

# On Transient Electric Field and Ionisation Phenomena

In Gas and at Dielectric Interfaces Under Impulsive Energisation

Timothy Wong

A thesis presented for the degree of Doctor of Philosophy  
Department of Electronic and Electrical Engineering  
University of Strathclyde  
2024

On Transient Electric Field and Ionisation Phenomena in Gas and at  
Dielectric Interfaces Under Impulsive Energisation

---

Timothy Wong, MEng, AFHEA

*thesis presented for the degree of*

Doctor of Philosophy  
in Electronic and Electrical Engineering

High Voltage Technologies (HVT) Research Group  
Department of Electronic and Electrical Engineering  
University of Strathclyde, Glasgow, U.K.

*under the supervision of*

Dr Igor Timoshkin  
Prof. Scott MacGregor

*Cover art created using the multilayered model of Chapter 3.*

*Word count: 97,209.*

This thesis is the result of the author's original research. It has been composed by the author and has not been previously submitted for examination which has led to the award of a degree.

The copyright of this thesis belongs to the author under the terms of the United Kingdom Copyright Acts as qualified by University of Strathclyde Regulation 3.50. Due acknowledgement must always be made of the use of any material contained in, or derived from, this thesis.

In reference to IEEE copyrighted material which is used with permission in this thesis, the IEEE does not endorse any of University of Strathclyde's products or services. Internal or personal use of this material is permitted. If interested in reprinting/republishing IEEE copyrighted material for advertising or promotional purposes or for creating new collective works for resale or redistribution, please go to [http://www.ieee.org/publications\\_standards/publications/rights/rights\\_link.html](http://www.ieee.org/publications_standards/publications/rights/rights_link.html) to learn how to obtain a License from RightsLink.

The author hereby declares that all references to the author's previously published works, are to those works for which the author is the principal author. The extent of the author's contribution to these works is significant, including the conception of the research methodology, conducting of the research study, analysis of research results, and the synthesis of the first draft of the published work in its entirety.

Signed: Timothy Wong

Date: September 13, 2024

A handwritten signature in black ink that reads "Timothy Wong". The signature is written in a cursive, flowing style.

---

## Acknowledgements

---

Above all else, I would like to express my sincerest gratitude to Igor Timoshkin. To refer to you merely as a “supervisor” would be an insult to the role you played as a teacher, mentor, advisor and—most importantly—friend, over the course of both my undergraduate and postgraduate studies. If one day I could impart even a fraction of your wisdom, patience, and kindness to my own students, my career will have undoubtedly been a successful one. Let this work represent the culmination of your teachings over the past decade—it is as much yours as it is mine. Similarly, I would also like to express my deepest appreciation to Scott MacGregor, for providing me with the many opportunities for summer internships and for doctoral study; your unwavering support has made this work possible. The pulsed power group you have both collectively built is a truly special place that I had the fortune to be a part of—a rarity and oasis in the often hostile desert of academia.

I extend my appreciation to my fellow colleagues and co-authors: Mark Wilson, Martin Given, and Michelle Maclean. The success of this work is, in part, thanks to your invaluable feedback and advice that has greatly enhanced my abilities as a researcher and a writer. Let this work mark only the beginning of many future collaborations. To the HVT workshop technicians Andy, Sean, Louis, and Scott, whose expertise made parts of this work possible; and to Maureen—whose absence I’m sure would result in the HVT grinding to a halt!

I also take this opportunity to thank my friends and colleagues in the pulsed power and wider HVT research group for the many insightful and interesting discussions. This extends to all the brilliant people I have met through conferences and summer schools, to whom I wish the greatest of successes in whatever your future may hold.

Words cannot describe the heartfelt gratitude I would like to express to my family, particularly to my partner Jennifer. We embarked on our PhD journey together in what we knew would be a challenging time. Yet only through your care, compassion, and emotional support have I been able to produce the best version of my work. Finally, I thank my mum, dad, and sister, who have always been supportive of my scientific endeavours. Without your care and support (and food), this work would not have been possible.

*“How do you write like you’re running out of time?,  
Write day and night like you’re running out of time?”*

— Aaron Burr

in *Hamilton* by Lin-Manuel Miranda

*“For once in your life take a stand with pride,  
I don’t understand how you stand to the side!”*

— Alexander Hamilton  
in *Hamilton* by Lin-Manuel Miranda

---

## Abstract

---

Ever since the first creation of pulsed energy sources during the mid-to-late 20<sup>th</sup> century, the principles of pulsed power have been successfully applied to a multitude of applications. The realisation of pulsed power spans multiple scales and across multiple domains: from state-of-the-art facilities for high-energy-density research, aimed at probing the fundamental constituents of matter; to innovative techniques for tumour treatment and drug delivery through plasma medicine; or for the improvement of crop yields in plasma-assisted agriculture. From the extent of its impact alone, pulsed power technology should be considered nothing short of a technological marvel. However, ever-increasing requirements have introduced unprecedented levels of transient electrical stress on insulating system components. Progress in both fundamental and applied principles of dielectric and breakdown phenomena under fast-rising impulse action is, therefore, instrumental to ensure the continued success of pulsed power science and technology.

The present work addresses several poorly-understood aspects of impulsive breakdown phenomena in gas and within composite solid-solid and solid-gas insulator topologies. The application of a diverse set of methodologies has progressed towards a greater understanding of impulsive breakdown processes across its various stages: from the initial development of transient electric fields in composite materials, to complete impulsive flashover. Key issues addressed from extensive modelling work pertain to the time-dependency of electric field and ionisation processes, which focused on their effects on the overall breakdown evolution and on the properties of generated plasmas. Novel analytical descriptions of transient field behaviour, avalanche development, and streamer propagation—under impulse and overstressed conditions—have lent insight into: the coupling between dielectric relaxation and impulse waveshape in composite materials; provided new scaling relationships relating to streamer breakdown modes; and have introduced closed-form expressions for estimating overstressed breakdown strength and time. The experimental characterisation of impulsive flashover behaviour across five polymeric materials: PVC, Delrin, Ultem, Torlon, and Perspex, in solid-solid arrangements, has provided critical knowledge relating to the role of sharp surface features on the reduction of interfacial breakdown strength. Impulsive flashover tests across solid-gas configurations indicated that short-wavelength surface features provide a greater contribution to the enhancement of the flashover strength compared to long-wavelength undulations. Altogether, results and conclusions of this work have provided a solid foundation on which composite insulating technology for pulsed applications can be built.

---

## List of Research Contributions and Outputs

---

Listed below are research contributions in the form of peer-reviewed journal articles, conference proceedings, conference presentations, and awards associated with the present work.

### Journal Publications

1. **T. Wong**, I. Timoshkin, S. MacGregor, M. Wilson, and M. Given, “An Avalanche-to-Streamer Transition Criterion for Overstressed Breakdown on a Rising Slope,” *IEEE Trans. Plasma Sci.*, early access, doi: 10.1109/TPS.2024.3446243, Aug. 2024.
2. **T. Wong**, I. Timoshkin, S. MacGregor, M. Wilson, and M. Given, “The Breakdown and Surface Characteristics of Polymer Interfaces Under HV Impulses,” *IEEE Trans. Dielectr. Electr. Insul.*, early access, doi: 10.1109/TDEI.2024.3407728, May 2024.
3. **T. Wong**, I. Timoshkin, S. MacGregor, M. Wilson, M. Given, and M. Maclean, “A Many-shells Model for Cell Transmembrane Potentials for Pulsed Electric Field Applications,” accepted in *IEEE Trans. Plasma Sci.*, vol. 52, no. 5, pp. 1775–1786, May 2024.
4. **T. Wong**, I. Timoshkin, S. MacGregor, M. Wilson, and M. Given, “A computational study on the effects of fast-rising voltage on ionization fronts initiated in sub-mm air and CO<sub>2</sub> gaps,” *Sci. Rep.*, vol. 14, no. 1185, Jan. 2024.
5. **T. Wong**, I. Timoshkin, S. MacGregor, M. Wilson, and M. Given, “Dielectric Interfaces in High-Voltage Technology: Overview and Theoretical Approaches to the Modeling of Functional and Breakdown Behavior,” *IEEE Electr. Insul. Mag.*, vol. 39, no. 4, pp. 34–49, Aug. 2023.
6. **T. Wong**, I. Timoshkin, S. MacGregor, M. Wilson, and M. Given, “The Design of a Python Library for the Automatic Definition and Simulation of Transient Ionization Fronts,” *IEEE Access*, vol. 11, pp. 26577–26592, Mar. 2023.
7. **T. Wong**, I. Timoshkin, S. MacGregor, M. Wilson, and M. Given, “Modeling of the Transient Electric Field in Multilayer Dielectric Composites Under Impulsive HV Energization,” *IEEE Trans. Dielectr. Electr. Insul.*, vol. 30, no. 1, pp. 220–229, Feb. 2023.
8. **T. Wong**, I. Timoshkin, S. MacGregor, M. Wilson, and M. Given, “Modeling of the Transient Electric Field in Multilayer Dielectric Composites Under Impulsive HV

- Energization,” *IEEE Trans. Dielectr. Electr. Insul.*, vol. 30, no. 1, pp. 220–229, Feb. 2023.
9. **T. Wong**, I. Timoshkin, S. MacGregor, M. Wilson, and M. Given, “Characteristics of Impulse-driven Surface Flashover across Polymers with Different Surface Conditions,” in preparation for submission to *IEEE Trans. Dielectr. Electr. Insul.*

## Conference Publications

9. **T. Wong**, I. Timoshkin, S. MacGregor, M. Wilson, and M. Given, “Electrostatic Modelling of Gas-Filled Voids and Conductive Particles in Highly Non-uniform Electric Fields,” in *23rd Int. Symp. High Volt. Engr. (ISH)*, Glasgow, UK, Aug. 2023. (presented as oral presentation).
10. **T. Wong**, I. Timoshkin, S. MacGregor, M. Wilson, and M. Given, “Modelling of Transient Discharges Along a Sub-mm Air-Solid Dielectric Interfaces Under Fast-rising Ramp Voltages,” in *24th IEEE Int. Pulsed Power Conf. (PPC)*, San Antonio, TX, USA, Jun. 2023. (presented as oral presentation).
11. **T. Wong**, I. Timoshkin, S. MacGregor, M. Wilson, and M. Given, “Modelling The Impulsive Breakdown Characteristics of Sub-mm to mm Spheroidal Voids,” in *24th IEEE Int. Pulsed Power Conf. (PPC)*, San Antonio, TX, USA, Jun. 2023. (presented as oral presentation - and **awarded the IEEE NPSS Outstanding Student Paper Award**).
12. **T. Wong**, I. Timoshkin, S. MacGregor, M. Wilson, and M. Given, “A Python-based Adaptive Mesh Solver for Drift-Diffusion Modelling of Streamer Discharges,” in *23rd IEEE Int. Pulsed Power Conf. (PPC)*, Denver, CO, USA, Dec. 2021. (presented as poster presentation).
13. **T. Wong**, I. Timoshkin, S. MacGregor, M. Wilson, and M. Given, “Simulation of Streamer Discharges Across Solid Dielectric Surfaces Using the Open-source FEniCS Platform,” in *23rd IEEE Int. Pulsed Power Conf. (PPC)*, Denver, CO, USA, Dec. 2021. (presented as oral presentation).
14. **T. Wong**, I. Timoshkin, S. MacGregor, M. Wilson, and M. Given, “Electric Field Inside a Gas Cavity Formed at a Solid-Solid Dielectric Interface Stressed with HV Impulses,” in *8th Euro-Asian Pulsed Power Conf. (EAPPC)*, Biarritz, France, Sep. 2021. (presented as poster presentation and virtual oral presentation).

## Other Conference Presentations

14. **T. Wong**, I. Timoshkin, S. MacGregor, M. Wilson, and M. Given, “Simulation of nonthermal plasma discharges in air and CO<sub>2</sub> in sub-millimeter needle-plane gaps under fast-rising voltages,” in *75th Ann. Gaseous Electron. Conf. (GEC)*, Sendai, Japan, Oct. 2022. (as virtual oral presentation).
15. **T. Wong**, I. Timoshkin, S. MacGregor, M. Wilson, and M. Given, “Field Distribution in Layered Composite Insulation Under Fast-rising Impulsive HV Stress,” in *14th Univ. High Voltage Network Colloquium (UHVnet)*, Cardiff, UK, May 2022. (as oral presentation and **awarded the IEEE DEIS Best Presentation Award**).
16. **T. Wong**, I. Timoshkin, S. MacGregor, M. Wilson, and M. Given, “Modelling of Streamer Discharges in Air-filled Sub-millimeter needle-plane electrode gaps under fast-rising field conditions,” in *14th Univ. High Voltage Network Colloquium (UHVnet)*, Cardiff, UK, May 2022. (as poster presentation).

## Associated Awards

- Engineering and Physical Sciences Research Council (EPSRC) Doctoral Prize Fellowship 2024.
- IEEE Nuclear and Plasma Sciences Society (NPSS) Graduate Scholarship Award 2024.
- IEEE Nuclear and Plasma Sciences Society (NPSS) Outstanding Student Paper Award (at the 24th IEEE International Pulsed Power Conference, 2023).
- IEEE Dielectrics and Electrical Insulation Society (DEIS) Best Presentation Award (at the 14th Universities High Voltage Network Colloquium, 2022).

---

# Contents

---

<b>Declaration</b>	<b>i</b>
<b>Acknowledgements</b>	<b>ii</b>
<b>Abstract</b>	<b>v</b>
<b>List of Research Contributions and Outputs</b>	<b>vi</b>
<b>List of Acronyms and Symbols</b>	<b>xv</b>
<b>List of Tables</b>	<b>xxiii</b>
<b>List of Figures</b>	<b>xxv</b>
<b>1 Dielectric and Breakdown Phenomena as a Foundation of High Voltage and Pulsed Power Technology: An Introduction</b>	<b>1</b>
1.1 Scope and Objectives . . . . .	4
1.2 Novelty of Contributions . . . . .	6
1.3 Organisation and Structure . . . . .	7
Chapter 1 References . . . . .	12
<b>2 Preliminaries and State of the Art</b>	<b>15</b>
2.1 Pulsed Power and The Origin of Impulses . . . . .	16
2.1.1 Pulse Generation Through Capacitive Storage and Release . . . . .	17
2.1.2 Pulse Forming Using Transmission Lines . . . . .	19
2.2 Dielectric Phenomena and Interfacial Behaviour . . . . .	21
2.2.1 Dielectric Polarisation and Relaxation . . . . .	22
2.2.2 Charge Sources, Sinks, and Transport at Solid-Gas Interfaces . . . . .	24
2.3 Pre-breakdown and Breakdown Processes in Gas . . . . .	30
2.3.1 The Initial Electron . . . . .	31
2.3.2 Gas Kinetics and Collisions . . . . .	32
2.3.3 The Electron Avalanche . . . . .	34
2.3.4 Fast Transient Ionisation Fronts and Streamer Discharges . . . . .	36
2.3.5 From Streamer to Spark . . . . .	41
2.3.6 The Role of Gas Chemistry . . . . .	42
2.3.7 Gas Breakdown Scaling Relations . . . . .	44
2.4 Interfacial Breakdown . . . . .	46
2.4.1 Solid-Gas Surface Flashover and Surface Morphology . . . . .	47

2.4.2	Gas Cavity Driven Solid-Solid Interfacial Breakdown . . . . .	52
2.5	The Problem of Fast Transients and Overvoltages . . . . .	57
2.5.1	On Time-dependency . . . . .	57
2.5.2	Pulsed Breakdown Scaling . . . . .	59
	Chapter 2 References . . . . .	61
<b>3</b>	<b>On the Impulsive Electric Field Responses of Multilayered Composite Systems</b>	<b>73</b>
3.1	Introduction and Motivation . . . . .	74
3.2	A General View on Multilayered Geometries . . . . .	76
3.2.1	A Boundary Value Problem in Arbitrary Orthogonal Geometries . . . . .	77
3.2.2	Solution by Means of the Laplace Transform . . . . .	80
3.3	Multilayered Field Graders for Pulsed Power Applications . . . . .	84
3.3.1	Particular Solutions for One-dimensional Planar Geometries . . . . .	85
3.3.2	Grading Characteristics of Multilayered FGMs Under Fast-rising Impulses	88
3.3.3	Functionally Graded Spacers for Gas-Insulated Lines . . . . .	96
3.4	Multilayered Models of Dielectric Inclusions . . . . .	100
3.4.1	Particular Solutions for Prolate-Spheroidal Geometries . . . . .	101
3.4.2	Limiting Behaviours: Field Enhancement of Particles and Voids . . . . .	107
3.4.3	Further Validation: Microbiological Cell Transmembrane Potentials . . . . .	110
3.5	Chapter Conclusions, Contributions, and Outlook . . . . .	112
3.5.1	Academic Significance and Contributions . . . . .	113
3.5.2	Industrial Relevance . . . . .	114
3.5.3	Limitations and Future Outlook . . . . .	115
	Chapter 3 References . . . . .	118
<b>4</b>	<b>An Avalanche-to-Streamer Transition Criterion for Overstressed Breakdown on a Rising Slope</b>	<b>123</b>
4.1	Introduction and Motivation . . . . .	124
4.2	Overview of the Meek-Raether Criterion . . . . .	126
4.3	Transport of a Gaussian Electron Cloud and Streamer Transition . . . . .	127
4.3.1	The Diffusion Process . . . . .	128
4.3.2	Ionisation and Attachment . . . . .	129
4.3.3	Field-based Avalanche-to-Streamer Transition . . . . .	130
4.3.4	Nature of the Initial Electron Cloud . . . . .	131
4.4	Analytical Approximation for Ramp Electric Fields . . . . .	134
4.4.1	Electron Growth Rates and Ionisation Integral, $K$ . . . . .	136
4.4.2	The Importance of Diffusion for Impulsive Breakdown . . . . .	139

4.5	Closed-form Solutions and the Effect of Rate-of-Rise, $\mathcal{D}$ . . . . .	141
4.5.1	The Nature of Parameter $g$ . . . . .	145
4.6	Model Validation and Experimental Comparisons . . . . .	146
4.6.1	Pulsed Paschen Curves . . . . .	147
4.6.2	Field-Time Scaling Characteristics . . . . .	149
4.7	Chapter Conclusions, Contributions, and Outlook . . . . .	150
4.7.1	Academic Significance and Contributions . . . . .	152
4.7.2	Industrial Relevance . . . . .	153
4.7.3	Limitations and Future Outlook . . . . .	153
	Chapter 4 References . . . . .	156
<b>5</b>	<b>Development of a Python Library for the Modelling of Transient Ionisation</b>	
	<b>Fronts in Gas and Solid-Gas Topologies</b>	<b>159</b>
5.1	Introduction and Motivation . . . . .	160
5.2	Review of Low-Temperature Gas Discharge Modelling . . . . .	162
5.2.1	Modelling Strategies . . . . .	163
5.2.2	Selection and Bounds of Model Validity . . . . .	170
5.2.3	Notable Works on Non-thermal Gas Discharge Modelling . . . . .	171
5.3	Method and Platform . . . . .	174
5.3.1	The Finite Element Method . . . . .	175
5.3.2	The FEniCS Project . . . . .	176
5.4	Extended Hydrodynamic Model . . . . .	178
5.4.1	Advection-Diffusion-Reaction-Poisson Equation . . . . .	178
5.4.2	Source Terms and Plasma Chemistry . . . . .	179
5.4.3	Photoionisation . . . . .	180
5.4.4	The Local Field and Local Mean Energy Approximations . . . . .	182
5.4.5	Boundary Conditions . . . . .	184
5.5	Weak Formulation . . . . .	186
5.6	Adaptive Mesh Refinement and Time Stepping . . . . .	189
5.6.1	Adaptive Mesh Refinement . . . . .	190
5.6.2	Time Integration and Adaptive Time Stepping . . . . .	193
5.6.3	Miscellaneous Settings . . . . .	195
5.7	StrAFE Implementation and Syntax . . . . .	198
5.7.1	Automation of Problem Configuration and Definition . . . . .	199
5.7.2	Automation of Form Generation and System Assembly . . . . .	202
5.7.3	Main Solver Loop . . . . .	203

5.8	Code Verification and Comparison Studies . . . . .	204
5.8.1	Axisymmetric Positive Streamer . . . . .	205
5.8.2	Positive Streamer Attachment to Solid Dielectric . . . . .	209
5.8.3	Double-headed Streamers . . . . .	218
5.8.4	Counter-propagating Streamers Initiated From Needle-Needle Electrodes . . . . .	221
5.9	Chapter Conclusions, Contributions, and Outlook . . . . .	225
5.9.1	Academic Significance and Contributions . . . . .	226
5.9.2	Industrial Relevance . . . . .	227
5.9.3	Limitations and Future Outlook . . . . .	228
	Chapter 5 References . . . . .	231
<b>6</b>	<b>Characteristics of Overstressed Transient Ionisation Fronts and Streamers in Gas and Across Solid Interfaces</b> . . . . .	<b>239</b>
6.1	Introduction and Motivation . . . . .	240
6.2	A First Look at Streamer Development on a Rising Slope . . . . .	243
6.2.1	Computational Domain and Configuration . . . . .	243
6.2.2	Effects of Rate-of-Rise on Positive Streamer Development . . . . .	244
6.2.3	Effects of Rate-of-Rise on Negative Streamer Inception . . . . .	249
6.3	Overstressed Discharges in Sub-mm Air and CO <sub>2</sub> Gaps . . . . .	252
6.3.1	Computational Domain and Configuration . . . . .	253
6.3.2	Ionisation Front Morphology, Inception, and Propagation . . . . .	256
6.3.3	Effects of $dU/dt$ on Velocity and Electric Field . . . . .	262
6.3.4	Developed Electron Density and Plasma Composition . . . . .	266
6.3.5	Characteristics of the Cathode Sheath . . . . .	268
6.4	Overstressed Surface Streamers Along a Sub-mm Dielectric Surface . . . . .	275
6.4.1	Sub-mm Surface Discharge Morphology and Characteristics . . . . .	276
6.4.2	Electric Field and Separation of Discharge Phases . . . . .	281
6.4.3	Deposition of Surface Charge . . . . .	285
6.5	Influence of Non-uniform Surface Charge on Surface Streamer Development . . . . .	290
6.5.1	Computational Domain and Configuration . . . . .	291
6.5.2	Gaussian Distributed Homo- and Hetero-charge . . . . .	292
6.6	Chapter Conclusions, Contributions, and Outlook . . . . .	299
6.6.1	Academic Significance and Contributions . . . . .	300
6.6.2	Industrial Relevance . . . . .	303
6.6.3	Limitations and Future Outlook . . . . .	304
	Chapter 6 References . . . . .	307

<b>7</b>	<b>Impulsive Breakdown and Surface Roughness Characteristics of Solid-Solid Polymer Interfaces</b>	<b>313</b>
7.1	Introduction and Motivation . . . . .	314
7.2	A Theoretical Model for the Impulsive Breakdown of Solid-Solid Interfaces . . . . .	316
7.2.1	Hertzian Contact and the Equivalent Surface Approximation . . . . .	318
7.2.2	Transient Electric Field and Breakdown of Interfacial Voids . . . . .	322
7.2.3	On Intra-void Field Non-uniformity and the Uniform Approximation . . . . .	327
7.2.4	Breakdown of Contact Spots . . . . .	334
7.2.5	Model Predictions and Estimations . . . . .	337
7.3	Experimental Methodology . . . . .	343
7.3.1	Test Chamber and Circuit . . . . .	343
7.3.2	Surface Roughness Characterisation using Motifs . . . . .	346
7.3.3	Experimental Procedure . . . . .	352
7.3.4	Breakdown Data Processing and Statistical Treatment . . . . .	353
7.4	Impulsive Breakdown Results and Discussion . . . . .	355
7.4.1	Impulse Breakdown Strength and Material Choice . . . . .	355
7.4.2	Post-breakdown Surface Analysis . . . . .	359
7.4.3	Effects of Voltage Polarity . . . . .	360
7.4.4	Effects of $dU/dt$ . . . . .	361
7.4.5	Relationship with Surface Roughness Characteristics . . . . .	362
7.5	Comparison with Modelling Results . . . . .	365
7.5.1	Comparison of Theoretical and Practical Interfacial Breakdown Strengths . . . . .	366
7.6	Chapter Conclusions, Contributions, and Outlook . . . . .	368
7.6.1	Academic Significance and Contributions . . . . .	369
7.6.2	Industrial Relevance . . . . .	370
7.6.3	Limitations and Future Outlook . . . . .	371
	Chapter 7 References . . . . .	374
<b>8</b>	<b>Effects of Surface Condition on the Impulsive Flashover of Polymer-Gas Interfaces</b>	<b>379</b>
8.1	Introduction and Motivation . . . . .	380
8.2	Experimental Methodology . . . . .	381
8.2.1	Solid-Gas Test Cell and Circuit . . . . .	381
8.2.2	Sample Preparation and Roughness Characterisation . . . . .	384
8.2.3	Experimental Procedure . . . . .	386
8.2.4	Data Processing and Statistics . . . . .	387

- 8.3 Roughness and Waviness of “As received” and “Machined” Surfaces . . . . . 388
- 8.4 Surface Flashover Results . . . . . 393
  - 8.4.1 Comparison of Breakdown Voltages and Times . . . . . 393
  - 8.4.2 Effect of Surface Characteristics . . . . . 397
- 8.5 Chapter Conclusions, Contributions, and Outlook . . . . . 405
  - 8.5.1 Academic Significance and Contributions . . . . . 405
  - 8.5.2 Industrial Relevance . . . . . 407
  - 8.5.3 Limitations and Future Outlook . . . . . 407
- Chapter 8 References . . . . . 410
  
- 9 Concluding Remarks, Contributions, and Perspectives . . . . . 411**
  
- Appendix . . . . . i**
  - A Mathematical Derivations . . . . . i
  - B Additional and Supporting Material . . . . . xxii
  - C Miscellaneous Points of General Interest . . . . . xxxiii

---

## List of Acronyms and Symbols

---

### Acronyms

BOLSIG+	Electron Boltzmann equation solver		
DOLFIN	Dynamic Object-oriented Library for Finite Element Computation		
FEniCS	Finite Element Computational Software		
GMRES	Generalised Minimum Residual Method		
ICCD	Intensified Charge-Coupled Device		
ParMETIS	Parallel Graph Partitioning and Fill-reducing Matrix Ordering		
PETSc	Portable, Extensible Toolkit for Scientific Computing		
PT-SCOTCH	Parallel-Threaded library for Static Mapping and Matrix Reordering		
StrAFE	Streamers on Adaptive Finite Elements		
SUPG	Streamline Upward Petrov-Galerkin Method		
uBLAS	Boost Basic Linear Algebra System		
AC	Alternating Current	KDE	Kernel Density Estimate
ADR	Advection-Diffusion-Reaction	LFA	Local Field Approximation
AMG	Algebraic Multigrid	LI	Lightning Impulse
AMR	Adaptive Mesh Refinement	LMEA	Local Mean Energy Approximation
ATS	Adaptive Time Stepping	LTD	Linear Transformer Driver
BVP	Boundary Value Problem	MCC	Monte-Carlo Collisions
CST	Simulia CST Studio Suite	MEMS	Micro-electromechanical System
DC	Direct Current	MPI	Message-Passing Interface
DG	Discontinuous Galerkin	MW	Maxwell-Wagner
EDF	Energy Distribution Function	OpenMP	Open Multi-processing
EEDF	Electron EDF	PEEK	Polyether Ether Ketone
EPDM	Ethylene Propylene Diene Monomer	PEF	Pulsed Electric Field
EPR	Ethylene Propylene Rubber	PFL	Pulse Forming Line
ESP	Electrostatic Precipitation	PIC	Particle-in-Cell
FEM	Finite Element Method	PP	Polypropylene
FFC	FEniCS Form Compiler	PTFE	Polytetrafluoroethylene
FGM	Functionally Graded Material	PVC	Polyvinylchloride
FIAT	Finite Element Auto. Tabulator	SiR	Silicone Rubber
GIL	Gas-Insulated Line	STP	Standard Temperature and Pressure
GND	Ground	TMP	Transmembrane Potential
HDPE	High Density Polyethylene	UFC	Unified Form Assembly Code
HPC	High Performance Computing	UFL	Unified Form Language
HV	High Voltage	UV	Ultraviolet
HVDC	High Voltage Direct Current	XLPE	Cross-linked Polyethylene

SI units are used as standard throughout this work, unless otherwise stated. The nature of this work necessitates substantial usage of symbols and operators. To maintain consistency with the established and recognised symbols of known quantities, some symbols have different meanings within different chapters. Repeated symbols are indicated using superscripts (corresponding to the chapter) prepended to the descriptions. Variations of symbols, if similar enough, are also separated. Lists are organised in alphabetical order.

<b>Conventions</b>		<b>Units</b>
$\mathbf{A}$	Matrix	–
$\mathbf{A}^T, \vec{a}^T$	Matrix or vector transpose	–
$a$	Scalar variable or field	–
$\vec{a}$	Vector variable or field	–
$\hat{a}$	Unit vector	–
$ \vec{a} , a$	$L^2$ -norm (magnitude) of vector $\vec{a}$	–
$i, j, k$	Typical symbols for indexing sets, vectors, or matrix elements	–
$\ell, m$	Typical placeholder indices used in, e.g., summation ( $\Sigma$ ) or $\Pi$ -notation	–
	<sup>2</sup> $\ell$ : length along a transmission line	m
	<sup>3,7</sup> $\ell$ : Legendre function of order $\ell$	–
$n$	Typical symbol to indicate an arbitrary total quantity	1
<b>Additional Function Definitions</b>		<b>Units</b>
$\text{card}(\cdot)$	Cardinality (total number of elements) of a set	–
$\text{cov}(\cdot, \cdot)$	Statistical covariance of the function arguments	–
$\text{cosh}(\cdot)$	Hyperbolic cosine function	–
$\text{coth}(\cdot)$	Hyperbolic cotangent function, $\text{cosh}(\cdot)/\text{sinh}(\cdot)$	–
$\text{csch}(\cdot)$	Hyperbolic cosecant function, $1/\text{sinh}(\cdot)$	–
$\text{erf}(\cdot)$	Error function	–
$\text{erfc}(\cdot)$	Complementary error function, $1 - \text{erf}(\cdot)$	–
$\text{sinh}(\cdot)$	Hyperbolic sine function	–
$\text{sgn}(\cdot)$	Sign function, extracts the sign of the argument (+1, -1, or 0)	–
$\text{sech}(\cdot)$	Hyperbolic secant function, $1/\text{cosh}(\cdot)$	–
<b>Coordinate Systems</b>		<b>Units</b>
$(x, y, z)$	Cartesian coordinate system	–
$(r, \theta)$	Polar coordinate system	–
$(r, \theta, z)$	Cylindrical coordinate system	–
$(r, \theta, \phi)$	Spherical coordinate system	–
$(\mu, \nu, \theta)$	Prolate-spheroidal coordinate system	–
$(\psi, \zeta, \theta)$	Bi-spherical coordinate system	–
<b>Physical Constants</b>		<b>Units</b>
$c$	Speed of light in a vacuum	299 792 458 m/s
$\epsilon_0$	Permittivity of free space	$8.854\,187 \times 10^{-12}$ F/m
$h$	Planck's Constant	$6.626\,070 \times 10^{-34}$ J/s
$k_b$	Boltzmann Constant	$1.380\,649 \times 10^{-23}$ J/K
$\mu_0$	Permeability of free space	$1.256\,637 \times 10^{-6}$ H/m

$q_e$	Elementary Charge	$1.602\,176 \times 10^{-19} \text{ C}$
<b>Latin Symbols</b>		
$A_a$	Apparent contact area (contact mechanics)	$\text{m}^2$
$A, B$	Limit values for motif algorithm	$\text{m}$
	<sup>2</sup> $A, B$ : Arbitrary constants (Paschen's Law)	$\text{Pa m}, \text{V Pa}^{-1} \text{m}^{-1}$
	<sup>4</sup> $A_D, B_D$ : Fitting coefficients relating to electron diffusion	arb.
	<sup>3</sup> $A_i, B_i, \dots$ : Arbitrary time-dependent constants	arb.
	<sup>5</sup> $A_j, \lambda_j$ : Photoionisation model fitting coefficients	$\text{m}^{-1} \text{Pa}^{-2}, \text{m}^{-1} \text{Pa}^{-1}$
$AR_i$	Width of the $i$ -th motif	$\text{m}$
$AR^{[s]}, AW^{[s]}$	Mean roughness and waviness motif widths for surface $s$	$\text{m}$
$A_r$	Real area of contact (contact mechanics)	$\text{m}^2$
$\bar{A}_{\text{void}}$	Average interfacial void area	$\text{m}^2$
$A_\alpha, B_\alpha, C_\alpha$	Fitting coefficients relating to ionisation and attachment	arb.
$A_\mu, B_\mu$	Fitting coefficients relating to electron mobility	arb.
<b>A</b>	Generic FEM Matrix	–
$a$	Asperity aspect ratio	1
	<sup>7,8</sup> $a^{[\text{eq}]}$ : Asperity aspect ratio of the equivalent surface	1
	<sup>6</sup> $a, b$ : Lengths defining a hyperbola (needle electrode)	$\text{m}$
	<sup>3,7</sup> $a_\ell$ : $\ell$ -th order Fourier-Legendre series coefficient	arb.
	<sup>3,7</sup> $a_0$ : Focal distance in prolate spheroidal coordinates	$\text{m}$
$\vec{b}$	Right-hand vector in FEM matrix formulation	–
	<sup>3</sup> $\vec{b}$ : Known vector for $n$ -layer spheroid derivation	$\text{V/m}$
$\vec{B}$	Magnetic flux density vector	$\text{Wb}$
$C$	Capacitance	$\text{F}$
	<sup>2</sup> $C_0, C_L, C_M$ Marx stage, load, and erected capacitance	$\text{F}$
	<sup>4</sup> $C(t), C_0$ : Exponential coefficients in analytical electron cloud solution	$\text{V/m}$
$\mathcal{C}$	Set of cells in a computational mesh	–
$c_0, \dots, c_{n-1}$	Polynomial coefficients for $P_n$	1
$D_i$	Diffusion coefficient for charged species $i$	$\text{m}^2/\text{s}$
$\vec{D}_i$	Electric displacement field in layer $i$	$\text{C/m}^2$
$\mathcal{D}$	Rate of electric field rise	$\text{V m}^{-1} \text{s}^{-1}$
$d$	Measure of distance or length	$\text{m}$
	<sup>7</sup> $d_{\text{crit}}$ : Critical distance for polarity breakdown to be equal	$\text{m}$
	<sup>6</sup> $d_{\text{crit}}$ : Critical distance (for streamer propagation)	$\text{m}$
	<sup>7</sup> $d_s$ : Sample thickness (solid-solid interfaces)	$\text{m}$
	<sup>2,6</sup> $d_{st}$ : Streamer diameter	$\text{m}$
	<sup>7</sup> $\bar{d}_{\text{void}}$ : Average interfacial void length (square projection)	$\text{m}$
	<sup>7</sup> $\bar{d}_{\text{void}}^{\text{ellip}}$ : Average interfacial void length (elliptical projection)	$\text{m}$
$dU/dt$	Rate of voltage rise	$\text{V/s}$
$E$	Electric Field Strength	$\text{V/m}$
	$E_0$ : External (applied) field magnitude	$\text{V/m}$
	$E_b$ : Breakdown field strength	$\text{V/m}$
	<sup>7</sup> $E_{br}$ : Nominal 63.2% breakdown field strength	$\text{V/m}$
	<sup>4</sup> $E_{e,\text{max}}$ : Max. electron field magnitude	$\text{V/m}$
	<sup>3</sup> $E_i(t)_{DE}$ : Double exponential response of $n$ -layer planar composite	$\text{V/m}$
	<sup>2</sup> $E_m$ : Mean electric field (J. C. Martin)	$\text{kV/cm}$

	<sup>4</sup> $E_{net}$ : Net electric field strength	V/m
	<sup>2</sup> $E_{meek}$ : Electric field at avalanche head estimated by Meek	V/m
	<sup>3</sup> $E_{TJ}$ : Triple junction electric field magnitude	V/m
$\vec{E}$	Electric field vector	V/m
	<sup>3</sup> $\vec{E}_i$ : Electric field in layer $i$	V/m
	<sup>2</sup> $\vec{E}_g, \vec{E}_s$ : Electric field in gas/solid domain	V/m
	<sup>2</sup> $\vec{E}_\zeta$ : Surface charge induced electric field vector	V/m
$e_i$	Elliptical eccentricity	1
$F_a$	Apparent force (contact mechanics)	N
$F_\ell^\mu, G_\ell^\mu$	$\ell$ -th order functions for spheroid model under non-uniform fields	1
$F_i, G_i$	Functions associated with $n$ -layer spheroid under uniform fields	1
$F_r$	Real force (contact mechanics)	N
$\mathcal{F}$	Refinement function vector in AMR algorithm	–
	<sup>7</sup> $\mathcal{F}_\ell$ : Enhancement factor nonuniform geometries	1
$\vec{F}$	Force vector	N
$f$	Arbitrary function	–
	<sup>2,3</sup> $f$ : Field enhancement factor	1
	<sup>4</sup> $f \cdot E(t_b)$ : Arbitrary fraction of applied field at breakdown	V/m
	<sup>3</sup> $f_k$ : Arbitrary function used in expansion of separated potential	arb.
	<sup>2</sup> $f_{MB}$ : Maxwell-Boltzmann distribution	s/m
	<sup>7</sup> $f(p; \alpha, \beta)$ : Two-parameter Weibull distribution for variable $p$	arb.
	<sup>2</sup> $f(\vec{r}, \vec{v}, t)$ : 6-dimensional phase-space probability distribution	$s^3 m^{-6} kg^{-3}$
$G$	Mechanical toughness	J/m <sup>3</sup>
$\mathcal{G}$	Geometric function for spatial component of external potential	1
$g \cdot E(t_b)$	Arbitrary fraction of breakdown electric field	V/m
$H_i$	Single motif height	m
$HR_i$	Single motif $y$ -bounds	m
$H(t)$	Heaviside step function	1
$\vec{H}$	Magnetic field vector	A/m
$h_j$	Scale factor for coordinate $j$	arb.
	<sup>5</sup> $h_j$ : Reaction rate coefficient for reaction $j$	m <sup>3</sup> /s or m <sup>6</sup> /s
	<sup>3</sup> $h_n(t)$ : Impulse response of $n$ -layer system to Dirac delta, $\delta(t)$	–
	<sup>7</sup> $h_s$ : Motif profile standard height	m
$I$	Electric Current	A
	<sup>2</sup> $I_0, {}^8I_D$ : Townsend external current, Capacitive displacement current	A
$I(\cdot), f(\cdot)$	Functions associated with Zheleznyak's photoionisation model	m <sup>3</sup> /s, m <sup>-1</sup>
$\mathcal{I}(t), \mathcal{A}(t)$	Equivalent ionisation and attachment rate function for ramp fields	1
$J$	Current density magnitude	A/m <sup>2</sup>
	<sup>2</sup> $J_{FN}$ : Fowler-Nordheim emission current density magnitude	A/m <sup>2</sup>
	<sup>2</sup> $J_{Schottky}$ : Schottky emission current density magnitude	A/m <sup>2</sup>
	<sup>2</sup> $J_{thermionic}$ : Thermionic emission current density magnitude	A/m <sup>2</sup>
$\vec{J}$	Current density vector	A/m <sup>2</sup>
	<sup>2</sup> $\vec{J}_{emission}$ : Surface emission current density vector	A/m <sup>2</sup>
	<sup>2</sup> $\vec{J}_{se}$ : Secondary emission current density vector	A/m <sup>2</sup>
$K$	Ionisation integral	1
$K_0$	Distance-independent component of $K$	–
	<sup>3,7</sup> $K_i$ : Elliptical axis ratio (minor divided by major)	1

List of Acronyms and Symbols

---

	<sup>3</sup> $K_\ell$ : Arbitrary constants in partial fraction expansion	1
$K_{\text{ramp}}$	Equivalent $K$ value for ramp fields	1
$\mathcal{K}$	Refinement tolerances vector in AMR algorithm	–
$k_{1-4}$	Convenience parameters for electron cloud derivation	1
$L$	Characteristic length of a system	m
	<sup>2</sup> $L$ : Total length of transmission line	m
	<sup>6</sup> $L(t)$ : Streamer length	m
	<sup>5</sup> $L(u)$ : Arbitrary differential operator acting on function $u$	–
$\mathcal{L}$	Laplace transform operator	–
$\mathbb{L}$	Likelihood function	arb.
$\ell_m$	Mean free path	m
$\mathbf{M}$	Matrix for $n$ -layer spheroid derivation	1
$\mathcal{M}$	Representation of a computational mesh	–
	<sup>5</sup> $\mathcal{M}_b, \mathcal{M}_0, \mathcal{M}_j$ : Base, initial, and $j$ -th mesh in AMR algorithm	–
$m$	Mass	kg
$N$	Neutral gas density	$\text{m}^{-3}$
	<sup>7</sup> $N$ : Total number of surface asperities	1
$N_e, N_0$	Number of electrons, and initial number of electrons	1
$\mathcal{N}$	Number of nodes per finite element	1
	<sup>7</sup> $\mathcal{N}$ : Normal distribution	–
	<sup>7</sup> $\mathcal{N}_{\text{eq}}$ : Normal peak height distribution of equivalent surface	$\text{m}^{-1}$
$n_0$	Initial electron density	$\text{m}^{-3}$
	<sup>4</sup> $n_0(t_0)$ : Time-dependent peak Gaussian electron density	$\text{m}^{-3}$
$n_e$	Electron density	$\text{m}^{-3}$
$n_\epsilon$	Electron energy density	$\text{J}/\text{m}^3$
	<sup>5</sup> $n_i$ : Density of charged species $i$	$\text{m}^{-3}$
$P$	Power	W
$P_\ell(\cdot)$	Legendre polynomial of $\ell$ -th order	1
$p_i^{\text{linear}}, p_i^{\text{U}}$	Layered FGM grading profiles	1 or S/m
$P_n$	Characteristic polynomial for $n$ -layer system	1
$P(\cdot), R(\cdot), S(\cdot)$	Arbitrary functions used in solution for planar composite	$\text{S}^{n-1}\text{m}^{n-1}$
$p$	Pressure	Pa
	<sup>7</sup> $p_a$ : Apparent contact pressure	Pa
	<sup>5</sup> $p$ : Length of solution vector in StrAFE	1
	<sup>5</sup> $p_{O_2}, p_q$ : Partial pressure of $O_2$ in air, Quenching pressure	Pa
$p_s$	Significance value	1
$pd_{\text{min}}$	Paschen minimum	Pa m
$\vec{p}$	Momentum vector	kg m/s
$Q$	Arbitrary charge	C
$Q_\ell(\cdot)$	Legendre functions of the second kind of $\ell$ -th order	1
$q$	Electric charge	C
$q_i^j$	$j$ -th coordinate line along position $i$	arb.
$\vec{q}$	Generalised coordinate vector $\vec{q} = q^1, q^2, \dots, q^n$	arb.
$R$	Electrical Resistance	$\Omega$
	<sup>2</sup> $R_0$ : Charging resistance	$\Omega$
	<sup>2</sup> $R_f, R_t$ : Marx front and tail resistance	$\Omega$
$R_a$	Surface roughness (Zhao <i>et al.</i> )	m

List of Acronyms and Symbols

---

	<sup>7</sup> $R_i$ : Single motif mean height	m
	<sup>5,6</sup> $R_i$ : Set of reactions involving reactant $i$	–
$R^{[s]}, W^{[s]}$	Mean roughness and waviness motif heights for surface $s$	m
$\mathcal{R}(\cdot)$	Rank function	–
	<sup>5,6</sup> $\mathcal{R}_j$ : Set of all reactants involved in reaction $j$	–
$\mathbb{R}^3$	3-dimensional Real coordinate space	–
$r_c$	Hertzian elastic sphere contact radius	–
$r_w$	Weighted residual	1
$S$	Switch (circuit element)	–
$SAR^{[s]}, SAW^{[s]}$	RMS roughness and waviness motif widths for surface $s$	m
$S_i$	Source terms in ADR equations	$\text{m}^3/\text{s}$
	<sup>5</sup> $S_{\text{ion}, S_{\text{ph}}}$ : Ionisation source term, Photoelectron source term	$\text{m}^3/\text{s}$
$SR^{[s]}, SW^{[s]}$	RMS roughness and waviness motif heights for surface $s$	m
$\mathcal{S}$	Set of all charged species	–
$\mathbf{S}$	Representation of 3-dimensional sphere in $\mathbb{R}^3$	–
$s$	Complex frequency (Laplace) variable $i$	$\text{s}^{-1}$
$s_0$	Initial variance of a Gaussian distribution	m
$T_1, T_2, T_3$	Rise, duration, and fall times associated with trapezoidal pulse	s
$T$	Thermodynamic temperature	K
	<sup>5</sup> $T_i$ : Thermodynamic temperature of species $i$	K
	<sup>7</sup> $T_i$ : Single motif depth	m
	<sup>2</sup> $T_\ell$ : Electrical length of transmission line	s
$t$	Time	s
	$t_0$ : Initial time	s
	$t_0^+$ : Moment just after initial time	s
	<sup>7</sup> $t_{63.2}$ : 63.2% time-to-breakdown from Weibull analysis	s
	$t_{av}$ : Electron avalanche development time	s
	$t_b$ : Time-to-breakdown	s
	<sup>6</sup> $t_c, t_i$ : Ionisation wave time of contact and inception	s
	$t_p$ : Peak time	s
	$t_s$ : Statistical breakdown time delay	s
	$t_{st}$ : Streamer propagation time	s
	$t_{th}$ : Channel thermalisation time	s
	<sup>7</sup> $t_v$ : Void discharge time	s
$\mathcal{T}$	Triangulation of domain $\Omega$	–
$\mathbb{T}$	Adaptive timestepping tolerance	1
$U$	Voltage	V
	$U_0, U_L$ : Applied Voltage, Load Voltage	V
	<sup>5</sup> $U_i$ : Unknown coefficients in linear expansion of $u_h$	–
	<sup>5</sup> $\vec{U}$ : Unknown coefficient vector in FEM formulation	–
$\vec{u}$	Vector of arbitrary unknowns	arb.
	<sup>5</sup> $\vec{u}^H$ : Solution vector using coarse timestep in ATS algorithm	–
	<sup>5</sup> $\vec{u}^h$ : Solution vector using fine timestep in ATS algorithm	–
$V$	Arbitrary function space	–
	<sup>7</sup> $V_{63.2}$ : 63.2% breakdown voltage from Weibull analysis	V
	<sup>2,7</sup> $V_b$ : Breakdown voltage	V
$v$	Velocity magnitude	$\text{m}/\text{s}$

List of Acronyms and Symbols

---

	<sup>2</sup> $v_{av}$ : Avalanche propagation velocity	m/s
	<sup>2</sup> $v_\ell$ : Electromagnetic wave speed (transmission line)	m/s
	<sup>2,6</sup> $v_{st}$ : Streamer velocity	m/s
	<sup>5</sup> $v_{th,i}$ : Thermal velocity of species $i$	m/s
	<sup>5</sup> $v_{th,\varepsilon}$ : Thermal velocity of electron energy	m/s
$\vec{v}$	Velocity vector	m/s
	<sup>5,6</sup> $\vec{v}_d$ : Electron drift velocity	m/s
	<sup>5</sup> $\vec{v}, v_i$ : Vector and components of finite element test functions	–
$W$	Work/Energy	J
	<sup>4,6</sup> $W(\cdot)$ : Lambert– $W$ (product-log) function	–
$x_c$	Critical avalanche formation length from Meek	cm
$Y$	Elastic Modulus	Pa
$Y'$	Composite elastic modulus	Pa
$Z$	Electrical Impedance	$\Omega$
	<sup>2</sup> $Z_0, Z_L$ : Characteristic/Load impedance of transmission line	$\Omega$
	<sup>2,5</sup> $Z_j$ : Charge number of $j$ -th charged species	1
<b>Greek Symbols</b>		<b>Units</b>
$\alpha$	Ionisation coefficient	$\text{m}^{-1}$
	<sup>3</sup> $\alpha_k^i$ : Function coefficients for $k$ -th term in $i$ -th layer	arb.
$\bar{\alpha}$	Effective ionisation coefficient	$\text{m}^{-1}$
$\bar{\alpha}, \bar{\beta}$	Optimal scale and shape parameters from MLE Weibull fitting,	arb.
	<sup>2,3,7</sup> $\hat{\alpha}, \hat{\beta}$ : Double Exponential waveshaping parameters	$\text{s}^{-1}$
$\beta$	Asperity tip radius	m
$\beta^i$	Constant term for arbitrary potential in $i$ -th layer	V
$\beta_{i,j}$	Recombination coefficient between species $i$ and $j$	$\text{m}^3/\text{s}$
$\beta^{\text{eq}}$	Mean asperity radius for equivalent surface	m
$\Gamma(\cdot, \cdot)$	Incomplete gamma function	1
$\vec{\Gamma}_i$	Particle flux for species $i$	$\text{m}^{-2} \text{s}^{-1}$
	<sup>5</sup> $\vec{\Gamma}_\varepsilon$ : Electron energy flux	$\text{J m}^{-2} \text{s}^{-1}$
$\gamma$	Secondary emission coefficient	1
	<sup>2</sup> $\gamma$ : Representation of a single photon	–
$\gamma_1, \gamma_2$	Convenience parameters for closed-form electron cloud derivation	$\text{V m}^{-1} \text{s}^{-1}$
$\Delta E_j$	Electron energy change due to reaction $j$	J
$\Delta t$	Numerical timestep	s
$\Delta x_i$	Layer thickness for $i$ -th layer in prolate spheroidal coordinates	m
$\delta$	Hertzian contact deformation distance	m
	<sup>3</sup> $\delta(t)$ : Dirac delta function	–
	<sup>4</sup> $\vec{\delta}(t)$ : Displacement of electron cloud	m
$\varepsilon$	Absolute permittivity	F/m
$\varepsilon_r$	Relative permittivity	1
	<sup>3</sup> $\varepsilon_i$ : Relative permittivity of layer $i$	1
	<sup>7</sup> $\varepsilon_{g,l,b}$ : Relative permittivity of gas, intermediate layer, and bulk	1
$\bar{\varepsilon}$	Electron energy	eV
$\epsilon$	Estimation of truncation error	1
$\eta$	Attachment coefficient	$\text{m}^{-1}$
	<sup>7,8</sup> $\eta$ : Asperity density	$\text{m}^{-2}$

List of Acronyms and Symbols

---

	<sup>5</sup> $\eta_\ell$ : $\ell$ -th refinement tolerance in AMR algorithm	–
	<sup>7</sup> $\eta_E$ : Field utilisation factor	1
$\eta^{[\text{eq}]}$	Asperity density for equivalent surface	$\text{m}^{-2}$
$\theta$	Theta-scheme order parameter for timestepping	1
$\bar{\theta}$	Generic optimal parameters from MLE fitting $s$	arb.
$\kappa_1, \kappa_2$	Components of $K_{\text{ramp}}$	1
	<sup>5</sup> $\kappa_j$ : $j$ -th solid domain in StrAFE	–
$\lambda_1, \lambda_2$	Parameters associated with electron Diffusion length	m
	<sup>3</sup> $\lambda_i$ : Parameter related to relaxation times the $i$ and $(i + 1)$ -th layers	1
	<sup>5</sup> $\lambda_{E,M}, \nu_{E,M}$ : Energy and momentum dissipation length and frequency	$\text{m}, \text{s}^{-1}$
$\mu$	Absolute permeability	H/m
$\mu_r$	Relative permeability	1
	<sup>5,6</sup> $\mu_i$ : Electrical mobility of charged species $i$	$\text{m}^2 \text{V}^{-1} \text{s}^{-1}$
	<sup>7</sup> $\mu_T$ : Mean motif depths	m
$\nu_a$	Attachment frequency	$\text{s}^{-1}$
$\nu_i$	Ionisation frequency	$\text{s}^{-1}$
	<sup>5</sup> $\nu_u$ : Electron impact excitation frequency to level $u$	$\text{s}^{-1}$
$\bar{\nu}$	Effective ionisation frequency	$\text{s}^{-1}$
$\xi$	Photoionisation efficiency	1
	<sup>7</sup> $\xi_{1-4}$ : Convenience parameters for spheroid electric field	1
$\rho$	Volumetric charge density	$\text{C}/\text{m}^3$
$\rho_c$	Spearman's correlation coefficient	1
$\sigma$	Electrical conductivity	S/m
$\tilde{\sigma}_c$	Collision cross-sectional area	$\text{m}^2$
$\tilde{\sigma}_T$	Total collision cross-section area	$\text{m}^2$
$\sigma^{[\text{eq}]}$	Standard deviation of asperity peak heights for equivalent surface	m
$\sigma_{g,l,b}$	Electrical conductivity of gas, intermediate layer, and bulk	S/m
	<sup>3</sup> $\sigma_i$ : Electrical conductivity of layer $i$	S/m
	<sup>7</sup> $\sigma_T$ : Standard deviation of motif depths	m
$\bar{\sigma}_{\mathcal{R}}$	Standard deviation of rank	–
$\varsigma$	Surface charge density	$\text{C}/\text{m}^2$
	<sup>3</sup> $\varsigma_i$ : Surface charge density at interface $i$	$\text{C}/\text{m}^2$
$\tau$	Relaxation time constant	s
	<sup>5</sup> $\tau$ : Characteristic time for gas discharge process	s
$\tau_{av}$	Avalanche development (transition) time	s
$\tau_{is}$	Ionisation screening time	s
$\nu$	Poisson ratio	1
$\Phi^j$	$j$ -th separated potential function	arb.
$\phi_i$	Basis functions to the linear expansion of $u_h$	–
	<sup>7</sup> $\phi(z)$ : Asperity peak height distribution function	$\text{m}^{-1}$
$\bar{\phi}$	Work function	eV
$\varphi$	Scalar electric potential field	V
$\varphi_0$	Externally applied potential field	V
	<sup>3</sup> $\varphi_i$ : Electric potential in layer $i$	V
$\Omega$	Representation of a domain	–
	<sup>5,6</sup> $\Omega_g, \Omega_s$ : Gas domain, Solid domain	–
	<sup>5</sup> $\omega_j$ : Disjoint segments of an external boundary $\partial\Omega$	–
	<sup>2</sup> $\Omega$ : Solid angle	sr
$\partial\Omega$	Representation of external boundary of domain $\Omega$	–
$\omega(\mathcal{D})$	Function defined for closed-form pulsed breakdown equations	1

---

## List of Tables

---

<b>Chapter 2</b>	<b>15</b>
2.1 Typical characteristics of pulses used across pulsed power applications. . . . .	16
2.2 Typical characteristics required for common pulsed power applications. . . . .	17
<b>Chapter 3</b>	<b>73</b>
3.1 Double-exponential wave-shaping parameters for three impulses. . . . .	88
3.2 Cell parameters for multilayer inclusion model verification. . . . .	111
<b>Chapter 5</b>	<b>159</b>
5.1 Notable standalone software packages capable of gas discharge simulation. . . . .	173
5.2 Photoionisation fitting parameters for 3-term Helmholtz model in air. . . . .	207
5.3 Simulation data comparison to Bagheri <i>et al.</i> . . . . .	209
5.4 Simplified Plasma Chemistry of 80/20 N <sub>2</sub> /O <sub>2</sub> mixtures. . . . .	219
<b>Chapter 6</b>	<b>239</b>
6.1 Simplified Plasma Chemistry of CO <sub>2</sub> . . . . .	256
<b>Chapter 7</b>	<b>313</b>
7.1 Relevant material properties for investigated polymers. . . . .	316
7.2 Default parameters used to demonstrate solid-solid breakdown model. . . . .	339
7.3 Average motif parameters for practical dielectric samples. . . . .	363
7.4 Waveshaping parameters approximating practical waveforms. . . . .	366
<b>Chapter 8</b>	<b>379</b>
8.1 Significance testing results for “as received” and “machined” surface conditions. . .	391
8.2 Calculated Spearman’s correlation coefficients for solid-gas flashover study. . . . .	401

<b>Appendix</b>	<b>i</b>
A.1 All miscellaneous discharge simulation settings for computational work. . . . .	xxiv
A.2 MLE-fitted Weibull parameters: solid-solid experiments. . . . .	xxx
A.3 MLE-fitted Weibull parameters: solid-gas experiments—“as received”. . . . .	xxxii
A.4 MLE-fitted Weibull parameters: solid-gas experiments—“machined”. . . . .	xxxii

---

## List of Figures

---

<b>Chapter 1</b>	<b>1</b>
1.1 Areas of application of pulsed power technology. . . . .	2
1.2 Outline, layout, and organisation of this work. . . . .	8
<b>Chapter 2</b>	<b>15</b>
2.1 Circuit diagram of ideal Marx generator and erected equivalent circuit. . . . .	18
2.2 Circuit schematics of single pulse forming line and associated mechanism. . . . .	19
2.3 Circuit schematic of Blumlein generator and ideal impulse. . . . .	20
2.4 Two layer Maxwell-Wagner polarisation example. . . . .	24
2.5 Important mechanisms at the solid-gas interface. . . . .	25
2.6 Diagram for scattering cross section derivations. . . . .	32
2.7 Various depictions of electron avalanche mechanism. . . . .	35
2.8 Examples of ICCD-images streamer discharges in nitrogen-oxygen mixtures. . . . .	37
2.9 Colourised diagrams of Meek's streamer discharge mechanism. . . . .	38
2.10 Modern understanding of streamer structures from simulations. . . . .	39
2.11 Proposed structure of a leader channel and streamer region. . . . .	42
2.12 Example Paschen curves and discharge regimes. . . . .	45
2.13 Diagram of factors influencing surface flashover behaviour. . . . .	48
2.14 Spark breakdown channel morphologies and comparison. . . . .	49
2.15 Simulation and experimental images of surface-initiated streamers. . . . .	50
2.16 Tangential and perpendicular field components at solid-solid interfaces. . . . .	52
2.17 Diagram of interfacial voids at a solid-solid interface. . . . .	54
2.18 CCD images of partial discharges inside an artificial void. . . . .	56
<b>Chapter 3</b>	<b>73</b>
3.1 Diagram of generalised orthogonal coordinate system. . . . .	77
3.2 Two types of potential boundary condition. . . . .	79
3.3 Diagram of a one-dimensional planar composite energised between electrodes. . . . .	86
3.4 Three impulsive waveforms for evaluating multilayer FGM performance. . . . .	89

3.5	Linear and “U”-shaped multilayer FGM grading profiles. . . . .	90
3.6	Field responses for 20-layer permittivity graded FGM under 50/500 ns impulse. . .	91
3.7	Field responses for 20-layer conductivity graded FGM under 50/500 ns impulse. . .	93
3.8	Transient electric fields for 20-layer FGM subjected to three impulsive waveforms. .	95
3.9	Radially-graded FGM structure using polar coordinates. . . . .	96
3.10	3D model of simple disk-type GIL spacer geometry. . . . .	97
3.11	Simulated field enhancement in uniform and multilayered FGM spacers in GIL. . .	98
3.12	Field distributions along spacer interface for graded and ungraded GIL spacers. . .	99
3.13	Prolate spheroidal coordinate system for multilayered inclusions. . . . .	102
3.14	Analytical colour plots of enhancement around inclusions. . . . .	108
3.15	Two-layer inclusion against eccentricity and convergence in the spherical limit. . .	110
3.16	Diagram of 5-layer cell geometry for demonstration. . . . .	112
3.17	Comparison of transmembrane potentials using multilayered inclusion model. . . .	113
<b>Chapter 4</b>		<b>123</b>
4.1	Simplified transport of a Gaussian electron distribution. . . . .	128
4.2	Volumetric render of electron avalanche under ramp field. . . . .	132
4.3	Sliced 2D view of avalanche development under ramp voltage energisation. . . . .	133
4.4	Effective $K$ value for ramp fields including electron diffusion. . . . .	139
4.5	Dependency of $K$ value for ramp fields on $\mathcal{D}$ and diffusion constants. . . . .	140
4.6	Peak of net electric field as alternative transition criterion. . . . .	143
4.7	Closed-form estimations of breakdown strength and time-to-breakdown. . . . .	144
4.8	Pulsed Paschen curves compared to experimental and simulated data. . . . .	147
4.9	Plot of $pd$ scaling behaviour of the predicted breakdown voltage. . . . .	149
4.10	Predicted field-time scaling for breakdown in air, nitrogen, and CO <sub>2</sub> . . . . .	151
<b>Chapter 5</b>		<b>159</b>
5.1	Matrix of simulation software development issues. . . . .	161
5.2	High-level overview of the main algorithmic loop for PIC simulations. . . . .	165
5.3	Comparison of 2D/3D particle/fluid approaches for positive streamer. . . . .	167
5.4	Example of branching streamers using tree-like models. . . . .	168
5.5	Example of other methods used to characterise non-thermal gas discharges. . . . .	169
5.6	Approximate validity bounds for kinetic, hybrid, and fluid plasma models. . . . .	171
5.7	Validity bounds for the fluid approach for gas discharge modelling. . . . .	172

5.8	Block diagram of FEniCS software architecture. . . . .	177
5.9	Cylindrical photoionisation integral in Zheleznyak’s model. . . . .	181
5.10	Regions of validity for LMEA and LFA in air. . . . .	184
5.11	Flow diagram outlining the AMR algorithm implemented in StrAFE. . . . .	192
5.12	Block diagram of StrAFE software architecture. . . . .	198
5.13	Flow diagram of the main solver time loop implemented in StrAFE. . . . .	204
5.14	Computational domain for positive streamer comparison study. . . . .	206
5.15	Results of axisymmetric positive streamer comparison study. . . . .	208
5.16	Computational domain for surface streamer attachment study. . . . .	210
5.17	Results from positive streamer attachment study—seed distance. . . . .	212
5.18	Magnified image of the head of a positive surface streamer. . . . .	213
5.19	Magnified image of streamer surface attachment for different permittivity. . . . .	214
5.20	Results from positive streamer attachment study—surface permittivity. . . . .	215
5.21	Results from positive streamer attachment study—applied voltage. . . . .	217
5.22	Computational domain for double-headed streamer study. . . . .	218
5.23	Electric field results from double-headed streamer study. . . . .	220
5.24	Electron density results from double-headed streamer study. . . . .	221
5.25	Computational domain for needle-needle counter-propagating streamer study. . . . .	222
5.26	Streak image comparison of counter-propagating streamers. . . . .	224
5.27	Inter-electrode gap electric field for counter-propagating streamers. . . . .	225
<b>Chapter 6</b>		<b>239</b>
6.1	Chapter outline matrix. . . . .	242
6.2	Adapted computational domain for streamer simulations under different $dU/dt$ . . . . .	244
6.3	Electric field and electron density of positive streamers at different $dU/dt$ . . . . .	245
6.4	Max. field strength and streamer velocity for overstressed positive streamers. . . . .	246
6.5	Time for overstressed positive streamers to propagate same distance. . . . .	247
6.6	Electron density profiles of overstressed positive streamers at same length. . . . .	247
6.7	Streamer diameter and $v/a_s^2$ for overstressed positive streamers. . . . .	248
6.8	Electric field strength and electron density of overstressed negative streamers. . . . .	251
6.9	Computational domains used for the study of sub-mm ionisation waves. . . . .	254
6.10	Time evolution of the ionisation front in an air-filled needle-plane gap. . . . .	257
6.11	Time evolution of the ionisation front in a CO <sub>2</sub> -filled needle-plane gap. . . . .	258
6.12	Time evolution of the ionisation fronts in air and CO <sub>2</sub> needle-needle gaps. . . . .	259

6.13	Streamer inception time scaling with $(dU/dt)^{-1}$ . . . . .	260
6.14	Sensitivity of $\omega(\mathcal{D})$ to $\mathcal{D}$ . . . . .	261
6.15	Instantaneous velocity over time for positive and negative ionisation fronts in air. . .	262
6.16	Evolution and mean propagation velocities for air and CO <sub>2</sub> ionisation waves. . . .	264
6.17	Maximum electric field over time for air and CO <sub>2</sub> needle-plane ionisation waves. . .	265
6.18	Electric field across axis of symmetry for needle-needle ionisation waves. . . . .	266
6.19	Electron density along axis of symmetry for needle-plane gaps at time of contact. . .	267
6.20	Plasma composition plots for needle-plane gaps at time of contact. . . . .	269
6.21	Cathode sheath thicknesses for needle-plane ionisation waves in air and CO <sub>2</sub> . . . .	270
6.22	Electron mobility and photoionisation on cathode sheath thickness variation. . . .	271
6.23	Additional sheath thicknesses for ionisation waves in air without photoionisation. . .	273
6.24	Suppression of negative waveform formation at slower rates of rise in CO <sub>2</sub> . . . . .	274
6.25	Computational domains used for the study of sub-mm surface ionisation waves. . .	276
6.26	Electric field and electron density for sub-mm surface ionisation waves in air. . . .	277
6.27	Electric field and electron density for sub-mm surface ionisation waves in CO <sub>2</sub> . . .	279
6.28	Maximum electric field over time for positive surface ionisation waves. . . . .	280
6.29	Surface wavefront propagation phases based on maximum electric field. . . . .	282
6.30	Evolution of maximum electric field at different propagation phases. . . . .	282
6.31	Locations of maximum electric field for surface ionisation waves in air and CO <sub>2</sub> . . .	284
6.32	Deposited surface charge of negative surface ionisation wavefronts in air and CO <sub>2</sub> . .	286
6.33	Diagrams of analytical surface charge critical field calculations. . . . .	287
6.34	Electric field due a to Gaussian surface charge as a function of $k =  x/s_0 $ . . . . .	289
6.35	Computational domain for streamers interacting with non-uniform surface charge. . .	291
6.36	Development of a positive surface streamer across an uncharged surface. . . . .	292
6.37	Surface streamer with a peak surface charge density of $-400$ pC/mm <sup>2</sup> . . . . .	293
6.38	Surface streamer with a peak surface charge densities of $-600$ and $-800$ pC/mm <sup>2</sup> . . .	294
6.39	Close approach of positive surface streamer to negative Gaussian charge patch. . . .	296
6.40	Development of a surface-charge induced double-headed streamer. . . . .	298
<b>Chapter 7</b>		<b>313</b>
7.1	Diagram of solid-solid interfacial breakdown model and components. . . . .	317
7.2	Depiction of rough surface contact with ideal rigid plane. . . . .	318
7.3	Diagram of classical Hertzian elastic contact of spherically-tipped asperity. . . . .	319
7.4	Diagram of interfacial voids and their approximation. . . . .	321

---

7.5	Diagram of single, triple layer, gas-filled void. . . . .	322
7.6	Diagram of spheroidal voids in non-uniform electrode geometries. . . . .	328
7.7	Electric field distributions of spheroidal voids in non-uniform external fields. . . . .	329
7.8	Intra-void field utilisation factor as a function of proximity to curved electrode. . . . .	330
7.9	Intra-void field utilisation factor as a function of void semi-major radius. . . . .	330
7.10	Diagram of interfacial contact spots. . . . .	334
7.11	Comparison of models for contact spot tracking. . . . .	336
7.12	Detail flowchart of impulsive solid-solid interfacial breakdown model. . . . .	337
7.13	Modelled intra-void and contact spot electric fields for a dry-mate interface. . . . .	339
7.14	Modelled intra-void and contact spot electric fields for a wet-mate interface. . . . .	341
7.15	Modelled intra-void and contact spot electric fields for an oil-mate interface. . . . .	342
7.16	3D CAD model of solid-solid interface test chamber for experimental study. . . . .	343
7.17	Photographs of square solid material samples. . . . .	344
7.18	Photograph of shoulder mill used to treat sample surfaces. . . . .	345
7.19	Circuit diagram of test circuit for solid-solid interface breakdown tests. . . . .	345
7.20	Handysurf 35+ manual profilometer for surface roughness characterisation. . . . .	346
7.21	Example measurement of a primary surface height profile. . . . .	347
7.22	Example diagram of a single motif and a motif profile. . . . .	348
7.23	Example of motif decomposition of primary surface profile. . . . .	350
7.24	Diagram showing the features used to characterise the asperity aspect ratio. . . . .	352
7.25	Flowchart of solid-solid interfacial breakdown test procedure. . . . .	352
7.26	Example oscillograms from impulse breakdown across solid-solid interfaces. . . . .	354
7.27	Nominal breakdown fields and times for solid-solid interfaces. . . . .	356
7.28	Photographs of post-breakdown surfaces and categories of post-breakdown traces. . . . .	359
7.29	Magnified image showing different interfacial breakdown paths. . . . .	360
7.30	Maximum widths of post-breakdown affected region over all tests. . . . .	361
7.31	Nominal breakdown field against motif parameters for all interfaces. . . . .	364
7.32	Nominal breakdown field against asperity aspect ratio for all interfaces. . . . .	365
7.33	Measured and theoretical impulsive breakdown voltages of solid-solid interfaces. . . . .	366
7.34	Comparison of predicted/measured breakdown strengths of solid-solid interfaces. . . . .	367
<b>Chapter 8</b>		<b>379</b>
8.1	3D CAD model of test cell for solid-gas impulsive flashover tests. . . . .	381
8.2	Photograph of cylindrical solid samples for impulsive flashover tests. . . . .	382

---

8.3	Comparison of fresh and used gramophone needles under magnification. . . . .	383
8.4	Circuit diagram of test circuit for solid-gas flashover tests. . . . .	384
8.5	Photographs of cylindrical sample surfaces for solid-gas flashover tests. . . . .	385
8.6	Revised surface roughness measurement system for cylindrical samples. . . . .	386
8.7	Example oscillograms from solid-gas flashover events. . . . .	387
8.8	Comparison of “as received” and “machined” surface motif parameters. . . . .	389
8.9	Comparison of “as received” and “machined” surface roughness parameters. . . . .	390
8.11	Breakdown voltage and time-to-breakdown for TG-01 flashover tests. . . . .	393
8.12	Simulated field distribution in solid-gas test cell. . . . .	394
8.13	Simulated electric field magnitude across solid sample. . . . .	395
8.14	Time to breakdown for Blumlein flashover tests. . . . .	396
8.15	Breakdown voltage against motif parameters for TG-01 flashover events. . . . .	399
8.16	Breakdown voltage against compound parameters for TG-01 flashover events. . . . .	400
8.17	Time to breakdown against motif parameters for all Blumlein flashover events. . . . .	402
8.18	Time to breakdown compound parameters for all Blumlein flashover events. . . . .	403

**Appendix****i**

A.1	Comparison of spheroidal enhancement factor to literature. . . . .	xxiii
A.2	Selected surface height distributions for machined experimental samples. . . . .	xxv
A.3	Demonstration of void-shielding at moment of discharge. . . . .	xxvi
A.4	Field enhancement between two discharged voids. . . . .	xxvii
A.5	Sensitivity of void and bulk electric fields to layer permittivity. . . . .	xxviii
A.6	Sensitivity of void and bulk electric fields to layer conductivity. . . . .	xxix
A.7	Comparison of LSQ and MLE fittings for Weibull distributions. . . . .	xxx
A.8	Examples of dynamic meshes generated in StrAFE during simulations. . . . .	xxxv
A.9	Results from basic parallel scaling test of StrAFE up to 16 MPI processes. . . . .	xxxvi
A.10	Example plasma chemistry input file for StrAFE. . . . .	xxxvi
A.11	Additional nonuniform field enhancement plots for dielectric inclusions. . . . .	xxxvii
A.12	Additional post-breakdown photographs of solid-solid interfaces. . . . .	xxxviii
A.13	Additional pre-breakdown photographs of cylindrical solid-gas sample surfaces. . . . .	xxxix



# Dielectric and Breakdown Phenomena as a Foundation of High Voltage and Pulsed Power Technology

## An Introduction

---

THE pioneering work of J. C. Martin [1,2] set into motion an avalanche of research and development, culminating in what has become the modern field of Pulsed Power Science and Technology. Since Martin, pulsed power has seen rapid growth driven by great successes in applying the principles of pulsed power to numerous industrial applications. The central idea to pulsed power technology is the rapid release of accumulated energy, stored over comparatively long timescales, to attain substantial peak output power in the form of electrical impulses. Over the last few decades, a vast array of technologies have been developed that operate on the basis of pulsed power techniques; including those that have benefited from the direct effects induced by pulse compression and release, or through the properties of the low-temperature plasmas that can be generated using pulsed power systems. Applications have been realised over multiple scales in terms of size, peak power, repetition rate, and pulse characteristics; prominent examples of which have been outlined in Figure 1.1, ordered approximately by their spatial scale.

On one end, high voltage (HV) pulse generators attaining peak power outputs the range of MW to TW form part of the critical infrastructure for conducting high energy density scientific research [3–5], including particle acceleration experiments [6,7], high energy radiation science [8],

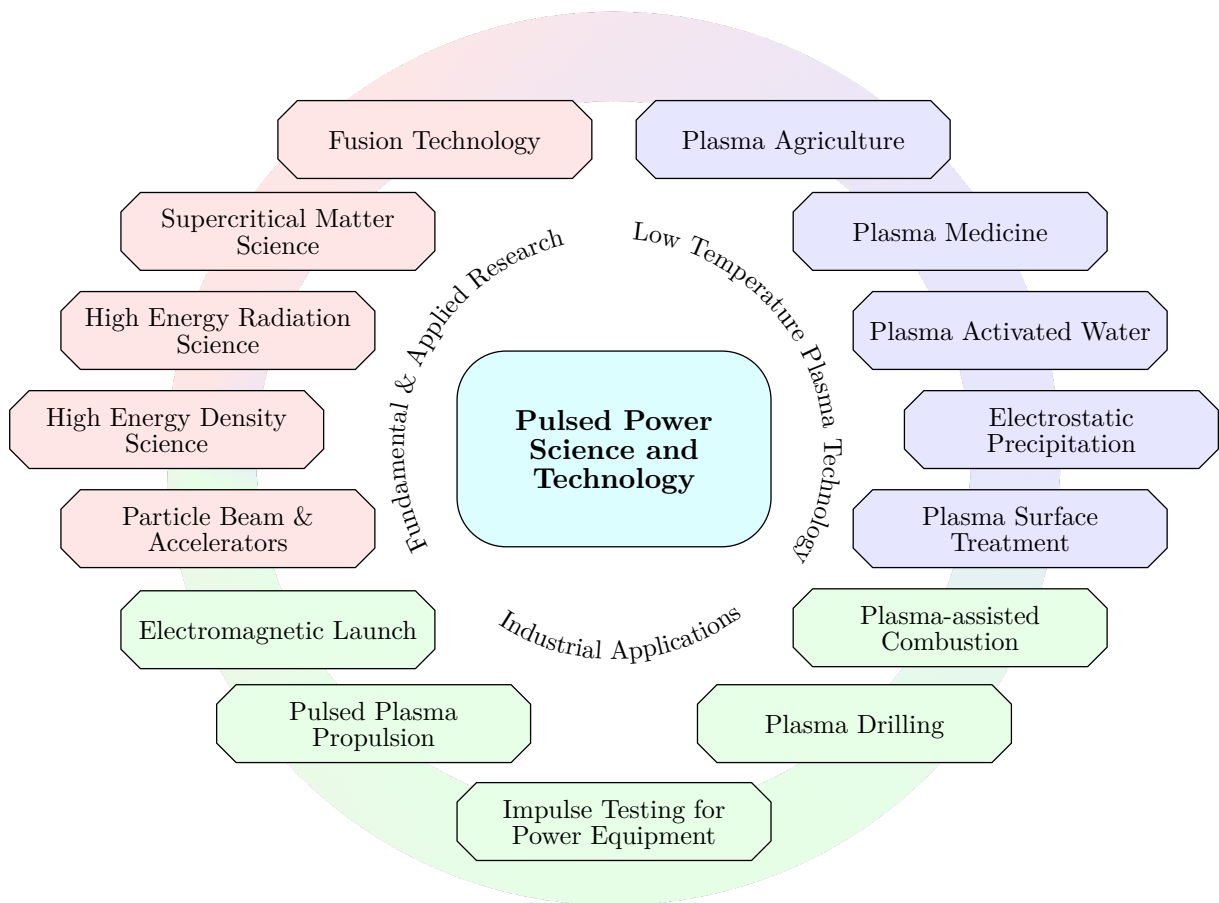


**Figure 1.1:** Areas of application benefiting from the principles of Pulsed Power Science and Technology, ordered roughly by scale according to colour.

plasma compression and confinement techniques [9,10], and for the development of novel solutions moving towards commercial fusion technology [11]. Major pulsed power facilities have led to scientific progress in numerous fields, contributing towards the understanding of plasma pinch physics [12], of celestial objects [13], and of material science [14]. In addition, harnessing the peak power capabilities of intense HV impulses is necessary for technologies that employ electromagnetic launch [15], with relevance to defence and military technology [16]; for research on hypersonic shocks [17]; and for understanding matter under extreme compression [18].

Medium-scale applications include the use of high-power impulses for drilling and liberation of ores and minerals [19] or for the pulverisation of solid matter [20,21]. Manufacturing industries have also benefited from pulsed power techniques, which has seen success, for example, from applying pulsed nanosecond discharges for surface treatment and modification [22,23]. For chemical processing purposes, these have additionally been shown effective for the production

---

of active chemical species and free radicals [24]. Moreover, the efficiency of environmental air cleaning technology based upon the principles of electrostatic precipitation has been shown to improve with application of repetitive pulsed electric fields [25], extending the uses of pulsed power to the area of particulate capture and treatment of flue gases [26,27]. In the power industry, pulsed power research has contributed fundamental knowledge towards the understanding of dielectric breakdown phenomena under pulse action [28,29], which is of particular importance to the understanding of system transients such as lightning or switching impulses. This has continued to aid in the development and coordination of HV insulation for power transmission and protection equipment.

On smaller scales, biomedical applications such as pulsed electric field (PEF) treatment are well-known methods used for sterilisation and decontamination [30,31], drug delivery [32], and for the treatment of tumours, which includes the possibility of less invasive surgery for cancers and neurodegenerative diseases [33,34]. The development of PEF has also impacted the food processing [35] and biomass extraction industries [36], favoured for its efficiency and capability to ensure minimal detrimental effects to the treated medium due to heating [37]. Novel areas of application continue on an upward trend as the pace of pulsed power research increases. Recent examples utilising pulsed discharges include plasma assisted combustion [38], a promising method to improve fuel efficiency and enhance engine performance for the automotive and aerospace industries; or plasma-activated water [39] within the wider field of plasma agriculture [40], which appears to stimulate effective nutrient uptake and promote plant growth.

The need to fully understand the interaction of pulsed electric fields with matter is a common issue shared by all of the applications described above. On one hand, the generation of HV transient electrical impulses necessitates the development of robust and performant electrical insulation; otherwise there is a risk of dielectric breakdown that may possibly lead to catastrophic system failure. The drive towards system miniaturisation while maintaining similar operational ratings can greatly improve energy efficiency, but presents significant challenges for insulation coordination due to elevated electric field stresses. Recent developments in the semiconductor, power electronic, and micro-electromechanical systems (MEMS) industries have begun to face similar issues [41,42]. Despite low operating voltages, increasing operational requirements and device density have led to unprecedented levels of electrical stress on such devices, with some crossing a threshold where dielectric breakdown becomes a tangible risk. On the other hand, certain classes of pulsed power equipment, e.g., high-speed plasma-closing (spark-gap) switches, are reliant upon the ability to induce precise, controllable, and repeatable electrical

breakdown [43]. Similarly, applications exploiting the many properties of low-temperature plasma must necessarily operate within a regime close to breakdown, considering that the generation of plasma results directly from gas discharge phenomena.

It follows that, regardless of the application, a solid understanding of the interactions between pulsed electric fields, dielectrics, conductors, and electrical (pre-)breakdown phenomena, is foundational to the success of pulsed power technologies, now and in the future. Systems that feature different combinations of gas-, liquid-, or solid-phase materials are commonplace within HV pulsed power equipment, which may be formed from materials used as insulation, or be part of the treatment medium like in applications such as PEF. Often, composite systems are also unavoidable when phase-specific properties are necessary for different components (e.g., solid dielectrics as necessary mechanical support in an otherwise gas-insulated system). As a result of the extensive research efforts directed towards the development of power transmission and distribution equipment, dielectric and breakdown phenomena under steady-state AC and DC regimes are typically far better understood than for fast transient stresses like impulses. This is especially true for non-standard waveforms often used in pulsed power applications, particularly when combined with configurations exhibiting high field non-uniformity or using atypical materials uncommon to power applications. Hence, to support the continued development of HV pulsed power technologies now and in the future, a deeper understanding of dielectric phenomena and electrical (pre-)breakdown under impulsive energisation, specifically under non-standard waveforms and using atypical materials that depart from those of power-centric research, must be gained. Innovations in this direction would be of significant and far-reaching benefit to many, encompassing the many applications described in this introductory section. These aspects greatly motivated the present work and formed the basis of the ideas explored, and contributions presented, herein.

### 1.1 Scope and Objectives

This work concerns itself with aspects pertaining predominantly to systems incorporating gaseous dielectrics, and was largely focused on the quantification of effects due to fast-rising impulse action on discharge and (pre-)breakdown behaviour in gas and across solid-gas and solid-solid interfaces. Particular attention was paid to providing further clarity on aspects relating to dielectric phenomena, pre-breakdown processes, and breakdown characteristics incorporating topologies subjected to transient impulse action and under overstressed conditions.

It was recognised that there existed many poorly-understood processes relating to impulse-driven gas breakdown throughout the multiple stages of pulsed energisation and in relation to composite systems: starting from the development of the initial field distribution, to the initiation of electron transport and multiplication processes; through to charge-dominated ionisation processes and pre-breakdown phenomena, that may eventually lead to breakdown and voltage collapse. This work therefore aimed to provide a comprehensive view across a range of physical factors affecting impulsive breakdown, and to advance the understanding of the following:

- Considering the varied nature of materials that may feature within pulsed power applications, understand how differences in the material's electrical responses affect the electric fields developed within composite (multilayered) systems subjected to fast-rising HV impulses of different rise and fall characteristics. Can these effects be of consequence?
- Explore the origins of the known tendency for overstressed pulsed breakdown to occur at higher field strengths than the static case in gas. How can this difference be better explained, and how can it be better characterised or predicted? How are the various stages leading up to complete breakdown affected by fast-rising overvoltages?
- What are the defining characteristics of ionisation wavefronts and streamer discharges that are initiated under fast-rising overstressed conditions and in geometries of practical relevance? Specifically, how does the rate of voltage rise affect their inception and subsequent propagation, including across solid dielectric surfaces?
- What is the role of surface condition and roughness in practical breakdown across solid-solid and solid-gas interfaces under different impulse waveforms? What are the effects of different rates-of-rise?
- Can the analysis of combined experimental breakdown and surface roughness data provide a greater understanding of impulsive breakdown across solid-solid and solid-gas interfaces?

To answer these questions, this work employed a diverse set of methods encompassing analytical, computational, and experimental techniques to gain a comprehensive understanding of processes across the various phases of pulsed breakdown. Numerous novel results relating to dielectric phenomena, pre-breakdown gas discharges, and overstressed breakdown in gas, solid-gas, and solid-solid system topologies were attained from this work and are given in summary form in the following section.

## 1.2 Novelty of Contributions

It is firstly remarked that detailed statements which report on the per-chapter novel contributions can be found within the conclusion sections included at the end of each chapter. These provide standalone discussion of the contributions within the context of their respective chapters, with greater specificity to the work presented within that chapter and provides further discussion relating to academia and industrial relevance. Here, a condensed list highlighting the overall key novelties are given in summary form.

- Advancement of analytical techniques for the estimation of intra-layer electric fields developed inside complex, multilayered, and poorly-conducting composites under time-dependent energisation. Under impulsive energisation, showed that the coupling between interfacial relaxation times and characteristic impulse rise- and fall-times may impact insulator performance. For the first time, generalisation of the analytical Maxwell-Wagner method to numerous arbitrary multilayer geometries, with the potential to impact the way in which complex layered materials will be modelled in the future.
- Development of novel analytical and semi-empirical models describing electron avalanche growth under fast-rising overstressed conditions. Mathematical analyses provided new perspectives on the reasons for increased gas breakdown strength with faster rising voltages based upon an argument of competing rates-of-change. Limits to where electron diffusion may become important to overstressed breakdown were deduced. Novel closed-form approximations for the time-to-breakdown and breakdown voltage for overstressed breakdown were found to be in good agreement with experimental data.
- Development and introduction of StrAFE (**Streamers on Adaptive Finite Elements**), a new framework for the simulation of gas discharge phenomena in the form of a Python library built atop open-source software. Verification studies indicated comparable performance and accuracy to both commercial software and state-of-the-art custom codes.
- Conducted novel simulations of fast transient ionisation events in short and long gaps. Comprehensive analyses has provided new scaling relationships for overstressed streamer characteristics and revealed cathode-sheath effects in CO<sub>2</sub> affecting sub-mm gap discharges. It has further contributed towards a deeper understanding of fundamental characteristics of primary gas discharges initiated under overstressed conditions, including electric field strengths, propagation velocities, and developed plasma densities. Effects of surface ionisation wavefronts and streamers have additionally provided novel insights into surface charging dynamics and its effects on subsequent discharges.

- Experimentally characterised impulse-driven breakdown events across solid-solid interfaces formed between five different polymers: PVC, Delrin, Torlon, Perspex, and Ultem; under two different impulse waveshapes and considering surface roughness. Results indicated differences in breakdown path that were dependent on rate-of-rise, and that effects relating to surface asperity aspect ratio may be important in determining solid-solid flashover strength under low mating pressure, different from that conventionally known for high mating pressure. Interfacial breakdown strengths were also found to be generally lower than those of gas alone due to interfacial field enhancement. A novel solid-solid interfacial breakdown model for time-dependent energisation was found to support the experimental findings.
- Experimentally characterised impulsive flashover behaviour across the same five materials in a solid-gas arrangement for “as received” and “machined” surface conditions. Statistical analysis combined with surface profilometry data suggested that short-wavelength surface features contribute substantially more to an increased flashover strength relative to long-wavelength surface undulations.

### 1.3 Organisation and Structure

Onward from the current introductory chapter, this work proceeds with *Chapter 2: Preliminaries and State of the Art* which details the theoretical basis upon which this work is based. This incorporates the basic principles of pulsed power and impulse generation to gain an understanding of their origin and characteristics. Then, relevant aspects of electromagnetic theory, kinetic theory, and both classical and current theories explaining gas discharge and breakdown phenomena are detailed. The mechanisms driving solid-solid and solid-gas breakdown are additionally described, primarily delivered through an overview of successive pieces of literature that have made significant contributions towards understanding the associated phenomena. The review and critique of the literature is concluded with an approximate analysis of the characteristic timescales of gas discharge phenomena, and from this, why pulsed breakdown represents a limit in which many classical gas breakdown theories developed under static conditions become inapplicable.

Six technical chapters then follow, comprising the significant findings of this work. Each chapter begins with an individual *Introduction and Motivation* section, which provides specific context relating to the issues that the work presented within the chapter aimed to address. Correspondingly, each chapter is closed with an appropriate conclusion and discussion of the

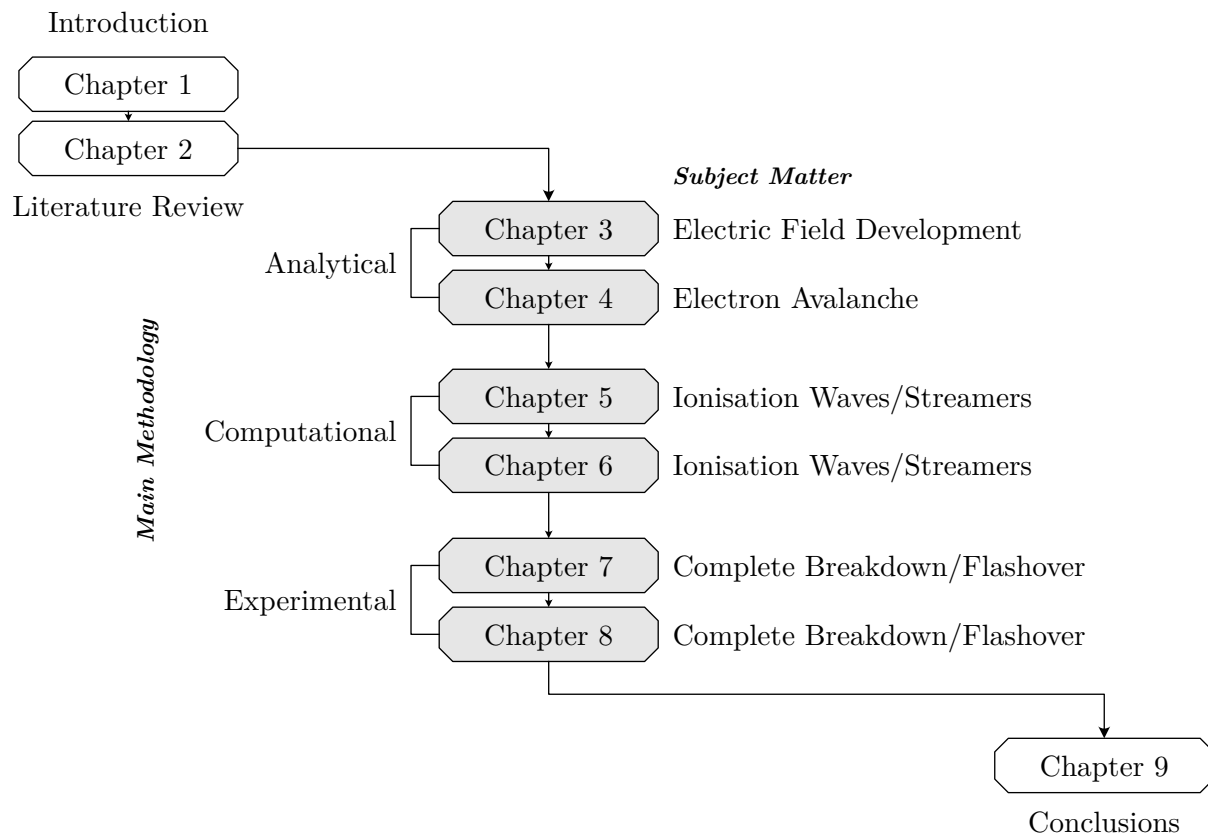


**Figure 1.2:** Flowchart outlining the organisation and layout of this work. Main technical chapters are shaded grey, with the corresponding subject matter and main methodology provided as labels. Full descriptions of each chapter given in main text.

limitations of the study. The novel academic contributions of the chapter are reiterated, the relevance of the chapter’s conclusions to industrial system development is discussed, and aspects that would benefit from additional study are identified.

The subject matter of each chapter is detailed in Figure 1.2, to which the reader should refer in the descriptions that follow. Each technical chapter shown in Figure 1.2 has additionally been labelled with the main research methodology which was applied: analytical, computational, or experimental, which corresponds also to the style of presentation the reader may expect within the respective chapter’s main text. Broadly, the technical chapters are purposefully ordered to follow the chronological development of breakdown: field development → avalanche → streamer → spark, which has further been indicated in Figure 1.2. A summary of the contents of each technical chapter is as follows.

**Chapter 3 (analytical):** *On the Impulsive Electric Field Responses of Multilayered*

### ***Composite Systems***

Motivated by the wide range of materials and pulse waveforms often used in pulsed power applications, Chapter 3 details the mathematical analysis of  $n$ -layer composite materials under time-dependent impulse action. This begins with a generalised approach in arbitrary coordinates, before specific solutions are constructed for cases of practical interest. Several case studies are included within this chapter for the purposes of model validation, involving the comparison of limiting cases and comparison to numerically-simulated results. Chapter 3 additionally presents the application of the multilayered approach to the problem of functionally-graded materials (FGMs), where the impact of such a material structure on field grading performance under impulse action is determined and demonstrated.

### ***Chapter 4 (analytical): An Avalanche-to-Streamer Transition Criterion for Overstressed Breakdown on a Rising Slope***

Progressing from the transient field analysis of Chapter 3, Chapter 4 presents a new analytical model for the spatio-temporal development of an electron avalanche under time-dependent energisation. The morphological characteristics of the predicted avalanche evolution is compared to the literature, before a semi-empirical formulation of the original problem under linearly-rising voltages facilitates several mathematical arguments that partially explain the known tendencies of overstressed breakdown, and further allowed the proposal of a new criterion relating to the role of electron diffusion. Building on this, closed-form approximations are presented as an alternative and convenient model for fast-rising overstressed breakdown with explicit incorporation of the field rate-of-rise as a parameter. Chapter 4 is concluded with a comparison of the model predictions to simulated and experimental data.

### ***Chapter 5 (computational): Development of a Python Library for the Modelling of Transient Ionisation Fronts in Gas and Solid-Gas Topologies***

Linking between the avalanche-centric work of Chapter 4 and the results on ionisation waves and streamers in Chapter 6, Chapter 5 documents the development of StrAFE, a novel computational framework for the finite-element simulation of gas discharge phenomena. Chapter 5 begins with a self-contained and comprehensive literature review of streamer discharge modelling, providing also the motivation and justification to develop a brand-new software program. This includes the discussion of different modelling approaches and of their respective limitations, which ultimately informed the implementation of the hydrodynamic approximation in StrAFE. Two main sections then follow in Chapter 5: the first, an account detailing the implementation of StrAFE; and the second, the presentation of a number of code verification studies comparing StrAFE to other

software, both commercially-available and custom implementations.

***Chapter 6 (computational): Characteristics of Overstressed Transient Ionisation Fronts and Streamers in Gas and Across Solid Interfaces***

Using StrAFE, Chapter 6 is split into four main sections presenting various novel simulations of fast ionisation wavefronts and streamers, broadly split by gap distance and whether a solid dielectric surface was considered. A first section presents results arisen from a “first-look” study on the basic characteristics of overstressed streamer discharges using a minimal model. Advancing in complexity, a second and third section details overstressed discharges initiated within sub-mm needle-plane and needle-needle gaps, in a case study comparing atmospheric air and CO<sub>2</sub>. The former is concerned with discharges in gas only, while the latter includes a vertical dielectric barrier and additionally discusses surface charging phenomena. A fourth and final section builds upon the idea of surface charge, presenting simulations that aimed to provide further understanding of non-uniform surface charge distributions, focused particularly on their effects on the development of subsequent surface streamers.

***Chapter 7 (experimental): Impulsive Breakdown and Surface Roughness Characteristics of Solid-Solid Polymer Interfaces***

Shifting the focus to the complete breakdown process and to interfaces, Chapter 7 is the first of two experimental chapters, detailing the experimental arrangements and results from impulse breakdown experiments performed across solid-solid polymer interfaces formed from PVC, Delrin, Torlon, Ultem, and Perspex. As support, Chapter 7 begins by detailing the development of a theoretical solid-solid breakdown model for impulse energisation, which partially incorporates the techniques described within Chapters 3 and 4 and is based on the theory of gas-void driven breakdown. The experimental methodology and test configuration is then described, encompassing the details regarding the method of profilometry, surface characterisation, and data processing using Weibull statistics. This is followed by the presentation and analysis of the results, which includes the comparison of experimental tendencies to those predicted by the developed model.

***Chapter 8 (experimental): Effects of Surface Condition on the Impulsive Flashover of Polymer-Gas Interfaces***

Complementary to Chapter 7, Chapter 8 presents a second experimental study using the same polymers, aimed at the characterisation of impulsive flashover across solid-gas interfaces. The revised methodology and experimental arrangements are first presented, once again featuring surface profilometry and roughness characterisation. Analysis and discussion of the flashover

results are supported by appropriate numerical simulations of field distributions.

**Chapter 9: Conclusions, Contributions, and Perspectives** closes with a summary and overarching conclusions drawn over the entire work, alongside final remarks on future outlook and progression.

It is further noted that the Appendix which is referred to throughout this work is split into three distinct sections. Appendix [A](#) contains supporting mathematical derivations relating mainly to analytical work, Appendix [B](#) encloses supporting results in the form of plots or diagrams that are auxiliary to the main argument, and Appendix [C](#) includes extra content that may be tangentially related but form points of general interest. Relevant references are provided on a per-chapter basis and can be found appended to the end of each chapter.

## Chapter 1 References

- [1] J. Martin, “Nanosecond pulse techniques,” *Proceedings of the IEEE*, vol. 80, no. 6, pp. 934–945, 1992.
- [2] J. C. Martin, *J. C. Martin on Pulsed Power*, T. H. Martin, A. H. Guenther, and M. Kristiansen, Eds. “London”: Springer New York, NY, 2013.
- [3] D. B. Sinars, M. A. Sweeney, C. S. Alexander, D. J. Ampleford, T. Ao, J. P. Apruzese *et al.*, “Review of pulsed power-driven high energy density physics research on Z at sandia,” *Phys. Plasmas*, vol. 27, no. 7, p. 070501, 2020.
- [4] J. Deng, W. Xie, S. Feng, M. Wang, H. Li, S. Song *et al.*, “From concept to reality – a review to the primary test stand and its preliminary application in high energy density physics,” *Matter Radiat. Extrem.*, vol. 1, no. 1, pp. 48–58, 2016.
- [5] J. Deng, J. Shi, W. Xie, L. Zhang, S. Feng, J. Li *et al.*, “Overview of pulsed power research at CAEP,” *IEEE Trans. Plasma Sci.*, vol. 43, no. 8, pp. 2760–2765, 2015.
- [6] O. Bayard, “The supply of the 148 MW pulsed power to the CERN SPS and the associated mains voltage stabilization and filtering,” *IEEE Trans. Nucl. Sci.*, vol. 26, no. 3, pp. 4066–4068, 1979.
- [7] J. Holma and M. J. Barnes, “Prototype inductive adders with extremely flat-top output pulses for the compact linear collider at CERN,” *IEEE Trans. Plasma Sci.*, vol. 46, no. 10, pp. 3348–3358, 2018.
- [8] B. Cadilhon, L. Pécastaing, T. Reess, A. Silvestre de Ferron, P. Pignolet, S. Vauchamp *et al.*, “High pulsed power sources for broadband radiation,” *IEEE Trans. Plasma Sci.*, vol. 38, no. 10, pp. 2593–2603, 2010.
- [9] M. K. Matzen, M. A. Sweeney, R. G. Adams, J. R. Asay, J. E. Bailey, G. R. Bennett *et al.*, “Pulsed-power-driven high energy density physics and inertial confinement fusion research,” *Phys. Plasmas*, vol. 12, no. 5, p. 055503, 2005.
- [10] M. E. Cuneo, M. C. Herrmann, D. B. Sinars, S. A. Slutz, W. A. Stygar, R. A. Vesey *et al.*, “Magnetically driven implosions for inertial confinement fusion at sandia national laboratories,” *IEEE Trans. Plasma Sci.*, vol. 40, no. 12, pp. 3222–3245, 2012.
- [11] M. R. Gomez, S. A. Slutz, P. F. Knapp, K. D. Hahn, M. R. Weis, E. C. Harding *et al.*, “Assessing stagnation conditions and identifying trends in magnetized liner inertial fusion,” *IEEE Trans. Plasma Sci.*, vol. 47, no. 5, pp. 2081–2101, 2019.
- [12] J. L. Giuliani, F. N. Beg, R. M. Gilgenbach, V. L. Kantsyrev, B. R. Kusse, V. V. Ivanov *et al.*, “Plasma pinch research on university pulsed-power generators in the united states,” *IEEE Trans. Plasma Sci.*, vol. 40, no. 12, pp. 3246–3264, 2012.
- [13] R. E. Falcon, G. Rochau, J. Bailey, J. Ellis, A. Carlson, T. Gomez *et al.*, “An experimental platform for creating white dwarf photospheres in the laboratory,” *High Energy Density Phys.*, vol. 9, no. 1, pp. 82–90, 2013.
- [14] D. B. Reisman, B. S. Stoltzfus, W. A. Stygar, K. N. Austin, E. M. Waisman, R. J. Hickman *et al.*, “Pulsed power accelerator for material physics experiments,” *Phys. Rev. ST Accel. Beams*, vol. 18, p. 090401, 2015.

- 
- [15] M. D. Fitzgerald, J. D. Pecover, N. Petrinic, and D. E. Eakins, "A 0-d electric gun model for the optimization of flyer acceleration to hypervelocities," *IEEE Trans. Plasma Sci.*, vol. 51, no. 8, pp. 2347–2357, 2023.
- [16] T. A. Mehlhorn, "National security research in plasma physics and pulsed power: Past, present, and future," *IEEE Trans. Plasma Sci.*, vol. 42, no. 5, pp. 1088–1117, 2014.
- [17] M. R. Betney, B. Tully, N. A. Hawker, and Y. Ventikos, "Computational modelling of the interaction of shock waves with multiple gas-filled bubbles in a liquid," *Phys. Fluids*, vol. 27, no. 3, p. 036101, 2015.
- [18] E. M. Escauriza, J. P. Duarte, D. J. Chapman, M. E. Rutherford, L. Farbaniec, J. C. Jonsson *et al.*, "Collapse dynamics of spherical cavities in a solid under shock loading," *Sci. Rep.*, vol. 10, no. 1, p. 8455, 2020.
- [19] U. Andres, J. Jirestig, and I. Timoshkin, "Liberation of minerals by high-voltage electrical pulses," *Powder Technol.*, vol. 104, no. 1, pp. 37–49, 1999.
- [20] I. Timoshkin, J. Mackersie, and S. MacGregor, "Plasma channel miniature hole drilling technology," *IEEE Trans. Plasma Sci.*, vol. 32, no. 5, pp. 2055–2061, 2004.
- [21] X. Zhu, Y. Luo, and W. Liu, "On the rock-breaking mechanism of plasma channel drilling technology," *J. Petroleum Sci. Engr.*, vol. 194, p. 107356, 2020.
- [22] F. Massines, C. Sarra-Bournet, F. Fanelli, N. Naudé, and N. Gherardi, "Atmospheric pressure low temperature direct plasma technology: Status and challenges for thin film deposition," *Plasma Process. Polym.*, vol. 9, no. 11-12, pp. 1041–1073, 2012.
- [23] B. Rakhadilov, D. Buitkenov, Z. Idrisheva, M. Zhamanbayeva, S. Pazylbek, and D. Baizhan, "Effect of pulsed-plasma treatment on the structural-phase composition and tribological properties of detonation coatings based on ti-Si-C," *Coatings*, vol. 11, no. 7, 2021.
- [24] D. Wang and T. Namihira, "Nanosecond pulsed streamer discharges: II. physics, discharge characterization and plasma processing," *Plasma Sources Sci. Technol.*, vol. 29, no. 2, 2020.
- [25] A. C. Mermigkas, I. V. Timoshkin, S. J. MacGregor, M. J. Given, M. P. Wilson, and T. Wang, "Superposition of DC voltage and submicrosecond impulses for energization of electrostatic precipitators," *IEEE Trans. Plasma Sci.*, vol. 40, no. 10, pp. 2388–2394, 2012.
- [26] H.-H. Kim, "Nonthermal plasma processing for air-pollution control: A historical review, current issues, and future prospects," *Plasma Process. Polym.*, vol. 1, no. 2, pp. 91–110, 2004.
- [27] K. Shimizu, K. Kinoshita, K. Yanagihara, B. Rajanikanth, S. Katsura, and A. Mizuno, "Pulsed-plasma treatment of polluted gas using wet-/low-temperature corona reactors," *IEEE Trans. Ind. Appl.*, vol. 33, no. 5, pp. 1373–1380, 1997.
- [28] S. Okabe, J. Takami, T. Tsuboi, G. Ueta, A. Ametani, and K. Hidaka, "Discussion on standard waveform in the lightning impulse voltage test," *IEEE Trans. Dielectr. Electr. Insul.*, vol. 20, no. 1, pp. 147–156, 2013.
- [29] S. Okabe, T. Tsuboi, and J. Takami, "Basic study of possible waveforms generated in lightning impulse withstand voltage test on UHV equipment," *IEEE Trans. Dielectr. Electr. Insul.*, vol. 16, no. 4, pp. 1127–1133, 2009.

- [30] S. Qin, P. Li, G. Liang, J. Liu, S. Huang, and J. Meng, "Pulsed electric field treatment of raw milk and its effect on protein-free amino acids transition," *IEEE Trans. Plasma Sci.*, vol. 50, no. 4, pp. 911–919, 2022.
- [31] M. Sato, N. Ishida, A. Sugiarto, T. Ohshima, and H. Taniguchi, "High-efficiency sterilizer by high-voltage pulse using concentrated-field electrode system," *IEEE Trans. Ind. Appl.*, vol. 37, no. 6, pp. 1646–1650, 2001.
- [32] U. Pliquet and J. C. Weaver, "Feasibility of an electrode-reservoir device for transdermal drug delivery by noninvasive skin electroporation," *IEEE Trans. Biomed. Engr.*, vol. 54, no. 3, pp. 536–538, 2007.
- [33] S. Beebe, P. Fox, L. Rec, K. Somers, R. Stark, and K. Schoenbach, "Nanosecond pulsed electric field (nsPEF) effects on cells and tissues: apoptosis induction and tumor growth inhibition," *IEEE Trans. Plasma Sci.*, vol. 30, no. 1, pp. 286–292, 2002.
- [34] M. Zamponi, R. Petrella, and P. A. Mollica, "Picosecond pulsed electric fields and promise in neurodegeneration research," *Bioelectricity*, vol. 3, no. 3, pp. 176–185, 2021.
- [35] G. Ghoshal, "Comprehensive review on pulsed electric field in food preservation: gaps in current studies for potential future research," *Heliyon*, vol. 9, no. 6, p. e17532, 2023.
- [36] R. Zhang, O. Parniakov, N. Grimi, N. Lebovka, L. Marchal, and E. Vorobiev, "Emerging techniques for cell disruption and extraction of valuable bio-molecules of microalgae *nannochloropsis* sp." *Bioproc. Biosyst. Engr.*, vol. 42, no. 2, pp. 173 – 186, 2019.
- [37] U. Roobab, A. Abida, J. S. Chacha, A. Athar, G. M. Madni, M. M. A. N. Ranjha *et al.*, "Applications of innovative non-thermal pulsed electric field technology in developing safer and healthier fruit juices," *Molecules*, vol. 27, no. 13, 2022.
- [38] M. Li, Z. Wang, R. Xu, X. Zhang, Z. Chen, and Q. Wang, "Advances in plasma-assisted ignition and combustion for combustors of aerospace engines," *Aerospace Sci. Technol.*, vol. 117, p. 106952, 2021.
- [39] Q.-Y. Han, X. Wen, J.-Y. Gao, C.-S. Zhong, and Y.-Y. Ni, "Application of plasma-activated water in the food industry: A review of recent research developments," *Food Chem.*, vol. 405, p. 134797, 2023.
- [40] P. Ranieri, N. Sponsel, J. Kizer, M. Rojas-Pierce, R. Hernández, L. Gatiboni *et al.*, "Plasma agriculture: Review from the perspective of the plant and its ecosystem," *Plasma Process. Polym.*, vol. 18, no. 1, p. 2000162, 2021.
- [41] Y.-L. Tsai, T.-C. Chang, Y.-C. Tsao, M.-C. Tai, H.-Y. Tu, Y.-T. Chien *et al.*, "Improving breakdown voltage in AlGaN/GaN metal-insulator-semiconductor HEMTs through electric-field dispersion layer material selection," *IEEE Trans. Device Mat. Reliab.*, vol. 21, no. 3, pp. 320–323, 2021.
- [42] W. A. de Groot, J. R. Webster, D. Felnhofer, and E. P. Gusev, "Review of device and reliability physics of dielectrics in electrostatically driven MEMS devices," *IEEE Trans. Device Mat. Reliab.*, vol. 9, no. 2, pp. 190–202, 2009.
- [43] A. Larsson, "Gas-discharge closing switches and their time jitter," *IEEE Trans. Plasma Sci.*, vol. 40, no. 10, pp. 2431–2442, 2012.

---

## CHAPTER 2

---

# Preliminaries and State of the Art

---

THIS chapter provides a review of relevant literature which pertains to the subject of the present work. Namely, the context within which this work sits—high voltage pulsed power technology and interfacial phenomena—are detailed, emphasis of which is placed on the foundational physical principles that underpin their application within engineered systems. Included are the fundamental concepts behind impulsive electric field behaviour in composite dielectrics, gaseous pre-breakdown and breakdown phenomena, and important physical processes present at dielectric interfaces. This review further encompasses classical and recent theories on (pre-)breakdown behaviours from both theoretical and experimental works while highlighting opportunities for further study, referring also to those addressed in the present work. The review of literature found in this chapter pertains to the overarching topic of this work which relates to transient electric field characteristics and (pre-)breakdown behaviours of gas, solid-gas, and solid-solid interfaces under impulse action and their associated physics. Targeted reviews of specific aspects (e.g., computational modelling schemes and methods as used in Chapter 5) are instead included at the beginning of the respective chapters for which these aspects are relevant. Sections 2.1 to 2.3 firstly focus on reviewing the physical preliminaries necessary to understand the origin of impulsive transient fields and interfacial phenomena under the context of pulsed power technology. Section 2.4 then provides a review of the current state of research and recent

---

This chapter was partially adapted, and may be quoted verbatim, from the following publication(s) with permission: T. Wong, I. Timoshkin, S. MacGregor, M. Wilson, and M. Given, “Dielectric Interfaces in HV Technology: Overview and Theoretical Approaches to the Modelling of Functional and Breakdown Behaviour,” *IEEE Electr. Insul. Mag.*, vol. 39, no. 4, pp. 34–49, Jun. 2023. © IEEE 2023.

**Table 2.1:** Typical electrical characteristics of pulses used across pulsed power applications, according to [1].

Energy per pulse	$1 - 10^7$ J
Peak power	$10^6 - 10^{14}$ W
Peak voltage	$10^3 - 10^7$ V
Peak current	$10^3 - 10^8$ A
Pulse width	$10^{-10} - 10^{-5}$ s

progress, both experimental and theoretical, that has moved towards deepening the understanding of impulse action on breakdown processes across solid-gas and solid-solid interfaces.

## 2.1 Pulsed Power and The Origin of Impulses

At the core of the present study resides the field of pulsed power science and technology, which has seen significant growth in recent decades within both small- and large-scale applications as outlined within Chapter 1. Regardless of the application, the core operating principle underpinning pulsed power technology is the rapid release of stored electrical energy accumulated over a comparatively long time. Consider the definition

$$P = \frac{dW}{dt}, \quad (2.1)$$

where  $P$  is the instantaneous power; expressed as the change in energy (work),  $W$ , over time,  $t$ . Equation (2.1) suffices to show that even a low amount of stored energy, if released sufficiently quickly, may result in significant peak power delivery. Ultimately, the optimal pulsed conditions in terms of energy, voltage, current, and power delivery depend entirely on the nature and purpose of the application. While the possible pulse parameters differ significantly between applications, Lehr and Ron [1] provided typical ranges of values which are tabulated in Table 2.1. For approximate requirements for specific applications, Schamiloglu *et al.* [2] provides a useful summary, their table of which has been reproduced as Table 2.2. Note particularly the wide range of parameters, spanning several magnitudes, that may be encountered for different applications.

Effective pulse generation technologies to achieve waveforms of the desired properties are equally as varied, with common systems including capacitive storage based Marx generators and Linear Transformer Drivers (LTD) [3, 4], inductive pulse transformers [5], and pulse-forming lines (PFL) [6]. The former two techniques and their derivatives are typical examples of energy

**Table 2.2:** Typical electrical characteristics required for common pulsed power applications, according to [2].

Application	Electrical Energy	Pulse Length	Peak Power	Burst Avg. Power
High Energy Density Plasma Physics	20 MJ	100 ns	> 10 TW	n/a
Intense Electron Beam Radiography	200 kJ	70 ns	< 1 TW	n/a
High Power Microwave (Narrowband)	10 kJ	100 ns	100 GW	100 kW
High Power Microwave (Ultra-Wideband)	10 J	1 ns	10 GW	10 kW
Ion Beam Modification of Materials	< 10 kJ	100 ns	30 GW	small
Bioelectrics	0.1 mJ–few J	10–100’s ns	10 kW–100 MW	mW–few W

accumulation followed by near-instantaneous release, while PFLs operate on the principle of electromagnetic wave interactions along transmission lines. The design and advancement of effective pulse generation systems itself forms an active area of research, with which the present work is largely unconcerned. The reader is referred to [1] and references therein for additional reading. Relevant, however, to the present work are the basic principles driving the operation of simple capacitive storage pulse generators and pulse formation using PFLs, which have either featured directly or have informed modelling decisions within this work.

### 2.1.1 Pulse Generation Through Capacitive Storage and Release

The straightforward generation of high voltage impulses may be achieved by exploiting capacitive energy storage elements and their subsequent discharge into the desired electrical load. The simplicity and well-understood dynamics of capacitive discharge enables the generation of tunable HV impulses with relative ease compared to more sophisticated designs [1]. Of particular importance is the case of the  $n$ -stage *Marx generator*, shown in Figure 2.1(a), which is able to deliver impulse waveforms based on the parallel charging of  $n$  capacitors that are subsequently discharged in series into the load. Figure 2.1(b) shows the equivalent circuit of the *erected* Marx (capacitors switched to be connected in series) assuming a capacitive load, which has a nominal peak voltage multiplication factor equal to  $n$ , resulting ideally in an open circuit load voltage of  $U_L = nU_0$ . Series connection of the  $n$  Marx stages is facilitated through a number of switches that fire sequentially or simultaneously. Traditionally, these are plasma-closing switches designed for high-speed and repeatable operation with low jitter (a measure of the deviation in the switch closure time), which is critical for erecting the Marx and achieving the desired voltage

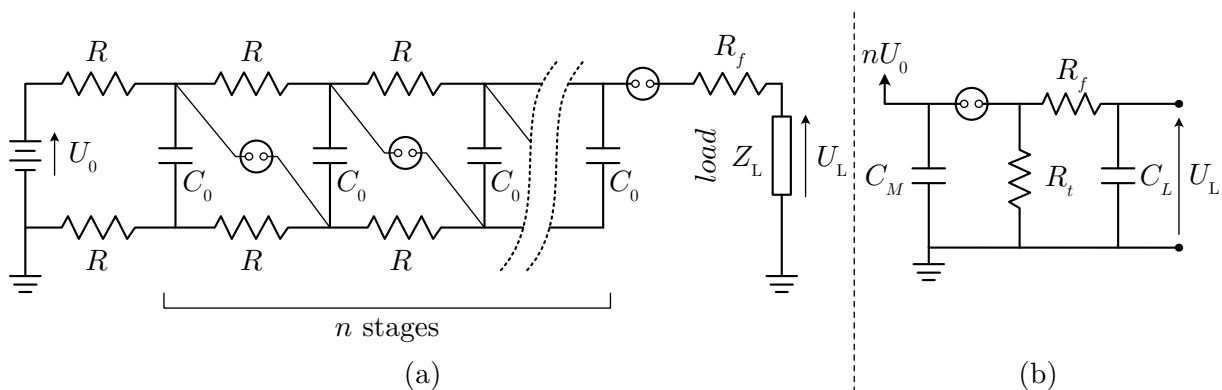


**Figure 2.1:** (a) Circuit diagram of an  $n$ -stage ideal Marx generator with charging resistances  $R$ , stage capacitance  $C_0$ , and front resistance  $R_f$ . (b) Equivalent circuit of an ideal erected Marx generator with erected capacitance  $C_M$  and tail resistance  $R_t$ , connected to a capacitive load  $C_L$  with load voltage  $U_L$ .

multiplication [1, 7–9]. However, recent advances have seen these replaced with solid-state power electronics within some compact applications [3, 10, 11].

The ideal Marx generator (in the absence of stray capacitance and inductance) delivers characteristic *double-exponential* output impulses based on the simple lumped-element analysis of the erected equivalent circuit of Figure 2.1(b). Following the analysis of [1], the resulting load voltage is given by

$$U_L(t) = \frac{nU_0(t)}{R_f C_L (\hat{\beta} - \hat{\alpha})} \left( e^{-\hat{\alpha}t} - e^{-\hat{\beta}t} \right), \quad (2.2)$$

where the waveshaping parameters  $\hat{\alpha}$  and  $\hat{\beta}$  determine the front and tail characteristics of the double exponential impulse and which are related to the circuit elements with

$$\begin{aligned} \hat{\alpha} + \hat{\beta} &= \frac{1}{R_f C_M} + \frac{1}{R_t C_M} + \frac{1}{R_f C_L}, \\ \hat{\alpha} \hat{\beta} &= \frac{1}{R_f R_t C_M C_L}, \\ t_p &= \frac{1}{\hat{\beta} - \hat{\alpha}} \ln \left( \frac{\hat{\beta}}{\hat{\alpha}} \right), \end{aligned} \quad (2.3)$$

where  $t_p$  is the peak time of the waveform. Equations (2.3) enable the selection of circuit element parameters to produce the desired transient characteristics of an output impulse. The introduction of the Marx generator formed a foundation for many subsequent pulse generation technologies developed using similar principles, and the exact expression for the produced double-exponential waveshape (2.2) is particularly convenient for modelling tasks within power and pulsed power

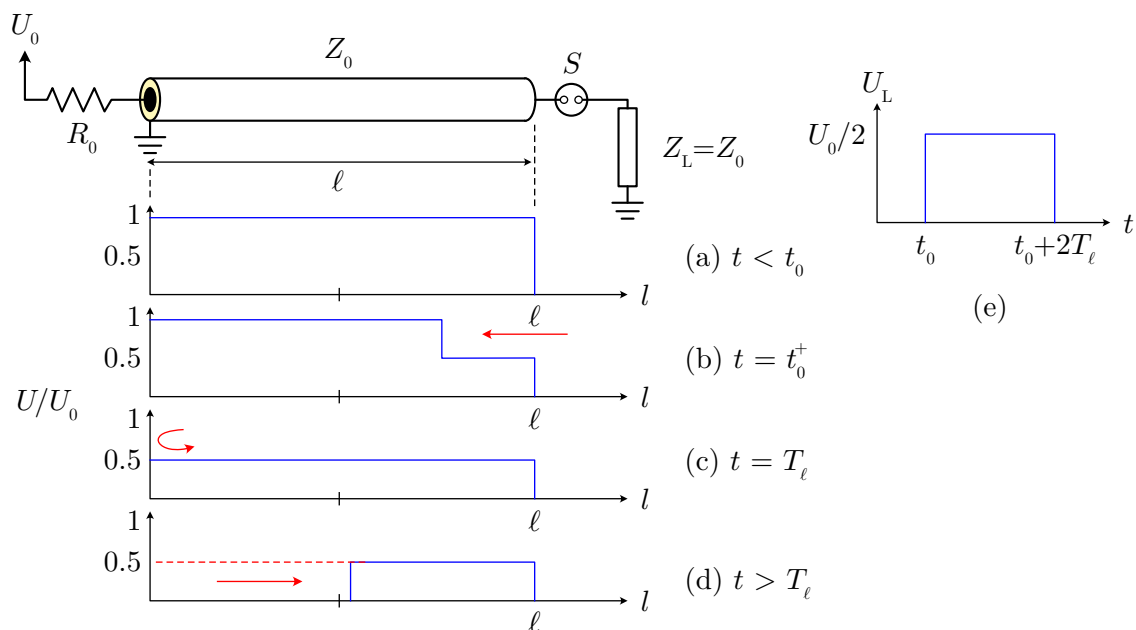


**Figure 2.2:** Circuit schematic of a single, matched-load, transmission line PFL, showing the ideal line voltage at times (a) before triggering: fully charged to  $U_0$ , (b) right after triggering: load-side wave propagating towards source, (c) after a time equal to one line delay: wave reflects back from source side, (d) some time after one line delay: reflected wave returns to load side. Sub-figure (e) shows the ideal pulse of width  $2T_\ell$ .

engineering disciplines. For instance, IEC-60060 [12] prescribes a  $1.2\ \mu\text{s}$  rise,  $50\ \mu\text{s}$  time-to-half impulse as standard for lightning impulse testing of power equipment which is well-represented in the double-exponential form.

### 2.1.2 Pulse Forming Using Transmission Lines

Of no less importance to pulsed power technology are pulse forming transmission lines. In contrast to the devices relying on capacitive storage and release, PFLs operate on the principles of electromagnetic wave propagation, reflection, and interference. Consider the simplest case of a single transmission line charged to a voltage  $U_0$  through charging resistance  $R_0$  and switched by an ideal switch denoted  $S$  to supply load  $Z_L$ , as shown in Figure 2.2. For a matched load  $Z_L = Z_0$ , where  $Z_0$  is the characteristic impedance of the transmission line, a voltage of  $U_0/2$  develops across the load ( $l = \ell$ ) upon switch closure. A  $-l$ -travelling wave also develops at this time with voltage  $-U_0/2$ , which takes a time  $T_\ell = \ell/v_\ell$  to reach the charging resistor, where  $\ell$  and  $v_\ell$  are the length and wave propagation velocity along the line, respectively. The reflection

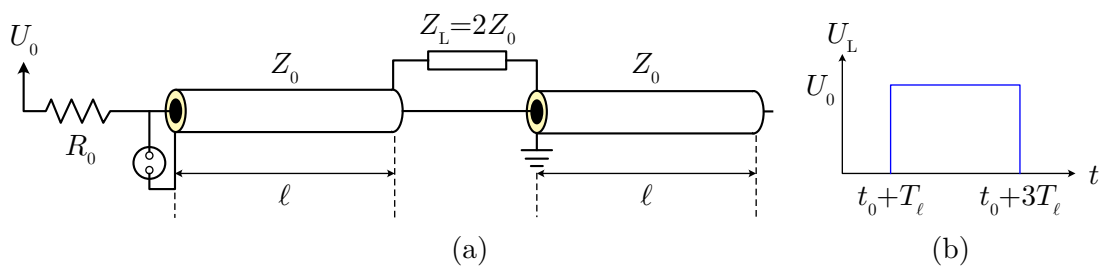


**Figure 2.3:** (a) Circuit schematic of matched-load Blumlein PFL, (b) ideal square impulse generated of  $2T_\ell$  pulse width at full charging voltage  $U_0$ .

coefficient

$$\Gamma = \frac{Z - Z_0}{Z + Z_0} \quad (2.4)$$

at the source is effectively 1 due to the far greater source impedance, fully reflecting the wave along the line until it reaches the load. The load voltage is sustained for a time equal to  $2T_\ell$  at  $U_0/2$  with an ideally square-pulse characteristic, as illustrated in Figure 2.2(a)–(e). Note that for a matched load, the load reflection coefficient  $\Gamma_L$  is zero, resulting in no additional reflections returning back onto the transmission line. For unmatched loads, some fraction of load-incident waves reflect back-and-forth along the line until they eventually dissipate. The relevant design parameters necessary for PFLs include the characteristic impedance,

$$Z_0 = \sqrt{\frac{L}{C}}, \quad (2.5)$$

where  $L$  and  $C$  are the inductance and capacitance of the line, respectively. The propagation velocity,  $v_\ell$ , is given by

$$v_\ell = \frac{c}{\sqrt{\mu_r \varepsilon_r}}, \quad (2.6)$$

where  $c$  is the speed of light, and  $\mu_r$ ,  $\varepsilon_r$  are the relative permeability and permittivity of the material used in the line construction.

PFL-based generators are often preferable for applications requiring considerably faster pulse delivery, as they mitigate limitations relating to inductance in, for example, Marx generators which may substantially limit pulse rise-times [1]. However, basic single-line PFLs as shown in Figure 2.2 are rarely used due to their low peak output voltage. The Blumlein PFL was developed to address this problem, which has since become ubiquitous within pulsed power technology. Figure 2.3 shows a basic schematic of a single Blumlein generator, comprised of two single PFLs on opposing sides of a central load. Upon switch closure, the operating principle

of a single Blumlein is identical to that of the PFL, with the exception that travelling waves are established on both transmission lines of equal length, interacting with the load in such a way that the full charging voltage  $U_0$  can be developed across a matched load for the same pulse width  $2T_\ell$ . Note that in this case a matched load is twice the characteristic impedance due to the additional line,  $Z_L = 2Z_0$ , and an additional line delay of  $T_\ell$  precedes the appearance of the pulse across the load, corresponding to the propagation time of the initial wave from source to load. Often, Blumlein generators are further combined in various arrangements to achieve some desired factor of voltage multiplication in so-called *stacked* Blumlein topologies [13–15]. In a manner reminiscent of the Marx generator principle, parallel Blumleins may equally be charged in parallel and released simultaneously to the load with a theoretical multiplication factor of  $n$  for  $n$  stacked Blumlein generators, though in practise, this factor is unavoidably lower due to inefficiencies.

Here, an overview of two essential pulse generation techniques has been conducted, systems of which are central to many pulsed power technologies. It is remarked that unlike systems found within, for example, the power industry, pulsed power technologies are not typically required to conform to standards in terms of waveform, materials, or construction. Effective characterisation of pulsed electrical stress on system components therefore presents a substantial challenge given the significantly greater number of possible combinations, configurations, and system characteristics. Some of these challenges are explored in greater detail within the following sections, which begin to focus on aspects of dielectrics, electrical insulation, and interfaces relating to high voltage equipment, and particularly, to pulsed power technology.

## 2.2 Dielectric Phenomena and Interfacial Behaviour

High voltage technologies, which encapsulates the applications of pulsed power, would not be possible without a deep understanding of the interaction between matter and electric fields. Of particular importance are dielectric materials for their role as electrical insulation, providing the backbone on which high voltage systems can safely and reliably operate. Challenges and shifts in global electricity generation, transmission, and distribution have shone a spotlight on the subject of dielectrics and interfaces, with great emphasis on insulation coordination for power systems. Substantial research effort has therefore been made to better understand dielectric breakdown and interfacial effects for voltage stresses relevant to power apparatus. This largely includes steady-state AC [16–19], long-term unipolar DC [20–23] (and related effects such as field inversion [24–26]), and a limited selection of standard impulses, e.g., lightning [27–30] or

switching impulses [31–33] (or some combination of the above standardised waveforms such as AC-DC or AC-LI superimposed voltages [34–37]).

Insulation often serves much the same purpose within pulsed power systems, however, the operation of many pulsed power systems (e.g., plasma-closing switches [38, 39] and pulsed plasma sources [40, 41]) also rely upon precise, controllable, and reliable electrical breakdown of dielectrics, as opposed to outright prevention. In addition, the problem of impulse breakdown is inherently time-dependent, thereby necessitating the lifting of steady-state assumptions when developing physical models or theories. Compounding this, non-standardisation and the many possible pulsed system configurations (as discussed within Section 2.1) often results in the inability to directly apply results arising from power-centric research without careful consideration. This section therefore concerns itself with the review of fundamental dielectric phenomena and effects present at dielectric interfaces, with emphasis on the incorporation of transience and time-dependency. This includes elements of the classical macroscopic theory of electromagnetism in continuous media and microscopic processes pertaining to charge sources and transport in the presence of interfaces. The phenomena described here is mostly limited to dielectric behaviour not concerning the initiation of pre-breakdown or breakdown phenomena, which is instead detailed from Section 2.3 onwards.

### 2.2.1 Dielectric Polarisation and Relaxation

The behaviour of linear isotropic media (which is assumed for all materials considered herein) under the effects of an electric field is governed by Maxwell’s equations. Of particular importance to multiple aspects of this work, Gauss’ Law (2.7) and the Ampère-Maxwell Law (2.8) may be written

$$\vec{\nabla} \cdot (\varepsilon_0 \varepsilon_r \vec{\mathbf{E}}) = \rho, \quad (2.7)$$

$$\vec{\nabla} \times \vec{\mathbf{H}} = \left[ \vec{\mathbf{J}} + \frac{\partial}{\partial t} (\varepsilon_0 \varepsilon_r \vec{\mathbf{E}}) \right], \quad (2.8)$$

where the terms  $\vec{\nabla} \times \vec{\mathbf{H}}$ ,  $\vec{\mathbf{J}} = \sigma \vec{\mathbf{E}}$ , and  $\partial/\partial t (\varepsilon_0 \varepsilon_r \vec{\mathbf{E}})$  represent the total, conduction, and displacement current densities, respectively, and  $\rho$  is the space (volumetric) charge density. Symbols  $\vec{\mathbf{H}}$  and  $\vec{\mathbf{E}}$  are the magnetic and electric fields, respectively. Materials are characterised by their permittivity,  $\varepsilon$ , and electrical conductivity,  $\sigma$ , which determine their response to an applied electric field. Note that the permittivity is more often given as the non-dimensional *relative permittivity*,  $\varepsilon_r$ , such that  $\varepsilon = \varepsilon_0 \varepsilon_r$ , where  $\varepsilon_0$  is the permittivity of free space. In

this text the notation  $\varepsilon_i$ , where  $i$  may be a non-zero integer or letter, denotes the *relative* permittivity in a region assigned the symbol  $i$ . The presence of an external electric field induces the alignment of bound charges and the transport of free charges, giving rise to displacement and conduction currents, respectively. When considering time-dependent field quantities, an important consequence of (2.7) and (2.8) is

$$\frac{\partial \rho}{\partial t} = -\frac{\sigma}{\varepsilon_0 \varepsilon_r} \rho = -\vec{\nabla} \cdot \vec{\mathbf{J}} = -\vec{\nabla} \cdot (\sigma \vec{\mathbf{E}}), \quad (2.9)$$

for homogeneous materials, which takes the form of a first-order relaxation equation with time constant  $\tau = \varepsilon_0 \varepsilon_r / \sigma$ , indicating some form of delay in the response of the medium when subjected to time-varying electric fields with a characteristic time related to its electrical properties. Based on (2.9), this time delay is manifested due to the finite time necessary for charge transport and accumulation. The result (2.9) is crucial for the characterisation of matter under time-dependent electric field action as it underpins the relaxation behaviour of spatially-inhomogeneous materials with non-zero electrical conductivity. In the most general case, i.e., assuming neither limit of ideal conductor ( $\sigma \rightarrow \infty$ ) nor ideal dielectric ( $\sigma \rightarrow 0$ ) is applicable, (2.9) governs the transport and accumulation of charges based on the balance of current density at any point within the medium. Ultimately, the self-consistent solution of Maxwell's equations enable the prediction of electric fields within a specified domain of interest.

Interfaces formed between two or more materials with different characteristics can be considered a limiting case of spatially-inhomogeneous media, in that the material properties exhibit a step change at the interfacial boundary. It is instructive to consider the simplest case of two different contacting materials with an electric field applied perpendicular to the interface, as shown in Figure 2.4. For (2.9) to hold across the discontinuity where the current densities  $\vec{\mathbf{J}}_1$  and  $\vec{\mathbf{J}}_2$  are unequal, the conservation of charge dictates that charge must necessarily be accumulated at the interface. Under the simplification that charges only exist and accumulate directly at the interfacial boundary, (2.9) gives the interfacial charging time as the elementary result

$$\tau_{MW} = \frac{\varepsilon_2 d_1 + \varepsilon_1 d_2}{d_1 \sigma_2 + d_2 \sigma_1} \varepsilon_0, \quad (2.10)$$

where  $\tau_{MW}$  is known as the Maxwell-Wagner relaxation time constant, after the effect going by the same name, and  $d_{1,2}$  are the sample thicknesses. Notably, the relaxation characteristic of a simple two-layer system is dependent on the properties of both layers, which in part also determines the time-evolution of the electric fields uniquely developed inside each layer. In dealing with time-dependent impulsive voltages, dielectric relaxation and the Maxwell-Wagner

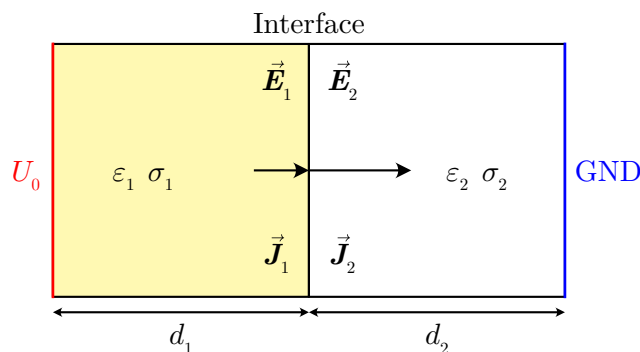


**Figure 2.4:** Textbook example of Maxwell-Wagner polarisation at an interface between two poorly-conducting materials. If the conduction currents  $\vec{J}$  are mismatched, free surface charge accumulates at the interface.

effect can therefore have considerable effects on the response of composite systems comprised of multiple different materials. Since the time evolution of the electric field may be influenced by this phenomenon, so too may the breakdown characteristics of the medium considering that electrical breakdown is principally induced by the electric field. The convenience stemming from the simplicity of this approach has promoted its application as a model within a number of areas, including PEF technology [42–45], HV cable development [46, 47], and for energy storage applications [48]. In Chapter 3, this idea is explored in greater detail through extended mathematical modelling of the Maxwell-Wagner process, generalised for the first time to complex multilayered geometries.

### 2.2.2 Charge Sources, Sinks, and Transport at Solid-Gas Interfaces

Within the interfacial component of this work, focus was placed on solid-gas and solid-solid interfaces, where the leading theory of breakdown for the latter was also considered gas-driven through the mechanism of interfacial void discharge (see the later Section 2.4.2 for details). The case of the solid-gas interface is therefore of particular relevance and importance to the body of work presented here, where much of the modern understanding stemmed from the earlier descriptions of Sudarshan and Dougal [49], with more recent developments comprehensively discussed within Li *et al.* [50]. Specific characteristics that relate to solid-gas interfaces which impact on the production, reduction, or transport of charge; or ultimately influences the breakdown dynamics, are detailed in the following section. Mechanisms specific to surface flashover, however, are discussed in Section 2.4.1. For convenience, labelled illustrations have been provided as Figure 2.5, to which the subheadings refer in the descriptions given here.

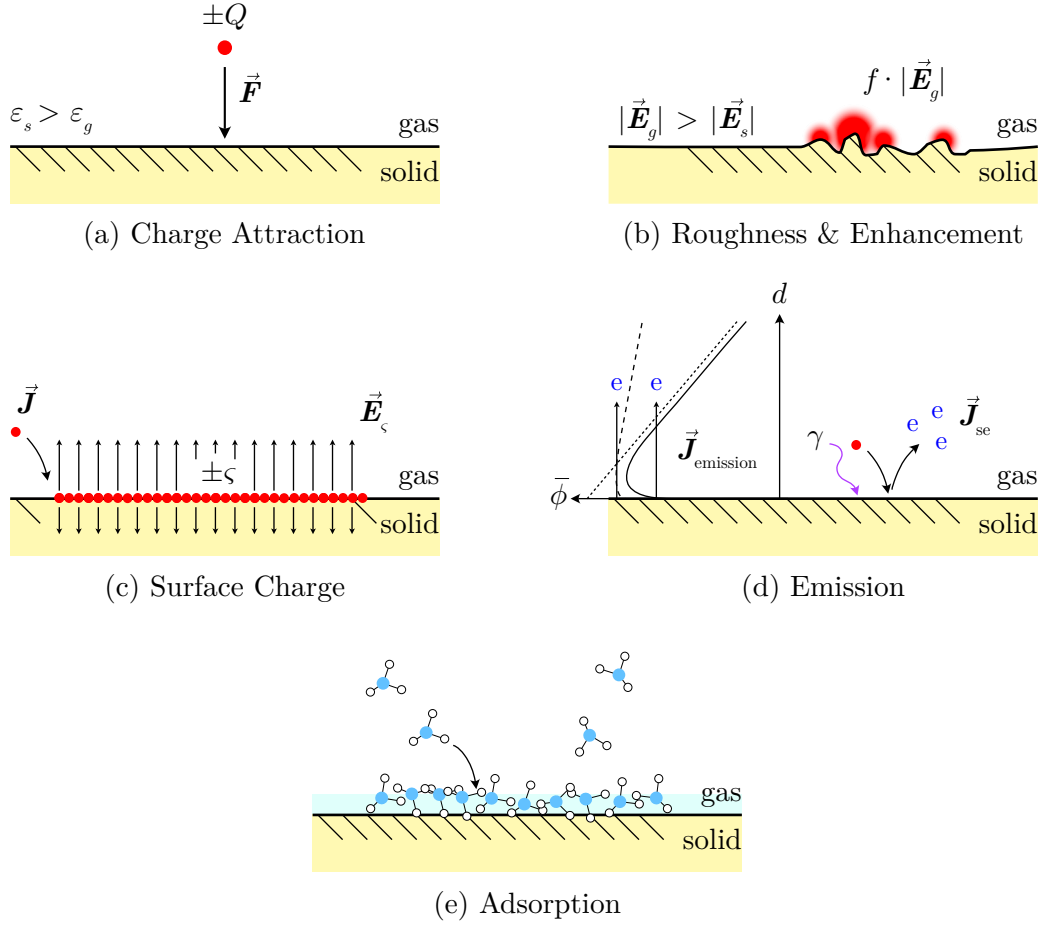


**Figure 2.5:** Mechanisms present at solid-gas interfaces acting as charge sources, sinks, or that may influence charge transport dynamics. Detailed discussions given in main text, labelled in correspondence with this figure.

### (a) Dielectric Attraction of Charges

First and foremost, a point charge  $Q$  inside a gaseous medium (relative permittivity  $\epsilon_g = 1$ ) located at distance  $d$  from a dielectric with  $\epsilon_s > 1$  [as shown in Figure 2.5(a)] experiences a force of attraction,  $F$ , towards the dielectric due to polarisation, with the magnitude [51]

$$F = \frac{Q^2 \epsilon_s - 1}{4d^2 \epsilon_s + 1} \quad (2.11)$$

which is independent of charge polarity. Therefore, in absence of other competing forces, charged species—whether pre-existing or produced due to gas discharge events—tend to move towards solid dielectrics and impinge on their surfaces. It should be noted that this does not stipulate that all charges must therefore be moving towards a dielectric surface at all times, as other

external forces directed away from the surface may be dominant.

### (b) Field Enhancement and Surface Morphology

When considering equation (2.8) and the condition of current continuity across a discontinuous interface, it implies that

$$\left(\vec{J}_1 + \frac{\partial \vec{D}_1}{\partial t}\right) \cdot \hat{n} = \left(\vec{J}_2 + \frac{\partial \vec{D}_2}{\partial t}\right) \cdot \hat{n} \quad (2.12)$$

must hold at an interface between the materials identified by the subscripts 1 and 2. Symbol  $\vec{D}$  is the electric displacement and  $\hat{n}$  is the surface normal perpendicular to the interface. Even in the absence of unbound charges (and thus no conduction current), (2.12) reduces to the elementary  $\vec{D}_1 \cdot \hat{n} = \vec{D}_2 \cdot \hat{n}$  stipulating the continuity of electric displacement, where  $\vec{D} = \epsilon_0 \epsilon_r \vec{E}$ . From these familiar boundary conditions, electric fields developed within the dielectric possessing the lower permittivity *enhances*, due to the requirement for the displacement field to be continuous across the interface. The larger the difference in  $\epsilon_1$  and  $\epsilon_2$ , the greater the degree of field enhancement. System geometry may also influence the severity of enhancement, including features such as triple junctions [52] or irregular and high aspect ratio features [53].

Along similar lines, the surface condition of solid dielectrics in a solid-gas system may have considerable impact on charge generation and transport. This may refer to non-ideal surface roughness found on all practical surfaces, or to intentional surface modifications that may be introduced for various purposes. Multiple effects can result from irregular surface texture. For one, electric fields become enhanced in the near vicinity of irregularities or high aspect ratio surface features as described above. Inevitable rough-surface features exposed at solid-gas interfaces may therefore cause significant localised distortion or enhancement, potentially influencing the overall system breakdown characteristics. The exact nature of these effects are specific to the system geometry involved, and where the above-described mechanisms may be of various levels of impact. In Section 2.4, a review of breakdown across solid-gas and solid-solid interfaces is provided, encompassing experimental breakdown studies along with current theories behind the observed breakdown behaviours. This includes recent efforts attempting to exploit engineered surface features as a potential method to *increase* surface flashover strength. The studies presented as Chapter 7 and 8 of this work were also focused on methods to characterise rough-surface geometry in order to quantify its effects on interfacial breakdown behaviour.

**(c) Surface Charging**

Incident charge fluxes impinging on a solid surface may lead to the deposition of free surface charge. Consider that (2.12) with (2.9) in the presence of free charges yields the more general condition

$$\left(\vec{D}_2 - \vec{D}_1\right) \cdot \hat{n} = \varsigma, \quad (2.13)$$

where  $\varsigma$  is the free surface charge density developed at the interface. Allowed to accumulate, the induced electric field due to the presence of these charges may become significant, locally distorting or enhancing the net electric field near the surface. In practise, HV insulators possess non-zero electrical conductivity and are classified as poorly-conducting. Deposition of any form of charge, surface-bound or otherwise, may require significant time to naturally decay, potentially impacting the insulator's performance. Studies suggest that repeated partial or complete discharges (as is often intentional in many pulsed power systems) may result in significant surface charge accumulation across solid surfaces [54–56], with the potential to modify the subsequent breakdown behaviour of the same system [56–59]. Following from the classical argument of the Gaussian pillbox, a local value of surface charge density  $\varsigma$  induces an electric field immediately above or below the surface as given by

$$\vec{E} = \frac{\varsigma}{2\varepsilon_0\varepsilon_r} \cdot \hat{n}, \quad (2.14)$$

where  $\hat{n}$  is the surface normal, and is valid for a point on any surface geometry considering an infinitesimal region around said point\*. Pedersen and Blaszczyk [60] has used this approach to estimate *saturation* charge values in the context of discharge-induced surface charging, providing a means to estimate the maximum levels of surface charge required to prevent additional surface charging. The method has since been adopted by Meyer *et al.* [61] for the investigation of surface discharges and re-strike behaviour. It is also noted that surface *trapping* and *de-trapping* mechanisms, referring to the capturing and release of charges due to imperfections, impurities, or defect sites on the solid surface, may additionally influence the dynamics of surface charge accumulation [62]. These processes are of particular importance for long-term steady-state energisation regimes, as the balance of trapping and de-trapping rates may influence the accumulation of volumetric charge [63]. As part of a series of computational studies associated with the present work, a study on the influence of a non-uniform distribution of surface charge on primary surface discharge behaviour is detailed within Chapter 6.

---

\*Note that when considering charged conductors of finite thickness, an additional factor of 2 arises such that  $\vec{E} = \varsigma/\varepsilon_0\varepsilon_r \cdot \hat{n}$ .

**(d) Emission Mechanisms at Electrodes and Dielectric Surfaces**

As will be made clear in Section 2.3, inception of discharges in gas and along solid surfaces relies upon the existence of an initial source of electrons. The subsequent evolution and propagation of discharges is also reliant upon being continuously fed by produced charges, the main generation mechanisms of which are detailed in Section 2.3. The presence of solid-gas interfaces may contribute, in several ways, as an initial or continuous charge source which may influence the breakdown properties of the system. These are discussed here under the broad term of *surface and secondary emission* processes, in reference to electron emission due to the presence of a solid surface due to various phenomena.

Relevant mainly to metallic surfaces (e.g., electrodes), high temperatures may induce *thermionic emission* of electrons from metal surfaces should the electron become sufficiently energetic to overcome the material *work function*,  $\bar{\phi}$ . Leading theories for the thermionic emission current density generally admit the form [64]

$$J_{\text{thermionic}} \propto T^2 \exp\left(\frac{-\bar{\phi}}{k_b T}\right), \quad (2.15)$$

where  $T$  is the temperature and  $k_b$  is the Boltzmann constant. Over time, the constant of proportionality has been subject to modifications and corrections based on advances in quantum-mechanical understanding [65, 66] and also material-specific properties [67, 68]. Under combined thermal and electric fields, the related *Schottky effect* may be used to describe the emission effect with the corresponding injection current

$$J_{\text{Schottky}} \propto T^2 \exp\left[\frac{-(\bar{\phi} - \Delta\bar{\phi})}{k_b T}\right], \quad (2.16)$$

where the modification,  $\Delta\bar{\phi}$ , to the effective work function describes the phenomena of barrier lowering due to the applied electric field, facilitating the escape of the electron from the surface.

Under strong electric fields ( $\gtrsim 10^7$  V/cm [69]), the potential barrier may become sufficiently distorted as to substantially increase the probability of quantum tunnelling. The phenomena of *field emission* was known experimentally but not understood until Fowler and Nordheim [69], who successfully explained the phenomena using the, at the time, recently developed quantum theory based on exact solutions to the Schrödinger equation. They predicted the tunnelling of electrons through a field-modified potential barrier based on the quantum wavefunction, which showed the non-zero and field-increasing probability of electron escape that would have otherwise

been impossible based on classical physics. The Fowler-Nordheim type equations of the form

$$J_{\text{FN}} \propto \frac{|\vec{E}|^2}{\bar{\phi}} \exp\left(\frac{-c\bar{\phi}^{3/2}}{|\vec{E}|}\right) \quad (2.17)$$

were developed (and subsequently improved in [70] and references therein) and were found to describe the field-emission current density, where the associated constant of proportionality and the parameter  $c$  are material-dependent. Note that due to local field enhancement that may result from surface irregularities or asperities, the magnitude of an applied electric field may not need to be above the field emission threshold. Localised emission may still occur depending on the degree of local field enhancement.

Electron emission may also result from the bombardment of a solid surface with other charged species or photons, corresponding to the general phenomena of *secondary emission* (where the latter may also be referred to as *photoemission*). Incident ions, electrons, or photons with sufficient energy may liberate electrons from the material surface with some yield, typically assigned the symbol  $\gamma_{\text{se}}$ , describing the average number of electrons produced per unit incident ion or photon flux. Sources of surface-incident fluxes are described in more detail within the discussion of the gas discharge process included as Section 2.3. In general, a secondary emission current may then arise of the form

$$J_{\text{se}} = \sum_i \gamma_i \bar{J}_i, \quad (2.18)$$

where the sum over  $i$  runs over all possible secondary emission sources with yields  $\gamma_i$  resulting from the surface-directed flux  $\bar{J}_i$  impinging on the surface. At the time of writing, ion-impact secondary electron yields remain poorly characterised for many materials, as are the effects and yields due to photoemission, with studies reporting a large possible range of values, see for example, [57, 71–73]. This is primarily due to the difficulty in obtaining a complete fundamental description of secondary emission that successfully captures the effects such as incident angle, scattering, material structure, and more. The reader is referred to comparisons of different approaches in Dionne [74] including commonly used semi-empirical equations developed by the same author. Secondary emission, however, undoubtedly forms an area of continued interest that would be of great benefit if further addressed.

### (e) Gas Adsorption

Recent works by Li *et al.* [75] and Li *et al.* [76] have theorised that the adsorption of gas molecules at the solid surface leads to the formation of a *gas adsorption layer* across the surface. Their

measurements suggest that the gas adsorption layer is of higher density than the bulk gas, and is the main region in which surface discharges propagate. Li *et al.* [76] suggests that despite the higher pressure region, adsorbed gas may increase the efficiency of charge trapping, distorting the local surface field. They argue this may further influence electron emission rates from the surface, substantially affecting any charge transport, pre-breakdown, or breakdown processes occurring at the interface. This theory, however, is a recent development and the extent of its influence on the overall characteristics of surface discharge evolution has yet to be fully explored.

### 2.3 Pre-breakdown and Breakdown Processes in Gas

In the broadest sense, the term *electrical breakdown* describes the abrupt transition of a normally insulating medium to an electrical conductor under the application of a potential difference. Insulators limit the ability for electrical currents to conduct due to the negligible number of unbound electrons available in their atomic structure. To become a good conductor, the applied potential difference must somehow induce a sudden and significant increase (of several magnitudes) in the number of unbound electrons. The source of these electrons and the nature of their growth forms the basis of any study relating to electrical breakdown phenomena.

As was previously mentioned, the electrical breakdown component of the present work focused on gas, solid-gas, and solid-solid interfaces. The occurrence of dielectric breakdown in all three cases is predominantly associated with gas discharge, though the latter two are aided by the various surface effects described in Section 2.2.2. It is therefore instructive to provide a review of the fundamental concepts behind pre-breakdown and breakdown events in gases alone as the commonality linking between these types of composite system. The current understanding of breakdown mechanisms specific to solid-gas and solid-solid interfaces are discussed further in Section 2.4.

In this section, the subject is limited to gaseous dielectrics where the electronic source is well-known to be predominantly impact ionisation. From the initial electron through to the development of highly energetic and thermalised plasma arcs, this section provides an overview of the current understanding of gas breakdown phenomena, detailing the stages of their development based on classical theories and recent advances in understanding.

### 2.3.1 The Initial Electron

Initiation of a gas discharge requires three primary ingredients: (a) a sufficiently strong electric field, (b) initial electrons, and (c) electron multiplication. Evidently, the converse is also true: to reduce the probability of breakdown in HV systems, one would aim to reduce peak electric field stresses, remove electron sources, and suppress discharge development and growth. These aspects form the basis to all HV insulation technologies and inform design decisions in, for example: the choice of gas used within gas-insulated equipment [77]; the design of field grading materials [78]; or in the development of vacuum-insulated systems [79]. In practise, initial electrons will inevitably exist within any insulating medium, due to the many unavoidable electron sources. These include natural cosmic radiation [80], spontaneous emission and photoionisation [81], or injection from electrodes and nearby surfaces, several mechanisms of which were discussed in Section 2.2.2. Some of these sources are stochastic in nature and difficult to fully characterise, such that it remains a challenge to quantify both the spatial distribution of background electrons and the distribution of their time of appearance. The existence of initial electrons is crucial to understanding the *statistical time lag* associated with electrical breakdown, which refers to the time delay between the application of an external field and the appearance of an initial electron that begins the breakdown process. Within experimental work, the total time-to-breakdown,  $t_b$ , is typically measured between the moment of voltage application to the moment of voltage collapse (see Chapter 7 and 8 for experimental work relevant to these aspects), which may be considered as a composition of several distinct time delays, following

$$t_b = t_s + (t_{av} + t_{st} + t_{th}) = t_s + t_f, \quad (2.19)$$

where  $t_s$  is the statistical time lag;  $t_{av}$  is the time associated with initial electron multiplication processes;  $t_{st}$  is the streamer propagation time, relating to a phase of space charge dominated transport and establishment of an initial conductive channel; and  $t_{th}$  may be interpreted as the time required for the thermalisation of the channel on its transition to a spark. The exact processes pertaining to each of these stages are detailed in the sections that follow. The total time  $t_{av} + t_{st} + t_{th}$  is often referred to collectively as the *formative breakdown time*,  $t_f$ . In pulsed breakdown experiments, it is often assumed (and suggested by breakdown results, e.g., in [82]) that the statistical time dominates the total measured time-to-breakdown, such that  $t_s \gg t_f$  and where  $t_f$  is approximately constant for the same breakdown configuration. Progress has nevertheless been made towards characterising the statistical time, for example, in computational studies utilising Monte-Carlo methods in attempt to understand the distribution of statistical

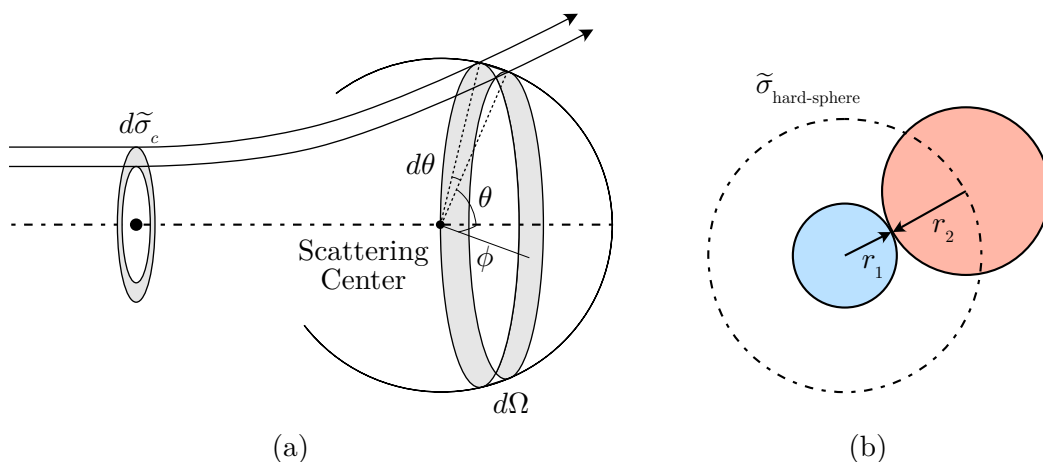


**Figure 2.6:** (a) Diagram illustrating the classical treatment of collisional cross-sections, based on the differential cross section integrated over the solid angle [84]. (b) Depiction of the hard-sphere approximation as a useful simplification of the scattering cross sections of particles.

time lags within simple systems [83].

For theoretical purposes, models concerned with the development of gas discharges typically assume that an initial electron (or distribution of electrons) already exists, disregarding the exact details of its origins. These initial electrons are also assumed to always lead directly to the pre-breakdown or breakdown process under study, which may not necessarily be true in practise. For practical breakdown, unless specific measures (e.g., irradiation using an ultraviolet light source) are taken to ensure sufficient pre-ionisation, a statistical time lag is unavoidable and can only be quantified in terms of a distribution due to its stochastic nature.

### 2.3.2 Gas Kinetics and Collisions

Suppose that an initial electron is accelerated by an applied electric field and begins its transport through a gas. Electron-neutral collisions will take place determined by the density of gas molecules and the *collisional cross sections*,  $\tilde{\sigma}_c$ , between the electron and neutral, which may be elastic or inelastic in nature. The classical treatment of collisional cross sections stems from the analysis of *scattering* by considering a two-particle (binary) interaction, depicted in Figure 2.6(a). A general form for the total scattering cross section is given as in [84] to be an integral of the *differential cross section*,  $d\tilde{\sigma}_c/d\Omega$ , over the entire solid angle ( $d\Omega = \sin\theta d\theta d\phi$ ) such that

$$\tilde{\sigma}_c = \int_0^{2\pi} \int_0^\pi \frac{d\tilde{\sigma}_c}{d\Omega} \sin\theta d\theta d\phi. \quad (2.20)$$

Various approximations for the differential cross section exist, which range from simple hard-sphere collision models derived from classical mechanics to complex descriptions such as the Born-Bethe approximation arising from quantum theory, which is accurate for high-energy collisions. For a detailed review of various scattering theories and models, the reader is referred to [84]. For engineering purposes, the simplest definition for  $\tilde{\sigma}_c/d\Omega$  as provided under the hard-sphere approximation suffices, such that [84]

$$\frac{d\tilde{\sigma}_c^{\text{hard-sphere}}}{d\Omega} = \frac{1}{4}(r_1 + r_2)^2 \quad (2.21)$$

which when evaluated using (2.20) (assuming also that scattering in the azimuth angle,  $\phi$ , is isotropic) provides the cross section as

$$\tilde{\sigma}_c^{\text{hard-sphere}} = \pi(r_1 + r_2)^2, \quad (2.22)$$

giving the area around a particle-pair with radii  $r_1$  and  $r_2$ , respectively, and which would result in direct collision, as illustrated in Figure 2.6(b). Collisions occur stochastically and are collectively characterised by the *mean free path*,  $\ell_m$ , describing the mean distance travelled between collisions, given by

$$\ell_m = \frac{1}{\tilde{\sigma}_T N}, \quad (2.23)$$

where  $N$  is the neutral gas density and  $\tilde{\sigma}_T$  is the total collisional cross section. Collisions act to change the particles' energy, velocity, and deflection of its trajectory; the probabilistic nature of collisions, and sheer number of particles within a gas, renders it virtually impossible to predict the behaviour of an ensemble of particles within practical gas volumes based on per-particle interactions. The field of *statistical mechanics* addresses this by alternatively describing large systems of particles in terms of probability distributions. The kinetic Boltzmann equation [85] describes the collective evolution of interacting particles in a 6-dimensional momentum-position phase space, valid even when the system is in thermodynamic non-equilibrium, according to

$$\frac{\partial f}{\partial t} + \frac{\vec{p}}{m} \cdot \vec{\nabla} f + \vec{F} \cdot \frac{\partial f}{\partial \vec{p}} = \left( \frac{\partial f}{\partial t} \right)_{\text{coll}}, \quad (2.24)$$

where  $f(\vec{r}, \vec{v}, t)$  is the phase-space distribution function with  $\vec{r}, \vec{v}$  being the position and velocity vectors, respectively, and  $t$  is time. Symbol  $\vec{p} = m\vec{v}$  is the momentum,  $m$  is the particle mass, and  $\vec{F}$  represents the exertion of an external force. For charged particles,  $\vec{F}$  is often the Lorentz force  $\vec{F} = q\vec{E} + \vec{v} \times \vec{B}$  where  $q$  is the electric charge and  $\vec{E}, \vec{B}$  are the electric field and magnetic flux density, respectively. The right-hand term represents the change to the distribution  $f$  due

to collisions. For ideal gases at thermodynamic equilibrium, Chapman-Enskog theory shows that (2.24) yields the Maxwell-Boltzmann distribution [86],

$$f_{MB} = 4\pi v^2 \left( \frac{m}{2\pi k_b T} \right) \exp \left( -\frac{mv^2}{2k_b T} \right), \quad (2.25)$$

of velocities and energies, where  $k_b$  is the Boltzmann constant and  $T$  is the kinetic temperature. Gases and plasma whose constituent particles follow the distribution (2.25) are referred to as *Maxwellian*, with the corresponding term *non-Maxwellian* used for those whose distributions may stray significantly from the form of (2.25) [87,88].

For charged particles (e.g., an initial electron) accelerated by an electric field through a sea of neutral gas molecules, collective *swarm* parameters can be computed from the solution of (2.24) over the many collisions and interactions the particle may engage in along its path of travel [89]. These parameters characterise the transport of these charges on an averaged basis. Of particular importance within the context of this work, the *mobility*,  $\mu_i$ , of a charged particle  $i$ , characterises the average *drift velocity* of charges when advected by an electric field,  $\vec{E}$ , according to

$$\vec{v}_i = \mu_i \vec{E} \quad (2.26)$$

and which is dependent on the type of particle and frequency of collisions along its path. Collisions also determine the net energy gain or loss over the duration of a particles' transport. In this case, if sufficient energy is gained by the initial electron to breach the ionisation energy threshold of the gas, collisions with neutrals may be *ionising* and so establishes a basis from which electron multiplication—thus electrical breakdown—may eventually occur, as explained in the following sections.

### 2.3.3 The Electron Avalanche

Should the electric field be sufficiently strong to accelerate electrons beyond the ionisation energy of the gas, ionising collisions of the form



where  $M$  is an arbitrary neutral gas atom or molecule, can begin to occur. Additional electrons produced from (2.27) may be further accelerated by the field, ultimately causing an electron multiplication process known as the *electron avalanche*, reported originally by Townsend [90] and

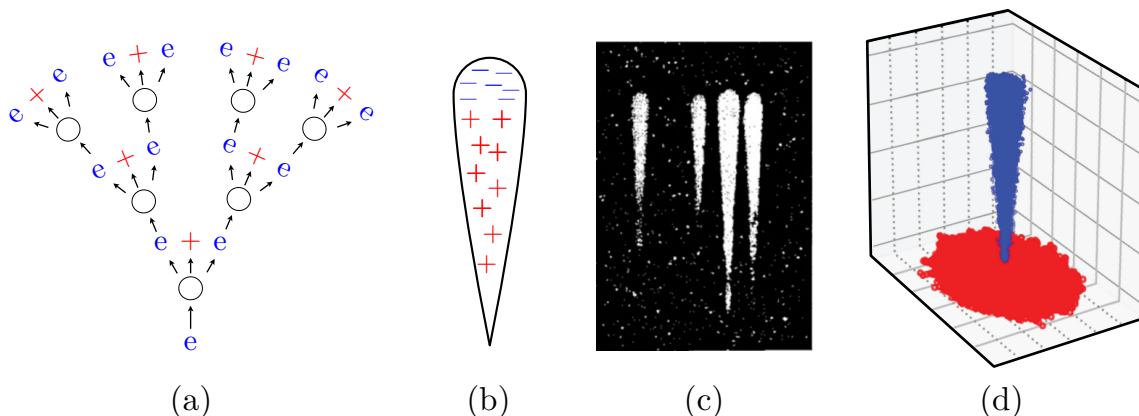


**Figure 2.7:** Various depictions of Townsend’s electron avalanche. (a) Tree-like diagram showing the exponential growth of electrons due to impact ionisation, (b) typical rendering of a developing electron avalanche, showing the distribution of charges, (c) electron avalanches imaged using a cloud chamber by Raether [91], (d) simulated electron avalanche from Jovanović *et al.* [83] using particle-based kinetic methods. Image (d) adapted from [83] under CC BY 4.0.

depicted in various forms within Figure 2.7. Thus was discovered the basic process driving gas discharges, and from whom the basic type of *Townsend Discharge* received its name. Townsend deduced, for the first time, a description for electron growth [90],

$$\frac{dn_e}{dx} = \alpha n_e, \quad (2.28)$$

describing the exponential growth in the number of electrons,  $n_e$ , travelling in the  $x$ -direction between two plane electrodes and where  $\alpha$  is the *ionisation coefficient*, describing the number of electrons per unit length produced due to collisional ionisation. Exponential electron growth from electron avalanches would provide the source of electrons necessary for the initially insulating gas to begin its transition towards becoming conductive, giving rise also to a measurable discharge current. Holst and Oosterhuis [92–94] later found that should positive ions remaining from the collisional process have sufficient time to return to the cathode, the liberation of secondary electrons (as described in Section 2.2.2) from their bombardment with the electrode surface<sup>†</sup> may fuel a self-sustaining mode of discharge that would not depend on an external current source (also referred to as *ignition*).

<sup>†</sup>Note that Townsend [90] originally assumed the secondary source of negative charges would be produced simply due to positive charges ionising other neutrals rather than from collision with the cathode. Townsend characterised this process using individual per-unit-length  $\alpha$  coefficients for the ionisation rates for both positive and negative charges.

The growth of the discharge current,  $I$ , was deduced as

$$I = I_0 \frac{e^{\alpha d}}{1 - \gamma(e^{\alpha d} - 1)} \quad (2.29)$$

for a uniform field between plane electrodes separated by distance  $d$ . The symbol  $\gamma$  is the secondary emission coefficient as described in Section 2.2.2, and  $I_0$  represents an initial current injected through stimulated photoemission or otherwise. Townsend [90], Holst and Oosterhuis [92–94] recognised that the singular solution to (2.29) corresponded to a case where unbounded current growth becomes possible disregarding the presence of an external source, thus establishing a theoretical condition for a self-sustaining discharge as  $\gamma(e^{\alpha d} - 1) = 1$ .

In the modern view, Townsend discharge is characterised by the Townsend ionisation coefficient  $\alpha$ , attachment coefficient  $\eta$ , and secondary emission coefficient,  $\gamma$ . The first was previously described as the number of electrons produced due to collisional ionisation per unit length, while the second characterises the number of electrons lost to attachment processes, also per unit length. The coefficients  $\alpha$  and  $\eta$  are often combined as the *effective* ionisation coefficient,  $\bar{\alpha} = \alpha - \eta$  indicating the net number of electrons produced per unit length and which, in general, is dependent on the the type of gas, the thermodynamic conditions of the gas, and the applied electric field. The field value where  $\bar{\alpha} = 0$  is referred to as the *critical field* of the gas—the threshold field value where ionisation balances attachment. Beyond the critical field, exponential electron growth—and electrical breakdown—becomes possible.

### 2.3.4 Fast Transient Ionisation Fronts and Streamer Discharges

Outside of experimental conditions similar to those of Townsend, limitations to Townsend’s theory soon became apparent. According to Townsend’s avalanches, discharges propagate at the electron drift velocity solely driven by the acceleration imparted by the external field. Observations previous [95] and subsequent [96] to Townsend’s theory described a class of highly energetic gas discharge that developed rapidly, far exceeding that of drift velocity, that prompted further investigation. These were successfully described following the work of Loeb, Meek, and Raether [91,97–99] as the *streamer discharge*, corresponding to self-sustaining wavefronts driven by intense impact ionisation. Included as Figure 2.8 are experimentally-imaged streamer discharges, made possible due to advancements in instrumentation and diagnostics. The proposed mechanism begins initially as an electron avalanche, however, under configurations where a propagating avalanche is allowed to continuously grow—and the density of free charge increases beyond a certain threshold—the space charge induced field must also be considered as it begins

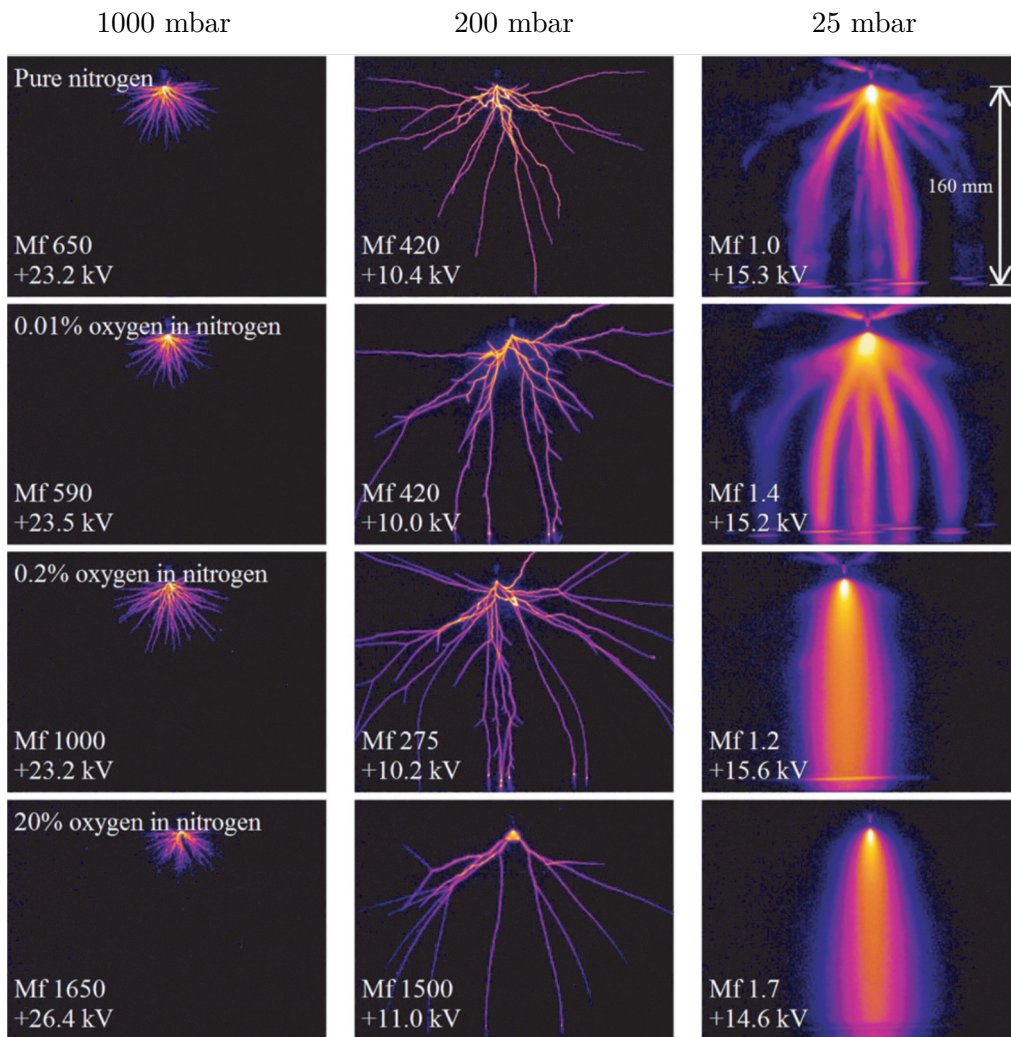


**Figure 2.8:** ICCD images of various streamer morphologies, initiated within nitrogen-oxygen mixtures of different proportions and at different voltages and pressures. The label “Mf” is the multiplication factor for the image intensity, giving an indication of the discharge intensity. Image adapted with permission from [100], © 2010 IOP Publishing.

to distort the effective (net) electric field. Conceptually, the far lighter electrons drift quickly away from the heavy ions within an avalanche front, resulting in charge separation that distorts the electric field, provided that the magnitude of charge is sufficiently large.

With reference to Figure 2.9, Meek [101] originally described the streamer formation mechanism as the moment when secondary avalanches contribute to the growth of a dense patch of ions deposited near the anode surface after the crossing of an avalanche. As the charge density grows, the space charge induced field grows to be on the order of the external field magnitude and

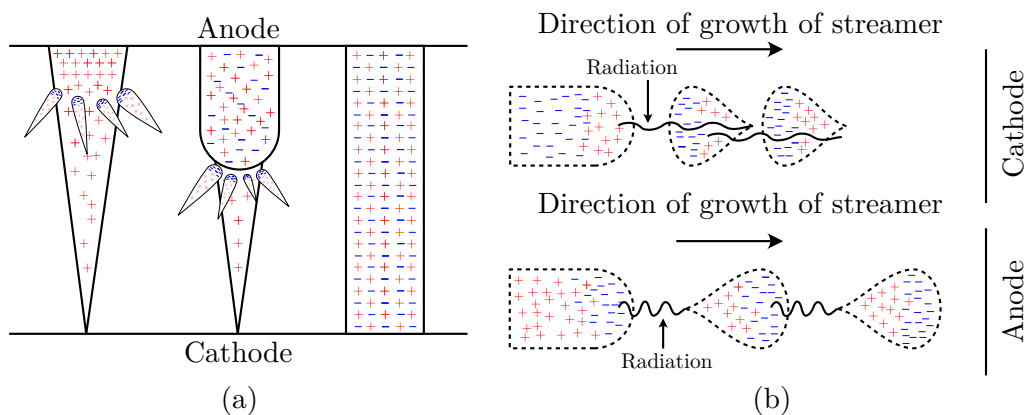


**Figure 2.9:** Coloured versions of positive and negative streamer development from Meek and Craggs [101]. (a) The mechanism of positive-streamer formation from a positive ion patch remaining from an avalanche, (b) streamer growth mechanisms due to (top) incoming avalanches to a positive streamer head, and (bottom) avalanches developed ahead of negative streamer fronts. The radiation of (b) refers to the occurrence of photoionisation—see Section 2.3.6.

leads to local field enhancement at the avalanche head—a moment now known as the *avalanche-to-streamer transition*. While the classical diagrams drawn by Meek [101] have undoubtedly deepened the knowledge of the streamer discharge process, more recent work leveraging modern computational power has provided a means to understand the physical structure and processes at a level of detail unattainable during the time of Meek and Raether. It is deemed only appropriate for this review to describe the subsequent evolution of the streamer discharge based on modern computational simulations, in reference to Figure 2.10.

Beginning with panel (a-i) of Figure 2.10, which shows the enhanced field due to a positive charge density as proposed by Meek, collisional ionisation therefore takes place ahead of the charge density driven by incoming electrons (a source of which may also be photoionisation, depending on the gas) as shown in panels (a-i)–(a-iv). Electrons produced through ionisation eventually reach a critical density and reduces the electric field behind the initial positive charges due to their upward drift (a-i)–(a-ii). The screened interior of a streamer begins to emerge, leading to the enhancement of the electric field at the forming streamer “head” (a-ii)–(a-iii). Charge separation results in the development of a thin layer of positive charge, into which incoming electrons are accelerated (a-x). The enhanced electric field at the streamer front becomes predominantly supported by the developing, conductive, plasma channel (a-vi)–(a-viii), and where the intense ionisation caused by incoming electrons enables the streamer head to advance forward in the form of a *wavefront of ionisation* (a-iv). The formation mechanism of a negative (*anode-directed*) streamer shown in Figure 2.10(b) is similar, with the main difference

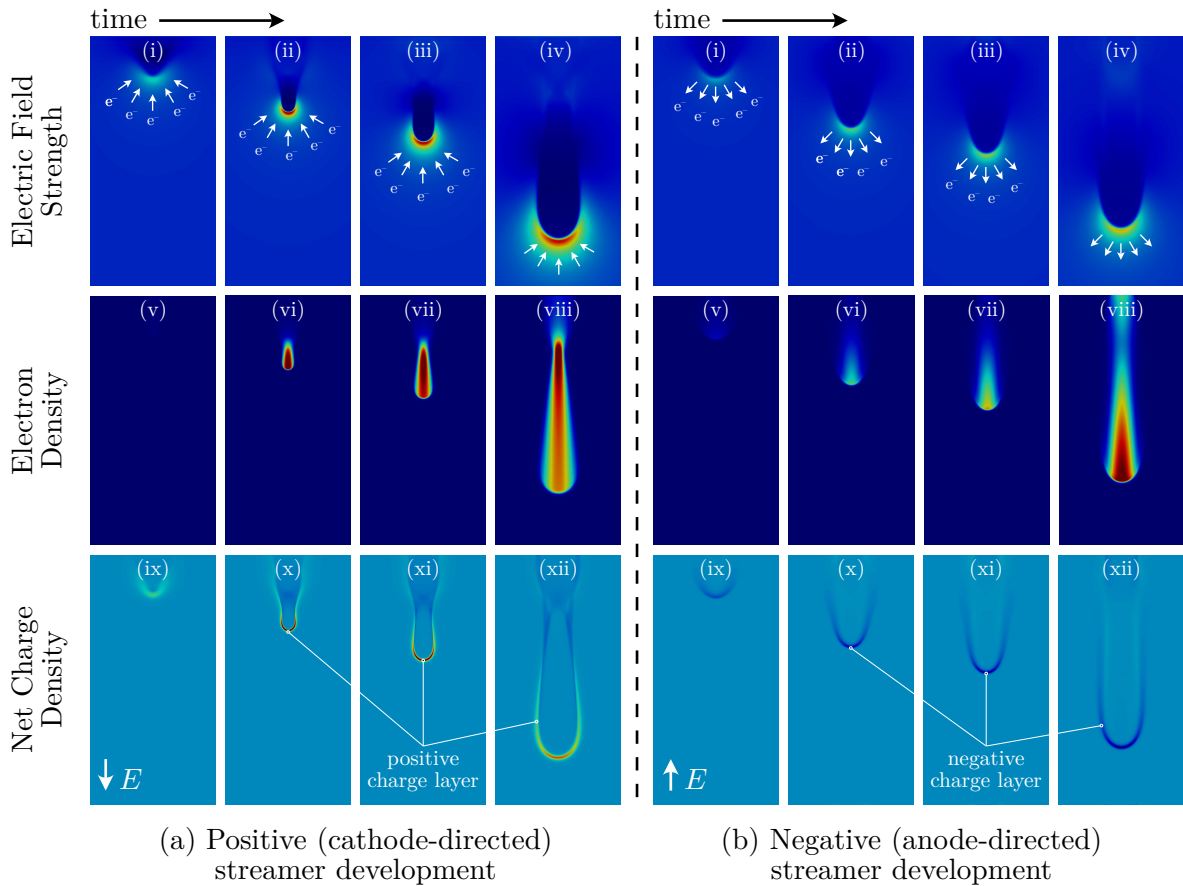


**Figure 2.10:** Modern understanding of streamer development and structure based on charge transport simulations, (a) positive (cathode-directed) streamer, (b) negative (anode-directed) streamer). From the top, rows correspond to the electric field magnitude, electron density, and the net charge density. Contrast these to the classical diagrams of Meek (Figure 2.9). Simulations computed using the framework presented within Chapter 5.

that electrons are accelerated from the streamer channel into and away from the streamer head, in the same direction that the streamer propagates (b-i)–(b-iv) and a negative charge sheath is thus created instead (b-ix)–(b-xii). For instance, a growing electron avalanche with sufficient distance ahead of it may transition into a negative streamer if the electron density at its head becomes significant.

The self-driven enhancement ahead of these ionising wavefronts permit streamers initiated in regions above the critical field to penetrate into regions below criticality, a common example being in systems incorporating non-uniform field geometries. The plasma left in the wake of the wavefront increases the conductivity of the gas, seeding the possibility for it to develop into a sufficiently conductive pathway for a large current to flow. It is noted, however, that the bridging

of electrodes within HV systems by either a Townsend discharge or by one or more streamers does not necessarily result in full breakdown of the medium, but may register as a *partial* discharge or pre-breakdown event. The transition to full voltage collapse necessitates the heating of the gas and formation of a far more conductive and thermalised channel associated with electric sparks and arcs. In Chapter 5, the mechanisms of streamer formation and propagation are described in substantially more detail within the review of simulation methodologies for streamer discharges. Chapter 6 additionally presents numerous novel results based on computational simulations of streamer discharges, which formed a significant portion of the present work.

Meek had described a *positive* or *cathode-directed* streamer, providing alongside an analytical estimate for the electric field strength ahead of the initiating charge density,

$$E_{\text{meek}}(x) \approx \frac{q\alpha e^{\alpha x}}{3\sqrt{\frac{2D_e x}{\mu_e E}}}, \quad (2.30)$$

where  $D_e$  is the electron diffusion coefficient,  $E$  is the applied field strength, and where it was assumed that the charge would be uniformly distributed within a sphere of  $r = \sqrt{2D_e t}$ . Raether [91] conducted similar analysis with minor differences relating to the diffusion length, arriving at a similar expression. The now-ubiquitous Meek-Raether criterion is based upon this approach to estimate the avalanche-to-streamer transition, given that the general solution to Townsend's original avalanche growth equation (2.28) may be written as

$$n_e = n_0 \exp\left(\int_{\ell} \bar{\alpha} d\ell\right), \quad (2.31)$$

where  $n_e$  is the electron density and  $n_0$  is the initial condition, often assumed to be a single electron. The path-dependent growth rate in the exponent is typically assigned the symbol  $K$  and referred to as the *ionisation integral*. Then, based on either Meek or Raether's field expressions, Meek and Craggs [101] present this quantity in the form

$$K = \bar{\alpha}x_c = K_0 + \ln x_c, \quad (2.32)$$

where  $x_c$  in this case has units of centimetres, describing the critical length beyond which an avalanche may transition into a streamer, and  $K_0 \approx 18 - 20$  [101] in air and under a static, uniform, electric field. In many cases, this approach adequately describes the gas breakdown process which has driven its widespread usage within research and as a design rule for practical HV systems. However, increasing system complexity has exposed the limitations to

this semi-empirical approach: for one, estimating breakdown singularly on the basis of a (highly approximate) threshold of charge density invites improvement. Secondly, the value for  $K$  appears strongly dependent on the specific breakdown conditions, including the type and parameters of the gas, field non-uniformity, and nature of the energising signal. As such, different studies report various values for  $K$  [102–107], and in some cases, arbitrary values are often selected solely to explain experimental data with little consideration given to the exact value chosen. However, in the absence of a new breakdown criterion that is as straightforward to apply and provides a comparable level of accuracy, the Meek-Raether criterion remains a useful tool. To address the avalanche-to-streamer transition in the context of overstressed breakdown, Chapter 4 encloses several analytical results arising from the revisiting and extending of the Meek-Raether approach.

### 2.3.5 From Streamer to Spark

On the road to breakdown, the second transition from the streamer mechanism to full breakdown remains poorly understood at the time of writing. Streamers bridging an electrode gap do not necessarily lead to spark breakdown, nor can the non-thermal plasma channel left in the wake of an ionising wavefront be sufficient to explain the substantial breakdown currents associated with complete breakdown. In principle, rapid gas heating must occur to ultimately develop a thermalised plasma bridging between the electrodes, thus enabling the conductance of a substantial breakdown current observed as a spark or arc. Beyond the primary streamer stage, some authors describe subsequent phases including secondary [108] or further, tertiary [109] streamers; each propagating successively along the primary streamer channel and contributing to the increase in plasma density and conductivity.

An important process within certain thermodynamic conditions is the streamer-to-leader transition. This is similar in nature to the transition of streamer to spark, however, it may do so mid-flight without initially bridging the electrodes [110, 111]. Figure 2.11 depicts a typical illustration of the structure of a propagating leader, thought to be fed by an active streamer (or corona) region at its head comprised of multiple streamers which act to inject significant current into the leader stem or channel. The experimental observation of several distinct modes of streamer, streamer-to-leader transition, and leader breakdown regimes appear definitive, but the rapid physical processes occurring within these regimes remain challenging to experimentally quantify. Approximate modelling of these processes has been attempted in [111, 112], but in general, large-scale and high-fidelity computational models of streamer-to-leader transition remain out of reach. Beyond thermalisation sees the establishment of sparks and possibly arcs,

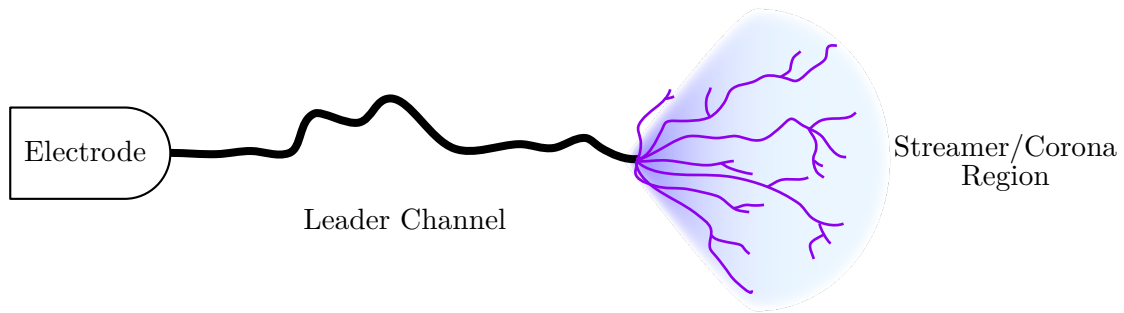


**Figure 2.11:** Present understanding of the structure of a leader, comprising of a thermalised channel fed by a streamer or corona region at its head.

the characteristics of which are important to be understood for a range of power and pulsed power systems, e.g., in circuit breakers [113], and hence subject to much study. However, the properties, processes, and applications beyond this stage were not of concern to this work, as such, are not detailed any further.

### 2.3.6 The Role of Gas Chemistry

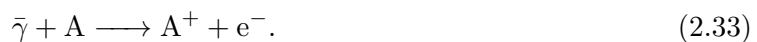
The preceding sections of this chapter have broadly outlined the gas breakdown process with sufficient detail to understand the core principles. However, the ultimate determinant of the gas breakdown characteristics for a particular system lies within the composition and chemistry of the working gas itself. The Townsend parameters introduced in Section 2.3.3 merely act as collective *swarm* parameters which are themselves representative averages, but which are dependent on the underlying kinetic and chemical interactions. Most importantly for gas discharges are reactions which act as charge sources or sinks, as these influence the the availability of charges, the energy of electrons, the electric field distribution, and therefore, the discharge evolution. Aside from the necessary ionisation reaction as in (2.27), other underlying inelastic chemical interactions that are of primary importance include [114]

- Excitation,  $e^- + M \longrightarrow M^* + e^-$
- Electron attachment,  $e^- + M \longrightarrow M^-$
- Dissociative attachment,  $e^- + M_2 \longrightarrow M^- + M^*$
- Ion-Electron recombination,  $e^- + M^+ \longrightarrow M$
- Ion-Ion recombination,  $M^+ + M^- \longrightarrow 2M$
- Ionic Dissociation,  $e^- + M_2 \longrightarrow M^+ + M^- + e^-$

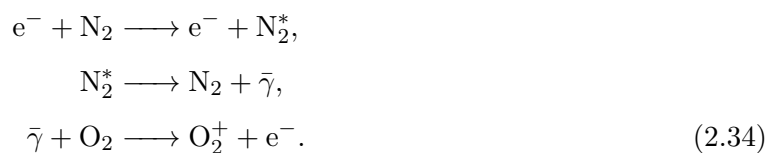
Other processes, e.g., three-body processes, ion-ion interactions, production of metastables,

and Penning ionisation etc. [1] may also be of contribution. Combinations of reactions act to influence the composition of electrons, ions, and neutrals, which may impact the overall discharge characteristics. Each type of reaction occurs at a different rate, dependent on the conditions in which the discharge was initiated. These processes often underpin the characterisation of gaseous dielectrics for use in HV systems. For example, the *electronegativity* of a gas has long been relevant to the optimisation of gas-insulated equipment, acting as a measure of the tendency for electrons in a gas to attach and form negative ions. Sulphur hexafluoride (SF<sub>6</sub>) is a prime example of a highly electronegative gas which has resulted in its dominating presence within, for example, gas-insulated power equipment, for its remarkably high dielectric strength and arc-quenching capabilities [115, 116].

In certain cases, photoionisation of gas molecules may also be of significance and influence the evolution of a discharge. This may be in a reaction of the form<sup>‡</sup>



In some gases, including air, the initiation of sufficiently intense collisional processes may alone result in the production of photons that may induce ionisation. In other cases, photoionisation may be intentionally induced, e.g., in laser-triggered switches [117], as a means of pre-ionisation or as a triggering mechanism. For streamers in air, the collisional excitation of diatomic Nitrogen followed by subsequent emissive de-excitation provides a source of photons that photoionise molecular Oxygen, following the sequence of reactions



As such, the production rate of photoelectrons may also be tightly coupled to the intensity of ionisation. Photons are able to propagate some distance away from the region of their initial production before ionising a neutral, determined by its absorption length. In atmospheric air, photoionisation is widely believed to be a dominant source of electrons fuelling the propagation of positive streamers [118]. In other work, lasers have been shown to be capable of guiding streamer

---

<sup>‡</sup>The included reaction assumes only single-photon ionisation. Other mechanisms such as multiphoton, tunnelling, and over-barrier ionisation are also possible at substantially stronger electric field magnitudes (e.g., application of high-power lasers), but are not of relevance to this work.

discharges in oxygen-nitrogen mixtures, made possible by laser pre-ionisation effects [119].

The chemical properties of the low-temperature gas discharge phase forms the basis of many novel plasma-based technologies as discussed within Chapter 1. Since electrons within this regime are accelerated to sufficient energies for plasma chemical processes to occur without the heating of the parent gas, efficient and non-thermal production of useful active species can be achieved [41]. Knowledge of the individual reaction rates that determine the efficiency of these processes are therefore paramount to the optimisation of these types of technology. While plasma composition does not form a major focus of the present work, the streamer simulation framework presented in Chapter 5 includes the capability to evaluate the composition of plasmas developed from the passage of non-thermal ionisation fronts. Details relating to the use of known reaction rates and electron energy loss coefficients to substantially increase modelling fidelity are additionally described.

### 2.3.7 Gas Breakdown Scaling Relations

It has been shown that, fundamentally, gas breakdown is governed by the transport and interactions of charges on subatomic to atomic spatial scales. The applicability of gas discharge theories to the design and construction of HV equipment was in part facilitated by several scaling relationships, which enabled these models to be extended to systems beyond those used in the original experiments. Townsend [90] introduced the concept of scaling laws for gas discharge processes, on the knowledge that electrons accelerated by an electric field gain energy with direct proportion to the electric field magnitude,  $W \propto E$ . The average collision-free length travelled by an electron is the *mean free path*,  $\ell_m$ , which is inversely proportional to the gas number density,  $N$ , from (2.23). It follows that

$$W \propto \frac{E}{N} \iff \ell_m \propto \frac{1}{N} \quad (2.35)$$

since  $W = qE\ell_m$ . In consequence, energy distributed among all electrons within a gas scales with  $E/N$ , also known as the *reduced electric field*. This serves as a useful scaling factor for many physical properties relating to gas discharge phenomena, and has motivated the unit of the Townsend (Td) arising from this definition, where  $1 \text{ Td} = 10^{21} \text{ V m}^2$ .

On a similar note, the  $\ell_m \propto 1/N$  proportionality also explains the well-known *Paschen's Law* [120],

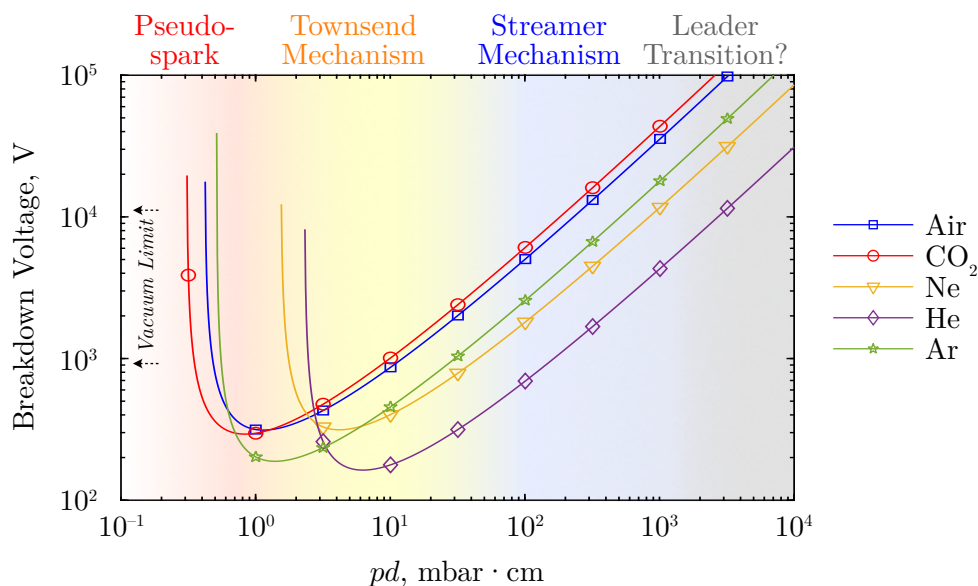


**Figure 2.12:** Paschen curves from common gases, plotted using the parameters from Raizer and Allen [121]. Background colour and associated labels indicate the approximate boundaries between different discharge regimes. The colour gradient serves to indicate that there are no definite boundaries at any one particular value, and is highly dependent on the exact breakdown configuration. A leader transition and breakdown regime has been proposed in [122] for very high  $pd$ .

canonically written

$$V_b = \frac{Bpd}{\ln(Apd) - \ln\left[\ln\left(1 + \frac{1}{\gamma}\right)\right]}, \quad (2.36)$$

where  $V_b$  is the breakdown voltage and  $A$  and  $B$  are gas-specific constants (over certain ranges of reduced electric field). The gas pressure,  $p$ , and gap distance,  $d$ , together form the so-called  $pd$  product. In accordance with (2.36), the breakdown voltage scales with  $pd$ , and estimates the occurrence of a minimum breakdown voltage for some value of  $pd_{min}$ , see the example *Paschen curves* of Figure 2.12. Conceptually, high pressurisation of gas reduces the mean free path such that electrons fail to gain sufficient energy prior to collision for it to be ionising, increasing  $V_b$ . In contrast, low pressurisation reduces the probability of any collision in general, disregarding whether the electron has reached ionisation energy or not, also increasing  $V_b$ . As for the gap distance,  $d$ , longer gaps reduce the overall electric field, leading to less energy imparted to accelerated electrons and naturally increasing  $V_b$ . For small gaps, however, the condition of the critical distance may become important, and avalanches may simply be unable to form over short distances, also increasing  $V_b$ .

Scaling with  $pd$  continues to be a powerful tool for HV design, with gases are often characterised

in part by its Paschen curve as an indicator of performance. It is, however, not without its limitations, primarily concerning very low and very high values of  $pd$ . According to (2.36), Paschen's law diverges towards an infinite value of  $V_b$  for small  $pd$ , a limitation of the model confirmed by experimentation [123–126]. This concerns cases where  $\ell_m \sim d$  and breakdown voltage decreases with reducing  $d$ , in disagreement with (2.36). Though the exact mechanisms remain an open question, authors have considered aspects such as field emission [127] and ballistic electron conduction [128] to possibly be dominant within this regime, leading to a rapid reduction of breakdown voltage with  $pd$  instead. For large  $pd$ , (2.36) once again diverges in practise as the streamer mechanism described in Section 2.3.4 dominates. There have been suggestions for further regime changes for even larger values of  $pd$ , corresponding to the previously-described leader discharge modes [122]. Furthermore, as the basis of Paschen's law was the Townsend mechanism, it also suffers similar inaccuracies as the nature of the electrode configuration or waveform begins to increase in complexity. Of relevance to this work is the upward shifting of Paschen's curve observed experimentally with faster rising voltages [129, 130], which is discussed in more detail within Chapter 4.

## 2.4 Interfacial Breakdown

Increasing complexity in pulsed power systems have driven the need for composite and novel insulation solutions which, in turn, has provoked research efforts to characterise and understand insulation characteristics. Expansion and maintenance efforts for power transmission and distribution systems have highlighted key issues relating to dielectric interfaces. These have included concerns regarding surface flashover across solid insulating spacers or at cable joints and connecting components, generally considered under power frequency AC, DC, and on occasion, included tests using standard LI waveforms. The atypical system topologies and non-standard, fast-rising, waveforms as featured in pulsed power applications currently do not possess a strongly-established body of literature concerning insulation interfaces. However, the underlying physical breakdown processes between AC, DC, and impulsive regimes are fundamentally the same, thus the relevance of these past works cannot be wholly discounted. As such, the following sections nevertheless provide an overview of the present state of experimental and theoretical understanding of solid-gas and solid-solid breakdown behaviour that is of relevance to the present work. It is noted that the following does not concern itself with the review of bulk solid breakdown since this work exclusively focused on configurations where discharges are gas-initiated. Besides, under most standard operating conditions, discharges initiate within the weaker, gaseous, dielectric within solid-gas composite systems and is the primary mode of failure [50].

### 2.4.1 Solid-Gas Surface Flashover and Surface Morphology

In general, surface flashover behaviour at solid-gas interfaces is an issue of considerable complexity and has been the subject of intensive study in the past few decades. This has largely been driven by the importance of successful mitigation of surface flashover within power equipment, where solid-gas interfaces are pervasive and unavoidable. In the vast majority of cases, the dielectric strength of an insulation system will be limited by the medium with the lowest breakdown strength, and generally, gaseous dielectrics are far weaker than bulk solids under most standard operating conditions. At solid-gas interfaces, discharges thus incept within the gas phase, but are known to be heavily influenced by the presence of solid dielectrics in their near vicinity [49, 50].

Despite this, a complete understanding has not yet been attained owing to the plethora of processes occurring at the solid-gas interface during breakdown initiation and development. Much of the modern literature is focused on the processes detailed within Section 2.2.2, for which Figure 2.13 has been adapted from [50] that provides a comprehensive summary for reference. Within the scope of the present work, the aspects explored relating to solid-gas interfaces were mainly concerned with surface charge and surface morphology. Literature that is relevant to these aspects are summarised in the following.

Experimental work had established that the presence of solid dielectrics may lead to the reduction of the system breakdown strength, relative to that of an identical gas-only system [50]. Studies have attempted to understand the effects of the relative permittivity of solid spacer materials, as it would be reasonable to assume that polarisation may have some influence over the breakdown process. However, studies such as those conducted by Pillai and Hackam [131] found little effect of permittivity on the DC flashover voltages across Teflon, Plexiglas, and Pyrex of the same insulator length. Trémas *et al.* [132] performed impulse flashover tests initiated from a needle electrode situated above various solid materials which included polytetrafluoroethylene (PTFE), polycarbonate, epoxy resin, epoxy silica composites, and polyphthalamide-glass fibre composites over a 5 cm air gap. Flashover voltage dependency with permittivity was inconclusive in the case that the ground electrode was oriented to produce a largely parallel field with the solid surface. However, a weak correlation appeared in the case that the electrode was placed behind the solid surface, inducing a field with far stronger components normal to the surface, where higher permittivity materials tended to result in lower flashover voltages. This is consistent with the findings of Marskar and Meyer [133], who simulated far faster streamer development over textured dielectric surfaces in a perpendicular field geometry when comparing to those of Li *et al.* [54] who found only a weak dependence on permittivity using a parallel geometry. In

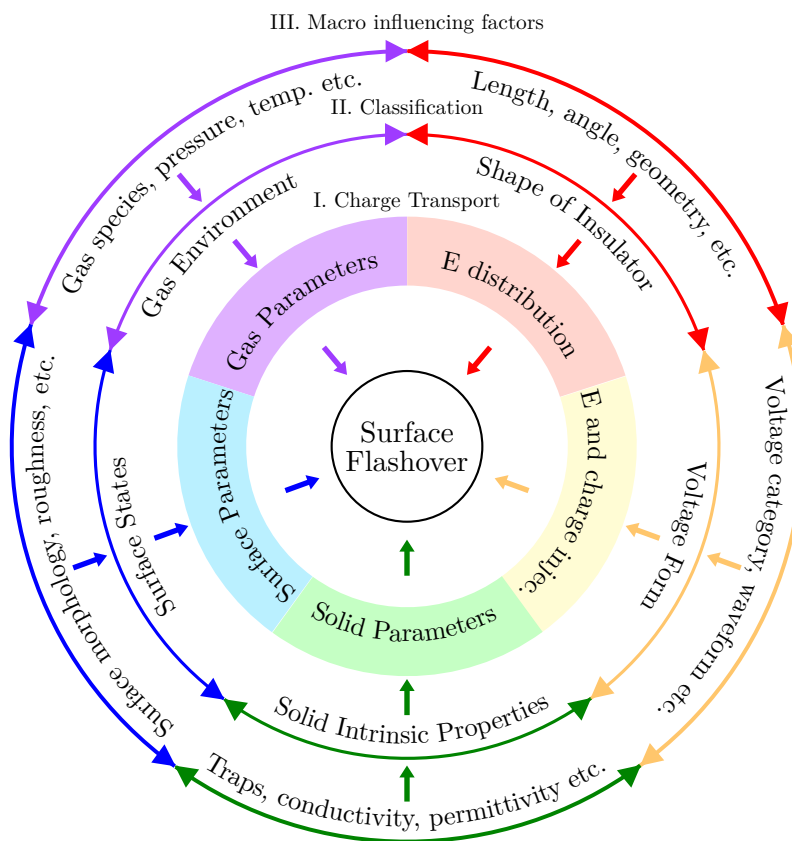


**Figure 2.13:** Diagram showing the many factors that ultimately determine the nature of surface flashover across insulators. Aspects explored within this work include surface roughness, voltage waveform (impulse), and to some extent, surface charge. Image adapted from [50] under CC BY 4.0.

impulsive flashover tests conducted by Wang *et al.* [134], flashover events across  $\approx 4$  cm long spacers made from high-density polyethylene (HDPE), polyoxymethylene (Delrin), PTFE, and the glass-ceramic Macor [135] were studied in dry air, nitrogen, and carbon dioxide environments. Under  $\approx 1.9$   $\mu$ s rise-time impulses, the authors also report an inconclusive effect of permittivity. In contrast, work conducted under switching impulses by Lazaridis and Mikropoulos [136] report an increase to the breakdown voltage with increasing permittivity. In other work, Macpherson *et al.* [137] reported a weak reduction of flashover voltage with higher values of permittivity, for flashover under negative  $\approx 100$  ns rise-time impulses and under various levels of relative humidity, but remark that these were not of statistical significance. In general, experimental evidence for permittivity is inconclusive at best; which is somewhat against modelling studies such as in Li *et al.* [54, 57] or as studied by Dubinova [138], showing the electrostatic attraction of streamer discharges towards dielectric surfaces regardless of polarity, that becomes stronger with higher

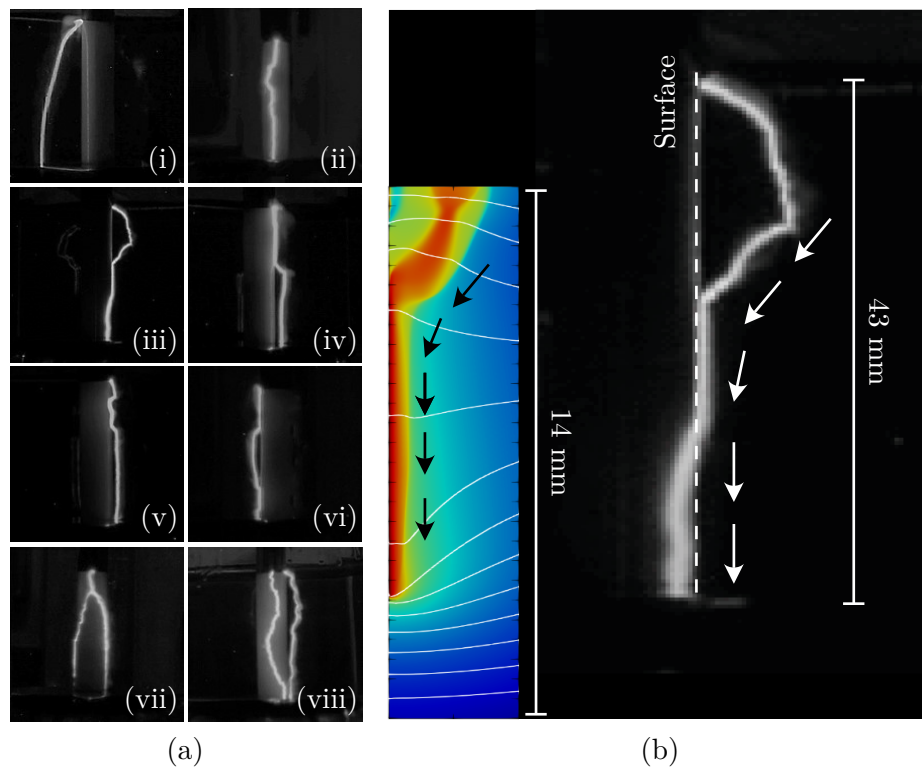


**Figure 2.14:** (a) Different morphologies of spark breakdown channels across a solid-gas interface capturing using open-shutter photography in Wang *et al.* [134]. Note the different categories including spontaneous surface attachment and detachment behaviours. (b) Comparison of spark morphology from [134] to a simulated positive streamer attaching to a dielectric surface, from Wong *et al.* [139]. Images (a) and (b) adapted with permission from [134] and [139], respectively, © 2020 and 2023 IEEE.

permittivity solid materials. However, given the large number of processes at play during a practical breakdown event, it may not be unreasonable to assume other factors dominate over the attraction behaviour found from simulations. The direct measurement of the effects of permittivity in isolation may therefore be a greater challenge than generally expected.

On that note, it is important to remark on the morphological similarities between the surface-attaching streamers of Li *et al.* [54,57] compared to spark channels imaged using open-shutter techniques in Wang *et al.* [134]. While in Li *et al.* [57] the attraction was explained to be purely due to polarisation (as must be the case based on the limited physics present in the simulation model), Wang *et al.* [134] posited that the different spark breakdown categories which were imaged (and reproduced as Figure 2.14(a) from the comparison of Wong *et al.* [139]) may also be due to the effects of surface charge. While surface charges were not explicitly measured in [134], other simulation and experimental studies strongly suggest that significant

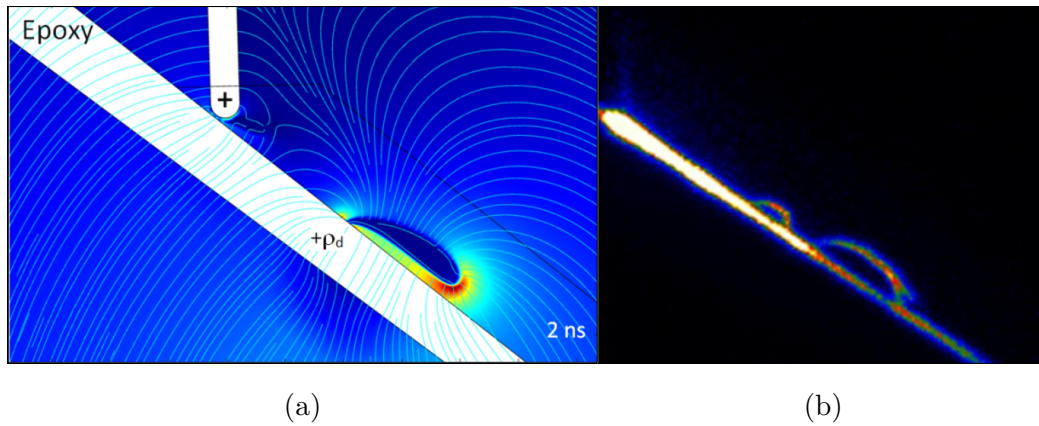


**Figure 2.15:** (a) Simulated and (b) experimentally-imaged streamers in Florkowski [141]. Simulated streamer was initiated from a patch of surface charge placed on the dielectric surface, believed to explain the experimental findings, which Florkowski referred to as *airborne streamers*. Image adapted with permission from [141], © 2021 Elsevier.

surface charge can be deposited from the prior passage of surface streamers. Negative surface streamers simulated in Li *et al.* [54] charged adjacent surfaces to peak surface charge densities of  $\varsigma \approx -300 \text{ pC/mm}^2$  to  $-400 \text{ pC/mm}^2$  and which were found to increase with greater values of background electric field. In contrast, positive surface streamers were found to negligibly charge the same surface, which the authors justify as the tendency for electrons to move away from the surface due to the direction of the local electric field. These charge magnitudes are supported by other work, e.g., in Meyer *et al.* [56, 140]. To further understand the role of surface charge, Florkowski *et al.* [141] compared simulated streamer development on an inclined dielectric barrier with a pre-set surface charge patch included as an initial condition. The author finds that with sufficient charge, the surface field local to the charge patch can initiate a streamer directly from the surface in qualitative agreement to experimentally-imaged streamers, a comparison of which has been reproduced as Figure 2.15. This may be consequential for solid-gas systems operating in repetitive discharge modes, entertaining the possibility that accumulated surface charge from previous discharges may significantly alter the subsequent discharge behaviour. Several other works investigating surface charging come to similar conclusions [58, 142, 143], however, the general understanding of its effects currently remain at a basic level. For instance, the magnitude and distribution of charges resulting from different types of discharge are not yet well-understood, and the subsequent behaviour including charge decay dynamics and influence on system performance have only recently received some, but growing, attention.

In recent efforts to enhance hold-off voltages at solid-gas interfaces, studies have investigated the feasibility and effectiveness of *surface modifications* on the solid surface [144–147]. Incidentally,

this is strongly related to other studies attempting to understand the effects of *surface roughness* on surface flashover events [148–150]. In general, certain types of rough or modified surface appear to increase the surface flashover strength without compromising on mechanical strength. For example, Zhao *et al.* [149] found increasing flashover voltage for dry silicone rubber (SiR) interfaces with roughness values of  $R_a > 3\ \mu\text{m}$ . This was similarly found in Xue *et al.* [148], attributing the difference to a number of surface changes including surface conductivity, which they observed to have increased with increased roughness. They further find changes to the surface trap distribution that was believed to help suppress the number of available charge carriers participating in the surface discharge, enhancing the overall flashover strength. In the series of works by Meyer *et al.* [56, 61, 140, 147], Marskar and Meyer [133], and in Meyer, Marskar, and Mauseth [151], effects of the purposeful modification of the surface texture, by introducing either square or semicircular surface profiles, was studied experimentally and supported by simulations. Profiles with characteristic dimensions of  $500\ \mu\text{m}$  to  $1000\ \mu\text{m}$  were studied (which is far greater than typical surface roughness features), from which the authors reported: increased hold-off voltage resulting from the impeding of discharge development from triple junctions due to the surface profile [147]; proposal of a streamer re-ignition mechanism that facilitated streamer propagation across textured surfaces [133]; and found that narrower profile spacing appear to be more effective at inhibiting surface streamer growth. Macpherson *et al.* [146] reported similar increases to the hold-off voltage for knurled solid spacers [polyetherimide (Ultem), Delrin, and HDPE] under impulse action of around  $100\ \text{ns}$  rise-time and  $700\ \text{ns}$  time-to-half, though only for positive energisation. In contrast, a decrease in hold-off voltage was found for the corresponding negative cases. The authors explain this in terms of the greater path length that required traversal by a positive surface streamer and the greater voltage required to support its development; an argument similar to those of Meyer *et al.* [133].

These developments pertaining to surface texture and morphology are recent, especially considering the far longer history of solid-gas spacer technology itself. However, they hold great promise as a low-cost and simple process that could greatly enhance the dielectric performance of solid-gas interfaces within power and pulsed power equipment, without compromising mechanical strength. It is therefore of great importance to gain a deeper understanding of the processes along textured and rough solid surfaces, which ultimately contribute towards the identification of optimal surface features to maximise flashover strength. In Chapter 8, results from impulsive flashover tests across polymer interfaces considering different surface conditions are presented, in a contribution towards the understanding of surface texture on flashover strength.

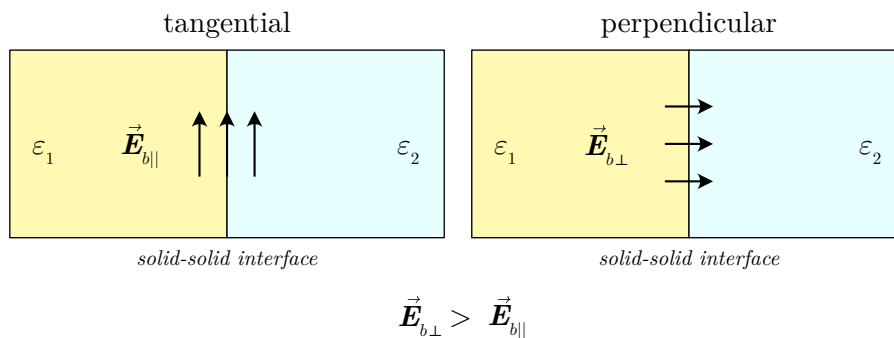


**Figure 2.16:** Diagram showing tangential compared to perpendicular field components relative to the interfacial axis. Configurations where there exists a substantial tangential component are at greater risk of interfacial breakdown.

### 2.4.2 Gas Cavity Driven Solid-Solid Interfacial Breakdown

In several systems described within Chapter 1, contact between different solid dielectric insulators may be unavoidable, for instance, inside HV cables [46], at cable joints and terminations [152], or between layers of laminate used in composite materials [153]. It is well known that the breakdown strength across solid-solid interfaces can be significantly lower than that of bulk solids [154], which increases the probability of unwanted partial or complete electrical breakdown if left unaddressed. Most importantly, configurations where there exist significant electric field components in the direction of the interface are particularly vulnerable, as the tangential breakdown strength has been previously found to be substantially lower than in the perpendicular direction [155], see the illustration of Figure 2.16. The semi-permeable nature of solid-solid interfacial contacts also greatly increases the risk of contamination or water ingress, which is especially relevant to technologies that operate in the presence of, or immersed in, liquids; such as undersea cables [152].

For a long time, breakdown across solid-solid interfaces were of lesser concern until the mass global deployment and integration of HV electrical infrastructure. Even then, only with the dire consequences of ageing and the modern push for higher operating voltages with smaller geometric footprints has greater emphasis been placed on solid-solid interfaces. Studies that aimed to delve deeper into these issues have therefore only been conducted relatively recently. Earlier work by Fournier, Lamarre, and Dang *et al.* [156–161] investigated cross-linked polyethylene (XLPE) and ethylene-propylene diene monomer rubber (EPDM) under steady-state AC and DC energisation. The results of Fournier, Dang, and Paquin [157] showed a marked increase of the interfacial breakdown strength from two separate factors: (i) increasing the interfacial mating pressure and (ii) with the application of a dielectric grease during the mating process, which improved the dielectric performance for both fresh and aged samples. This was in agreement to Fournier and

Lamarre [156], who had similar conclusions for EPDM interfaces under 0 kPa to 100 kPa mating pressure subjected to power-frequency AC stress. The authors of [156] additionally considered the effects of interfacial length, indicating a reduction in dielectric strength from approximately 13 kV/mm to 5 kV/mm when the length of the interface was increased from 1 mm to 10 mm for greased interfaces. For dry-mate (no application of grease) interfaces, they further record an unexpected minimisation of the breakdown strength at around 4 mm, which they attribute to Paschen-like behaviour on the suggestion that *air cavities* at the interface may play a role in the discharge evolution. Behavioural similarities between greased contact and bulk breakdown further implied that gas cavities may be partially responsible for the observed reductions. Fournier [158] later investigated homogeneous (same-material) and heterogeneous (different-material) interfaces between XLPE and EPDM, observing an almost threefold increase to the interfacial breakdown strength when the XLPE was sanded (150-grit) and greased, compared to a dry-mate and untreated surface. EPDM-EPDM interfaces were found not to differ substantially whether greased or ungreased, while XLPE-XLPE interfaces exhibited 2 to 3 times greater breakdown strength for untreated surfaces over sanded surfaces when under dry-mate conditions.

Aged cable joints were further investigated in Dang and Fournier [160] with specific focus on surface roughness and mating pressure. EPDM-EPDM interfaces were found to maintain their dielectric strength with age, while EPDM-XLPE interfaces decreased with time. This was despite the reduction of the EPDM-EPDM interfacial contact pressure to under half of its original value. The authors of [160] attributed this to surface properties, reinforcing the tendencies observed in previous studies that ultimately led to the identification that the *surface morphology*, *contact pressure*, and *material hardness* are critical parameters that, at least in part, determine the interfacial breakdown strength. Dang [160] explicitly linked these observations to the theory of trapped gas cavities<sup>§</sup> between the contacting rough surfaces, as shown in Figure 2.17, believed to explain the far lower interfacial breakdown strength compared to bulk solids. Increased contact pressure and smoother surfaces were hypothesised to decrease the interfacial cavity size and increase the effective contact area, enhancing the interfacial breakdown strength. Greased contacts were suggested to initially improve breakdown strength across EPDM-XLPE interfaces on the basis that the air gaps were replaced instead with grease that had higher dielectric strength. With ageing, decreasing contact pressure allowed the re-introduction of air cavities due to grease

---

<sup>§</sup>Note that past studies have typically referred to the gaps formed at the interface as *cavities*. However, in this work the term *interfacial void* is used interchangeably, on the basis that the *cavities* are partially open, while *voids* refer to regions which are fully enclosed, such as the gaps found at interfaces. In any case, interfacial *cavities* and *voids* may be treated equally within this text.

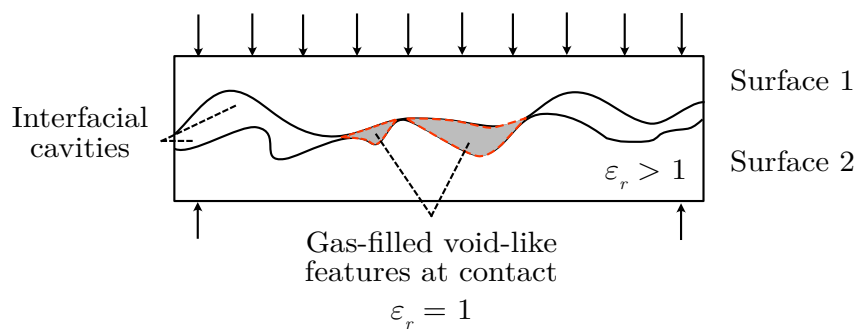


**Figure 2.17:** Diagram depicting gas-filled interfacial voids found at practical solid-solid interfaces due to inevitable surface roughness. Due to the higher relative permittivity values of the bulk solids, the electric field is enhanced inside the voids. Understood to be the primary cause of solid-solid interfacial breakdown. Image adapted with permission from [162], © 2024 IEEE.

seepage, reducing the breakdown strength once again. Dang [160] further remarked that for EPDM-EPDM interfaces (formed of a softer material), grease seepage may have improved the dielectric performance since it would facilitate the tighter adherence of the two surfaces and instead reduce the size of gas-filled cavities.

At the turn of the century, studies continued to build upon the theory of gas-cavity driven breakdown at solid-solid interfaces. Kunze *et al.* [163] studied interfaces within extruded XLPE cables considering also SiR and ethylene-propylene rubber (EPR) under power-frequency AC and impulse energisation. Their results were consistent with previous theories, where an increased surface roughness (characterised by an increase to the surface asperity heights of around  $5\ \mu\text{m}$  to  $50\ \mu\text{m}$ ) was reported to nearly halve the breakdown voltage. AC and impulsive tests were claimed to behave characteristically the same, but the authors did not provide details relating to the type of impulse waveshape, though this can likely be assumed to be the standard LI waveform considering the context of power engineering surrounding their work. Similarly, Shibata *et al.* [164] studied interfaces between epoxy rubber and SiR using disk electrodes embedded at the interface and under similar energisation conditions as Kunze *et al.* [163]. The air gap dimension between the two dielectrics was varied to approximate interfacial cavities of various size. A reduction in the dielectric strength was observed with increasing gap distance for positive energisation, but was found to decrease for negative energisation once a back electrode was included. The authors of [164] explain this observation under the framework of streamer breakdown, referring to the increased inception strength of negative streamers which may have increased the breakdown strength. Using image processing techniques, Du and Gu [165] investigated aged XLPE-SiR interfaces with a particular focus on the physical propagation of

discharges across the interface under different contact pressures. Higher mating pressure (studied for the values of 20, 100, and 200 kPa) was found to suppress discharge propagation and rendered the tracking failure of the samples more difficult, thereby increasing the measured breakdown voltages.

In more recent work, Hasheminezhad *et al.* [166, 167] and Kantar *et al.* [168–173] began to combine the numerous suspected factors that influence the interfacial breakdown strength, as uncovered in the works that preceded them. Hasheminezhad, Ildstad and Nysveen [166] applied a rough surface contact model [174] alongside the principles of gas breakdown in an attempt to predict the AC breakdown strength of XLPE-XLPE interfaces based on the gas cavity theory, finding reasonable agreement between theoretical and experimentally-obtained values. This was found, however, only in the case when the cavities were assumed to be *vented*, i.e., at atmospheric pressure, assuming that cavities were sufficiently exposed such that the contained gas would equalise in pressure with its surroundings. This rejected their earlier hypotheses that pressurised gas within cavities may have contributed to an observed increase to the interfacial breakdown strength. Importantly, Hasheminezhad’s work demonstrated, for the first time, that the cavity size at an interface as estimated using surface profilometry data can yield results of practical significance to HV system design. A later study by the same author [167] found greater deviations between modelled and experimental breakdown strengths, particularly with smoother surfaces. They associated this discrepancy with discharges initiating within cavities larger than predicted, as the developed model assumed breakdown would be due to a statistically average cavity, when in reality, cavity sizes will exist as a distribution across the surface.

Kantar *et al.* [168–173] built upon Hasheminezhad’s work, not only by widening the range of materials characterised to include SiR, epoxy resin, and polyether ether ketone (PEEK), but also introduced a deterministic surface contact model [173] as a means for comparison with the statistical model used previously in [171], which was based on the classical statistical theories of Greenwood and Williamson [174]. The various works of Kantar *et al.* consolidated the parameters of contact pressure, surface roughness, and elastic modulus, alongside the principles of gas breakdown, into a single model for AC interfacial breakdown. Discharge monitoring experiments were additionally conducted in Kantar and Ildstad [172] using glass-PEEK interfaces which allowed the imaging of discharges within interfacial voids, see the images reproduced as Figure 2.18. The correlation of interfacial breakdown strength with the predicted cavity discharge inception strength was successfully reported in [171, 173]. The developments of Kantar *et al.* further suggested that materials with higher values of elastic modulus tended to create

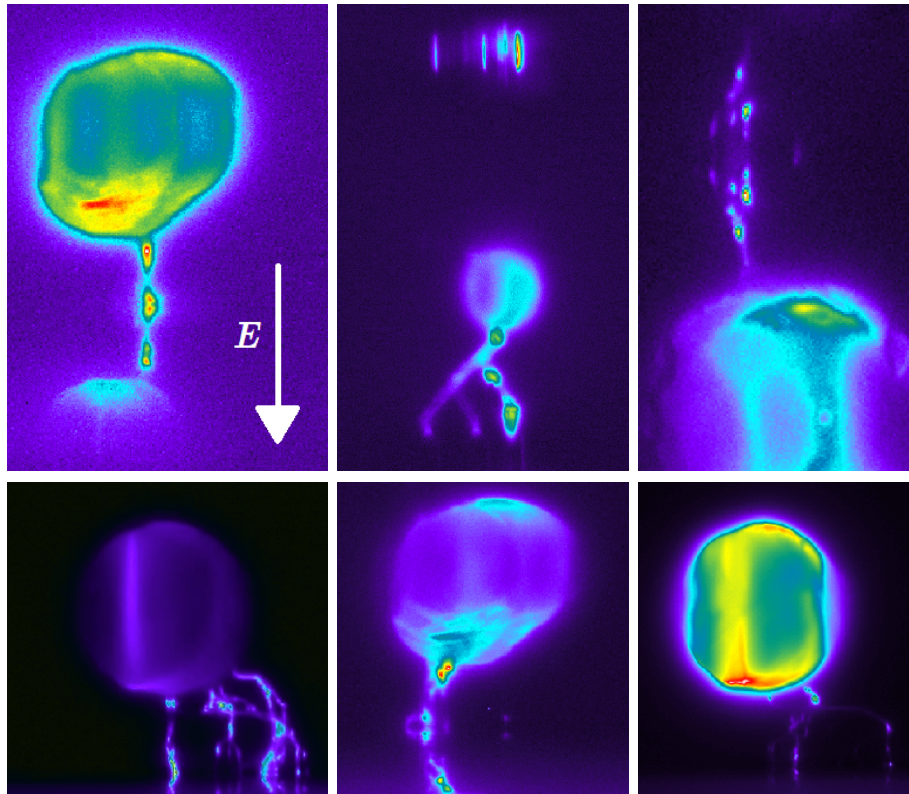


**Figure 2.18:** CCD images of partial discharges initiated within artificial voids at a PEEK-glass interface from Kantar *et al.* [172]. Image adapted with permission from [172], © 2019 IEEE.

larger cavities when placed in homogeneous contact, which was subsequently confirmed using profilometry techniques, and moreover, corresponded to a measurable reduction in the interfacial breakdown strength. One additional aspect introduced within the works of Kantar *et al.* was the idea that the interfacial *contact spots* are crucial to the overall evolution of breakdown across a solid-solid interface, which was later supported by the work of a number of authors including in Zhu *et al.* [175].

The studies described here were deemed the most significant in developing the understanding of the core mechanisms driving solid-solid interfacial breakdown. It is again apparent, however, that both the characterisation and modelling of solid-solid breakdown has almost exclusively been confined to power industry-aligned materials, geometries, and energisation regimes. Yet, solid insulators form an increasingly important part of pulsed power systems incorporating non-standard materials, fast-rising impulses, and under atypical conditions. The lack of appropriate design and characterisation data severely impedes the development of pulsed power systems.

In Chapter 7, this work begins to extend the theory and techniques developed in the past to conduct, for the first time, the characterisation of solid-solid interfaces formed between several non-standard materials in the overstressed impulsive breakdown regime, with a particular emphasis on rate of voltage rise and surface roughness.

## 2.5 The Problem of Fast Transients and Overvoltages

The preceding sections have collectively mapped out the context in which the present work is set. While many challenges surrounding dielectric phenomena, electrical breakdown, and interfacial behaviours have been successfully addressed through the pivotal ideas of numerous past authors; as many challenges remain that must be addressed for the successful development of next-generation pulsed power technology. In one final section of this chapter, emphasis is placed on a central and overarching idea that this work aimed to progress: that of time-dependency, fast transients, and of the overstressed breakdown regime typical of many applications within the pulsed power disciplines. Most importantly, the reason that new approaches are fundamentally necessary to characterise these processes are illustrated, and the lack of scaling relationships for pulsed breakdown is further highlighted.

### 2.5.1 On Time-dependency

Within many steady-state applications, it often suffices to consider the breakdown behaviour of dielectric media as characterised under static and unchanging electric fields, i.e., as if it were energised in a static DC system. This assumption is also largely applicable to the extensively studied steady-state AC waveforms at power frequency, considering that the characteristic time of a 50 or 60 Hz waveform on the millisecond range is longer by several magnitudes than typical processes associated with electrical discharge and breakdown events.

To demonstrate, using electron mobility data from [176, 177], one may estimate  $\mu_e \approx 0.05 \text{ m}^2 \text{ V}^{-1} \text{ s}^{-1}$  in atmospheric air based on a near-critical field strength of 2.8 kV/mm. It follows from (2.26) that the drift velocity of electrons and corresponding velocity of an electron avalanche would be

$$v_{av}(E = 2.8 \text{ kV/mm}) = \mu_e E \approx 0.14 \text{ mm/ns} \quad (2.37)$$

such that across, for example, a 1 cm gap, the associated time-of-flight would be  $t_{av} \approx 70 \text{ ns}$ . Timescales necessary for the transition from avalanche-to-streamer follows from the electron

growth equation (2.31), from which one finds

$$\tau_{av} \approx \frac{K}{\bar{\alpha}\mu_e E}, \quad (2.38)$$

which is predominantly determined by the time-dependency of the energising field,  $E$ , but in a static field assuming  $K = 18$  and a field just above critical gives  $\tau_{av} \sim 30$  ns. Within the streamer breakdown regime, one may additionally consider the Maxwell time according to (2.9), applied here to a plasma with conductivity  $\sigma = qn_e\mu_e$  (assuming the positive ion current is negligible) and where  $\varepsilon_r = 1$ :

$$\tau_{MW} = \frac{\varepsilon_0}{q_en_e\mu_e}, \quad (2.39)$$

which may be considered a measure of the time necessary for the electric field within a streamer channel to be screened. Based on the critical field of  $E \approx 3$  kV/mm in atmospheric air, a characteristic timescale on the scale of  $\tau_{MW} \sim 1$  ns results. Note that Teunissen, Sun, and Ebert [178] improved this approximation by additionally considering ionisation, giving the ionisation screening time as

$$\tau_{is} = \frac{1}{\bar{\alpha}\mu_e E} \ln \left( 1 + \frac{\bar{\alpha}\varepsilon_0 E}{q_en_0} \right), \quad (2.40)$$

where  $n_0$  is the initial electron density. However, for the purposes here these two approaches provide same order-of-magnitude estimates on the scale of nanoseconds. Finally, empirical estimates of streamer propagation velocities,  $v_{st}$ , can be attained from the fittings of Briels *et al.* [179], finding typical streamer velocities within the range  $v_{st} \approx 0.5$  mm/ns to 4 mm/ns (where negative-polarity streamers were reported to be around 25% slower than the positive), and who also provide the phenomenological relation

$$v_{st} \approx \frac{1}{2} d_{st}^2 \quad (2.41)$$

with units mm/ns, where  $d_{st}$  is the streamer diameter in millimetres. This relation was found to fit all measured streamers, regardless of polarity. Thus, in typical gaps of  $10^{-3}$  m to  $10^{-2}$  m, streamer propagation times,  $t_{st}$ , can be similarly estimated to be on the order of nanoseconds to tens-of-nanoseconds.

Generally speaking, the total avalanche and streamer formation process completes within timescales of  $\sim 10$  ns to 100 ns, which can reasonably be treated as instantaneous within most steady-state applications. However, the reader is reminded of typical timescales associated with many pulsed power technologies as outlined in Section 2.1, which may lie within the sub-nanosecond or shorter range. Under these conditions, timescales associated with ionisation

and breakdown development are not negligible and must be accounted for. Resulting effects include the so-called *overvolted* or *overstressed* breakdown regime—referring to the tendency for impulse-driven breakdown to occur at voltages and fields greater than the static case [180]. A similar argument holds for dielectric relaxation times associated with material interfaces described in Section 2.2. Materials that are moderately conductive with finite relaxation times in the nano- or micro-second may not influence electric field distributions when energised with waveforms changing over comparatively long timescales. Under fast-rising impulses, however, the change in temporal behaviour may lead to the invalidity of classical breakdown approaches that were developed assuming static conditions. Thus, for pulsed applications where it is important to characterise both the breakdown strength and the breakdown *time*, studies addressing these issues with the purposeful consideration of *time* are critical to the success of future pulsed power technology.

### 2.5.2 Pulsed Breakdown Scaling

Scaling relations such as Paschen’s Law (2.36) have acted as a powerful design curve for HV equipment when its application can be justified. It is evident, however, that neither Paschen’s Law nor the classical criteria of Meek [99] nor Raether [91] consider non-uniform or rapidly-changing background fields. From, for example, Levko, Arslanbekov, and Kolobov [130], Paschen curves exhibit an upward shift with faster-rising voltages, a characteristic feature of overstressed impulsive breakdown which is not successfully captured within the classical approaches.

Experimentalists have progressed towards understanding the scaling behaviour of impulse-driven breakdown based on fitted curves to empirical data, by incorporating measurements of both breakdown strength and time-to-breakdown. For example, well-known fittings include J. C. Martin’s equation [181]

$$E_m t_b^{\frac{1}{6}} d^{\frac{1}{6}} = C \left( \frac{p}{p_0} \right)^n, \quad (2.42)$$

where  $E_m$  is the mean electric field across the gap in kV/cm,  $d$  is the gap distance in cm, and  $t_b$  is the breakdown time in microseconds. The ratio  $p/p_0$  is the ratio of the gas pressure to atmospheric pressure, and  $n$ ,  $C$ , are constants determined through fitted curves to experimental data. Similarly, T. H. Martin [182] provided a closer fit based on the inclusion of additional datapoints,

$$p t_b = 97800 \left( \frac{E_b}{p} \right)^{-3.44}, \quad (2.43)$$

where  $t_b$  is the breakdown time in seconds,  $E_b$  is the breakdown field strength in kV/cm, and  $p$

is the gas pressure in  $\text{g/cm}^3$ . Both expressions suggest an intrinsic relationship between field strength, and importantly, *time*. As pulse waveforms grew increasingly varied over time, it was clear that both of these types of expression were limited in their applicability. The lack of solid theoretical explanations for these phenomenological scaling laws certainly invites improvement. A deeper understanding of the fundamental processes that render pulsed breakdown different from the static case would inform the development of scaling relationships with far wider application. While these aspects form a central theme throughout the present work, Chapter 4 directly addresses the idea of an alternative scaling law by presenting analytical progress attained through the explicit incorporation of a rate-of-rise parameter to the field-time scaling characteristic for pulsed breakdown.

## Chapter 2 References

- [1] J. Lehr and P. Ron, *Foundations of Pulsed Power Technology*, ser. 2053-2563. Wiley-IEEE Press, 2018.
- [2] E. Schamiloglu, R. Barker, M. Gundersen, and A. Neuber, “Modern pulsed power: Charlie martin and beyond,” *Proc. IEEE*, vol. 92, no. 7, pp. 1014–1020, 2004.
- [3] Z. Zhong, J. Rao, H. Liu, and L. M. Redondo, “Review on solid-state-based marx generators,” *IEEE Trans. Plasma Sci.*, vol. 49, no. 11, pp. 3625–3643, 2021.
- [4] R. D. McBride, W. A. Stygar, M. E. Cuneo, D. B. Sinars, M. G. Mazarakis, J. J. Leckbee *et al.*, “A primer on pulsed power and linear transformer drivers for high energy density physics applications,” *IEEE Trans. Plasma Sci.*, vol. 46, no. 11, pp. 3928–3967, 2018.
- [5] O. Liebfried, “Review of inductive pulsed power generators for railguns,” *IEEE Trans. Plasma Sci.*, vol. 45, no. 7, pp. 1108–1114, 2017.
- [6] G.-H. Rim, E. Pavlov, H.-S. Lee, J. Kim, and Y.-W. Choi, “Pulse forming lines for square pulse generators,” *IEEE Trans. Plasma Sci.*, vol. 31, no. 2, pp. 196–200, 2003.
- [7] A. Larsson, D. Yap, and Y. W. Lim, “Time jitter study of a corona-stabilized closing switch,” *IEEE Trans. Plasma Sci.*, vol. 40, no. 10, pp. 2646–2652, 2012.
- [8] A. Larsson, D. Yap, and J. Au, “Operating conditions and switching delay time of a corona-stabilized switch during repetitive operation,” *IEEE Trans. Plasma Sci.*, vol. 41, no. 10, pp. 2605–2608, 2013.
- [9] A. Larsson, “Gas-discharge closing switches and their time jitter,” *IEEE Trans. Plasma Sci.*, vol. 40, no. 10, pp. 2431–2442, 2012.
- [10] X. Ren, T. Sugai, A. Tokuchi, and W. Jiang, “Solid-state marx generator circuit based on inductive energy storage,” *IEEE Trans. Plasma Sci.*, vol. 49, no. 11, pp. 3377–3382, 2021.
- [11] T. Sakamoto and H. Akiyama, “Solid-state dual marx generator with a short pulsewidth,” *IEEE Trans. Plasma Sci.*, vol. 41, no. 10, pp. 2649–2653, 2013.
- [12] “High-voltage test techniques - part 1: General definitions and test requirements,” International Electrotechnical Commission (IEC), Geneva, CH, International Standard, 2010.
- [13] F. Davanloo, D. Borovina, C. Collins, F. Agee, and L. Kingsley, “Repetitively pulsed high power stacked blumlein generators,” *Nucl. Instrum. Methods Phys. Res. B: Beam Interact. Materials Atoms*, vol. 99, no. 1, pp. 713–716, 1995, application of Accelerators in Research and Industry '94.
- [14] J. Rossi and M. Ueda, “A 100 kV/200 A blumlein pulser for high-energy plasma implantation,” *IEEE Trans. Plasma Sci.*, vol. 34, no. 5, pp. 1766–1770, 2006.
- [15] I. C. Somerville, S. J. MacGregor, and O. Farish, “An efficient stacked-blumlein HV pulse generator,” *Meas. Sci. Technol.*, vol. 1, no. 9, p. 865, 1990.
- [16] H. Li, Y. Zheng, P. Zhang, X. Han, and W. Zhou, “Effect of temperature on insulation properties of SF<sub>6</sub>/N<sub>2</sub> mixed gas under AC voltage,” *IEEE Trans. Plasma Sci.*, vol. 48, no. 4, pp. 914–920, 2020.
- [17] C. Zhou and G. Chen, “Space charge and AC electrical breakdown strength in polyethylene,” *IEEE Trans. Dielectr. Electr. Insul.*, vol. 24, no. 1, pp. 559–566, 2017.

- [18] J. Obrzut and K. Kano, "Impedance and nonlinear dielectric testing at high AC voltages using waveforms," *IEEE Trans. Instrum. Meas.*, vol. 54, no. 4, pp. 1570–1574, 2005.
- [19] R. Piccin, A. R. Mor, P. Morshuis, A. Girodet, and J. Smit, "Partial discharge analysis of gas insulated systems at high voltage AC and DC," *IEEE Trans. Dielectr. Electr. Insul.*, vol. 22, no. 1, pp. 218–228, 2015.
- [20] T. Christen, "The effect of injection properties of contacts on the dynamics of unipolar space-charge limited currents," *IEEE Trans. Dielectr. Electr. Insul.*, vol. 23, no. 6, pp. 3712–3724, 2016.
- [21] Z. Li and B. Du, "Polymeric insulation for high-voltage dc extruded cables: challenges and development directions," *IEEE Electr. Insul. Mag.*, vol. 34, no. 6, pp. 30–43, 2018.
- [22] G. Rizzo, P. Romano, A. Imburgia, and G. Ala, "Partial discharges in HVDC cables - the effect of the temperature gradient during load transients," *IEEE Trans. Dielectr. Electr. Insul.*, vol. 28, no. 5, pp. 1767–1774, 2021.
- [23] E. Peschke and R. von Olshausen, *Cable Systems for High and Extra-High Voltage: Development, Manufacture, Testing, Installation and Operation of Cables and Their Accessories*. Wiley, 2019.
- [24] B. X. Du, J. G. Zhang, and D. S. Liu, "Interface charge behavior of multi-layer oil–paper insulation under dc and polarity reversal voltages," *IEEE Trans. Dielectr. Electr. Insul.*, vol. 22, no. 5, pp. 2628–2638, 2015.
- [25] B. Du, J. Dong, H. Liang, and X. Kong, "Polarity reversal and over voltage affecting discharge inception of tri-post insulator in  $\pm 800$  kV gil," *IEEE Trans. Dielectr. Electr. Insul.*, vol. 29, no. 1, pp. 223–230, 2022.
- [26] X. Chen, X. Wang, K. Wu, Z. R. Peng, Y. H. Cheng, and D. M. Tu, "Effect of voltage reversal on space charge and transient field in LDPE films under temperature gradient," *IEEE Trans. Dielectr. Electr. Insul.*, vol. 19, no. 1, pp. 140–149, 2012.
- [27] T. Zhang, W. Zhou, J. Yu, and Z. Yu, "Insulation properties of C4F7N/CO2 mixtures under lightning impulse," *IEEE Trans. Dielectr. Electr. Insul.*, vol. 27, no. 1, pp. 181–188, 2020.
- [28] T. Wen, Q. Zhang, L. Zhang, J. Ma, C. Guo, M. Chen *et al.*, "Discussion on lightning impulse test waveform according to breakdown characteristics of SF6 gas gaps," *IEEE Trans. Dielectr. Electr. Insul.*, vol. 24, no. 4, pp. 2306–2313, 2017.
- [29] C. Guo, Q. Zhang, H. You, J. Ma, Y. Li, T. Wen *et al.*, "Influence of electric field non-uniformity on breakdown characteristics in SF6/N2 gas mixtures under lightning impulse," *IEEE Trans. Dielectr. Electr. Insul.*, vol. 24, no. 4, pp. 2248–2258, 2017.
- [30] M. Hanai, T. Nakamoto, and H. Ikeda, "Dielectric breakdown characteristics of an insulator with a sharp edge in SF6 gas under lightning impulse voltage," *IEEE Trans. Dielectr. Electr. Insul.*, vol. 14, no. 2, pp. 321–327, 2007.
- [31] S. Chen, R. Zeng, C. Zhuang, Z. Yu, and J. He, "Switching impulse breakdown characteristics of large sphere-plane air gaps compared with rod-plane air gap," *IEEE Trans. Dielectr. Electr. Insul.*, vol. 20, no. 3, pp. 839–844, 2013.

- [32] Y. Liao, R. Li, C. Gao, G. Wang, and Z. Liu, “Flashover tests on air gap of  $\pm 800\text{kV}$  dc transmission line under composite dc and switching impulse voltage,” *IEEE Trans. Dielectr. Electr. Insul.*, vol. 21, no. 5, pp. 2095–2101, 2014.
- [33] Y. Wang, X. Wen, L. Lan, Y. An, M. Dai, D. Gu *et al.*, “Breakdown characteristics of long air gap with negative polarity switching impulse,” *IEEE Trans. Dielectr. Electr. Insul.*, vol. 21, no. 2, pp. 603–611, 2014.
- [34] G. Ueta, T. Tsuboi, J. Takami, S. Okabe, and A. Ametani, “Insulation characteristics of gas insulated switchgear under lightning impulse and ac superimposed voltage,” *IEEE Trans. Dielectr. Electr. Insul.*, vol. 21, no. 3, pp. 1026–1034, 2014.
- [35] X. Li, M. Wu, X. Hu, P. Jiang, J. Han, K. Zhao *et al.*, “Discharge characteristics of insulation defects in GIS under AC/LI superimposed voltage,” *IEEE Trans. Dielectr. Electr. Insul.*, vol. 29, no. 5, pp. 2017–2025, 2022.
- [36] S. Zhang, Z. Peng, C. Zhou, and G. Chen, “Numerical analysis on space charge and AC-DC combined breakdown strength in polyethylene,” *IEEE Trans. Dielectr. Electr. Insul.*, vol. 26, no. 3, pp. 826–834, 2019.
- [37] C. He, L. Zhang, X. Zhang, J. Li, and X. Yao, “Study on the influence of switching impulse superposition phase on AC partial discharge of epoxy surface in  $\text{SF}_6$  gas,” *IEEE Trans. Power Deliv.*, vol. 35, no. 3, pp. 1596–1598, 2020.
- [38] Y. Yao, I. V. Timoshkin, S. J. MacGregor, M. P. Wilson, M. J. Given, and T. Wang, “Breakdown characteristics of plasma closing switch filled with air,  $\text{N}_2$ ,  $\text{CO}_2$ , and  $\text{Ar/O}_2$ ,” *IEEE Trans. Plasma Sci.*, vol. 46, no. 10, pp. 3574–3583, 2018.
- [39] Y. Yao, I. V. Timoshkin, S. J. MacGregor, M. P. Wilson, M. J. Given, and T. Wang, “Postbreakdown transient characteristics of a gas-filled plasma closing switch,” *IEEE Trans. Plasma Sci.*, vol. 49, no. 2, pp. 942–951, 2021.
- [40] T. Huiskamp, “Nanosecond pulsed streamer discharges part I: Generation, source-plasma interaction and energy-efficiency optimization,” *Plasma Sources Sci. Technol.*, vol. 29, no. 2, p. 023002, 2020.
- [41] D. Wang and T. Namihira, “Nanosecond pulsed streamer discharges: II. physics, discharge characterization and plasma processing,” *Plasma Sources Sci. Technol.*, vol. 29, no. 2, p. 023001, 2020.
- [42] T. Kotnik, D. Miklavčič, and T. Slivnik, “Time course of transmembrane voltage induced by time-varying electric fields—a method for theoretical analysis and its application,” *Bioelectrochem. Bioenergetic.*, vol. 45, no. 1, pp. 3–16, 1998.
- [43] T. Kotnik and D. Miklavčič, “Second-order model of membrane electric field induced by alternating external electric fields,” *IEEE Trans. Biomed. Engr.*, vol. 47, no. 8, pp. 1074–1081, 2000.
- [44] C. Yao, D. Mo, C. Li, C. Sun, and Y. Mi, “Study of transmembrane potentials of inner and outer membranes induced by pulsed-electric-field model and simulation,” *IEEE Trans. Plasma Sci.*, vol. 35, no. 5, pp. 1541–1549, 2007.

- [45] I. V. Timoshkin, S. J. MacGregor, R. A. Fouracre, B. H. Crichton, and J. G. Anderson, “Transient electrical field across cellular membranes: pulsed electric field treatment of microbial cells,” *J. Phys. D: Appl. Phys.*, vol. 39, no. 3, p. 596, 2006.
- [46] S. Delpino, D. Fabiani, G. Montanari, C. Laurent, G. Teyssedre, P. Morshuis *et al.*, “Feature article - polymeric HVDC cable design and space charge accumulation. part 2: insulation interfaces,” *IEEE Electr. Insul. Mag.*, vol. 24, no. 1, pp. 14–24, 2008.
- [47] T. T. N. Vu, G. Teyssedre, S. L. Roy, and C. Laurent, “Maxwell–wagner effect in multi-layered dielectrics: Interfacial charge measurement and modelling,” *Technol.*, vol. 5, no. 2, 2017.
- [48] M. Feng, Y. Feng, T. Zhang, J. Li, Q. Chen, Q. Chi *et al.*, “Recent advances in multilayer-structure dielectrics for energy storage application,” *Adv. Sci.*, vol. 8, no. 23, p. 2102221, 2021.
- [49] T. S. Sudarshan and R. A. Dougal, “Mechanisms of surface flashover along solid dielectrics in compressed gases: a review,” *IEEE Trans. Electr. Insul.*, vol. EI-21, no. 5, pp. 727–746, 1986.
- [50] Z. Li, J. Liu, Y. Ohki, G. Chen, H. Gao, and S. Li, “Surface flashover in 50 years: Theoretical models and competing mechanisms,” *High Volt.*, vol. 8, no. 5, pp. 853–877, 2023.
- [51] J. D. Jackson, *Classical Electrodynamics*, 3rd ed. Wiley, 1998.
- [52] T. Takuma and T. Kawamoto, “Field enhancement at a triple junction in arrangements consisting of three media,” *IEEE Trans. Dielectr. Electr. Insul.*, vol. 14, no. 3, pp. 566–571, 2007.
- [53] T. Wong, I. Timoshkin, S. MacGregor, M. Wilson, and M. Given, “Electrostatic modelling of gas-filled voids and conductive particles in highly non-uniform electric fields,” in *23rd Int. Symp. on High Voltage Engr.* Institution of Engineering and Technology, 2023, pp. 1022–1028.
- [54] X. Li, A. Sun, and J. Teunissen, “A computational study of negative surface discharges: Characteristics of surface streamers and surface charges,” *IEEE Trans. Dielectr. Electr. Insul.*, vol. 27, no. 4, pp. 1178–1186, 2020.
- [55] J. Deng, H. Mu, G. Zhang, S. Matsuoka, A. Kumada, and K. Hidaka, “Residual charge distribution of surface leader discharge under positive impulse voltage,” *IEEE Trans. Plasma Sci.*, vol. 41, no. 4, pp. 999–1004, 2013.
- [56] H. K. Meyer, F. Mauseth, R. Marskar, A. Pedersen, and A. Blaszczyk, “Streamer and surface charge dynamics in non-uniform air gaps with a dielectric barrier,” *IEEE Trans. Dielectr. Electr. Insul.*, vol. 26, no. 4, pp. 1163–1171, 2019.
- [57] X. Li, A. Sun, G. Zhang, and J. Teunissen, “A computational study of positive streamers interacting with dielectrics,” *Plasma Sources Sci. Technol.*, vol. 29, no. 6, p. 065004, 2020.
- [58] S. Kumara, S. Alam, I. R. Hoque, Y. V. Serdyuk, and S. M. Gubanski, “DC flashover characteristics of a polymeric insulator in presence of surface charges,” *IEEE Trans. Dielectr. Electr. Insul.*, vol. 19, no. 3, pp. 1084–1090, 2012.
- [59] M. Florkowski, D. Krześniak, M. Kuniewski, and P. Zydrón, “Surface discharge imaging in presence of deposited space charges in non-uniform DC electric field,” *High Volt.*, vol. 6, no. 4, pp. 576–589, 2021.

- [60] A. Pedersen and A. Blaszczyk, "An engineering approach to computational prediction of breakdown in air with surface charging effects," *IEEE Trans. Dielectr. Electr. Insul.*, vol. 24, no. 5, pp. 2775–2783, 2017.
- [61] H. K. Meyer, A. Blaszczyk, M. Schueller, F. Mauseth, and A. Pedersen, "Surface charging of dielectric barriers in short rod-plane air gaps-experiments and simulations," in *2018 IEEE International Conference on High Voltage Engineering and Application (ICHVE)*, 2018, pp. 1–4.
- [62] D. K. DAVIES, "Trapped charges on dielectrics," *Nature*, vol. 203, pp. 290–291, 1964.
- [63] Z. Xing, C. Zhang, H. Cui, Y. Hai, Q. Wu, and D. Min, "Space charge accumulation and decay in dielectric materials with dual discrete traps," *Appl. Sci.*, vol. 9, no. 20, 2019.
- [64] O. W. Richardson, "On the negative radiation from hot platinum," *Proc. Cambridge Philosophical Soc.: Math. Phys. Sci.*, vol. 11, pp. 286–295, 1902.
- [65] C. R. Crowell, "The richardson constant for thermionic emission in schottky barrier diodes," *Solid-State Electron.*, vol. 8, no. 4, pp. 395–399, 1965.
- [66] E. L. Murphy and R. H. Good, "Thermionic emission, field emission, and the transition region," *Phys. Rev.*, vol. 102, pp. 1464–1473, 1956.
- [67] Y. S. Ang, H. Y. Yang, and L. K. Ang, "Universal scaling laws in schottky heterostructures based on two-dimensional materials," *Phys. Rev. Lett.*, vol. 121, p. 056802, 2018.
- [68] S.-J. Liang and L. K. Ang, "Electron thermionic emission from graphene and a thermionic energy converter," *Phys. Rev. Appl.*, vol. 3, p. 014002, 2015.
- [69] R. H. Fowler and L. Nordheim, "Electron emission in intense electric fields," *Proc. Royal Soc. London. Series A, Containing Papers of a Mathematical and Physical Character*, vol. 119, no. 781, pp. 173–181, 1928.
- [70] R. G. Forbes, "Refining the application of fowler–nordheim theory," *Ultramicroscopy*, vol. 79, no. 1, pp. 11–23, 1999.
- [71] M. Fujihira, T. Hirooka, and H. Inokuchi, "Photoemission from compounds containing benzene, naphthalene and anthracene ring systems," *Chem. Phys. Lett.*, vol. 19, no. 4, pp. 584–587, 1973.
- [72] A. Jaksts and J. Cross, "The influence of a solid dielectric spacer on electron avalanches in nitrogen at atmospheric pressure," *Can. Electr. Engr. J.*, vol. 6, no. 2, pp. 14–18, 1981.
- [73] A. Buzulutskov, A. Breskin, and R. Chechik, "Photoemission through thin dielectric coating films," *J. Appl. Phys.*, vol. 81, no. 1, pp. 466–479, 1997.
- [74] G. F. Dionne, "Effects of secondary electron scattering on secondary emission yield curves," *J. Appl. Phys.*, vol. 44, no. 12, pp. 5361–5364, 1973.
- [75] S. Li, Y. Huang, D. Min, G. Qu, H. Niu, Z. Li *et al.*, "Synergic effect of adsorbed gas and charging on surface flashover," *Sci. Rep.*, vol. 9, no. 1, p. 5464, 2019.
- [76] Z. Li, S. Li, H. Xu, G. Qu, H. Niu, Y. Huang *et al.*, "The mechanism of gas pressure and temperature dependent surface flashover in compressed gas involving gas adsorption," *Appl. Surf. Sci.*, vol. 539, p. 148107, 2021.
- [77] S. Xiao, X. Zhang, J. Tang, and S. Liu, "A review on SF6 substitute gases and research status of cf3i gases," *Energ. Rep.*, vol. 4, pp. 486–496, 2018.

- [78] X. Yang, X. Zhao, J. Hu, and J. He, “Grading electric field in high voltage insulation using composite materials,” *IEEE Electr. Insul. Mag.*, vol. 34, no. 1, pp. 15–25, 2018.
- [79] H. C. Miller, “Flashover of insulators in vacuum: the last twenty years,” *IEEE Trans. Dielectr. Electr. Insul.*, vol. 22, no. 6, pp. 3641–3657, 2015.
- [80] M. M. Pejović, “Experimental results of breakdown voltage and electrical breakdown time delay of geiger-muller chamber,” in *2022 57th International Scientific Conference on Information, Communication and Energy Systems and Technologies (ICEST)*, 2022, pp. 1–4.
- [81] N. Brenning, I. Axnas, J. Nilsson, and J. Eninger, “High-pressure pulsed avalanche discharges: formulas for required preionization density and rate for homogeneity,” *IEEE Trans. Plasma Sci.*, vol. 25, no. 1, pp. 83–88, 1997.
- [82] T. Liu, I. Timoshkin, M. P. Wilson, M. J. Given, and S. J. MacGregor, “The nanosecond impulsive breakdown characteristics of air, N<sub>2</sub> and CO<sub>2</sub> in a sub-mm gap,” *Plasma*, vol. 5, no. 1, pp. 12–29, 2022.
- [83] A. P. Jovanović, M. N. Stankov, V. L. Marković, and S. N. Stamenković, “Simulation of the statistical and formative time delay of townsend-mechanism-governed breakdown in argon at low pressure,” *Contrib. Plasma Phys.*, vol. 63, no. 3-4, p. e202200161, 2023.
- [84] W. Yang, “A tutorial overview of the angular scattering models of electron–neutral, ion–neutral, neutral–neutral, and coulomb collisions in monte carlo collision modeling on low-temperature plasma,” *Plasma Sources Sci. Technol.*, vol. 33, no. 2, p. 023001, 2024.
- [85] I. Rafatov and A. Kudryavtsev, *Introduction to Simulation Methods for Gas Discharge Plasmas*, ser. 2053-2563. IOP Publishing, 2020.
- [86] C. Cercignani, *The Boltzmann Equation and Its Applications*. Springer New York, NY, 2012.
- [87] J. Li, C. Yuan, Z. Zhou, A. A. Kudryavtsev, X. Wang, and X. Chen, “Effects of druyvesteyn distribution to transmission coefficients in plasma,” in *2018 12th Int. Symp. Antennas, Propagation and EM Theory (ISAPE)*, 2018, pp. 1–3.
- [88] D. Darian, S. Marholm, M. Mortensen, and W. J. Miloch, “Theory and simulations of spherical and cylindrical langmuir probes in non-maxwellian plasmas,” *Plasma Phys. Control. Fusion*, vol. 61, no. 8, p. 085025, 2019.
- [89] G. J. M. Hagelaar and L. C. Pitchford, “Solving the boltzmann equation to obtain electron transport coefficients and rate coefficients for fluid models,” *Plasma Sources Sci. Technol.*, vol. 14, no. 4, p. 722, 2005.
- [90] J. S. E. Townsend, *The Theory of Ionization of Gases by Collision*. Constable and Company Ltd., London, 1910.
- [91] H. Raether, *Electron Avalanches and Breakdown in Gases*. Butterworths, London, 1964.
- [92] G. Holst and E. Oosterhuis, “The sparking potentials of gases,” *Physica*, vol. 1, 1921.
- [93] G. Holst and E. Oosterhuis, “The sparking potentials of gases,” *Comptes Rendus*, vol. 175, 1922.
- [94] G. Holst and E. Oosterhuis, “The sparking potentials of gases,” *Phil. Mag.*, vol. 46, 1923.
- [95] J. J. Thomson, *Notes on the Recent Researches in Electricity and Magnetism*. Oxford: Clarendon Press, 1893.

- [96] W. Rogowski, “Stoßspannung und durchschlag bei gasen,” *Archiv für Elektrotechnik*, vol. 20, pp. 99–106, 1928.
- [97] L. B. Loeb and A. F. Kip, “The mechanism of spark discharge in air at atmospheric pressure,” *J. Appl. Phys. II*, vol. 10, p. 459, 1939.
- [98] L. B. Loeb and J. M. Meek, *The Mechanism of the Electric Spark*. Stanford University Press, 1941.
- [99] J. M. Meek, “A theory of spark discharge,” *Phys. Rev.*, vol. 57, pp. 722–728, 1940.
- [100] S. Nijdam, F. M. J. H. van de Wetering, R. Blanc, E. M. van Veldhuizen, and U. Ebert, “Probing photo-ionization: experiments on positive streamers in pure gases and mixtures,” *J. Phys. D: Appl. Phys.*, vol. 43, no. 14, p. 145204, 2010.
- [101] J. M. Meek and J. D. Craggs, *Electrical Breakdown of Gases*. Oxford: Clarendon Press, 1953.
- [102] R. T. Waters and W. B. Stark, “Characteristics of the stabilized glow discharge in air,” *J. Phys. D: Appl. Phys.*, vol. 8, no. 4, p. 416, 1975.
- [103] W. S. Zaengl and K. Petcharakas, *Application of Streamer Breakdown Criterion for Inhomogeneous Fields in Dry Air and SF<sub>6</sub>*. Boston, MA: Springer US, 1994, pp. 153–159.
- [104] L. Niemeyer, “A generalized approach to partial discharge modeling,” *IEEE Trans. Dielectr. Electr. Insul.*, vol. 2, no. 4, pp. 510–528, 1995.
- [105] J. J. Lowke and F. D’Alessandro, “Onset corona fields and electrical breakdown criteria,” *J. Phys. D: Appl. Phys.*, vol. 36, no. 21, p. 2673, 2003.
- [106] G. V. Naidis, “Conditions for inception of positive corona discharges in air,” *J. Phys. D: Appl. Phys.*, vol. 38, no. 13, p. 2211, 2005.
- [107] P. N. Mikropoulos and V. N. Zagkanas, “Threshold inception conditions for positive DC corona in the coaxial cylindrical electrode arrangement under variable atmospheric conditions,” *IEEE Trans. Dielectr. Electr. Insul.*, vol. 22, no. 1, pp. 278–286, 2015.
- [108] M. Janda, V. Martišovič, A. Buček, K. Hensel, M. Molnár, and Z. Machala, “Influence of repetition frequency on streamer-to-spark breakdown mechanism in transient spark discharge,” *J. Phys. D: Appl. Phys.*, vol. 50, no. 42, p. 425207, 2017.
- [109] T. Suzuki, “Transition from primary streamer to arc in negative point-to-plane corona,” *J. Appl. Phys.*, vol. 44, no. 10, pp. 4534–4544, 1973.
- [110] C. Peng, X. Dong, Y. Zhao, Z. Li, Y. Zheng, X. Pei *et al.*, “Discharge characteristics of leader inception and development under 10m long air gap—experimental observation and simulation results,” *High Volt.*, vol. 8, no. 6, pp. 1151–1160, 2023.
- [111] L. Arevalo and V. Cooray, “Unstable leader inception criteria of atmospheric discharges,” *Atmosphere*, vol. 8, no. 9, 2017.
- [112] C. L. da Silva and V. P. Pasko, “Dynamics of streamer-to-leader transition at reduced air densities and its implications for propagation of lightning leaders and gigantic jets,” *J. of Geophys. Res.: Atmos.*, vol. 118, no. 24, pp. 13,561–13,590, 2013.
- [113] R. Ma, M. Rong, F. Yang, Y. Wu, H. Sun, D. Yuan *et al.*, “Investigation on arc behavior during arc motion in air DC circuit breaker,” *IEEE Trans. Plasma Sci.*, vol. 41, no. 9, pp. 2551–2560, 2013.

- [114] G. Franz, *Low Pressure Plasmas and Microstructuring Technology*. Springer-Verlag, Berlin, Heidelberg, 2009.
- [115] W. M. Leeds, T. E. Browne, and A. P. Strom, “The use of SF<sub>6</sub> for high-power arc quenching,” *Electr. Engr.*, vol. 76, no. 9, pp. 788–791, 1957.
- [116] Y.-K. Choi, “Interaction of dynamic electric arc plasma and flow field in thermal-puffer SF<sub>6</sub> gas circuit breaker,” *IEEE Trans. Plasma Sci.*, vol. 43, no. 4, pp. 1082–1087, 2015.
- [117] A. Larsson, D. Yap, J. Au, and T. E. Carlsson, “Laser triggering of spark gap switches,” *IEEE Trans. Plasma Sci.*, vol. 42, no. 10, pp. 2943–2947, 2014.
- [118] A. A. Kulikovskiy, “The role of photoionization in positive streamer dynamics,” *J. Phys. D: Appl. Phys.*, vol. 33, no. 12, p. 1514, 2000.
- [119] S. Nijdam, E. Takahashi, J. Teunissen, and U. Ebert, “Streamer discharges can move perpendicularly to the electric field,” *New J. of Phys.*, vol. 16, no. 10, p. 103038, 2014.
- [120] F. Paschen, “Ueber die zum funkenübergang in luft, wasserstoff und kohlendioxid bei verschiedenen drucken erforderliche potentialdifferenz,” *Ann. Phys.*, vol. 273, no. 5, pp. 69–96, 1889.
- [121] Y. P. Raizer and J. E. Allen, *Gas Discharge Physics*. Springer-Verlag, Berlin, Heidelberg, 1991.
- [122] F. Boakye-Mensah, “Numerical modelling of streamer discharges for medium voltage electro technical applications,” Theses, Université Grenoble Alpes [2020-....], 2021.
- [123] D. B. Go and D. A. Pohlman, “A mathematical model of the modified paschen’s curve for breakdown in microscale gaps,” *J. Appl. Phys.*, vol. 107, no. 10, p. 103303, 2010.
- [124] A. M. Loveless and A. L. Garner, “A universal theory for gas breakdown from microscale to the classical paschen law,” *Phys. Plasmas*, vol. 24, no. 11, p. 113522, 2017.
- [125] A. M. Loveless, G. Meng, Q. Ying, F. Wu, K. Wang, Y. Cheng *et al.*, “The transition to paschen’s law for microscale gas breakdown at subatmospheric pressure,” *Sci. Rep.*, vol. 9, no. 1, p. 5669, 2019.
- [126] A. Peschot, C. Poulain, N. Bonifaci, and O. Lesaint, “Electrical breakdown voltage in micro- and submicrometer contact gaps (100nm - 10µm) in air and nitrogen,” in *2015 IEEE 61st Holm Conference on Electrical Contacts (Holm)*, 2015, pp. 280–286.
- [127] Y. Li, R. Tirumala, P. Rumbach, and D. B. Go, “The coupling of ion-enhanced field emission and the discharge during microscale breakdown at moderately high pressures,” *IEEE Trans. Plasma Sci.*, vol. 41, no. 1, pp. 24–35, 2013.
- [128] S. Datta, ser. Cambridge Studies in Semiconductor Physics and Microelectronic Engineering. Cambridge University Press, 1995.
- [129] L. P. Babich, *High-Energy Phenomena in Electric Discharges in Dense Gases*. Futurepast, Arlington, Virginia, 2003, vol. 2.
- [130] D. Levko, R. R. Arslanbekov, and V. I. Kolobov, “Modified paschen curves for pulsed breakdown,” *Phys. Plasmas*, vol. 26, no. 6, p. 064502, 2019.
- [131] A. S. Pillai and R. Hackam, “Surface flashover of solid insulators in atmospheric air and in vacuum,” *J. Appl. Phys.*, vol. 58, no. 1, pp. 146–153, 1985.

- 
- [132] L. Trémas, O. Lesaint, N. Bonifaci, B. Ohl, and F. Gentils, “Breakdown in air along insulating solid surfaces of different natures, parallel or perpendicular to the field direction,” in *IEEE Conf. Electr. Insul. and Dielectr. Phenom. (CEIDP)*, 2016, pp. 412–415.
- [133] R. Marskar and H. K. H. Meyer, “A kinetic monte carlo study of positive streamer interaction with complex dielectric surfaces,” *Plasma Sources Sci. Technol.*, vol. 32, no. 8, p. 085010, 2023.
- [134] Z. Wang, I. V. Timoshkin, M. P. Wilson, M. J. Given, T. Wang, and S. J. MacGregor, “Impulsive breakdown characteristics of solid–gas interfaces,” *IEEE Trans. Plasma Sci.*, vol. 49, no. 1, pp. 365–377, 2021.
- [135] *MACOR Machinable Glass Ceramic Data Sheet*, Corning Inc.
- [136] L. A. Lazaridis and P. N. Mikropoulos, “Flashover along cylindrical insulating surfaces in a nonuniform field under positive switching impulse voltages,” *IEEE Trans. Dielectr. Electr. Insul.*, vol. 15, no. 3, pp. 694–700, 2008.
- [137] R. W. Macpherson, M. P. Wilson, I. V. Timoshkin, S. J. Macgregor, and M. J. Given, “Impulsive flashover characteristics and weibull statistical analysis of gas-solid interfaces with varying relative humidity,” *IEEE Access*, vol. 8, pp. 228 454–228 465, 2020.
- [138] A. Dubinova, “Modeling of streamer discharges near dielectrics,” Phd Thesis 2 (Research NOT TU/e / Graduation TU/e), Applied Physics and Science Education, 2016, proefschrift.
- [139] T. Wong, I. Timoshkin, S. MacGregor, M. Wilson, and M. Given, “Dielectric interfaces in high-voltage technology: Overview and theoretical approaches to the modeling of functional and breakdown behavior,” *IEEE Electr. Insul. Mag.*, vol. 39, no. 4, pp. 34–49, 2023.
- [140] H. K. Meyer, F. Mauseth, A. Pedersen, and J. Ekeberg, “Breakdown mechanisms of rod-plane air gaps with a dielectric barrier subject to lightning impulse stress,” *IEEE Trans. Dielectr. Electr. Insul.*, vol. 25, no. 3, pp. 1121–1127, 2018.
- [141] M. Florkowski, “Imaging and simulations of positive surface and airborne streamers adjacent to dielectric material,” *Meas.*, vol. 186, p. 110170, 2021.
- [142] M. Yuan, L. Zou, Z. Li, L. Pang, T. Zhao, L. Zhang *et al.*, “A review on factors that affect surface charge accumulation and charge-induced surface flashover,” *Nanotechnol.*, vol. 32, no. 26, p. 262001, 2021.
- [143] C. Li, C. Lin, B. Zhang, Q. Li, W. Liu, J. Hu *et al.*, “Understanding surface charge accumulation and surface flashover on spacers in compressed gas insulation,” *IEEE Trans. Dielectr. Electr. Insul.*, vol. 25, no. 4, pp. 1152–1166, 2018.
- [144] C. Li, J. He, and J. Hu, “Surface morphology and electrical characteristics of direct fluorinated epoxy-resin/alumina composite,” *IEEE Trans. Dielectr. Electr. Insul.*, vol. 23, no. 5, pp. 3071–3077, 2016.
- [145] Q. Xie, T. Wang, H. Huang, K. Fu, Y. Xu, and T. Shao, “Surface morphology and flashover performance of epoxy resin in SF6 after discharge aging,” *IEEE Trans. Dielectr. Electr. Insul.*, vol. 24, no. 6, pp. 3395–3404, 2017.

- [146] R. W. Macpherson, M. P. Wilson, I. V. Timoshkin, M. J. Given, and S. J. MacGregor, "Flashover of smooth and knurled dielectric surfaces in dry air," *IEEE Trans. Dielectr. Electr. Insul.*, vol. 31, no. 1, pp. 204–211, 2024.
- [147] H. K. Meyer, R. Marskar, H. G. Osberg, and F. Mauseth, "Surface flashover over a microprofiled cylinder in air," *IEEE Trans. Dielectr. Electr. Insul.*, vol. 30, no. 6, pp. 2862–2869, 2023.
- [148] J. Xue, H. Wang, J. Chen, K. Li, Y. Liu, B. Song *et al.*, "Effects of surface roughness on surface charge accumulation characteristics and surface flashover performance of alumina-filled epoxy resin spacers," *J. Appl. Phys.*, vol. 124, no. 8, p. 083302, 2018.
- [149] Y. Zhao, Y. Xiang, S. Gu, B. Du, B. Dong, N. Xiang *et al.*, "Effect of surface roughness on flashover characteristics of silicone rubber," *J. Electrostat.*, vol. 99, pp. 41–48, 2019.
- [150] Z. Zhan, Q. Zhang, F. Lü, Y. Liu, W. Liu, Z. Li *et al.*, "Effect of the surface roughness of epoxy resin on its creeping flashover characteristics in C4F7N-CO2 gas mixtures," *AIP Adv.*, vol. 9, no. 4, p. 045129, 2019.
- [151] H. K. H. Meyer, R. Marskar, and F. Mauseth, "Evolution of positive streamers in air over non-planar dielectrics: experiments and simulations," *Plasma Sources Sci. Technol.*, vol. 31, no. 11, p. 114006, 2022.
- [152] E. Kantar, "Dielectric strength of polymeric solid–solid interfaces under dry-mate and wet-mate conditions," *Energies*, vol. 14, no. 23, 2021.
- [153] E.-S. Eugene Shin, D. A. Scheiman, and M. Lizcano, "Lightweight, durable, and multifunctional electrical insulation material systems for high voltage applications," in *2018 AIAA/IEEE Electric Aircraft Technologies Symposium (EATS)*, 2018, pp. 1–21.
- [154] R. Ross, "Dealing with interface problems in polymer cable terminations," *IEEE Electr. Insul. Mag.*, vol. 15, no. 4, pp. 5–9, 1999.
- [155] T. Takahashi, T. Okamoto, Y. Ohki, and K. Shibata, "Breakdown strength at the interface between epoxy resin and silicone rubber—a basic study for the development of all solid insulation," *IEEE Trans. Dielectr. Electr. Insul.*, vol. 12, no. 4, pp. 719–724, 2005.
- [156] D. Fournier and L. Lamarre, "Effect of pressure and length on interfacial breakdown between two dielectric surfaces," in *Conf. Rec. 1992 IEEE Int. Symp. Electr. Insul.*, 1992, pp. 270–272.
- [157] D. Fournier, C. Dang, and L. Paquin, "Interfacial breakdown in cable joints," in *Proc. 1994 IEEE Int. Symp. Electr. Insul.*, 1994, pp. 450–452.
- [158] D. Fournier, "Effect of the surface roughness on interfacial breakdown between two dielectric surfaces," in *Conf. Rec. IEEE Int. Symp. Electr. Insul.*, vol. 2, 1996, pp. 699–702 vol.2.
- [159] D. Fournier, "Aging of defective electrical joints in underground power distribution systems," in *Electrical Contacts - 1998. Proc. Forty-Fourth IEEE Holm Conf.on Electr. Contacts (Cat. No.98CB36238)*, 1998, pp. 179–192.
- [160] C. Dang and D. Fournier, "A study of the interfacial breakdown in cable joints," in *Proc. IEEE Conf. Electr. Insul. Dielectr. Phenom. - (CEIDP'94)*, 1994, pp. 518–523.
- [161] C. Dang and D. Fournier, "Dielectric performance of interfaces in premolded cable joints," *IEEE Trans. Power Deliv.*, vol. 12, no. 1, pp. 29–32, 1997.

- [162] T. Wong, I. Timoshkin, S. MacGregor, M. Wilson, and M. Given, “The breakdown and surface characteristics of polymer interfaces under HV impulses,” *IEEE Trans. Dielectr. Electr. Insul.*, pp. 1–1, 2024.
- [163] D. Kunze, B. Parmigiana, R. Schroth, and E. Gockenbach, “Macroscopic internal interfaces in high voltage cable accessories,” *Int. Council Large Electr. Syst.*, 2000.
- [164] K. Shibata, Y. Ohki, T. Takahashi, and T. Okamoto, “Breakdown strength at the interface between epoxy resin and silicone rubber,” in *2003 Ann. Rep. Conf. Electr. Insul. Dielectr. Phenom.*, 2003, pp. 289–292.
- [165] B. Du and L. Gu, “Effects of interfacial pressure on tracking failure between XLPE and silicon rubber,” *IEEE Trans. Dielectr. Electr. Insul.*, vol. 17, no. 6, pp. 1922–1930, 2010.
- [166] S. M. Hasheminezhad, E. Ildstad, and A. Nysveen, “Breakdown strength of solid|solid interface,” in *2010 10th IEEE Int. Conf. Solid Dielectr.*, 2010, pp. 1–4.
- [167] M. Hasheminezhad and E. Ildstad, “Application of contact analysis on evaluation of breakdown strength and PD inception field strength of solid-solid interfaces,” *IEEE Trans. Dielectr. Electr. Insul.*, vol. 19, no. 1, pp. 1–7, 2012.
- [168] E. Kantar, F. Mauseth, and E. Ildstad, “Effect of pressure and elastic modulus on tangential breakdown strength of solid-solid interfaces,” in *2016 IEEE Electr. Insul. Conf. (EIC)*, 2016, pp. 431–435.
- [169] E. Kantar, F. Mauseth, E. Ildstad, and S. Hvidsten, “Interfacial breakdown between dielectric surfaces determined by gas discharge,” in *2017 IEEE Conf. Electr. Insul. Dielectr. Phenom. (CEIDP)*, 2017, pp. 556–559.
- [170] E. Kantar, F. Mauseth, E. Ildstad, and S. Hvidsten, “Longitudinal AC breakdown voltage of XLPE-XLPE interfaces considering surface roughness and pressure,” *IEEE Trans. Dielectr. Electr. Insul.*, vol. 24, no. 5, pp. 3047–3054, 2017.
- [171] E. Kantar, S. Hvidsten, F. Mauseth, and E. Ildstad, “A stochastic model for contact surfaces at polymer interfaces subjected to an electrical field,” *Tribol. Int.*, vol. 127, pp. 361–371, 2018.
- [172] E. Kantar and E. Ildstad, “A novel methodology to monitor partial discharges in microvoids at solid-solid interfaces,” in *2019 IEEE Conf. Electr. Insul. Dielectr. Phenom. (CEIDP)*, 2019, pp. 113–117.
- [173] E. Kantar and S. Hvidsten, “A deterministic breakdown model for dielectric interfaces subjected to tangential electric field,” *J. Phys. D: Appl. Phys.*, vol. 54, no. 29, p. 295503, 2021.
- [174] J. A. Greenwood, J. B. P. Williamson, and F. P. Bowden, “Contact of nominally flat surfaces,” *Proc. Royal Soc. London. Series A. Math. Phys. Sci.*, vol. 295, no. 1442, pp. 300–319, 1966.
- [175] B. Zhu, Z. Jia, H. Hu, X. Ouyang, and X. Wang, “Relationship between the interfacial ramped DC breakdown voltage and the morphology of the XLPE/SiR interface,” *IEEE Trans. Dielectr. Electr. Insul.*, vol. 26, no. 3, pp. 689–697, 2019.
- [176] T. Liu, I. V. Timoshkin, S. J. MacGregor, M. P. Wilson, M. J. Given, N. Bonifaci *et al.*, “Field-time breakdown characteristics of air, N<sub>2</sub>, CO<sub>2</sub>, and SF<sub>6</sub>,” *IEEE Trans. Plasma Sci.*, vol. 48, no. 10, pp. 3321–3331, 2020.

- [177] B. Bagheri, J. Teunissen, U. Ebert, M. M. Becker, S. Chen, O. Ducasse *et al.*, “Comparison of six simulation codes for positive streamers in air,” *Plasma Sources Sci. Technol.*, vol. 27, no. 9, p. 095002, 2018.
- [178] J. Teunissen, A. Sun, and U. Ebert, “A time scale for electrical screening in pulsed gas discharges,” *J. Phys. D: Appl. Phys.*, vol. 47, no. 36, p. 365203, 2014.
- [179] T. M. P. Briels, J. Kos, G. J. J. Winands, E. M. van Veldhuizen, and U. Ebert, “Positive and negative streamers in ambient air: measuring diameter, velocity and dissipated energy,” *J. Phys. D: Appl. Phys.*, vol. 41, no. 23, p. 234004, 2008.
- [180] M. Balmelli, Y. Lu, R. Färber, L. Merotto, P. Soltic, D. Bleiner *et al.*, “Breakdown of synthetic air under nanosecond pulsed voltages in quasi-uniform electric fields,” *IEEE Access*, vol. 10, pp. 53 454–53 467, 2022.
- [181] J. C. Martin, *J. C. Martin on Pulsed Power*, T. H. Martin, A. H. Guenther, and M. Kristiansen, Eds. London: Springer New York, NY, 2013.
- [182] T. Martin, “An empirical formula for gas switch breakdown delay,” in *7th Pulsed Power Conf.*, 1989, pp. 73–79.

# On the Impulsive Electric Field Responses of Multilayered Composite Systems

---

As a prerequisite to understanding electrical breakdown under fast-rising electric fields in composite dielectric systems, one must first establish how the dielectric system will respond to an externally-applied field. This must be done considering the possibly complex relaxation behaviour arising from the different polarisation characteristics of the various dielectrics involved. For the transient impulsive waveforms of interest to this work, steady-state assumptions may not always be applicable and yet knowledge of the time-course of developed electric fields is critical for the understanding of ionisation processes that may be subsequently initiated. In this chapter, new mathematical models for the transient electric field based on the mechanism of Maxwell-Wagner polarisation are presented, which have been generalised to include poorly-conducting multilayered geometries in several coordinate descriptions. Important characteristics of multilayered composite materials, inferred from the derived mathematical description, are presented; as are results from subsequent analyses pertaining to the coupling between interfacial relaxation times and the time-course of the applied field. Several case studies that utilise the

---

This chapter was partially adapted, and may be quoted verbatim, from the following publication(s) with permission: T. Wong, I. Timoshkin, S. MacGregor, M. Wilson, and M. Given, “Modeling of the Transient Electric Field in Multilayer Dielectric Composites Under Impulsive HV Energization,” *IEEE Trans. Dielectr. Electr. Insul.*, vol. 30, no. 1, pp. 220–229, Feb. 2023. © IEEE 2023.

T. Wong, I. Timoshkin, S. MacGregor, M. Wilson, M. Given, and M. Maclean, “A Many-shells Model for Cell Transmembrane Potentials for Pulsed Electric Field Applications,” *IEEE Trans. Plasma Sci.*, vol. 52, no. 5, pp. 1775–1786, May 2024. © IEEE 2024.

developed model within the pulsed power domain are additionally presented, which includes its application to functionally-graded materials (FGMs) and for the advanced modelling of microbiological cells relating to PEF technology.

## 3.1 Introduction and Motivation

In systems that feature interfaces, characterisation of the electric field distribution often begins with the analysis of basic two- or three-layer systems under the consideration of Maxwell-Wagner polarisation as explained in Section 2.2.1. See for instance the numerous discussions on the topic of space charge accumulation within cables using simplified planar models [1, 2] or cylindrical geometries [3, 4]. This method has been commonly applied to HVDC transmission problems with the aim to quantify space charge migration leading to phenomena such as field inversion, enhancement, or accelerated insulation degradation [5, 6]. It has, however, become clear in recent studies that the sole application of Maxwell-Wagner theory is often inaccurate [4, 7], since a true description of spatially-distributed volumetric charge is not considered within this basic approach. Furthermore, important issues of prolonged unipolar currents in HVDC applications are strongly related to the temperature and field dependency of electrical conductivity, generally requiring some form of multi-physical modelling to be an adequate representation of reality, see for instance the numerous recent simulation works [8–10].

However, this work realised the opportunity to revisit the Maxwell-Wagner approach for fast-rising impulsive energisation, with its applicability informed mainly by the additional considerations that:

- Over short timescales typically used within pulsed power applications (e.g., nanosecond to millisecond range, from Chapter 2), any temperature variation can be considered negligible.
- Similarly, significant space charge is unlikely to accumulate over such timescales (assuming no breakdown at this stage).
- For moderate peak field magnitudes ( $10^5$  V/m to  $10^7$  V/m), material conductivity may only have a weak dependence on the electric field magnitude, see for instance [11].
- For particularly fast signals, the time necessary for conductivity to change as a function of field may also be far longer, based on the relaxation time of the conduction process in certain materials, e.g., see [12, 13].

The Maxwell-Wagner approach has seen previous success in pulsed power related fields, for

example, in PEF applications where microbiological cells have often been modelled as multilayered dielectric inclusions subject to pulsed external fields [14–18]. In these cases, reasonable estimates of cell transmembrane potentials (TMPs) and developed intra-layer electric fields can be obtained [19], further suggesting that the above assumptions may be valid for impulsive conditions. Given the growing interest in composite materials for HV applications, for instance: inhomogeneous field grading technology [20, 21], where some authors propose layered topologies [22, 23]; or laminates for more electric aircraft [24], it seemed instructive to reconsider the Maxwell-Wagner approach for the estimation of transient electric fields within the pre-breakdown regime. Moreover, it would be of great benefit to extend and generalise this approach to match pace with the increasing complexity of composite electrical systems. There was the additional motivation to provide an alternative, analytical, means for estimating potential and electric field quantities in complex layered dielectric systems; particularly in the context of interfaces. In many cases, there is the tendency to default to the use of mesh-based computational methods for such geometries, such as finite-element or finite-volume methods, e.g., in [22, 25], as they have become widely available and accessible most prominently in the form of commercial software packages. These computational methods are undoubtedly powerful, especially for practical geometries where analytical representation may be impractical or impossible. However, a number of issues relating to mesh-based numerical methods certainly invites improvement and motivates the progression of analytical techniques:

- The requirement to use computational meshes places great restriction on the relative dimensions of certain geometrical features. For example, modelling microscale or smaller features (e.g., voids, microbiological cells, droplets, thin material layers) contained within a host region with characteristic dimensions larger by several magnitudes. Extremely fine meshes are necessary to attain accurate results, but the total number of mesh elements may become prohibitively expensive due to the large external area under analysis. Modern multiscale modelling techniques like dynamic mesh adaptation alleviates some of the imposed computational load, but is far from a complete solution.
- The requirement to use numerical time stepping. As emphasised within Chapter 2, impulsive electric fields come inherently with the additional consideration of time-dependency and transience. Typical waveforms used in pulsed power applications span a wide range of characteristic times (the reader is reminded of Chapter 2, Table 2.1), while system relaxation times may span a comparable or wider range depending on the materials involved. The issue with multiple timescales is similar to the previous point, wherein sufficiently small timesteps must be employed to capture the fastest behaviour in a system lest risk significant

inaccuracies due to truncation errors. This quickly becomes prohibitive as the requirements on computational resources and time increases rapidly; particularly problematic for studies focused on time periods that are long relative to the required timestep.

- It is necessary when using mesh-based numerical methods to ensure sufficient spatial and temporal resolution to have confidence in the attained results. Typically, this would require mesh convergence studies (repeated cycle of refine, re-solve, evaluate error until it meets an acceptable threshold), again contributing to the total time required for model development and analysis.
- Numerical methods, while powerful, often provides little information regarding the underlying physical mechanisms. Contrast this with analytical approaches derived from first principles, which can lead to robust mathematical explanations offering a deeper intuition of physical phenomena. Ultimately, numerical methods excel at resolving equations which describe the physical phenomena, but are not a means to describe the physical phenomena alone.
- Analytical solutions to physical problems are necessary to verify numerical models.

Section 3.2 first details the theoretical framework and method underpinning the models developed within this chapter. This is initially conducted within arbitrary orthogonal coordinates, to make clear the generality of the results. Useful variations of the model are presented and validated against numerical simulations within relevant industrial contexts presented in Sections 3.3 and 3.4. This includes their application to layered field graders, insulation defects, and microbiological cell models for PEF applications. This chapter is concluded with a summary and discussion of the contributions that this modelling work has made towards the understanding of composite insulation and pulsed power system design.

## 3.2 A General View on Multilayered Geometries

Throughout this modelling work, it was firstly assumed that no breakdown nor pre-breakdown phenomena had yet occurred; the aim was to solely characterise the intra-layer electric field responses in space charge free composite materials according to the macroscopic theory. Here, any dielectric in contact with another of different properties is considered an *interface*, irrespective of their phases of matter, and where the adjacent regions in contact are electrically characterised by their (dimensionless) relative permittivity,  $\epsilon_i$ ; electrical conductivity,  $\sigma_i$ ; and some measure of thickness,  $d_i$ , as illustrated in Figure 3.1. Note that the subscript  $i$  refers to the  $i$ -th layer in an arbitrary layered geometry with  $n$  layers, separated by  $n - 1$  interfaces.

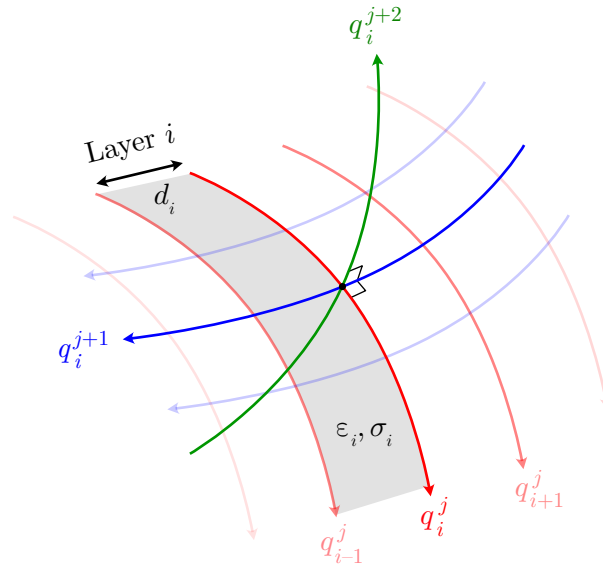


**Figure 3.1:** Pictorial representation of an orthogonal coordinate system, where the coordinate lines  $q_i^j$ ,  $q_i^{j+1}$ , and  $q_i^{j+2}$  meet at right angles.

The main quantity of interest is the electric potential field,  $\varphi_i$ , developed within each layer, from which knowledge of the electric field can be obtained. In physical problems, one must choose an appropriate coordinate definition which best describes the geometry under study to establish a boundary value problem (BVP) to be subsequently solved. Typically, the most natural description will align the geometry of interest along lines described by a single spatial coordinate, e.g., the use of spherical coordinates for spheres, etc. The present section first introduces this concept in a generalised manner with the use of an arbitrary geometrical coordinate representation. The purpose is to illustrate that the relaxation properties of multilayered poorly-conducting composites exhibit complex coupling between the individual relaxation behaviours of all  $n$  layers, irrespective of the coordinate system used. A link is established between the mathematical results and the physical system, demonstrating that the analytical results describe the underlying processes of charge transport and interfacial charge accumulation occurring at layer interfaces over the course of energisation.

### 3.2.1 A Boundary Value Problem in Arbitrary Orthogonal Geometries

Consider the real coordinate space  $\mathbb{R}^3$  described by orthogonal coordinates  $\vec{q} = (q^1, q^2, q^3)$  and where a region (or *layer*),  $i$ , is defined as the space between the curves  $q_{i-1}^j$  and  $q_i^j$ . The analysis was limited to orthogonal systems for their prevalence and relative simplicity. The extension of this approach to skew-coordinate systems, or other generalised curvilinear coordinates, is

nontrivial and left as a matter for future work. Letting  $h_j$  be the scale factor associated with coordinate  $q^j$ , the Laplacian of the potential field in layer  $i$ ,  $\varphi_i$ , following the space charge free assumption, must satisfy

$$\vec{\nabla}^2 \varphi_i(\vec{q}, t) = \frac{1}{\prod_j h_j} \frac{\partial}{\partial q^k} \left( \frac{\prod_j h_j}{h_k^2} \frac{\partial \varphi_i(\vec{q}, t)}{\partial q^k} \right) = 0, \quad (3.1)$$

where  $j = 1, 2, 3$ . Symbol  $t$  represents time, and summation over indices  $k$  is implied from Einstein notation\*. At each interface, two boundary conditions must be satisfied according to Maxwell's equations. The first dictates that the potential must be continuous at the interface, such that

$$\varphi_i(q_i^j, t) = \varphi_{i+1}(q_i^j, t), \quad (3.2)$$

while current continuity imposes the condition

$$\left[ \sigma_i \vec{\nabla} \varphi_i(q_i^j, t) + \varepsilon_0 \varepsilon_i \frac{\partial \vec{\nabla} \varphi_i(q_i^j, t)}{\partial t} \right] \cdot \hat{\mathbf{n}} = \left[ \sigma_{i+1} \vec{\nabla} \varphi_{i+1}(q_i^j, t) + \varepsilon_0 \varepsilon_{i+1} \frac{\partial \vec{\nabla} \varphi_{i+1}(q_i^j, t)}{\partial t} \right] \cdot \hat{\mathbf{n}}, \quad (3.3)$$

which describes the accumulation of a surface charge density,  $\varsigma_i(t)$ , at the  $i$ -th interface due to interface-directed currents as explained in Chapter 2, Section 2.2.2. A discontinuity in the electric displacement is therefore induced; condition (3.3) is the expansion of the classical continuity condition from Section 2.2.2:

$$\left[ \vec{D}_i(q_i^j, t) - \vec{D}_{i+1}(q_i^j, t) \right] \cdot \hat{\mathbf{n}} = \varsigma_i(t). \quad (3.4)$$

The ability to obtain self-consistent analytical solutions to (3.1) is dependent on: (i) the nature of the coordinate system and (ii) the potential boundary conditions. Addressing point (i), it is often convenient for simple orthogonal coordinate systems to be used (e.g., cartesian, polar, spherical etc.) which approximates the geometry of interest well. In the general case considered here, analytical solutions may be found when the potential in (3.1) is *separable*, that is, satisfies

$$\varphi(\vec{q}, t) = \Phi^1(q^1, t) \Phi^2(q^2, t) \Phi^3(q^3, t), \quad (3.5)$$

where  $\Phi^j$  are functions dependent only on one spatial coordinate, allowing the method of separation of variables to be applied. In the case of orthogonal coordinates, the Laplace equation is known to be separable on 13 coordinate systems [26], to which the analysis here is therefore

---

\*Sum over indices such that  $q^k \equiv \sum_k^D q^k$  for  $\mathbb{R}^D$ .

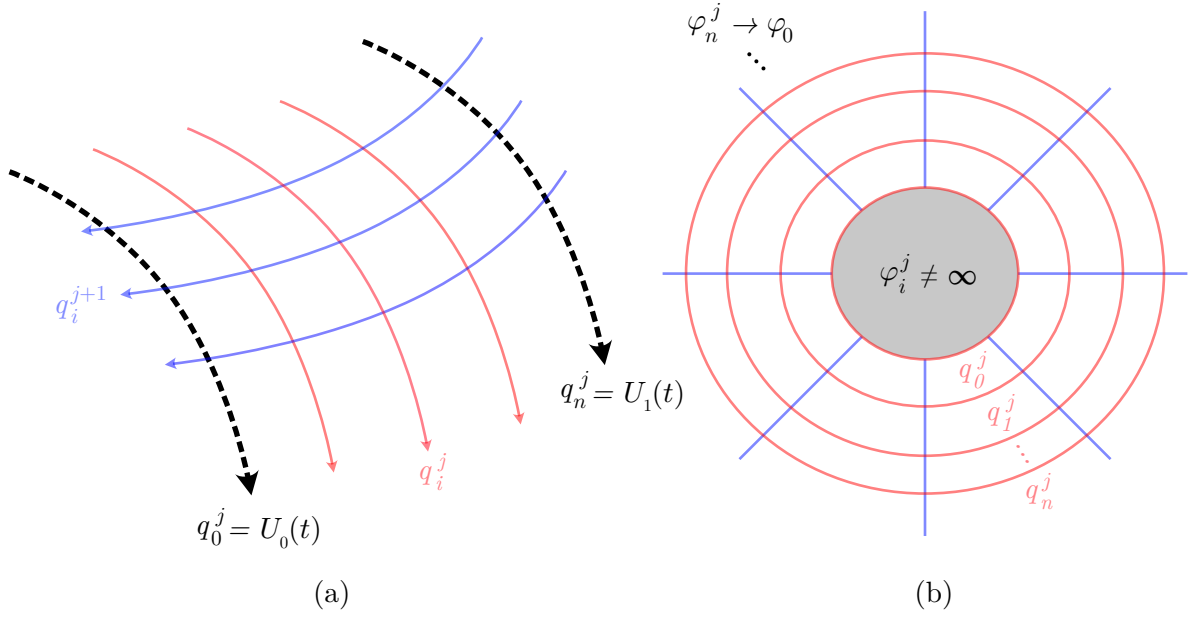


**Figure 3.2:** Two types of potential boundary conditions considered here, (a) where there exist Dirichlet conditions on surfaces described by a single coordinate  $q_i^j$ , (b) where the coordinate system creates closed loops, and the far-field condition requires  $\varphi_i^j$  to become self-consistent with the external potential,  $\varphi_0$ , far from the region of interest. Any enclosed region must also possess a non-singular potential.

limited. Further simplification can be achieved by exploiting common symmetries such as for rotationally-symmetric domains. In these cases,  $\varphi$  becomes invariant along some direction  $q^j$  often leading to the dimensional reduction of (3.1) and allowing simpler solutions to be recovered. As for point (ii), there are two cases of potential boundary condition that are of interest, illustrated in Figure 3.2:

- (a) Where Dirichlet conditions exist for the potential, i.e.,  $\varphi_i(q_i^j, t) = U_0(t)$  which may represent the application of a voltage on an electrode described by  $q_i^j$ .
- (b) Far-field conditions such as those used for modelling particles, voids, or bubbles in dielectrics [27–29], where the potential field far from the region of interest must become self-consistent with an externally applied field,  $\varphi_0(\vec{q}, t)$ . In these cases, enclosed regions as shown in Figure 3.2(b) must not contain any singularities in the electric potential.

Thus is stated that general form of the BVP associated with multilayered geometries in orthogonal coordinates. Solutions to  $\varphi_i(\vec{q}, t)$  of (3.1) subject to the conditions (3.2), (3.3), and any external potential conditions allow the time-domain electric field responses to be obtained. In Section 3.2.2, the typical solution process by means of the Laplace transform is illustrated, where the

complex coupling between the interfacial relaxation times is analytically demonstrated for this generalised representation.

### 3.2.2 Solution by Means of the Laplace Transform

For convenience, the interfacial conditions (3.2) and (3.3) may be reduced from their differential form to a purely algebraic representation by application of the Laplace transform. Letting  $s$  be the complex frequency variable, the transform  $\partial/\partial t \rightarrow s$  may be performed. The conditions (3.2) and (3.3) become the set of linear algebraic equations

$$\begin{aligned} \varphi_i(q_i^j, s) &= \varphi_{i+1}(q_i^j, s) \\ \vec{\nabla} \varphi_i(q_i^j, s) \cdot \hat{\mathbf{n}} &= \lambda_i \vec{\nabla} \varphi_{i+1}(q_i^j, s) \cdot \hat{\mathbf{n}}, \end{aligned} \quad (3.6)$$

where the symbol  $\lambda_i$  has been substituted for brevity, defined as

$$\lambda_i := \frac{\sigma_{i+1} + \varepsilon_0 \varepsilon_{i+1} s}{\sigma_i + \varepsilon_0 \varepsilon_i s} \equiv \frac{\varepsilon_{i+1} \left( s + \frac{1}{\tau_{i+1}} \right)}{\varepsilon_i \left( s + \frac{1}{\tau_i} \right)} \quad (3.7)$$

which relates to the intrinsic relaxation times,  $\tau_i := \varepsilon_0 \varepsilon_i / \sigma_i$ , of directly-adjacent layers. For static geometrical configurations (where the geometry itself does not change with time, which is true for most practical cases of interest), one may assume that the separated functions,  $\Phi^j$ , of (3.5) themselves are separable in time, and without the loss of generality, may be expressed

$$\Phi^j(q^j, s) = \beta(s) + \sum_k \alpha_k(s) f_k(q^j) \quad (3.8)$$

such that  $\alpha_k(s)$  is the  $s$ -domain coefficient to an arbitrary  $k$ -th function  $f_k(q^j)$ , which, importantly, is dependent only on the geometrical coordinate  $q^j$ ; and  $\beta$  is some spatially-constant term. Note that the summation over indices  $k$  is up to the number of terms comprising  $\Phi^j$ . It follows that with the definitions (3.7) and (3.8), the equation set (3.6) may be expressed as

$$\begin{aligned} \beta^i(s) + \sum_k \alpha_k^i(s) f_k(q_i^j) &= \beta^{i+1}(s) + \sum_k \alpha_k^{i+1}(s) f_k(q_i^j) \\ \sum_k \alpha_k^i(s) \frac{\partial}{\partial q^j} f_k(q_i^j) &= \lambda_i \sum_k \alpha_k^{i+1}(s) \frac{\partial}{\partial q^j} f_k(q_i^j), \end{aligned} \quad (3.9)$$

where it should be noted that by the condition of separability, any other function  $\Phi \neq \Phi^j$  from (3.5) cancel on both sides of the equation, as they are independent of the coordinate  $q_i^j$ . Similarly,

orthogonality allows the simplification of the normal component of the gradient operator to the partial derivative with respect to only  $q_i^j$ , and where the scaling factors of  $1/h_j$  also cancel<sup>†</sup>. The problem now becomes one concerning the existence of the coefficients  $\alpha_k^i(s)$  for consecutive layers. Equations (3.9) may be combined by subtraction to yield

$$\beta^i(s) + \sum_k \alpha_k^i(s) \left[ f_k(q_i^j) - \frac{\partial}{\partial q^j} f_k(q_i^j) \right] = \beta^{i+1}(s) + \sum_k \alpha_k^{i+1}(s) \left[ f_k(q_i^j) - \lambda_i \frac{\partial}{\partial q^j} f_k(q_i^j) \right]. \quad (3.10)$$

The reader is reminded that the coefficients  $\alpha_k^i(s)$ ,  $\beta^i(s)$ , if obtained, fully characterises the time-evolution of the electric potential as provided by the definition (3.8). That is, in a system with  $n$  layers, solutions to  $\alpha_k^1(s) \dots \alpha_k^n(s)$  and subsequent application of an inverse Laplace transform provides a full analytical solution to the electric potential in all layers, and by extension, all electric field distributions. The significance, however, of (3.10) is that it takes the form of a recurrence relation. The coefficients of the  $i$ -th layer are dependent on those characterising the next,  $(i+1)$ -th layer. Correspondingly, coefficients of the  $i$ -th layer must also be dependent on those of the previous,  $(i-1)$ -th, layer. In consequence, it must be true that the time-domain response of any layer  $i$  in a complex  $n$ -layer composite is affected by *all other layers present in the composite*.

The presence of  $\lambda_i$  in (3.10) is of further importance. As will be demonstrated in the following and in Section 3.3 and 3.4, analytical solutions exist to (3.10) under certain conditions, showing that the combination of all  $\lambda_i$  characterises the layer relaxation times due to Maxwell-Wagner polarisation. This is best illustrated for the simple case where only one term exists in the expansion of  $\Phi^j$  (i.e.,  $k=1$ ). With an appropriate choice of coordinate definition, the application of potential boundary conditions will generally provide information on  $\beta^i$ . For instance, the spatially-constant terms  $\beta^1$  and  $\beta^n$  will typically be known for multilayer systems bounded by a pair of electrodes (e.g., see the later Section 3.3.1). This can be verified from (3.8), since the application of a potential on some coordinate  $q^j$  representing an electrode will be, by definition, an equipotential. Thus,  $\beta$  alone will be equal to the applied potential. For the sake of illustration, it is assumed that  $\beta^1$  and  $\beta^n$  are known. The details of the derivation of the following step are of less importance than the result, and have thus been demoted to Appendix A.1, from which

<sup>†</sup>Since, by definition, the gradient operator is given by  $\vec{\nabla}\varphi = \sum_j \frac{1}{h_j} \frac{\partial\varphi}{\partial q^j} \cdot \hat{q}^j$ , and in orthogonal systems the unit normal  $\hat{n}$  on a surface  $q^j = \text{const.}$  is always  $\hat{q}^j$ . Hence,  $\vec{\nabla}\varphi \cdot \hat{n} = \vec{\nabla}\varphi \cdot \hat{q}^j = \frac{1}{h_j} \frac{\partial\varphi}{\partial q^j}$ .

the following expression

$$\beta^1(s) - \beta^n(s) = \sum_{\ell=1}^n \sum_k \alpha_k^i(s) \frac{\sigma_i + \varepsilon_0 \varepsilon_i s}{\sigma_\ell + \varepsilon_0 \varepsilon_\ell s} [f_k(q_\ell^j) - f_k(q_{\ell+1}^j)] \quad (3.11)$$

can be shown to hold in general, and in the most simple case of  $k = 1$ , yields the closed-form

$$\alpha^i(s) = \frac{\beta^1(s) - \beta^n(s)}{\sum_{\ell=1}^n \frac{\sigma_i + \varepsilon_0 \varepsilon_i s}{\sigma_\ell + \varepsilon_0 \varepsilon_\ell s} [f(q_\ell^j) - f(q_{\ell+1}^j)]} \quad (3.12)$$

for the  $\alpha$  coefficients of the  $i$ -th layer. For the assumptions applied here,  $q_\ell^j$  are constant, describing the geometry of the interfacial boundaries. It remains that to successfully recover time-domain solutions to  $\alpha_k^i(s)$ , an analytical inverse Laplace transform of (3.12) must be recoverable. The significance of (3.12) lies in the form of its denominator. The compounded effect of many layers stacked adjacently is revealed by the summation, which ultimately expands into a *characteristic polynomial* in  $s$  with order<sup>‡</sup>  $n - 1$ ,

$$P_n := \sum_{p=0}^{n-1} c_p s^{(n-p-1)} = c_0 s^{n-1} + c_1 s^{n-2} + \dots + c_{n-2} s^1 + c_{n-1} s^0, \quad (3.13)$$

where  $c_0 \dots c_{n-1}$  are constant coefficients. This allows (3.12) to alternatively be expressed as

$$\frac{\alpha^i(s)}{\beta^1(s) - \beta^n(s)} = \frac{1}{c_0 \prod_{\ell=1}^{n-1} \left(s + \frac{1}{\tau_\ell}\right)} = \sum_{\ell=1}^{n-1} \frac{K_\ell}{\left(s + \frac{1}{\tau_\ell}\right)} \quad (3.14)$$

when factored, where  $K_\ell$  are constant coefficients from the partial fraction expansion. Here it is evident, and perhaps expected, that the net effect of the Maxwell-Wagner interfacial charging effect is in the form of a superposition of  $n - 1$  first-order exponential responses, as evidenced by the  $\left(s + \frac{1}{\tau}\right)$  terms<sup>§</sup>. Equation (3.14) is the transfer function for the coefficients  $\alpha_i$  based on the time-varying nature of  $\beta^1$  and  $\beta^n$  representing the applied potentials. The factors of  $P_n$  therefore provide a means to compute the *interfacial relaxation time constants* describing the characteristic time of charge accumulation and decay at the  $i$ -th interface, and due to the  $f_k(q_\ell^j)$

---

<sup>‡</sup>The term *order* is used in this work to refer to the highest exponent of the polynomial, for which the term *degree* is equally valid.

<sup>§</sup>Since  $\mathcal{L}^{-1}\left(\frac{1}{s-a}\right) = e^{at}$ .

terms of (3.12), accounting also for the geometry of the problem, i.e.:

$$\tau_\ell = -\frac{1}{\text{roots}(P_n)_\ell}. \quad (3.15)$$

As a consequence of (3.14), as long as the known coefficients,  $\beta$ , have analytical inverse Laplace transforms, the partial fraction expansion of (3.14) allows the recovery of time-domain coefficients as a *sum of exponentials*. For instance, the *impulse response*,  $h_n(t)$ <sup>¶</sup>, of the multilayered system corresponds to the case when  $\beta^1(s) - \beta^n(s) = 1$ , thus

$$h_n(t) = \mathcal{L}^{-1} \left\{ \frac{\alpha^i(s)}{1} \right\} = \sum_{\ell=1}^{n-1} K_\ell e^{-\frac{t}{\tau_\ell}} \quad (3.16)$$

for an  $n$ -layer system.

The necessity to compute (3.15) for the relaxation time constants, however, imposes a limit to the maximum number of layers  $n$  for which fully closed-form solutions can be obtained. According to the Abel-Ruffini theorem [30], the roots of polynomials can be expressed in radicals only when its order is less than 5. Fully closed-form solutions to (3.14) are therefore obtainable only when  $n \leq 5$ , corresponding to attainable closed-form solutions to (3.15). This, however, does not equate to the model becoming invalid for  $n > 5$ , as (3.15) can equally be solved numerically using common algorithms (e.g., using the eigenvalue theorem). As long as the roots are computed accurately, closed-form solutions are equally obtainable (though with the additional numerical component, may be considered as *semi-closed-form*). For the case of  $n = 1$ , this simply corresponds to a single solid bulk material and  $P_n$  reduces to a constant. If  $n = 2$ ,  $P_n$  is a simple linear equation solvable by means of algebraic rearrangement that provides a single value of  $\tau_\ell$ , representing the interfacial relaxation time of the simple two-layer system. For  $n = 3, 4$ , or  $5$ ,  $P_n$  has order 2, 3, and 4, respectively. Closed-form solutions can therefore be sought through the quadratic, cubic, and quartic formulas as appropriate.

The mathematical forms derived here are in agreement with the present physical understanding of Maxwell-Wagner polarisation. Consider that a component of the electric field developed in the  $i$ -th layer originates from free charges which have accumulated at the bounding interfaces (due to mismatching conduction currents). It would be reasonable to assume that *all interfacial charges*, including those at interfaces not belonging immediately to the bounded region  $i$ , would

---

<sup>¶</sup>Note that *impulse response* here refers to the system response to the Dirac delta function,  $\delta(t)$ , rather than to impulsive waveforms in the context of pulsed power engineering.

also induce a component of electric field in the layer  $i$ , contributing to the net field as per superposition. Given that the magnitude of total interfacial charges, free and bound, are determined by the electrical conductivity and permittivity of the material layers, respectively; the constantly-changing balance of charges at each interface results in a strong coupling between every layer present in the composite. The present model hereby provides a powerful means to describe and to analyse this charging process.

The generalised analysis conducted in this section is perhaps more abstract, but is important from the perspective of mathematical rigour. Most importantly, it has been shown that the characteristic polynomial,  $P_n$ , governs the time-domain electric field response of multilayered poorly-conducting systems. Theoretical limits to the number of layers for which there exist closed-form solutions, and methods to reach beyond these limits, have been established. This has purposefully been conducted within a generalised coordinate reference frame with only the imposition of orthogonality and separability of the electric potential as constraints. While mesh-based methods remain vastly superior for complex geometries without simple analytical descriptions, problem domains which can be well-represented under the present assumptions benefit greatly from the approach described here. Moving away from the present abstractions into the tangible realm of practical design, Sections 3.3 and 3.4 demonstrate particular solutions relevant to important practical problems within pulsed power engineering, showing how they may be applied.

### 3.3 Multilayered Field Graders for Pulsed Power Applications

In this section, the theory developed in Section 3.2 is applied to the development of novel field-grading materials for power and pulsed power applications. The methods and results of this section are based on the published paper [31], aiming to demonstrate the relevance of this model within an industrial context and to provide a practical example of where the intra-layer coupling of time constants become important. Field grading refers to the purposeful design and coordination of system geometry and/or insulation to achieve and control the electric field distribution developed within a particular system. Existing methods may be based on geometrical modifications to system components and accessories [32], the use of conductive coatings and tapes for surface grading [33, 34], or the use of adaptive FGMs [20, 35].

FGMs may be broadly split into two categories. The first involves adaptive materials with field-dependent electrical characteristics (permittivity, electrical conductivity) [20, 32, 36]. Such

materials, when subjected to non-uniform electric fields, will exhibit a spatially inhomogeneous response based on the local electric field strength, typically designed to purposefully reduce localised field enhancement and maintain a greater overall degree of field uniformity. The main focus of this section, however, is on a second type of functional grading (also commonly referred to as FGMs) involving specialised composite materials that possess spatially non-uniform distributions of either permittivity, electrical conductivity, or both [37,38]. In response to modern requirements for system miniaturisation, this category of FGM has received significant research attention, where both continuous FGMs [37] and multilayered FGMs [22] have been explored as possible solutions for effective electric field control. At the time of writing, these types of FGM remain under development and have yet to be widely adopted. However, recent efforts focused on performance characterisation and on methods of fabrication have been significant, see for instance [39–42]. Continued progress may see FGMs be deployed in the near future to support systems within both power and pulsed power applications.

In contribution to the advancement of modern FGM technology, the generalised methodology of Section 3.2 was applied as a means to estimate layered FGM grading performance for impulsive applications. To do so, Section 3.3.1 firstly derives  $n$ -layer closed-form field solutions in a one-dimensional planar case using the general solution of (3.12), representing a graded composite. Section 3.3.2 follows with the analysis of the field-grading characteristics of a 20-layer laminate under impulsive energisation, which includes an evaluation of the effects of three different impulsive waveforms. This also acts to demonstrate the complex coupling between the individual layer relaxation times and the signal rise/fall characteristics. Then, the simple extension of the planar case to incorporate cylindrical geometries is presented in Section 3.3.3, demonstrating the relevance of this novel approach to FGM spacers that are proposed to be used within gas-insulated lines (GIL).

### 3.3.1 Particular Solutions for One-dimensional Planar Geometries

To begin, the reader is referred to the diagram of Figure 3.3 which illustrates the one-dimensional planar geometry considered here. Consider an  $n$ -layer laminate of poorly-conducting material stacked between two planar electrodes, where the electrode at  $z = z_0$  is energised with some arbitrary time-dependent potential  $U_0(t)$  in volts, while the electrode at  $z = z_n$  is grounded. As in Section 3.2, each layer is characterised by some value of constant relative permittivity,  $\epsilon_i$ , electrical conductivity,  $\sigma_i$ , in S/m, and thickness  $\Delta z_i = z_i - z_{i-1}$  in meters, where  $z_i$  is the coordinate representing the  $i$ -th interface with  $z_0 = 0$  m. In this simple one-dimensional geometry,

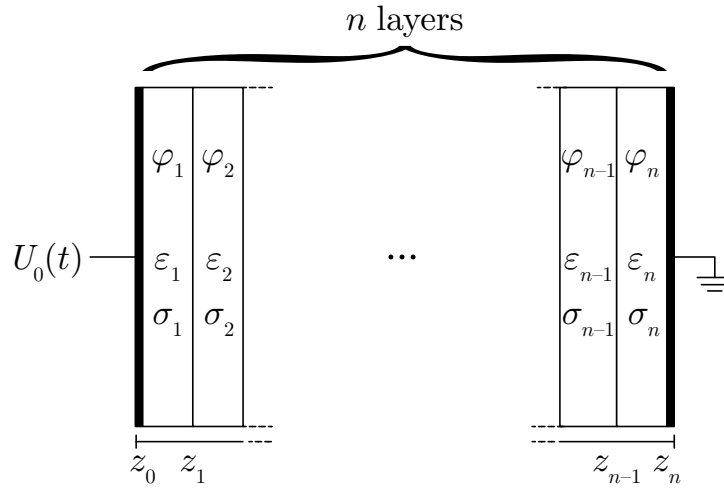


**Figure 3.3:** Diagram of a one-dimensional planar,  $n$ -layered, composite energised between two electrodes. Image adapted with permission from [31], © 2023 IEEE.

the Laplace equation (3.1) becomes

$$\frac{d^2 \varphi_i(z, t)}{dz^2} = 0, \quad (3.17)$$

where  $\varphi_i(z, t)$  is once again the time-dependent electric potential. Equation (3.17) has the elementary general solution

$$\varphi_i(z, t) = A_i(t)z + B_i(t), \quad (3.18)$$

where  $A_i(t)$  and  $B_i(t)$  are time-dependent coefficients characterising the response of the  $i$ -th layer. By  $\vec{E} = -\vec{\nabla}\varphi$ , the electric field developed within the  $i$ -th layer must be of the form

$$\vec{E}_i(z, t) = -A_i(t) \cdot \hat{z}. \quad (3.19)$$

At this point, one may wish to continue the derivation as was presented in [31], however, comparing the form of the potential (3.18) to (3.8) shows that the general solution (3.12) established for  $k = 1$  is exactly applicable. The additional Dirichlet conditions on the electrodes take the form

$$\begin{aligned} \varphi_1(z = 0, t) &= U_0(t) \\ \varphi_n(z = z_n, t) &= 0 \end{aligned} \quad (3.20)$$

for the HV and ground electrodes, respectively, and hence from (3.12),

$$A_i(s) = \frac{U_0(s)}{\sum_{\ell=1}^n \frac{\sigma_\ell + \varepsilon_0 \varepsilon_{i\ell} s}{\sigma_\ell + \varepsilon_0 \varepsilon_{\ell s}} (z_\ell - z_{\ell+1})}, \quad (3.21)$$

which is equivalent to equation (13) of [31] with minor notational differences. From (3.19),  $A_i(s)$  alone defines the electric field in the  $i$ -th layer for an appropriate choice of  $U_0(s)$  in (3.21). As the interest is in fast-rising impulsive energisation,  $U_0(t)$  was assumed to take a double-exponential form as typical for capacitive-storage based pulse generators (e.g., Marx generators as described in Section 2.1), given generally in both the time- and  $s$ -domains by

$$U_0(s) = \mathcal{L}\{U_0(t)\} = \mathcal{L}\left\{A_0 U_0 \left(e^{-\hat{\alpha}t} - e^{-\hat{\beta}t}\right)\right\} = A_0 U_0 \left(\frac{1}{s + \hat{\alpha}} - \frac{1}{s + \hat{\beta}}\right), \quad (3.22)$$

where  $U_0$  is the peak voltage in volts,  $A_0$  is a constant scaling factor, and  $\hat{\alpha}$ ,  $\hat{\beta}$  are wave-shaping parameters with units  $s^{-1}$ , which characterise the rise and fall characteristics of the impulse. Combination of (3.21) with (3.22) and (3.19) with the application of a partial fraction expansion (see Appendix A.2<sup>¶</sup>) allows the inverse  $s$ -transform to be performed analytically as a sum of exponentials. A fully closed-form time-domain solution to the electric field magnitude in [31] was hence recovered as

$$E_i(t)_{\text{DE}} = -\frac{A_0 U_0}{a_0} \left[ \frac{P(\hat{\alpha})}{Q(\hat{\alpha})} e^{-\hat{\alpha}t} - \frac{P(\hat{\beta})}{Q(\hat{\beta})} e^{-\hat{\beta}t} + (\hat{\beta} - \hat{\alpha}) \sum_{m=1}^{n-1} \frac{R(m)}{S(m)} e^{-\frac{t}{\tau_{n+m}}} \right], \quad (3.23)$$

where

$$\begin{aligned} P(x) &= \prod_{j=1, j \neq i}^n \sigma_j (1 - x\tau_j), & Q(x) &= \prod_{m=1}^{n-1} \left( \frac{1}{\tau_{n+m}} - x \right), \\ R(x) &= \prod_{j=1, j \neq i}^n \sigma_j \left( 1 - \frac{\tau_j}{\tau_{n+x}} \right), \\ S(x) &= \left( \hat{\alpha} - \frac{1}{\tau_{n+x}} \right) \left( \hat{\beta} - \frac{1}{\tau_{n+x}} \right) \prod_{\substack{k=1 \\ k \neq x}}^{n-1} \left( \frac{1}{\tau_{n+k}} - \frac{1}{\tau_{n+x}} \right), \end{aligned} \quad (3.24)$$

<sup>¶</sup>Note that the formulation here has a number of notational differences compared to the prior work published as [31], but are mathematically identical. See Appendix A.2 for details.

**Table 3.1:** Double-exponential wave-shaping parameters for the utilised impulsive waveforms.

Waveform Specification	$A_0$	$\alpha, \text{s}^{-1}$	$\beta, \text{s}^{-1}$
50/500 ns	1.1454	$144.8861 \times 10^4$	$49.8516 \times 10^6$
0.5/5 $\mu\text{s}$	1.1418	$144.7250 \times 10^3$	$50.2967 \times 10^5$
1.2/50 $\mu\text{s}$	1.0305	$13.9621 \times 10^3$	$24.8658 \times 10^5$

and  $a_0$  is the leading coefficient of the polynomial (see Appendix A.2 for its differences compared to  $c_0$  used in the more general form). The first  $n$  indices of the time constants  $\tau$  are defined  $\tau_i := \varepsilon_0 \varepsilon_i / \sigma_i : i \leq n$  representing the intrinsic layer relaxation times, while  $\tau_i : n < i \leq (2n - 1)$  are the interfacial relaxation times accounting for Maxwell-Wagner polarisation arisen from the characteristic polynomial due to (3.13). Equation (3.23) along with the definitions (3.24) enable the transient electric field to be calculated in closed-form within any layer  $i$  in an  $n$ -layer laminate, and is free from the aforementioned limitations of mesh-based methods discussed in Section 3.1.

### 3.3.2 Grading Characteristics of Multilayered FGMs Under Fast-rising Impulses

On the basis of equation (3.23), this section validates the analytical solution against numerically simulated solutions using Quickfield Professional [43], a standard numerical computing software capable of transient electric field analysis. This was firstly conducted through the analysis of the developed intra-layer electric fields for a 20-layer graded composite under the energisation of a 50/500 ns (50 ns rise-time, 500 ns full-width-half-maximum) waveform with peak magnitude 150 kV, as shown in Figure 3.4 (dashed line). For the sake of illustration, the layer thicknesses were assumed to be equal at  $\Delta z_i = 0.25$  cm, resulting in a total electrode gap distance of 5 cm. This comparison is also used to demonstrate the effects of permittivity and conductivity grading in separate, complementary, studies involving two different grading profiles. The effects of the applied voltage waveshape were further investigated through the comparison of the time-domain intra-layer field responses developed under three impulsive waveforms with different characteristic timescales. These included the mentioned 50/500 ns waveform, a 0.5/5  $\mu\text{s}$  waveform, and a standard (IEC-60060 [44]) 1.2/50  $\mu\text{s}$  lightning impulse (Figure 3.4). The waveshaping parameters characterising these waveshapes were attained used a custom swarm-like optimisation technique which solved for the required parameters, tabulated in Table 3.1. A brief description of this method can be found attached as Appendix B.1.

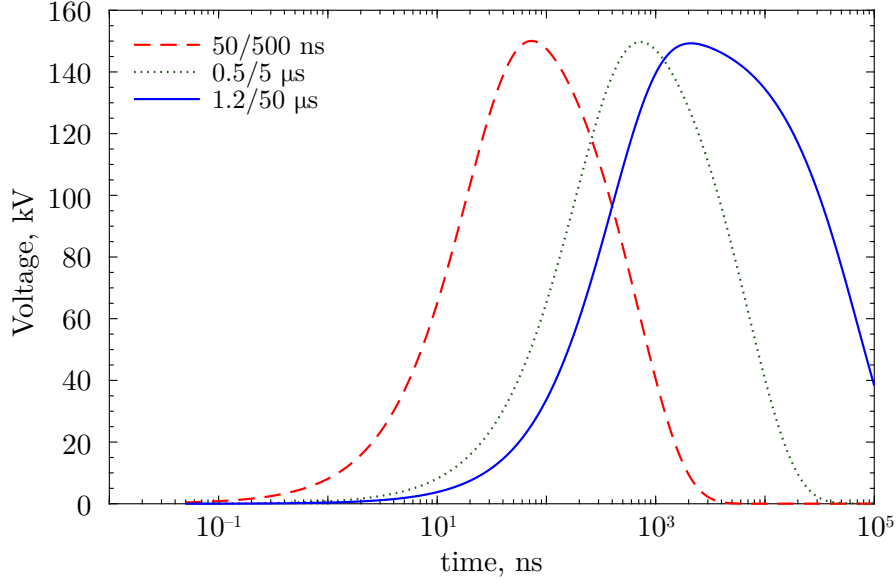


**Figure 3.4:** Time-course of the three waveforms used within this chapter to evaluate the effects of multilayered field graders for impulsive applications. Waveshape specification given as rise-time/FWHM. Image adapted with permission from [31], © 2023 IEEE.

### 3.3.2.1 Grading Profiles

For a multilayer composite with  $n = 20$ , the parameter values of two different grading profiles are conveniently provided by the evaluation of (3.25) and (3.26):

$$p_i^{\text{linear}} = p_{\max} + \frac{p_{\max} - p_{\min}}{z_{n-1}} z_{i-1}, \quad (3.25)$$

$$p_i^{\text{U}} = \frac{16(p_{\max} - p_{\min})}{z_{n-1-a}^4} \left( z_{i-1} - \frac{z_{n-1-a}}{2} \right)^4 + p_{\min}, \quad (3.26)$$

where  $p_i$  is the parameter of interest for the  $i$ -th layer; either relative permittivity,  $\varepsilon_i$ , or electrical conductivity,  $\sigma_i$ . The value of  $a = (1 - (-1)^n)/2$  is either 1 or 0 depending on  $n$ . The former equation (3.25) corresponds to a linearly-decreasing profile from  $p_{\max}$  to  $p_{\min}$ , while the latter (3.26) returns a symmetrical “U”-shaped profile assuming values of  $p_{\max}$  at the edges with a minimum of  $p_{\min}$  at the centre. Figure 3.5 provides example plots for graded permittivity profiles using values of  $\varepsilon_{\max} = 15$  and  $\varepsilon_{\min} = 2$ . This range of relative permittivity may be considered to reflect common materials used for electrical insulation purposes. For example, polymeric materials such as XLPE or polypropylene (PP) have typical values of  $\varepsilon_r \in [2 - 3]$  [45], while some ceramics like Macor or Alumina have  $\varepsilon_r \in [6 - 9]$  [46]. An upper range of  $\varepsilon_r \in [12 - 15]$  can be attained by some novel composite grading materials [47]. For the conductivity grading

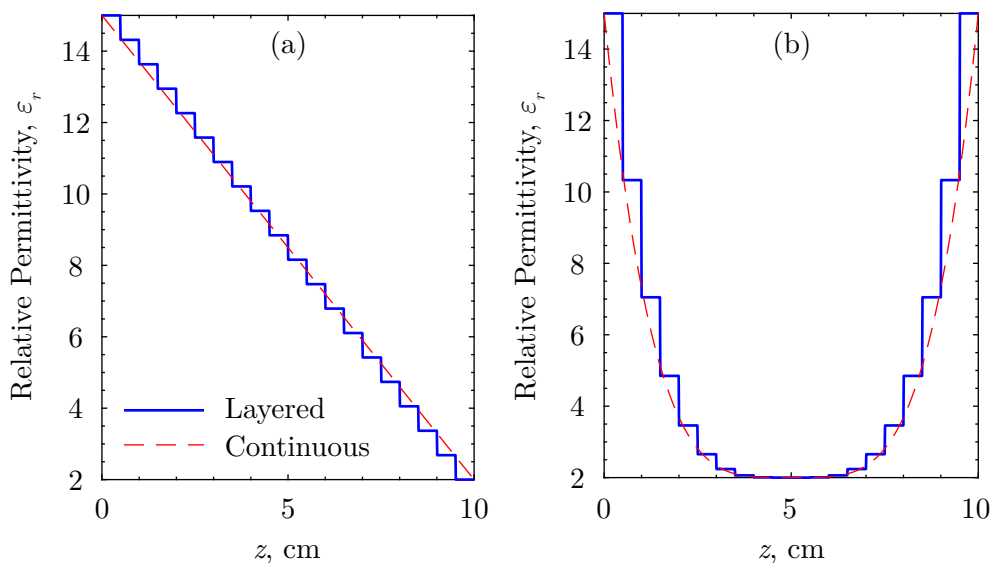


**Figure 3.5:** Multilayered grading distributions used in this work, (a) linear profile according to (3.25), (b) “U”-shaped profile according to (3.26). Blue solid lines show the multilayered profiles as an approximation to the continuous distributions shown as dashed red lines. Image adapted with permission from [31], © 2023 IEEE.

study, the corresponding parameters were chosen as  $\sigma_{\min} = 10^{-14}$  S/m and  $\sigma_{\max} = 10^{-4}$  S/m, with values in the lower end of the range being typical for engineering polymers, while the upper end may be attained by commercially available conductive grading tapes [48].

### 3.3.2.2 Effects of Graded Permittivity

Based on the graded permittivity profiles of Figure 3.5, Figure 3.6(a)–(b) plots the electric field distribution across all layers of the 20-layer composite with the assumption that all layers were perfect dielectrics ( $\sigma_i = 0$  S/m) alongside data simulated using QuickField. Fields are shown at  $t_p = 73.1$  ns, corresponding to the peak of the applied field as shown by the transient field plots of Figure 3.6(c); for layers  $i = 1, 5, 10,$  and  $15$ , using the linear grading profile. Note that simulated data could only be gathered at linearly spaced timesteps which begin to overlap on Figures 3.6(c) and 3.7(c) due to the logarithmic scale. Markers have therefore been removed after  $1 \mu\text{s}$  to ensure visibility, but do continue to follow the analytical solution. All comparisons find excellent agreement between the numerical results and the derived analytical solution of (3.23).

In the non-conductive limit, the absence of conduction currents prevents surface charge accumulation, leading to the observed electrostatic response. Reduction of the intra-layer field magnitudes due to polarisation was observed, with proportion to the layer permittivity, which is

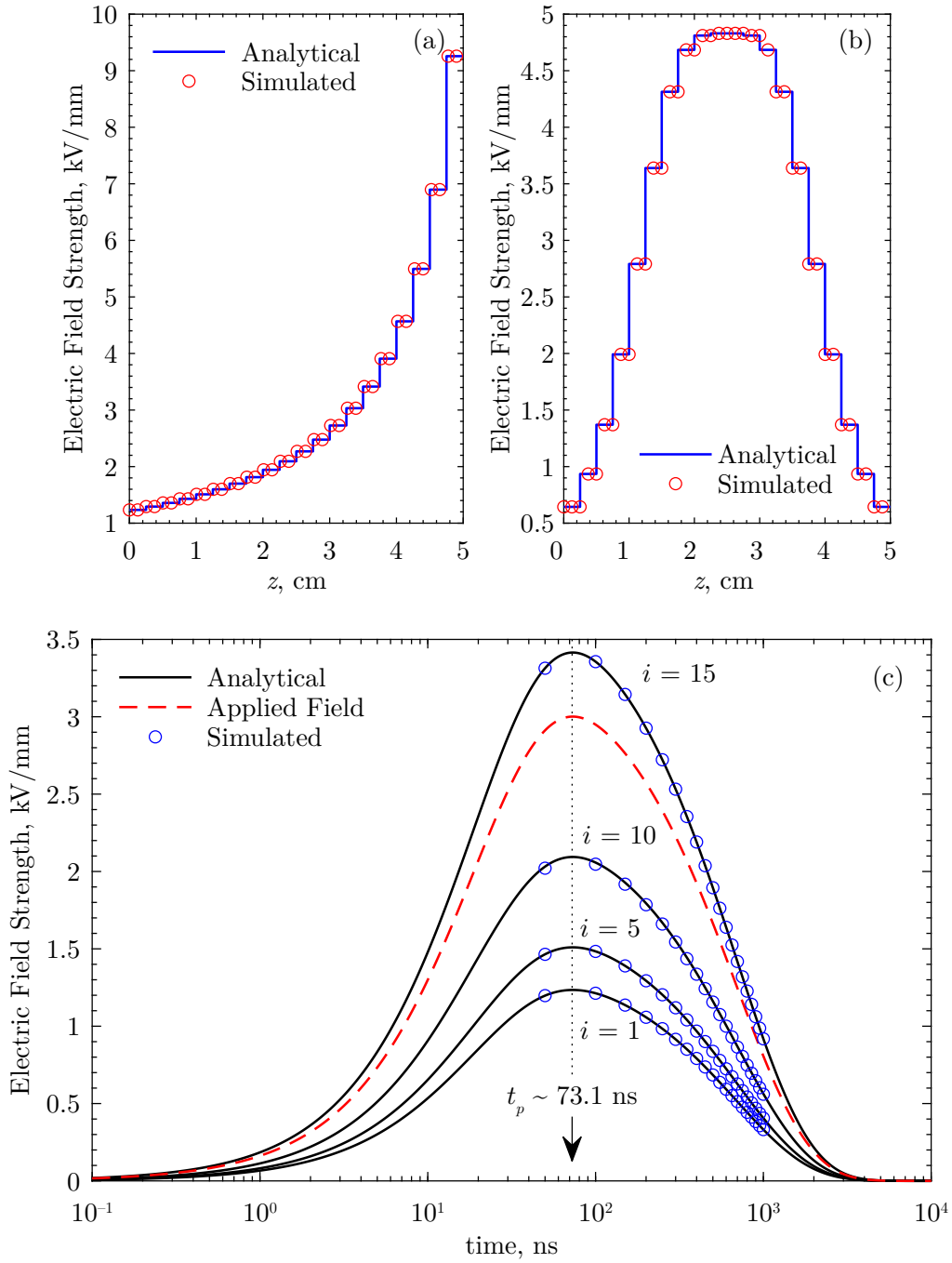


**Figure 3.6:** Field responses for a 20-layer graded permittivity composite (zero conductivity) under 50/500 ns impulse. Field distributions at  $t_p$  for (a) linear grading profile, (b) “U”-shaped grading profile. Sub-figure (c) shows the electric field strength over time for layers  $i = 1, 5, 10,$  and  $15,$  comparing the analytical solution to FEM simulated data (linear profile). Image adapted with permission from [31], © 2023 IEEE.

reflective of the applied grading profile. The net effect is the redistribution and reduction of the electric field magnitude away from the regions of highest permittivity, alongside the enhancement of the field in layers of lower permittivity. Without significant charge displacement in the system (modelled by zero conductivity), the intra-layer electric fields reach their peak simultaneously with identical rise and fall characteristics to the applied voltage and field.

#### 3.3.2.3 Effects of Graded Conductivity

As a complementary study to permittivity grading, Figure 3.7(a)–(b) similarly plots the spatial field distribution inside the composite, and Figure 3.7(c) shows the corresponding transient responses of the fields developed in layers 1, 5, 10, and 15. These plots were generated using the graded conductivity profiles as described in Section 3.3.2.1 with relative permittivity set to  $\varepsilon_r = 2$  for all layers.

For conductivity-graded materials, charge transport across each layer give rise to conduction currents. Consequently, additional surface charge accumulates at interfacial boundaries based on the local balance of currents, leading to a distinctly different response compared to the non-conductive, permittivity-graded, case. Both the peak field magnitude and peak time in each layer was found to be strongly affected by the grading profile, resulting from the different relaxation times now associated with the interfaces between layers. In this particular arrangement, using the linear grading profile, the time to field maximum is prolonged for lower conductivity layers. This behaviour can be explained through the relative charging times between the set of interfaces, which act to modify the intra-layer electric fields and manifests different timescales for the accumulation of surface charge. The difference in the characteristic times between the applied field and the surface charge induced field, in any layer,  $i$ , acts to modify the rise and fall characteristics of the net developed field within the layer. Layers of lower conductivity impart a longer charging time to their respective interfacial boundaries, leading to the observed prolonging of the time necessary for the field to peak. The opposite is true for layers of higher conductivity. In Figure 3.7(c), using the linearly-decreasing conductivity profile, this results in a “domino” like effect where each layer experiences its field maximum in sequence from  $i = 1$  (highest conductivity) up to  $i = 20$  (lowest conductivity). From the same phenomenon, consecutive field reversal of each layer is observed on the falling edge past  $t \approx 1 \mu\text{s}$  due to the decaying surface charge at the interfaces. The time necessary for surface charge to dissipate is governed by the same set of charging time constants, therefore, the field in the  $i$ -th layer becomes momentarily reversed when charges on one interface decays more rapidly than the opposing side (affected also

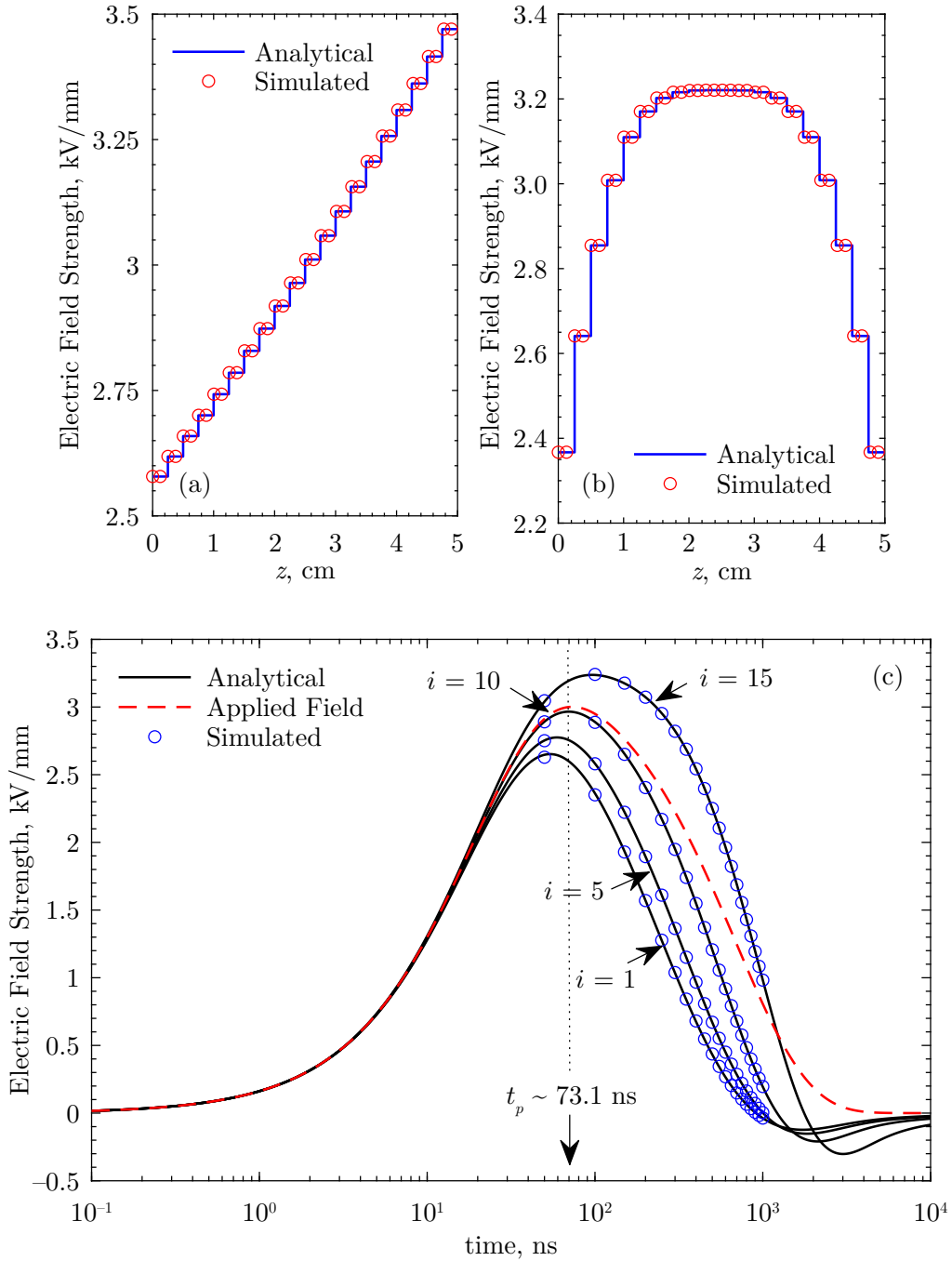


**Figure 3.7:** Field responses for a 20-layer graded conductivity composite (equal permittivity) under 50/500 ns impulse. Field distributions at  $t_p$  for (a) linear grading profile, (b) “U”-shaped grading profile. Sub-figure (c) shows the electric field strength over time for layers  $i = 1, 5, 10,$  and  $15$ , comparing the analytical solution to FEM simulated data (linear profile). Image adapted with permission from [31], © 2023 IEEE.

by the field magnitude of the adjacent layers). The time for field reversal therefore follows the same pattern when under the present linearly-decreasing conductivity grading profile.

#### 3.3.2.4 Effects of Applied Pulse Parameters

To address one of the main motivators for the development of the present model, this section aims to compare the intra-layer electric field responses for multilayered composites subjected to impulsive waveforms with different rise and fall characteristics. The relevance of this is not limited to the present case study of graded insulators for pulsed power systems, but results of which are applicable to any system featuring interfacial contacts between many different dielectric and/or poorly-conducting materials.

Again using the 20-layer composite described within the preceding sections, and maintaining the same 150 kV peak voltage, the three double-exponential waveforms shown in Figure 3.4 and defined by the parameters of Table 3.1 were applied to the 20-layer system using (3.23). In this case, combined permittivity and conductivity grading was utilised following the “U”-shaped profile (3.26) with the same parameters used previously in Sections 3.3.2.2 and 3.3.2.3. Using this profile, the strongest fields develop at the centre of the composite, while the weakest are developed at the layers closest to the electrodes. Figure 3.8 therefore plots the transient field responses for layers  $i = 1$  (outermost) and  $i = 10$  (centre) for energisation under all three waveforms. It is remarked that due to the symmetry of the grading profile, field responses were correspondingly mirrored about the interface between layers 10 and 11. That is, layers  $i = 1, 20$  and  $i = 2, 19$  etc. have identical field responses.

The grading effect is immediately evident, based on the reduction of the peak electric field strength by around 85% in the layers nearest the electrodes. Despite the same peak field magnitude of the three applied waveforms, the peak field strength developed at the centre of the composite differs significantly. The peak electric field for the 0.5/5  $\mu\text{s}$  impulse is approximately 10% higher than that of the 50/500 ns impulse, while the 1.2/50  $\mu\text{s}$  impulse developed a peak almost 40% higher than the 0.5/5  $\mu\text{s}$  impulse. The difference can again be explained in terms of the interfacial time constants. For the grading parameters used here, the relaxation times computed from the laminate’s characteristic polynomial range between  $\approx 1 \mu\text{s}$  (outermost interfaces) to a maximum of  $\approx 23 \text{ ms}$  (innermost interfaces); most were found to be between 1 and 10  $\mu\text{s}$ . The relative difference between the rise-time of the applied field and the interfacial charging time is critical in characterising the observed differences in developed peak field magnitude. For the 50/500 ns case, even the fastest-charging interfaces charged on a timescale longer than the characteristic time

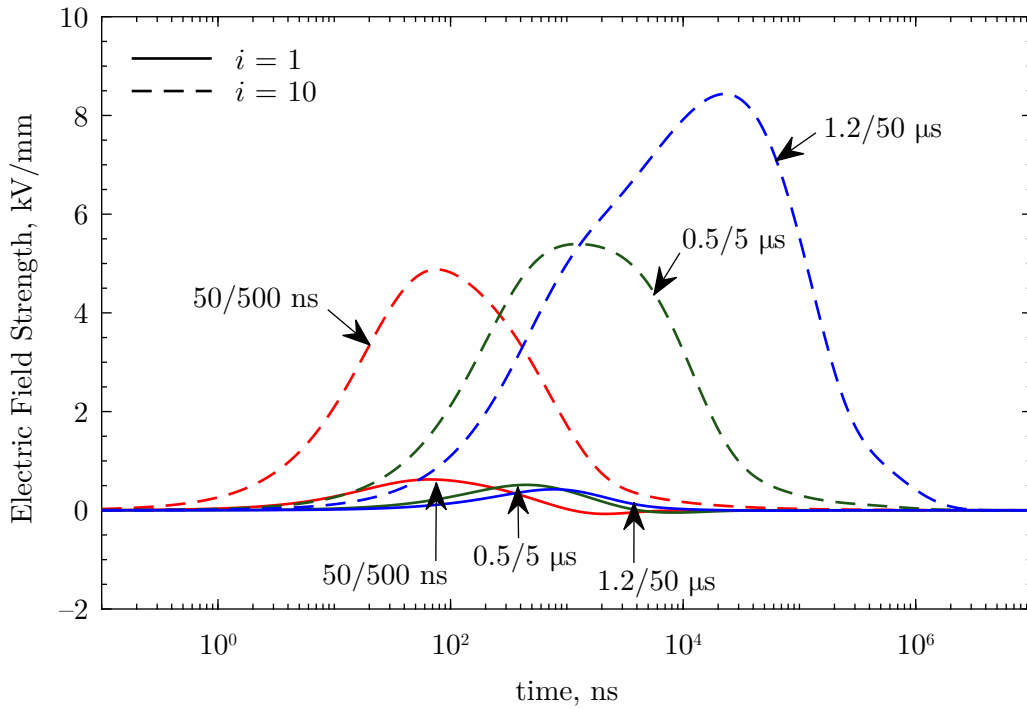


**Figure 3.8:** Comparison of transient field responses in layers  $i = 1$  and  $10$ , in a 20-layer “U”-shaped FGM using combined permittivity/conductivity grading, under 50/500 ns, 0.5/5  $\mu$ s, and 1.2/50  $\mu$ s impulses. Image adapted with permission from [31], © 2023 IEEE.

required for the impulse to rise (and fall). The composite is therefore unable to react sufficiently quickly (and establish significant interfacial charge) to substantially redistribute the electric field from the outer layers towards the centre, thus the enhancement of the field at the centre is less significant. This is supported by the stronger peak field found in the electrode-adjacent layers ( $i = 1, 20$ ). For the 0.5/5  $\mu$ s and 1.2/50  $\mu$ s impulses, their rise-times are comparable in magnitude to the charging times of the majority of interfaces, allowing significant interfacial charge to accumulate within the time necessary for the applied field to peak. The effects of this surface charge are therefore considerable, acting to enhance the electric field at the composite centre and leading to a greater degree of field reduction near the electrodes.

The results imply that the grading performance of multilayered composites under impulsive (and more generally, time-dependent) voltages is highly dependent on the nature of the applied waveforms. This extends to any pulsed power system that incorporates composite materials or laminates, whereby careful consideration should be given to the system relaxation times compared to the characteristic times of the applied waveform(s), to ensure design specifications are satisfied. Failure to do so may result in higher-than-expected peak field stresses and compromise system

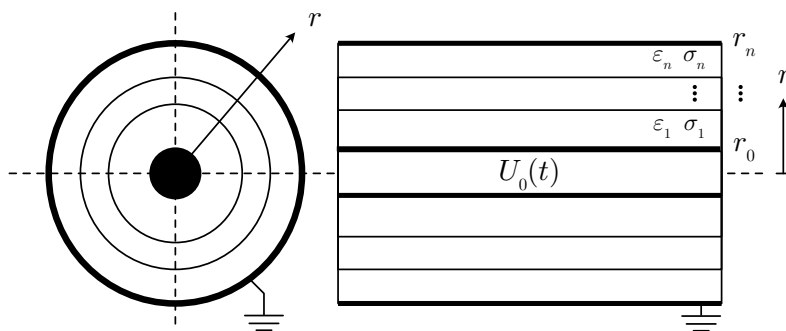


**Figure 3.9:** Structure of a multilayered cylindrical geometry, graded in the radial direction. Assuming a the length in the  $z$  direction is far greater than the radius, may be accurately represented using one-dimensional polar coordinates. Image adapted with permission from [31], © 2023 IEEE.

integrity. The possibility of catastrophic electrical breakdown occurrence, if critical field thresholds are exceeded due to improper insulation coordination, may become a risk. In the following section, results arising from the combined application of permittivity and conductivity grading to FGMs for novel GIL spacer technology are presented, demonstrating the possible value of this approach for the estimation of field redistribution for next-generation composite insulation design.

### 3.3.3 Functionally Graded Spacers for Gas-Insulated Lines

By means of a simple coordinate transform, the solution to the one-dimensional planar case (3.21) can be extended to incorporate cylindrical geometries of infinite length as shown in Figure 3.9. This extends the application of the novel multilayered model to common systems exhibiting cylindrical symmetry with an inner conductor and outer grounded sheath, e.g., power transmission cables or gas insulated lines. Despite the infinite length assumption, this section seeks to also show that the model may be applied as a useful approximation of the surface electric field across a functionally graded spacer in GIL.

Considering the geometry of Figure 3.9, the radially-symmetric Laplace's equation admits general solutions of the form

$$\varphi_i(r, t) = C_i(t) \ln r + D_i(t), \quad (3.27)$$

where  $r$  is the radial coordinate, and  $C_i(t)$ ,  $D_i(t)$  are time-dependent coefficients; the equivalent to  $A_i(t)$  and  $B_i(t)$  from the previously-described planar case. The similarity to (3.18) is evident, and by the general form (3.8) the function  $f_1(q^j) \rightarrow \ln r$ . The transform from  $(z_\ell - z_{\ell+1}) \rightarrow (\ln r_k - \ln r_{k+1})$  in (3.21) is therefore the sole step necessary to extend the model to the cylindrical

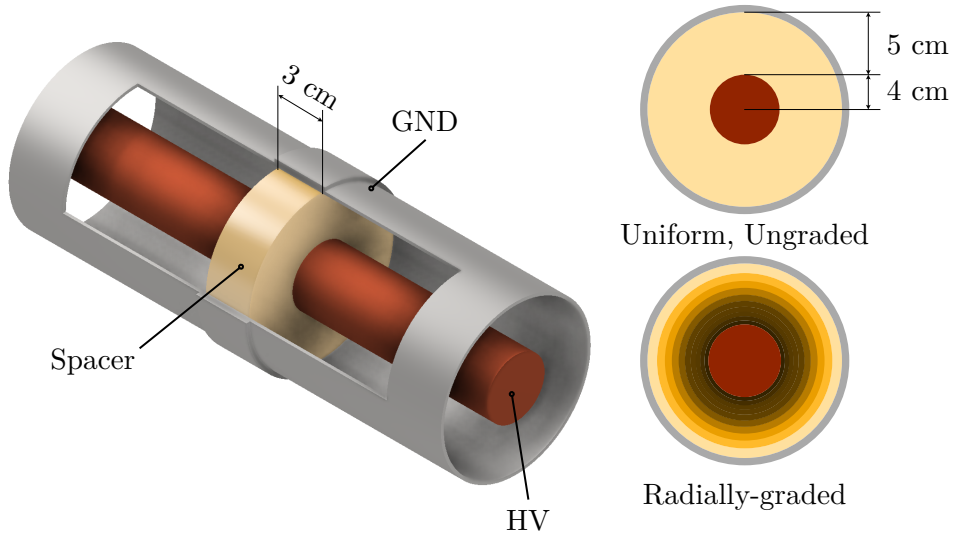


**Figure 3.10:** 3D-cutaway CAD model of a simple disk-type GIL spacer geometry, acting as mechanical support for an inner HV conductor. Shown are examples of uniform and radially-graded spacer types.

domain. The corresponding electric field from (3.27) then also assumes a radial decay with

$$\vec{E}_i^{\text{cyl}} = -\frac{C_i(t)}{r} \cdot \hat{r}. \quad (3.28)$$

The spacer geometry of interest is shown in Figure 3.10. For GIL spacers, the electric field distribution along the gas-spacer interface is of great importance. The triple junctions formed at the inner (HV) and outer (GND) conductors can induce significant field enhancement, bringing with them an increased risk of surface flashover. Graded GIL spacers have been proposed as one possible solution to reduce this risk, by using tailored inhomogeneous distributions of permittivity and/or conductivity to reduce peak field stresses across the spacer surface [25, 37]. Recent developments in the field of FGM spacers have seen great success for reducing the triple junction field [49], and studies on optimal grading profiles have also aided in their development [50, 51].

The spacer considered here takes the form of a radially-symmetric disk-type spacer; approximated using the geometry of Figure 3.9. It is remarked that this geometry is a simplification, particularly when compared to modern cone-type spacers used in current power equipment. However, spacers that are close to disk-like [52, 53] remain common in smaller-scale and non-standard systems used in some pulsed applications, which can be well represented with the present geometry. The considered GIL topology consisted of a total radial dimension,  $r_n - r_0$ , of 5 cm; a spacer width of 3 cm; and a conductor core radius of  $r_0 = 4$  cm. The applied potential to the conductor followed

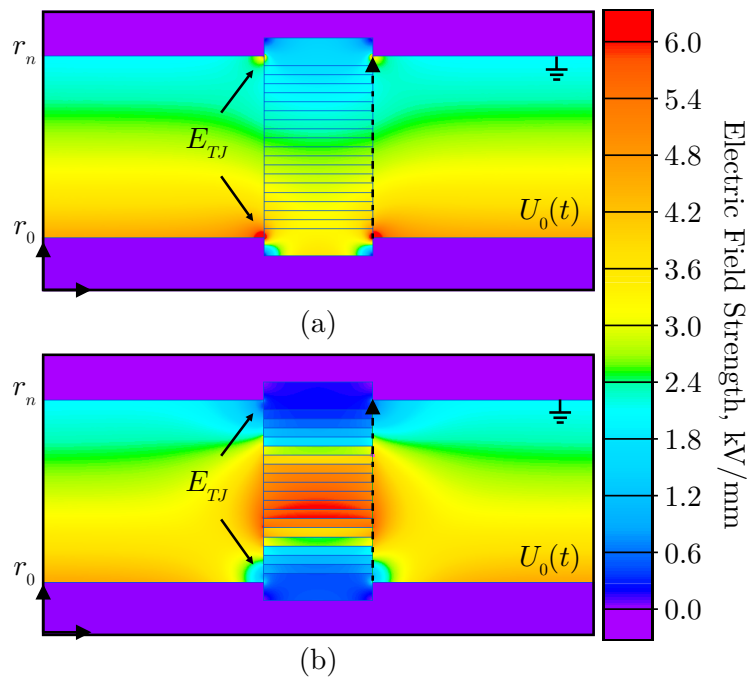


**Figure 3.11:** Simulated electric field distribution around disk-type GIL spacer for (a) uniform spacer material and (b) 20-layer  $\varepsilon/\sigma$  radially-graded spacer using the “U”-profile. Images taken when the field enhancement at the interface was at its maximum. Dashed arrow indicates the contour of measurement for Figure 3.12, taken on the side of the gas. The electrodes of the analytical model were set to align with  $r_0$  and  $r_n$ . Image adapted with permission from [31], © 2023 IEEE.

the 150 kV 1.2/50  $\mu$ s lightning impulse shown in Figure 3.4 described by the corresponding parameters of Table 3.1. To evaluate the grading effectiveness, a 20-layer ungraded spacer with  $(\varepsilon_i, \sigma_i) = (2.3, 10^{-14} \text{ S/m}) \forall i$  was compared to a graded spacer following the “U”-shaped profile of (3.26). Combined permittivity and conductivity grading was assumed with the same parameters as used in Sections 3.3.2.2 and 3.3.2.3. The electric field magnitude along the spacer-gas interface was of primary interest, thus, both graded and ungraded cases were simulated using QuickField, before the graded case was also compared to the approximation provided by the closed-form model (3.28). Figure 3.11 shows the simulated electric field distributions of ungraded and graded spacers at the moment of maximum field stress, with the locations of the triple junctions indicated. Figure 3.12(a) and (b) plots the electric field strength across the gas-spacer interface for graded and ungraded cases, respectively, alongside the estimated field based on the analytical model. This is additionally compared to the simulated field inside the spacer bulk (down the centre-line of the spacer).

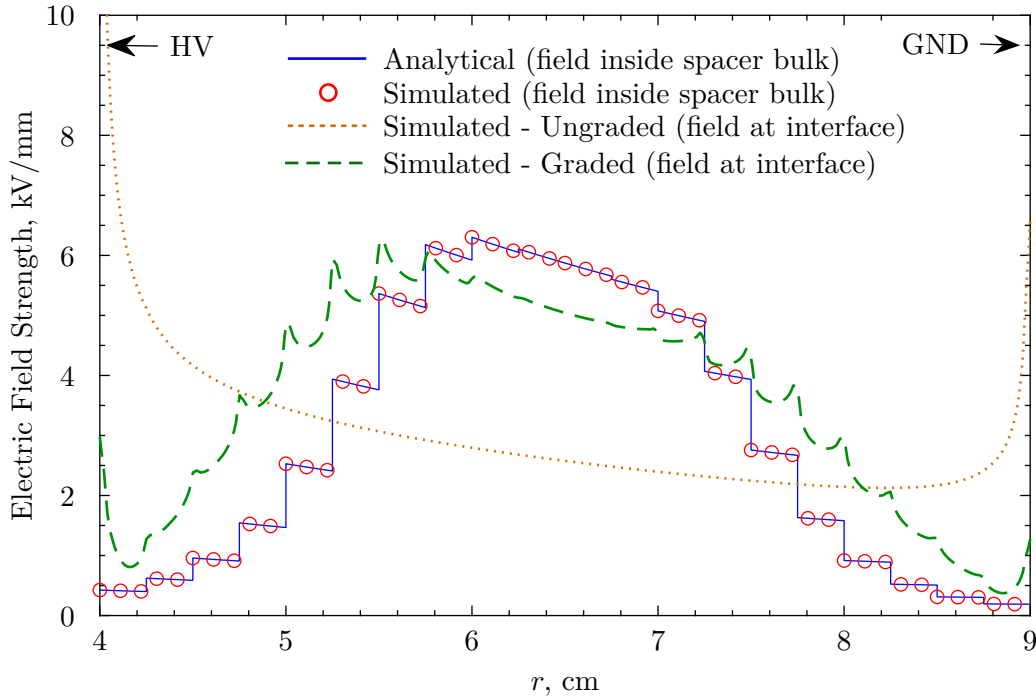


**Figure 3.12:** Comparison of predicted bulk field in the composite to the simulated field along the gas-spacer interface. Field measurement is taken along the contour of Figure 3.11 on the side of the gas. Simulation results for the bulk are taken down the centre-line of the spacer. All data recorded at the time when the peak electric field magnitude was reached inside the domain. Dotted and dashed lines are therefore taken at different times, while the solid line arising from (3.28) is calculated at the same time as the dashed line. Image adapted with permission from [31], © 2023 IEEE.

The grading effect is evident in Figures 3.11 and 3.12, where the magnitude of the electric field was significantly reduced at both triple junctions compared to the ungraded case. Maximum values simulated for the ungraded spacer were found to be  $\approx 14$  kV/mm at the anode and  $\approx 6$  kV/mm at the cathode, respectively. With the addition of the “U”-shaped graded spacer, these reduce to  $\approx 3$  kV/mm and  $\approx 1.3$  kV/mm, respectively, corresponding to a reduction of around 78% in each case. Based on the analytical solution (solid blue line of Figure 3.12) compared to the full solution (dashed green line), one finds that the model provides a reasonable approximation to the surface field at the spacer-gas interface despite not explicitly incorporating this geometry, and most importantly, was found applicable at any time  $t$ . The analytical model is unable to provide exact peak field values at the spacer-gas interface, however, the general shape of the redistributed field was able to be approximated both spatially and temporally. The novel approach developed here therefore additionally provides a convenient method for estimating the field distribution in systems incorporating FGMs in similar geometries to this case study,

which may aid in accelerating the design process by facilitating rapid iteration of novel FGM designs. When used as an approximation, the model may not provide exact field values, but the tendencies of the redistributed field are captured reasonably well to be capable of informing the optimisation of grading profiles. This is particularly important for transient energisation, as the present method can readily provide these estimates for any time,  $t$ . Used in combination with more sophisticated tools like existing computational models, they may inform important design decisions for composite insulation coordination in pulsed power systems of the future.

It is further remarked that the generality of this approach means that it is far from limited to just FGMs or solely for double-exponential descriptions of impulsive signals. Equation (3.22) permits the application of any analytical  $s$ -transformable waveform, and further supports variable thicknesses for each layer. Applications including PEF chamber design, multilayered capacitor design, composite insulation for more-electric aircraft, or any other system incorporating dielectric multilayered geometries may benefit from this model and from models of this type. Of course, modelling alone does not consider the practical limitations in terms of fabrication and manufacturing of layered composite insulation. Incidentally, experimental validation would be invaluable to evaluate the degree to which these models are representative, but at the time of writing, techniques to accurately probe intra-layer electric fields under fast-rising waveforms do not yet exist. Addressing these issues are of high priority, but to do so falls outside the scope of the purely theoretical work conducted here.

## 3.4 Multilayered Models of Dielectric Inclusions

Following from the one-dimensional planar case of Section 3.3.1, this section considers a scenario of greater geometric complexity in the ongoing analysis of multilayered materials under impulse action. The examples presented in this section include the analysis of multilayered structures using prolate-spheroidal coordinates, for a number of reasons:

- To demonstrate that the novel  $n$ -layer interfacial solutions may be applied to different coordinate systems, particularly those which are considerably more complex than the one-dimensional case of Section 3.3.1.
- As demonstration of the handling of far-field boundary conditions, rather than simple Dirichlet conditions prescribed to constant coordinate surfaces.
- To introduce a different class of industrial pulsed power applications that can benefit from the developed interface modelling approach.

- To act as support for Chapter 7, where the particular solutions developed in this section are further employed in the modelling of interfacial voids at solid-solid interfaces for the purposes of interfacial breakdown prediction.

It should be noted that the contents of this section is partially based on the published article [19]. Focus was placed on the analysis of dielectric *inclusions*, which are defined here as embedded regions within a bulk material which may have different properties than those of its host. In this work, it was also assumed that inclusions may have an arbitrary number of layers, with each layer completely encapsulating the previous. Models of dielectric inclusions have been of critical importance in the analysis of defects relating to electrical insulation. For example, features such as gas bubbles in liquid dielectrics, gas voids in solid insulation, or contaminant particles in gas-insulated systems [27, 28] have often been modelled as dielectric inclusions [29]. Mentioned previously on multiple occasions is PEF technology, in which multilayered dielectric inclusions are commonly used to estimate TMPs across microbiological cell membranes to study the dynamics of the electroporation process [15, 16]. In [54–56], authors included models of multilayered inclusions for the study of partial discharge inception in voids. Other applications for which interfacial charging processes are important, like in electrostatic precipitation (ESP) technology [57], composite material development involving fillers [58], or nanocomposites [59], have similarly employed the inclusion modelling approach. The advancement of this pervasive theoretical approach would therefore be of benefit to many fields of research. Spheroidal and spherical inclusions are most commonly used in the applications listed above, acting generally as good approximations of features like voids, bubbles, or particulates. This is therefore also the geometry of choice presented in the following sections.

### 3.4.1 Particular Solutions for Prolate-Spheroidal Geometries

The orthogonal system of choice that can offer a convenient representation of both spherical and spheroidal inclusions is the prolate-spheroidal coordinate system, characterised by the coordinates  $(\mu, \nu, \theta)$  which relate to the Cartesian system  $(x, y, z)$  with

$$\begin{aligned}x &= a_0 \cosh \mu \cos \nu, \\y &= a_0 \sinh \mu \sin \nu \sin \theta, \\z &= a_0 \sinh \mu \sin \nu \cos \theta,\end{aligned}\tag{3.29}$$

where  $a_0$  is the focal distance, as illustrated in Figure 3.13. Surfaces of constant  $\mu$  therefore

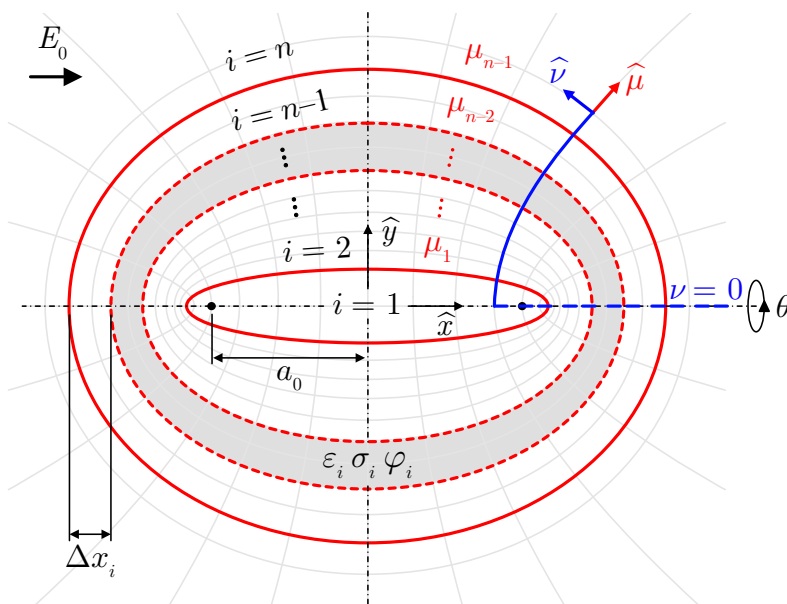


**Figure 3.13:** Diagram of a rotationally-symmetric prolate spheroidal coordinate system, where the dielectric layers are formed between consecutive coordinate surfaces of constant  $\mu$ . Image adapted with permission from [19], © 2024 IEEE.

represent spheroids and conveniently model the geometries of interest, while constant  $\nu$  form confocal hyperboloids. Under this definition, the multilayered structure is formed between consecutive values of  $\mu_i$ . The elliptical eccentricity may further be defined as

$$e_i := \sqrt{1 - K_i^2}, \quad (3.30)$$

where  $K_i$  is the ratio of the minor to major axis of the interfacial boundary described by  $\mu_i$ , which additionally satisfies  $K_i = \tanh \mu_i$  from (3.29). In the limit  $e_i \rightarrow 0$ , the geometry tends towards an ideal sphere. By nature of this coordinate definition, a limitation is that the *layer thickness* cannot be uniform for all  $\nu$ . That is, as the number of layers,  $n$ , becomes large, so too does  $K_i$  such that  $K_n \rightarrow 1$  or equally,  $e \rightarrow 0$ , regardless of the eccentricity of the innermost region. Here, the definition for the *layer thickness* is taken to be the distance between Cartesian  $x$ -coordinates of adjacent interfaces at an angle of  $\nu = 0$  such that

$$\Delta x_i = a_0 (\cosh \mu_{i+1} - \cosh \mu_i) \quad (3.31)$$

for  $i \in [1, n - 2]$ . The  $n$ -layered inclusion was assumed to be subjected to some time-varying external potential field,  $\varphi_0(\mu, \nu, t)$ . For the intended purposes of this model within the context of the present work, the additional assumption that the geometry is rotationally-symmetric around

$\theta$  was further applied. This does impose restrictions on the form that  $\varphi_0$  may assume since this external field must also exhibit the same symmetry. This, however, does not pose an issue for the problems considered in this work. Analysis of asymmetric field configurations increases the mathematical complexity of the problem considerably and is considered an aspect for future extensions to this approach. Under these constraints, the Laplace equation may be written [60] [where functional notation has been omitted for brevity,  $\varphi(\mu, \nu, t) \rightarrow \varphi$ ]

$$\vec{\nabla}^2 \varphi = \frac{1}{h^2} \left( \frac{\partial^2 \varphi}{\partial \mu^2} + \frac{\partial^2 \varphi}{\partial \nu^2} + \coth \mu \frac{\partial \varphi}{\partial \mu} + \cot \nu \frac{\partial \varphi}{\partial \nu} \right) = 0, \quad (3.32)$$

where the scale factor  $h = a_0 \sqrt{\cosh^2 \mu - \cos^2 \nu}$ . Following the full derivation included as Appendix A.3, the general solution to (3.32) assumes the form

$$\varphi = \sum_{\ell=0}^{\infty} [A_{\ell} P_{\ell}(\cos \nu) + B_{\ell} Q_{\ell}(\cos \nu)] [C_{\ell} P_{\ell}(\cosh \mu) + D_{\ell} Q_{\ell}(\cosh \mu)], \quad (3.33)$$

where  $P_{\ell}$  and  $Q_{\ell}$  are the  $\ell$ -th degree Legendre functions of the first and second kinds, respectively, and  $A_{\ell}$ ,  $B_{\ell}$ ,  $C_{\ell}$ , and  $D_{\ell}$  are time-dependent coefficients. In contrast to Section 3.3.1 where Dirichlet potential conditions were applied to fixed coordinate surfaces, the application of an external field to the present inclusion geometry necessitates the second set of conditions as described in Section 3.2.1. The first is the far-field condition stipulating that

$$\lim_{\mu \rightarrow \infty} \varphi = \varphi_0, \quad (3.34)$$

ensuring that the potential field becomes self-consistent with the external applied potential far from the inclusion. The second pertains to the non-singular nature of the electric potential such that

$$\varphi \neq \infty \quad \forall (\mu, \nu) \quad (3.35)$$

for the recovery of a physical solution. Imposition of (3.34) and (3.35) allows (3.33) to be reduced. Most importantly,  $Q_{\ell}(\cos \nu)$  becomes singular when  $\nu = k\pi : k \in \mathbb{Z}$  in violation of (3.35), implying that the coefficients  $B_{\ell}$  must be zero regardless of the layer. Similarly,  $Q_{\ell}(\cosh \mu)$  is singular at the origin, thereby requiring that the coefficients  $D_{\ell}$  be zero for the innermost region ( $i = 1$ ) of the inclusion. In the far-field limit, condition (3.34) can be satisfied for any  $\varphi_0$  expressible in terms of a Fourier-Legendre series to match the form of (3.33). That is, an

external potential field of the form

$$\varphi_0 = \sum_{\ell=0}^{\infty} a_{\ell} P_{\ell}(\cos \nu) \quad (3.36)$$

satisfies (3.33). The details to obtain the expansion coefficients,  $a_{\ell}$ , are included in Appendix A.4, resulting in

$$a_{\ell} = \frac{2\ell + 1}{2} \int_0^{\pi} \varphi_0 P_{\ell}(\cos \nu) \sin \nu \, d\nu. \quad (3.37)$$

In the limit  $\mu \rightarrow \infty$ , therefore, (3.33) in combination with (3.36) requires that

$$A_{\ell} = \frac{a_{\ell}}{P_{\ell}(\cosh \mu)}. \quad (3.38)$$

The derivation so far permits an arbitrary choice of  $\varphi_0$  as long as the integral (3.37) can be evaluated analytically. However, the remainder of this section will continue with the derivation with the added assumption that the external field,  $\varphi_0$ , represents a uniform applied field (i.e., linearly decreasing potential) directed in the positive Cartesian  $x$ -direction. This is sufficiently representative of the configurations studied here and in Chapter 7, where due to the small dimensions of the considered inclusions relative to the non-uniformity of the external fields, the fields could be considered essentially uniform across the distances of interest. More specific details pertaining to use of this model to study interfacial voids and the justification for this assumption are explored in greater detail within Chapter 7. Appendix C.5 additionally encloses examples of solutions for non-uniform external fields. The contents of this appendix were included in support of the contents of Chapter 7, but together with the derivations of Appendix A.15 may be of mathematical interest relating to non-uniform fields discussed here.

### 3.4.1.1 Particular Case of the Uniform External Field

For a positive  $x$ -directed uniform electric field,  $E_0 \cdot \hat{x}$ , the corresponding expression for the external potential after transforming to  $(\mu, \nu)$ -coordinates gives

$$\varphi_0 = -a_0 E_0 \cosh \mu \cos \nu, \quad (3.39)$$

where the reader is reminded that  $E_0 \equiv E_0(t)$  is time-dependent, but functional notation has been omitted for clarity. The form of this external potential is unique, in that it may be fully represented using only the zero- and first-degree terms ( $\ell = 0, 1$ ) of the Fourier-Legendre series, verifiable by application of (3.39) in (3.37). With the knowledge that only a two-term expansion

is necessary, the potential fields described previously by the infinite series (3.33) may be collapsed to (see Appendix A.5 for the full derivation of this section)

$$\varphi_i = [A_i + B_i F_i] \cosh \mu \cos \nu \quad (3.40)$$

for the  $i$ -th layer, and where the function  $F_i$  has been introduced for brevity, equal to

$$F_i = F(\mu_i) = \operatorname{sech} \mu_i - \ln \sqrt{\frac{\cosh \mu_i + 1}{\cosh \mu_i - 1}}. \quad (3.41)$$

The reader is hereby reminded of the most general form of the potential from Section 3.2.2, equation (3.8), for which the established form of the potential (3.40) has now assumed. The significance here is that the subsequent analysis conducted in arbitrary orthogonal coordinates equally applies here. The equivalent system of linear  $s$ -domain equations characterising the intra-layer time-domain responses must therefore follow from (3.9), giving

$$\begin{aligned} A_i + B_i F_i &= A_{i+1} + B_{i+1} F_i \\ A_i + B_i G_i &= \lambda_i (A_{i+1} + B_{i+1} G_i), \end{aligned} \quad (3.42)$$

where the function  $G_i$  has been introduced for convenience, equal to

$$G_i = G(\mu_i) = \coth \mu_i \operatorname{csch} \mu_i - \frac{1}{2} \ln \left( \coth \frac{\mu_i}{2} \right) \quad (3.43)$$

and which satisfies the relationship

$$G_i \sinh \mu = \frac{\partial}{\partial \mu} (F_i \cosh \mu). \quad (3.44)$$

The functions  $F_i$  and  $G_i$  are dependent solely on the coordinate  $\mu$ , and their significance in the calculation of local field enhancement factors is shown later in Section 3.4.2. Again following the analysis of Section 3.2.2, solutions to the coefficients of (3.42) provides all necessary information to reconstruct the potential (and electric) fields through (3.40). This case differs from the example of Section 3.3.1 due to the differences in the boundary conditions, since the far-field (3.34) and non-singular (3.35) conditions were instead imposed. The solution process and the recovery of the interfacial relaxation times requires a more involved process than in Section 3.3.1, owing to the considerably more complex geometry. This process, however, may be facilitated by realising that the linear equations (3.42) may be written in the form  $\mathbf{M}\vec{\mathbf{u}} = \vec{\mathbf{b}}$ , where  $\mathbf{M}$  is a tridiagonal matrix with a regular structure,



Appendix A.5, and takes the form of a second-order recurrence relation

$$\begin{aligned}
 P_n &= (F_{n-1} - G_{n-1}\lambda_{n-1})P_{n-1} - F_{n-1}G_{n-1}(\lambda_{n-1} - 1) \\
 &\times \left[ (\lambda_{n-2} - 1)P_{n-2} + \frac{G_{n-2} - F_{n-2}\lambda_{n-2}}{F_{n-2}G_{n-2}(\lambda_{n-2} - 1)} [P_{n-1} - (F_{n-2} - G_{n-2}\lambda_{n-2})P_{n-2}] \right] \quad (3.48)
 \end{aligned}$$

for  $n \geq 3$ , with the conditions that

$$\begin{aligned}
 P_1 &= 1, \\
 P_2 &= F_1 - G_1\lambda_1. \quad (3.49)
 \end{aligned}$$

One observes that despite the added complexity of the prolate-spheroidal geometry under study, the conclusions of the analyses on interfacial relaxation times and the method of their determination from Section 3.2 continue to hold. The time-response of the developed intra-layer fields are fundamentally determined by the roots of the characteristic polynomial,  $P_n$ . It follows that the familiar  $s$ -domain form (representative of the summed exponential time-domain form) can be recovered from (3.47) to be

$$A_1^n = -\frac{a_0 E_0 \sigma_n (1 + \tau_n s)}{c_0 \sigma_1 (1 + \tau_1 s)} \prod_{\ell=1}^{n-1} \frac{F_\ell - G_\ell}{\left(s + \frac{1}{\tau_{\ell+n}}\right)}, \quad (3.50)$$

where, once again, the interfacial relaxation times,  $\tau_{\ell+n}$  are given by (3.15), where the first  $n$  values of  $\tau$  correspond to the intrinsic layer relaxation times,  $\tau_i = \varepsilon_0 \varepsilon_i / \sigma_i$ . Backward substitution of the coefficient  $A_1^n$  given by (3.50) into the linear set (3.42) allows the determination of all other coefficients in  $\vec{u}$ , thus completing the solution. It is noted that the limitation on the maximum number of layers for fully closed-form solutions remains, due to the necessity to factor the characteristic polynomial (3.48). However, the semi-analytical approach suggested in Section 3.2.2 remains valid. Several typical problems in power and pulsed power engineering are presented in the next sections to validate the prolate-spheroidal model, included to demonstrate further applications that may benefit from the present theoretical work.

### 3.4.2 Limiting Behaviours: Field Enhancement of Particles and Voids

As a first case study, this section aims to show that well-known theoretical limits to the field enhancement factors inside dielectric inclusions and on the surface of conductive particles can be recovered from the approach of Section 3.4.1. Focus is placed on the elementary limits for a two-layer inclusion system (e.g., single inclusion embedded in a bulk material) of spherical

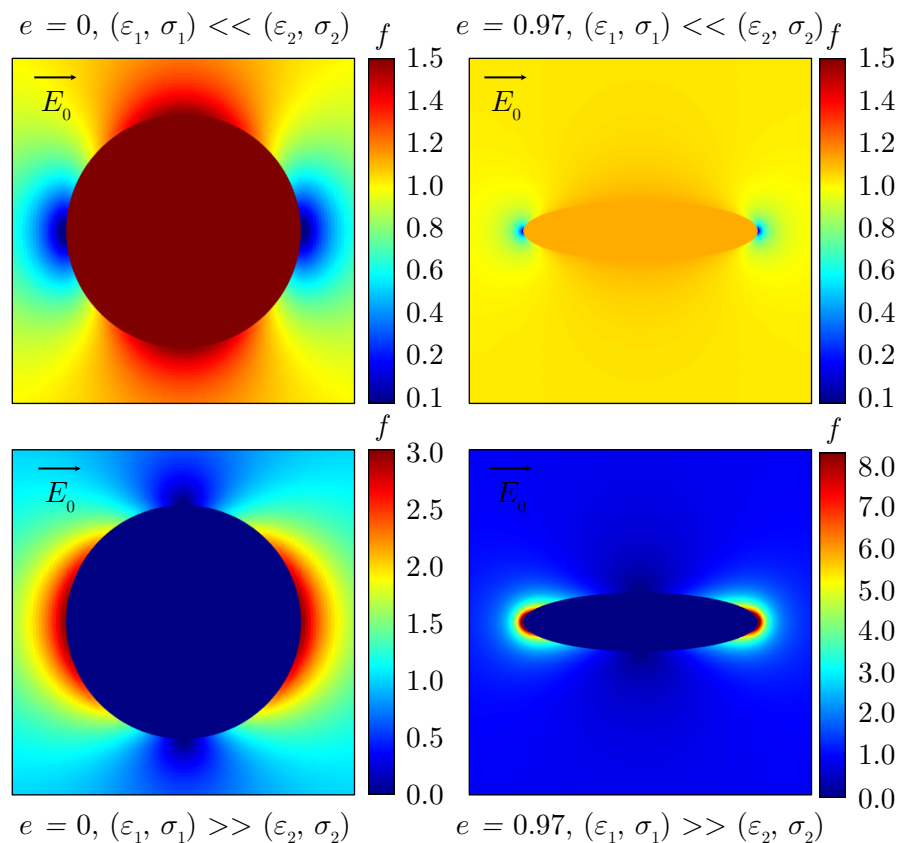


**Figure 3.14:** Analytically-determined colour plots of enhancement around inclusions in the two limiting cases. Shown for a spherical ( $e = 0$ ) and spheroidal particle with  $e = 0.97$  (or axis ratio,  $K$  of 0.25).

( $e \rightarrow 0$ ) geometry, where it is well established that (corresponding to Figure 3.14):

- When the inclusion represents a conductive particle embedded in a dielectric bulk,  $(\varepsilon_1, \sigma_1) \gg (\varepsilon_2, \sigma_2)$ , the maximum field enhancement factor found at the surface of the particle tends to  $f = 3$ .
- When the inclusion represents a dielectric particle or void inside a bulk of far greater permittivity,  $\varepsilon_1 \ll \varepsilon_2, \sigma_i = 0 \forall i$ , the field enhancement factor *inside* the inclusion reaches a maximum of  $f = 3/2$ .

These limits may be established within the framework of this model by first using (3.47) and (3.48) to determine the coefficient  $A_1^2$  for  $n = 2$ . Since by definition,  $P_2 = F_1 - G_1\lambda_1$ ,

$$A_1^2 = -a_0 E_0 \frac{\lambda_1 (F_1 - G_1)}{F_1 - G_1 \lambda_1} \quad (3.51)$$

while  $A_2^2 = -a_0 E_0$  is already known alongside  $B_1^2 = 0$  from the applied potential boundaries. This leaves the substitution of (3.51) into (3.42) to determine  $B_2^2$  as

$$B_2^2 = -\frac{A_2^2}{F_1} = \frac{a_0 E_0}{F_1} \quad (3.52)$$

and hence, the expression for the electric fields in both layers from the gradient of (3.40) can be recovered to be

$$\begin{aligned} \vec{E}_1^2 &= \frac{a_0 E_0}{h} \frac{\lambda_1 (F_1 - G_1)}{F_1 - G_1 \lambda_1} \sinh \mu \cos \nu \cdot \hat{\boldsymbol{\mu}} + \frac{a_0 E_0}{h} \frac{\lambda_1 (F_1 - G_1)}{F_1 - G_1 \lambda_1} \cosh \mu \sin \nu \cdot \hat{\boldsymbol{\nu}}, \\ \vec{E}_2^2 &= \frac{a_0 E_0}{h} \left[ 1 - \frac{G(\mu)}{F_1} \right] \sinh \mu \cos \nu \cdot \hat{\boldsymbol{\mu}} + \frac{a_0 E_0}{h} \left[ 1 - \frac{G(\mu)}{F_1} \right] \cosh \mu \sin \nu \cdot \hat{\boldsymbol{\nu}}. \end{aligned} \quad (3.53)$$

Evaluating the first limiting case when  $(\varepsilon_1, \sigma_1) \gg (\varepsilon_2, \sigma_2)$  for a conducting particle,  $\lambda_1 \rightarrow 0$  causes the field inside the particle to also vanish,  $\vec{E}_1^2 \rightarrow 0$ , as one would expect. The maximum enhancement at the surface occurs at  $\nu = 0$  and  $\pi$ , and should be normalised by the external uniform field magnitude,  $E_0$ , which simply yields

$$f_{(\varepsilon_1, \sigma_1) \gg (\varepsilon_2, \sigma_2)} = \max \frac{|\vec{E}_2^2|}{E_0} = \frac{|\vec{E}_2^2(\mu = \mu_1, \nu = 0)|}{E_0} = 1 - \frac{G_1}{F_1}. \quad (3.54)$$

Correspondingly, the second limiting case when  $\varepsilon_1 \ll \varepsilon_2$  requires the explicit computation of the inclusion field magnitude,

$$|\vec{E}_1^2(\mu_1)| = \sqrt{\frac{(a_0 E_0)^2}{a_0^2} \left[ \frac{\lambda_1 (F_1 - G_1)}{F_1 - G_1 \lambda_1} \right]^2 \frac{\sinh^2 \mu \cos^2 \nu + \cosh^2 \mu \sin^2 \nu}{\sinh^2 \mu + \sin^2 \mu}} = E_0 \frac{\lambda_1 (F_1 - G_1)}{F_1 - G_1 \lambda_1} \quad (3.55)$$

which is uniform in nature, since it is independent of both  $\mu$  and  $\nu$ . Taking the limit for the inclusion field enhancement factor, one obtains

$$f_{\varepsilon_1 \ll \varepsilon_2} = 1 - \frac{F_1}{G_1}. \quad (3.56)$$

The results (3.54) and (3.56) show that in both cases, the field enhancement factor is governed only by geometry. Recalling the definition  $K = \tanh \mu$  from Section 3.4.1 where  $K$  is the ratio of the minor to major axes, the limiting field enhancement factors are determined solely by the eccentricity of the particle or void. One may utilise these equations to evaluate numerical limits in the case of an ideal sphere. Figure 3.15 plots (3.54) and (3.56) as a function of eccentricity, showing the convergence towards the theoretical limits of  $f = 3$  for the maximum

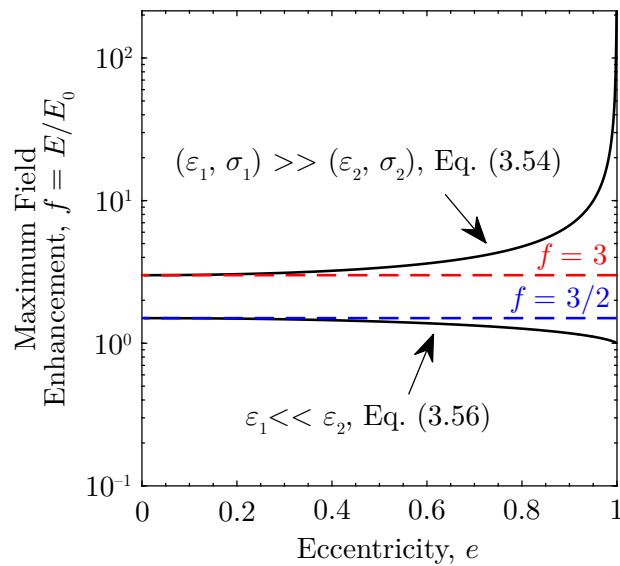


**Figure 3.15:** Plot of the predicted maximum field enhancement factor against eccentricity for a simple 2-layer inclusion, for the limiting conditions of (3.54) and (3.56). Note the convergence towards the well-known limits of  $f = 3$  and  $f = 3/2$  for spherical geometries, respectively. Image adapted with permission from [19], © 2024 IEEE.

field enhancement on the surface of a conductive particle, and  $f = 3/2$  for the interior of a gas void in a far more susceptible bulk. For arbitrary eccentricities, Lekner [62] had previously derived analytical solutions using a different formulation which are equivalent to the expressions presented in this work. Similarly, the solutions given by Crichton, Karlsson and Pedersen [55] were further compared and found to be identical to the present model. A comparison between these three analytical models can be found in Appendix B.2.

### 3.4.3 Further Validation: Microbiological Cell Transmembrane Potentials

In this section, a second case study investigating the transmembrane potentials (TMPs) across microbiological cells is presented in brief, with the purpose to further compare the developed multilayered model against known results. Pulsed electric field treatment of microorganisms is a well-established technology arising from pulsed power research, developed within the last few decades [63]. The technology aims to induce irreversible or reversible electroporation of microbiological cells, with wide ranging applications such as bacterial inactivation, sterilisation, and decontamination [64, 65], treatment of tumours and cancers [66, 67], or food processing [68].

**Table 3.2:** Cell parameters for multilayer inclusion model verification.

Parameter	Value	Parameter	Value
$\varepsilon_1$	72.28	$\sigma_1$	0.3 S/m
$\varepsilon_2$	49.69	$\sigma_2$	$3 \times 10^{-7}$ S/m
$\varepsilon_3$	72.28	$\sigma_3$	0.3 S/m
$\varepsilon_4$	46.69	$\sigma_4$	$3 \times 10^{-7}$ S/m
$\varepsilon_5$	46.69	$\sigma_5$	1.2 S/m
$\Delta x_1$	3 $\mu\text{m}$ – 5 nm	$\Delta x_3$	7 $\mu\text{m}$ – 10 nm
$\Delta x_2$	5 nm	$\Delta x_4$	5 nm

This is achieved through the application of pulsed electric fields with various rise-times and pulse widths (in sub-fields now often referred to as  $\mu\text{s}$ -PEF or  $\text{ns}$ -PEF, etc.), which induces the formation of nanopores on cell membrane layers. Depending on the size and density of the created pores, the process may allow the introduction of external material (e.g., drugs) into the cell, or result in cell death [69]. It is widely accepted that the electric potential across various membranes of a biological cell correlates to the mode of electroporation and whether the process will be reversible.

Multilayered dielectric models of microbiological cells have typically been used to estimate cell TMPs. Each layer in the stack represents a different cell layer, commonly in geometries identical to the model developed here, and each characterised by values of permittivity and electrical conductivity. Kotnik and Miklavčič [15] pioneered this approach, originally by using simple two- and three-layer cell geometries, though the complexity of these models quickly grew with the inclusion of ellipsoids [60], in arbitrary orientations [17], and with additional numbers of layers [16]. To the best of the author’s knowledge, this work is the first to establish the theoretical closed-form limit of  $n = 5$ , and the first to suggest a methodology to reach beyond this limit. Given the numerous multilayered models developed for PEF purposes, it seemed instructive to compare the present model to some well-known cases to ensure mathematical consistency with established literature. For additional reading, the paper from which this section was adapted [19] also features a full PEF-based study demonstrating a model incorporating 6 layers.

Comparison to the work of Kotnik and Miklavčič [70] and to Nath, Sinha and Thaokar [71] was conducted and is presented here, involving a spherical model with five layers. Kotnik and Miklavčič [70] derive their model under spherical coordinates, while Nath, Sinha and Thaokar [71] assume prolate-spheroidal coordinates as was similarly used in the present work. Figure 3.16 shows the considered geometry, while Table 3.2 provides the relevant layer parameters, sourced from [70]. The TMPs across the outer and inner membranes were calculated using the method

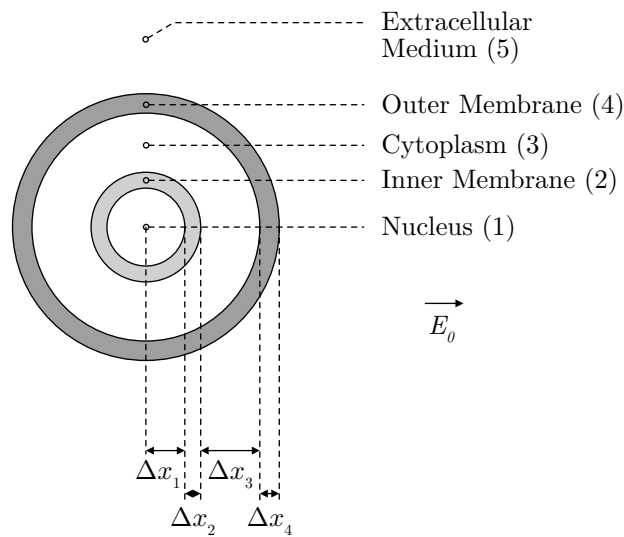


**Figure 3.16:** Diagram of 5-layer cell geometry used in [70] and [71]. Image adapted with permission from [19], © 2024 IEEE.

of Section 3.4.1 under a trapezoidal field of magnitude 15 kV/mm according to

$$E(s) = E_0 \left[ \frac{1 - e^{-sT_1}}{s^2 T_1} - \frac{e^{-s(T_1+T_2)}(1 - e^{-sT_3})}{s^2 T_3} \right] \quad (3.57)$$

as originally used in [70], where  $T_1 = T_3 = 1$  ns are the rise and fall times, and  $T_2 = 10$  ns is the pulse width. Figure 3.17 shows the modelling results, compared to both the approaches used in [70] and [71]. Note that all three approaches are analytical in nature, thus, plotting three lines would simply overlap. Selected datapoints from [70] and [71] have therefore been plotted against the solid line representing the present model, where excellent agreement was found.

The multilayered method developed in this work allows this type of microbiological cell model to be extended beyond the 5 layer limit, without the necessity of mesh-based methods. This may contribute towards increased modelling fidelity for the exploration of various bio-electric effects in the future, facilitating the analysis of cells with particularly complex structures. The inclusion model is revisited within Chapter 7 as a model for interfacial voids between solid-solid insulation, demonstrating yet another application for the techniques developed in this chapter.

### 3.5 Chapter Conclusions, Contributions, and Outlook

In summary, this chapter has introduced novel analytical solutions for the time-dependent potential and electric fields in multilayered poorly-conducting composite materials. This was

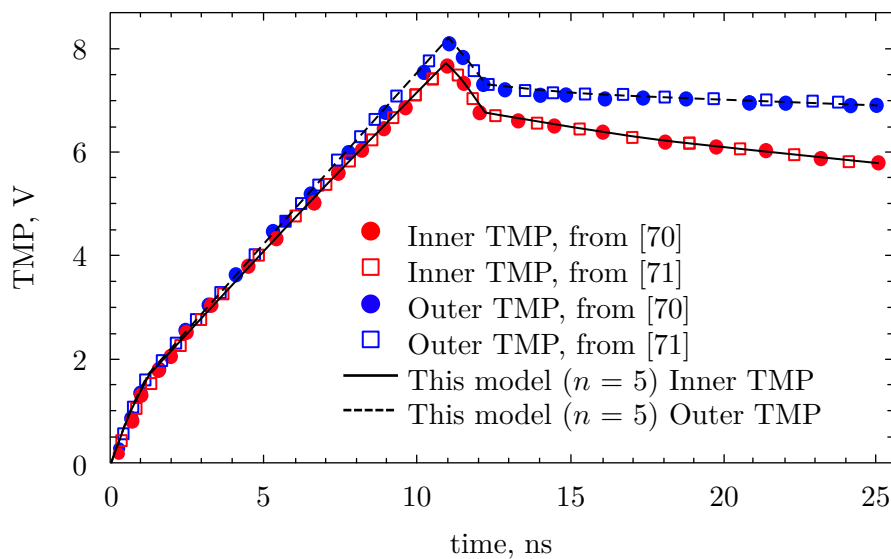


**Figure 3.17:** Comparison of cell transmembrane potentials for a 5-layer cell calculated using the present approach to the solutions of [70] and [71]. Note that discrete points have been sampled from [70] and [71] for visibility, though all three models are analytical and thus produce smooth, overlapping, curves. Image adapted with permission from [19], © 2024 IEEE.

driven by the need to understand the development of transient electric fields in the presence of interfaces under impulsive voltages, prior to the inception of any breakdown or pre-breakdown phenomena. Two main variations of the multilayered problem was solved and demonstrated in the context of important pulsed power technologies. The first demonstrated its potential application to support the development of novel field-grading materials in power and pulsed power equipment; and the second, as an advanced model for the analysis of complex dielectric inclusions, such as insulation defects like voids and conductive particles. In a third example, the approach has also been shown to have progressed a common technique for estimating TMPs across complex microbiological cells in PEF applications.

### 3.5.1 Academic Significance and Contributions

Beginning the analysis in an arbitrary coordinate reference frame, the generalised BVP governing the evolution of the electric potential in  $n$ -layered geometries was defined for the first time. By employing boundary conditions based on the classical macroscopic theory of Maxwell-Wagner polarisation, it was shown that under the assumptions of orthogonality and separability, analytical descriptions of the electric potential, and by extension, the electric fields, are obtainable. This was shown possible by means of the Laplace transform and reduction of the governing system

of differential equations to simple algebraic forms. Importantly, the *characteristic polynomial* encoding the time-dependent behaviour of the system was extracted, showing that the interfacial relaxation time constants are recovered from the roots of this polynomial. The generalised form of the field response in an arbitrary layer was therefore shown to be tightly coupled to all other layers in a composite, exhibiting an impulse response in the form of a summed-exponential. The new results thus also act to unify a number of variations of the Maxwell-Wagner approach that have been prevalent in various fields, providing mathematical explanations of the emergent time-domain behaviour.

From the need to obtain the roots of the characteristic polynomial, a novel theoretical limit to the existence of closed-form time-domain solutions has been established. These have been shown possible for  $n \leq 5$  on the basis of the Abel-Ruffini theorem, though, numerical factorisation allows this limit to be overcome in an alternative semi-analytical approach, extending the model's applicability to  $n > 5$ . Overall, the results obtained through this theoretical analysis advances the understanding of the Maxwell-Wagner approach for modelling multilayered dielectric geometries; elucidating the details behind interfacial charging through studying the properties of the underlying mathematics.

#### 3.5.2 Industrial Relevance

The conducted analyses contribute towards additional design knowledge and a greater understanding of composite materials and of their interaction with electric fields. Of particular importance are results pertaining to the coupling between applied field time-domain characteristics and the relaxation times of the multilayered material. It has been shown that both the field magnitude and time-evolution of developed electric fields inside multilayered composites are dependent on the interfacial relaxation times relative to the applied field rise and fall characteristic times. For impulse energisation, the model developed here has emphasised that the material composition of a system may substantially affect the nature of developed electric field stresses, both in space and in time. Failure to consider such issues when developing insulation for pulsed power systems has the potential to lead to field stresses in excess of the system breakdown strength.

In two separate case studies, the developed multilayer approach has been demonstrated as a predictive tool that may aid in the development of current and future technologies involving multilayered composite media. In the first case, the ability to rapidly estimate time-dependent field distributions developed inside multilayered field-grading material has been demonstrated,

alongside an example of its application to graded spacers in GIL for the approximation of the gas-spacer surface field. The method allows the avoidance of expensive mesh-based computational methods that are traditionally necessary, at least for geometries which are well-represented or approximated. Used alongside more sophisticated numerical modelling techniques, the model may aid in the development of novel insulation technology by facilitating rapid iteration during the initial design phase, or accelerate parametric and optimisation studies of new composite materials.

Extending this approach, the multilayered model was solved with a different variation of boundary conditions, allowing the representation of  $n$ -layered dielectric inclusions embedded inside a host bulk material. This is relevant to the analysis of insulation defects such as gas voids in solid/liquid dielectrics, or as a model for conductive contaminant particles within high voltage equipment. Analytical limits have been recovered from the present formulation, showing that the model is consistent with well known results for the theoretical maximum field enhancement factors in gas voids and on the surface of metallic particles. In a second case study, the novel model has been demonstrated in the context of pulsed electric field technology, showing its capability to model the TMPs across complex multilayered microbiological cells. This not only offers an alternative to mesh-based numerical analysis capable of rapidly obtaining exact theoretical solutions, but also provides a method to surpass the upper limit of 5 layers to model cells of considerable complexity.

### 3.5.3 Limitations and Future Outlook

In the development of the multilayered model, a number of assumptions were applied as outlined at the beginning of Section 3.1. These were necessary simplifications for the present derivations to be analytically attainable. However, a number of limitations result directly from the imposition of these assumptions.

Perhaps most significantly, is the assumption of constant electrical conductivity,  $\sigma_i$ , which assumes that it is completely independent of any other system parameter. It is well established that  $\sigma_i$  is generally field- and temperature-dependent,  $\sigma_i \rightarrow \sigma_i(E, T)$ , which is the source of many issues relating to the development of cables and accessories for HVDC transmission. Heating under prolonged unipolar currents may give rise to non-uniform conductivity distributions, causing space-charge accumulation and phenomena such as field inversion [2–5]. This was assumed negligible under pulsed conditions, on the basis that there would be no significant heating over the course of nano- to micro-seconds. However, given that the models have been developed

with the capability to accept any analytical time-dependent energising potential or field (which includes the possibility of any combination of sinusoidal AC, DC, step functions, pulse trains, etc.), it is important to emphasise that this model may lead to significant inaccuracy due to the absence of these dependencies. It would be of great interest to explore the effects of  $\sigma_i(E, T)$  in future, which may ultimately allow a similar approach to be extended to longer-term energisation and increasing its relevance to the power industry. Similarly, the assumption of field-independent conductivity may no longer hold true for impulses with substantial peak field strengths, and additional work would have to be conducted to ascertain the effects within these issues considered.

Fundamentally, the analytical approach used in this work also has inherent limitations to the types and forms of geometry that can be modelled. As with all analytical approaches, they can rarely match the flexibility of computational methods which essentially allow any arbitrary geometry—as accurate to the real system as desired. While significant effort has been made in the development of this model to generalise to as many analytical geometries as possible, the model can only be taken as an approximation when used to estimate real-system performance in many cases. This is also true in relation to the presence of volumetric charge, which would produce a Poissonian field that may not be well represented using the this approach.

Despite this, the developed model has nevertheless provided an advancement to the theoretical knowledge of multilayered dielectric systems. The generality of the model opens up many opportunities for further study, including:

- Expansion of the analysis to other time-dependent signals. As derived in Section 3.2.2, arbitrary  $s$ -transformable signals can be used within the model to obtain equally valid field responses. Investigation of the applicability of this modelling approach for other waveforms, including various AC signals, may expand the relevance of this model.
- Advancement of FGM fabrication capabilities alongside suitable diagnostics may allow the electric field strengths to be measured in practise. This would provide a means for model validation and evaluation of the extent these models can be used as predictive tools. Successfully doing so could be a significant step forward for the development of novel composite dielectrics.
- The present model may be used to approximate continuous distributions of electrical parameters, for example, the grading profiles shown in Section 3.3.2. They may therefore be considered a discrete version of the continuous problem. In the limit as the layer thickness tends to an infinitesimal i.e.,  $\Delta x \rightarrow dx$ , can analytical descriptions of the electric field for the

continuous profiles  $\varepsilon(q^j, q^{j+1}, q^{j+2})$ ,  $\sigma(q^j, q^{j+1}, q^{j+2})$  be recovered? Do the surface charge distributions in the limit reconstruct the full volumetric space charge expression? (see Appendix C.1 for preliminary analysis in a 1D case that lends credence to this possibility).

- Could the analytical approach here break free of the orthogonality-separability condition? For example, it is currently unknown whether solutions may be sought within arbitrary skew coordinates, or as a stronger result, generalised curvilinear coordinates. Methods such as conformal mapping may allow these possibilities to be entertained. Success could potentially allow analytical solutions to be found for an even greater set of complex geometries.

## Chapter 3 References

- [1] T. T. N. Vu, G. Teyssedre, S. L. Roy, and C. Laurent, “Maxwell–wagner effect in multi-layered dielectrics: Interfacial charge measurement and modelling,” *Technol.*, vol. 5, no. 2, 2017.
- [2] J. Li, B. X. Du, and H. Xu, “Suppressing interface charge between LDPE and EPDM for HVDC cable accessory insulation,” *IEEE Trans. Dielectr. Electr. Insul.*, vol. 24, no. 3, pp. 1331–1339, 2017.
- [3] D. Fabiani, G. C. Montanari, C. Laurent, G. Teyssedre, P. H. F. Morshuis, R. Bodega *et al.*, “Polymeric HVDC cable design and space charge accumulation. part 1: Insulation/semicon interface,” *IEEE Electr. Insul. Mag.*, vol. 23, no. 6, pp. 11–19, 2007.
- [4] S. Delpino, D. Fabiani, G. Montanari, C. Laurent, G. Teyssedre, P. Morshuis *et al.*, “Feature article - polymeric HVDC cable design and space charge accumulation. part 2: insulation interfaces,” *IEEE Electr. Insul. Mag.*, vol. 24, no. 1, pp. 14–24, 2008.
- [5] Z. Li and B. Du, “Polymeric insulation for high-voltage dc extruded cables: challenges and development directions,” *IEEE Electr. Insul. Mag.*, vol. 34, no. 6, pp. 30–43, 2018.
- [6] G. Rizzo, P. Romano, A. Imburgia, and G. Ala, “Partial discharges in HVDC cables - the effect of the temperature gradient during load transients,” *IEEE Trans. Dielectr. Electr. Insul.*, vol. 28, no. 5, pp. 1767–1774, 2021.
- [7] Y. Wang, Y. Wang, X. Yang, A. Ma, and Y. Yin, “Interfacial charge dynamics of XLPE/EPDM double layers by simultaneous measurement of space charge and relaxation current,” *IEEE Trans. Dielectr. Electr. Insul.*, vol. 28, no. 2, pp. 569–577, 2021.
- [8] S. L. Roy, P. Segur, G. Teyssedre, and C. Laurent, “Description of bipolar charge transport in polyethylene using a fluid model with a constant mobility: model prediction,” *J. Phys. D: Appl. Phys.*, vol. 37, no. 2, p. 298, 2003.
- [9] M. Zhu, Y. Gao, J. Chen, J. Li, Q. Yu, and C. Li, “Effect of XLPE/EPDM interface on space charge behavior in cable accessory,” *IEEE Access*, vol. 7, pp. 183 554–183 564, 2019.
- [10] H. Shimakawa, A. Kumada, K. Hidaka, M. Sato, T. Yasuoka, Y. Hoshina *et al.*, “One-dimensional modeling of charge transport in epoxy for DC-GIS insulating spacer,” *IEEE Trans. Dielectr. Electr. Insul.*, vol. 28, no. 4, pp. 1457–1464, 2021.
- [11] V. Adamec and J. H. Calderwood, “Electric-field-enhanced conductivity in dielectrics,” *J. Phys. D: Appl. Phys.*, vol. 10, no. 6, p. L79, 1977.
- [12] J. H. Simpson, “The time delay in conduction and breakdown processes in amorphous solids,” *Proc. Phys. Soc. A*, vol. 63, no. 2, p. 86, 1950.
- [13] G. Eriksson, H. Greijer, M. Pradhan, and M. Unge, “Stress dependent conductivity of field grading materials under time varying electrical fields,” in *2012 Annual Report Conference on Electrical Insulation and Dielectric Phenomena*, 2012, pp. 165–169.
- [14] I. V. Timoshkin, S. J. MacGregor, R. A. Fouracre, B. H. Crichton, and J. G. Anderson, “Transient electrical field across cellular membranes: pulsed electric field treatment of microbial cells,” *J. Phys. D: Appl. Phys.*, vol. 39, no. 3, p. 596, 2006.

- 
- [15] T. Kotnik, D. Miklavčič, and T. Slivnik, “Time course of transmembrane voltage induced by time-varying electric fields—a method for theoretical analysis and its application,” *Bioelectrochem. Bioenerg.*, vol. 45, no. 1, pp. 3–16, 1998.
- [16] C. Yao, D. Mo, C. Li, C. Sun, and Y. Mi, “Study of transmembrane potentials of inner and outer membranes induced by pulsed-electric-field model and simulation,” *IEEE Trans. Plasma Sci.*, vol. 35, no. 5, pp. 1541–1549, 2007.
- [17] J. Gimsa and D. Wachner, “Analytical description of the transmembrane voltage induced on arbitrarily oriented ellipsoidal and cylindrical cells,” *Biophys. J.*, vol. 81, no. 4, pp. 1888–1896, 2001.
- [18] T. Kotnik and D. Miklavčič, “Second-order model of membrane electric field induced by alternating external electric fields,” *IEEE Trans. Biomed. Engr.*, vol. 47, no. 8, pp. 1074–1081, 2000.
- [19] T. Wong, I. Timoshkin, S. MacGregor, M. Wilson, M. Given, and M. Maclean, “A many-shells model for cell transmembrane potentials for pulsed electric field applications,” *IEEE Trans. Plasma Sci.*, pp. 1–12, 2024.
- [20] T. Christen, L. Donzel, and F. Greuter, “Nonlinear resistive electric field grading part 1: Theory and simulation,” *IEEE Electr. Insul. Mag.*, vol. 26, no. 6, pp. 47–59, 2010.
- [21] L. Donzel, F. Greuter, and T. Christen, “Nonlinear resistive electric field grading part 2: Materials and applications,” *IEEE Electr. Insul. Mag.*, vol. 27, no. 2, pp. 18–29, 2011.
- [22] M. Kurimoto, H. Ozaki, T. Sawada, T. Funabashi, T. Kato, and Y. Suzuoki, “FEM simulation of local field enhancement close to lamination interface of permittivity-graded material,” *Electron. Commun. Jap.*, vol. 101, no. 6, pp. 48–57, 2018.
- [23] S. Li, “Improvement of surface flashover in vacuum,” *High Volt.*, vol. 5, no. 2, pp. 122–133, 2020.
- [24] E.-S. Eugene Shin, D. A. Scheiman, and M. Lizcano, “Lightweight, durable, and multifunctional electrical insulation material systems for high voltage applications,” in *2018 AIAA/IEEE Electric Aircraft Technologies Symposium (EATS)*, 2018, pp. 1–21.
- [25] M. Talaat, A. El-Zein, and M. Amin, “Electric field simulation for uniform and FGM cone type spacer with adhering spherical conducting particle in GIS,” *IEEE Trans. Dielectr. Electr. Insul.*, vol. 25, no. 1, pp. 339–351, 2018.
- [26] P. M. Morse and H. Feshbach, *Methods of Theoretical Physics*. McGraw-Hill, 1953.
- [27] V. M. Atrazhev, V. S. Vorob’ev, I. V. Timoshkin, S. J. Macgregor, M. J. Given, M. P. Wilson *et al.*, “Breakdown processes in gas micro-bubbles in liquids under electric stress,” *IEEE Trans. Dielectr. Electr. Insul.*, vol. 19, no. 5, pp. 1552–1558, 2012.
- [28] Y. Belkacem and B. ZEGNINI, “Electric field and potential distribution within a XLPE insulated cable containing a void-defect,” in *2016 International Conference on Electrical Sciences and Technologies in Maghreb (CISTEM 2016)*, 2018.
- [29] T. Wong, I. Timoshkin, S. MacGregor, M. Wilson, and M. Given, “Electrostatic modelling of gas-filled voids and conductive particles in highly non-uniform electric fields,” in *23rd Int. Symp. High Voltage Engr.* Institution of Engineering and Technology, 2023, pp. 1022–1028.

- [30] H. H. Abel, *Mémoire sur les équations algébriques: où on démontre l'impossibilité de la résolution de l'équation générale du cinquième degré*, *Oeuvres Complètes de Niels Henrik Abel*. Grøndahl & Søn, 1824.
- [31] T. Wong, I. Timoshkin, S. MacGregor, M. Wilson, and M. Given, "Modeling of the transient electric field in multilayer dielectric composites under impulsive HV energization," *IEEE Trans. Dielectr. Electr. Insul.*, vol. 30, no. 1, pp. 220–229, 2023.
- [32] A. Can-Ortiz, L. Laudebat, Z. Valdez-Nava, and S. Diahm, "Nonlinear electrical conduction in polymer composites for field grading in high-voltage applications: A review," *Polymers*, vol. 13, no. 9, 2021.
- [33] B. X. Du, Z. H. Wang, J. Li, H. C. Liang, and Z. H. Li, "Epoxy insulator with surface graded-permittivity by magnetron sputtering for gas-insulated line," *IEEE Trans. Dielectr. Electr. Insul.*, vol. 27, no. 1, pp. 197–205, 2020.
- [34] J. Li, H. C. Liang, B. X. Du, and Z. H. Wang, "Surface functional graded spacer for compact HVDC gaseous insulated system," *IEEE Trans. Dielectr. Electr. Insul.*, vol. 26, no. 2, pp. 664–667, 2019.
- [35] M. Pradhan, H. Grejjer, G. Eriksson, and M. Unge, "Functional behaviors of electric field grading composite materials," *IEEE Trans. Dielectr. Electr. Insul.*, vol. 23, no. 2, pp. 768–778, 2016.
- [36] X. Zhao, X. Yang, J. Hu, H. Wang, H. Yang, Q. Li *et al.*, "Grading of electric field distribution of AC polymeric outdoor insulators using field grading material," *IEEE Trans. Dielectr. Electr. Insul.*, vol. 26, no. 4, pp. 1253–1260, 2019.
- [37] Rachmawati, H. Kojima, N. Hayakawa, K. Kato, and N. Zebouchi, "Electric field simulation of permittivity and conductivity graded materials ( $\epsilon/\sigma$ -FGM) for HVDC GIS spacers," *IEEE Trans. Dielectr. Electr. Insul.*, vol. 28, no. 2, pp. 736–744, 2021.
- [38] M. Kurimoto, K. Kato, M. Hanai, Y. Hoshina, M. Takei, and H. Okubo, "Application of functionally graded material for reducing electric field on electrode and spacer interface," *IEEE Trans. Dielectr. Electr. Insul.*, vol. 17, no. 1, pp. 256–263, 2010.
- [39] N. Hayakawa, J. Ishiguro, H. Kojima, K. Kato, and H. Okubo, "Fabrication and simulation of permittivity graded materials for electric field grading of gas insulated power apparatus," *IEEE Trans. Dielectr. Electr. Insul.*, vol. 23, no. 1, pp. 547–554, 2016.
- [40] X.-R. Li, Z. Liu, W.-D. Li, G.-Y. Sun, J.-Y. Xue, C. Wang *et al.*, "3d printing fabrication of conductivity non-uniform insulator for surface flashover mitigation," *IEEE Trans. Dielectr. Electr. Insul.*, vol. 26, no. 4, pp. 1172–1180, 2019.
- [41] N. Hayakawa, Y. Miyaji, H. Kojima, and K. Kato, "Simulation on discharge inception voltage improvement of GIS spacer with permittivity graded materials ( $\epsilon$ -FGM) using flexible mixture casting method," *IEEE Trans. Dielectr. Electr. Insul.*, vol. 25, no. 4, pp. 1318–1323, 2018.
- [42] T. Imai, Y. Hoshina, H. Kojima, and N. Hayakawa, "Resin injection behavior in process of manufacturing insulation spacer with permittivity gradient using computational fluid dynamics," *IEEE Trans. Dielectr. Electr. Insul.*, vol. 26, no. 5, pp. 1669–1677, 2019.
- [43] Tera Analysis. (2024) Quickfield professional v. 6.4. [Online]. Available: <https://quickfield.com>

- 
- [44] “High-voltage test techniques - part 1: General definitions and test requirements,” International Electrotechnical Commission (IEC), Geneva, CH, International Standard, 2010.
- [45] Y. Zhou, S. Peng, J. Hu, and J. He, “Polymeric insulation materials for HVDC cables: Development, challenges and future perspective,” *IEEE Trans. Dielectr. Electr. Insul.*, vol. 24, no. 3, pp. 1308–1318, 2017.
- [46] *MACOR Machinable Glass Ceramic Data Sheet*, Corning Inc.
- [47] M.-R. Halloum, B. S. Reddy, and G. N. Reddy, “Stress control for polymeric outdoor insulators using nonlinear resistive field grading materials operating under different conditions,” *IEEE Trans. Dielectr. Electr. Insul.*, vol. 29, no. 3, pp. 1175–1182, 2022.
- [48] A. Naeini, E. A. Cherney, and S. H. Jayaram, “Effect of conductivity on the thermal and electrical properties of the stress grading system of an inverter-fed rotating machine,” *IEEE Trans. Dielectr. Electr. Insul.*, vol. 26, no. 1, pp. 179–186, 2019.
- [49] Rachmawati, H. Kojima, K. Kato, N. Zebouchi, and N. Hayakawa, “Electric field grading and discharge inception voltage improvement on HVDC GIS/GIL spacer with permittivity and conductivity graded materials ( $\epsilon/\sigma$ -FGM),” *IEEE Trans. Dielectr. Electr. Insul.*, vol. 29, no. 5, pp. 1811–1817, 2022.
- [50] S. Hidayat, F. Damanik, and U. Khayam, “Electric field optimization on 150 kV GIS spacer using functionally gradient material,” in *2nd Int. Conf. Indus. Mech. Electr. Chem. Engr. (ICIMECE)*, 2016, pp. 254–259.
- [51] M. Talaat, A. El-Zein, and M. Amin, “Developed optimization technique used for the distribution of u-shaped permittivity for cone type spacer in GIS,” *Electr. Power Syst. Res.*, vol. 163, pp. 754–766, 2018, advances in HV Transmission Systems.
- [52] A. Cookson, “Review of high voltage gas breakdown and flashover of insulators in compressed sulfur hexafluoride,” in *Proc. 3rd Int. Conf. Appl. Dielectr. Mater.*, 1991, pp. 369–376 vol.1.
- [53] N. Zebouchi and M. A. Haddad, “A review on real-size epoxy cast resin insulators for compact high voltage direct current gas insulated switchgears (GIS) and gas insulated transmission lines (GIL)—current achievements and envisaged research and development,” *Energies*, vol. 13, no. 23, 2020.
- [54] G. Crichton, A. Karlsson, and A. Pedersen, “A theoretical derivation of the transients related to partial discharges in ellipsoidal voids,” in *Conf. Rec. 1988 IEEE Int. Symp. Electr. Insul.*, 1988, pp. 238–241.
- [55] G. Crichton, P. Karlsson, and A. Pedersen, “Partial discharges in ellipsoidal and spheroidal voids,” *IEEE Trans. Electr. Insul.*, vol. 24, no. 2, pp. 335–342, 1989.
- [56] H. Illias, G. Chen, and P. L. Lewin, “Comparison between three-capacitance, analytical-based and finite element analysis partial discharge models in condition monitoring,” *IEEE Trans. Dielectr. Electr. Insul.*, vol. 24, no. 1, pp. 99–109, 2017.
- [57] K. Adamiak, “Rate of charging of spherical particles by monopolar ions in electric fields,” *IEEE Trans. Ind. Appl.*, vol. 38, no. 4, pp. 1001–1008, 2002.
- [58] L. Chen, C. Ong, B. Tan, and C. Deng, “Effective permittivity of layered dielectric sphere composites,” *J. Mater. Sci.*, vol. 33, p. 5891–5894, 1998.

- [59] T. Tanaka, M. Kozako, N. Fuse, and Y. Ohki, "Proposal of a multi-core model for polymer nanocomposite dielectrics," *IEEE Trans. Dielectr. Electr. Insul.*, vol. 12, no. 4, pp. 669–681, 2005.
- [60] T. Kotnik and D. Miklavčič, "Analytical description of transmembrane voltage induced by electric fields on spheroidal cells," *Biophys. J.*, vol. 79, no. 2, pp. 670–679, 2000.
- [61] L. H. Thomas, "Elliptic problems in linear difference equations over a network," Columbia University, New York, USA, Tech. Rep., 1949.
- [62] J. Lekner, *Electrostatics of Conducting Cylinders and Spheres*. AIP Publishing LLC, 2021.
- [63] R. P. Joshi, A. L. Garner, and R. Sundararajan, "Review of developments in bioelectrics as an application of pulsed power technology," *IEEE Trans. Plasma Sci.*, vol. 51, no. 7, pp. 1682–1717, 2023.
- [64] S. Qin, P. Li, G. Liang, J. Liu, S. Huang, and J. Meng, "Pulsed electric field treatment of raw milk and its effect on protein-free amino acids transition," *IEEE Trans. Plasma Sci.*, vol. 50, no. 4, pp. 911–919, 2022.
- [65] M. Sato, N. Ishida, A. Sugiarto, T. Ohshima, and H. Taniguchi, "High-efficiency sterilizer by high-voltage pulse using concentrated-field electrode system," *IEEE Trans. Ind. Appl.*, vol. 37, no. 6, pp. 1646–1650, 2001.
- [66] S. Beebe, P. Fox, L. Rec, K. Somers, R. Stark, and K. Schoenbach, "Nanosecond pulsed electric field (nsPEF) effects on cells and tissues: apoptosis induction and tumor growth inhibition," *IEEE Trans. Plasma Sci.*, vol. 30, no. 1, pp. 286–292, 2002.
- [67] K. H. Schoenbach, S. J. Hargrave, R. P. Joshi, J. F. Kolb, R. Nuccitelli, C. Osgood *et al.*, "Bioelectric effects of intense nanosecond pulses," *IEEE Trans. Dielectr. Electr. Insul.*, vol. 14, no. 5, pp. 1088–1109, 2007.
- [68] B. M. Novac, P. Sarkar, I. R. Smith, W. Whittow, and C. Greenwood, "An innovative and non-invasive technology for PEF food processing," in *2009 IEEE Pulsed Power Conf.*, 2009, pp. 737–741.
- [69] L. Buchmann and A. Mathys, "Perspective on pulsed electric field treatment in the bio-based industry," *Front. Bioengr. Biotechnol.*, vol. 7, 2019.
- [70] T. Kotnik and D. Miklavčič, "Theoretical evaluation of voltage inducement on internal membranes of biological cells exposed to electric fields," *Biophys. J.*, vol. 90, no. 2, pp. 480–491, 2006.
- [71] S. Nath, K. P. Sinha, and R. M. Thaokar, "Development of transmembrane potential in concentric spherical, confocal spheroidal, and bispherical vesicles subjected to nanosecond-pulse electric field," *Phys. Rev. E*, vol. 101, p. 062407, 2020.

# An Avalanche-to-Streamer Transition Criterion for Overstressed Breakdown on a Rising Slope

---

FOLLOWING from the analysis of Chapter 3, which focused on the pre-avalanche and pre-breakdown electric field evolution in composite systems under impulse action, this chapter moves to the next stage of the breakdown process as outlined in Figure 1.2. Namely, the focus is shifted to the initiation and development of the *electron avalanche* in gas, with the aim to unravel the nature of electron growth and of the avalanche-to-streamer transition under fast-rising voltage waveforms, as is characteristic of many pulsed power applications. An analytical approach was again taken, which sought to extend the knowledge of electron avalanche development by adapting the classical Meek criterion and to incorporate the rate-of-rise of the applied field as an explicit model parameter. The derivation was based on Montijn and Ebert’s simplified electron transport model [1], allowing the effects of electron diffusion to be incorporated into a novel avalanche-to-streamer transition criterion for fast-rising electric fields. Results include an

---

This chapter was partially adapted, and may be quoted verbatim, from the following publication(s) with permission: T. Wong, I. Timoshkin, S. MacGregor, M. Wilson, and M. Given, “An Avalanche-to-Streamer Transition Criterion for Overstressed Breakdown on a Rising Slope,” *IEEE Trans. Plasma Sci.*, early access, doi: 10.1109/TPS.2024.3446243, Aug. 2024. © IEEE 2024.

T. Wong, I. Timoshkin, S. MacGregor, M. Wilson, and M. Given, “Modelling the Impulsive Breakdown Characteristics of Sub-mm to mm Spheroidal Voids,” *IEEE International Pulsed Power Conference (PPC)*, San Antonio, TX, USA, 2023. © IEEE 2023.

analytical explanation of higher streamer inception fields with greater rate-of-rise; semi-analytical expressions modelling the non-constant and time-increasing electron growth factor under rising voltages; and a new set of explicit, closed-form, solutions for the breakdown voltage and time for the overstressed breakdown regime. Moreover, the developed model is shown to exhibit agreement with several experimental datasets for the field-time scaling of pulsed breakdown, and is further able to recreate the upward shift to Paschen's curve with greater voltage rate-of-rise. Approximate analytical limits for when electron diffusion becomes important to avalanche development under rising voltages have additionally been established, an aspect which has been typically neglected both in Meek's original approach and in many subsequent analyses and interpretation of impulsive breakdown experiments.

## 4.1 Introduction and Motivation

Beyond the pre-breakdown development of the electric field, a natural next-step in the study of electrical breakdown is to investigate the initiating stages of the breakdown itself. As mentioned, the focus of this work was primarily on systems where breakdown is gas-driven, therefore, the effects of fast-rising impulsive voltages on the development of electron avalanches in gas are important to characterise.

There is reason to suspect that electron growth during the avalanche stage would differ significantly under time-dependent pulsed voltages compared to the static case. From a physical perspective, important parameters which determine the process of avalanche evolution include the electron mobility,  $\mu_e$ , effective ionisation coefficient,  $\bar{\alpha}$ , and diffusion coefficient,  $D_e$ , which all exhibit dependence on the applied electric field\*. Under a time-dependent field, it would be reasonable to assume that these parameters will exhibit variation with time that may give rise to non-trivial behaviour. To the best of the author's knowledge, characterising this process has never been approached analytically.

As further motivation to better quantify the avalanche process under impulsive waveforms, there is a distinct lack of theoretical predictive models focused on impulsive breakdown. A common approach involves the fitting of empirical curves to experimental data, however, these are typically limited in validity to the specific ranges of the obtained data, and further, do not provide any

---

\*Strictly speaking, dependence on the *electron energy*, since the swarm parameters essentially describe collective collision dynamics from a kinetic perspective. This distinction only becomes important in regions of exceptionally high field or intense ionisation occurring over considerably shorter timescales than those studied in this chapter. This is discussed in further detail in the context of streamer modelling within Chapter 5.

meaningful links to the underlying physical processes. Many authors therefore resort to the classical Meek-Raether criterion, which has stood the test of time since its introduction from the pioneering work of Meek [2], Raether [3], and Loeb [4–6]. The reader is reminded of the review on the Meek-Raether criterion in Section 2.3.5, though the technical details will be reiterated in brief for the purposes of clarity in the sections that follow. As discussed in Section 2.3.5, the highly approximate approach, though favoured for its simplicity, applicability, and moderate accuracy in many cases, invites improvement. In particular, this is with regards to the seemingly arbitrary choice of  $K$  values to fit experimental data. At the very least, efforts should be made to extend this analysis for energisation regimes that clearly no longer satisfy the original assumptions. The extension to the fast-rising overstressed breakdown regime therefore forms the subject of the present chapter.

The structure of this chapter is as follows. Section 4.2 provides a brief overview and critique of the classical Meek-Raether criterion, before Section 4.3 introduces the derivation for a variation of a model developed by Montijn and Ebert [1] based on the transport of a Gaussian distribution of electrons. This section also establishes a set of governing equations applicable to an arbitrary, time-dependent, applied field and for which numerical solutions are demonstrated. In Section 4.4, the analysis is extended for the particular case of a linearly-increasing (ramp) electric field, in an investigation of the effects of rate-of-rise. Here, semi-analytical solutions to the full set of equations are presented, providing insight into the vastly different electron growth rates under fast-rising voltages. Additional analyses on the effects of diffusion on the  $K$  value for overstressed breakdown are also presented. This is followed by Section 4.5, which aims to show further results that are obtainable under additional assumptions of a non-diffusive and non-attaching gas, from which closed-form approximations to the breakdown field and breakdown time have been successfully derived. The model was validated against experimental impulsive breakdown data and computational simulations, where comparisons are shown within Section 4.6, notably for  $pd$ -scaling and for field-time scaling characteristics. The model developed in this chapter additionally provided an explanation to an observed scaling relationship of the streamer inception time simulated later in Chapter 6. The chapter is concluded with a summary of contributions, the limitations of the modelling approach, and a commentary on the implications of the modelling results on the understanding of avalanche development and breakdown in the overstressed breakdown regime.

## 4.2 Overview of the Meek-Raether Criterion

The classical approach describes electron growth in terms of the first-order differential equation

$$\frac{\partial N_e}{\partial \ell} = \bar{\alpha} N_e, \quad (4.1)$$

where  $N_e$  is the number of electrons, and  $\partial \ell$  is a differential distance in the direction of electron transport. The solution to (4.1) is elementary, yielding the exponential growth/decay equation

$$N_e = N_0 \exp\left(\int_{\ell} \bar{\alpha} d\ell\right) \quad (4.2)$$

depending on the sign of  $\bar{\alpha}$  and where  $N_0$  is the initial condition, equivalent to the result introduced in Section 2.3.5. As was also described in Section 2.3.5, the exponent of (4.2) is typically assigned the letter  $K$  and may be referred to as the *ionisation integral*. Since the present study deals primarily with time-dependent signals, it is convenient to re-cast (4.2) and the  $K$  number in terms of time,  $t$ , instead. This can be done since the effective ionisation frequency satisfies  $\bar{\nu} = \bar{\alpha}|\vec{v}_d|$ , where  $\vec{v}_d$  is the electron drift velocity. Hence,

$$K = \ln \frac{N_e}{N_0} = \int_{\ell} \bar{\alpha} d\ell = \int_t \bar{\nu} dt', \quad (4.3)$$

reflecting the spatio-temporal development of electron avalanches. The well-known Meek-Raether criterion arises from Meek's estimations of  $K = 18 - 20$  for an avalanche to accumulate sufficient space charge and transition into a streamer [2], in a process described previously within Section 2.3.5. This was originally conducted under the assumptions of atmospheric air and a uniform and unchanging external field, which found good agreement with the empirical estimates of Raether [3]. This range of values have since come under intense scrutiny and have been used extensively to describe experimental breakdown results, generally finding very good agreement in many cases, e.g., in [1, 7, 8].

However, with the advancement of high voltage and pulsed power technology, increasing system complexity has highlighted the limitations of the Meek-Raether criterion in several ways. In systems featuring irregular and non-uniform electrode geometries, exotic gases, or non-standard transient impulsive waveforms, there is the increasing realisation that the value of  $K$  has many yet-unknown dependencies [9–15]. Montijn and Ebert [1] conducted improved analyses with the aim to include the effects of electron diffusion, an aspect they note was not satisfactorily included within Meek's original model. They conclude from their results that the effects of diffusion should

not be considered negligible, particularly for avalanches formed in weaker electric fields [1]. Their analysis indicated that under static background fields, diffusive reduction to the electron density can significantly delay the moment of avalanche-to-streamer transition, due to the corresponding delay in the moment that the electron field becomes capable of distorting the external field [1]. As such, they conclude that electronic diffusion can have a substantial influence on the value of  $K$ .

Experimental results additionally suggest that electron attachment and field non-uniformity may be additional factors that impacts the value of  $K$ , see for instance, in Chvyreva *et al.* [16]. Based on the aforementioned argument within Montijn and Ebert’s analysis [1], since fast-rising electric fields must necessarily pass through an initial low-field region, one should expect that the rate at which the field is rising would have some influence on the extent to which diffusive and attachment processes may dominate. By extension, one could theorise that the rate-of-rise will also influence the value of  $K$ , potentially supported by experimental works such as [17]. Building upon the approach of Montijn and Ebert [1], this dependency is addressed in the present work.

### 4.3 Transport of a Gaussian Electron Cloud and Streamer Transition

Following initially from the approach of Montijn and Ebert [1], the transport of a Gaussian-distributed “cloud” of electrons under the action of a uniform electric field was considered. This was also conducted assuming that space-charge distortion is negligible up to the point of streamer transition<sup>†</sup>. Suppose some localised collection of electrons may be modelled by the density (which by the central limit theorem would be a reasonable assumption [1])

$$n_e(r, t_0) = n_0(t_0) \exp\left(-\frac{r^2}{2s_0^2}\right), \quad (4.4)$$

where  $n_e(r, t)$  is the local density of electrons at the (origin-centred) radius  $r$  and time  $t$ ,  $n_0(t)$  is the time-dependent peak value of the Gaussian, and  $s_0$  is the deviation controlling the initial spread of the distribution. Note that this model does not consider the statistical appearance of initial electrons and assumes that a localised density already exists inside the gas. Equation (4.4) was then assumed to evolve in space and in time according to simplified laws of diffusion

---

<sup>†</sup>In this work, avalanche-to-streamer transition was assumed to occur when the space charge induced field equals the external field multiplied by a factor. This is more formally defined within Section 4.3.3

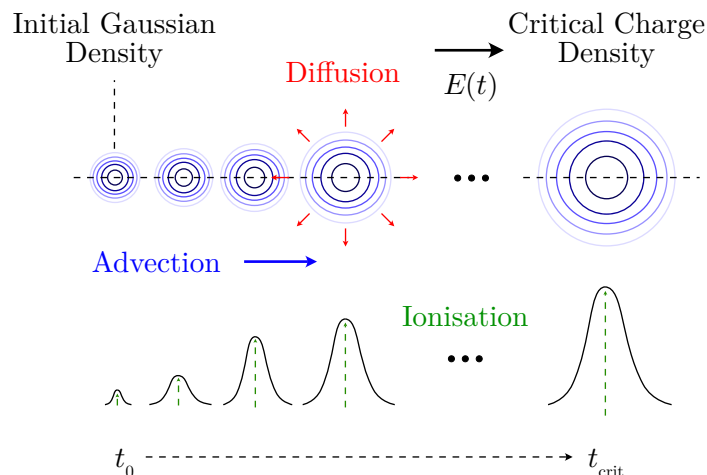


**Figure 4.1:** Graphical depiction of the simplified transport of a Gaussian-distributed electron “cloud” under the action of diffusion and ionisation, modelling the growth of an electron avalanche. Viewed from the moving reference frame of the distribution itself, assuming an origin-centred distribution, and where the avalanche is far from any boundaries, advection can be ignored. Image adapted with permission from [18], © IEEE 2023.

and ionisation, the concept of which is graphically depicted in Figure 4.1. The mathematical treatment of each of these processes are explained in the following sections.

### 4.3.1 The Diffusion Process

It was firstly assumed that (4.4) evolves due to the action of diffusion, characterised by the time-dependent coefficient,  $D_e(t)$ . Time-dependency was assumed since the diffusion coefficient is, in general, field dependent. Thus, for the consideration of an arbitrarily time-varying (but spatially-uniform) field,  $E(t)$ ,  $D_e \rightarrow D_e(t)$  will also change in time. Assuming further that diffusion is isotropic, Fick’s law dictates that (4.4) will evolve like

$$n_e(r, t) = n_0(t) \frac{(2\pi s_0^2)^{3/2}}{\lambda_2^3} \exp\left(-\frac{r^2}{\lambda_1^2}\right) \quad (4.5)$$

following Appendix A.6, where  $\lambda_1$  and  $\lambda_2$  vary with time and are related to the diffusion length by

$$\begin{aligned} \lambda_1 &= \sqrt{2s_0^2 + 4 \int_{t_0}^t D_e(t') dt'}, \\ \lambda_2 &= \sqrt{2\pi s_0^2 + 4\pi \int_{t_0}^t D_e(t') dt'}. \end{aligned} \quad (4.6)$$

Here is a good place to remark on the form of (4.5), which describes the outward diffusive spreading of the initial Gaussian cloud (4.4) as determined by a time-dependent diffusion process. It is also important that (4.5) maintains a Gaussian form, as this enables the electric field distribution to be obtained in closed-form as is critical to the analysis of Section 4.3.3 onwards. Note that this therefore limits this analysis to the case of a uniform or weakly non-uniform external field where electron transport can be assumed spatially-independent.

### 4.3.2 Ionisation and Attachment

Next, growth and decay of the electron density necessitated the inclusion of ionisation and attachment processes. Note that for simplicity, separate rates for processes such as recombination, detachment, or specific chemical interactions were not considered, nor were they necessary for this analysis which focused on rate-of-rise. Besides, most major electronic sources and sinks should be included within the net rates described by the Townsend parameters. Using the effective ionisation coefficient,  $\bar{\alpha}(t)$ , the generation and removal of free electrons is assumed to contribute only to the modification of the Gaussian peak magnitude,  $n_0(t)$ , of (4.5), following the ordinary differential equation

$$\frac{\partial n_0(t)}{\partial t} = \bar{\alpha}(t)|\vec{v}_d(t)|n_0(t), \quad (4.7)$$

where the drift velocity  $\vec{v}_d(t) = \mu_e(t)\vec{E}(t)$  has been previously defined as (2.26), but is rewritten here to show the explicit time-dependency of both the field and electron mobility. For completeness, one may further include the motion of the electron cloud as the avalanche advances, which may be assumed to be at drift velocity following

$$\frac{\partial \vec{\delta}(t)}{\partial t} = \mu_e(t)\vec{E}(t), \quad (4.8)$$

where  $\vec{\delta}(t)$  is the displacement of the electron cloud. Note that the location of the avalanche is not strictly necessary for avalanche-to-streamer transition prediction for electrodeless configurations or when the gap distance is known to be greater than the critical distance. This is true because the moment of transition was considered to be based only on the field magnitude; as long as the Gaussian does not collide with any boundaries, its evolution may be followed from a moving reference frame which tracks the centre of the distribution. From this perspective, the overall drift of the electron cloud need not be considered.

On the subject of ionisation, it is remarked that the spatio-temporal evolution of the trail of

positive ions left in the wake of the avalanche head could be computed by solving

$$\frac{\partial n_+(r, t)}{\partial t} = \max\left(\frac{\partial n_e(r, t)}{\partial t}, 0\right) \quad (4.9)$$

for the positive ion density,  $n_+(r, t)$ . However, this is valid only when assuming that positive ion production results solely from impact ionisation, and that no other process contributes either source nor sink. The use of the max function ensures that positive ions are only generated when the corresponding rate of change of the electron density is positive (i.e., are being produced through ionisation). Negative components must be ignored, since electron attachment has no influence on the balance of positive ions. It does lead to the generation of negative ions, however, these are not tracked in the present model.

### 4.3.3 Field-based Avalanche-to-Streamer Transition

One major motivation to adopt the present Gaussian method is that the electron-induced electric field may be obtained in closed-form from the solution of the Poisson equation (2.7). The classical theory of avalanche-to-streamer transition is based on the moment that the space charge induced field becomes sufficiently strong to distort the applied field. This is largely supported also by numerical simulations, and is essentially approximated in Meek's original theory with the concept of a critical charge density represented by the value of  $K$ . Using the present method, the electron-induced electric field due to (4.5) has the explicit solution [1]

$$E_e(r, t) = q_e n_0(t) \frac{(2\pi s_0^2)^{3/2}}{4\pi\epsilon_0} \left[ \frac{1}{r^2} \operatorname{erf}\left(\frac{r}{\lambda_1}\right) - \frac{2}{r\lambda_1\sqrt{\pi}} \exp\left(-\frac{r^2}{\lambda_1^2}\right) \right], \quad (4.10)$$

where  $q_e$  is the elementary charge and  $\operatorname{erf}(\cdot)$  is the error function. Note also that the relative permittivity has been assumed unity, since this approach deals only with gas. A general condition for the moment of transition from avalanche-to-streamer may then be written

$$\max_{r,t} E_e(r, t) = f \cdot E(t_b), \quad (4.11)$$

where  $f \cdot E(t_b)$  is some factor of the applied field, since the moment of transition may not necessarily align exactly with the moment the fields become equal. For instance in [1], authors considered a value of  $f = 1.03$  based on numerical simulations, corresponding to a 3% enhancement ahead of the avalanche front. Assuming then that the streamer propagation, thermalisation, and spark stage is far shorter than the avalanche development phase, the value of  $t = t_b$  recovered from solving (4.11) can be considered the formative time-to-breakdown. Hence, values for the

breakdown strength,  $E_b$ , and any corresponding breakdown voltage (e.g., if the field was generated between planar electrodes),  $V_b$ , may be estimated with knowledge of  $t_b$ .

The approach here only considers the electron field as part of the space charge induced field and neglects field components arising from the positive ion trail. Primarily, this is due to the considerably more complex structure of the ion trail [from equation (4.9)], which generates an electric field that cannot be easily described analytically. Naturally, any field components arising from positive charges would act in opposition to the electron field, thus would reduce the net field and likely prolong the time necessary for distortion. Analysis conducted in [1] came to similar conclusions, that the omission of the positive ion field would have the tendency to underestimate the breakdown strength based on (4.11). Over short timescales or when diffusion can be neglected, however, authors of [1] also concluded that the positive ion trail may not have any meaningful impact on the streamer transition moment. At present it is unclear how large an effect the positive ion trail may have on avalanche development under fast-rising or impulsive conditions, and given the potentially large scope of such an investigation, it has been left as an aspect for future study.

#### 4.3.4 Nature of the Initial Electron Cloud

Of equal importance to the development of the model itself is the selection of initial conditions. In general, however, it is difficult to accurately characterise the nature of the initial electron density distribution. This is made more difficult since initial conditions may vary greatly depending upon the conditions and environment where the discharge is initiated. Throughout this chapter, including the results presented in Sections 4.4 to 4.6, the initial electron parameters  $n_0(t_0)$  and  $s_0$  have been kept the same; their values determined by estimations based on typical values of background ionisation levels.

From [19], a value of  $n_b = 10^9 \text{ m}^{-3}$  was estimated as a typical level of background ionisation density, which was assumed to be uniformly distributed. Based on this value, a peak value,  $n_0(t_0) = 10^{13} \text{ m}^{-3}$  is assumed for the initial Gaussian cloud, a representative value that has previously been used in various modelling studies [20]. Considering that this represents a peak value (representing a localised packet of electrons) rather than being uniformly distributed throughout space, it could conceivably exist due to ionisation from background sources, or remaining from a previous discharge within a laboratory setting [21]. The choice of the initial deviation parameter,  $s_0 = 10^{-4} \text{ m}$ , was based on approximate dimensions of simulated electron avalanches in [22] using particle kinetic methods. Since the work of this chapter considered an

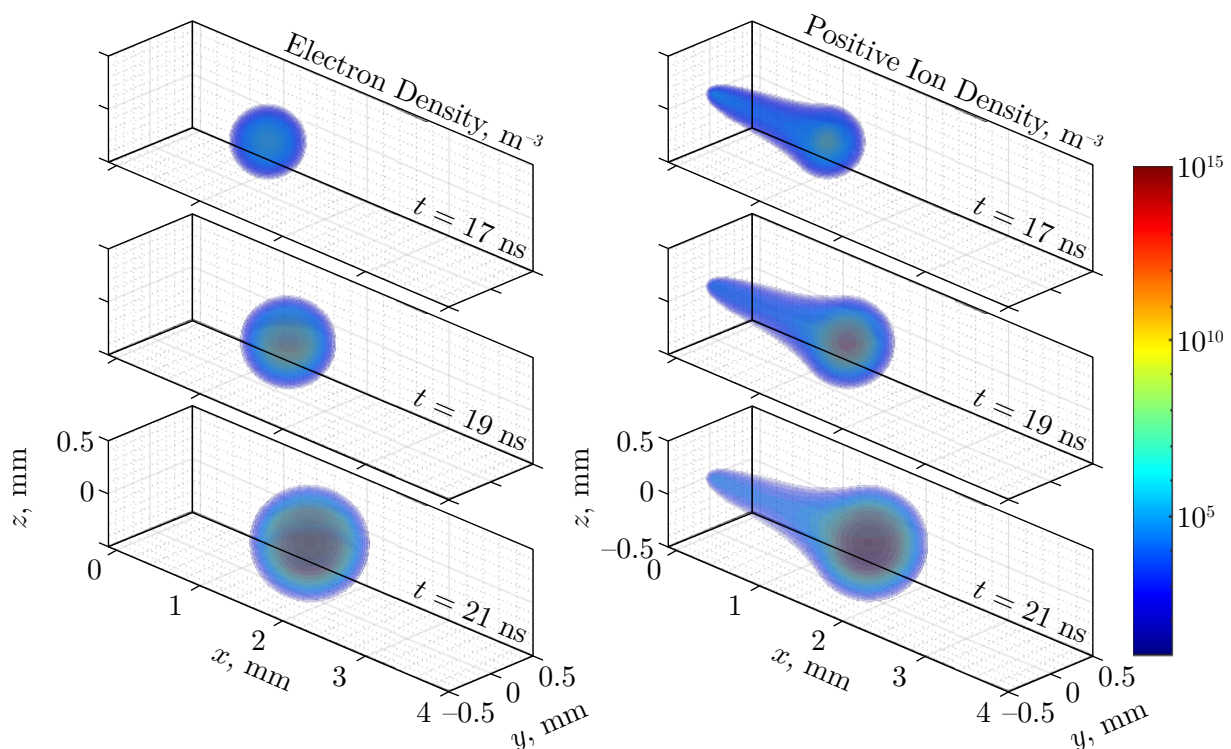


**Figure 4.2:** Volumetric rendering of the estimated (left) electron density (right) positive ion density of an electron avalanche developed across a 4 mm air gap energised with a ramp voltage at 0.5 kV/ns at  $t = 17, 19,$  and  $21$  ns. This figure is from numerical solution of the full model (4.4)–(4.11). Image adapted with permission from [23], © IEEE 2024.

initial *density* of electrons to facilitate the incorporation of avalanche initiation from multiple electrons (or multiple localised avalanches that merge and act effectively as a single, larger, avalanche), one may calculate the total number of electrons based on the assumed value of  $n_0(t_0)$  by

$$N_e = \int_0^{2\pi} \int_0^\pi \int_0^\infty n_0(t_0) \exp\left(-\frac{r^2}{2s_0^2}\right) r^2 \sin\theta \, dr \, d\theta \, d\phi \quad (4.12)$$

where the volume integral over  $\mathbb{R}^3$  is the total electron number in the Gaussian (see Appendix A.7). An assumed value for  $s_0$  on the order of  $10^{-4}$  meters corresponds to  $N_e$  on the order of  $10^2$ , which was sufficiently low and deemed feasible as a reasonable initial condition. Within the assumed uniform background density of  $10^9 \text{ m}^{-3}$ , a similar number of electrons would be expected in a volume of  $(\approx 5 \text{ mm})^3$ .

Equations (4.5)–(4.11) forms the full equation set of this approach, solutions to which, in general, require numerical methods. For example, Figure 4.2 and Figure 4.3 encloses 3D-renderings and corresponding 2D cross-sections of the electron and positive ion densities forming an avalanche

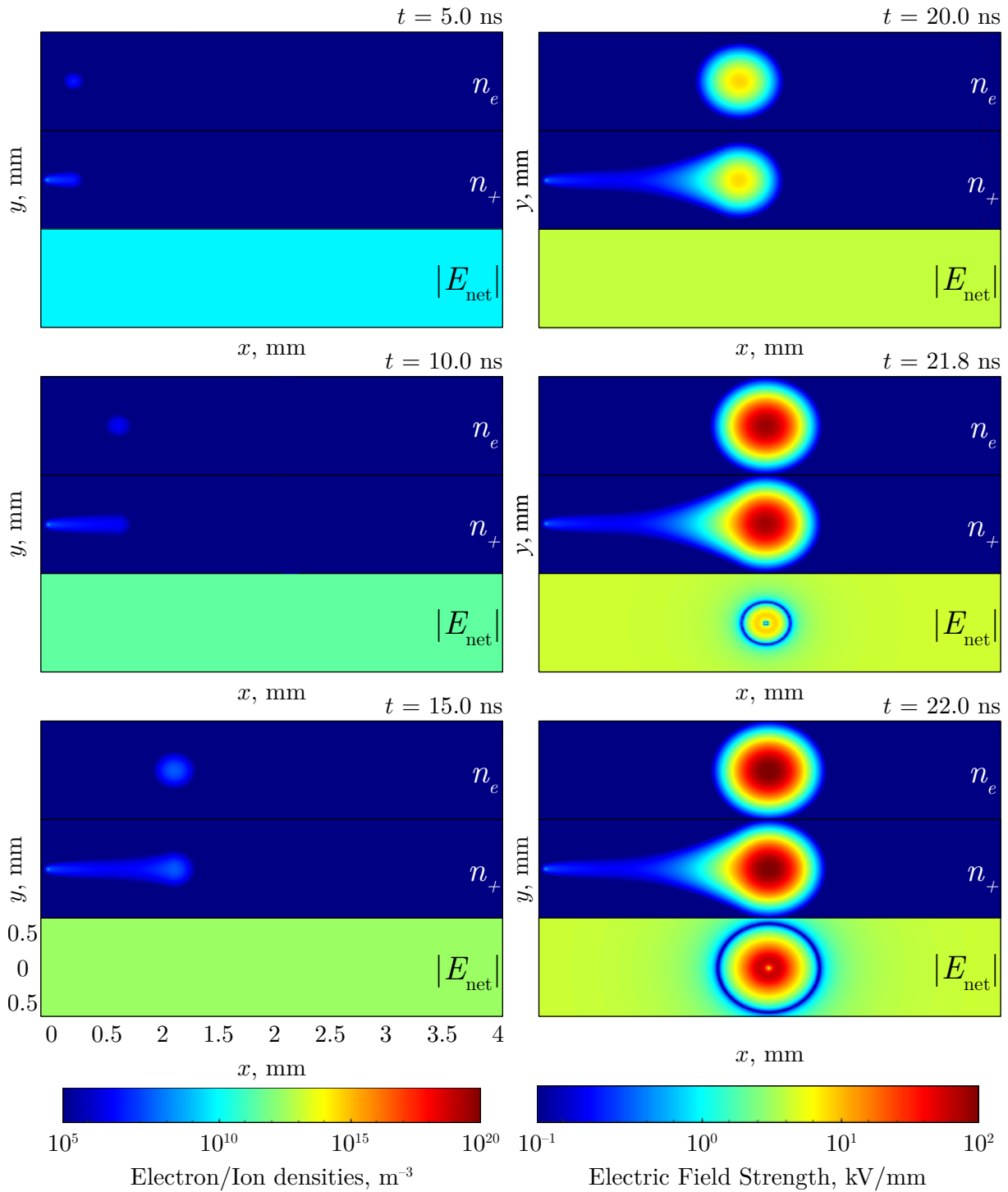


**Figure 4.3:** Sliced 2D view of the electron avalanche of Figure 4.2, showing also the net electric field strength at  $t = 5, 10, 15, 20, 21.8,$  and  $22$  ns. The avalanche-to-streamer transition occurs between 20 and 21.8 ns, when the field first becomes distorted.

computed from (4.4)–(4.11) using MATLAB Simulink [24]. The conditions used here incorporated a ramp voltage rising at 0.5 kV/ns in a 4 mm air gap, using empirical transport parameter expressions from [7]. Qualitatively, the morphology of the developed avalanche recreates the familiar and classical “teardrop” shape as originally observed in cloud chambers [3], often drawn by authors to represent avalanches [25, 26], and simulated using kinetic models [22]. Figure 4.3 shows the corresponding net electric field, which rises linearly (remaining undistorted) up until the moment that the Gaussian reaches a critical charge density. In the section that follows, it is shown that with the application of a few additional assumptions and approximations, (4.4)–(4.11) may yield analytical solutions, capable of providing far deeper insights into the nature of electron avalanches under fast-rising fields.

#### 4.4 Analytical Approximation for Ramp Electric Fields

From the general set of governing equations as defined in Section 4.3, this section returns back to the main subject matter of fast-rising fields and voltages. Of particular interest here, as briefly mentioned in Section 4.1, is the *overstressed* or *overvolted* breakdown regime. This is defined as electrical breakdown occurring at fields or voltages higher than that of the static breakdown values [27], and which is characteristic of impulsive breakdown. For many pulsed power systems, overstressed breakdown is achieved by application of fast-rising impulses with high peak voltage, often in an effort to guarantee breakdown occurrence on the rising slope. Of main interest were therefore the processes pertaining to avalanche development during a fast-rising slope, which was approximated by the linearly-increasing field

$$E(t) = \mathcal{D}t \tag{4.13}$$

where  $\mathcal{D}$  is the *rate-of-field-rise*, or  $dE/dt$ . This is an appropriate approximation considering that the region of interest lies solely on the rising slope during overstressed breakdown. Moreover, the simplicity of a linearly increasing field with constant rate-of-rise facilitates a systematic investigation on the effects of  $\mathcal{D}$ , results of which better generalise to all practical impulse waveforms where the rate-of-rise may change over the course of the rising edge.

To attain analytical results, (4.7) must also be analytically solved for the peak electron density,  $n_0(t)$ . The main barrier here is the existence of analytical functions describing the transport parameters  $\bar{\alpha}(t)$  and  $\mu_e(t)$ . In general, no exact expressions exist for these parameters, and it is more typical to use either empirical fittings or tabulated values in other modelling tasks, for

example, see Chapters 5 and 6 on streamer modelling which make extensive use of tabulated transport data. However, a semi-analytical approach may be applied here by assuming that  $\bar{\alpha}(t)$  and  $\mu_e(t)$  can be fit using the commonly-used functions

$$\begin{aligned}\bar{\alpha}(t) &\approx A_\alpha \exp\left[-\frac{B_\alpha}{E(t)}\right] - C_\alpha, \\ \mu_e(t) &\approx A_\mu E(t)^{-B_\mu}, \\ D_e(t) &\approx A_D E(t)^{B_D},\end{aligned}\tag{4.14}$$

where  $A_\alpha$ ,  $B_\alpha$ ,  $C_\alpha$ ,  $A_\mu$ ,  $B_\mu$ ,  $A_D$ , and  $B_D$  are constant coefficients unique to the gas under consideration. Functions like (4.14) have been used in the past to describe electron transport parameters over certain ranges of reduced electric field [7]. A clear limitation arising from this assumption is that the model will only be valid over the range for which the fittings of (4.14) are also valid. However, with the electron transport parameters in this form, along with the linear field (4.13), the original differential equation (4.7) can be restated as

$$\frac{\partial n_0(t)_{\text{ramp}}}{\partial t} = t^{k_1-1} \left[ k_2 \exp\left(\frac{k_3}{t}\right) - k_4 \right] n_0(t)_{\text{ramp}},\tag{4.15}$$

where the constants  $k_{1-4}$  represent the absorbed constants with the definitions:

$$\begin{aligned}k_1 &= 2 - B_\mu, & k_2 &= A_\alpha A_\mu \mathcal{D}^{k_1-1}, \\ k_3 &= B_\alpha / \mathcal{D}, & k_4 &= A_\mu C_\alpha \mathcal{D}^{k_1-1}.\end{aligned}\tag{4.16}$$

Equation (4.15), following Appendix A.8, can be shown to admit solutions of the form

$$n_0(t)_{\text{ramp}} = n_0(t_0) \exp\left[ k_2 k_3^{k_1} \Gamma\left(-k_1, \frac{k_3}{t}\right) - \frac{k_4}{k_1} t^{k_1} \right],\tag{4.17}$$

where  $\Gamma(a, t)$  is the upper incomplete gamma function with the definition

$$\Gamma(a, t) := \int_t^\infty \xi^{a-1} e^{-\xi} d\xi.\tag{4.18}$$

As a result, a closed solution for the electron field (4.10) can now be successfully constructed due to the expression (4.17). However, the transition criterion given by (4.11) requires the location of the maximum of  $E_e(r, t)$  to be determined, which has no exact solution. Despite this, the authors of [1] show that the location  $r = \lambda_1$  approximates the location of the field maximum

well, yielding

$$E_{e,\max}(t) \approx \frac{q_e n_0(t)}{4\pi\epsilon_0} \frac{(2\pi s_0^2)^{3/2}}{\lambda_1^2} \left[ \operatorname{erf}(1) - \frac{2}{e\sqrt{\pi}} \right]. \quad (4.19)$$

Thus, for a ramp field of the form (4.13), an analytical transition criterion is recovered by substitution of the ramp field into (4.19), resulting in the criterion

$$\frac{q_e n_0(t)_{\text{ramp}}}{4\pi\epsilon_0} \frac{(2\pi s_0^2)^{3/2}}{\lambda_1^2} \left[ \operatorname{erf}(1) - \frac{2}{e\sqrt{\pi}} \right] = f \cdot \mathcal{D}t. \quad (4.20)$$

This form of the transition criterion no longer necessitates a full numerical solution, in contrast to (4.4)–(4.11). Instead, it may be conveniently evaluated based solely on the intersection of two curves, given by the left and right side of (4.20) which are readily computable.

#### 4.4.1 Electron Growth Rates and Ionisation Integral, $K$

The explicit form of the electron density obtained as (4.17) provides a means to gain a greater understanding of the electron growth rates under fast-rising conditions. In particular, the nature of the electronic growth rate over the course of a fast-rising external field can be compared to the static case. As a reminder, the solution to the classical equation was given by (4.2), which may be written in terms of ionisation and attachment frequencies as

$$N_e(t) = N_0 \exp(\nu_i t - \nu_a t), \quad (4.21)$$

where  $\nu_i$  and  $\nu_a$  are constant ionisation and attachment frequencies, respectively. The net rate  $(\nu_i - \nu_a)$  therefore represents the balance between ionisation and attachment processes, which collectively determine the electron growth and decay dynamics and ultimately controls the avalanche development. By comparison of the ramp field solution (4.17) to the standard equation (4.21), one finds that the exponential form of the equation remains the same, but the growth rate is now considerably more complex, with

$$\nu_i t \rightarrow k_2 k_3^{k_1} \Gamma\left(-k_1, \frac{k_3}{t}\right) = \mathcal{I}(t), \quad (4.22)$$

$$\nu_a t \rightarrow \frac{k_4}{k_1} t^{k_1} = \mathcal{A}(t), \quad (4.23)$$

corresponding to the new ionisation rate of growth,  $\mathcal{I}(t)$ , and attachment rate of decay,  $\mathcal{A}(t)$ . Emphasis is placed here on the nature of the time-dependency of  $\mathcal{I}(t)$  and  $\mathcal{A}(t)$ , which is highly nonlinear in time compared to the constant-growth case found under static background fields.

The ionisation rate,  $\mathcal{I}(t)$ , is described by the upper incomplete gamma function which initially exhibits a slow increase, slower than that of the linear  $\nu t$  (i.e., constant  $\nu$  under a static field), but increases rapidly with time to exceed linear growth, closer to something akin to a power law. Counteracting this is the attachment rate,  $\mathcal{A}(t)$ , acting as an electron sink, and according to (4.23), follows a power law with time. Ultimately, the exact electron evolution will be determined by the constants  $k_{1-4}$ , which by the chain of dependencies, means that  $\mathcal{D}$  must also influence this evolution. To show the explicit dependence on the rate-of-rise,  $\mathcal{D}$ , it is convenient to introduce the constants

$$\begin{aligned}\gamma_1 &= A_\alpha A_\mu B_\alpha^{k_1}, \\ \gamma_2 &= \frac{A_\mu C_\alpha}{k_1},\end{aligned}\tag{4.24}$$

such that (4.23) may be redefined as

$$\begin{aligned}\mathcal{I}(t) &\rightarrow \frac{\gamma_1}{\mathcal{D}} \Gamma\left(-k_1, \frac{B_\alpha}{\mathcal{D}t}\right), \\ \mathcal{A}(t) &\rightarrow \frac{\gamma_2}{\mathcal{D}^{1-k_1}} t^{k_1}.\end{aligned}\tag{4.25}$$

The implication here is that the attachment rate  $\mathcal{A}(t)$  is dependent upon the value of  $k_1 = 2 - B_\mu$ . The value of  $B_\mu$  is typically less than unity [7], meaning that  $\mathcal{A}(t)$  has the tendency to be greater with increased  $\mathcal{D}$  for the same time. The nature of the ionisation rate,  $\mathcal{I}(t)$ , is not as clear, due to the reciprocal relation both in the coefficient and inside the incomplete gamma function. Overall, the rate of ionisation always grows over time at a given rate-of-rise. However, the inverse proportion of  $\mathcal{I}(t)$  to the rate-of-rise,  $\mathcal{D}$ , results in an initially lower value of  $\mathcal{I}(t)$ , but also increases the rate at which  $\mathcal{I}(t)$  subsequently increases as time advances. The implication here is that while ionisation activity grows in time regardless of  $\mathcal{D}$ , the *rate* at which it grows differs depending on the value of  $\mathcal{D}$  itself. The expected behaviour with a faster-rising field would be a reduced time-to-breakdown as the required field for breakdown would be established more quickly. However, the breakdown field is known to increase. Equation (4.25) offers one possible explanation of this behaviour: faster rates of rise,  $\mathcal{D}$ , tend to decrease the initial value of  $\mathcal{I}(t)$ , but increases the rate at which  $\mathcal{I}(t)$  increases in time. Consequently, ionisation activity and charge production must correspondingly increase, leading also to an increase in the rate at which the electron-induced field,  $E_{e,\max}(t)$ , increases. However, by definition, the external linearly-rising field is rising at a rate equal to  $\mathcal{D}$ , such that for the electron-induced field to become close to the magnitude of the external field, there is a competition between the rate at which the electron

field increases relative to the rate at which the external field increases. One may confirm that based on the limit

$$\lim_{\mathcal{D} \rightarrow \infty} \frac{E(t)}{E_{e,\max}(t)} = \lim_{\mathcal{D} \rightarrow \infty} \frac{\mathcal{D}t}{C(t) \exp[\mathcal{I}(t) - \mathcal{A}(t)]} = \infty, \quad (4.26)$$

where  $C(t)$  is used as shorthand for the coefficients of the exponential in (4.19), that as the rate-of-rise increases, the external electric field increases faster with  $\mathcal{D}$  compared to the electron-induced electric field. Hence, the external field at the moment of transition is necessarily higher, as the electron-induced electric field becomes increasingly delayed relative to the external field. With faster rates-of-rise, the gap between these two rates becomes increasingly wide, explaining the phenomenon of higher breakdown strengths under faster-rising field stress. In Section 4.5, this aspect is elaborated further detail using closed-form approximations.

Further analysis may be conducted on an effective value of  $K$  which arises from this novel description of the avalanche, since the definition (4.3) may equally be applied to (4.17). Let  $K_{\text{ramp}}$  be the effective  $K$  value in the case of the ramp field considered here. Based on the original form of the Gaussian electron cloud (4.5) and the newly-derived growth rate equation (4.17),  $K_{\text{ramp}}$  may be expressed in terms of two components,

$$K_{\text{ramp}} = \kappa_1(t, \mathcal{D}, \bar{\alpha}, \mu_e) + \kappa_2(t, D_e), \quad (4.27)$$

the first term of which accounts for its dependence on ionisation, attachment, and the rate-of-rise,  $\mathcal{D}$ ; while the second is a contribution arising from electron diffusion. From the definitions (4.25),  $K_{\text{ramp}}$ , in accordance with (4.3) and (4.17) may be expressed in the form

$$\begin{aligned} K_{\text{ramp}}(t) &= \ln \left[ \frac{n_e(0, t)}{n_0(t_0)} \right] + \ln \left[ \frac{\lambda_2^3}{(2\pi s_0^2)^{3/2}} \right] \\ &= \underbrace{\frac{\gamma_1}{\mathcal{D}} \Gamma \left( -k_1, \frac{B_\alpha}{\mathcal{D}t} \right) - \frac{\gamma_2}{\mathcal{D}^{1-k_1}} t^{k_1}}_{\kappa_1(t, \mathcal{D}, \bar{\alpha}, \mu_e)} + \underbrace{\ln \left[ \frac{\lambda_2^3}{(2\pi s_0^2)^{3/2}} \right]}_{\kappa_2(t, D_e)}. \end{aligned} \quad (4.28)$$

Using fitting coefficients for air obtained in [7], Figure 4.4 plots  $K_{\text{ramp}}(t_b)^\ddagger$  alongside its two constituent components against  $\mathcal{D}$  in the range  $\mathcal{D} \in [10^{10}, 10^{16}] \text{ V m}^{-1} \text{ s}^{-1}$ . These values may be taken to represent rising slopes of impulses peaking at tens to hundreds of kV within the

---

<sup>‡</sup>It is important to note that the components of  $K_{\text{ramp}}(t_b)$  both inherit a dependency on diffusion, since the breakdown time  $t_b$  is diffusion-dependent, despite (4.28).

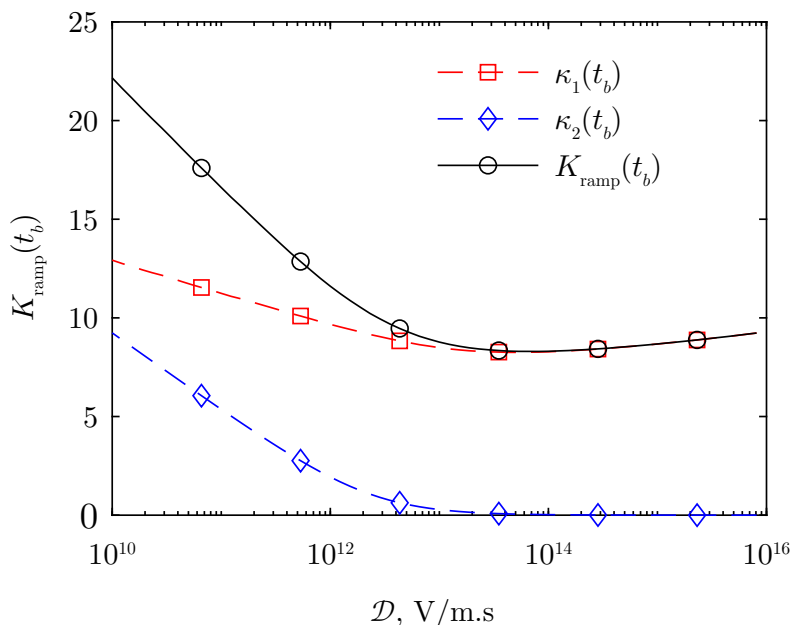


**Figure 4.4:** Plot of the effective  $K_{\text{ramp}}$  at the estimated breakdown time,  $t_b$ , including the components arising from ionisation,  $\kappa_1$ , and diffusion,  $\kappa_2$ , for air.

nanosecond to hundreds of microsecond range, in gap separations on the order of tens of millimetres. Parameters for the initial electron cloud were chosen following the strategy discussed in Section 4.3.4. The resulting plot indicates a declining relationship of  $K_{\text{ramp}}(t_b)$  with the rate of field rise  $\mathcal{D}$  for slower-rising fields ( $\mathcal{D} \lesssim 10^{14} \text{ V m}^{-1} \text{ s}^{-1}$  in this particular case), suggesting that more significant space charge must be accumulated to sufficiently distort the external field with slower-rising fields. It should be emphasised, however, that this does not imply that the breakdown strength,  $E_b$  decreases with  $\mathcal{D}$  as it would in a static case, since the applied field would also be rising at a different rate. The dependency of the breakdown strength on  $\mathcal{D}$  is analysed further in Section 4.5. The present model also predicts the occurrence of a minimum, past which  $K_{\text{ramp}}(t_b)$  increases. This can be explained by the relative importance of diffusion, as discussed in the following section.

#### 4.4.2 The Importance of Diffusion for Impulsive Breakdown

There has been limited exploration of the effects of diffusion for impulsive breakdown, and it is often assumed to be negligible based on the typical timescales involved. In [28], authors concluded using fluid simulations that diffusion may not be significant for pulsed breakdown. The line showing  $\kappa_2$  in Figure 4.4 is of interest here, since by (4.28),  $\kappa_2$  represents the main component of

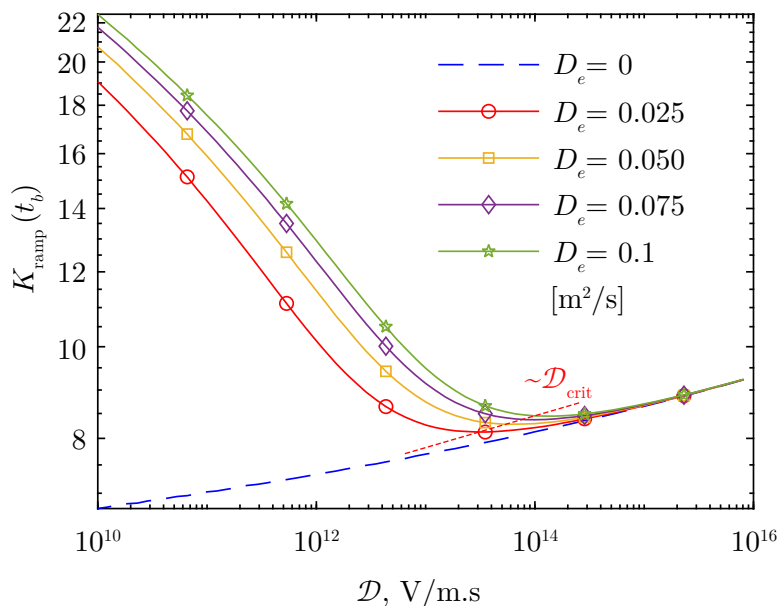


**Figure 4.5:** Plot of the effective value of  $K_{\text{ramp}}(t_b)$  as a function of  $\mathcal{D}$  and for different values of diffusion constant  $D_e$  (using transport parameters for Nitrogen). Emphasis is placed on the vanishing effect of  $D_e$  for higher values of  $\mathcal{D}$ . Image adapted with permission from [23], © IEEE 2024.

the effective  $K$  value which has arisen due to diffusion. Physically, and similarly described in [1], diffusion tends to reduce the peak magnitude of the Gaussian electron cloud, such that strong diffusive action also reduces the maximum magnitude of the electron field. Naturally, this also influences the moment of field distortion in accordance with the condition (4.20). It is clear from Figure 4.4, however, that  $\kappa_2$  tends to zero for high values of  $\mathcal{D}$ , suggesting that there exists a limit for which diffusion is important for breakdown on a rising slope.

The plot of Figure 4.4 was generated assuming a field-dependent diffusion coefficient following the parameters in [29]. For illustrative clarity, however, it is more useful in the following analysis to assume discrete values of constant  $D_e$  over some range. Figure 4.5 plots  $K_{\text{ramp}}(t_b)$  using several different values of constant  $D_e$ , and which includes the non-diffusive case of  $D_e = 0$ . There is a clear influence from  $D_e$  that tends to increase the effective  $K$  value below a critical limit  $\mathcal{D}_{\text{crit}}$ , beyond which diffusion ceases to have any significant effect as evidenced by the convergence of all lines irrespective of  $D_e$  beyond  $\mathcal{D} \approx 10^{14} \text{ V m}^{-1} \text{ s}^{-1}$ . This can be explained based on the relative timescales required for electron diffusion to have a sufficiently impactful role in reducing the peak electric field, compared to the time for the field to increase based on  $\mathcal{D}$ . While no closed-form solution to the equation  $\partial K_{\text{ramp}}/\partial \mathcal{D} = 0$  can be obtained, it may be argued from (4.28) that  $\kappa_2$

becomes negligible when  $\kappa_2 \rightarrow 0$ , hence

$$\ln \left[ \frac{\lambda_2^3}{(2\pi s_0^2)^{3/2}} \right] \rightarrow 0 \iff \int_{t_0}^{t_b} D_e(t) dt \ll \frac{s_0^2}{2}, \quad (4.29)$$

or in the case of constant diffusion, simplifies to

$$1 \ll \frac{s_0^2}{2D_e t_b} \quad (4.30)$$

where  $s_0^2/2D_e$  is the diffusion time, which provides an intuitive physical interpretation of the tendencies of Figure 4.5. Diffusion becomes negligible when breakdown occurs sufficiently fast that diffusion is unable to significantly affect the initial spread and peak of the electron distribution by the time of breakdown. From (4.28) and Figure 4.5, however, where diffusion is important, it tends to increase the effective  $K$  value necessary for avalanche-to-streamer transition in agreement with the results from [1]. The conditions (4.29) and (4.30) derived here may therefore be used to separate and identify the regions where diffusion has strong influence for impulsive breakdown, and where its effects can be ignored. This result may be consequential for future modelling efforts, particularly for overstressed gas breakdown phenomena, and may further support the interpretation of experimental breakdown results gathered within this regime.

## 4.5 Closed-form Solutions and the Effect of Rate-of-Rise, $\mathcal{D}$

In this section, closed-form approximations to the impulsive breakdown time and fields are shown to be attainable under the application of an additional layer of simplification. The additional analyses which these expressions have facilitated provided further insights into fundamental aspects of overstressed breakdown, while also providing convenient formulas that possess predictive power for practical system design.

The analysis here was focused on the limiting case where diffusion and attachment can be treated as negligible ( $D_e = C_\alpha = 0$ ). As was discussed in Section 4.4.2, diffusion may not necessarily be negligible and is subject to the condition (4.29) derived previously, and zero attachment can only be assumed for gases of low electronegativity. Imposition of these constraints was done out of mathematical necessity to conduct the present analysis, however, it is shown in the following sections that the introduction of a auxiliary parameter during the process of derivation may be able to account for (to some extent) diffusion and attachment despite their initial omittance. While the analysis of Section 4.4 arrived at an analytical solution to the electron evolution by

approximating the location of the maximum field and by making use of fitted functions for transport parameters; it remains that the actual condition for transition, (4.20), was not solved in closed-form but was obtained based on the intersection of (4.13) and (4.19). Here, this is addressed in a new approximation and approach.

Consider that the approximate maximum electron field established as (4.19) may be written in the form

$$E_{e,\max}^{D_e, C_\alpha=0} = C_0 \exp \mathcal{I}(t) \quad (4.31)$$

since the imposition of the non-attaching assumption drives  $\mathcal{A}(t)$  to zero, and the zero-diffusion assumption reduces the coefficient  $C(t)$  to a constant,  $C_0$ , given by:

$$C_0 = \frac{q_e n_0(t_0)}{4\pi\epsilon_0} \frac{(2\pi s_0^2)^{3/2}}{2s_0^2} \left[ \operatorname{erf}(1) - \frac{2}{e\sqrt{\pi}} \right]. \quad (4.32)$$

One may arrive at a very good approximation the transition criterion of (4.20) by instead solving

$$\frac{\partial}{\partial t} [f\mathcal{D}t_p - C_0 \exp \mathcal{I}(t_p)] = f\mathcal{D} - C_0 \frac{\partial \mathcal{I}(t_p)}{\partial t} \exp \mathcal{I}(t_p) = 0 \quad (4.33)$$

for the time  $t_p$  when the *electron field rate of change is equal to the rate of change of the external field (times the factor  $f$ )*. In other words, (4.33) solves for the *maximum of the net electric field*. This contrasts the previous criterion of (4.20) which required that the magnitudes be equal and solves for the breakdown time previously assigned the symbol  $t_b$ . However, at breakdown field magnitudes, the rapid growth of the electron density causes the electron field to increase equally as fast, fast enough that the moment of field distortion happens sufficiently quickly such that  $t_b \approx t_p$  is a reasonable approximation, see as illustrated in Figure 4.6. It is remarked that, defining the moment that the net field collapses as the moment of breakdown is perhaps more similar to the definition of breakdown used in experimental work, where the *beginning* of the voltage collapse is often used to indicate the onset of breakdown (see for example, Chapter 7 and 8). If the initial electron field is small, which would be the case assuming the avalanche is initiated from typical background ionisation levels, then at time  $t = t_0^+$  the applied field rises significantly faster than the electron field. In this case,  $E_{e,\max}(t_p)$  must necessarily be lower than the external  $E(t_p)$  when their rates become equal. Without loss of generality, the electron field may then be expressed as some fraction  $g$  of the applied field,  $E_{e,\max}(t_b) = g \cdot E(t_b)$ . Then (4.33)

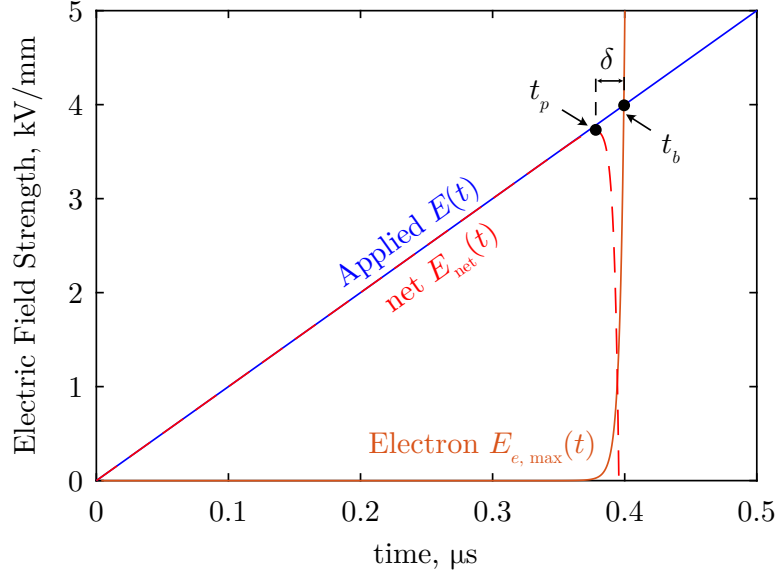


**Figure 4.6:** Example of the electric field strength over time for the applied ramp,  $E(t)$ ; max. electron field  $E_{e,\max}(t)$ ; and net electric field,  $E_{\text{net}}(t)$ . Indicated are the time for the electron field and applied field to equal in magnitude,  $t_b$ , and the time for the net field to reach a maximum,  $t_p$ . The difference,  $\delta$ , is assumed negligible for the derivation of the closed-form approximation. Image adapted with permission from [23], © IEEE 2024.

can be restated as

$$\begin{aligned} \frac{\partial \mathcal{I}(t_p)}{\partial t} \underbrace{C_0 \exp \mathcal{I}(t_p)}_{g \cdot E(t_b)} &= f \mathcal{D} \\ \frac{\partial \mathcal{I}(t_p)}{\partial t} g E(t_b) &= f \mathcal{D} \\ t_b \frac{\partial \mathcal{I}(t_p)}{\partial t} &= \frac{f}{g}. \end{aligned} \quad (4.34)$$

The fraction  $g$  essentially becomes a fitting factor, however, the significance and selection of  $g$  is discussed further in Section 4.5.1. Equation (4.34) can be shown to have the closed-form solution (see Appendix A.9)

$$t_b = \frac{B_\alpha}{\mathcal{D} k_1 \omega(\mathcal{D})} \quad (4.35)$$

for the time-to-breakdown, where the function  $\omega(\mathcal{D})$  is defined as

$$\omega(\mathcal{D}) := W \left[ \frac{1}{k_1} \left( \frac{g \gamma_1}{f \mathcal{D}} \right)^{1/k_1} \right], \quad (4.36)$$

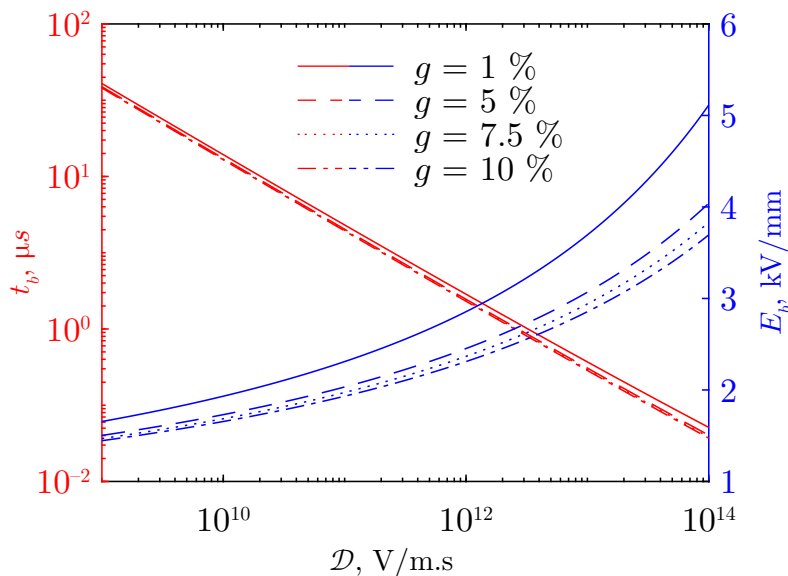


**Figure 4.7:** Plots of the closed-form estimations for breakdown time,  $t_b$ , and breakdown field magnitude,  $E_b$ , in the zero-diffusion, non-attaching limit (4.35), (4.37) as a function of  $\mathcal{D}$ . Plots at different values of  $g$  also shown. Image adapted with permission from [23], © IEEE 2024.

where  $W(\cdot)$  is the principal branch of the Lambert- $W$  (or product-log) function<sup>§</sup>. Correspondingly, the breakdown strength and breakdown voltage (assuming the external field was generated between two planar electrodes with separation  $d$ ) can be written

$$E_b = \frac{B_\alpha}{k_1 \omega(\mathcal{D})}, \quad V_b = \frac{B_\alpha d}{k_1 \omega(\mathcal{D})}. \quad (4.37)$$

Figure 4.7 plots the breakdown time,  $t_b$ , and breakdown field,  $E_b$ , as a function of  $\mathcal{D}$  over a similar range as used in Section 4.4.2, also for nitrogen. Several different values of  $g$  are also included which are discussed later in Section 4.5.1. As for general tendencies, the time-to-breakdown decreases with faster-rising fields, as expected, due to the more rapid onset of ionisation and avalanche development. However, the present closed-form approximations also capture the increasing breakdown strength with  $\mathcal{D}$ , in agreement with characteristic trends observed experimentally for overstressed impulsive breakdown.

Under the assumptions applied here of zero-diffusion and of a non-attaching gas, both the applied field and electron field are monotonically increasing functions with time. Where no

<sup>§</sup>The Lambert- $W$  function is a known special function which is the solution  $y(x)$  of equations with the form  $ye^y = x$  for  $x \geq 0$ .

significant pre-ionisation exists, the rate of increase of the electron field is always lower than that of the applied field, which rises at a constant rate  $\mathcal{D}$ . The moment that the net electric field is maximised must therefore equal the moment when the rate-of-rise of the electron field becomes equal to  $\mathcal{D}$ , which is stipulated by (4.33). With an increase to  $\mathcal{D}$ , the increase to the rate-of-rise of the applied field is greater than the increase induced on the electron field, as was concluded based on the limit (4.26).

Therefore, the electron field requires an increasing amount of time to reach a rate of  $\mathcal{D}$  at greater values of  $\mathcal{D}$ , increasing the breakdown field. This is relative to the breakdown time,  $t_b$ , which continues to decrease with greater  $\mathcal{D}$ . One may further be reminded of the definitions (4.14) and their relation to the electron transport parameters. It may be said that the above effect is due to the differing rates at which the ionisation coefficient,  $\alpha(t)$ , and electron mobility,  $\mu_e(t)$  change with increasing electric field (and by extension, change with  $\mathcal{D}$  since in the case of a ramp field, the field magnitude has a linear dependence on  $\mathcal{D}$ .) Based on the functions (4.14), ionisation activity increases with increased  $E$ , while mobility decreases. Their rates of change, however, are not equal, with ionisation increasing like  $\exp(-1/E)$  and mobility decreasing with  $E^{-B\mu}$ . The rate at which mobility decreases with field is therefore faster than the rate that ionisation may increase. This ultimately limits the net rate of change that  $E_{e,\max}$  can attain with increasing  $\mathcal{D}$ , such that (4.26) becomes imposed. This is consistent with the analysis presented in Section 4.4.1, which considered the ionisation rate in terms of the upper incomplete gamma function and its growth with respect to differing values of  $\mathcal{D}$ .

The scaling of the breakdown time  $t_b$  with  $\mathcal{D}$  according to (4.35) is revisited within Chapter 6, where it helps to explain the observed streamer inception times from numerical modelling results. Section 4.6 also deals directly with model validation by comparing model predictions to experimental data.

#### 4.5.1 The Nature of Parameter $g$

Returning to the derivation step (4.34) and to Figure 4.7, the significance of the fraction  $g$  has yet to be addressed. As introduced originally in (4.34),  $g \cdot E(t_p)$  represents the magnitude of the electron field at the moment that the net field reaches a maximum as a fraction,  $g$ , of the applied field. In general,  $g$  will be dependent on  $\mathcal{D}$ , gas parameters, and on the initial field condition given by the constant  $C_0$ , though from the present analysis alone the exact nature of its dependencies remains unclear. It was found that  $g$  need not exceed  $\approx 10\%$  to provide excellent agreement between the closed-form approximation (4.35) and the full numerical model (4.4)–(4.11) over

several magnitudes of  $\mathcal{D}$ . This is detailed further in Section 4.6 within experimental validation results. This suggests that the sensitivity of  $g$  to the rate-of-rise  $\mathcal{D}$  may not be significant. However, it does suggest that nearing the moment of breakdown, the electron field is typically  $<10\%$  of the applied field, but the subsequent ionisation processes occur with such intensity and rapidity that their magnitudes become equal within a sufficiently short time for the assumption of  $t_p \approx t_b$  to become a good approximation.

As mentioned, the fraction  $g$  also depends on the electron transport parameters. Therefore, using  $g$  as a fitting parameter could also be said to account for (to some degree) any subsequent reduction of the electron field during its transport due to diffusion or attachment, which were initially omitted. There may be the view that  $g$  essentially takes the place of the parameter  $K$  within the classical Meek-Raether criterion, which is often chosen arbitrarily to match experimental results. However, it is remarked that the value of  $g$  can be determined by comparison with the full numerical model (4.4)–(4.11), from which 1–10% was found to be typical values which provided good experimental fits (see Figure 4.10 of Section 4.6.2). Since  $g$  was introduced during the simplification of the analytical model (4.20) to attain the closed-form (4.35), it can be considered to be more of a fitting parameter to ensure that the approximation is corrected to the full physical model, rather than solely as an empirical fitting parameter. This is considered a significant advantage and improvement upon the classical Meek-Raether criterion. It is acknowledged, however, that the investigation of the nature of  $g$  should be of high priority in future work. Understanding its dependencies may be an important step forward for impulsive breakdown modelling and prediction.

## 4.6 Model Validation and Experimental Comparisons

This section validates the developed model by means of comparison to available data sourced from literature. This includes simulated data arising from modelling approaches of considerably greater complexity, and also experimental breakdown results. This is split into two sections. The first addresses the capability for the present model to predict the upward shift of the Paschen minimum with greater rate-of-rise, and the second, presents a new analytical field-time scaling relationship of overstressed breakdown on the rising slope, where the rate-of-rise has been included as an explicit parameter.

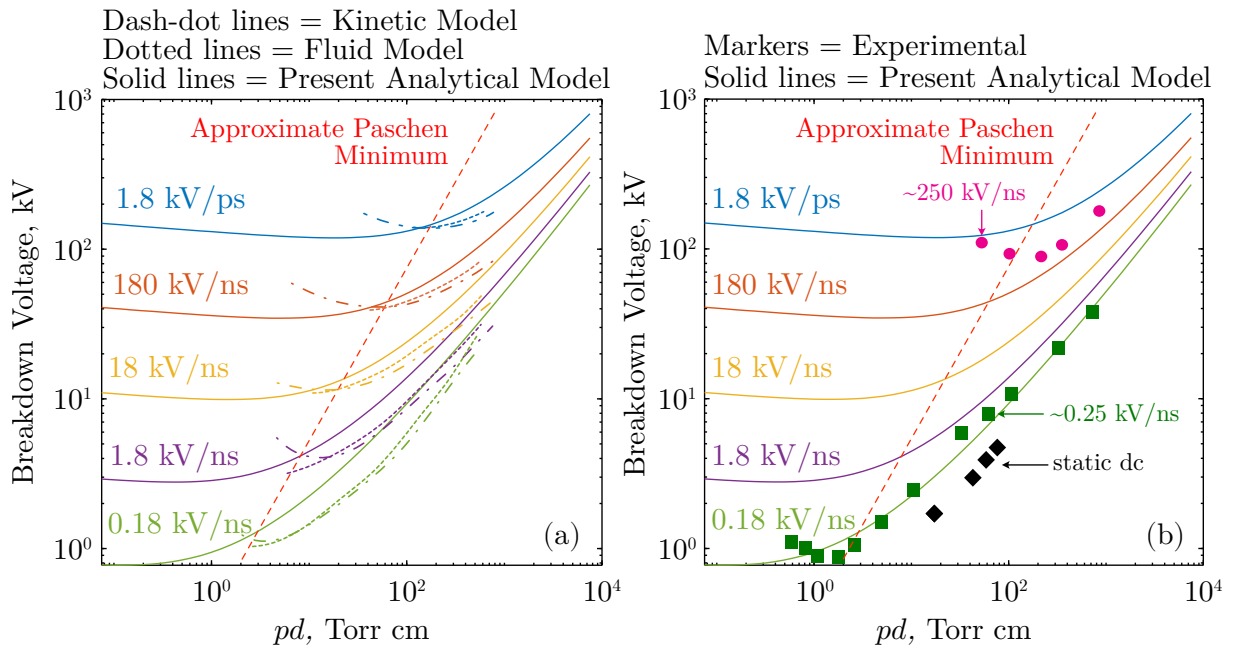


**Figure 4.8:** Comparison of Paschen curves for Nitrogen subject to ramp voltages at various rate-of-rise as predicted by the analytical model (4.20). Comparison to (a) fluid and kinetic simulation data from [28], (b) experimental data from [30]. Solid black diamond markers are the static breakdown case, while the red dashed lines indicate the approximate position of the estimated Paschen minimum, where the model predictions begin to diverge. Image adapted with permission from [23], © IEEE 2024.

#### 4.6.1 Pulsed Paschen Curves

As reviewed in Section 2.3.7, Paschen’s law forms a cornerstone of high voltage engineering, describing the scaling relationship of the gas breakdown voltage with the pressure-distance product. Importantly, Paschen’s law provided a model capable of capturing the *Paschen minimum*, a combination of  $pd$  which results in a minimum breakdown voltage. However, it has been known for some time that under fast-rising voltage impulses, the canonical form (2.36) no longer applies. As shown in [28], Paschen curves, including the position of the minimum, tend to be shifted upward and towards higher values of  $pd$ , including the position of the Paschen minimum.

For any breakdown model focused on impulsive waveforms, the so-called *pulsed* Paschen curves are important to be able to recreate. Here, computational data sourced from Levko *et al.* [28] and experimental data according to Babich [30] are used as a means of comparison to the present model (4.20). Figure 4.8 plots these results for the parameters used in [28], which incorporated a ramp voltage rising to 180 kV over a range of times which result in the values of  $dV/dt$  specified by the figure labels. The gap considered was 1 cm and filled with nitrogen, fitting coefficients

of which were again obtained from [7]. As shown in Figure 4.8, reasonable agreement is found between the present model when compared to both fluid simulations, kinetic simulations, and also to experimental data. At least to the right of Paschen curves, the model adequately describes the upward shift induced by faster-rising voltages. Disparities arisen particularly in the comparison with computational models [Figure 4.8(a)] are likely to be partially due the difference in initial conditions used, which were not rigorously specified in [28], and for the simple fact that these models differ greatly in complexity. Considering this, the agreement appears quite reasonable.

To the left of the Paschen curves, the situation is clearly different. In this region, the present model fails to recreate the upward trend for small  $pd$ . However, given that the main mechanism behind the present model is avalanche-to-streamer transition, the intended region of applicability would naturally be on the right-side of the minimum anyway. Levko *et al.* [28] also remarked that their fluid model was unable to accurately capture the tendencies to the left of the minimum, to which they attribute to non-local electron kinetics, which the present model also does not consider<sup>¶</sup>. To further ensure that  $pd$  scaling is indeed exhibited by the present model, Figure 4.9 plots the predicted breakdown voltage as a colour map over the two dimensional  $pd$  space, defined within the range  $p \in [0, 7500]$  Torr (1 to 10 bar), and  $d \in [0, 5]$  cm. This plot aims to show that the predicted breakdown voltage correctly scales with  $pd$ , evidenced by the equipotential lines that align approximately with curves of constant  $pd$ , since by definition, the breakdown voltage should be the same for the same values of  $pd$ . This confirms that the model indeed exhibits  $pd$ -scaling over the full space and is consistent with experimental trends. Moreover, according to [31], the Lambert- $W$  function,  $W(x)$ , is asymptotic to  $\ln x - \ln(\ln x)$ . In which case, the closed-form breakdown voltage from (4.37) can be further approximated to have the proportionality (see Appendix A.10):

$$V_b \propto \frac{pd}{\ln [k(p^a d)^b] - \ln [\ln k(p^a d)^b]} \quad (4.38)$$

by realising that  $B_\alpha$  in the chosen form depends on the number density,  $N$ , and by extension, dependent on the pressure,  $p$ . Here  $k$ ,  $a$ , and  $b$  represent constants for a given gas and value of  $\mathcal{D}$ . Note particularly the form of (4.38), which bears a striking resemblance to that of the classical Paschen's Law (2.36).

---

<sup>¶</sup>For more discussion on non-locality and its effects, see Chapter 5, Section 5.2.2.

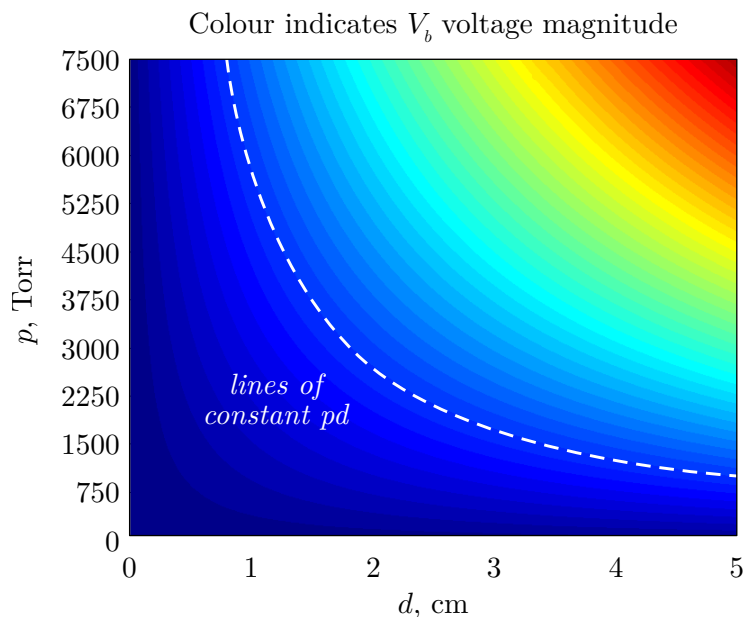


**Figure 4.9:** Colour map of the  $pd$  space from  $p$  up to 7500 Torr (10 bar), and  $d$  up to 5 cm. Colour indicates the magnitude of the predicted breakdown voltage, warmer colours correspond to higher values. Equipotential lines align with curves of constant  $pd$ , satisfying  $pd$  scaling. No colour bar is shown as the exact voltage values are unimportant here. Image adapted with permission from [23], © IEEE 2024.

#### 4.6.2 Field-Time Scaling Characteristics

For impulsive breakdown data, where both the breakdown time and breakdown strength are important quantities, a different type of scaling has often been employed to compare breakdown datasets. See for instance in [8], which involves plotting the scaled breakdown time,  $Nt_b$ , against the reduced breakdown field,  $E_b/N$ , where  $N$  is the neutral gas density. In Liu *et al.* [8], a number of experimental datasets were compared in this way, and also compared to a well-known empirical relation introduced by T. H. Martin [32]. Liu *et al.* [8] also compared these experimental results to the classical Meek criterion, assuming a value of  $K = 18$ , where the characteristic curve describing this scaling relation follows from (4.3) to be

$$Nt_b = \frac{K}{\bar{\alpha}\mu_e} \cdot \frac{1}{E_b/N}. \quad (4.39)$$

Using the closed-form approximation derived in this work, equations (4.35), (4.37) can be combined to yield a characteristic in the same form (following from Appendix A.11),

$$Nt_b = \frac{B_\alpha^2}{k_1^2 \mathcal{D} \omega^2(\mathcal{D})} \cdot \frac{1}{E_b/N}, \quad (4.40)$$

but which now shows a direct dependence on the rate of field rise,  $\mathcal{D}$ . Liu *et al.* [8] had previously shown that the original criterion (4.39) adequately described the gathered experimental data. The relation (4.40) developed here can be considered the same as (4.39), but in its derivation as presented in Section 4.5, provided far deeper insight into the avalanche process and its dependency on the gas transport parameters and rate-of-rise. Figure 4.10 compares (4.40) to the collated experimental datasets in [8], which included work by Carboni *et al.* [33]; Felsenthal and Proud [34]; Kumar *et al.* [17]; Mankowski *et al.* [35]; Tao *et al.* [36]; fluid modelling results from Liu *et al.* [7]; and Martin’s [32] empirical curve, for reference. This is shown for air, nitrogen, and CO<sub>2</sub>, using parameters from [7]. Furthermore, solutions to the full numerical model (4.5)–(4.11) are also compared to the closed-form approximation (4.40) at values of  $g = 1\%$ ,  $5\%$ , and  $10\%$  of the applied field to show sensitivity. Reasonable agreement was found across the entire range of reduced electric field for all three gases considered. Larger discrepancies are apparent in the lower field regions, for example, for CO<sub>2</sub> in the region where  $E_b/N < 10^2$  Td. This is close to the critical field of each gas, and corresponds mainly to the limit of validity for the fitting coefficients which have been used. It should also be noted that the shown values for CO<sub>2</sub> were calculated in Liu *et al.* [8] based only on the average electric field in the weakly non-uniform gap used in the study of Kumar *et al.* [17], which may have led to an underestimation of the breakdown field. In general, there is a clear lack of impulsive breakdown data for CO<sub>2</sub> that reports on both breakdown strength and breakdown time, which should act to inform future studies. Some discrepancies also arise in air and N<sub>2</sub> leading up to around  $10^3$  Td, though these are likely explained by the effects of the statistical time lag, which is believed to be significant compared to the formative time for the datasets of Tao *et al.* and Mankowski *et al.* In both these works, no specific arrangements were implemented to ensure pre-ionisation or initial electrons, through the use of ultraviolet (UV) irradiation or otherwise. Thus, this may explain the longer breakdown time recorded in these datasets.

## 4.7 Chapter Conclusions, Contributions, and Outlook

In pursuit of advancing the understanding the effects of fast-rising voltages on the avalanche phase of gas breakdown, this chapter has introduced a novel theoretical model to estimate the moment

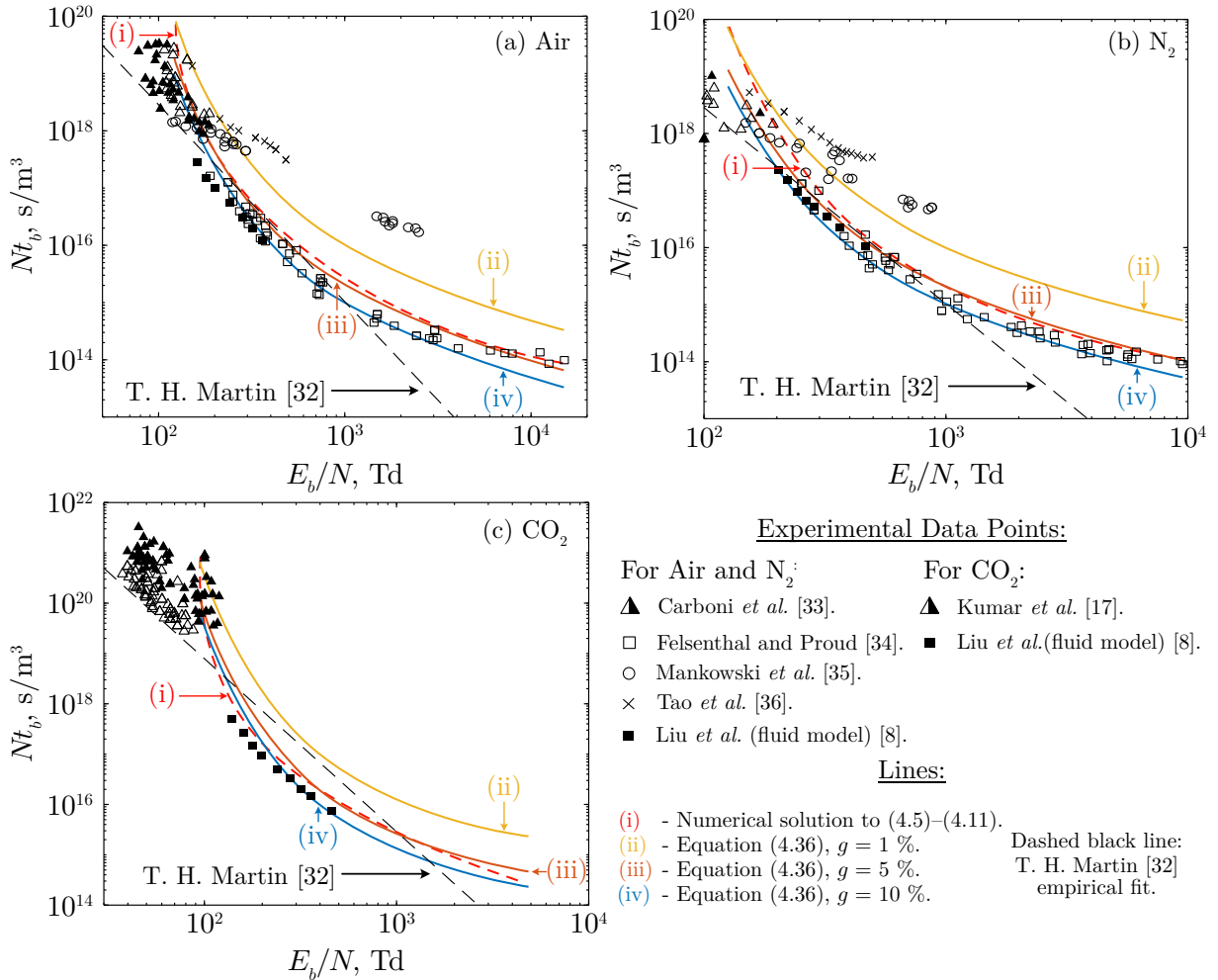


**Figure 4.10:** Field-time scaling curves for (a) air, (b) nitrogen, (c) carbon dioxide, comparing experimental datapoints with the solution to the full numerical model and its closed-form approximation, (4.40), at different values of the parameter  $g$ . References to experimental data provided in the shared figure legend. Image adapted with permission from [23], © IEEE 2024.

of avalanche-to-streamer transition under linearly-increasing electric fields. A hierarchy of models have been explored, starting from the development of a set of governing equations describing the avalanche growth. Subsequent simplifications have led to analytical and closed-form breakdown models being derived in succession. Each offered different insights into the effects of fast-rising fields on avalanche development during the early stages of gas breakdown. The model has offered theoretical explanations of typical characteristics observed for overstressed impulsive breakdown, such as the increasing breakdown strength with rate-of-rise. The model has also been validated against experimental and simulated data, finding excellent agreement across numerous datasets.

#### 4.7.1 Academic Significance and Contributions

Building upon the Gaussian-cloud model developed by Montijn and Ebert [1], the present work has firstly presented a set of governing equations based on this approach, the numerical solutions of which describe impulsive overstressed breakdown results under arbitrary time-varying fields. Using a semi-analytical approach incorporating common empirical fitting functions for electron transport parameters, an analytical solution to the electron growth under ramp fields has been shown to be obtainable. Results indicated that avalanche development under fast-rising ramp voltages may be adequately described using the upper incomplete gamma function, exhibiting an initial period of slower growth, which then rapidly accelerates. With an analytical solution, the nature of the electron growth rates under ramp fields have been found to be highly nonlinear, contrasting that of the classical Meek Criterion which assumed constant rates. The effective value of  $K$  has been shown to exhibit a local minimum as a function of rate-of-rise, which has further been shown to relate to the dominance of electron diffusion. Hence, an approximate condition separating where diffusion is important for overstressed breakdown, and where diffusion can be safely assumed negligible, has been analytically deduced.

The imposition of a number of additional assumptions has allowed, for the first time, closed-form approximations for the overstressed impulsive breakdown strength and breakdown time to be derived. Moreover, these expressions have been obtained as explicit functions of the rate-of-rise, facilitating analysis that partly explains the reason for an increasing breakdown strength with faster-rising applied fields. This was explained in terms of the relative rate of change of the electron-induced electric field to the rate increase of the applied field. It has further been shown that overstressed impulsive breakdown may be described in terms of the Lambert- $W$  function, enabling the derivation of an alternative description of the field-time scaling characteristic for impulsive breakdown. Comparison with numerous experimental and computational datasets has

shown that the model correctly exhibits Paschen ( $pd$ ) scaling, recreates the upward shift to the Paschen curve, and also reasonably describes several experimental breakdown datasets over a wide range of reduced breakdown field and breakdown times.

### 4.7.2 Industrial Relevance

Despite the long history of high-voltage engineering and growing knowledge of gas breakdown, research focused on fast-rising impulsive breakdown is scarce compared to steady-state studies, especially from a theoretical perspective. As a result, breakdown predictions are very often evaluated using either empirical or phenomenological laws based on limited data, or classical theories that may no longer be absolutely applicable due to limitations surrounding the originally imposed assumptions. Many continue to be used in absence of better models that match their convenience and simplicity.

This work contributes a significant advancement in terms of convenient and easy to compute models for the overstressed breakdown regime. The closed-form breakdown expressions developed in this work have been validated against experimental data, showing the adequacy of its predictions for several common gases. Most importantly, the expressions are simple to compute, yet capture the intricacies between parameters of interest, particularly of known and controllable parameters such as the rate-of-rise. In this way, both the impulsive breakdown voltage and time-to-breakdown can be readily predicted using the model developed here. At the same time, the modelling approach can be traced back to fundamental and well-established processes, such that the limitations are also well understood. Overall, the model contributes further understanding of the impulsive breakdown process, while simultaneously providing expressions that can be used directly as a powerful predictive tool in the development of current- and next-generation pulsed power systems.

### 4.7.3 Limitations and Future Outlook

As with any model, there exists the inevitability of model limitations. Several limitations are evident from the nature of the model, or have previously been mentioned. Namely, the use of the empirical fitting functions, (4.14), provides a clearly-defined limit to the validity of this model, as the analysis requires expressions given by the form of (4.14) to draw its conclusions. Moreover, one may note that depending on the gas, multiple functions may be necessary to describe the transport parameters across a wide range [7]. Therefore, care must be taken to ensure that any predictions made using the model do not lay beyond the fitting limits of any one function. It

must also be stated that the entire approach relies on the transport parameters matching the form of (4.14). If these functions do not adequately describe the transport data, the present derivations are unlikely to provide reasonable values. However, depending on the form the fitting functions, alternative forms of the present model may still be obtainable.

Secondly, the approach assumes the prior existence of a localised electron distribution, which, as discussed in Section 2.3.1, is probabilistic in nature. In Section 4.6.2, experimental comparisons conducted here were to datasets that both used and did not use UV irradiation to provide starting electrons. Good agreement was found for a mixture of both types of data, but in general, it is difficult to decouple statistical effects from those arisen from the many other influencing factors that may be present, e.g., exact electrode configuration and gas conditions. Similarly, the initial conditions which define the initial cluster of electrons was chosen based on limited data;  $s_0$ ,  $n_0$  are both parameters with a high degree of uncertainty, particularly when considering the degree to which they may vary based on many scenario-dependent factors.

Along the same lines, the assumption that the initial electron distribution maintains a Gaussian shape throughout its transport is an approximation that may only be valid for the case of an ideal uniform field. This was assuming that electrons are under the action of the external field alone and therefore move along field lines at drift velocity (in the same direction), thereby not deviating far from their initial Gaussian form. Comparing to imaged avalanches [3] and kinetic simulations [22], this indeed seems reasonable for the uniform case studied here. However, the expectation is that for highly non-uniform fields (where the field rapidly changes across the characteristic dimension of the avalanche), an initial Gaussian may be perturbed into a substantially different distribution, invalidating this assumption.

Based on these limitations and on the various aspects of this model's development, a number of recommendations for future work are listed below. These points are considered most important to further advance the understanding of the present modelling approach, and includes aspects pertaining to impulsive breakdown that have arisen from the study of these processes:

- Validation of the model against an extended set of experimental data, including both common and exotic gases that are relevant to industry, for example, SF<sub>6</sub> replacements. This of course necessitates that the transport parameters be determined and functions in the form of (4.14) fitted. (The full numerical model, however, can be used with tabulated data).
- What are the dependencies of  $g$ , and how could knowledge of these dependencies lead

to better modelling of avalanche development? Does the adjustment of  $g$  adequately compensate for missing processes ignored during derivation? (e.g., diffusion, attachment).

- Can reliance on empirically-fit transport parameters ever be removed? Are there more fundamental analyses that could be conducted, that would allow accurate analytical representations of electron transport parameters (possibly deriving from collisional cross-sections), that would mitigate the need for empirical fittings?
- For more complex waveforms, possibly full impulses of various types, can similar semi-analytical solutions be found (potentially described by other special mathematical functions, in a similar way the upper incomplete gamma function described the ramp case)? What about other, non-impulsive, signals?
- Could a similar approach be used to study avalanche development in certain non-uniform field geometries? For instance, if the field non-uniformity is only significant over the distance which the avalanche transports, but is effectively uniform over the characteristic length of the Gaussian density. In this case, can the field over some path  $E[\vec{r}(t)]$  be treated as simply time-dependent given that the path  $\vec{r}(t)$  is known analytically? Are there any combinations of field and paths that could yield analytical solutions in this case?
- What is the nature of the positive ion field, and are there any conditions where this field can be modelled or approximated in a simple way?

## Chapter 4 References

- [1] C. Montijn and U. Ebert, “Diffusion correction to the raether–meek criterion for the avalanche-to-streamer transition,” *J. Phys. D: Appl. Phys.*, vol. 39, no. 14, p. 2979, 2006.
- [2] J. M. Meek, “A theory of spark discharge,” *Phys. Rev.*, vol. 57, pp. 722–728, 1940.
- [3] H. Raether, *Electron Avalanches and Breakdown in Gases*. Butterworths, London, 1964.
- [4] L. B. Loeb and J. M. Meek, “The Mechanism of Spark Discharge in Air at Atmospheric Pressure. I,” *J. Appl. Phys.*, vol. 11, no. 6, pp. 438–447, 1940.
- [5] L. B. Loeb and J. M. Meek, “The Mechanism of Spark Discharge in Air at Atmospheric Pressure. II,” *J. Appl. Phys.*, vol. 11, no. 7, pp. 459–474, 1940.
- [6] L. B. Loeb and J. M. Meek, *The Mechanism of the Electric Spark*. Stanford University Press, 1941.
- [7] T. Liu, I. V. Timoshkin, S. J. MacGregor, M. P. Wilson, M. J. Given, N. Bonifaci *et al.*, “Field-time breakdown characteristics of air, N<sub>2</sub>, CO<sub>2</sub>, and SF<sub>6</sub>,” *IEEE Trans. Plasma Sci.*, vol. 48, no. 10, pp. 3321–3331, 2020.
- [8] T. Liu, I. Timoshkin, M. P. Wilson, M. J. Given, and S. J. MacGregor, “The nanosecond impulsive breakdown characteristics of air, N<sub>2</sub> and CO<sub>2</sub> in a sub-mm gap,” *Plasma*, vol. 5, no. 1, pp. 12–29, 2022.
- [9] R. T. Waters and W. B. Stark, “Characteristics of the stabilized glow discharge in air,” *J. Phys. D: Appl. Phys.*, vol. 8, no. 4, p. 416, 1975.
- [10] W. S. Zaengl and K. Petcharakas, *Application of Streamer Breakdown Criterion for Inhomogeneous Fields in Dry Air and SF<sub>6</sub>*. Boston, MA: Springer US, 1994, pp. 153–159.
- [11] L. Niemeyer, “A generalized approach to partial discharge modeling,” *IEEE Trans. Dielectr. Electr. Insul.*, vol. 2, no. 4, pp. 510–528, 1995.
- [12] J. J. Lowke and F. D’Alessandro, “Onset corona fields and electrical breakdown criteria,” *J. Phys. D: Appl. Phys.*, vol. 36, no. 21, p. 2673, 2003.
- [13] G. V. Naidis, “Conditions for inception of positive corona discharges in air,” *J. Phys. D: Appl. Phys.*, vol. 38, no. 13, p. 2211, 2005.
- [14] P. N. Mikropoulos and V. N. Zagkanas, “Threshold inception conditions for positive DC corona in the coaxial cylindrical electrode arrangement under variable atmospheric conditions,” *IEEE Trans. Dielectr. Electr. Insul.*, vol. 22, no. 1, pp. 278–286, 2015.
- [15] M. Seeger, P. Stoller, and A. Garyfallos, “Breakdown fields in synthetic air, CO<sub>2</sub>, a CO<sub>2</sub> / O<sub>2</sub> mixture, and CF<sub>4</sub> in the pressure range 0.5–10 MPa,” *IEEE Trans. Dielectr. Electr. Insul.*, vol. 24, no. 3, pp. 1582–1591, 2017.
- [16] A. Chvyreva, S. Pancheshnyi, T. Christen, and A. J. M. Pemen, “Raether–meek criterion for prediction of electrodeless discharge inception on a dielectric surface in different gases,” *J. Phys. D: Appl. Phys.*, vol. 51, no. 11, p. 115202, 2018.
- [17] S. Kumar, T. Huiskamp, A. Pemen, M. Seeger, J. Pachin, and C. M. Franck, “Electrical breakdown study in CO<sub>2</sub> and CO<sub>2</sub>-O<sub>2</sub> mixtures in AC, DC and pulsed electric fields at 0.1–1 MPa pressure,” *IEEE Trans. Dielectr. Electr. Insul.*, vol. 28, no. 1, pp. 158–166, 2021.

- [18] T. Wong, I. Timoshkin, S. MacGregor, M. Wilson, and M. Given, "Modelling the impulsive breakdown characteristics of sub-mm to mm spheroidal voids," in *2023 IEEE Pulsed Power Conf. (PPC)*, 2023, pp. 1–5.
- [19] S. Pancheshnyi, "Role of electronegative gas admixtures in streamer start, propagation and branching phenomena," *Plasma Sources Sci. Technol.*, vol. 14, no. 4, p. 645, 2005.
- [20] B. Bagheri, J. Teunissen, and U. Ebert, "Simulation of positive streamers in CO<sub>2</sub> and in air: the role of photoionization or other electron sources," *Plasma Sources Sci. Technol.*, vol. 29, no. 12, p. 125021, 2020.
- [21] S. Nijdam, G. Wormeester, E. M. van Veldhuizen, and U. Ebert, "Probing background ionization: positive streamers with varying pulse repetition rate and with a radioactive admixture," *J. Phys. D: Appl. Phys.*, vol. 44, no. 45, p. 455201, 2011.
- [22] A. P. Jovanović, S. N. Stamenković, M. N. Stankov, and V. L. Marković, "Monte carlo simulation of electron avalanches and avalanche size distributions in methane," *Contrib. Plasma Phys.*, vol. 59, no. 3, pp. 272–283, 2019.
- [23] T. Wong, I. Timoshkin, S. MacGregor, M. Wilson, and M. Given, "An avalanche-to-streamer transition criterion for overstressed breakdown on a rising slope," *IEEE Transactions on Plasma Science*, pp. 1–13, 2024.
- [24] Mathworks. Simulink v. 2022a. [Online]. Available: <https://uk.mathworks.com/products/simulink>
- [25] A. Chirokov, A. Gutsol, and A. Fridman, "Atmospheric pressure plasma of dielectric barrier discharges," *Pure Appl. Chem.*, vol. 77, no. 2, pp. 487–495, 2005.
- [26] A. Sun, C. Huo, and J. Zhuang, "Formation mechanism of streamer discharges in liquids: a review," *High Volt.*, vol. 1, no. 2, pp. 74–80, 2016.
- [27] M. Balmelli, Y. Lu, R. Färber, L. Merotto, P. Soltic, D. Bleiner *et al.*, "Breakdown of synthetic air under nanosecond pulsed voltages in quasi-uniform electric fields," *IEEE Access*, vol. 10, pp. 53 454–53 467, 2022.
- [28] D. Levko, R. R. Arslanbekov, and V. I. Kolobov, "Modified Paschen curves for pulsed breakdown," *Phys. Plasmas*, vol. 26, no. 6, p. 064502, 2019.
- [29] B. Bagheri, J. Teunissen, U. Ebert, M. M. Becker, S. Chen, O. Ducasse *et al.*, "Comparison of six simulation codes for positive streamers in air," *Plasma Sources Sci. Technol.*, vol. 27, no. 9, p. 095002, 2018.
- [30] L. Babich, *High-energy Phenomena in Electric Discharges in Dense Gases: Theory, Experiment and Natural Phenomena*, ser. ISTC science and technology series. Futurepast, 2003.
- [31] R. M. Corless, G. H. Gonnet, D. E. G. Hare, D. J. Jeffrey, and D. E. Knuth, "On the LambertW function," *Adv. Comput. Math.*, vol. 5, pp. 329–359, 1996.
- [32] T. Martin, "An empirical formula for gas switch breakdown delay," in *7th Pulsed Power Conf.*, 1989, pp. 73–79.
- [33] V. Carboni, H. Lackner, D. Giri, and J. Lehr, "The breakdown fields and risetimes of select gases under the conditions of fast charging ( $\sim$  20 ns and less) and high pressures (20-100 atmospheres),"

- in *PPPS-2001 Pulsed Power Plasma Sci., 28th IEEE Int. Conf. Plasma Sci., 13th IEEE Int. Pulsed Power Conf. Digest of Papers (Cat. No.01CH37251)*, vol. 1, 2001, pp. 482–486 vol.1.
- [34] P. Felsenthal and J. M. Proud, “Nanosecond-pulse breakdown in gases,” *Phys. Rev.*, vol. 139, pp. A1796–A1804, 1965.
- [35] J. Mankowski, J. Dickens, and M. Kristiansen, “High voltage subnanosecond breakdown,” *IEEE Trans. Plasma Sci.*, vol. 26, no. 3, pp. 874–881, 1998.
- [36] S. Tao, S. Guangsheng, Y. Ping, W. Jue, Y. Weiqun, S. Yaohong *et al.*, “An experimental investigation of repetitive nanosecond-pulse breakdown in air,” *J. Phys. D: Appl. Phys.*, vol. 39, no. 10, p. 2192, 2006.

# Development of a Python Library for the Modelling of Transient Ionisation Fronts in Gas and Solid-Gas Topologies

---

THE natural progression from the topics of Chapter 3 and 4 are phenomena relating to *fast transient ionisation fronts*, including the development of *streamer discharges*. The preceding chapters have enhanced the understanding of fast-rising electric fields on composite dielectric systems in the pre-avalanche regime, and has further studied its influence on avalanche development under overstressed conditions. Upon avalanche-to-streamer transition, however, analytical models can seldom be used due to the presence of significant space charge, where the charge-induced electric fields can no longer be assumed negligible. The reader is reminded of the review conducted on fast ionisation wavefronts in Chapter 2, Section 2.3.5. Within this regime of space charge dominated transport, alternative methods must be employed to reflect the additional

---

This chapter was partially adapted, and may be quoted verbatim, from the following publication(s) with permission: T. Wong, I. Timoshkin, S. MacGregor, M. Wilson, and M. Given, “The Design of a Python Library for the Automatic Definition and Simulation of Transient Ionization Fronts,” *IEEE Access*, vol. 11, pp. 26577–26592, Mar. 2023.

T. Wong, I. Timoshkin, S. MacGregor, M. Wilson, and M. Given, “A Python-based Adaptive Mesh Solver for Drift-Diffusion Modelling of Streamer Discharges,” *IEEE Int. Pulsed Power Conf.*, Denver, CO, USA, Mar. 2022. © IEEE 2022.

T. Wong, I. Timoshkin, S. MacGregor, M. Wilson, and M. Given, “Simulation of Streamer Discharges Across Solid Dielectric Surfaces Using the Open-Source FEniCS Platform,” *IEEE Int. Pulsed Power Conf.*, Denver, CO, USA, Mar. 2022. © IEEE 2022.

coupling between physical processes to successfully understand the emergent phenomena.

To progress the subject of this thesis to the next phase of breakdown, this chapter details a novel computational framework; developed to perform high-fidelity computational simulations aimed at understanding transient and charge-dominated ionisation events in gas and solid-gas geometries. In recent decades, significant advances in semiconductor technology has increased the availability of highly capable computer hardware. As a result, high-fidelity numerical simulations have become widespread across all areas of science and engineering, facilitating the exploration of tightly-coupled multi-physical processes that were once considered out of reach. Research in gas discharge phenomena is one beneficiary of these advancements, evidenced by the recent development of numerous software codes, by numerous international groups. These have subsequently enabled the investigation of important charge transport processes relating to gas breakdown.

This chapter presents a novel simulation framework, StrAFE (**Streamers on Adaptive Finite Elements**), as a flexible piece of software dedicated to the finite-element simulation of fast ionisation events in gas and solid-gas topologies. This chapter is primarily concerned with the implementation details of StrAFE, and concludes with a comprehensive set of verification studies comparing the simulated results to several existing works. The developed code was employed for the analyses presented later in Chapter 6, which were aimed at the understanding of fast ionisation phenomena under various conditions and makes heavy reference to the techniques presented in the present chapter. As the field of gas discharge modelling is vast in scope, being itself an established field of research, an integrated and self-contained review of advances in low-temperature gas discharge modelling has been included as Section 5.2.

## 5.1 Introduction and Motivation

The primary goal for computational modelling was the exploration of transient ionisation wavefronts (including streamer discharges) under time-dependent fields and in complex solid-gas domains. In an ideal piece of simulation software, the design issues outlined in Figure 5.1 would be fully satisfied. However, with the current state of computing technology, no single piece of software is yet able to completely satisfy these requirements. Developed software must find a suitable balance between these design issues, depending on the purpose and requirements of those using the software under development. While there exists both commercial solutions and openly-available custom codes that are capable of conducting such simulations, a number of

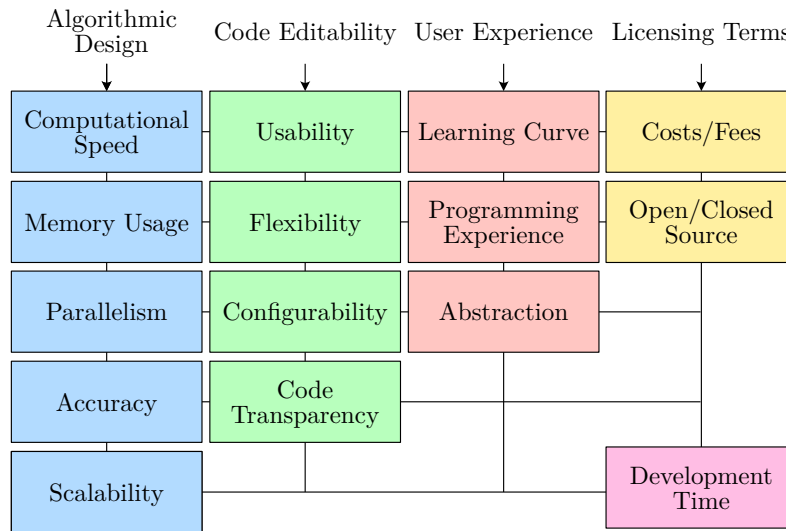


**Figure 5.1:** Matrix showing issues relating to simulation software development, organised into loose categories. All issues cannot, in general, be satisfied, and the developer must target specific issues considered relevant. The amount of development time may be an additional consideration.

specific requirements necessitated a new solution to be developed, namely:

- To have support and/or ability to be modified to support curved boundaries, enabling the accurate representation of practical geometries of interest.
- Be highly user-configurable, in that the simulation problem, solver settings, mesh, etc. can be readily changed.
- Possess a low entry barrier and be simple to use without significant computational expertise or knowledge of low-level programming languages.
- Be built in such a way that facilitates modification for the interests of future work, which may see the extension of the software to incorporate additional physics.

The third requirement listed above was imposed with the purpose to ensure that future users of the developed framework would require minimal training or programming knowledge to successfully configure and simulate complex problems. This was deemed important when considering the often deeply mathematical nature of numerical computing, where much of the underlying algorithmic design is generally unimportant for users from engineering disciplines, who are more concerned with the application of the results. Yet, as engineered systems become more complex, the requirements imposed on simulation software has increased correspondingly. Therefore, it was equally important to build in flexibility, such that, if necessary, advanced users may have full

programmatic control for highly specialised simulations.

Commercial solutions were found to be mostly unsuitable due to their inability to be freely modified. On the other hand, previously developed proprietary codes were either closed-source in nature; were developed in part with commercial software (e.g. in [1]) as a backend; or had specific limitations, for instance, the code described in [2,3] had no support for curved geometries at the time of writing. A tabulation of existing and notable software, including their main innovations and features, has been included in Section 5.2. To ensure that all requirements were satisfied, a custom approach was thus taken and the developed framework is described in this chapter. To begin, however, a brief review of gas discharge modelling techniques is first provided.

## 5.2 Review of Low-Temperature Gas Discharge Modelling

Despite computational advances, fast transient ionisation waves and streamer discharges remain highly challenging to accurately model, primarily due to the multiple spatial and temporal scales involved [4,5]. As explained in Section 2.3.5, streamers are emergent phenomena from space charge dominated transport processes, where the electric field induced by the presence of free charge is sufficiently strong to influence the evolution of the charges themselves, in a self-driven and self-organised manner. Moreover, isolated streamers rarely occur outside laboratory settings, and as shown by simulations in [2] and experimentally in [6,7], may influence the propagation of their neighbours. Coupled then with other complexities such as the type of working gas; thermodynamic conditions; streamer branching events; their interaction with nearby surfaces, droplets, and dust, etc.; renders the efficient and accurate simulation of streamer discharge phenomena a highly nontrivial problem.

Fundamentally, three main components are necessary for any description of ionisation wavefronts: (i) a representation of free charges in a gas, (ii) a method to determine the net electric field arising from these charges combined with the applied electric fields, and (iii) knowledge of the charge sources and sinks responsible for supplying and maintaining the discharge over time. The exact implementation and computation of these quantities is, in general, problem-specific and also dependent on the scale of the simulation. Progress has been made with the development of a number of modelling strategies encompassing all spatial scales of streamer phenomena, summarised in the following.

### 5.2.1 Modelling Strategies

A recent and comprehensive review of streamer discharges can be found in [5], to which the reader is referred; the strategies below are only discussed in brief. The modelling strategy should be selected to reflect the type of information that one considers important to extract from the simulation, balanced with the computational time and resources required for completion. For streamer simulations, a number of aspects are true (or can be assumed) irrespective of the modelling strategy:

- The developed plasma is not at thermodynamic equilibrium, as the electron temperature far exceeds that of the ions and neutrals, which are generally assumed to equal the gas temperature.
- The developed plasma is non-Maxwellian; the electron energy distribution function typically does not follow a Maxwell-Boltzmann distribution.
- The effects of magnetic fields can be assumed negligible under most conditions without a significant external magnetic field (i.e., outside of artificially-generated magnetic fields with strengths unattainable by the streamer currents alone [5,8]).

A direct approach to modelling charge transport naturally arises from the understanding of gas kinetics under the framework of statistical mechanics. The solution to the  $n$ -body collisional problem would theoretically provide an exact solution to the Boltzmann equation (2.24), thus predicting the evolution of collectively-interacting charges and any emergent macroscale phenomena. Unfortunately, it remains impossible (and probably will be for some time yet) to track each individual electron, ion, neutral, and their corresponding interactions within a discharge. Fortunately, techniques have been developed as useful approximations. In increasing levels of abstraction:

#### 5.2.1.1 Kinetic, Particle-Based Approach

A kinetic approach known as the Particle-in-Cell (PIC) method [9–11] is commonly used for plasma simulation studies. The method tracks discrete particles in a Lagrangian sense, while field quantities are computed on a computational grid based on projected charge densities in an Eulerian approach. Particles are advected based on the Lorentz force, such that for a particle  $i$ , the equation of motion is

$$\frac{\partial \vec{v}_i}{\partial t} = \frac{q_i}{m_i} \left( \vec{E}_i + \vec{v}_i \times \vec{B}_i \right) \quad (5.1)$$

while continuous field quantities are calculated based on the projection of discrete charges onto a grid via some interpolation scheme. For example, a general expression for the grid-based charge density,  $\rho(\vec{r})$ , may be

$$\rho(\vec{r}) = \sum_j \rho_j \Phi(\vec{r}_j - \vec{r}), \quad (5.2)$$

where  $j$  denotes the nodes of the grid, and  $\Phi$  is some shape function that determines the particle-to-grid weighting scheme. Grid-based quantities can then be used to solve for the relevant fields, e.g., by solving the Poisson equation with (5.2) to attain a grid-based electric field,  $\vec{E}(\vec{r})$ . Since particles do not necessarily align with the grid nodes, similar interpolation schemes are used to project the closest field values,  $\vec{E}_j$ , back to the locations of the particles,  $\vec{E}_i$ , for use in (5.1).

In collisional plasmas, collisions are typically treated probabilistically using their collisional cross sections such as in Monte Carlo Collision (MCC) methods [11–13]. Characteristic parameters such as mobility, diffusion coefficient, and energy distribution functions therefore arise naturally from these descriptions as they directly approximate the Boltzmann equation (2.24). To lessen computational load, various *particle merge* schemes have been proposed, which occasionally combine *similarly behaving* particles into *superparticles* or *macroparticles* as an approximation. Various schemes have been designed to conserve properties such as energy or momentum, examples include [14–18]. A typical depiction of the algorithmic time-loop for PIC-MCC simulations is shown in Figure 5.2. Well implemented PIC-MCC and similar methods are often robust, providing the major benefit of including kinetic effects that may not be captured in other approximations. For instance, PIC-type methods are necessary when modelling the development of electron avalanches when initial pre-ionisation levels are low [19, 20], or where phenomena such as runaway electrons become important [11, 21]. A significant drawback is computational load; PIC-MCC methods are, by nature, time-consuming to compute, are difficult to parallelise, and have therefore not seen significant adoption outside of smaller geometric domains, with the exception of those studies with access to high performance computing (HPC) facilities. However, this may change with the development of novel algorithms like those recently introduced by Marskar [22].

### 5.2.1.2 Continuum/Fluid/Hydrodynamic Approach

In cases where the involved charge densities are sufficiently large, and where the mean free path of collisions compared to the characteristic length of the system (the Knudsen number,  $\ell_m/L$ ) is sufficiently low, a continuum approach may be derived from (2.24). As detailed in [23] and applying the assumptions for low-temperature plasmas, moments of the Boltzmann equation

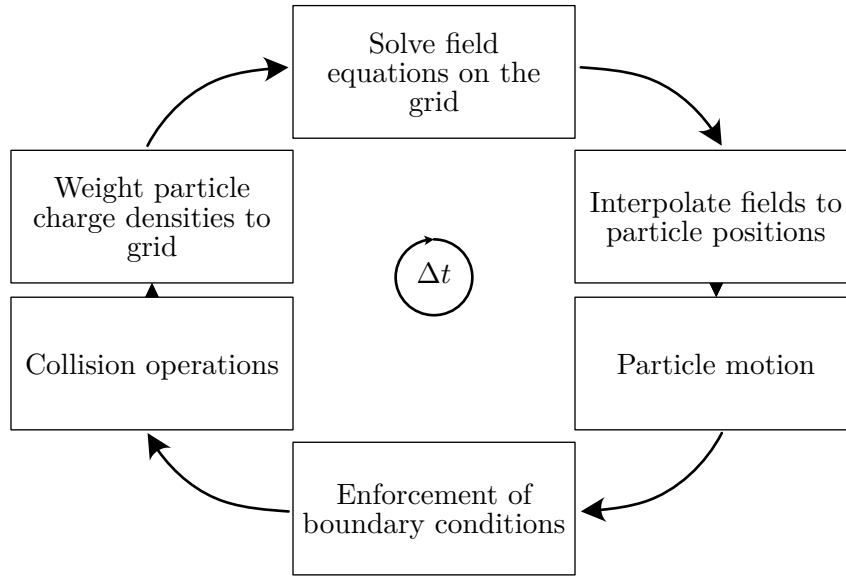


**Figure 5.2:** High-level overview of the main algorithmic loop for PIC simulations. Time steps are advanced after each successful computation of one cycle of the labelled operations.

(2.24) recover the *fluid* or *hydrodynamic* model that has recently attracted substantial interest among the fields of gas discharge modelling and high voltage engineering. At the core of the fluid model is the particle density continuity equation

$$\frac{\partial n_i}{\partial t} + \vec{\nabla} \cdot \vec{\Gamma}_i = S_i, \quad (5.3)$$

where  $n_i$  represents the volumetric density of a species  $i$  with sources and sinks given by  $S_i$ , while the flux  $\vec{\Gamma}_i$  under influence of an electric field  $\vec{E}$  is approximated by

$$\vec{\Gamma}_i = \text{sgn}(q_i)\mu_i n_i \vec{E} - D_i \vec{\nabla} n_i, \quad (5.4)$$

where the species' mobility,  $\mu_i$ ; and diffusion coefficient,  $D_i$ ; determines the nature of its transport under the presence of an electric field. Coupling between the electric field,  $\vec{E}$ , and the net charge density,  $\rho$ , is achieved through

$$\vec{\nabla} \cdot (\epsilon \vec{E}) = \rho = \sum_{j \in \mathcal{S}} q_j n_j, \quad (5.5)$$

where (5.5) is an expanded form of the Poisson equation (2.7), and where  $\mathcal{S}$  is the set of all charged species that are actively tracked in the simulation. In combination, the form of (5.3) and (5.4) follows that of an advection-diffusion-reaction (ADR) equation and is often referred to as the *drift-diffusion* approximation. It follows that many suitable numerical methods capable of

solving ADR equations (as is typical in the field of computational fluid dynamics) may be applied. The self-consistent solution of (5.3) and (5.5) therefore describes the spatio-temporal evolution of a set  $\mathcal{S}$  of charge densities and of the evolving electric field developed by these charges.

The source term  $S_i$  in (5.3) accounts for the sources and sinks of a charged species  $i$ , for example, due to various plasma chemical reactions. Where the hydrodynamic approach is a good approximation, it provides significant savings over pure kinetic methods in terms of computational cost. Mesh-based numerical methods such as the finite element method (FEM) or finite volume method (FVM) are also well-established mathematical techniques capable of solving this class of partial differential equation. The popularity of the hydrodynamic approach has thus grown, with numerous commercial and custom programs now with the capability to conduct hydrodynamic simulations of gas discharge phenomena (see Table 5.1 in Section 5.2.3). Figure 5.3 has been reproduced from [24], and highlights the differences between the fluid approach, 2D PIC approach, and 3D PIC approaches. The hydrodynamic approach forms the basis of the computational model implemented in StrAFE which is presented from Section 5.3 onward.

It is important to note that in deriving (5.3) from the Boltzmann equation (2.24), the assumption that the energy distribution function (EDF) is Maxwellian was necessarily applied. This is reasonable for heavy species, but clearly contradicts the non-Maxwellian nature of low-temperature plasmas when applied to electrons. For modelling purposes, the deviation of the electron energy distribution function (EEDF) away from the Maxwell-Boltzmann form is approximated by assuming certain dependencies of the electronic mobility,  $\mu_e$ ; the diffusion coefficient,  $D_e$ ; and any reaction rate coefficients. Two well-accepted methods have been implemented in the present work, detailed later in Section 5.4.4.

### 5.2.1.3 Macroscopic Tree Models

A class of model broadly dubbed the term *tree* models attempt to approximate the macroscopic and collective behaviour of multiple streamers [25]. As shown in Section 2.3.5 and suggested briefly at the beginning of Section 5.2, streamers rarely occur in isolation, and due to branching behaviour, often produces tree-like structures comprised of many discharge filaments originating from a single point, see for example, [26]. By raising the level of abstraction once again, tree models typically concern themselves with a simplified view of streamer channels, approximating them as growing conductive segments. In contrast to the kinetic and fluid approaches, where the macroscopic behaviour is emergent from microscale charge transport processes; the direct, macroscale, evolution of entire streamer discharge trees have been modelled by considering

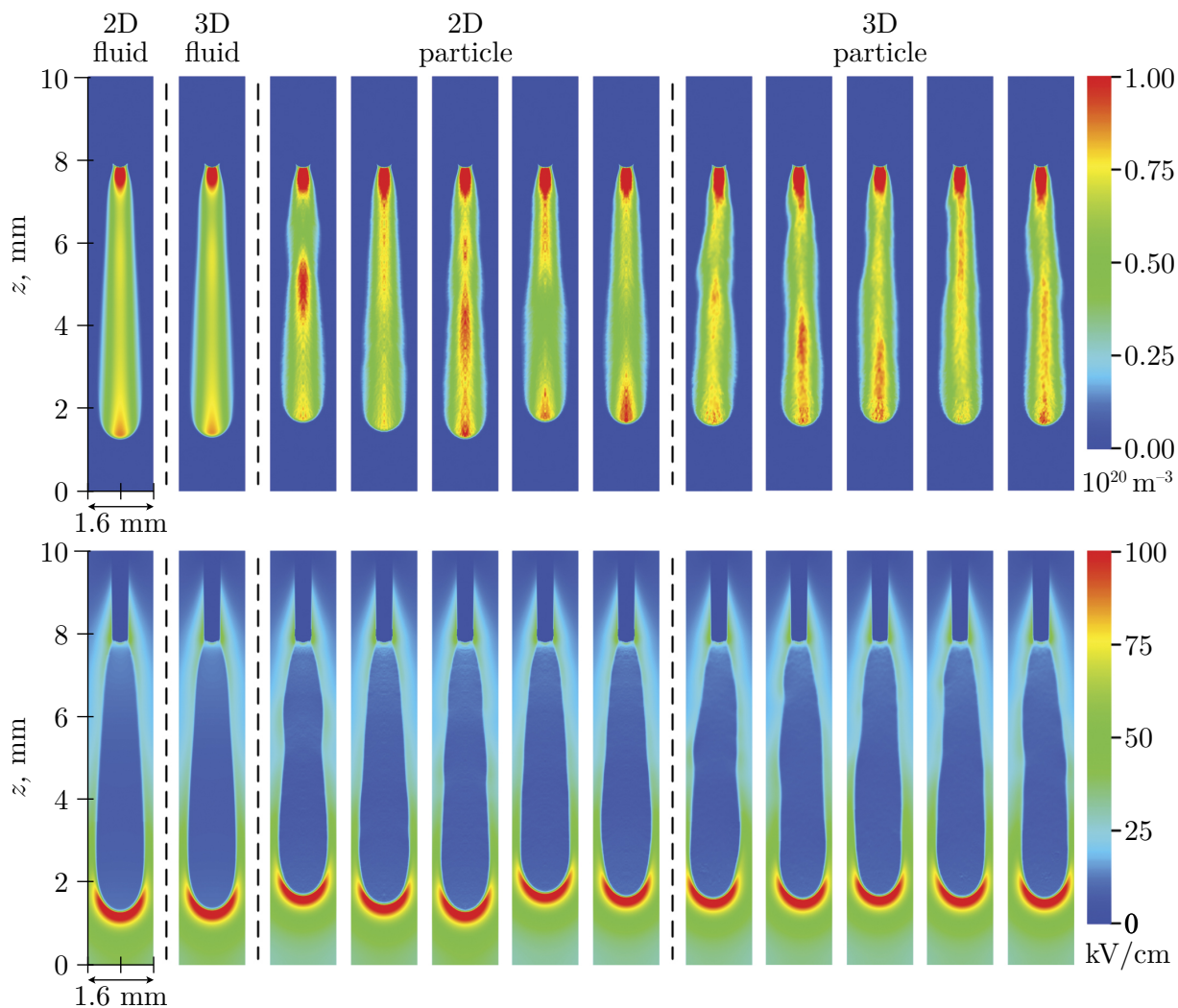


**Figure 5.3:** A comparison of a single positive streamer simulated using 2D fluid, 3D fluid, 2D particle, and 3D particle methods from [24]. Image adapted with permission from [24], © 2022 IOP Publishing.

the growth of these conductive segments using macroscopic conservation laws [25]. Figure 5.4 has been adapted from [25] and shows the ability for tree-like models to recreate branching, fractal-like, discharges resembling those imaged experimentally, e.g., as shown in Chapter 2, Figure 2.8.

#### 5.2.1.4 Other Models

Briefly, there exists a few additional approaches to gas discharge modelling that are less prevalent. While these are less widely used, they warrant a brief mention for completeness. Firstly, hybrid

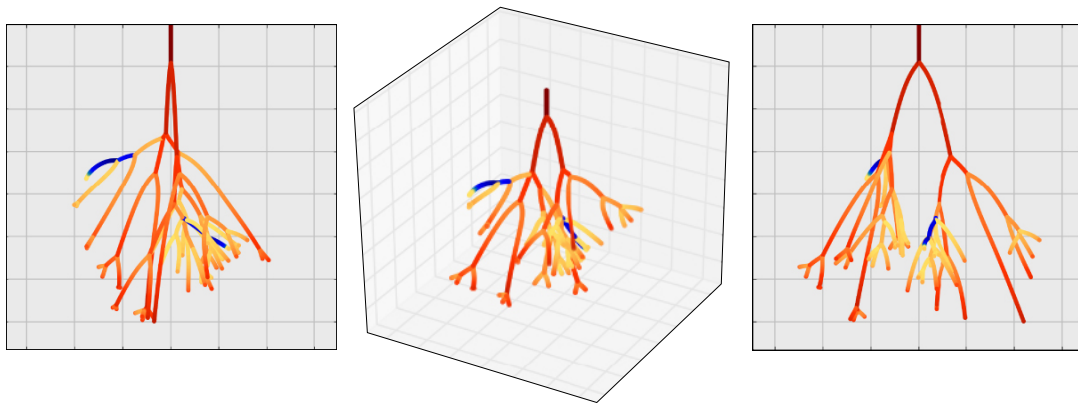


**Figure 5.4:** Example macroscopic streamer trees generated using tree-like propagation models. Images adapted from [25] under CC BY 3.0.

kinetic-fluid approaches have been explored in past works such as [27–29], which represent a combination of kinetic and fluid approaches. Conceptually, the simulation is partitioned into two regions, one which employs a kinetic approach, and the other, approximated using the fluid method. For streamers, the former region will typically be near the streamer head where density and field variations are incredibly steep; while the latter region must typically exhibit far slower changes in space and in time, e.g., within the streamer channel and away from strongly-ionising streamer heads, such that it may be accurately described using the simpler fluid approach. Combining approaches in this way ensures that kinetic effects are captured where necessary, but that a fallback to the much faster fluid approximation is done when these effects become negligible. Hybrid models therefore represent a balance between the two approaches, however, often at the cost of far greater implementation complexity. The reader is referred to Figure 5.5(a) adapted from [29] for an example of streamers simulated using hybrid techniques.

Recent works have further drawn parallels between dielectric breakdown and mechanical fracture mechanics [30–32]. Authors of [31] demonstrated successful simulations of breakdown in solid dielectrics, with strong qualitative agreement with experimental breakdown paths, using the *phase-field* approach shown in Figure 5.5(b). The phase-field approach is commonly employed to study mechanical fracture, by representing a solid material as two distinct phases: (i) the unfractured phase and (ii) the fractured phase. Transition from the unfractured phase to the fractured phase is generally estimated based upon some form of energy criterion. The authors of [30] extended this approach to dielectric breakdown, with corresponding phases representing (i) the dielectric in its insulating phase, and (ii) the dielectric in its electrically-broken and conductive phase. The generality of the approach developed in [31] holds great potential to

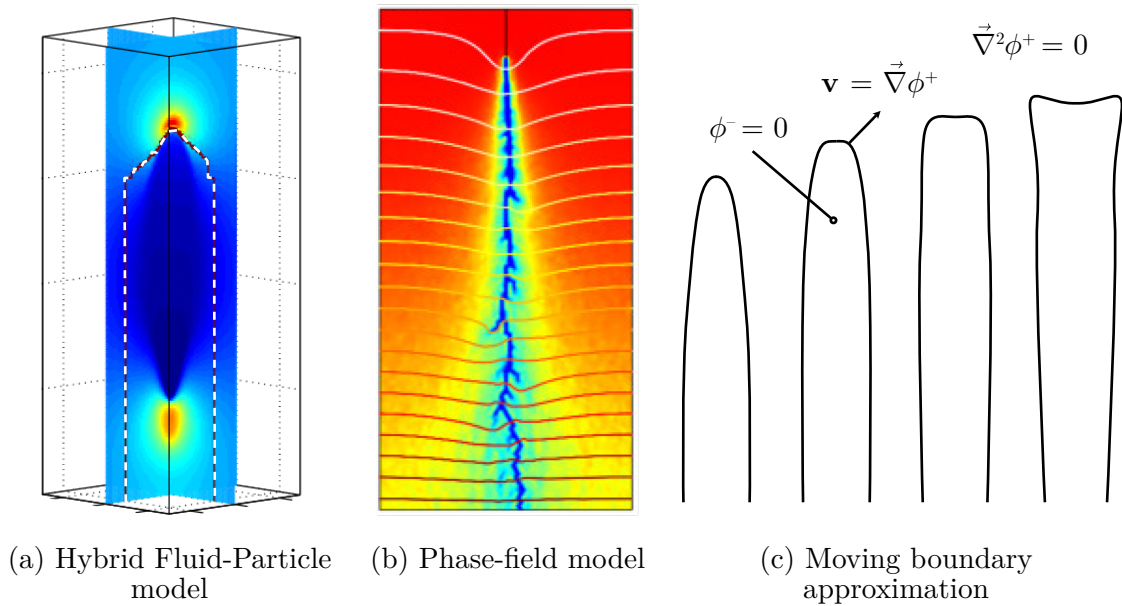


**Figure 5.5:** Examples of other methods/approximations used to study streamer discharge phenomena. (a) Hybrid fluid-particle approaches, where the white dashed line indicates the boundary between the fluid and particle descriptions, from [29], (b) phase-field model of dielectric breakdown from [30], and (c) moving boundary approximations of evolving interfaces, from [4]. Images adapted with permission from [29], © 2009 IOP Publishing; [30], © 2019 Elsevier; and [4], © 2006 IOP Publishing, respectively.

be extended to gas discharges in the future, if a link can be established between the energy parameters used in [30,31] with the known characteristics of gases.

Finally, there are *moving boundary approximations* [33,34], which model streamer channels as dynamically evolving boundaries in space and in time. The motivation behind moving boundary models is similar to that of phase-field approaches, where there is the recognition that the streamer (plasma) channel is a distinctive phase of matter compared to the gas in which it is developed. The two regions are separated by very steep charge gradients and thin charge sheaths [34], allowing their approximation as a moving boundary, in a manner depicted within Figure 5.5(c), to be reasonably effective. These types of model have not seen widespread usage for full streamer simulations, but have contributed to the mathematical explanation of various streamer phenomena. For example, analyses conducted in [34–38] have shown that the onset of streamer branching can arise even in fully deterministic models, challenging the previous understanding that branching was solely due to stochastic processes, such as photoionisation or inhomogeneities [34]

### 5.2.2 Selection and Bounds of Model Validity

Once again, an appropriate choice of model for any one study is entirely dependent on the behaviour which one wishes to capture. No single model as listed in Section 5.2.1 can adequately reproduce behaviour on all scales (at least not in reasonable time, at the time of writing). Understanding the limitations and validity bounds of various model types is therefore critical for the selection of a suitable method. Macroscopic tree models are typically applied only in the study of multiple streamers and branching trees; they do not typically contain sufficient information to recreate the detailed charge transport processes around isolated ionisation fronts or streamers. Kinetic and fluid models recreate single streamer processes to far greater fidelity, but modelling the collective behaviour of many streamers using these approaches requires significant computational power and novel algorithmic innovations. The development and optimisation of these algorithms has itself become a distinct area of research, see [3, 22, 39, 40]. As the characteristics of isolated ionisation wavefronts formed the focus of this work, establishing the bounds of validity between kinetic and fluid approaches was of greatest importance.

While exact validity bounds are highly problem-specific, attempts have been made to establish, approximately, conditions where kinetic effects become sufficiently important that the fluid model should be considered invalid. Kolobov and Arslanbekov [41] provided approximate bounds based on gas pressure and the characteristic length of the system under study, stating “*The non-local kinetic effects become important when the characteristic size of the system becomes smaller than the energy relaxation length*”; which relates to Figure 5.6 which has been adapted from [41]. Zhu *et al.* [42] conducted further analysis using a similar argument, deriving an approximate analytical criterion based on the momentum transfer time of collisions. Conceptually, *non-local* kinetic effects may pertain to situations of low electron density, such as the avalanche and discharge inception stage; to phenomena such as high-energy electrons (e.g., runaway electrons [21]) that may induce significant effects far from main ionisation wavefronts. Similarly, when the Knudsen number is close to or greater than unity, there exists the potential for electrons to become *ballistic*, travelling relatively large distances without collisions. Zhu *et al.* [42] therefore argue that for the fluid approach to be representative, the ionisation frequency,  $\nu_i$ , must be far less frequent than the inverse characteristic timescale,  $\tau$ , of the processes under study,

$$\nu_i \ll \tau^{-1}. \tag{5.6}$$

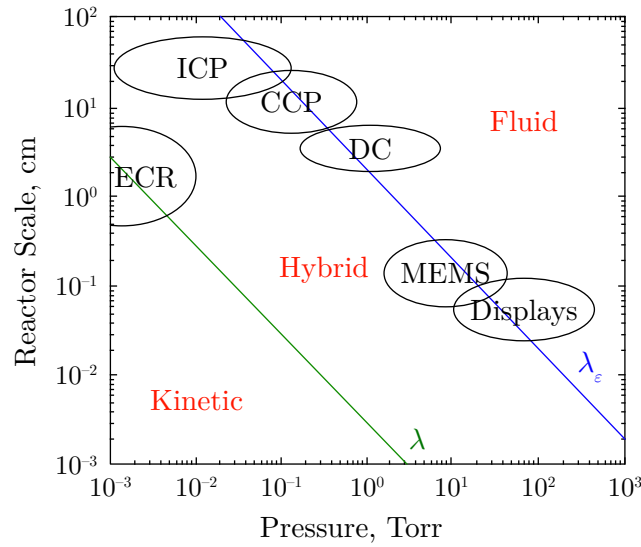


**Figure 5.6:** Approximate validity bounds for kinetic, hybrid, and fluid approaches based on the mean free path,  $\lambda$ , and the energy relaxation length,  $\lambda_\epsilon$ , according to [41]. Various plasma-related phenomena and technologies are shown in their approximate operating regimes. Abbreviations as follows: ICP = Inductively Coupled Plasma, ECR = Electron Cyclotron Resonance, CCP = Capacitively Coupled Plasma, DC = Direct Current (Plasma), MEMS = Micro-Electromechanical Systems. Image adapted with permission from [41], © 2003 Elsevier.

Specific to streamer discharges, [42] further provides a secondary condition,

$$\tau < t_{st}, \quad (5.7)$$

where  $t_{st}$  is the characteristic time of streamer propagation [42]. Conditions (5.6) and (5.7) are graphically represented as regions of validity in Figure 5.7 adapted from [42]. Note that the authors of [42] considered that (5.6) was satisfied when  $10 \cdot \nu_i \ll \tau^{-1}$  in the production of the figure, indicating also the inexactness of this condition. For example, a slight variation in the factor of 10 can cause a significant expansion or reduction of the region of validity, especially considering the logarithmic scale of Figure 5.7. In combination with Kolobov and Arslanbekov [41], however, these nonetheless provide two useful, albeit approximate, boundaries for appropriate model selection.

### 5.2.3 Notable Works on Non-thermal Gas Discharge Modelling

The popularity and interest in numerical gas discharge modelling has increased significantly in recent years, owing to the growing availability of capable software, affordability of capable

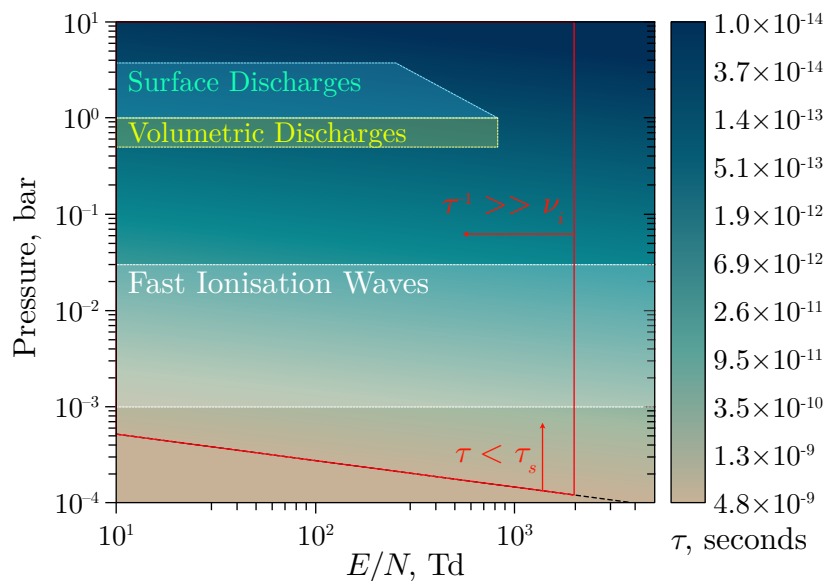


**Figure 5.7:** Validity of the hydrodynamic approximation according to the criteria derived in [42] (within the bounds of the red solid line), indicating typical regions for different categories of discharge. Note that their notation  $\tau_s = t_{st}$  in the context of this work. Image adapted with permission from [42], © 2021 IOP Publishing.

workstation computers, and the accessibility of supercomputing platforms. Various international research groups have developed custom discharge modelling codes using a variety of numerical algorithms. Many have taken advantage of commercially-available multiphysics solvers to achieve high-quality modelling results. In the following, a brief summary of notable software packages capable of gas discharge modelling is presented as Table 5.1. While there exist a significant number of modelling codes developed by numerous authors in the past few decades, the packages below represent the most recent and notable software codes currently in use. It is noted that those featured are completely standalone, in the sense that they are either custom-built for gas discharge simulation, or provides an integrated environment to do so. There is no shortage of other works that utilise standard numerical algorithms, or have developed proprietary code without the intention for it to be offered as an integrated platform for simulation. These works have undoubtedly contributed to the understanding of gas discharge physics in a variety of ways, but are not included within this listing on the basis that they are focused on the novelty of the explored phenomena rather than novelty in the software or algorithmic offerings.

**Table 5.1:** Notable standalone software packages capable of gas discharge simulation.

Software Name	Model	Summary	Ref.
COMSOL	Fluid	Main commercial offering. Includes plasma module and drift-diffusion modules. Selection of FEM solvers with graphical user interface. Cannot be modified, somewhat black-box in nature. High licensing fees.	[43]
ANSYS	Fluid	Commercial FEM offering. Also high licensing fees and cannot be edited on a code level. Offers a fluid module, but not as commonly used as COMSOL Multiphysics.	[44]
ARCoS	Fluid	Adaptive mesh FVM code using uniform Cartesian grids (cannot accurately represent curved geometry). Poisson equation solved using the Fortran-77 based FISHPACK [45] library. Open-source developed primarily in C.	[46]
PLASIMO	Fluid/PIC	Commercial dedicated plasma simulation software, with a variety of techniques encompassing various forms of plasma. Not openly available with limited information provided.	[47, 48]
Afivo-streamer	Fluid/PIC	Open-source and lightweight shared-memory parallelised FVM software. Utilises geometric multigrid methods and block-based adaptive meshes for efficient 2D and 3D simulations. At the time of StrAFE's development, Cartesian grids only (methods have been since been developed to address this [49]), with explicit time integration. Developed in Fortran.	[3]
MCPlas	Fluid	MATLAB automation interface to COMSOL, advantages and disadvantages therefore follow COMSOL. Not openly available.	[1]

---

PASSKEy	Fluid/PIC	Hybrid OpenMP to message-passing-interface (MPI) parallelised streamer simulation platform. Support for both fluid and kinetic descriptions. No information regarding if adaptive meshing was implemented. Recommended for HPC use only. Developed in Fortran and open for non-commercial use.	[50]
FEDM	Fluid	FEniCS-based fluid code interfaced through Python and is open-source. Supports adaptive time-steps but not adaptive meshes. Note that this code was independently developed by its authors at the same time as StrAFE which is presented in this work.	[51]
Cerman	Tree-like	Tree-like code based on Meek-Raether criterion developed to simulate streamer propagation in liquids. Simplified model that evaluates the Meek criterion at discrete grid points to determine streamer development. Aims to provide a more macroscopic view on streamer propagation. Open-source and developed in Python.	[52]
chombo-discharge	Fluid/PIC	Novel FVM fluid code that supports macroscopic drift-diffusion and microscopic drift-diffusion approaches based on Itô-diffusion [22]. Adaptive Mesh Refinement (AMR) capable code using Cartesian cut-cell approach for complex geometries and geometric multigrid solvers. Has demonstrated large-scale 3D simulations on HPC of fully branching streamer trees. Open-source and fully-featured, targeting HPC environments. Developed in C++. Was not yet available during the development of StrAFE.	[53]

---

### 5.3 Method and Platform

Based on the specifications of Section 5.1, and considering the types of phenomena which were of interest to this work, StrAFE was developed to solve the coupled continuum equations of the hydrodynamic approach (5.3)–(5.5). This section details the platform and method which was

ultimately employed and implemented StrAFE.

### 5.3.1 The Finite Element Method

The underpinning numerical method used in StrAFE is the finite element method (FEM). As the FEM is a well-established and well-documented method, only the most important concepts behind the FEM necessary for the present implementation are described. For details, the reader is referred to [54–56] and references therein. Let  $u$  denote the exact solution to an unknown function, and which satisfies a generic differential equation of the form

$$L(u) = f, \quad (5.8)$$

where  $L$  is some differential operator, and  $f$  is an arbitrary function in a bounded domain  $\Omega$  with external boundary  $\partial\Omega$ . Consider now that  $\Omega$  is discretised through some triangulation,  $\mathcal{T}$ , of mesh elements. The numerical approximation to  $u$  shall be denoted  $u_h$ , and in accordance with the FEM, is approximated by a linear combination of finite element basis functions,  $\phi_i$ , like

$$u \approx u_h = \sum_{i \in \mathcal{N}} U_i \phi_i, \quad (5.9)$$

where  $U_i$  are constant coefficients to  $\phi_i$ , and  $\mathcal{N}$  is the number of nodes of the discretisation. The *weighted residual*,  $r_w$ , which must be driven to zero, is found by the introduction of weight function  $v$  to (5.8) and integrating over the domain such that

$$r_w = \int_{\Omega} v L(u) \, d\Omega - \int_{\Omega} v f \, d\Omega = 0. \quad (5.10)$$

In the standard *continuous Galerkin* method,  $v$  belongs to an identical function space as  $\phi$ , and  $U_i$  must be sought such that (5.10) is satisfied (or to within an acceptable error tolerance). The application of (5.10) to each element in  $\mathcal{T}$  provides a linear system of the form

$$\mathbf{A}\vec{U} = \vec{b} \quad (5.11)$$

where  $\mathbf{A}$  is the system matrix and  $\vec{b}$  is a vector. The vector of coefficients  $\vec{U}$  can then be obtained via any suitable linear algebra solution method applied to (5.11). In many problems of practical significance, operator  $L$  is of order two. Should  $\mathcal{T}$  be comprised of first-order elements (which in general, are preferred due to their low computational cost) such that the basis functions  $\phi_i$  are linear, it imposes the condition that (5.10) must not contain derivatives of order greater than one.

Where higher derivative orders exist, therefore, (5.10) must be reduced by application of Green's identity to satisfy this constraint. The equation (5.10) is also known as the *weak* or *variational form* of the *strong* problem, since the relation holds *weakly* in the sense of a distribution on  $\Omega$  compared to the definitive relation defined by the full problem of (5.8). For the coupled Poisson-ADR equations (5.3)–(5.5), their weak formulations are included in Section 5.5, and details of their implementation can be found within Section 5.7.

While hyperbolic conservation laws like the ADR equation (5.3) generally benefit from locally-conservative methods (e.g., finite volume methods), FEM was used for its flexibility. A robust FEM implementation allows the order of the basis functions to be readily changed and without the need for substantial reprogramming, which strongly supports complex geometrical domains through the free choice of element shapes and discretisation order. FEM has also been widely demonstrated to be generally applicable to a wide range of physical problems, often favoured for its straightforward handling of geometry-conforming unstructured elements (see [57] relevant to streamer problems). As defined in the original motivation to develop StrAFE, these aspects are of considerable importance to the flexibility, usability, and to future development opportunities should StrAFE be extended to incorporate additional, multiphysical, capabilities.

### 5.3.2 The FEniCS Project

In alignment with the objectives for StrAFE, an open-source FEM framework, the FEniCS Project [54,58,59] was used as the foundation on which StrAFE was ultimately built. The FEniCS project is a collection of mathematical computing packages, designed to simplify and automate a significant portion of the configuration and solution of FEM problems. It does so by abstracting many core computational aspects such as the finite element basis function definition, the system matrix assembly, linear algebra solution algorithms etc., into simple and readable commands. The main interface of FEniCS, named DOLFIN, is comprised of the following software components (labelled in accordance to Figure 5.8, depicting the FEniCS software architecture):

- (i) *FEniCS Form Compiler (FFC)* [55,61,62] — Handles just-in-time (JIT) compilation and generation of finite element variational forms in high-speed C++ code.
- (ii) *Unified Form Assembly Code (UFC)* [63] — An interface for finite element assembly provided valid variational forms.
- (iii) *Unified Form Language (UFL)* [58,63] — A language developed for the discretisation of partial-differential equations, using syntax that closely resembles the original mathematical

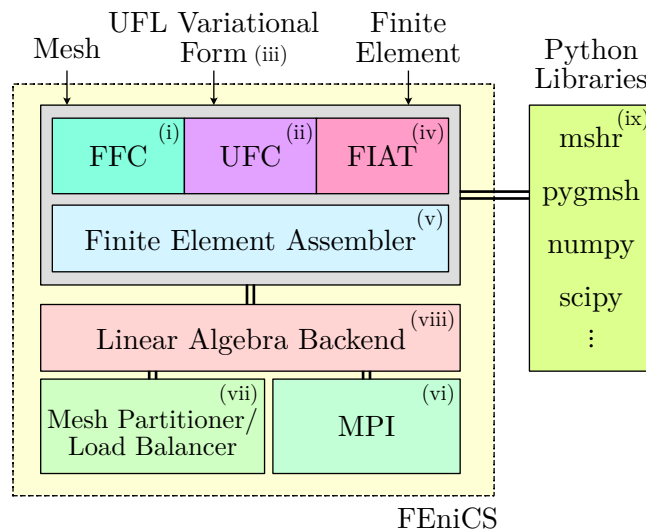


**Figure 5.8:** Block diagram of FEniCS software architecture, also showing its possible interconnection with useful third-party Python library. Descriptions of the labelled modules are given in the main text. Image adapted from [60] under CC BY 4.0.

formulation.

- (iv) *Finite Element Automatic Tabulator (FIAT)* [64] — Handles the generation of finite element basis functions and elements of arbitrary order.

While the backend for FEniCS is developed in C++, FEniCS also can be interfaced using Python through a dedicated interface. Python is a high-level programming language, known for its highly readable, English-like, syntax and low entry barrier. The majority of FEniCS functionality is exposed through the Python interface, allowing users to develop highly capable and efficient solvers for FEM problems with relative ease and without specific computational expertise. Aligning with this design philosophy, StrAFE was developed exclusively in Python and built atop FEniCS through the existing interface. StrAFE therefore inherits from the highly readable and interpretable Python code base, yet compromises little in terms of speed and efficiency, owing to the C++ backend. Also inherited from FEniCS are the following features (once again with labels corresponding to those of Figure 5.8):

- (v) *Finite Element System Assembler* — Consolidates the generated components from (i)–(iv) to form the system matrix.
- (vi) *Message Passing Interface (MPI)* — Support for distributed memory parallelisation, which functions based on the principle of domain decomposition. Multiple computational processes

work in parallel, with their own memory pool, to accelerate solution speed.

- (vii) *Mesh Partitioning and Load Balancing* — Complements MPI, by ensuring that the mesh is split evenly according to cell count such that the computational load on each process is similar. Either the PT-SCOTCH [65] or the ParMETIS [66] libraries are available by default.
- (viii) *Choice of Linear Algebra Backends* — FEniCS may be built against several different high-speed linear algebra backends, for example, uBLAS [67], Epetra [68], or PETSc [69, 70]. These provide efficient solvers for matrix equations of the type (5.11).
- (ix) *Third Party Library Integration* — The Python-based interface allows flexible integration with any third-party Python library. Custom applications for mesh generation, data visualisation, batch simulations, data processing, etc., can be built around FEniCS. This provides a great degree of configurability and customisability; all without the need to modify the C++ code base.

New classes and data structures introduced in StrAFE are specific to low-temperature plasma modelling, the syntax and usage of this code is detailed further within Section 5.7.

## 5.4 Extended Hydrodynamic Model

This section outlines the implemented mathematical model implemented in StrAFE for the modelling of low-temperature gas discharge phenomena. Section 5.4.1 further provides the strong mathematical formulation of the ADR-Poisson problem, including the various choices of boundary conditions, source terms, and approximations which the user may freely configure through StrAFE. Section 5.5 then details the weak formulations as directly implemented using the UFL and the FEniCS Python interface, as explained in Section 5.3.1.

### 5.4.1 Advection-Diffusion-Reaction-Poisson Equation

In StrAFE, the ADR equation following (5.3) forms the basis of the model, which considering the flux term (5.4), is restated as (5.12) for ease of reading,

$$\frac{\partial n_i}{\partial t} + \vec{\nabla} \cdot \left[ -\text{sgn}(q_i)\mu_i n_i \vec{\nabla} \varphi - D_i \vec{\nabla} n_i \right] = S_i, \quad (5.12)$$

where the electric field has been expanded using the potential,  $\varphi$ , according to  $\vec{E} = -\vec{\nabla}\varphi$  as the Poisson equation (5.5) is solved in the more general form

$$-\vec{\nabla} \cdot (\varepsilon \vec{\nabla} \varphi) = \rho = q_e \sum_{j \in \mathcal{S}} Z_j n_j \quad (5.13)$$

directly for the scalar electric potential, where  $Z_j$  is the charge number of the  $j$ -th species.

### 5.4.2 Source Terms and Plasma Chemistry

Two options are available in StrAFE to define the charge sources and sinks. A basic description of plasma may be gained by considering only two species: electrons and generic positive ions. The effective Townsend ionisation coefficient,  $\bar{\alpha}$ , may therefore be used to define the ionisation source term

$$S_{e,+} = \bar{\alpha} n_e \mu_e |\vec{\nabla} \varphi|, \quad (5.14)$$

where subscripts  $e$  and  $+$  denote electrons and positive ions, respectively. Alternatively,  $\bar{\alpha}$  may be decomposed into the ionisation-only coefficient,  $\alpha$ , and the attachment coefficient,  $\eta$ , such that three species (electrons, positive ions, negative ions) may be tracked as

$$\begin{aligned} S_e &= \bar{\alpha} n_e \mu_e |\vec{\nabla} \varphi|, \\ S_+ &= \alpha n_e \mu_e |\vec{\nabla} \varphi|, \\ S_- &= \eta n_e \mu_e |\vec{\nabla} \varphi|, \end{aligned} \quad (5.15)$$

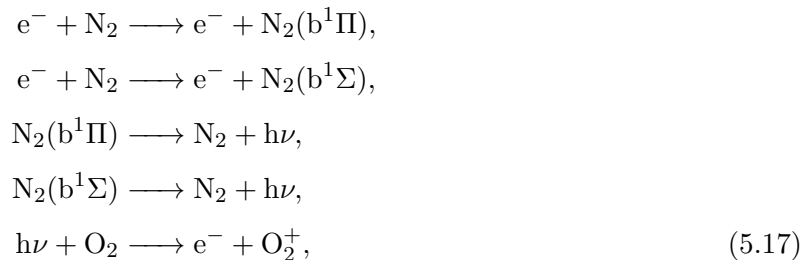
with one ADR equation per species. In some cases, advanced users may wish to study specific plasma composition. That is, to track individual chemical species developed during a discharge, while considering the chemical reactions in which they partake. In this case, StrAFE has full support for plasma chemistry with source terms computed following

$$S_i = \sum_{j \in R_i} \left( h_j k_j \prod_{m \in \mathcal{R}_j} n_m \right), \quad (5.16)$$

where  $R_i$  is the set of reactions which involve species  $i$ , and  $\mathcal{R}_j$  is the set of all reactants involved in reaction  $j$ . Symbol  $k_j$  is the reaction rate for reaction  $j$  and  $h_j$  is either  $+1$  or  $-1$  depending on whether the reaction is a source or sink to species  $i$ , respectively. The format in which a tabulated set of plasma chemical reactions can be passed directly to the solver is described later in Section 5.7.1.3.

### 5.4.3 Photoionisation

Studies [71–73] indicate that photoionisation is a critical process in sustaining positive streamer discharges. It is widely accepted that in certain gases (e.g., atmospheric air), photoionisation is a dominant process that provides free electrons ahead of positive streamer fronts to maintain their propagation [74]. This is currently better characterised in air compared to other gases, where the corresponding process of photoionisation may be described in the following reactions



describing the photoionisation of molecular  $\text{O}_2$  due to photons emitted from various excited  $\text{N}_2$  ( $\text{b}^2\Pi$ ) and  $\text{N}_2$  ( $\text{b}^1\Sigma$ ) states [75]. In recent work, progress has been made to characterise the importance of photoionisation in other gases, for example, in  $\text{CO}_2$  [76, 77].

In StrAFE, photoelectron source terms,  $S_{\text{ph}}$ , are assumed to follow Zheleznyak’s model [71], stipulating that the photoelectron source at point  $\vec{r}$  is due to the contribution of emission from originating points  $\vec{r}'$ , following

$$S_{\text{ph}}(\vec{r}) = \iiint_{\Omega} \frac{I(\vec{r}')f(|\vec{r} - \vec{r}'|)}{4\pi|\vec{r} - \vec{r}'|^2} d\Omega. \tag{5.18}$$

For example, Figure 5.9 encloses a figure adapted from [78], depicting this volumetric integral in cylindrical coordinates, providing the total contribution of photoionisation rates due to the rates of each differential volume element at the point  $\vec{r}$ . According to an approximation by Bourdon *et al.* [78], the implementation of functions  $I(\vec{r}')$  and  $f(|\vec{r} - \vec{r}'|)$  for air follow the definitions

$$\begin{aligned}
 I(\vec{r}) &= \frac{p_q}{p + p_q} \xi \frac{\nu_u}{\nu_i} S_{\text{ion}}(\vec{r}), \\
 f(|\vec{r} - \vec{r}'|) &= p_{\text{O}_2}^2 |\vec{r} - \vec{r}'| \sum_j A_j \exp(-\lambda_j p_{\text{O}_2} |\vec{r} - \vec{r}'|),
 \end{aligned} \tag{5.19}$$

for  $j = 1, 2$ , and  $3$  in the three-term approximation. Here,  $p$  is the pressure,  $p_q$  is the quenching pressure (accounting for collisional quenching and spontaneous emission [79]), and  $p_{\text{O}_2}$  is the partial pressure of oxygen in air. Symbol  $\nu_u$  is the frequency of excitation due to electron impact

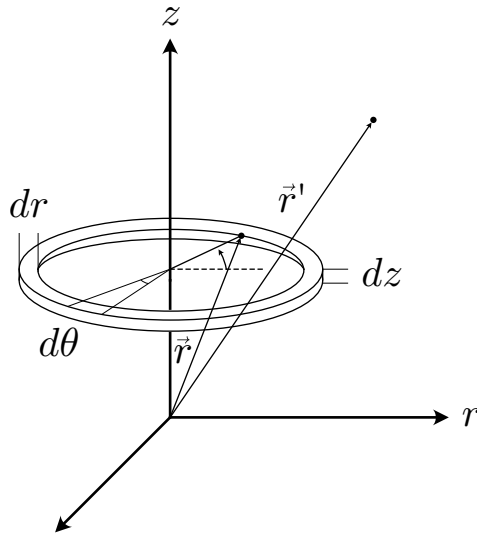


**Figure 5.9:** Diagrammatic representation of Zheleznyak's photoionisation integral in cylindrical coordinates. Photoionisation source term at position  $\vec{r}$  is the sum of all contributions from points  $\vec{r}'$ , which becomes an volume integral over the domain  $\Omega$  in the limit. In this case, the integral over differential rings in cylindrical coordinates.

resulting in excited state  $u$ ,  $\nu_i$  is the ionisation frequency, and  $\xi$  is the photoionisation efficiency. The factor  $\xi \frac{\nu_u}{\nu_i}$ , in general, is a field-dependent term [80], though has often been assumed constant since it is not appear highly sensitive to the field magnitude [80]. The source  $S_{\text{ion}}$  is the sum of the source terms as in Section 5.4.2, but only accounting for ionising sources (since it is assumed that the photoelectron production rate is proportional to the ionisation rate [78]). Fitting parameters  $A_j$  and  $\lambda_j$  are computed as described in [78], and are related to the photoionisation range and absorption lengths of irradiating photons. The approach of Bourdon *et al.* [78], and references therein, shows that the overall photoelectron source,  $S_{\text{ph}}$ , may then be approximated by solving equations of the Helmholtz form given by

$$\vec{\nabla}^2 S_{\text{ph},j} - (\lambda_j p_{\text{O}_2})^2 S_{\text{ph},j} = -A_j p_{\text{O}_2}^2 I(\vec{r}) \quad (5.20)$$

and summing the resulting sources such that

$$S_{\text{ph}} = \sum_j S_{\text{ph},j} \quad (5.21)$$

for  $j = 1, 2, 3$ , which is the implementation used within StrAFE. It is understood from [78] that boundary conditions for each term in (5.21) may significantly influence the computed

photoelectron source, which is particularly important for ionisation sources near boundaries. At the time of writing, StrAFE only supports Dirichlet-zero or (default) Neumann-zero conditions for  $S_{\text{ph},j}$  terms, though improvement to this has been identified as a valuable addition should the software be developed further.

It is also remarked that, at the time of writing, StrAFE does not account for *shadows*. That is, regions occluded by geometry where propagating photons may not reach, e.g., as shown in [81]. While this may incur error in simulations where shadows are important, none of the simulations presented in this work incorporated any occluded regions. The simpler approach provided by (5.20) is therefore applicable. As a second remark, the stochastic nature of photoionisation is thought to affect streamer development, particularly relating to streamer branching [82]. However, comparisons between the deterministic Helmholtz approach (5.20) and a stochastic model in Bagheri and Teunissen [83] indicated that the differences may not be very significant. Their simulations indicated that, in general, the continuum model agreed well with averaged stochastic simulations, and the onset of branching due to stochastic fluctuations was minimal under standard atmospheric conditions in air. Stochastic effects become more important for simulations with low electron sources, and where kinetic effects dominate [82, 83]. Coupling the fluid solver developed here with semi- or full-kinetic approaches would be of interest for future development, e.g., in a hybrid scheme as discussed in Section 5.2.1.4.

#### 5.4.4 The Local Field and Local Mean Energy Approximations

As was described in Section 5.2.1, the low-temperature plasma developed in the wake of an ionisation wave (or streamer) is non-Maxwellian in nature. However, in the derivation of the hydrodynamic approach, suitable moments of the Boltzmann equation (2.24) can only be obtained under the assumption of a Maxwellian energy distribution [23]. Given that the EEDF of the plasma will deviate significantly from Maxwellian, the electron transport characteristics must be set in such a way as to approximate the true EEDF. Broadly, there are two well-established approaches which have both been implemented in StrAFE, described below.

The simpler approach is the Local Field Approximation (LFA). Under the LFA, electron transport parameters are assumed to be a function of the local magnitude of the electric field, i.e.,  $\mu_e(|\vec{E}|)$  or  $D_e(|\vec{E}|)$  (or more typically, the reduced field  $|\vec{E}|/N$ ). In StrAFE, these can either be provided as analytic functions (for example, empirical functions fitted to experimental data, as in [84]), or as a tabulated data output from software solving various approximations of the Boltzmann equation (2.24) to determine transport parameters using cross-sectional data, for example, BOLSIG+ [85]

and others [86]. The LFA is, from an implementation perspective, simple and efficient, since the electric field data is already available from the Poisson solution (5.13). Transport parameters can therefore be readily computed from this field using either an analytic function, or efficiently interpolated from tabulated data. The exact syntax and usage in StrAFE is described in Section 5.7.1.3.

A second, more advanced, approach is the Local Mean Energy Approximation (LMEA). A significant drawback of the LFA is its limited applicability to regions of high or divergent electric fields as shown by Grubert, Becker, and Loffhagen [87]. By expanding the electron momentum distribution function by the commonly-used method of the two-term Legendre expansion, authors of [87] derive the approximate conditions for LFA validity for a one-dimensional case,

$$\begin{aligned} \frac{1}{\lambda_{E,M}(z, t, \bar{\varepsilon})} &\gg \frac{1}{E(z, t)} \frac{\partial E(z, t)}{\partial z}, \\ \nu_{E,M}(z, t, \bar{\varepsilon}) &\gg \frac{1}{E(z, t)} \frac{\partial E(z, t)}{\partial t}, \end{aligned} \quad (5.22)$$

where  $\bar{\varepsilon}$  is the electron energy,  $\lambda_E$ ,  $\lambda_M$  are the energy and momentum dissipation lengths, and  $\nu_E$  and  $\nu_M$  are the energy and momentum dissipation frequencies, respectively [87]. It follows, therefore, that care must be taken for simulations around sharp electrodes or solid dielectric surfaces if using the LFA, as significant error can be incurred by use of the LFA outside of its limits of validity [87]. A major factor influencing the limits of the LFA pertains to *locality*, and the assumption that the electron characteristics are influenced solely by the electric field immediately *local* to those electrons. In reality, and particularly in configurations with the mentioned high or divergent field conditions, *non-local* effects that contribute to the discharge characteristics should also be considered. Zhu *et al.* [42] considered the important case of simulations involving the formation of thin charge sheaths (e.g., see the simulations of Chapter 6, Section 6.3), deriving approximate boundaries for LFA/LMEA validity based on simulation mesh size and pressure, which has been adapted as Figure 5.10.

The LMEA attempts to incorporate non-locality to a certain extent, by stipulating that the electron transport parameters should instead be a function of the *local mean energy* of the electrons,  $\bar{\varepsilon}$ ; i.e.,  $\mu_e(\bar{\varepsilon})$  or  $D_e(\bar{\varepsilon})$ . This value of energy is dynamically computed during the simulation, following

$$\frac{\partial n_\varepsilon}{\partial t} + \vec{\nabla} \cdot \vec{\Gamma}_\varepsilon = q_e \vec{\Gamma}_\varepsilon \cdot \vec{\nabla} \varphi - \sum_{j \in \mathcal{R}_i} \left( \Delta E_j k_j \prod_{m \in \mathcal{R}_j} n_m \right), \quad (5.23)$$

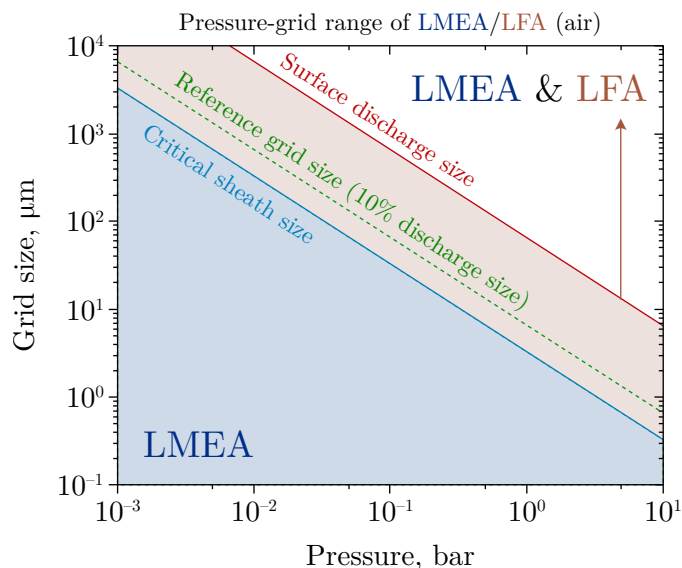


**Figure 5.10:** Regions of validity for the LMEA and LFA based on pressure, grid size, and sheath distances in air, according to [42]. Image adapted with permission from [42], © 2021 IOP Publishing.

where  $n_\varepsilon$  is the electron energy density, and  $\Delta E_j$  is the (signed) change in electron energy due to reaction  $j$ . The flux of the energy density,  $\vec{\Gamma}_\varepsilon$ , follows the definition of (5.4). This necessitates two additional parameters,  $\mu_\varepsilon$  and  $D_\varepsilon$ , which are the electron energy mobility and diffusion coefficients, respectively. Equation (5.23) therefore accounts for the transport of electron energy throughout the domain, including energy sources and sinks due to plasma chemical reactions. The  $q_e \vec{\Gamma}_e \cdot \vec{\nabla} \varphi$  term additionally accounts for the effects of Joule heating due to the development of the electronic current  $q_e \vec{\Gamma}_e$ . The local mean electron energy then follows from the ratio  $\bar{\varepsilon} = n_\varepsilon / n_e$ , and thus the non-local nature of this computed energy manifests in the electron transport behaviour through the  $\bar{\varepsilon}$  dependency of the electron transport parameters. Using the LMEA increases the simulation fidelity, though at a higher computational cost. The choice to use the LFA or the LMEA is solely decided by the user; the best approximation is dependent entirely on the nature of the simulated problem, and should be selected on a case-by-case basis.

#### 5.4.5 Boundary Conditions

The enforcement of boundary conditions has been kept flexible in StrAFE, in the sense that the user may configure arbitrary types of Dirichlet, Neumann, or Robin condition on any external or internal boundary of the domain. However, a number of common boundary conditions have been implemented for convenience and can be applied using straightforward syntax as shown later in

Section 5.7.1.4. The mathematical formulations of these boundaries are first discussed here.

On external boundaries and along lines of symmetry (see for instance, the cylindrically-symmetric approximations shown in Section 5.8.1), Neumann-zero conditions for the electric field ( $\vec{\mathbf{E}} \cdot \hat{\mathbf{n}} = 0$ ) and all tracked fluxes ( $\vec{\mathbf{\Gamma}}_i \cdot \hat{\mathbf{n}} = 0$ ) are applied by default. On boundaries defined as electrodes, the potential can be enforced through Dirichlet conditions which may be of constant value or be time-dependent. For solid boundaries (such as solid dielectrics or the electrodes themselves), it is important to have suitable boundary conditions to accurately capture the interaction of charged species and the surface. In this case, the default Neumann condition used for these types of boundary follows that of Hagelaar, de Hoog, and Kroesen [88] (but is here written in similar notation to Jovanović *et al.* [1]), such that

$$\vec{\mathbf{\Gamma}}_e \cdot \hat{\mathbf{n}} = \frac{1 - r_e}{1 + r_e} \left( |n_e \mu_e \vec{\nabla} \varphi \cdot \hat{\mathbf{n}}| + \frac{1}{2} n_e v_{\text{th},e} \right) - \frac{2}{1 + r_e} \gamma \sum_{\substack{j \in \mathcal{S} \\ j \neq e}} \max(\vec{\mathbf{\Gamma}}_j \cdot \hat{\mathbf{n}}, 0) \quad (5.24)$$

for electrons,

$$\vec{\mathbf{\Gamma}}_i \cdot \hat{\mathbf{n}} = \frac{1 - r_i}{1 + r_i} \left( |n_i \mu_i \vec{\nabla} \varphi \cdot \hat{\mathbf{n}}| + \frac{1}{2} n_i v_{\text{th},i} \right) \quad (5.25)$$

for heavy species, and

$$\vec{\mathbf{\Gamma}}_\varepsilon \cdot \hat{\mathbf{n}} = \frac{1 - r_e}{1 + r_e} \left( |n_\varepsilon \mu_\varepsilon \vec{\nabla} \varphi \cdot \hat{\mathbf{n}}| + \frac{1}{2} n_\varepsilon v_{\text{th},\varepsilon} \right) - \frac{2}{1 + r_e} \varepsilon \gamma \sum_{\substack{j \in \mathcal{S} \\ j \neq e}} \max(\vec{\mathbf{\Gamma}}_j \cdot \hat{\mathbf{n}}, 0) \quad (5.26)$$

for the electron energy density. The symbol  $r$  is the reflection coefficient for the species in the subscript,  $\gamma$  is the secondary emission coefficient of the surface, and  $v_{\text{th}}$  is the thermal velocity, given by

$$v_{\text{th},i} = \sqrt{\frac{8k_b T_i}{\pi m_i}}, \quad (5.27)$$

where  $k_b$  is the Boltzmann constant and  $T_i$ ,  $m_i$  are the temperature and mass of species  $i$ , respectively. When the LMEA as described in Section 5.4.4 is used, the electron temperature is computed from the energy, following

$$T_e = \frac{2n_\varepsilon}{3k_b n_e}. \quad (5.28)$$

The thermal velocity of electron energy is then

$$v_{\text{th},\varepsilon} = 2k_b T_e v_{\text{th},e}. \quad (5.29)$$

To accurately model discharges interacting with solid dielectric surfaces, one special case must

further be considered for internal interfacial boundaries. In StrAFE, interfacial boundaries between subdomains of different permittivity automatically has the following condition applied to the potential,

$$\epsilon \vec{\nabla} \varphi \cdot \hat{\mathbf{n}} = \varsigma, \quad (5.30)$$

where  $\varsigma$  is the surface charge density present at the interface. This condition accounts for the discontinuity in the electric displacement due to surface charge, as was explained in Chapter 2 - Section 2.2.1. Surface charge either exists as an initial condition (e.g., see Chapter 6, Section 6.4 and 6.5 for simulations which incorporate surface charge), or is dynamically accumulated over the simulation due to inbound charge fluxes. To account for the latter, the  $\varsigma$  distribution is computed by default for all interfacial boundaries according to

$$\frac{\partial \varsigma}{\partial t} = q_e \sum_{j \in \mathcal{S}} Z_j \vec{\Gamma}_j \cdot \hat{\mathbf{n}} + q_e \gamma \sum_{\substack{j \in \mathcal{S} \\ j \neq e}} \vec{\Gamma}_j \cdot \hat{\mathbf{n}} \quad (5.31)$$

which considers the normal incident flux on a surface from all charged species, including the residual positive charge remaining on the surface due to secondary emission. It is remarked that StrAFE does not yet support the definition of electrical conductivity for solid subdomains. In reality, volume conduction would introduce additional terms to (5.31) that gradually reduces the surface charge density (as was extensively considered within Chapter 3). However, most dielectric materials possess very low conductivity, resulting generally in a dielectric relaxation time that is several magnitudes slower than the typical nanosecond timescales for ionisation waves to develop and propagate. Since the simulations in this work exclusively considered materials possessing relaxation times far longer than characteristic streamer timescales, volume conduction was considered negligible and its omission justified.

## 5.5 Weak Formulation

Section 5.3.1 introduced the concept of the weak formulation, which allowed the re-expression of strong mathematical forms such that they hold only *weakly* with respect to some set of test functions. StrAFE leverages the UFL forms provided through FEniCS to directly implement the weak formulation of the present ADR-Poisson equation set (see syntactical details in Section 5.7.2.2), the formulation of which are presented in this section. To mirror the code implementation, let  $\vec{\mathbf{u}}$  be a vector of functions,  $\vec{\mathbf{u}} = [u_0, u_1, u_2, \dots, u_{p-1}, u_p]^T$ , where zero-based indexing is used to maintain consistency with the Python implementation. Each element of  $\vec{\mathbf{u}}$  represents a function on the domain  $\Omega$ , and the value  $p$  differs depending on the problem type (e.g., total number of

charged species, use of LFA or LMEA, photoionisation, etc.). The construction of  $\vec{u}$  adheres to the following rules:

- Index 0 is always the potential field,  $\varphi$ .
- Index 1 is always the electron density,  $n_e$ .
- Index 2 to  $\text{card}(\mathcal{S}) - 1^*$  are assigned the densities of all other charges species, e.g.,  $n_+$ ,  $n_-$ , etc.
- Index  $\text{card}(\mathcal{S})$  to  $\text{card}(\mathcal{S}) + 2$  are assigned the three components of the photoionisation source,  $S_{\text{ph},1}$ ,  $S_{\text{ph},2}$ , and  $S_{\text{ph},3}$ , if enabled.
- Index  $\text{card}(\mathcal{S}) + 3$  is assigned the surface charge,  $\varsigma$ , if there are subdomains.
- The final index,  $p$  (or equivalently in Python, index  $-1$ ) is assigned the electron energy density,  $n_\varepsilon$ , if the LMEA is used.

To summarise, the vector  $\vec{u}$  may alternatively be written

$$\vec{u} = \begin{bmatrix} u_0 \\ u_1 \\ u_2 \\ u_3 \\ \vdots \\ u_{\text{card}(\mathcal{S})-1} \\ u_{\text{card}(\mathcal{S})} \\ u_{\text{card}(\mathcal{S})+1} \\ u_{\text{card}(\mathcal{S})+2} \\ u_{\text{card}(\mathcal{S})+3} \\ u_p \end{bmatrix} \equiv \begin{bmatrix} \varphi \\ n_e \\ n_2 \\ n_3 \\ \vdots \\ n_{\text{card}(\mathcal{S})-1} \\ S_{\text{ph},1} \\ S_{\text{ph},2} \\ S_{\text{ph},3} \\ \varsigma \\ n_\varepsilon \end{bmatrix}. \quad (5.32)$$

For the construction of weak forms, let  $\vec{v} = [v_1, v_2, \dots, v_{p-1}, v_p]^T$  be a second vector of functions also of length  $p$ , where each element  $v_j$  stores the test function for the corresponding  $u_j$ . The weak forms of (5.12), (5.13), (5.20), and (5.23) are given in the following, using the process described in Section 5.3.1.

---

\* $\text{card}(x)$  is the cardinality of set  $x$ , giving the total number of elements in the set. The notation  $|\cdot|$  is also valid, but is not used here to differentiate from the vector norm.

For the Poisson equation (5.13), the weak form may be derived (see Appendix A.12 for full derivation) to be

$$\begin{aligned} \int_{\Omega} v_0 \vec{\nabla} \varepsilon \cdot \vec{\nabla} u_0 \, d\Omega + \int_{\Omega} v_0 \sum_{j \in \mathcal{S}} q_j n_j \, d\Omega \\ - \int_{\Omega} \vec{\nabla} (v_0 \varepsilon) \cdot \vec{\nabla} u_0 \, d\Omega + \int_{\partial\Omega} v_0 \varepsilon (\vec{\nabla} u_0 \cdot \hat{\mathbf{n}}) \, dS = 0, \end{aligned} \quad (5.33)$$

where  $\partial\Omega$  in the last integral denotes the external boundary of domain  $\Omega$ . The choice of the normal field term  $\varepsilon (\vec{\nabla} u_0 \cdot \hat{\mathbf{n}})$  determines the Neumann condition applied to  $\partial\Omega$  (such as the wall conditions of section 5.4.5). Different Neumann conditions can also be applied to disjoint sections of  $\partial\Omega$  in this way, by letting

$$\bigcup_j \omega_j = \partial\Omega \quad (5.34)$$

where  $\omega_j$  are sections of  $\partial\Omega$ . In this case, the boundary integral in (5.33) may be replaced more generally by

$$\sum_{\omega_j \in \partial\Omega} \int_{\omega_j} v_0 \varepsilon (\vec{\nabla} u_0 \cdot \hat{\mathbf{n}})_j \, dS_j. \quad (5.35)$$

For the ADR equation with strong form given by (5.12), the weak form follows from Appendix A.12 to yield

$$\begin{aligned} \int_{\Omega} \frac{\partial u_i}{\partial t} v_i \, d\Omega - \text{sgn}(q_i) \left[ \int_{\Omega} v_i \vec{\nabla} (u_i \mu_i) \cdot \vec{\nabla} \varphi \, d\Omega - \int_{\Omega} \vec{\nabla} (v_i u_i \mu_i) \cdot \vec{\nabla} \varphi \, d\Omega \right] \\ + \int_{\Omega} \vec{\nabla} (v_i D_i) \cdot \vec{\nabla} u_i \, d\Omega - \int_{\Omega} v_i \vec{\nabla} D_i \cdot \vec{\nabla} u_i \, d\Omega - \int_{\Omega} S_i v_i \, d\Omega \\ + \int_{\partial\Omega} v_i (\vec{\Gamma}_i \cdot \hat{\mathbf{n}}) \, dS = 0 \end{aligned} \quad (5.36)$$

for  $i \in [1..(\text{card}(\mathcal{S}) - 1)]^\dagger$ , and where the boundary flux integral in (5.36) can be similarly split according to (5.34). The energy balance equation (5.23) used in the LMEA follows an identical form to (5.12), except with the appropriate source terms from (5.23) replacing  $S_i$  in (5.12). The weak form of the Helmholtz equations for photoionisation (5.20) are derived in the same manner (Appendix A.12), yielding

$$\int_{\Omega} \vec{\nabla} v_i \cdot \vec{\nabla} u_i \, d\Omega + \int_{\Omega} v_i (p_{O_2} \lambda_j)^2 u_i \, d\Omega$$

---

<sup>†</sup>The shorthand notation of  $x \in [a..b]$  adopted here is equivalent to  $\{x \in \mathbb{Z} : a \leq x \leq b\}$ .

$$- \int_{\Omega} v_i \left( A_j p_{O_2}^2 \frac{p_q}{p + p_q} \xi \frac{\nu_u}{\nu_i} \right) S_{\text{ion}} d\Omega - \int_{\partial\Omega} v_i \left( \vec{\nabla} u_i \cdot \hat{\mathbf{n}} \right) dS = 0 \quad (5.37)$$

for  $i \in [\text{card}(\mathcal{S}) .. (\text{card}(\mathcal{S}) + 2)]$ , and where once again (5.34) applies to the boundary integral.

Splitting the domain of integration as done for boundaries in (5.35) equally applies to subdomains with differing  $\varepsilon$ . As explained in Section 5.4.5, StrAFE currently considers solid subdomains only. Therefore, when necessary, StrAFE internally splits the full domain  $\Omega$  into two groups:  $\Omega_g$  for gas and  $\Omega_s$  for solids. Since users are permitted to declare an arbitrary number of solid subdomains,  $\Omega$  may be decomposed like

$$\Omega = \Omega_g \cup \Omega_s = \Omega_g \cup \bigcup_{\kappa_j \in \Omega_s} \kappa_j, \quad (5.38)$$

where  $\kappa_j$  is the  $j$ -th solid subdomain. When subdomains are declared, the Poisson equation (5.13) continues to be solved over all  $\Omega$ , but the ADR (5.12) and Helmholtz equations (5.20) are restricted to  $\Omega_g$  only. Allowing for an arbitrary value of permittivity per solid subdomain, individual integrals must be appended for each subdomain  $\kappa$  such that a more general form of the first and third term of (5.33) would be

$$\int_{\Omega_g} \vec{\nabla} \cdot (\varepsilon_0 \vec{\nabla} \varphi) + \rho d\Omega_g + \sum_{\kappa_j \in \Omega_s} \int_{\kappa_j} \vec{\nabla} \cdot (\varepsilon_j \vec{\nabla} \varphi) d\kappa_j = 0 \quad (5.39)$$

assuming  $\varepsilon = \varepsilon_0$  for gases. The expansion of (5.39) for derivative order reduction then follows the form of (5.33). The realisation and programmatic implementation of these weak forms in StrAFE is detailed in Section 5.7.2.2.

## 5.6 Adaptive Mesh Refinement and Time Stepping

For the purposes of more effective multiscale modelling, StrAFE provides two important features to optimise the solution process: Adaptive Mesh Refinement (AMR) and Adaptive Time Stepping (ATS), described in the first two subsections of this section. Other miscellaneous solver settings relevant to numerical convergence, which are also exposed to the user, are then outlined in Section 5.6.3.

### 5.6.1 Adaptive Mesh Refinement

Transient ionisation waves and streamer discharges are multiscale phenomena [4], in that multiple spatial scales differing by several magnitudes are typical characteristics that must be necessarily resolved for a complete physical description. This arises from the very fact that the macroscopic coherent structures of ionisation wavefronts are emergent from atomic scale charge transport. From a simulation perspective, multiscale phenomena presents a difficult computational challenge, as all scales must be accurately represented within the numerical discretisation. By now it is well known [5] that the structure of ionisation waves and streamers exhibit highly nonlinear variations the charge density and steep gradients in the electric field, particularly at the heads of developed wavefronts. The characteristic thin layers of space charge formed around ionisation fronts must generally be resolved with micrometre accuracy, as do charge sheaths formed over electrodes [89, 90] or dielectric surfaces [91]. Yet, typical geometries of practical interest will possess characteristic lengths in the millimetre, centimetre, or even meter range.

One well-established method to approach multiple length scales when using mesh-based numerical methods is to employ *adaptive meshes*. AMR refers to the technique of decreasing (refining) the mesh cell size in regions of a simulation that require greater accuracy, and increasing (coarsening) the cell size in regions where the solution may be slowly-varying or of lesser interest. Since the numerical discretisation error is proportional to the cell dimension, the mesh becomes *adaptive*, ensuring that the solution is well-represented where necessary, but saving valuable computational time and memory by substantially decreasing the total number of required mesh cells. The technique of adapting cell dimension is also referred to as *h*-adaptivity, which is in contrast to *p*-adaptivity which adapts the order of the approximating basis functions within individual elements (or *hp*-adaptivity, which is a combination of both). At the time of development, FEniCS itself had support for per-cell refinement but no means for subsequent coarsening. StrAFE adds a fully custom AMR implementation capable of dynamic mesh refinement and derefinement, and which is developed to take advantage of MPI parallelism. Its implementation is described in the remainder of this subsection.

To overcome the inability to perform per-cell coarsening, a three-mesh method has been developed. A computational mesh is denoted  $\mathcal{M}$  and three meshes are defined:

- $\mathcal{M}_b$ , the *base* mesh.
- $\mathcal{M}_0$ , the *initial* mesh.

- $\mathcal{M}_j$ , the mesh *at the refinement step*  $j^\ddagger$ .

$\mathcal{M}_b$  is a coarse mesh whose resolution is defined in the settings by the user prior to engaging the solver. The base mesh represents the coarsest level which the mesh can attain during the AMR process. The initial mesh,  $\mathcal{M}_0$ , is also provided prior to solving, which must be significantly finer than that of  $\mathcal{M}_b$ . The purpose of  $\mathcal{M}_0$  is to provide an accurate solution for the initial potential and electric fields given the set of initial charge densities. This is a necessary first step for the AMR algorithm to obtain accurate function values for subsequent refinement and coarsening. As such,  $\mathcal{M}_0$  must be sufficiently fine to resolve the steepest of gradients for the first timestep. The third mesh,  $\mathcal{M}_j$ , is generated dynamically each time AMR is called, and differs depending on the state of the simulation. Note that by adopting this AMR scheme, per-cell derefinement is not used and the program has no memory of the mesh between refinement steps, nor is a parent-child hierarchy kept for each mesh cell. Instead, each refinement pass begins at the coarsest mesh and refines upwards, only refining cells that satisfy the AMR criteria. As such, mesh regions where the solution no longer satisfies the refinement criteria are coarsened automatically when re-projection is performed. It is further remarked that to ensure efficiency, StrAFE implements a function-based AMR criteria, such that functions which exist on the mesh are evaluated against some threshold to determine whether refinement should be performed in each cell, mirroring existing implementations [3]. This is in contrast to schemes based on computed estimates of the discretisation error, which are, in general, far more computationally expensive to repeatedly perform. Figure 5.11 provides a flowchart of the implemented AMR algorithm, which may also be described as the following sequence of steps:

1. If it is the beginning of the simulation, project the user-defined initial conditions onto  $\mathcal{M}_0$  and solve for  $\vec{\mathbf{u}}_0$ . Then store a temporary copy  $\vec{\mathbf{u}}_r \leftarrow \vec{\mathbf{u}}_0$ . If not, the temporary copy should be assigned from the current solution  $\vec{\mathbf{u}}_r \leftarrow \vec{\mathbf{u}}_k$ , where  $k$  is the current iteration. In either case, set up a temporary mesh as a copy of the coarsest base mesh,  $\mathcal{M}_r \leftarrow \mathcal{M}_b$ .
2. Construct a set of functions (or combination of functions),  $\mathcal{F}$ , from those in  $\vec{\mathbf{u}}_r$  which have been user-defined in the solver settings to be evaluated against refinement criteria.
3. Project  $\mathcal{F}$  onto  $\mathcal{M}_r$ . For  $f \in \mathcal{F}$ , each cell in  $\mathcal{M}_r$  should be marked for refinement if  $f \geq \eta_\ell$ , where  $\eta_\ell$  is the corresponding tolerance in the set of tolerances  $\eta_\ell \in \mathcal{K}_\ell$ , and where  $\ell$  is the refinement level, which is also user-defined.

---

<sup>‡</sup>Here  $j$  is defined as the *refinement step*, since AMR does not necessarily match the iteration number (denoted before as  $k$ ) due to timestepping.

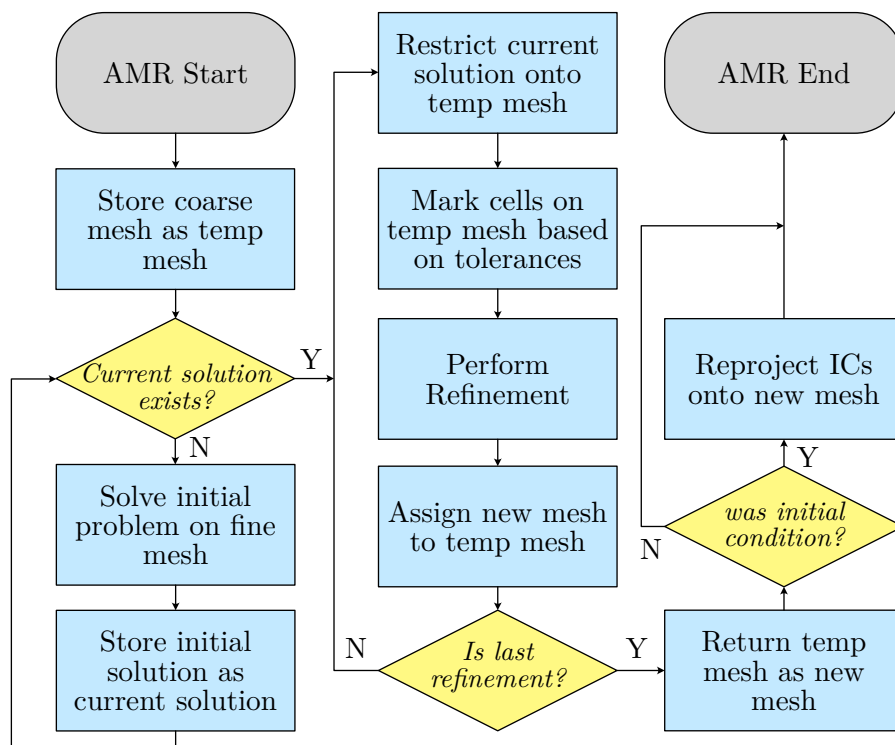


**Figure 5.11:** Flow diagram outlining the AMR algorithm implemented in StrAFE. Image adapted from [60] under CC BY 4.0.

4. (Optional) grow the region of cells which are marked for refinement, by marking all cells within a distance  $d_r$  of a marked cell in  $\mathcal{M}_r$ .
5. Call the FEniCS refinement function on the marked  $\mathcal{M}_r$  giving a refined mesh  $\mathcal{M}'_r$ , which should be reassigned like  $\mathcal{M}_r \leftarrow \mathcal{M}'_r$  and repeated for a user-defined number of refinements on the current level  $\ell$ , starting from step 3.
6. If  $\mathcal{K}_\ell$  has been exhausted on this level  $\ell$ , iterate  $\ell$  and repeat from step 3 until the last  $\ell$ .
7. Return the fully refined mesh  $\mathcal{M}_r$ .
8. If this was the beginning of the simulation, re-project the initial conditions onto  $\mathcal{M}_r$  before re-solving for  $\vec{u}_0$ . In any case, reassign  $\mathcal{M}_j \leftarrow \mathcal{M}_r$ .
9. Project the current solution (and any past solutions necessary for the desired time-stepping scheme)  $\vec{u}_k$  onto  $\mathcal{M}_j$  and re-assemble the variational problem. Timestepping can then be recommenced using the refined mesh.

Step 3 of the above algorithm necessitates the projection of functions from the current solution onto  $\mathcal{M}_r$ , which is under the process of refinement. As such, the technique for projection must

account for the mismatch in the number and location of mesh nodes. However, because the projection function values are used only for the purposes of refinement rather than part of the solution process, accurate interpolation of mesh values is not necessary, and computationally cheaper options can be utilised as an alternative. Namely, StrAFE implements nearest-neighbour searches and copies these values through two different schemes, the choice of which may be set by the user:

1. Simple nested loops, over the mesh cells then over the cell vertices. The nodal value of the vertex identified with the minimum euclidean distance to the query point is copied as the function value.
2. The use of *kd*-tree nearest neighbour searching. In this case, a *kd*-tree is constructed to accelerate nearest-neighbour searches with the two sets of nodal points; one set from  $\mathcal{M}_k$ , and the other from  $\mathcal{M}_r$  as the query points.

The choice of which method should be toggled is problem-dependent. From testing, simple loops are typically slower than the use of *kd*-trees, even when factoring in the time required to initialise the tree structure. However, the memory requirements from the use of *kd*-tree method far exceeds that of using loops. The choice should therefore be made based on the user's requirements and hardware specifications. It is also remarked here that the above AMR algorithm has been developed with MPI in mind. Since the MPI implementation in FEniCS operates on the principle of mesh decomposition (i.e., the mesh is fragmented and distributed to each computational process), information regarding function values must be communicated between processes during AMR. This is accounted for in StrAFE, and global mesh data is shared between all processes before AMR commences. In this way, the present implementation of AMR is not performance limited by a single process with MPI enabled; each process uses the shared mesh data to perform refinement marking in parallel. Results from a basic parallel scaling test are included in Appendix C.3, and examples of adaptively-refined meshes using this scheme can be found in Appendix C.2.

### 5.6.2 Time Integration and Adaptive Time Stepping

While FEniCS automatically handles the discretisation of the FEM problem given the weak formulation, temporal discretisation must be dealt with separately. By default, StrAFE uses the

$\theta$ -scheme for time discretisation, such that the rate of change in time is approximated by

$$\frac{\partial \vec{u}}{\partial t} \approx \frac{\vec{u}_{k+1} - \vec{u}_k}{\Delta t} = \theta f_{k+1}[t, \vec{u}_{k+1}] + (1 - \theta) f_k[t, \vec{u}_k] \quad (5.40)$$

where  $\Delta t$  is the time-step, and where the parameter  $0 \leq \theta \leq 1$  is freely chosen by the user. One may recover common schemes based on the choice of  $\theta$ . For instance, setting  $\theta = 0$  recovers the explicit Euler scheme, while  $\theta = 1$  gives the implicit Euler scheme both of first-order accuracy. The default option is  $\theta = 1/2$  corresponding to the second-order accurate Crank-Nicolson scheme. The choice of time-step is also user-defined, unless adaptive time stepping is enabled. It should be noted that the user is responsible for evaluating whether a given time-step is appropriate for their simulation, for example, use of the explicit Euler scheme requires that the Courant-Friedrichs-Lewy (CFL) condition be satisfied to maintain stability.

Adaptive Time Stepping is an additional feature often impactful for time-dependent numerical modelling. This refers to the dynamic adaptation of the computational time-step used over the course of the simulation. Slow-varying solutions in time generally do not require very fine steps to achieve reasonable accuracy, however, where a solution begins to exhibit rapid changes in time, the time-step must be sufficiently small to not incur significant truncation errors. StrAFE implements a typical version of Adaptive Time Stepping, by allowing the user to define a custom control law that will dynamically adjust the time-step based on a value of the maximum estimated truncation error. By default, the truncation error is estimated by comparison of *coarse* and *fine* solutions: the former generated using the current step size  $\Delta t$ , and the latter from two fine steps of  $\Delta t' = 0.5\Delta t$ . Let  $\vec{u}_k^H$  and  $\vec{u}_k^h$  denote the coarse and fine solutions at iteration  $k$ , respectively, StrAFE computes the estimated truncation error via Richardson extrapolation,

$$\epsilon := \frac{\|\vec{u}_{k+1}^h - \vec{u}_{k+1}^H\|}{2^w - 1}, \quad (5.41)$$

where  $w$  is equal to unity unless  $\theta = 1/2$ , in which case  $w = 2$ . User-defined routines may utilise  $\epsilon$  to inform the nature of the time-step update. If none is specified, a simple control law is implemented by default, such that the new timestep  $\Delta t^{k+1}$  is given by

$$\Delta t^{k+1} = \left( \frac{0.8\mathbb{T}}{\epsilon} \right)^{\frac{1}{w}} \Delta t^k \quad (5.42)$$

where  $\mathbb{T}$  is a user-defined tolerance.

### 5.6.3 Miscellaneous Settings

This section briefly outlines a number of other settings available through StrAFE that were designed to aid in numerical convergence in certain cases. These settings are generally less important for general use, but may provide superior performance and/or convergence in specific, problem-dependent cases.

#### 5.6.3.1 Mesh Pre-Refinement

While the AMR algorithm as described in Section 5.6.1 generally performs well, certain problems benefit from an additional layer of mesh refinement prior to the engagement of the main solver time loop. For example, for domains that feature high aspect ratio features that the base mesh must conform to, or along solid dielectric surfaces that often experience steep density and field gradients in their vicinity. A number of functions allowing a user-defined number of pre-refinement passes on the base mesh are available, of the following types:

- Refine all mesh cells within a radial distance of a given set of points.
- Refine all mesh cells within a distance around a line parallel to the  $x$ ,  $y$ , or  $z$  axes.
- Refine all mesh cells contained near the boundary of a circle or sphere given a centre and radius.

Pre-refinement modifies the base mesh prior to the engagement of the solver loop. Therefore, AMR can be applied atop pre-refinement, therefore providing an exceptional level of user control to refine precisely where needed.

#### 5.6.3.2 Refinement Partitioning

Additional mesh refinement controls are also available in the form of *refinement partitions*. Two main components exist that allow further control of mesh refinement regions, described below.

The first, for a given mesh  $\mathcal{M}$ , refinement may be limited solely to a set of cells  $\mathcal{C} \subseteq \text{cells}(\mathcal{M})$ . Function threshold values are evaluated in the same way as in Section 5.6.1, but those not contained in  $\mathcal{C}$  are skipped during refinement marking. This may be useful for complex simulations incorporating complex solid-gas topologies, and where there is *a priori* knowledge of the regions where the discharge will occur. AMR can be limited to act only in this region.

Secondly, and separate from the cell-partitioning above, a subset of cells  $\mathcal{C}$  may also be defined to

limit the region from which refinement thresholds should be calculated. For example, a refinement criterion based on the maximum value of the electric field (e.g.,  $|\vec{E}| \geq \max(g \cdot |\vec{E}|)$ , where  $g$  is some fraction) will be highly ineffective for discharges exhibiting the formation of cathode sheaths. The electric field inside the sheath will generally possess a magnitude far greater than that of the rest of the domain (including any propagating wavefronts), and therefore this type of criterion would fail to refine near streamer heads. Using this method, the region from which the value of  $\max |\vec{E}|$  is obtained can be set to ignore the sheath region, ensuring that the maximum field of the streamer head is instead used for refinement marking. The AMR scheme then correctly refines around both the cathode sheath and the streamer head.

The combination of the two schemes introduced here effectively allows different AMR thresholds to be defined on different subsets of cells( $\mathcal{M}$ ), which is useful since the effectiveness of an AMR scheme is generally dependent on the type and conditions of a discharge. This is shown to be highly effective in the examples detailed in Section 5.8.3 and Section 5.8.4, where simultaneous counter-propagating positive and negative streamers use different AMR schemes on a single domain.

### 5.6.3.3 Preservation of Positive Densities

A common problem encountered in using the fluid approach is ensuring positivity for all charge densities. Negative densities are unphysical, but may manifest in a number of different ways during numerical simulations. This includes numerical tolerance issues when densities are near zero, near very steep density gradients, or in the case of the re-projection method used within the final step of the AMR algorithm. The introduction of initially small erroneous negative values can quickly grow, resulting in numerical instability and ultimately non-convergence. Several methods have been implemented in StrAFE, which may be selected by the user. In order of increasing complexity:

- Setting all density values less than zero back to zero between each timestep. This method is only effective for small numerical errors, and may incur great inaccuracies in other cases.
- Setting all density values less than zero back to its value in the previous timestep. This method is useful for errors arisen from AMR re-projection, introduces a small amount of numerical diffusion, but is useful nonetheless for AMR-enabled simulations near steep fronts.
- Addition of an additional charge source term following implementations such as COMSOL [92]. These additional terms vanish at large densities, but are in place to ensure that

densities approaching zero do not cross into the unphysical domain.

- Active stabilisation through Streamline Upwind Petrov-Garlerkin (SUPG) terms — This is an experimental, and as of the time of writing, largely untested feature. However, users may enable SUPG [93] to append stabilisation terms to the weak formulation in attempt to smooth out steep gradients. This method also introduces some degree of artificial diffusion, but is a well-established technique in computational fluid dynamics, particularly for high Péclet<sup>§</sup> number flows.

#### 5.6.3.4 Linear Solver

StrAFE was developed with FEniCS built against the PETSc backend [70] and utilises a custom Newton solver for the nonlinear problem. The inner linear problem is solved, by default, using the Generalised Minimum Residual (GMRES) method preconditioned using the provided algebraic multigrid preconditioner (AMG) [94]. However, users may explore all available options as listed in [54] including Biconjugate Gradient and various other relaxation methods. Relative or absolute solver tolerances can also be set as described by FEniCS documentation [54]. These are all standard linear solvers, as such, require no introduction within this work.

#### 5.6.3.5 Built-in Initial Charge Conditions

For the definition of initial charge conditions, there exist a number of common charge distributions used in past literature. To facilitate rapid problem generation, a number of these have been implemented as convenient defaults alongside the ability to define fully custom initial conditions. For background ionisation, simple uniform distributions (with and without random perturbations as used in [2]) are available. Gaussian distributions following the form of

$$n_i = n_0 \exp\left(-\frac{(x - x_0)^2 + (y - y_0)^2 + (z - z_0)^2}{s_0^2}\right) \quad (5.43)$$

are also available, where  $n_0$  is the peak initial density and  $s_0$  is the initial spread of the seed, as used in e.g., [95]. The capsule-like seed of [91] has further been included following the provided definition. These seeds are typically used to model patches of pre-ionisation within a domain, from which streamers may initiate from.

---

<sup>§</sup>The non-dimensional Péclet (Pe) number characterises fluid flows by the ratio of advective to diffusive transport rates.

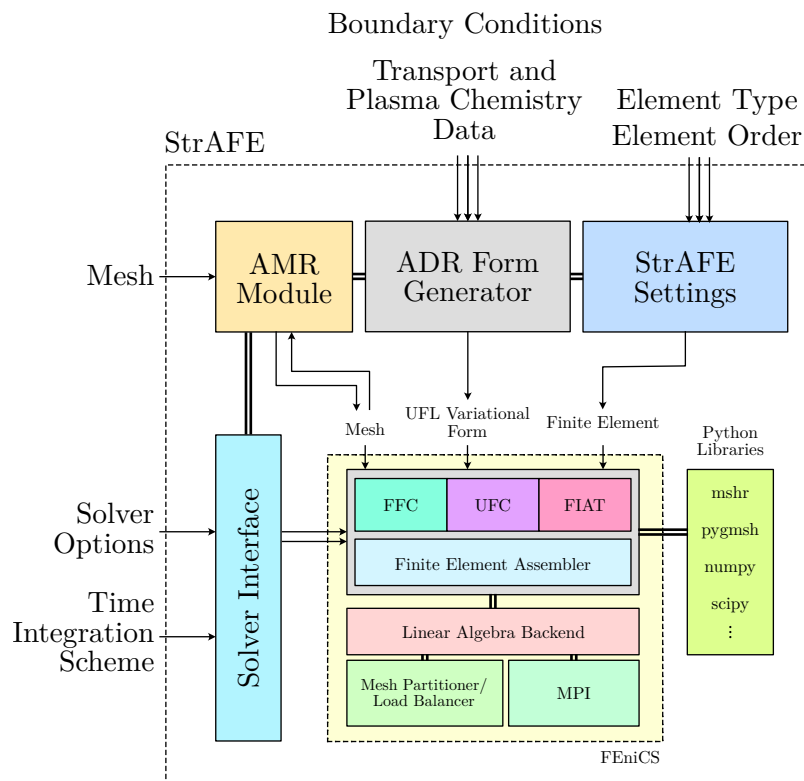


**Figure 5.12:** Block diagram outlining the software architecture of StrAFE, as built upon the FEniCS framework previously shown as Figure 5.8. Image adapted from [60] under CC BY 4.0.

## 5.7 StrAFE Implementation and Syntax

To ensure that the developmental aims of Section 5.1 were met, the entire mathematical formulation of the problem as described in Section 5.4.1 must be translated, at a sufficiently high level of abstraction, to result in a user-friendly, yet highly-configurable, software package. This section describes the computational realisation of the described mathematical model using the Python interface to FEniCS. Figure 5.12 provides a block diagram showing the architecture of StrAFE and its relationship to the core FEniCS components as was included in Figure 5.8. In the sections that follow, references to several inherited FEniCS features and software classes are made, for which in-depth explanations are outside the scope of this work. For details, the reader is referred to the FEniCS documentation [54] and references therein.

To successfully define and solve a problem using StrAFE, three main stages are involved; broadly described as:

1. The user inputs the desired simulation conditions and solver configuration.
2. Solver is invoked; finite element forms are generated and the system is assembled based on defined inputs.
3. Time-stepping loop is engaged, solution is sought at every timestep and solutions are output at user-defined save intervals.

Sections 5.7.1 to 5.7.3 describe each of these stages in sequence, detailing the automation tools introduced with StrAFE to allow the high-level abstraction of the problem to be translated into a mathematical FEM problem of considerable complexity, and then solved.

## 5.7.1 Automation of Problem Configuration and Definition

### 5.7.1.1 Main Problem Environment

The top-level user-facing interface of StrAFE comes in the form of the `DriftDiffusionProblem` class. This class contains all the necessary data and settings for one simulation instance which the user must set up before invoking the solver. Attributes of the simulation problem are then defined using `.set` methods. For example<sup>¶</sup>

```

1   from strafe import *           # Import the strafe package
2
3   prob = DriftDiffusionProblem() # Instantiates a problem environment
4   prob.set_approximation('LMEA') # Sets the approximation to LMEA
5   prob.set_base_mesh(mesh)      # Sets the base mesh
6   prob.set_timestep(10**-9)     # Sets dt to one ns

```

### 5.7.1.2 Meshed Domain

For any simulation, one begins with a `mesh` object representing the discretised computational domain  $\Omega$ . While StrAFE has the basic ability to generate simple meshed domains (e.g., simple polygons and combinations of polygons), it may also accept any mesh file saved as `.xdmf` or `.xml` formats output from third-party software or other python packages. The latter option provides native support for intricate and complex domains and is generally recommended. All meshes used in the present work were generated from the Python package `pygmsh` [96], allowing a single-script solution to combined mesh generation and FEM problem solving. Instantiated mesh objects (whether generated in StrAFE or read-from-file) are supplied to the problem environment using `prob.set_base_mesh(mesh)` as shown.

---

<sup>¶</sup>Wildcard import using `*` is generally not recommended due to possible namespace conflicts. It is, however, used here for illustrative clarity.

### 5.7.1.3 Declaration of Tracked Species

A single type of charged species to be included in a simulation can be defined through the use of the `ChargedSpecies` class. The class attributes include the name, charge, mass, transport parameters, and initial conditions of the represented charged species. Transport parameters can be provided as a custom python `function` handle or as a file path pointing to tabulated data. For example, a `ChargedSpecies` object representing electrons is instantiated, with its mobility and ionisation coefficient populated, like

```

1     def function mu_e(E, N):           # Define mobility function of E, N
2         return f(E,N)
3
4     alpha_path = 'filepath/mobility.txt' # Filepath to tabulated alpha
5
6     # Set the attributes of the charged species
7     electrons = ChargedSpecies('electron', q_e, m_e)
8     electrons.set_mobility(mu_e)
9     electrons.set_ionisation(alpha_path)

```

A completed Python `list` of `ChargedSpecies` must then be passed to the solver environment by calling the `.set_charged_species` of `DriftDiffusionProblem`. Alternatively, StrAFE also supports input via plaintext `.txt` files enclosing a table of active species, associated transport data, and plasma chemical reactions. An example of the format of these files is shown in Appendix C.4, which act to substantially simplify the generation of complex multi-species problems, as each charged species need not be manually defined. With the file path of the plaintext file, one may use the dedicated `TabulatedSpecies` class to automatically generate a `list` of an arbitrary number of `ChargedSpecies` to be included in the problem, complete with all transport data using the much simplified syntax

```

1     reaction_table = 'filepath/reactions.txt'
2
3     problem = DriftDiffusionProblem()
4     table = TabulatedSpecies(reaction_table)
5     problem.set_charged_species(table.get_species_list())

```

### 5.7.1.4 Declaration of Boundary Conditions and Solid Subdomains

The enforcement of boundary conditions involves the declaration of *marker functions* using the FEniCS `SubDomain` class [54]. When called, the `.inside` method of `SubDomain` returns a `True` boolean flag for each node of the mesh that determines whether the node should be considered as part of the represented boundary. For instance, the class method

```

1     def inside(self, r, on_boundary):

```

```
2     return on_boundary and near(r[1], 0.0, tol)
```

evaluates the coordinate vector  $\vec{r} = (x, y, z)$  for a node on the mesh. The function `near` accounts for the finite accuracy of floating point number representations, such that `near(x, a, b)` is equivalent to `(x >= a-b) and (x <= a+b)` where `b` is the tolerance. The status flag `on_boundary` is `True` only for nodes that lie on the external boundary  $\partial\Omega$ . In the example above, the marker function therefore returns `True` only for nodes that lie near  $y = 0$  and lie on the external boundary.

StrAFE implements additional wrapper functions around `SubDomain` to further streamline the boundary marking process. Namely, the StrAFE classes `DirichletCondition` and `NeumannCondition` can be initialised with an index to the function vector  $\vec{u}$  referring to the function to which it should be prescribed (in accordance with the indexing scheme of Section 5.5), a user-defined boundary marker function, and a boundary expression. When passed to the main solver environment (as a `list`, using `.set_dirichlet_conditions` and `.set_neumann_conditions`, respectively) these conditions are automatically sorted by type and append the corresponding boundary integrals to the weak form expression.

To streamline and simplify this process further, the additional classes `Wall` and `Electrode` have also been introduced in StrAFE. The former inherits from `NeumannCondition` and automatically prescribes the wall conditions as described by (5.24), (5.25), and (5.26) (if the LMEA is used) to the marked mesh nodes for the provided charge species (either by index or by species name). The `Wall` condition is also automatically applied by StrAFE to the outer surfaces of any solid subdomains declared in the simulation (though this can be overridden if necessary). The latter `Electrode` condition inherits from `DirichletCondition`, and allows the quick definition of an electrode boundary when provided with a value for voltage. The voltage can be passed as either a constant value or as a time-dependent function if desired. All `Electrode` boundaries also have the `Wall` boundary applied for charge fluxes by default, unless overridden. An example of setting these conditions is shown below, assuming that `hv_electrode`, `gnd_electrode`, and `surface` are `SubDomain` classes with the `.inside` method that indicate which mesh nodes are part of their boundary definitions. These could, for instance, represent an electrode pair and a dielectric surface.

```
1     prob = DriftDiffusionProblem()
2
3     d_bc_hve = Electrode(hv_electrode, 100e3) # 100 kV on HV electrode
4     d_bc_gnd = Electrode(gnd_electrode, 0.0) # 0 kV on GND electrode
5     n_bc_sym = Wall(surface, 'electron') # Wall conditions for electrons
6
7     # Declare conditions to solver environment
8     prob.set_dirichlet_conditions([d_bc_hve, d_bc_gnd])
```

```
9 prob.set_neumann_conditions([n_bc_sym])
```

Marker functions passed to the `SubDomain` class are similarly used to declare solid subdomains. The StrAFE class `SolidSubDomain` can be initialised with a marker function (in this case, marking mesh *cells* instead of nodes for boundary conditions) alongside a value of relative permittivity. Once passed to the solver environment, automatic assignment of the permittivity and splitting the weak form integral following (5.39) is performed. By default, accumulation of surface charge is considered and  $\vec{u}$  is adjusted accordingly with (5.31) and the condition (5.30) is added to the weak form. The external boundaries of all  $\Omega_s$  are computed and marked automatically based on mesh connectivity data.

## 5.7.2 Automation of Form Generation and System Assembly

### 5.7.2.1 Representation of Functions

In StrAFE, all functions are represented using the FEniCS-provided `Function` class which can be instantiated given an appropriate function space. The exact nature of the function space is determined by the user's choice of basis function and element order (set from `.set_global_element` and `.set_global_element_order`, respectively). By default, linear Lagrange elements are used, however, a general function belonging to a space  $V$  is instantiated in the format

```
1 V = FunctionSpace(mesh, element, element_degree)
2 f = Function(V)
```

where `f` is a function which stores a single scalar value for each node in the `mesh`. To represent the main function vector,  $\vec{u}$ , of (5.32), a vector function space of dimension  $p + 1$  is necessary, which is constructed by defining a `VectorElement` with the appropriate number of dimensions such that

```
1 element = VectorElement(element, mesh.ufl_cell(), element_degree, dim)
2 N = FunctionSpace(mesh, element)
3 u = Function(N)
```

where `dim` is determined beforehand and is equal to  $p + 1$  in accordance with the rules in Section 5.5. For vector fields such as the electric field, three dimensional vector function spaces are automatically generated on initial problem setup. Individual components of  $\vec{u}$  may be accessed by calling the `.split` method followed by indexing (again using the scheme of Section 5.5) as illustrated below:

```
1 u_s = u.split()
2 phi = u_s[0] # This returns the function for the potential field
3 n_e = u_s[1] # This returns the function for the electron density
```

### 5.7.2.2 Automated Weak Form Generation

Based on the user configuration, StrAFE must translate the physical problem into a weak formulation in UFL format that is understandable by the FEniCS form compiler. At this stage, the following items are assumed to have been defined in the `DriftDiffusionProblem` class:

- A `mesh` object representing the domain.
- A `list` of `ChargedSpecies` providing charge and transport data for all tracked species.
- A `list` of `DirichletCondition`, which may include `Electrode` conditions.
- A `list` of `NeumannCondition`, which may include `Wall` conditions.
- Solver settings such as timestepping scheme, whether AMR or ATS are enabled, etc.

Upon calling `.solve()`, a `list_of_forms` is stored as an attribute to `DriftDiffusionProblem`, which is populated by parsing the user inputs and appending the UFL-constructed form expressions to this attribute. StrAFE automatically differentiates between volume integrals over the full domain, subdomains, external facets, or internal facets, and applies the correct integration measures. For example, the Poisson form (5.33) for the gaseous domain is included by

```

1     form = c.vacuum_permittivity()*dot(grad(u_[0]), grad(v[0]))*dx(0)
2         - q_source*v[0]*dx(0)
3
4     self.list_of_forms.append(form)      # Append the form to the list of forms

```

where FEniCS defines the integration measure `dx` for volumes, `ds` for external facets, and `dS` for internal facets. These may be followed by a bracketed index when subdomains are present, to limit the form to only apply within the identified mesh regions. For instance, the above example of `dx(0)` restricts integration to the subdomain marked with index 0, which exclusively identifies the gas domain  $\Omega_g$  in StrAFE. Upon the completion of form generation, `sum` is called on the `list_of_forms` and is stored as the attribute `nonlinear_variational_form`. Note that the form is reassembled each time AMR completes execution, as the form is intrinsically linked to the computational mesh which may have changed during mesh adaptation. The main solver loop described in Section 5.7.3 accesses the stored form to assemble and solve the system.

### 5.7.3 Main Solver Loop

The processes involved within the main solver loop may be visualised as Figure 5.13 and has a simple structure. Problem initialisation is performed only once during initial solver launch. This utilises the initial mesh  $\mathcal{M}_0$  to generate high-quality initial potential and field distributions,

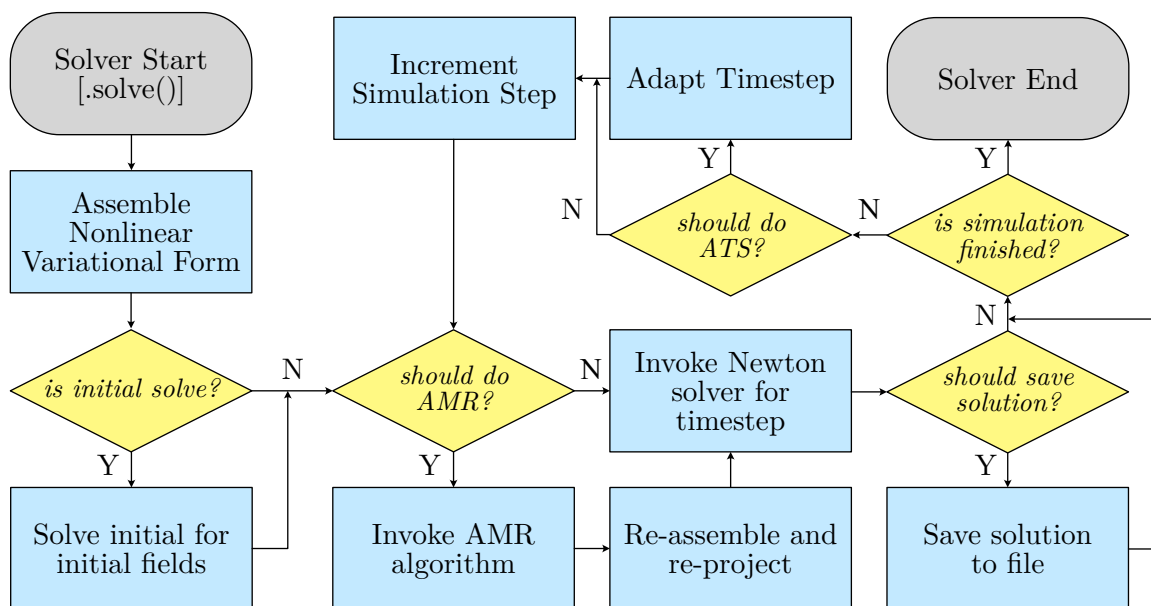


**Figure 5.13:** Flow diagram of the main solver time loop implemented in StrAFE.

from which the UFL forms may be defined (since they involve these field quantities within their definitions). StrAFE checks, at every time-step, whether AMR or ATS should be called based on the user settings. Solution output settings are also provided, which includes the options `save_path` and `save_interval`, defining the filepath and time interval separating solution outputs, respectively. As with FEniCS, StrAFE collates parallelised solution data and outputs as `.hdf5` and `.xdmf` file pairs, enclosing all mesh and function data from  $\vec{u}$  for each saved time-step. A separate file may be generated for the electric field with vector components separated into scalar fields, if desired. These may be visualised in any capable data visualisation packages, such as Paraview [97].

## 5.8 Code Verification and Comparison Studies

The present sections aims to present a number of code verification studies conducted using StrAFE. The purpose of these tests were to ensure the correctness of StrAFE’s code implementation. This is primarily conducted via comparison to results available in the literature that were simulated using either commercial software or other custom codes. Evaluation of the system assembly code from FEniCS and detailed numerical properties of the utilised PETSc solvers is out of the scope of this work. Besides, since these are both frameworks of considerable maturity, benchmarking exercises have been thoroughly conducted elsewhere [59, 98, 99]. The concern lies solely with evaluating the plasma modelling components of StrAFE which have been subsequently developed

in this work and described in this chapter.

Each verification case study aimed to test a different aspect implemented in StrAFE. All cases were performed using triangular elements with linear Lagrange basis functions. Simulations were executed on either 16-core (AMD Ryzen 9 5950X) or 18-core (Intel Xeon W-2295) workstation computers equipped with 64 GB memory, running inside a Docker [100] container, and with MPI enabled. It is remarked that StrAFE has been developed with the ability to perform full 3D simulations. However, verification case studies were restricted to 2D cases due to their far greater prevalence and availability in literature, providing a strong basis for comparison. At the time of writing, full 3D simulations have only recently become possible, and it would be difficult to evaluate code accuracy based on limited data. It is, however, of great interest to conduct 3D simulations using StrAFE in future investigations and to evaluate StrAFE's capability in HPC environments.

### 5.8.1 Axisymmetric Positive Streamer

This first case aims to conduct an evaluation of StrAFE based on the comparison study of Bagheri *et al.* [95]. At the time of writing, standard methods to verify non-thermal plasma modelling codes remain under development. That is, no standardised test problems exist to benchmark and evaluate codes of this nature, since the feasibility of efficient streamer modelling remains a relatively recent development. The work of Bagheri *et al.* [95] is the first work that attempted to address this, by conducting a comparison study in collaboration with several international research groups using a test simulation with defined parameters. All output data collated in [95] was also made openly available to facilitate comparison by other authors. Comparison of the simulation results computed by StrAFE to the various datasets available through [95] was therefore prioritised.

#### 5.8.1.1 Problem Configuration

Of the three test problems described in [95], the “Case 3” study was recreated, which incorporated a cylindrically-symmetric positive streamer initiated from an initial Gaussian distribution of positive ions, and with the inclusion of photoionisation using the Helmholtz approach (5.20). This case was chosen specifically for its inclusion of photoionisation, allowing the implementation of this process in StrAFE to be verified. Figure 5.14 shows a diagram of the computational domain and boundary conditions, based on the details provided in [95]. The mathematical model follows that which was described in [95], which is given in summary form here. The minimal plasma

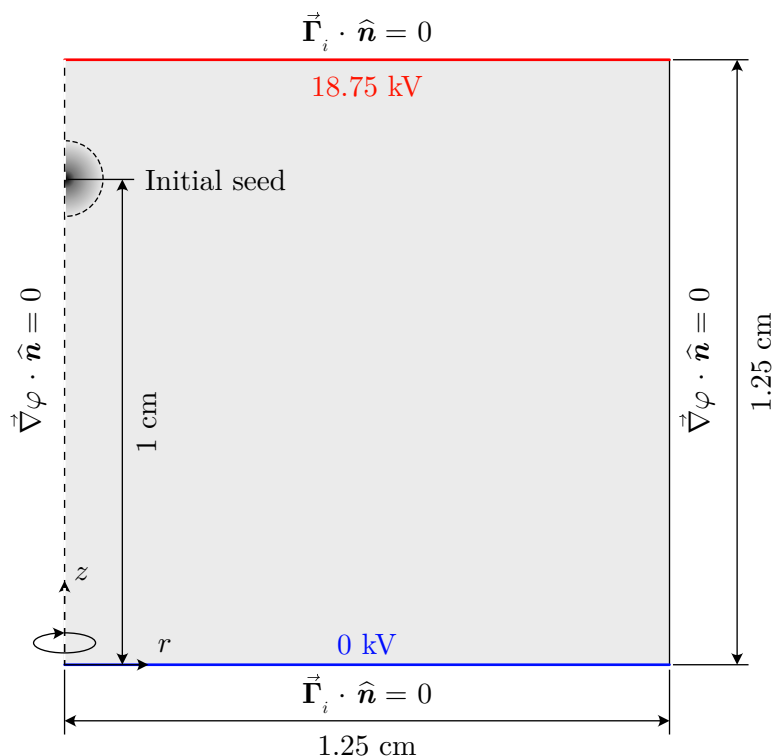


**Figure 5.14:** Cylindrically-symmetric domain used for the positive streamer comparison study of [95] labelled with dimensions, boundary conditions, and initial Gaussian seed placement.

model including only electrons and generic positive ions was used under the LFA. The general ADR equation (5.12) therefore reduces to the coupled pair of particle continuity equations

$$\begin{aligned} \frac{\partial n_e}{\partial t} + \vec{\nabla} \cdot \vec{\Gamma}_e &= \bar{\alpha} \mu_e n_e |\vec{\nabla} \varphi| + S_{\text{ph}}, \\ \frac{\partial n_+}{\partial t} + \vec{\nabla} \cdot \vec{\Gamma}_+ &= \bar{\alpha} \mu_e n_e |\vec{\nabla} \varphi| + S_{\text{ph}}, \end{aligned} \quad (5.44)$$

where  $S_{\text{ph}}$  is given by the solution of the Helmholtz equation (5.20) and with the Poisson equation source term determined by the sum of only two charged species

$$\vec{\nabla}^2 \varphi = -\frac{q_e (n_+ - n_e)}{\epsilon_0}. \quad (5.45)$$

An initial density of positive ions in the form (5.43) was placed at  $z_0 = 1$  cm, which acted to enhance the uniform background field and initiate a cathode-directed streamer. This initial seed possessed a peak density of  $n_0 = 5 \times 10^{18} \text{ m}^{-3}$  and an initial spread of  $s_0 = 0.4$  mm, placed in the domain alongside a uniform background density of both  $n_e$  and  $n_i$  of  $10^9 \text{ m}^{-3}$ . Townsend

coefficients for air were used according to the empirical formulae provided in [95], repeated as (5.46) for completeness,

$$\begin{aligned}\mu_e &= 2.398|\vec{E}|^{-0.26} [\text{m}^2 \text{V}^{-1} \text{s}^{-1}], \\ D_e &= 4.3628 \times 10^{-3}|\vec{E}|^{0.22} [\text{m}^2/\text{s}], \\ \bar{\alpha} &= \left( 1.1944 \times 10^6 + \frac{4.3666 \times 10^{26}}{|\vec{E}|^3} \right) \exp\left(\frac{-2.73 \times 10^7}{|\vec{E}|}\right) - 340.75 [\text{m}^{-1}].\end{aligned}\quad (5.46)$$

Positive ions were considered non-diffusive and immobile over the course of the  $\sim 15$  ns simulation. Parameters controlling the photoionisation process were also given in [95], originally taken from Bourdon *et al.* [78] for the three-term Helmholtz model and provided in Table 5.2, with the factor  $\xi \frac{\nu_u}{\nu_i}$  assumed constant at 0.075 and the pressures  $p_{\text{O}_2} = 150$  Torr,  $p_q = 40$  mbar. All other miscellaneous computational settings are provided in Appendix B.3.

### 5.8.1.2 Simulation Results

Figure 5.15 encloses colour plots showing the time-evolution of the electron density and electric field distribution at various timesteps of the simulation. In Figures 5.15(c) and 5.15(d), a quantitative comparison of the streamer length and maximum electric field at the streamer head is shown, comparing the predictions of StrAFE to other groups involved in [95]. Additional information regarding the software and numerical aspects used by all other groups is included as Table 5.3. Considering the many potential differences in numerical implementation, mesh size, timestep, discretisation order, etc., between each code; StrAFE compares well to all other groups. The predictions computed by StrAFE lie within a reasonable margin when compared to other code implementations, many which are considered state-of-the-art streamer modelling platforms. In both Figure 5.15(c) and 5.15(d), the characteristics of the streamer modelled using StrAFE is most similar to group “DE”, whose simulations were computed using the commercially-available multiphysics software COMSOL (using MCPlas as in Table 5.1 [1]). This is perhaps unsurprising, given that COMSOL also employs FEM with a similar selection of linear solvers as available in StrAFE. The description provided in [95] by group “DE” indicated that linear elements and

**Table 5.2:** Photoionisation fitting parameters for 3-term Helmholtz model in air [95].

$j$	$A_j, \text{cm}^{-2} \text{Torr}^{-2}$	$\lambda_j, \text{cm}^{-1} \text{Torr}^{-1}$
1	$1.986 \times 10^{-4}$	0.0553
2	0.0051	0.1460
3	0.4886	0.8900

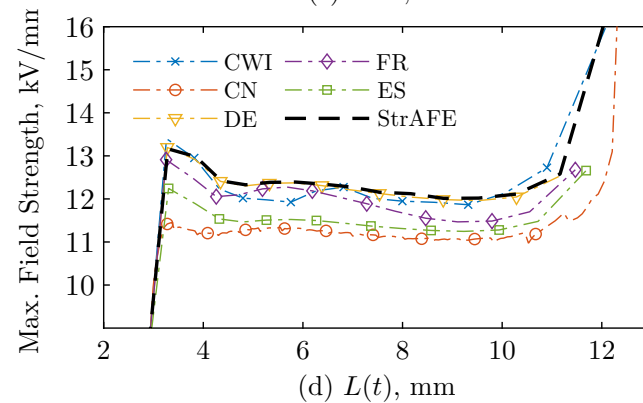
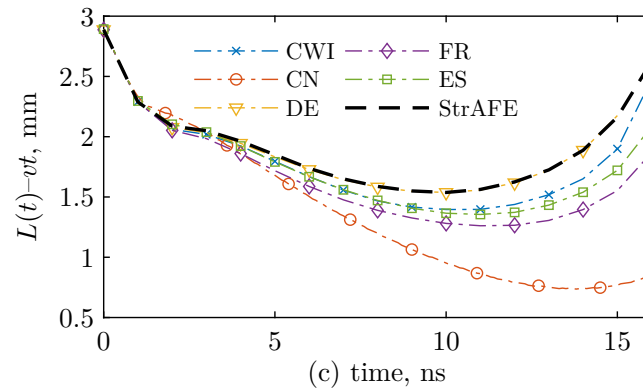
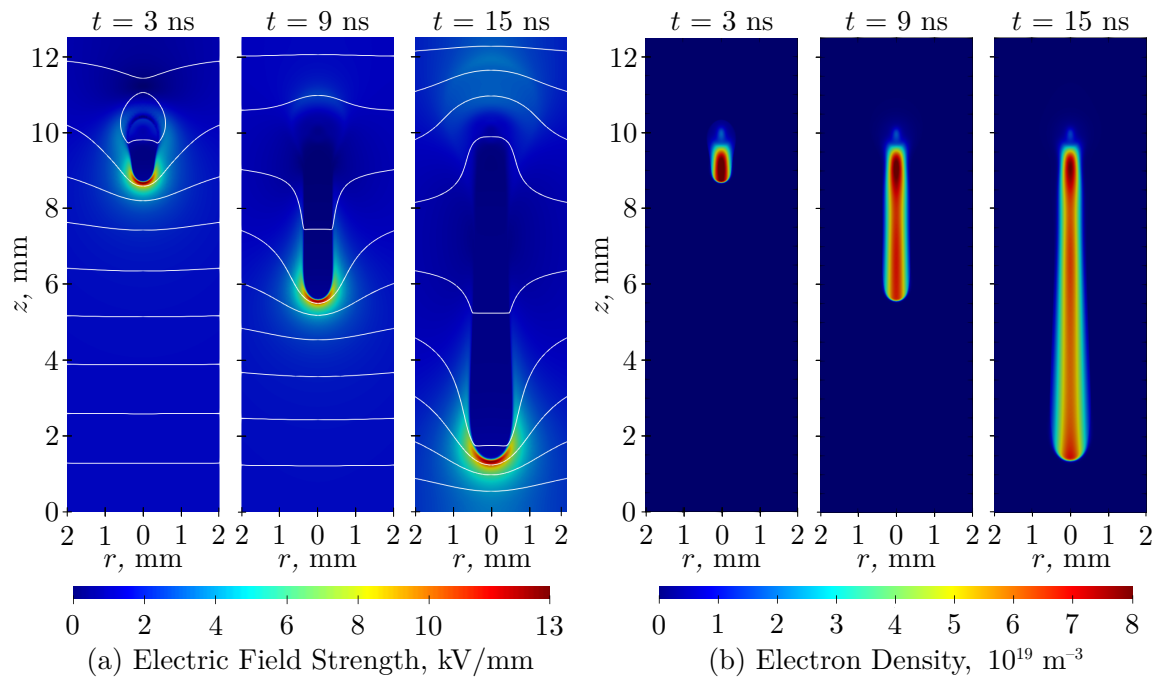


**Figure 5.15:** Resulting positive streamer as computed using StrAFE. Colour plots of the (a) electric field strength (equipotentials spaced by 2 kV), (b) electron density at  $t = 3, 9,$  and  $15$  ns. Comparison of (c) streamer length over time, (d) max. electric field vs. streamer length with other groups' data from [95]. Images (c) and (d) adapted from [60] under CC BY 4.0.

**Table 5.3:** Comparison of relevant simulation settings to data from [95]. Table reproduced with permission from [101], © IEEE 2021.

	CWI	ES	FR	CN	DE	<b>StrAFE</b>
FV/FE	FV	FV	FV	FE (COMSOL)	FE (COMSOL)	FE
Unstructured Grid				✓	✓	✓
Spatial Order	2	2	2	1	1	1
Temporal Order	2	2	2	1–2	1–5	2
Mesh refinement	✓	✓	✓	✓	✓	✓
AMR	✓	✓		✓		✓
Parallel	✓		✓	✓	✓	✓
Tabulated Data	✓	✓				
Min. grid, $\mu\text{m}$	3.0	3.9	6.0	2.0	4.1	2.2
Max. grid, $\mu\text{m}$				8.0	5.0	
Max. $N$ -cells, $10^5$	0.76	20	2.9	7.2	7.6	7.8
Time step	dyn.	1.0 ps	dyn.	dyn.	dyn.	dyn.
CPU Cores	4	1	1	4	6	16
Run time	< 5 min	72 h	34 min	26 h	42 h	4 h

adaptive-timestepping were also used, mirroring the methods used with StrAFE. Given these similarities, it would be reasonable to assume that these two methods would provide similar results. Thus, the results presented in Figure 5.15 provided confidence that the implementation of the fluid model in StrAFE would demonstrate a comparable level of accuracy to state-of-the-art custom codes and to well-established commercial software.

## 5.8.2 Positive Streamer Attachment to Solid Dielectric

As a second verification case study, the implementation of solid dielectric subdomains as described in Section 5.5, was evaluated. To do so, various results from the study [91], which focused on positive surface streamers, were recreated using StrAFE. This also aimed to demonstrate the effective usage of the mesh pre-refinement routines described in Section 5.6.3.1 to provide increased mesh density near dielectric surfaces to support the resolution of field and density gradients.

### 5.8.2.1 Problem Configuration

The main characteristics of the original work included the initiation of a positive streamer from a charged seed, which propagates briefly through air alone before attaching to a nearby solid dielectric surface, due to electrostatic forces. A number of parameters affecting the streamer development were systematically investigated in [91], including the offset distance of the seed

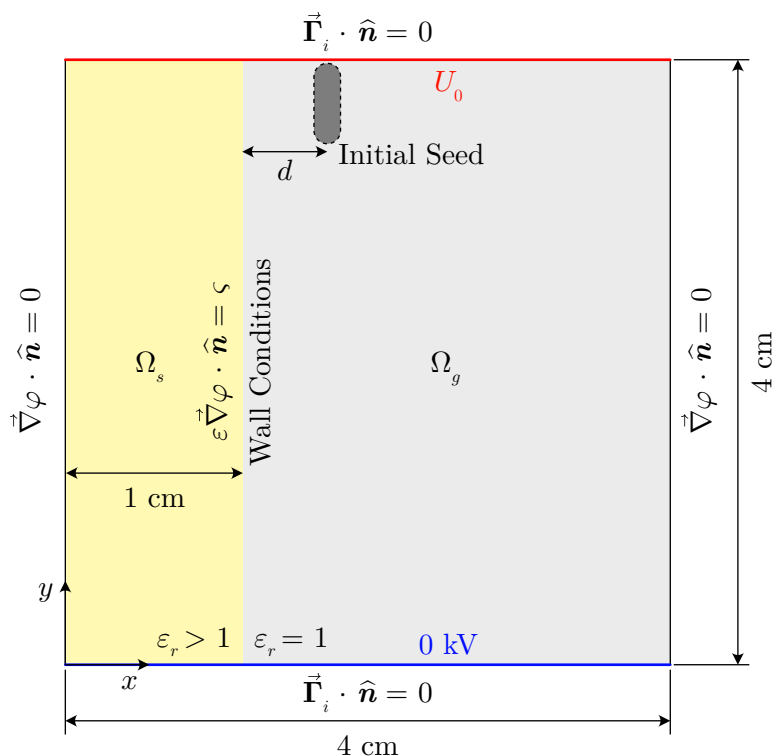


**Figure 5.16:** 2D domain used for the study of streamer attachment to solid dielectric surfaces from [91] labelled with dimensions, boundary conditions, and initial capsule seed placement.  $\Omega_g$  and  $\Omega_s$  indicate the gas and solid domains as per (5.38), respectively. Wall conditions refer to (5.24)–(5.26).

away from the surface, the permittivity of the surface, and the applied voltage magnitude. Several results and tendencies were recreated using StrAFE and are presented here. Figure 5.16 shows the problem domain and boundary conditions as described in [91], including the definition of the initial capsule-like seed (and which is implemented as a default in StrAFE, using the **Capsule** initial condition class). Three species were included in this case: electrons ( $e$ ), positive ions ( $+$ ), and negative ions ( $-$ ). For brevity, the three density balance equations are not repeated here. In a change from the original work, electron-ion and ion-ion recombination processes were additionally included using constant rates alongside the standard Townsend coefficients, such that the source terms for each respective charge were

$$\begin{aligned}
 S_e &= n_e \mu_e (\alpha - \eta) |\vec{\nabla} \varphi| + S_{\text{ph}} - n_e n_+ \beta_{e+}, \\
 S_+ &= n_e \mu_e |\vec{\nabla} \varphi| + S_{\text{ph}} - n_e n_+ \beta_{e+} - n_+ n_- \beta_{+-}, \\
 S_- &= n_e \mu_e \eta |\vec{\nabla} \varphi| - n_+ n_- \beta_{+-},
 \end{aligned} \tag{5.47}$$

where  $\beta$  are recombination coefficients with subscript “e+” for electron-position ion, “e-” for electron-negative ion, and “+-” for ion-ion recombination. All three recombination rates were assumed constant at  $2 \times 10^{-13} \text{ m}^3/\text{s}$  [102], while ions were once again treated as non-diffusive, but assumed ionic mobilities of  $\mu_+, \mu_- = 3 \times 10^{-4} \text{ m}^2 \text{ V}^{-1} \text{ s}^{-1}$  in following [91]. Electron transport parameters were defined in functional form following Section 5.7.1.3 using analytical fitting functions from Liu *et al.* [84] for air at standard temperature and pressure (STP) conditions. Note that [91] also conducted analyses on the effects of secondary emission (including photoemission) from the surface. No attempt to recreate these results were conducted using StrAFE, for three reasons: (i) simulation studies conducted throughout the present work were focused more on system topology and the effects of fast-rising voltages, rather than secondary emission; (ii) for practical engineering purposes, coefficients characterising secondary emission (whether from electron or photon bombardment) are not well known nor can be easily determined; and (iii) the conclusions of the original study [91] indicated that the effects of secondary and photoemission were both essentially trivial, at least for the conditions used here. It would have therefore been difficult to compare simulation results, since it would not be clear whether differences were arisen from varying the secondary emission parameter, or from differences in modelling and implementation. It is also noted that the full output data of [91] was not made openly available, thus, the comparisons made here are either qualitative in nature based on general streamer morphology, or quantitative only in comparing parameters based on approximate ranges or values. The focus is placed therefore on quantities which were directly reported in [91], namely, maximum electric field strength and propagation velocity.

For all simulations relating to this case study, AMR was utilised on top of mesh pre-refinement, which provided two initial refinement passes along the location of the dielectric surface ( $x = 10 \text{ mm}$ ). Other numerical settings have are included within Appendix B.3.

### 5.8.2.2 Effects of Seed Position

In a first set of simulations, the distance,  $d$ , of the initial seed away from the dielectric surface was varied, for values of  $d = 0.5, 1.0, \text{ and } 2.0 \text{ mm}$ . Figure 5.17 encloses colour plots of the electron density at  $t = 20 \text{ ns}$  for the three distances used, showing the propagating streamers developing towards the dielectric surface of  $\varepsilon_r = 2$ . The further away the initiating seed, the farther the streamer travelled through the gas before contacting the surface. Plots of the maximum electric field magnitudes and instantaneous streamer velocities over time are included within Figure 5.17(b) and (c).

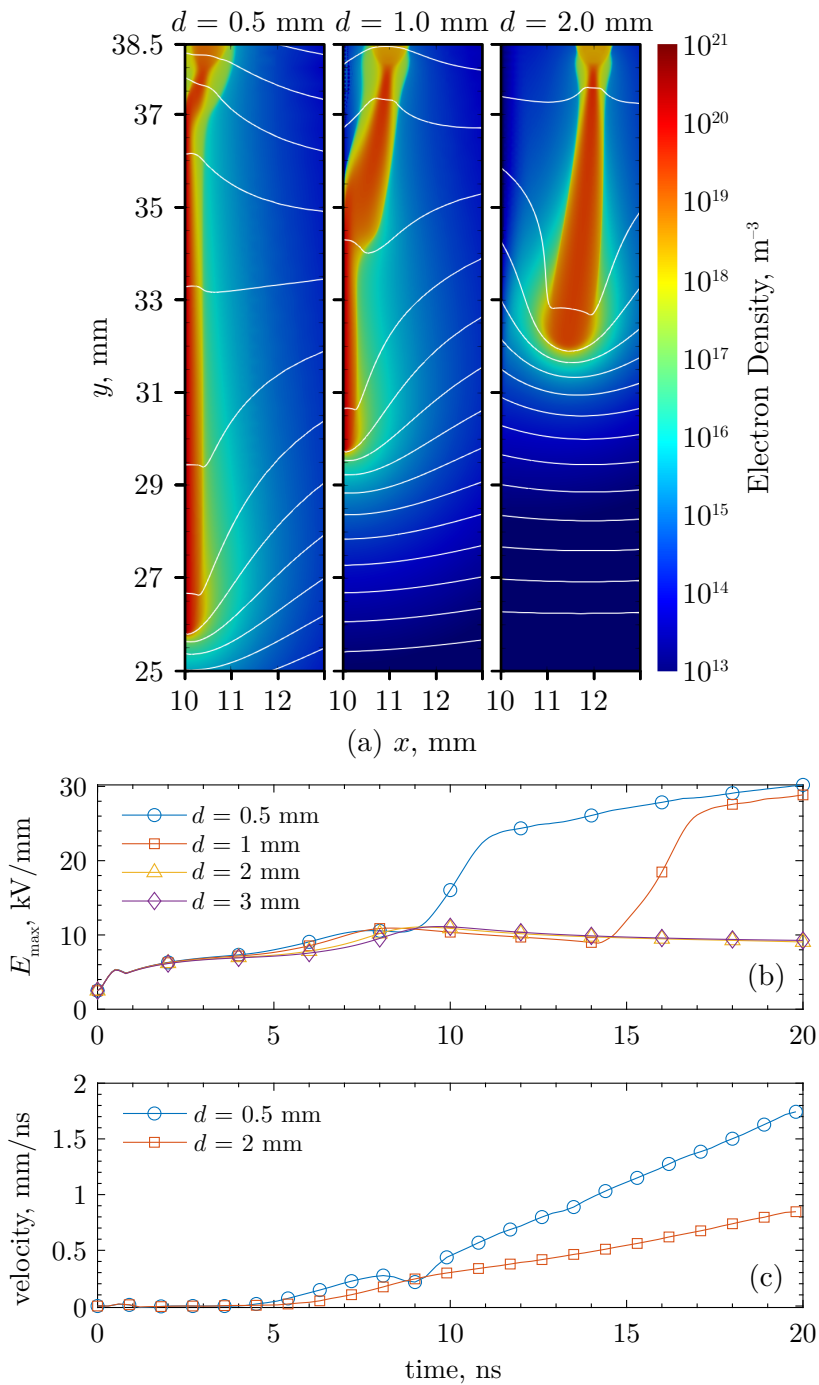


**Figure 5.17:** StrAFE results of the streamer attachment study at different seed offset distances,  $d$ . Surface located at  $x = 10$  mm. (a) Colour plot of the developed electron density at 20 ns for cases  $d = 0.5$ , 1.0, and 2.0 mm (equipotential lines spaced by 2 kV), (b) maximum electric field over time for  $d = 0.5$ , 1.0, 2.0, and 3.0 mm, (c) propagation velocity for a surface-attaching streamer ( $d = 0.5$  mm) and for one that does not attach ( $d = 2.0$  mm). Velocity for  $d = 3.0$  mm not shown since it did not attach and is almost identical to the  $d = 2.0$  mm case. Images adapted with permission from [103], © 2021 IEEE.

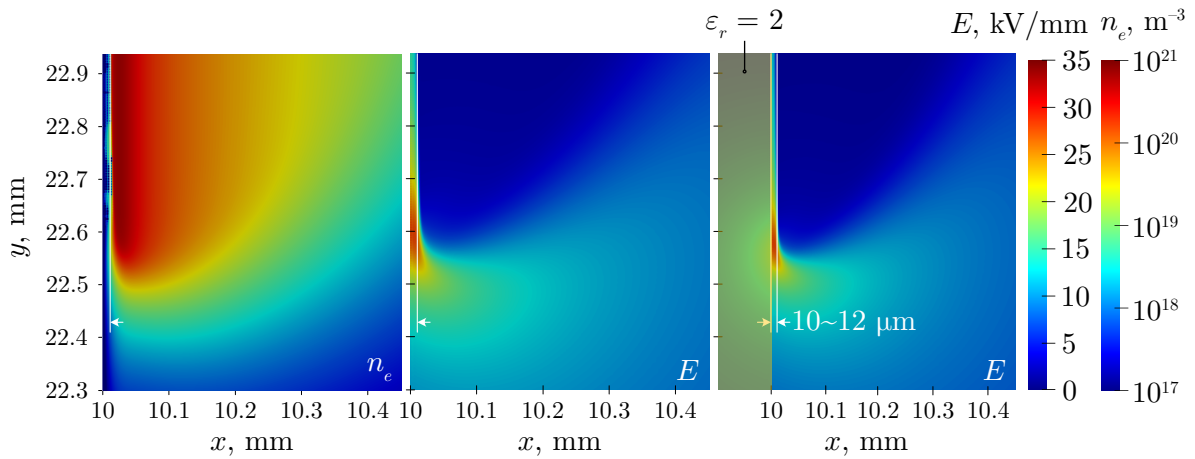


**Figure 5.18:** Magnified image of surface streamer head as it propagates along the solid dielectric, showing the approximate thickness of the dielectric sheath with low electron density. (left) electron density, (middle) electric field magnitude, (right) electric field magnitude, but shifted in the  $x$  direction to partially show the solid domain.

Agreement in terms of general propagation characteristics and streamer morphology was found when compared to [91]. This includes the sudden increase in maximum electric field as the streamer contacts the solid dielectric, marking its transition to a surface streamer. The maximum field value then becomes located within the thin sheath between the streamer channel and the solid surface, nearest the streamer head. At this moment, the streamer also accelerates at a greater rate, driven by the intense ionisation activity occurring at the streamer head resulting from the strongly enhanced electric field. Reaching velocities in the range of 0.5 to 2 mm/ns over the duration of the surface streamer’s propagation; with maximum electric field strengths around 10 kV/mm at inception, rising to around 30 kV/mm by 20 ns, these values are in quantitative agreement with those reported in [91]. Streamers in [91] achieve a slightly higher value of maximum electric field, though this can be explained due to the inclusion of recombination rates used in this work. The addition of these processes tend to reduce the charge densities, resulting in a reduction of the overall developed electric fields, and consequently, reduction in the propagation velocity. As such, streamers in [91] have travelled a few millimetres farther by  $t = 20$  ns than those simulated here.

Figure 5.18 provides magnified colour plots of the streamer head at  $t = 20$  ns for the  $d = 1.0$  mm case, showing the location of the maximum electric field developed within the surface sheath. The sheath distance was measured to be around 10 to 12  $\mu\text{m}$  in thickness, also in approximate agreement with [91], and was adequately resolved using the pre-refinement and AMR routines implemented in StrAFE.

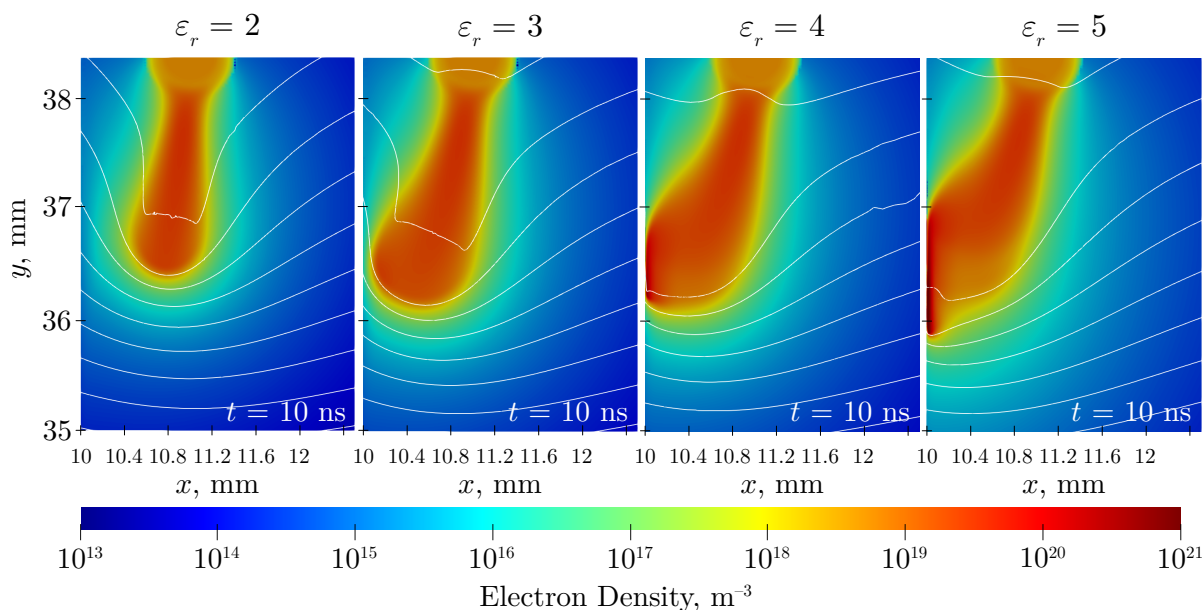


**Figure 5.19:** Magnified image of the initial stages of the streamer development at  $t = 10$  ns with  $d = 0.5$  mm and the solid surface relative permittivity  $\epsilon_r = 2, 3, 4,$  and  $5$ . Equipotential lines are spaced by 2 kV.

### 5.8.2.3 Effects of Relative Permittivity

A second set of simulations aimed to recreate the effects of different values of relative permittivity assigned to the solid subdomain. As in [91], values of  $\epsilon_r = 2, 3, 4,$  and  $5$  were studied, where the work of [91] concluded that higher permittivity surfaces resulted in a stronger attraction of the streamer towards the dielectric surface; facilitating a more rapid transition from gas to surface streamer. Using StrAFE, the initiation stage of streamers placed at  $d = 1.0$  mm away from the surface for different relative permittivity values is shown in Figure 5.19. All four plots of Figure 5.19 have been recorded at  $t = 10$  ns, showing faster attachment and transition to a surface streamer for higher permittivity values, in support of the conclusions of [91]. Figure 5.20 shows colour plots of the electron density at  $t = 20$  ns for  $\epsilon_r = 2, 3,$  and  $4$ , alongside graphs of maximum electric field strengths and the propagation velocities. Once again, quantitative agreement between the electric field strengths and propagation velocities was found, including the tendencies for increased maximum field and velocity for greater values of permittivity. Note that the initial reduction in velocity at the moment of surface attachment is caused by the method used to calculate velocity, which tracks the location of the maximum  $y$  component of the electric field. At the moment of attachment, the redistribution of the field momentarily moves the peak field from the tip of the streamer head into the (developing) surface sheath, therefore, it is manifested as a momentary decrease in velocity. This is a feature which was also found in [91].

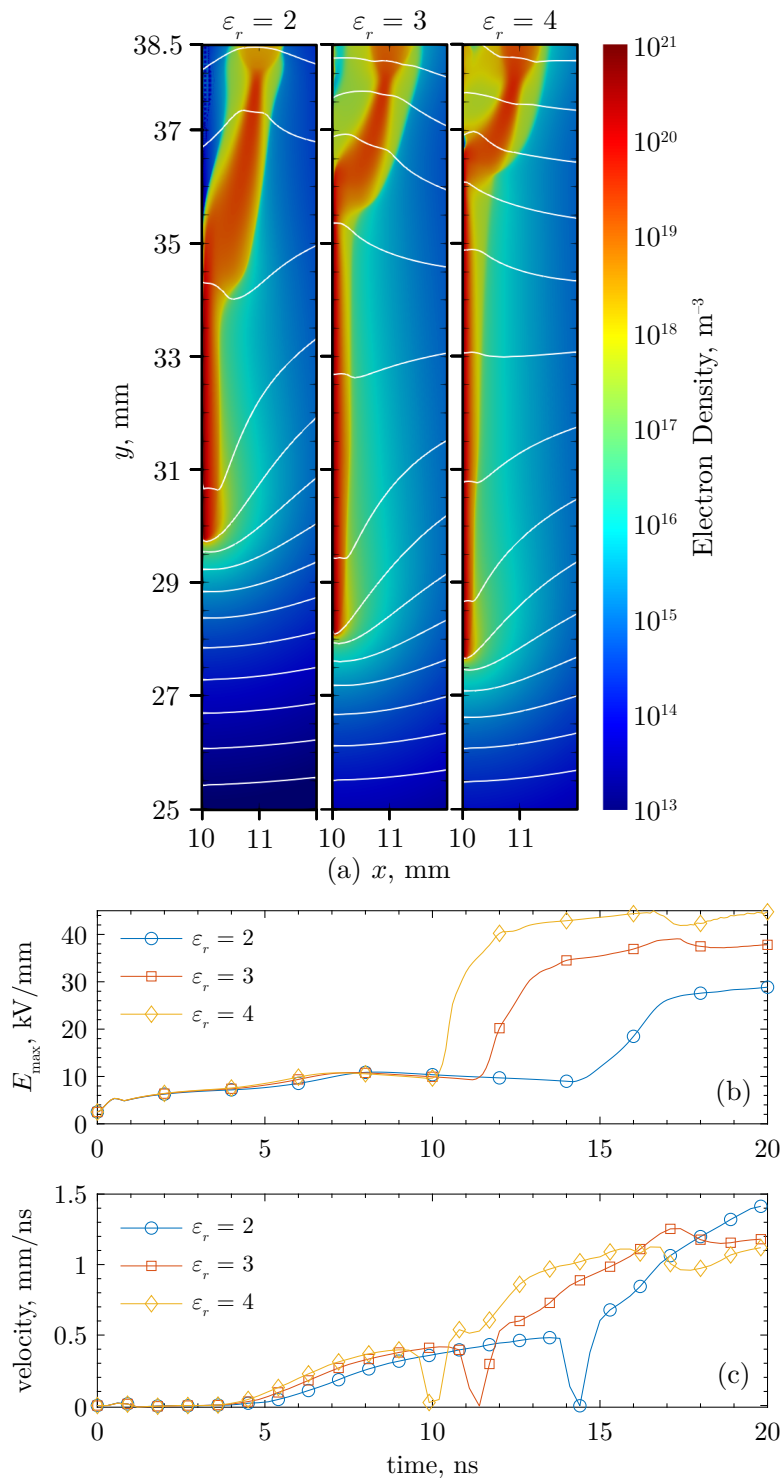


**Figure 5.20:** StrAFE results of the streamer attachment study at different surface relative permittivities,  $\epsilon_r$ . Surface located at  $x = 10$  mm. (a) Colour plot of the developed electron density at 20 ns (equipotential lines spaced by 2 kV), (b) maximum electric field over time, (c) propagation velocity for a surface-attaching streamer for cases  $\epsilon_r = 2, 3$ , and 4. Images adapted with permission from [103], © 2021 IEEE.

Beyond around  $t = 15$  ns, streamer velocities produced by StrAFE appear to fluctuate for higher values of permittivity, which may be due to numerical artefacts or insufficient mesh density, since higher permittivity values also tended to increase the charge and field gradients near the surface. However, this is not entirely clear, since propagation velocities beyond  $y = 33$  mm (14 ns) were not shown in the original work [91] so there is no basis for comparison. However, since the characteristics up to the point with various values of permittivity were successfully recreated, the comparison was considered satisfactory for code verification purposes.

#### 5.8.2.4 Effects of Applied Voltage

In a third, and final, set of simulations for this case study, the energising voltage,  $U_0$ , was varied for  $U_0 = 90, 95, 100,$  and  $105$  kV. These were compared to [91] where the effects of the background electric field were studied using  $E = 2.3, 2.5,$  and  $2.8$  kV/mm. Figure 5.21 provides the same set of electron density colour plots, maximum electric field over time, and propagation velocity over time for this case study. Agreement was once again found between the simulations conducted using StrAFE to those in [91], with an increased background field resulting in a more rapid streamer development during the gas stage, leading to earlier surface attachment. In an expected manner, the streamer also propagates farther and attains a higher velocity after 20 ns due to the greater intensity of ionisation activity induced by higher background fields. Note that the increased acceleration for  $U_0 = 105$  kV (beyond 15 ns) results from additional field enhancement due to the proximity of the streamer head to the cathode, since it had almost bridged the full electrode gap within the simulated time. Away from the electrodes, however, the surface streamers appear to accelerate at similar rates regardless of the applied voltage, at least for the range simulated here.

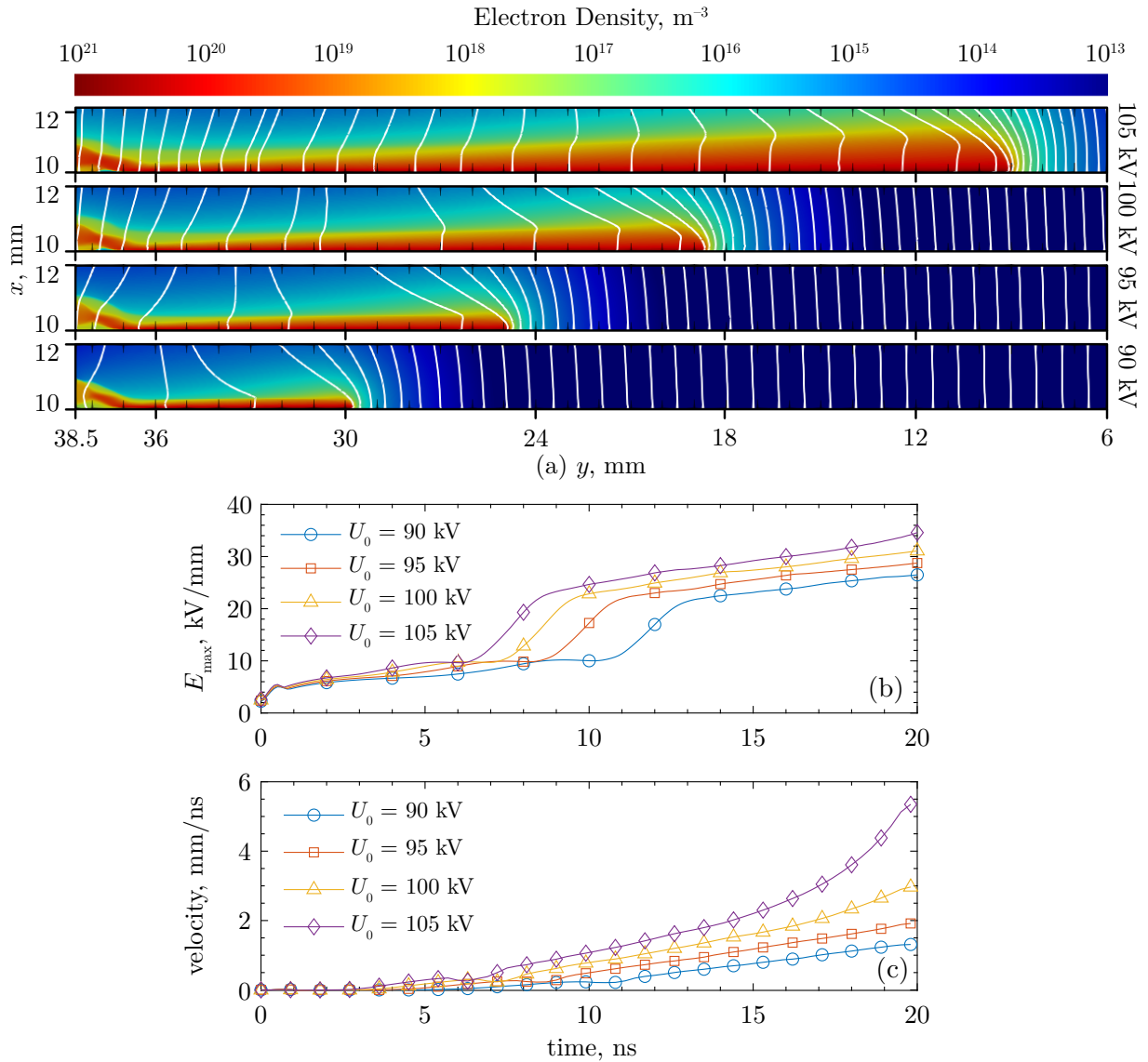


**Figure 5.21:** StrAFE results of the streamer attachment study at different applied voltages,  $U_0$ . Surface located at  $x = 10$  mm. (a) Colour plot of the developed electron density at 20 ns (equipotential lines spaced by 2 kV), (b) maximum electric field over time, (c) propagation velocity for a surface-attaching streamer for cases  $U_0 = 90, 95, 100,$  and  $105$  kV. Image reproduced with permission from [103], © 2021 IEEE.

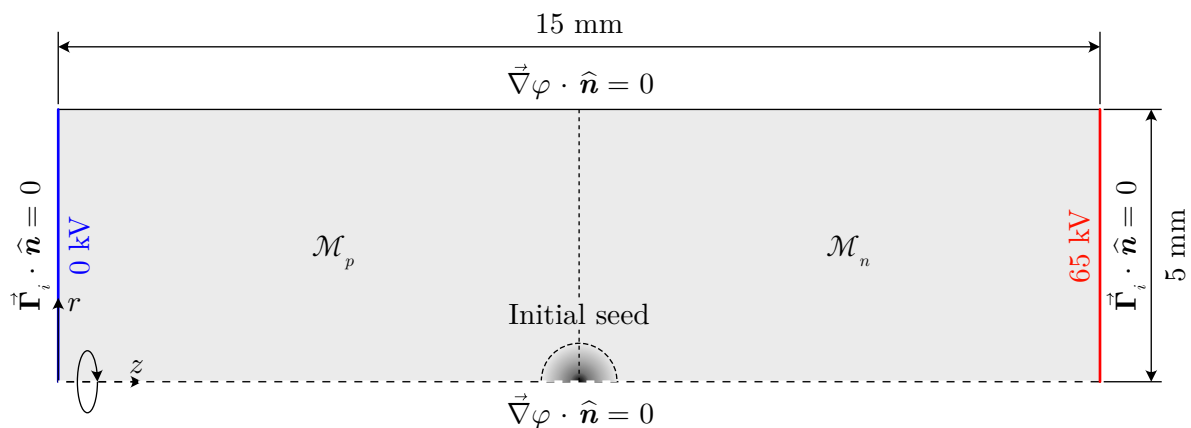


**Figure 5.22:** Cylindrically-symmetric domain used for the double-headed streamer study from [104] labelled with dimensions, boundary conditions, and initial Gaussian seed placement.  $\mathcal{M}_p$  and  $\mathcal{M}_n$  indicate the separate regions used for partitioned AMR.

### 5.8.3 Double-headed Streamers

Two major features included in StrAFE for greater modelling fidelity was evaluated in a third verification case study. Here, the plasma chemistry input module as described in Section 5.4.2 and Section 5.7.1.3 was tested, using a simulation problem that was specifically chosen to also take advantage of the refinement partitioning feature as in Section 5.6.3.2. The simulation concerns so-called *double-headed* streamers [104–106], referring to the near-simultaneous inception and propagation of positive and negative streamers from a common point.

#### 5.8.3.1 Problem Configuration

The case study conducted here follows similar parameters to that of [104], where the authors studied the inception of double-headed streamers in uniform background fields with magnitudes greater than the critical field in air. These types of discharge are relevant to, for example, geophysical phenomena occurring in the upper atmosphere [105]. Figure 5.22 shows the simple axisymmetric geometry and boundary conditions used, which incorporated an initial Gaussian charge patch of  $\text{N}_2^+$  ions and electrons centred along the line of symmetry with  $n_{\text{N}_2^+} = n_e = 5 \times 10^{18} \text{ m}^{-3}$  and  $s_0 = 0.2 \text{ mm}$ , with a uniform background density of the same charges at  $10^9 \text{ m}^{-3}$ . The LMEA was additionally used in this simulation in contrast to [104], however, either the LFA or LMEA were expected to provide similar results in this configuration since there was no violation of any of the validity conditions discussed in Section 5.4.4.

Instead of using the effective ionisation rate as done in Sections 5.8.1 and 5.8.2, the plasma chemistry module according to Section 5.7.1.3 was used including the reactions listed in Table

**Table 5.4:** Plasma chemical reactions used in example simulations for 80/20 air. Notation  $f(\bar{\epsilon})$  means that the reaction rate was an empirical function of the local electron energy. Chemical symbol M represents  $O_2$  or  $N_2$ . Data from the BOLSIG+ solver [85] was computed using the Phelps' database [107–109].

R	Description	Reaction	Rate	Unit	Ref.
$R_1$	Impact Ionisation (15.6 eV)	$e^- + N_2 \longrightarrow N_2^+ + 2e^-$	BOLSIG+	$m^3/s$	[85]
$R_2$	Impact Ionisation (18.8 eV)	$e^- + N_2 \longrightarrow N_2^+ + 2e^-$	BOLSIG+	$m^3/s$	[85]
$R_3$	Impact Ionisation	$e^- + O_2 \longrightarrow O_2^+ + 2e^-$	BOLSIG+	$m^3/s$	[85]
$R_4$	Attachment	$e^- + 2O_2 \longrightarrow O_2^- + O_2$	$f(\bar{\epsilon})$	$m^6/s$	[110]
$R_5$	Rapid $O_2^+$ Production	$N_2^+ + N_2 + M \longrightarrow N_4^+ + M$	$5 \times 10^{-41}$	$m^6/s$	[110]
$R_6$	Rapid $O_2^+$ Production	$N_4^+ + O_2 \longrightarrow O_2^+ + 2N_2$	$2.5 \times 10^{-16}$	$m^3/s$	[110]
$R_7$	Rapid $O_2^+$ Production	$N_2^+ + O_2 \longrightarrow O_2^+ + N_2$	$6 \times 10^{-17}$	$m^3/s$	[110]
$R_8$	$O_2^+$ to $O_4^+$ Conversion	$O_2^+ + 2N_2 \longrightarrow O_2^+N_2 + N_2$	$9 \times 10^{-43}$	$m^6/s$	[110]
$R_9$	$O_2^+$ to $O_4^+$ Conversion	$O_2^+N_2 + N_2 \longrightarrow O_2^+ + 2N_2$	$4.3 \times 10^{-16}$	$m^3/s$	[110]
$R_{10}$	$O_2^+$ to $O_4^+$ Conversion	$O_2^+N_2 + O_2 \longrightarrow O_4^+N_2$	$1 \times 10^{-15}$	$m^3/s$	[110]
$R_{11}$	$O_2^+$ to $O_4^+$ Conversion	$O_2^+ + O_2 + M \longrightarrow O_4^+ + M$	$2.4 \times 10^{-42}$	$m^6/s$	[110]
$R_{12}$	Electron-ion Recombination	$e^- + O_4^+ \longrightarrow 2O_2$	$f(\bar{\epsilon})$	$m^3/s$	[110]
$R_{13}$	Electron-ion Recombination	$e^- + O_2^+ \longrightarrow 2O$	$f(\bar{\epsilon})$	$m^3/s$	[110]
$R_{14}$	Ion-ion Recombination	$O_2^- + O_4^+ \longrightarrow 3O_2$	$1 \times 10^{-13}$	$m^3/s$	[110]
$R_{15}$	Ion-ion Recombination	$O_2^- + O_4^+ + M \longrightarrow 3O_2 + M$	$2 \times 10^{-37}$	$m^6/s$	[110]
$R_{16}$	Ion-ion Recombination	$O_2^- + O_2^+ + M \longrightarrow 2O_2 + M$	$2 \times 10^{-37}$	$m^6/s$	[110]
$R_{17}$	Excitation/Emission	$e^- + N_2 \longrightarrow e^- + N_2 + \gamma$	Zheleznyak.	–	[71]
$R_{18}$	Photoionisation	$\gamma + O_2 \longrightarrow e^- + O_2^+$	Zheleznyak.	–	[71]

5.4, which incorporated seven tracked species ( $e^-$ ,  $N_2^+$ ,  $O_2^+$ ,  $N_4^+$ ,  $O_4^+$ ,  $O_2^+N_2$ , and  $O_2^-$ ) involved in 18 reactions. Photoionisation was also included following [78] using the Helmholtz model with the same parameters as Table 5.2.

As there was *a priori* knowledge that simultaneous positive and negative streamers would propagate in opposite directions, the partitioned mesh refinement feature could be used to great effect. Since the maximum electric fields strengths at positive and negative streamer heads, in general, cannot be assumed to be of the same magnitude, the application of an AMR criteria based solely on a single value of electric field (e.g., refine everywhere where  $|\vec{E}| \geq 0.9 \max |\vec{E}|$ ) may correctly refine around the positive streamer head, but omit regions around the negative streamer where the field is lower than 90% of its positive counterpart. To address this, the mesh,  $\mathcal{M}$ , is split into the subregions  $\mathcal{M}_p : z \leq L/2$  and  $\mathcal{M}_n : z > L/2$  where  $\mathcal{M} = \mathcal{M}_p \cup \mathcal{M}_n$ , with two separate instances of the AMR criterion applied to each sub-mesh. In this case, the maximum field value used for refinement was based only on the sub-mesh for which the refinement criterion was active, ensuring that both streamer heads were sufficiently refined relative to their own maximum field. In addition, maximum field-based AMR was set to enable only once  $t \geq 4$  ns, since the initial condition containing a neutral charge seed creates no distortion to the background field. Therefore, a static field-based AMR scheme would over-refine the entire domain if enabled

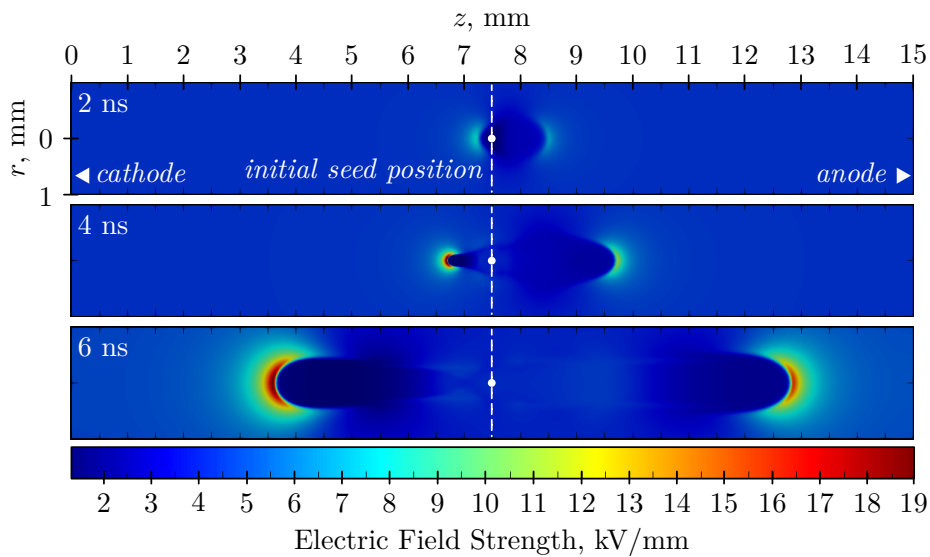


**Figure 5.23:** Resulting double-headed streamer simulated using StrAFE. Colour plots of electric field magnitude for  $t = 2, 4,$  and  $6$  ns. Dashed line and white dot indicates the original location of the initial seed. Image adapted from [60] under CC BY 4.0.

prior to charge separation. Density-based AMR, however, was enabled for the entire simulation. Other simulation settings are again included within Appendix B.3.

### 5.8.3.2 Simulation Results

Colour maps of the electron density and electric field magnitude for  $t = 2, 4,$  and  $6$  ns are shown in Figure 5.23 and 5.24. The double-headed streamer was successfully resolved using StrAFE and with characteristics that match those of previous works. Namely, the earlier inception of the positive streamer compared to the negative streamer; the more diffuse front and lower peak electric field for the negative streamer; and the initial higher velocity of the negative front were all characteristic of the double-headed streamers simulated in [104]. Maximum electric field magnitudes at the streamer heads are within  $17$  kV/mm to  $18$  kV/mm for the positive front, and  $15$  kV/mm to  $16$  kV/mm for the negative, in good agreement with [104]. The distance traversed over  $6$  ns is also comparable with the results simulated using StrAFE.

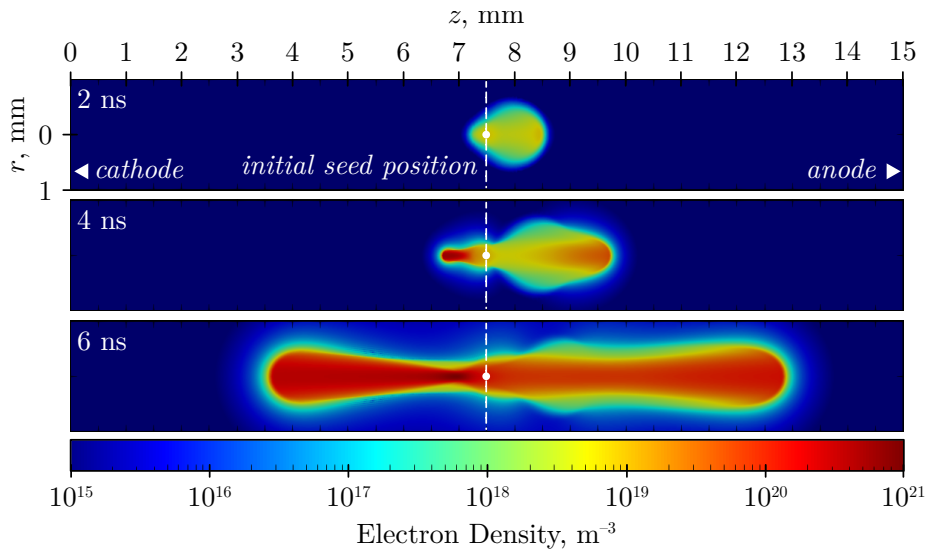


**Figure 5.24:** Resulting double-headed streamer simulated using StrAFE. Colour plots of electron density for  $t = 2, 4,$  and  $6$  ns. Dashed line and white dot indicates the original location of the initial seed. Image adapted from [60] under CC BY 4.0.

#### 5.8.4 Counter-propagating Streamers Initiated From Needle-Needle Electrodes

In one final verification case study, time-dependent boundary conditions, the LMEA, and an electrode geometry with significant curvature were further included atop the previously-tested features in one single, computationally challenging, simulation. The study in question stemmed from [111], where primary ionisation fronts were simulated in a typical laboratory breakdown configuration involving two needle electrodes. Positive and negative streamers once again initiate almost simultaneously, this time resulting solely due to field enhancement at the needle tips, before propagating towards each other and ultimately merging near the centre of the gap.

##### 5.8.4.1 Problem Configuration

The computational domain incorporating opposed needle electrodes is shown in Figure 5.25, where StrAFE in axisymmetric mode was once again used. No initial charged seeds were included in this simulation, as the streamers would incept directly from the enhanced field at the needle tips. In the original study [111], the authors utilised a pulsed waveform obtained from electromagnetic simulations using CST studio suite [112] that was not made openly available. However, since the simulation was only performed on the rising slope, the waveform was instead approximated

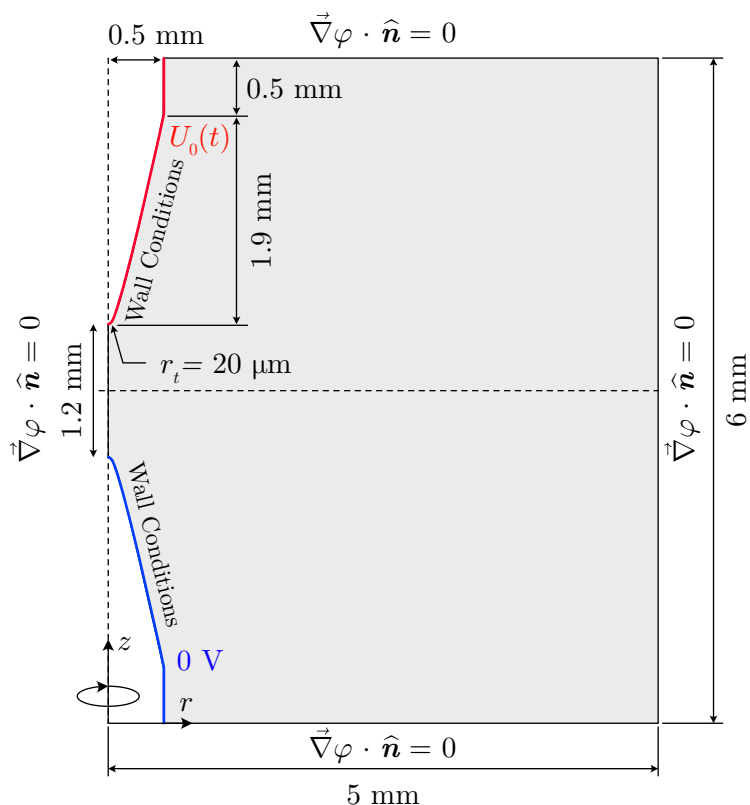


**Figure 5.25:** Cylindrically-symmetric domain used for the needle-needle counter-propagating study from [111] labelled with dimensions and boundary conditions. Wall conditions refer to (5.24)–(5.26).

using a ramp voltage of the form

$$U_0(t) = \frac{dU}{dt} \cdot t, \quad (5.48)$$

where  $dU/dt$  was set to 75 kV/ns to roughly align with the slope of the waveform used in [111]. Due to the size of the gap and the proximity of the electrodes, the LMEA was used to circumvent the limitations of the LFA, which was considered unlikely to provide accurate results in the geometry studied here, as discussed in Section 5.4.4. Besides, the LMEA was also employed in the original study. The plasma chemistry set for air according to Table 5.4 was once again used, and also assuming immobile and non-diffusive heavy species, since the entire discharge was completed within 1 ns.

AMR, ATS, and partitioned refinement were all enabled for this case study. The partitioning scheme was split into two regions along the  $r$  direction down the centre, similar to Section 5.8.3.1. However, for the sub-mesh containing the cathode, the maximum field value used for field-based refinement is constrained to be taken from 0.15 mm above the cathode tip. This ensured that the

high field developed inside the cathode sheath formed over the electrode would not be considered, as it is typically far higher than the field magnitude at the streamer head. Miscellaneous settings once again included within Appendix B.3.

#### 5.8.4.2 Simulation Results

To facilitate direct comparison to the results, the simulation outputs are presented in the same form as in [111]. Figure 5.26 shows streak images of the electric field strength and electron density, taken along the central axis and over 250 ps, compared to the corresponding Figure 8(a) and 8(b) of [111]. It is remarked that the simulation software used in [111] is the same as used by group “DE” in the first case study of Section 5.8.1. Tight agreement was again obtained between the results produced by StrAFE and those in [111], as evidenced by the similarities of the streak images which capture the behaviour of the main propagating wavefronts as they move simultaneously towards each other. Similar to the double-headed streamer of Section 5.8.3, the positive streamer initiated at a lower voltage than the negative, and due to their differing inception times and propagation velocities, the streamers do not merge at the exact centre of the inter-electrode gap, but closer to the anode as also found in [111].

Figure 5.27 plots the electric field magnitude along the line  $r = 0$  between the two needles for several timesteps, where the peak values of electric field originating from the two propagating wavefronts are compared to data taken from [111]. Good agreement was found in terms of both peak field magnitude and propagation velocity for the positive front. For the negative front, propagation time exhibited good agreement, however, peak electric field values estimated by StrAFE were consistently lower than that of [111] at the same timesteps. It is believed that this discrepancy can be explained by the differences between the approximate waveform used here compared to the full waveform of [111]. Boundary conditions applied at the electrodes and the exact set of plasma chemical reactions may also have been different, since these were not explicitly specified within [111]. Despite this, the overall characteristics of the simulated discharge compares very closely, qualitatively and quantitatively, despite the highly challenging conditions that this simulation study presented.

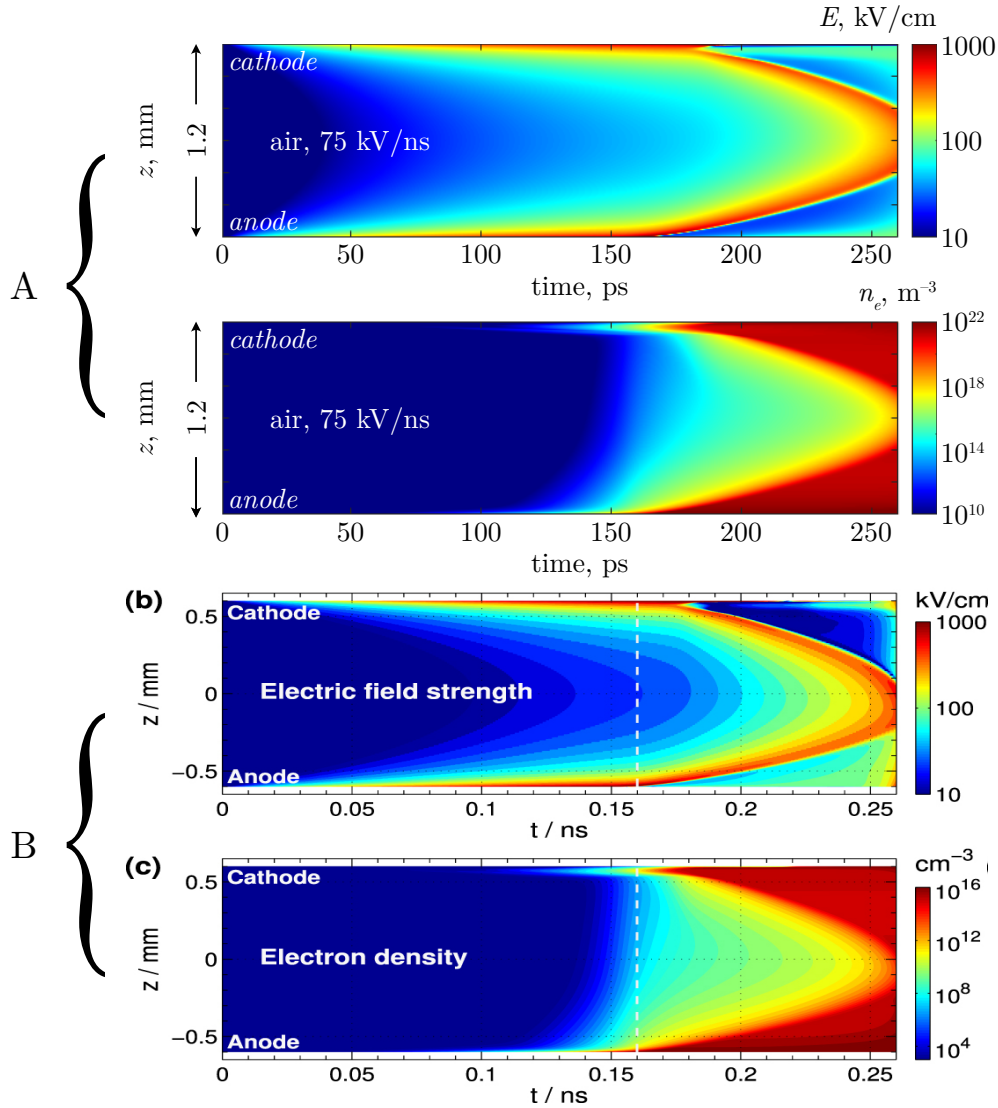


**Figure 5.26:** Streak images of the electric field magnitude and electron density down the central axis of Figure 5.25, (A) as computed by StrAFE, (B) original results from [111]. Images adapted from [111] and [60] under CC BY 4.0.

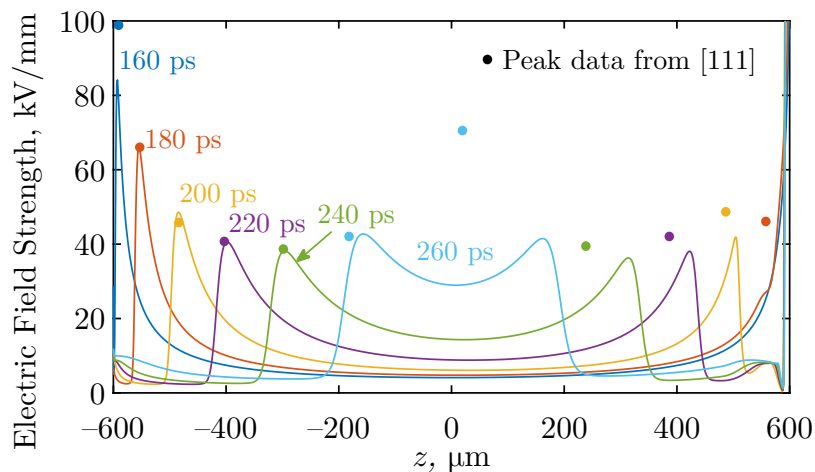


**Figure 5.27:** Electric field distribution along central axis of Figure 5.25 for indicated timesteps. Solid black circles show the peak data extracted from [111] for purposes of comparison. Image adapted from [60] under CC BY 4.0.

## 5.9 Chapter Conclusions, Contributions, and Outlook

Streamer discharges and fast transient ionisation waves are emergent from complex gas kinetics and possess characteristics that span multiple scales in space and in time. Recent advances in computational capabilities have enabled gas discharge phenomena to be simulated at increasing levels of fidelity, provided the appropriate software. While numerous custom codes have been developed in the past for the purpose of efficient streamer simulations, which includes commercially-available software, the balance between design issues such as computation speed, ease of use, feature set, accessibility, and configurability, remains. In the continued exploration of impulsive breakdown, it was desirable for a custom, fully-featured, but simple framework to be developed to study fast transient ionisation phenomena.

In this chapter, a novel Python library dedicated to the simulation of non-thermal gas discharge phenomena was presented. StrAFE (**S**reamers on **A**daptive **F**inite **E**lements) was built atop the open-source FEniCS [54,59] finite element platform, and aimed to provide a flexible and powerful, yet simple and accessible, platform for the automatic definition and simulation of non-thermal gas discharge phenomena including streamers and fast ionisation fronts. The software architecture of StrAFE has been presented in this chapter; the details of its implementation have been documented; and the developmental details that enable StrAFE to perform efficient multiscale modelling, using a high-level programming language, have been described. Notable features including the use of the hydrodynamic approximation, inclusion of solid dielectric subdomains, the

local energy approximation, plasma chemistry, and adaptive refinement, have been detailed; their implementation in StrAFE comprehensively described. The numerous powerful computational techniques that StrAFE inherits from its FEniCS parent have additionally been described, including distributed memory parallelism through the MPI protocol, automatic load-balancing, and a selection of efficient linear algebra solvers through the PETSc backend. The developed code was verified through a comprehensive set of comparison studies to past simulations using other well-established software, finding comparable performance and agreement over several case studies. StrAFE was thus used as the simulation platform for the computational studies presented in Chapter 6 of this work. Through the open-source nature of FEniCS, this work also acts as encouragement for interested parties to develop their own custom frameworks, for which the detailed account on aspects of software implementation provided in this chapter aims to facilitate.

### 5.9.1 Academic Significance and Contributions

The main contribution of this chapter was to demonstrate the capabilities of FEniCS as a developmental platform for a novel framework focused on simulating non-thermal gas discharge phenomena. Software programs such as StrAFE are instrumental in furthering the understanding of gas discharge phenomena, especially given the difficulty in experimentally characterising these types of fast transient events.

Successful simulations encompassing simple to complex domains, with models incorporating minimal to detailed physics, have been demonstrated using the StrAFE library. The platform showcases the potential of open-source code, and suggests one viable approach to implement a fully-featured plasma model for the exploration of complex ionisation and breakdown processes. The open-source nature of FEniCS, on which StrAFE was built, enables a cost-free alternative where code transparency, collaboration, or configurability is necessary; or where the licensing costs for commercial software is a limiting or undesirable factor. This chapter has provided detailed information that outlines the method from which similar custom frameworks can be developed. At the same time, verification studies provide confidence that the capabilities of the open-source code is able to match that of other state-of-the-art software.

These verification studies have not only served to ensure correct implementation, but provides further assurance that results in literature, simulated using other codes, are reproducible. This therefore contributes more generally to the collective development of streamer simulation codes, which is critical for fields of research such as gas discharge modelling, where standardised tests

or benchmarks have not yet been established.

### 5.9.2 Industrial Relevance

A major component in the design philosophy of StrAFE (as set out in Section 5.1) was built around the idea that practical geometries of interest must be well represented. This condition motivated the choice to employ the finite element method using a flexible open-source platform such as FEniCS. The ability for StrAFE to accept unstructured meshes in standard file formats greatly facilitates integration of StrAFE with external mesh generation software, allowing meshes to be built to exact and geometry conforming specifications, then imported for use within simulations. As such, allowable geometry is limited only by the available computational power, rather than the inability for the mesh to conform to complex shapes (i.e., if a Cartesian mesh were to be used instead). Refinement algorithms included with StrAFE have been developed with this in mind, ensured to work alongside MPI, to allow the load-balanced domain decomposition to handle large, complex, meshes. It is again remarked that StrAFE has full capability to perform 3D simulations using tetrahedral elements, though additional computational resources would be necessary to leverage this to its full effectiveness. Where this is available, however, StrAFE has the potential capability to simulate gas discharge phenomena within fully-detailed practical electrical systems.

Greater accessibility of computational tools for gas discharge research ultimately leads to a deeper knowledge of the underlying physical processes; with far reaching consequences for the coordination of electrical insulation systems, for geophysical research, and for the development of novel non-thermal plasma technologies. Computational tools like StrAFE may be used as predictive models for the onset of electrical breakdown, for example, in understanding discharge development across solid insulation spacers [91,113], or partial discharge inception within void defects [114]. The inclusion of plasma chemistry enables the possibility to estimate post-discharge plasma composition in chemical processing applications [115], or to evaluate the performance of novel, environmentally-friendly, gas alternatives for use in gas insulated equipment. The unparalleled flexibility provided through the physics-agnostic FEniCS platform permits future additions to StrAFE in terms of physics. In effect, StrAFE could be extended to incorporate fluid flows, gas heating, or combustion processes, opening it up to support the simulation of highly complex plasma interactions important in many other developing plasma technologies [116,117].

### 5.9.3 Limitations and Future Outlook

As a general limitation irrespective of the computational platform, StrAFE utilises the hydrodynamic approximation among the other possible methods described in Section 5.2.1. The limitations and boundaries for which this description is valid was also discussed in Section 5.2.2. For problems that sit outside the bounds of validity, e.g., discharges over very short timescales close to the relaxation time of the EEDF, or over very short distances, a kinetic description according to Section 5.2.1.1 should be used instead. It is remarked that it would be of great interest to couple a kinetic solver with StrAFE, either by use of StrAFE as the field solver alone, or for hybrid fluid-kinetic modelling.

It is also an inevitable truth that, at the time of writing, the balance of factors influencing simulation software design outlined in Figure 5.1 remains a limitation. Despite efforts to ensure that StrAFE was as fully-featured as possible, StrAFE targeted specific issues such as usability, flexibility, and aimed to lower the entry barrier to complex plasma simulations; at the unavoidable sacrifice of other desirable properties, as explained in the following points.

The first, and as briefly discussed in Section 5.3.1, pertains to conservation, whereby the continuous Galerkin method can only ensure globally-conserved properties. For conservation laws such as the continuity equations simulated here, local conservation is much preferred. It is acknowledged that at least some proportion of numerical errors may have arisen due to this constraint. Alternative formulations, such as finite-volume or discontinuous Galerkin methods allow this limitation to be circumvented. However, the trade-off is typically to the detriment of flexibility and configurability which were the main issues targeted by StrAFE.

Secondly, the choice to base StrAFE on the open-source FEniCS platform was important to ensure code transparency and to maintain accessibility of the low-level code, yet be able to accelerate development efforts by inheriting the well-established routines developed as part of the FEniCS project over its many active years. The physics-agnostic nature of FEniCS provided the perfect general-purpose platform on which StrAFE was able to be built, however, the same generality becomes a limiting factor for the computational speed and efficiency of the program to match that of specialised software. StrAFE helps to push forward the adoption of open-source code and usability, but does not concern itself with the development of novel or custom solvers to maximise computational speed, in contrast to codes such as [3, 22, 39]. As shown in Section 5.8.1, the pure computational performance of StrAFE is similar to that of the commercially-available multiphysics software, COMSOL.

Despite this, the foresight to develop StrAFE with an emphasis on flexibility opens up many possibilities and opportunities for future work and improvement:

- Code verification in the case of full 3D simulations and in HPC environments. Support already exists within StrAFE, such that with suitable computational resources the library is already prepared for evaluation. However, 3D simulations have only been recently demonstrated in a few studies by select research groups [2, 9, 10, 77]; typically investigating stochastic processes such as variations in the background ionisation density or discrete photon processes, with largely qualitative comparisons to experiments. Standard verification problems must be developed further for the proper testing of 3D gas discharge codes.
- Integration of kinetic models using StrAFE as the field solver, or for hybrid fluid-kinetic simulations. This potentially expands StrAFE to incorporate kinetic effects, allowing phenomena such as runaway electrons or discrete photoionisation processes to be accurately simulated using StrAFE.
- Expansion of the photoionisation model current implemented in StrAFE. This should also include the effects of shadowing such that models including occluded geometry can be accurately simulated.
- Expand the range of time integration methods to higher-order techniques, e.g., various order Runge-Kutta stepping methods.
- Development and/or modification of the existing code base, to incorporate accelerated methods of linear algebra solving, e.g., geometric multigrid methods.
- Exploration of the possible benefits of using higher-order basis functions and increasing the order of spatial discretisation. This should, in theory, increase the accuracy of the computed solution at lower element sizes. However, high-order elements also require greater computational effort. Understanding whether there are advantages to be gained from using high-order elements would be important to identify optimal numerical schemes for future gas discharge models.
- Can *hp*-adaptivity be achieved using FEniCS and implemented into StrAFE? Will adapting the element order as well as mesh size simultaneously provide any significant improvements to efficiency and/or accuracy?
- FEniCS (and thus StrAFE) has support for the discontinuous Galerkin (DG) method, a method more akin to finite-volume methods and guarantees local conservation. Could an alternative mode be introduced to StrAFE that makes use of DG-FEM to achieve greater accuracy? The discontinuous nature of DG-FEM is also potentially advantageous to the

modelling of solid boundaries, since these are, by definition, a material discontinuity in the domain which can only be approximated in CG-FEM.

- Leverage the flexibility and open-source nature of the code to explore parallel-in-time integration methods. The performance and stability of methods such as *Parareal* [118] to solve hyperbolic conservation laws is not yet understood. These, if developed, could potentially help to significantly accelerate the simulation of multiscale phenomena.

## Chapter 5 References

- [1] A. P. Jovanović, M. N. Stankov, D. Loffhagen, and M. M. Becker, “Automated fluid model generation and numerical analysis of dielectric barrier discharges using comsol,” *IEEE Trans. Plasma Sci.*, vol. 49, no. 11, pp. 3710–3718, 2021.
- [2] J. Teunissen and U. Ebert, “Simulating streamer discharges in 3d with the parallel adaptive afivo framework,” *J. Phys. D: Appl. Phys.*, vol. 50, no. 47, p. 474001, 2017.
- [3] J. Teunissen and U. Ebert, “Afivo: A framework for quadtree/octree amr with shared-memory parallelization and geometric multigrid methods,” *Comput. Phys. Commun.*, vol. 233, pp. 156–166, 2018.
- [4] U. Ebert, C. Montijn, T. M. P. Briels, W. Hundsdorfer, B. Meulenbroek, A. Rocco *et al.*, “The multiscale nature of streamers,” *Plasma Sources Sci. Technol.*, vol. 15, no. 2, p. S118, 2006.
- [5] S. Nijdam, J. Teunissen, and U. Ebert, “The physics of streamer discharge phenomena,” *Plasma Sources Sci. Technol.*, vol. 29, no. 10, p. 103001, 2020.
- [6] A. Luque, U. Ebert, and W. Hundsdorfer, “Interaction of streamer discharges in air and other oxygen-nitrogen mixtures,” *Phys. Rev. Lett.*, vol. 101, p. 075005, 2008.
- [7] S. Nijdam, C. G. C. Geurts, E. M. van Veldhuizen, and U. Ebert, “Reconnection and merging of positive streamers in air,” *J. Phys. D: Appl. Phys.*, vol. 42, no. 4, p. 045201, 2009.
- [8] Z. Wang, A. Sun, S. Dujko, U. Ebert, and J. Teunissen, “3d simulations of positive streamers in air in a strong external magnetic field,” arXiv, 2309.02300, 2024.
- [9] B. Guo, U. Ebert, and J. Teunissen, “3d particle-in-cell simulations of negative and positive streamers in C4F7N–CO2 mixtures,” *Plasma Sources Sci. Technol.*, vol. 32, no. 11, p. 115001, 2023.
- [10] A. Sun, J. Teunissen, and U. Ebert, “3-d particle modeling of positive streamer inception from a needle electrode in supercritical nitrogen,” *IEEE Trans. Plasma Sci.*, vol. 42, no. 10, pp. 2416–2417, 2014.
- [11] O. Chanrion and T. Neubert, “A PIC-MCC code for simulation of streamer propagation in air,” *J. Comput. Phys.*, vol. 227, no. 15, pp. 7222–7245, 2008.
- [12] C. Birdsall, “Particle-in-cell charged-particle simulations, plus monte carlo collisions with neutral atoms, PIC-MCC,” *IEEE Trans. Plasma Sci.*, vol. 19, no. 2, pp. 65–85, 1991.
- [13] V. Vahedi and M. Surendra, “A monte carlo collision model for the particle-in-cell method: applications to argon and oxygen discharges,” *Comput. Phys. Commun.*, vol. 87, no. 1, pp. 179–198, 1995, particle Simulation Methods.
- [14] M. Vranic, T. Grismayer, J. Martins, R. Fonseca, and L. Silva, “Particle merging algorithm for PIC codes,” *Comput. Phys. Commun.*, vol. 191, pp. 65–73, 2015.
- [15] P. T. Luu, T. Tückmantel, and A. Pukhov, “Voronoi particle merging algorithm for PIC codes,” *Compu. Phys. Commun.*, vol. 202, pp. 165–174, 2016.
- [16] J. Teunissen and U. Ebert, “Controlling the weights of simulation particles: adaptive particle management using k-d trees,” *J. Comput. Phys.*, vol. 259, pp. 318–330, 2014.

- [17] D. Faghihi, V. Carey, C. Michoski, R. Hager, S. Janhunen, C. Chang *et al.*, “Moment preserving constrained resampling with applications to particle-in-cell methods,” *J. Comput. Phys.*, vol. 409, p. 109317, 2020.
- [18] A. Muraviev, A. Bashinov, E. Efimenko, V. Volokitin, I. Meyerov, and A. Gonoskov, “Strategies for particle resampling in PIC simulations,” *Comput. Phys. Commun.*, vol. 262, p. 107826, 2021.
- [19] J. Teunissen and U. Ebert, “3d PIC-MCC simulations of discharge inception around a sharp anode in nitrogen/oxygen mixtures,” *Plasma Sources Sci. Technol.*, vol. 25, no. 4, p. 044005, 2016.
- [20] A. P. Jovanović, S. N. Stamenković, M. N. Stankov, and V. L. Marković, “Monte carlo simulation of electron avalanches and avalanche size distributions in methane,” *Contrib. Plasma Phys.*, vol. 59, no. 3, pp. 272–283, 2019.
- [21] O. Chanrion and T. Neubert, “Production of runaway electrons by negative streamer discharges,” *J. Geophys. Res.: Space Phys.*, vol. 115, no. A6, 2010.
- [22] R. Marskar, “Stochastic and self-consistent 3d modeling of streamer discharge trees with kinetic monte carlo,” *J. Comput. Phys.*, vol. 504, p. 112858, 2024.
- [23] I. Rafatov and A. Kudryavtsev, *Introduction to Simulation Methods for Gas Discharge Plasmas*, ser. 2053-2563. IOP Publishing, 2020.
- [24] Z. Wang, A. Sun, and J. Teunissen, “A comparison of particle and fluid models for positive streamer discharges in air,” *Plasma Sources Sci. Technol.*, vol. 31, no. 1, p. 015012, 2022.
- [25] A. Luque and U. Ebert, “Growing discharge trees with self-consistent charge transport: the collective dynamics of streamers,” *New J. Phys.*, vol. 16, no. 1, p. 013039, 2014.
- [26] P. O. Kochkin, A. P. J. van Deursen, and U. Ebert, “Experimental study of the spatio-temporal development of metre-scale negative discharge in air,” *J. Phys. D: Appl. Phys.*, vol. 47, no. 14, p. 145203, 2014.
- [27] C. Li, U. Ebert, and W. Hundsdorfer, “Spatially hybrid computations for streamer discharges with generic features of pulled fronts: I. planar fronts,” *J. Comput. Phys.*, vol. 229, no. 1, pp. 200–220, 2010.
- [28] C. Li, U. Ebert, and W. Hundsdorfer, “Spatially hybrid computations for streamer discharges : II. fully 3d simulations,” *J. Comput. Phys.*, vol. 231, no. 3, pp. 1020–1050, 2012, special Issue: Computational Plasma Physics.
- [29] C. Li, U. Ebert, and W. Hundsdorfer, “3d hybrid computations for streamer discharges and production of runaway electrons,” *J. Phys. D: Appl. Phys.*, vol. 42, no. 20, p. 202003, 2009.
- [30] Z. Cai, X. Wang, L. Li, and W. Hong, “Electrical treeing: A phase-field model,” *Extrem. Mech. Lett.*, vol. 28, pp. 87–95, 2019.
- [31] K. Chaitanya Pitike and W. Hong, “Phase-field model for dielectric breakdown in solids,” *J. Appl. Phys.*, vol. 115, no. 4, p. 044101, 2014.
- [32] Z. Mi, Y. Zhang, X. Hou, and J. Wang, “Phase field modeling of dielectric breakdown of ferroelectric polymers subjected to mechanical and electrical loadings,” *Int. J. Solids Struct.*, vol. 217-218, pp. 123–133, 2021.

- [33] F. Brau, B. Davidovitch, and U. Ebert, “Moving boundary approximation for curved streamer ionization fronts: Solvability analysis,” *Phys. Rev. E*, vol. 78, p. 056212, 2008.
- [34] U. Ebert, F. Brau, G. Derks, W. Hundsdorfer, C.-Y. Kao, C. Li *et al.*, “Multiple scales in streamer discharges, with an emphasis on moving boundary approximations,” *Nonlinearity*, vol. 24, no. 1, p. C1, 2010.
- [35] C. Montijn, B. Meulenbroek, U. Ebert, and W. Hundsdorfer, “Numerical simulations and conformal analysis of growing and branching negative discharge streamers,” *IEEE Trans. Plasma Sci.*, vol. 33, no. 2, pp. 260–261, 2005.
- [36] B. Meulenbroek, A. Rocco, and U. Ebert, “Streamer branching rationalized by conformal mapping techniques,” *Phys. Rev. E*, vol. 69, p. 067402, 2004.
- [37] J. Jadidian, M. Zahn, N. Lavesson, O. Widlund, and K. Borg, “Stochastic and deterministic causes of streamer branching in liquid dielectrics,” *J. Appl. Phys.*, vol. 114, no. 6, p. 063301, 2013.
- [38] N. Y. Babaeva and M. J. Kushner, “Streamer branching: The role of inhomogeneities and bubbles,” *IEEE Trans. Plasma Sci.*, vol. 36, no. 4, pp. 892–893, 2008.
- [39] R. Marskar, “An adaptive cartesian embedded boundary approach for fluid simulations of two- and three-dimensional low temperature plasma filaments in complex geometries,” *J. Comput. Phys.*, vol. 388, pp. 624–654, 2019.
- [40] R. R. Arslanbekov and V. I. Kolobov, “Implicit and coupled fluid plasma solver with adaptive cartesian mesh and its applications to non-equilibrium gas discharges,” *Plasma Sources Sci. Technol.*, vol. 30, no. 4, p. 045013, 2021.
- [41] V. Kolobov and R. Arslanbekov, “Deterministic boltzmann solver for electron kinetics in plasma reactors for microelectronics applications,” *Microelectron. Engr.*, vol. 69, no. 2, pp. 606–615, 2003, proceedings of the Symposium and Summer School on: Nano and Giga Challenges in Microelectronics Research and Opportunities in Russia.
- [42] Y. Zhu, X. Chen, Y. Wu, J. Hao, X. Ma, P. Lu *et al.*, “Simulation of ionization-wave discharges: a direct comparison between the fluid model and E-FISH measurements,” *Plasma Sources Sci. Technol.*, vol. 30, no. 7, p. 075025, 2021.
- [43] COMSOL AB. (2024) COMSOL multiphysics. [Online]. Available: [www.comsol.com](http://www.comsol.com)
- [44] Ansys. (2024) Ansys fluent. [Online]. Available: <https://www.ansys.com/products/fluids/ansys-fluent>
- [45] University of South Carolina. (2024) FISHPACK: A poisson equation solver. [Online]. Available: [https://people.math.sc.edu/Burkardt/f77\\_src/fishpack/fishpack.html](https://people.math.sc.edu/Burkardt/f77_src/fishpack/fishpack.html)
- [46] Centrum Wiskunde & Informatica. (2024) Multiscale plasma modeling: ARCoS. [Online]. Available: <https://www.cwimd.nl/doku.php?id=codes:arcos>
- [47] J. van Dijk, K. Peerenboom, M. Jimenez, D. Mihailova, and J. van der Mullen, “The plasma modelling toolkit plasimo,” *J. Phys. D: Appl. Phys.*, vol. 42, no. 19, p. 194012, 2009.
- [48] Plasma Matters & Eindhoven University of Technology. (2024) PLASIMO. [Online]. Available: <https://plasimo.phys.tue.nl/>

- [49] J. Teunissen and F. Schiavello, “Geometric multigrid method for solving poisson’s equation on octree grids with irregular boundaries,” *Comput. Phys. Commun.*, vol. 286, p. 108665, 2023.
- [50] Y. Zhu, C. X., and S. Starikovskaia. (2024) PASSKEy code. [Online]. Available: <http://www.plasma-tech.net/parser/passkey/>
- [51] A. P. Jovanović, D. Loffhagen, and M. M. Becker, “Introduction and verification of FEDM, an open-source FEniCS-based discharge modelling code,” *Plasma Sources Sci. Technol.*, vol. 32, no. 4, p. 044003, 2023.
- [52] I. Madshaven, O. Hestad, and P.-O. Åstrand, “Cerman: Software for simulating streamer propagation in dielectric liquids based on the townsend–meek criterion,” *Comput. Phys. Commun.*, vol. 265, p. 107987, 2021.
- [53] R. Marskar, “chombo-discharge: An AMR code for gas discharge simulations in complex geometries,” *Journal of Open Source Software*, vol. 8, no. 85, p. 5335, 2023.
- [54] A. Logg, K.-A. Mardal, and G. Wells, *Automated Solution of Differential Equations by the Finite Element Method: The FEniCS Book*. Springer, 2012.
- [55] G. Dhatt, G. Touzot, and Lefrançois, *A Finite Element Method*. Wiley-ISTE, 2012.
- [56] S. S. Rao, *The Finite Element Method in Engineering*, 5th ed. Elsevier Inc., 2011.
- [57] O. Ducasse, L. Papageorghiou, O. Eichwald, N. Spyrou, and M. Yousfi, “Critical analysis on two-dimensional point-to-plane streamer simulations using the finite element and finite volume methods,” *IEEE Trans. Plasma Sci.*, vol. 35, no. 5, pp. 1287–1300, 2007.
- [58] M. Alnæs, J. Blechta, J. Hake, A. Johansson, B. Kehlet, A. Logg *et al.*, “The FEniCS project version 1.5,” *Archive of Numerical Software*, vol. 3, no. 100, 2015.
- [59] The FEniCS Project. (2021) Fenics v. 2019.1.0. [Online]. Available: <https://fenicsproject.org/>
- [60] T. Wong, I. Timoshkin, S. MacGregor, M. Wilson, and M. Given, “The design of a python library for the automatic definition and simulation of transient ionization fronts,” *IEEE Access*, vol. 11, pp. 26 577–26 592, 2023.
- [61] K. B. Ølgaard and G. N. Wells, “Optimizations for quadrature representations of finite element tensors through automated code generation,” *ACM Trans. Math. Softw.*, vol. 37, no. 1, 2010.
- [62] R. C. Kirby and A. Logg, “A compiler for variational forms,” *ACM Trans. Math. Softw.*, vol. 32, no. 3, p. 417–444, 2006.
- [63] M. S. Alnæs, A. Logg, K. B. Ølgaard, M. E. Rognes, and G. N. Wells, “Unified form language: A domain-specific language for weak formulations of partial differential equations,” *ACM Trans. Math. Softw.*, vol. 40, no. 2, 2014.
- [64] R. C. Kirby, “Algorithm 839: FIAT, a new paradigm for computing finite element basis functions,” *ACM Trans. Math. Softw.*, vol. 30, no. 4, p. 502–516, 2004.
- [65] C. Chevalier and F. Pellegrini, “PT-Scotch: A tool for efficient parallel graph ordering,” *Parallel Computing*, vol. 34, no. 6, pp. 318–331, 2008, parallel Matrix Algorithms and Applications.
- [66] G. Karypis and K. Schoegel, “ParMETIS: Parallel graph partitioning and sparse matrix ordering library, version 4.0,” Dept. Comput. Sci. Engr., University of Minnesota, Minneapolis, USA, Tech. Rep., 2013.

- [67] J. Walter, M. Koch, and D. Bellot. (2021) Basic linear algebra library, ublas. [Online]. Available: [https://www.boost.org/doc/libs/1\\_85\\_0/libs/numeric/ublas/doc/index.html](https://www.boost.org/doc/libs/1_85_0/libs/numeric/ublas/doc/index.html)
- [68] T. T. P. Team. (2024) Epetra. [Online]. Available: <https://trilinos.github.io/epetra.html>
- [69] S. Balay, W. D. Gropp, L. C. McInnes, and B. F. Smith, *Efficient Management of Parallelism in Object-Oriented Numerical Software Libraries*. Boston, MA: Birkhäuser Boston, 1997, pp. 163–202.
- [70] S. Balay, S. Abhyankar, M. F. Adams, S. Benson, J. Brown, P. Brune *et al.*, “PETSc Web page,” <https://petsc.org/>, 2024. [Online]. Available: <https://petsc.org/>
- [71] M. B. Zheleznyak, A. K. Mnatsakanyan, and S. V. Sizykh, “Photo-ionization of nitrogen and oxygen mixtures by radiation from a gas-discharge,” *High. Temp.*, vol. 20, no. 3, pp. 357–362, 1982.
- [72] A. A. Kulikovskiy, “The role of photoionization in positive streamer dynamics,” *J. Phys. D: Appl. Phys.*, vol. 33, no. 12, p. 1514, 2000.
- [73] G. Wormeester, S. Pancheshnyi, A. Luque, S. Nijdam, and U. Ebert, “Probing photo-ionization: simulations of positive streamers in varying N<sub>2</sub>:O<sub>2</sub>-mixtures,” *J. Phys. D: Appl. Phys.*, vol. 43, no. 50, p. 505201, 2010.
- [74] S. Pancheshnyi, “Role of electronegative gas admixtures in streamer start, propagation and branching phenomena,” *Plasma Sources Sci. Technol.*, vol. 14, no. 4, p. 645, 2005.
- [75] Y. Li, Y. Fu, Z. Liu, H. Li, P. Wang, H. Luo *et al.*, “Effect of photoionisation on initial discharge in air under nanosecond pulse voltage,” *High Volt.*, vol. 8, no. 2, pp. 340–346, 2023.
- [76] X. Li, S. Dijcks, A. Sun, S. Nijdam, and J. Teunissen, “Investigation of positive streamers in CO<sub>2</sub>: experiments and 3d particle-in-cell simulations,” arXiv, 2304.01531, 2024.
- [77] R. Marskar, “A 3d kinetic monte carlo study of streamer discharges in CO<sub>2</sub>,” *Plasma Sources Sci. Technol.*, vol. 33, no. 2, p. 025023, 2024.
- [78] A. Bourdon, V. P. Pasko, N. Y. Liu, S. Célestin, P. Ségur, and E. Marode, “Efficient models for photoionization produced by non-thermal gas discharges in air based on radiative transfer and the helmholtz equations,” *Plasma Sources Sci. Technol.*, vol. 16, no. 3, p. 656, 2007.
- [79] P. Ségur, A. Bourdon, E. Marode, D. Bessieres, and J. H. Paillol, “The use of an improved eddington approximation to facilitate the calculation of photoionization in streamer discharges,” *Plasma Sources Sci. Technol.*, vol. 15, no. 4, p. 648, 2006.
- [80] N. Liu and V. P. Pasko, “Effects of photoionization on propagation and branching of positive and negative streamers in sprites,” *J. Geophys. Res.: Space Phys.*, vol. 109, no. A4, 2004.
- [81] J. Tungli, M. Horký, S. Kadlec, and Z. Bonaventura, “Capturing photoionization shadows in streamer simulations using the discrete ordinates method,” *Plasma Sources Sci. Technol.*, vol. 32, no. 10, p. 105009, 2023.
- [82] Z. Wang, S. Dijcks, Y. Guo, M. van der Leegte, A. Sun, U. Ebert *et al.*, “Quantitative modeling of streamer discharge branching in air,” *Plasma Sources Sci. Technol.*, vol. 32, no. 8, p. 085007, 2023.
- [83] B. Bagheri, J. Teunissen, and U. Ebert, “Simulation of positive streamers in CO<sub>2</sub> and in air: the role of photoionization or other electron sources,” *Plasma Sources Sci. Technol.*, vol. 29, no. 12, p. 125021, 2020.

- [84] T. Liu, I. V. Timoshkin, S. J. MacGregor, M. P. Wilson, M. J. Given, N. Bonifaci *et al.*, “Field-time breakdown characteristics of air, N<sub>2</sub>, CO<sub>2</sub>, and SF<sub>6</sub>,” *IEEE Trans. Plasma Sci.*, vol. 48, no. 10, pp. 3321–3331, 2020.
- [85] G. J. M. Hagelaar and L. C. Pitchford, “Solving the boltzmann equation to obtain electron transport coefficients and rate coefficients for fluid models,” *Plasma Sources Sci. Technol.*, vol. 14, no. 4, p. 722, 2005.
- [86] M. Flynn, A. Neuber, and J. Stephens, “Benchmarking the calculation of electrically insulating properties of complex gas mixtures using a multi-term boltzmann equation model,” *J. Phys. D: Appl. Phys.*, vol. 55, no. 1, p. 015201, 2021.
- [87] G. K. Grubert, M. M. Becker, and D. Loffhagen, “Why the local-mean-energy approximation should be used in hydrodynamic plasma descriptions instead of the local-field approximation,” *Phys. Rev. E*, vol. 80, p. 036405, 2009.
- [88] G. J. M. Hagelaar, F. J. de Hoog, and G. M. W. Kroesen, “Boundary conditions in fluid models of gas discharges,” *Phys. Rev. E*, vol. 62, pp. 1452–1454, 2000.
- [89] M. Černák, “Formation and evolution of the cathode sheath on the streamer arrival,” *AIP Conf. Proc.*, vol. 363, no. 1, pp. 136–145, 1996.
- [90] M. Černák, “Formation and evolution of the cathode sheath on the streamer arrival,” *AIP Conf. Proc.*, vol. 363, no. 1, pp. 136–145, 1996.
- [91] X. Li, A. Sun, G. Zhang, and J. Teunissen, “A computational study of positive streamers interacting with dielectrics,” *Plasma Sources Sci. Technol.*, vol. 29, no. 6, p. 065004, 2020.
- [92] COMSOL AB, *COMSOL Multiphysics v. 5.4., Plasma Module User’s Guide*, 2023.
- [93] T. Tezduyar, “Stabilized finite element formulations for incompressible flow computations,” ser. Advances in Applied Mechanics, J. W. Hutchinson and T. Y. Wu, Eds. Elsevier, 1991, vol. 28, pp. 1–44.
- [94] R. D. Falgout and U. M. Yang, “hypre: A library of high performance preconditioners,” in *Computational Science — ICCS 2002*, P. M. A. Sloot, A. G. Hoekstra, C. J. K. Tan, and J. J. Dongarra, Eds. Berlin, Heidelberg: Springer Berlin Heidelberg, 2002, pp. 632–641.
- [95] B. Bagheri, J. Teunissen, U. Ebert, M. M. Becker, S. Chen, O. Ducasse *et al.*, “Comparison of six simulation codes for positive streamers in air,” *Plasma Sources Sci. Technol.*, vol. 27, no. 9, p. 095002, 2018.
- [96] N. Schlömer. (Zenodo, 2024) pygymsh: A python frontend for gmsh.
- [97] J. P. Ahrens, B. Geveci, and C. C. Law, “Paraview: An end-user tool for large-data visualization,” in *The Visualization Handbook*, 2005. [Online]. Available: <https://api.semanticscholar.org/CorpusID:56558637>
- [98] J. Hoffman, J. Jansson, and N. Jansson, “FEniCS-HPC: Automated predictive high-performance finite element computing with applications in aerodynamics,” in *Parallel Processing and Applied Mathematics*, R. Wyrzykowski, E. Deelman, J. Dongarra, K. Karczewski, J. Kitowski, and K. Wiatr, Eds. Cham: Springer International Publishing, 2016, pp. 356–365.

- [99] L. Vynnytska, M. Rognes, and S. Clark, “Benchmarking FEniCS for mantle convection simulations,” *Comput. Geosci.*, vol. 50, pp. 95–105, 2013, benchmark problems, datasets and methodologies for the computational geosciences.
- [100] D. Merkel, “Docker: lightweight linux containers for consistent development and deployment,” *Linux J.*, vol. 2014, no. 239, 2014.
- [101] T. Wong, I. Timoshkin, S. MacGregor, M. Wilson, and M. Given, “A python-based adaptive mesh solver for drift-diffusion modelling of streamer discharges,” in *2021 IEEE Pulsed Power Conf. (PPC)*, 2021, pp. 1–5.
- [102] R. Morrow and J. J. Lowke, “Streamer propagation in air,” *J. Phys. D: Appl. Phys.*, vol. 30, no. 4, p. 614, 1997.
- [103] T. Wong, I. Timoshkin, S. MacGregor, M. Wilson, and M. Given, “Simulation of streamer discharges across solid dielectric surfaces using the open-source FEniCS platform,” in *2021 IEEE Pulsed Power Conf. (PPC)*, 2021, pp. 1–5.
- [104] A. Luque, V. Ratushnaya, and U. Ebert, “Positive and negative streamers in ambient air: modelling evolution and velocities,” *J. Phys. D: Appl. Phys.*, vol. 41, no. 23, p. 234005, 2008.
- [105] J. Qin, S. Celestin, and V. P. Pasko, “Formation of single and double-headed streamers in sprite-halo events,” *Geophys. Res. Lett.*, vol. 39, no. 5, 2012.
- [106] M. B. Garnung, S. Celestin, and T. Farges, “HF-VHF electromagnetic emissions from collisions of sprite streamers,” *J. Geophys. Res.: Space Phys.*, vol. 126, no. 6, p. e2020JA028824, 2021.
- [107] Plasma Data Exchange Project: Lxcat. (2024) Phelps database. [Online]. Available: <http://lxcat.net/Phelps>
- [108] A. V. Phelps and L. C. Pitchford, “Anisotropic scattering of electrons by N<sub>2</sub> and its effect on electron transport,” *Phys. Rev. A*, vol. 31, pp. 2932–2949, 1985.
- [109] S. A. Lawton and A. V. Phelps, “Excitation of the  $b^1\sigma_g^+$  state of o<sub>2</sub> by low energy electrons,” *J. Chem. Phys.*, vol. 69, no. 3, pp. 1055–1068, 1978.
- [110] S. V. Pancheshnyi and A. Y. Starikovskii, “Two-dimensional numerical modelling of the cathode-directed streamer development in a long gap at high voltage,” *J. Phys. D: Appl. Phys.*, vol. 36, no. 21, p. 2683, 2003.
- [111] H. Höft, M. M. Becker, J. F. Kolb, and T. Huiskamp, “Double-propagation mode in short-gap spark discharges driven by HV pulses with sub-ns rise time,” *Plasma Sources Sci. Technol.*, vol. 29, no. 8, p. 085002, 2020.
- [112] SIMULIA - Dassault Systèmes. (2022) CST studio suite electromagnetic field simulation software. [Online]. Available: <https://www.3ds.com/products/simulia/cst-studio-suite>
- [113] X. Li, A. Sun, and J. Teunissen, “A computational study of negative surface discharges: Characteristics of surface streamers and surface charges,” *IEEE Trans. Dielectr. Electr. Insul.*, vol. 27, no. 4, pp. 1178–1186, 2020.
- [114] N. Y. Babaeva and M. J. Kushner, “Structure of positive streamers inside gaseous bubbles immersed in liquids,” *J. Phys. D: Appl. Phys.*, vol. 42, no. 13, p. 132003, 2009.

- [115] A. Bogaerts, E. Neyts, R. Gijbels, and J. van der Mullen, “Gas discharge plasmas and their applications,” *Spectro. Acta B: Atom. Spectro.*, vol. 57, no. 4, pp. 609–658, 2002.
- [116] H.-H. Kim, “Nonthermal plasma processing for air-pollution control: A historical review, current issues, and future prospects,” *Plasma Process. Polym.*, vol. 1, no. 2, pp. 91–110, 2004.
- [117] T. Matsumoto, D. Wang, T. Namihira, and H. Akiyama, “Energy efficiency improvement of nitric oxide treatment using nanosecond pulsed discharge,” *IEEE Trans. Plasma Sci.*, vol. 38, no. 10, pp. 2639–2643, 2010.
- [118] J.-L. Lions, Y. Maday, and G. Turinici, “Résolution d’edp par un schéma en temps «pararéel »,” *Comptes Rendus de l’Académie des Sciences - Series I - Mathematics*, vol. 332, no. 7, pp. 661–668, 2001.

# Characteristics of Overstressed Transient Ionisation Fronts and Streamers in Gas and Across Solid Interfaces

---

WITH the developmental details of StrAFE addressed, the necessary context for the studies presented within this chapter have been established. This chapter moves to present analyses on transient ionisation phenomena, including streamer discharges. These self-sustained ionisation wavefronts not only form a critical part of the process leading up to complete breakdown, but are also a core component of technologies that aim to exploit the many properties of the low-temperature plasma developed in their wake. By leveraging the simulation capabilities of StrAFE, this chapter explores fast ionisation waves and streamer discharges with specific emphasis on the effects of time-dependent and fast-rising voltages. Simulations of fast transient ionisation events in gas and across solid dielectric surfaces are presented, providing additional insight into the interactions between non-thermal gas discharges and solid dielectric material. The conducted studies included geometries that incorporate long and short gaps, where the

---

This chapter was partially adapted, and may be quoted verbatim, from the following publication(s) with permission: T. Wong, I. Timoshkin, S. MacGregor, M. Wilson, and M. Given, "A computational study on the effects of fast-rising voltage on ionization fronts initiated in sub-mm air and CO<sub>2</sub> gaps," *Sci. Rep.*, vol. 14, no. 1185, Jan. 2024.

T. Wong, I. Timoshkin, S. MacGregor, M. Wilson, and M. Given, "Modelling of Transient Discharges Along a Sub-mm Air-solid Dielectric Interfaces Under Fast-rising Voltages," *IEEE Int. Pulsed Power Conf.*, San Antonio, TX, USA., Jun. 2023. © IEEE 2023.

former was aimed at deepening the understanding of the *streamer discharge* in the classical sense of a long, filamentary channel [1]; while the latter relates to phenomena better classified as *fast transient ionisation wavefronts* in short gaps, which have particular relevance to technologies such as micro-electromechanical systems (MEMS). Simulations in air and in CO<sub>2</sub> additionally feature in this work, motivated by the recent push towards SF<sub>6</sub> replacement in HV gas-insulated equipment, with some indication that CO<sub>2</sub> may be a strong potential candidate when mixed with various other gases.

## 6.1 Introduction and Motivation

Space charge driven processes, from which fast ionisation waves develop, have been of great interest since before their first description by Meek [2], Raether [3], and Loeb [4–6]. Such phenomena are notoriously difficult to characterise experimentally, at least with available diagnostics and instrumentation at the time of writing. Yet, fast ionisation events represent a critical stage of the gas breakdown process, acting to be the first stage to produce significant ionisation that substantially contributes to the establishment of a conductive channel through the gas. As was discussed within Chapter 5, this has motivated numerous subsequent studies that employed numerical modelling as a means to explore the characteristics of fast ionisation events that are not yet experimentally unattainable. Despite this, computational power remains a limitation, and significant progress has yet to be made for satisfactory code validation [1,7]. There therefore exist many facets to fast ionisation events that remain unknown or poorly understood.

In the continued exploration of impulse-driven breakdown phenomena, fast ionisation events initiated during the rising-slope and under overstressed conditions is one aspect that would benefit from further study. Reiterating the discussion of Chapter 4, there remains a reliance upon classical, possibly outdated, and highly phenomenological laws in much of the field of pulsed power engineering. Only by progressing both experimental and modelling works can design rules be improved to support the next generation of technology. The subsequent analyses presented in Chapter 4 demonstrated clear and significant effects that fast-rising voltages may have on the development of electron avalanches; motivating a similar investigation of their effects on the development and propagation of fast ionisation wavefronts. In the case of the electron avalanche, enhanced electron production rates on the rising slope were attributed to the time-increasing external field. Since the external field directly determined the electron transport parameters, which governed the avalanche development, it was reasonable to assume that it would similarly impact on the moment of avalanche-to-streamer transition, and which was subsequently deduced

to be the case.

However, the relationship is perhaps not so clear when space charge becomes dominant, as in the case of ionisation wavefronts. The governing equations for modelling these wavefronts, presented within Chapter 5, makes clear the coupling between the space charge magnitude and the net electric field. As a result, ionisation wavefronts and streamer discharges are self-propagating structures driven in part by their own electric field, developed due to the magnitude of free charge produced from intense collisional ionisation. If developed under a time-increasing field (like in the case of overstressed breakdown, where ionisation waves must necessarily have developed during the rising slope), there should be an expectation that there will be some influence on the field ahead of the wavefront. The exact nature of this influence, however, is unclear; as are the induced changes to other parameters such as the developed electron density, propagation velocity, and radius.

Limited work has been conducted in the past under such configurations, with those most relevant including simulations conducted by Babaeva and Naidis [8,9], who investigated streamer characteristics under exponentially-rising voltages within centimetre scale sphere-plane gaps. Their main results included the observation of greater streamer propagation velocities with faster-rising voltages, accompanied by an increase in the streamer diameter. In other work, Jadidian *et al.* [10] investigated streamer initiation within oil-filled gaps over full impulses, and in [11] with the inclusion of solid dielectric barriers. The authors of [10] found that the voltage rate-of-rise may affect characteristics such as the streamer radius and velocity when in oil. It must be noted, however, that the approach used in [10] follows that of the hydrodynamic approximation as presented in Section 5.4.1; its validity of application in liquid dielectrics is not well known, despite their inclusion of the Zener field ionisation process. The authors of [10] remarked that their modelled temperature distributions would indicate that vaporisation of the liquid into the gas phase would have occurred, however, separate domains representing the developed gas phase were not included. Comparison and extension of these trends to streamer development in gas alone must therefore be made with caution. Motivated by the largely-unexplored area of fast ionisation events under fast-rising voltages in gas, the work presented within this chapter partially addresses these deficiencies.

Similarly, this chapter also addresses the second major focus of the present work: dielectric interfaces. As discussed within the review of Section 2.4.1, a greater body of literature exists for the flashover behaviour of solid-gas interfaces, owing to their relevance to, and prevalence in, power equipment. Also reviewed were recent computational studies that had been made

		Dielectric Surface	
		N	Y
Gap Distance	Short, sub-mm	Section 6.3	Section 6.4
	Long, mm-cm	Section 6.2	Section 6.5

**Figure 6.1:** Outline of the four component sections of this chapter, based on the gap distance under study and whether solid dielectric surfaces were featured.

possible due the recent advances in gas discharge simulation techniques discussed in Chapter 5. These works have led exploration into highly-relevant issues including the effects of surface charge [12, 13] and propagation over textured surfaces [14, 15].

The configurations which were simulated and analysed in this chapter can be broadly split into two categories: (i) characteristics of streamer discharges developed within long (cm) gaps, and (ii) ionisation wavefronts initiated within short (sub-mm) gaps. Phenomena pertaining to surface streamers, surface charge, and comparative studies between air and CO<sub>2</sub> also feature. Figure 6.1 provides an outline of the four sections contained within this chapter; their respective contents is as follows:

- Section 6.2 — Using a minimal streamer model, this section includes a first look into positive and negative streamers developed in uniform, linearly-increasing, electric fields under gas-filled and overstressed gaps. Analysis is presented on the simulated streamer characteristics including their morphology, developed electric fields, electron densities, and the impact of the rate of voltage rise,  $dU/dt$ .
- Section 6.3 — A study on the effects of fast-rising voltages on ionisation wavefronts developed in sub-mm air and CO<sub>2</sub> needle-plane and needle-needle gaps. Resulting effects of  $dU/dt$  on the wavefront inception, development, and novel observations pertaining to the cathode sheath thickness in CO<sub>2</sub> are presented.
- Section 6.4 — A complementary study to Section 6.3 within a similar sub-mm needle-plane domain, but with the inclusion of a dielectric barrier, such that ionisation waves would be initiated directly from an electrode-solid-gas triple junction. Different values of  $dU/dt$  were again incorporated into this set of simulations, and results pertaining to surface charging are presented.

- Section 6.5 — A return to longer gaps and constant applied voltage, investigating the role of non-uniform (Gaussian distributed) surface charge on the inception and development of positive surface streamers. A needle electrode embedded within a solid dielectric was used in this study, to ensure the direct inception of streamers at the solid surface. The effects of surface heterocharge and homocharge were investigated.

All miscellaneous simulation settings not explicitly provided within the main text can once again be found in Appendix B.3 for each study presented here.

## 6.2 A First Look at Streamer Development on a Rising Slope

The analysis here begins with that of the most basic case: streamer discharges developed within uniform fields, using a minimal simulation model. The main objective was to provide a “first look” into streamer characteristics on the rising slope, in the absence of other complexities such as background field non-uniformity or surface effects. The configuration used in the comparison study of Bagheri *et al.* [16] (which was also used for the verification of StrAFE in Section 5.8.1) was considered highly appropriate for this purpose, especially considering that the static case was well reproduced using StrAFE and provides a good reference case for comparison.

### 6.2.1 Computational Domain and Configuration

It follows that the utilised simulation parameters and boundary conditions were identical to Section 5.8.1, with the following exceptions:

- The  $z$  height of the domain was increased to 2.5 cm to allow for the developed streamers to reach stable propagation regardless of which value of  $dU/dt$  was used. The initial seed was hence also moved upward to the position  $z_0 = 2.25$  cm, while its other parameters remained unchanged.
- The static 18.75 kV energising voltage was replaced with ramp voltages rising at 2.5, 5, 7.5, and 10 kV/ns in separate simulation runs to understand the effects of varying  $dU/dt$  (corresponding therefore to  $\mathcal{D} = 1 \times 10^{14}$ ,  $2 \times 10^{14}$ ,  $3 \times 10^{14}$ , and  $4 \times 10^{14}$  V m<sup>-1</sup> s<sup>-1</sup>, respectively, in the notation of Chapter 4 where  $\mathcal{D}$  is the rate of field rise.).

For convenience, the computational domain is shown in Figure 6.2 with the updated dimensions and boundary conditions. In each case, simulations were run for a total of 25 ns or until the streamer reached the opposite electrode, whichever occurred first.

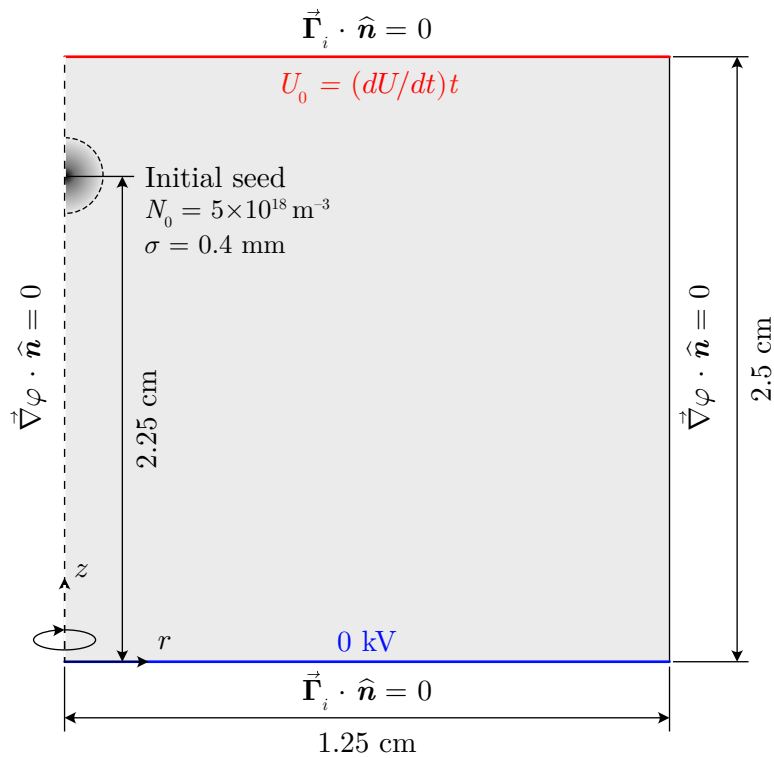


**Figure 6.2:** Adapted cylindrical domain from Section 5.8.1 to evaluate the role of  $dU/dt$  on streamer discharges, labelled with dimensions and boundary conditions. Note the equivalent notation  $\mathcal{D} \cdot d = dU/dt$  where  $\mathcal{D}$  is the rate of field rise as introduced in Chapter 4.

### 6.2.2 Effects of Rate-of-Rise on Positive Streamer Development

The spatio-temporal evolution of the developed streamers in the case of positive energisation are first presented. This is provided through Figure 6.3 which plots the electric fields and electron densities at  $t = 6, 8,$  and  $10$  ns (in correspondence to Figure 6.3(a), (b), and (c), respectively) for each value of studied  $dU/dt$ . Note that the usage of an axisymmetric domain ensured rotational symmetry of the computed results. To provide a compact presentation of the numerous simulation results, each panel of Figure 6.3 is split down the centre, showing the electric field magnitude and electron density on the left and right sub-panels, respectively. For Figures 6.3(a) and (b), none of the simulated streamers had propagated far enough to reach the mid-gap position. The panels have therefore been truncated to show only the top half of the domain.

In an identical manner to the static case of Section 5.8.1, positive streamers developed from the locally enhanced field induced by the presence of the initial charged seed. The electric field was then rapidly redistributed to form a streamer head, which then enabled its propagation through

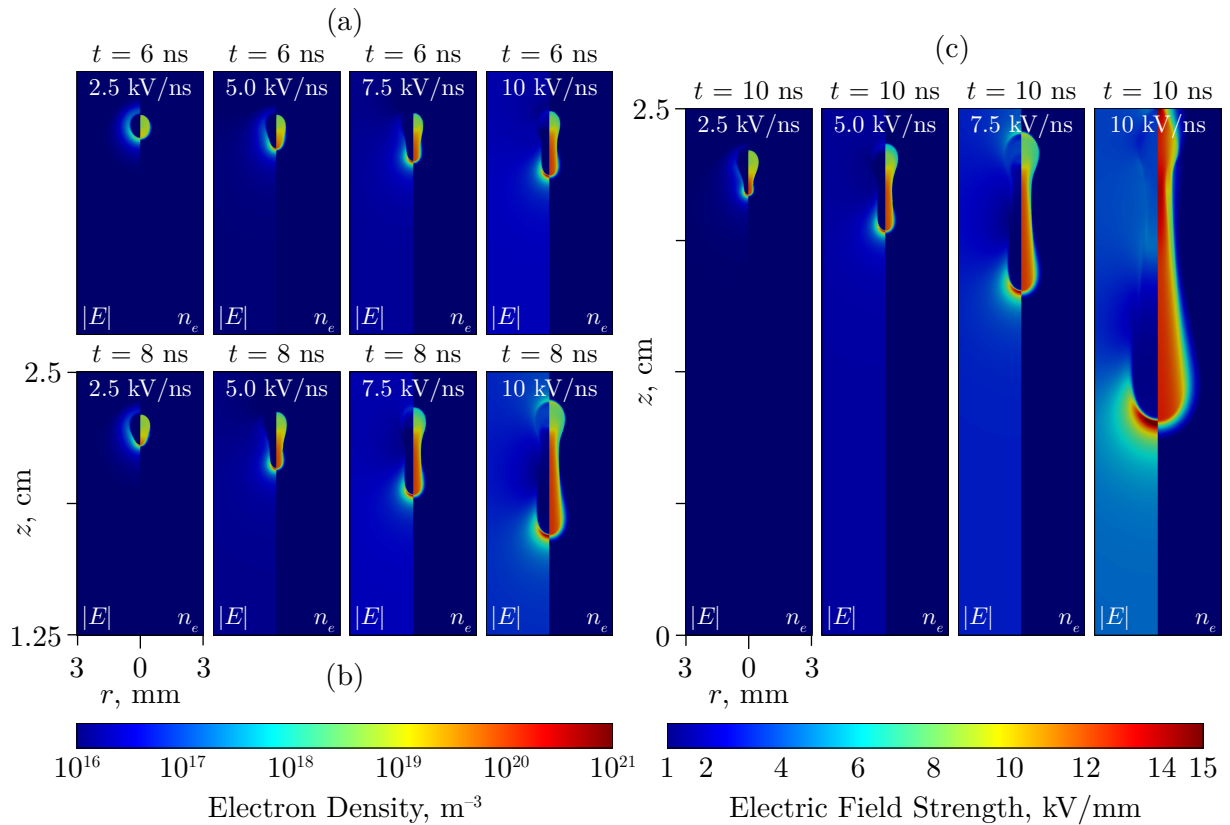


**Figure 6.3:** Spatio-temporal evolution of the electric field magnitude and electron density of positive streamers at  $dU/dt = 2.5, 5.0, 7.5,$  and  $10$  kV/ns at (a)  $t = 6$  ns, (b)  $t = 8$  ns, and (c)  $t = 10$  ns.

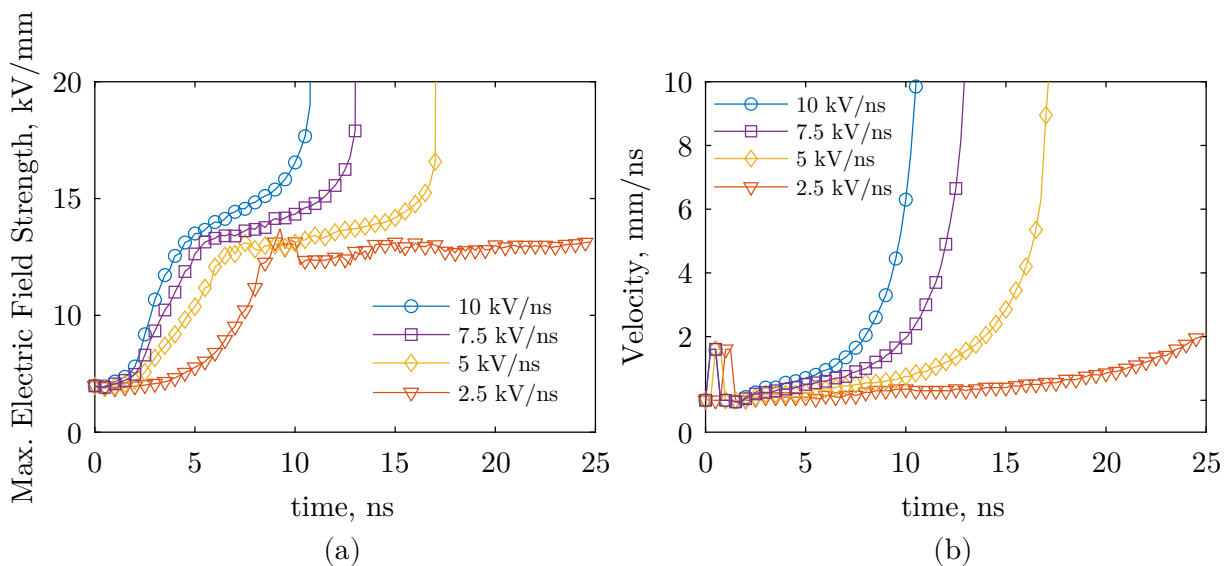
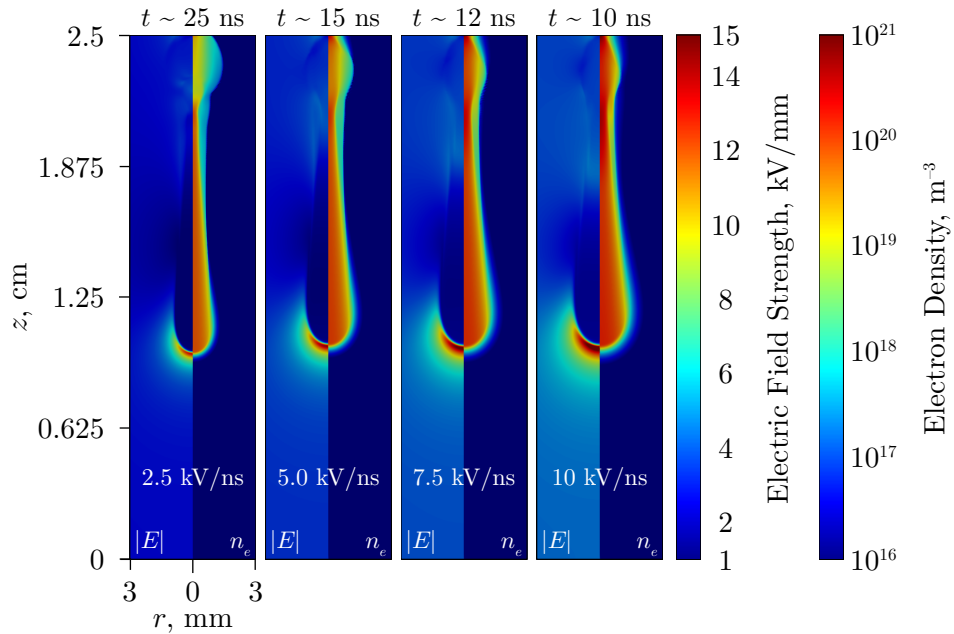


**Figure 6.4:** Plots of (a) maximum electric field strength and (b) streamer velocity over time for streamers initiated under  $dU/dt = 2.5, 5.0, 7.5,$  and  $10$  kV/ns ramp voltages. All cases apart from  $2.5$  kV/ns reached the ground electrode within  $25$  ns explaining the rapid increase in field and velocity due to proximity effects near the electrode boundary.

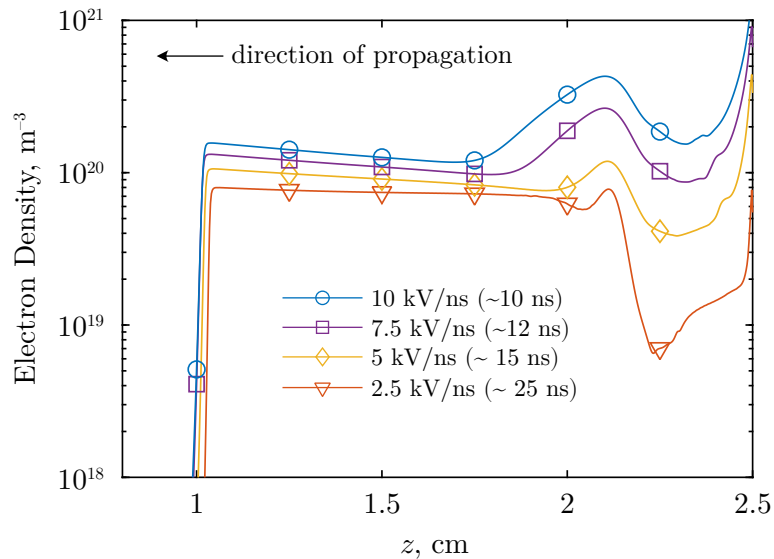
the gas, driven by intense collisional ionisation occurring at the wavefront. As is evident from Figure 6.3, faster-rising voltages resulted in an increasingly rapid development of the positive streamer due to the stronger electric fields developed at the streamer head at any given time. The electric field magnitudes along the axis of symmetry are plotted in Figure 6.4, alongside the streamer propagation velocities. It is reasonable that stronger electric fields lead to the enhancement of impact ionisation, allowing streamer fronts to reach greater velocities under faster-rising voltages.

Figure 6.5 shows colour plots corresponding to the four different cases of  $dU/dt$ , plotted at the moment that each streamer head had reached approximately  $z = 1$  cm. The corresponding times necessary for each streamer to do so has been annotated on each panel. Accordingly, the developed electron density inside the streamer channel (at the comparable propagation lengths shown in Figure 6.5) was also found to increase with faster-rising voltages, as plotted in Figure 6.6. This increase in the plasma density follows from the stronger field at the streamer head with greater overvoltage, which continued to increase over the duration of propagation due to the increasing strength of the applied field.

Tendencies of the streamer diameter,  $d_{st}$ , are further shown in Figure 6.7(a), showing increased streamer diameters with greater rate of voltage rise for a given time. Note that the streamer



**Figure 6.5:** Comparison of the time necessary for positive streamers initiated under  $dU/dt = 2.5, 5.0, 7.5,$  and  $10$  kV/ns ramp voltages to propagate the same length along the gap. Note also the differences in the streamer diameter.



**Figure 6.6:** Electron density profiles of positive streamers initiated under  $dU/dt = 2.5, 5.0, 7.5,$  and  $10$  kV/ns ramp voltages compared at times of equal propagation distance, according to those in Figure 6.5.

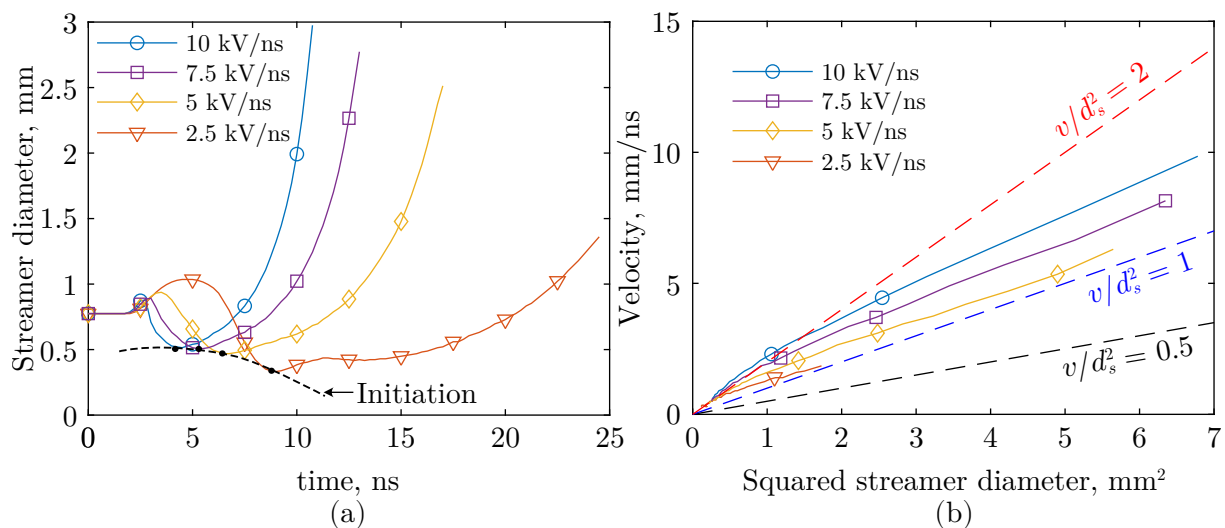


**Figure 6.7:** Plots of (a) streamer diameter over time and (b) streamer velocity against the ratio  $v/d_s^2$  for overstressed positive streamers initiated under  $dU/dt = 2.5, 5.0, 7.5,$  and  $10$  kV/ns ramp voltages.

diameter was defined as the  $r$ -coordinate of the point that corresponded to the maximum  $r$ -component of the electric field, recorded over time (as was also used in [16]). This increase is believed to once again reflect the stronger fields developed at the propagating streamer heads, which increases the effective size of the strongly-ionising region around the propagating wavefront, enabling the radial growth of the streamer. In Figure 6.7(b), the calculated streamer velocities have been plotted against the square of the streamer diameter, alongside the scaling relation discussed in Chapter 2 - Section 2.5.2,  $v = 0.5d_{st}^2$ , which is well known for the static case [17]. Under the present ramp voltages, the approximately linear relation undoubtedly remains. However, the ratio  $v/d_{st}^2$  was found to be greater than the standard case of 0.5, with values of  $v/d_{st}^2 \approx 1$  appearing a better fit to the data for  $dU/dt = 5, 7,$  and  $10$  kV/ns. In the case of  $2.5$  kV/ns,  $v/d_{st}^2 = 0.5$  remains a good fit, the difference of which provides some insight to the reason behind a value greater than 0.5 for faster-rising voltages. Consider that at  $2.5$  kV/ns, the maximum background field only reaches a maximum value of  $2.5$  kV/mm over the course of the  $25$  ns simulation. This field magnitude remains below the critical field for atmospheric air, such that the  $2.5$  kV/ns streamer does not technically qualify as a streamer initiated within the overstressed regime. This may explain the reason for the value of  $v/d_{st}^2$  to resemble that of the original cases studied in [17], where this expression was fitted based on experimental data of streamers propagating into regions of below-critical field. In an overvolted case, streamers produced larger ionising regions near their heads for a similar streamer diameter because of the already above-critical background field. It follows that a streamer of a certain diameter will

develop and (propagate) faster within a overstressed gap compared to a sub-critical gap.

Although a minimal streamer model was used in the present analysis, the results of this section also imply an intensification of plasma chemical processes occurring within discharges developed on the rising slope. For technologies involving nanosecond pulsed streamer discharges, the increased streamer velocities, diameters, and plasma densities found with faster rise-time (e.g., also reported experimentally such as in [18–21], and in other modelling studies [8, 9]), are in agreement with the simulations here. Considering that the streamers investigated in such studies were developed on the rising-edge, the situation is comparable to that of the ramp configuration used here. The observed effects with rise-time may therefore be directly explained by the stronger electric fields developed under overstressed conditions, facilitated by the fast-rising voltage capable of increasing significantly over the duration of the streamer flight.

### 6.2.3 Effects of Rate-of-Rise on Negative Streamer Inception

Complementing Section 6.2.2, simulations using negative ramp voltages were performed using the same domain of Figure 6.2, where the initial charged seed was also replaced with electrons instead of positive charges (with the same magnitude and variance), to reflect the change in polarity. Negative streamers would therefore be initiated and propagate downward towards the ground plane, mimicking the positive case. The total simulation runtime was also extended, since negative streamers exhibited a prolonged inception time. It should also be noted that the present configuration also led to the development of an upward-propagating positive streamer which travelled towards the negatively-charged plate (in the same way as the double-headed streamer shown previously in Section 5.8.3). In all cases, the simulation could not be progressed beyond the moment that the upward positive streamer contacted the electrode due to the formation of the cathode sheath. The dynamics of the cathode sheath cannot be resolved using the minimal model, as it would be in violation of the validity conditions of the local field approximation (LFA), as discussed within Section 5.4.4. Despite this, the initial stages of the negative streamer development and propagation remain valid and are sufficient for the investigation of the inception behaviour. It is remarked that even in a case where the full negative streamer evolution could be simulated in this way, there are indications from other works [22, 23] that kinetic and non-local phenomena, such as runaway electrons, are important for negative streamer development. If true, the LFA would certainly not be adequate to accurately capture negative streamer formation. Considering this, the discussion here is limited to the initiating stages of negative streamers from the initial charged seed.

The development of negatively-charged seeds into streamers is shown in Figure 6.8 using the same format as Figure 6.3, again showing the electric field and electron density distributions over time. Compared to their positive counterparts, negative streamers develop in a more diffuse manner, in agreement with other simulated work, e.g., in [24]. Upon voltage application, the initial electrons diffuse outward, forming a growing spherical charge volume (resembling the phenomena known as the *inception cloud* [25]). Due to downward electronic drift, it becomes distorted as the electric field increases in magnitude. Ionisation also permits the generation of electron-ion pairs near the bottom of this space charge volume, which eventually accumulate (in the cases that the field magnitude is sufficiently high) to form a streamer head.

During the initial stages of outward electron transport, the electron density experiences a period of sustained reduction. Combined with the reducing curvature of the space charge volume, a longer time was therefore necessary for the electric field to become sufficiently strong for a streamer to form. See for example the  $-2.5$  kV/ns case of Figure 6.8 row (a), where a streamer was unable to be formed within the 33 ns simulation time, partly due to the significant outward diffusion of the electron density during the slower-rising slope. For the  $-5.0$ ,  $-7.5$ , and  $-10$  kV/ns cases, the extent of the initial diffusive reduction is clearly reduced, evidenced by the far sharper boundary between the initial charge volume and the background gas. In other words, faster-rising background fields not only expedite the onset of ionisation, due to the development of stronger electric fields over shorter timescales, but the rate at which they rise also allow them to outpace the initial reduction during the inception stage due to outward electron diffusion.

These effects are identical to those derived analytically within Chapter 4 when analysing avalanche development. In the previous analysis, electrons experienced diffusion in a the uniform background field as space charge effects remained negligible during the initial avalanche stage (the reader is reminded of Figure 4.3, where the field was essentially undistorted up until the moment of transition). For the simulations conducted here, the enhanced field induced by the initial charge seed was also present as an initial condition. At  $t = 0$ , the field magnitude is radially symmetric around the centre of the charge seed, such that for a short period after  $t = t_0^+$ , the electron density spreads in all directions with radial symmetry (since the diffusion constant,  $D_e$ , is almost equal in all directions). However, as the field rises, these electrons are advected downward towards the anode, creating the asymmetry seen in Figure 6.8 columns (iii)–(vi). For cases where these electrons are accelerated beyond the ionisation threshold, the beginnings of a plasma channel begins to form and redistributes the electric field to the edge of the expanding charge volume (e.g., as seen in Figure 6.8 for  $dU/dt < -2.5$  kV/ns). This location at the lower extreme of the

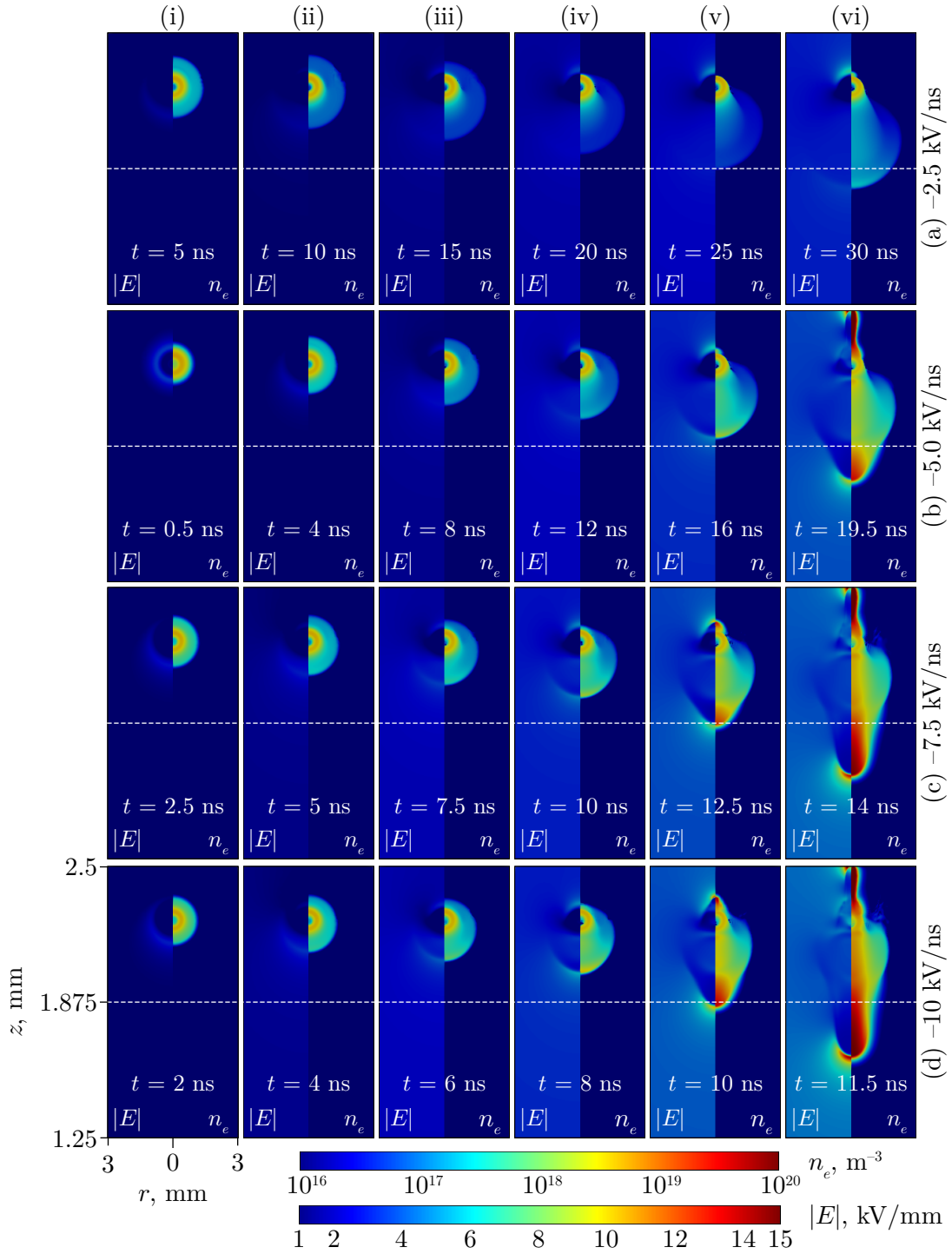


**Figure 6.8:** Spatio-temporal evolution electric field magnitude and electron density of negative streamers initiated under  $dU/dt = 2.5, 5.0, 7.5,$  and  $10$  kV/ns ramp voltages (a)–(d). Roman numerals advance in time (i)–(vi).

charge volume, extending towards the anode, ultimately becomes sufficiently enhanced that the main streamer front is developed.

The characteristics of the minimal case presented here sets out a number of base expectations for this discharge regime, establishing a reference case for the subsequent work. The following sections present additional studies of greater complexity, focusing on various aspects of fast ionisation events with greater practical relevance.

### 6.3 Overstressed Discharges in Sub-mm Air and CO<sub>2</sub> Gaps

Building upon the results of Section 6.2, this section presents a more extensive study on overstressed transient ionisation wavefronts under more specific and practically-relevant conditions. Note that the contents of this section are based on the published paper [26]. Namely, the system of interest pertains to primary discharges initiated within sub-mm electrode gaps. Motivated by the drive towards system miniaturisation in pulsed power, semiconductor, and power electronic industries; a strong understanding of the fundamental processes driving electrical breakdown within increasingly compact configurations is necessary to drive the development of related technologies. For instance, breakdown prevention within MEMS or novel power electronic devices [27], equipment used in pulsed power and low-temperature plasma systems [28], electrostatic precipitation systems [29], and systems for pulsed electric field treatment [30] are some potential beneficiaries from this type of study. Simulations in both air and CO<sub>2</sub> (at STP conditions) were conducted as part of this work, informed by the importance to characterise CO<sub>2</sub> in chemical processing applications such as CO<sub>2</sub> splitting [31], and for its potential to be used within gas mixtures that may act as replacements for the potent greenhouse gas, SF<sub>6</sub>, within gas-insulated power and pulsed power equipment [32–34].

Literature on sub-mm gaps (but larger than that of the lower Paschen limit of  $\lesssim 15 \mu\text{m}$  at 1 atmosphere [35]) is scarce, particularly for sub-mm gaps involving non-uniform electric fields combined with fast-rising voltages, yet, these are commonly encountered in practise. Experimentally, Hogg *et al.* [36,37] investigated the breakdown of bottled air in sub-mm point-plane gaps down to 250  $\mu\text{m}$ , pressurised between 0.1 and 0.35 MPa. The authors observed a dependency of the relative magnitudes of positive and negative breakdown voltages on the gap distance. While negative breakdown voltages exceeded those of its positive counterparts in longer gaps, for gaps shorter than a gas- and electrode-specific limit,  $d_{\text{crit}}$ , this relationship was inverted. Liu *et al.* [38] conducted impulsive breakdown experiments in common gases under fast-rising

nanosecond impulses in a 100  $\mu\text{m}$  needle-plane gap. Separate tests with gaps filled with air, CO<sub>2</sub>, and N<sub>2</sub> were conducted, from which the authors consistently recorded higher breakdown voltages at shorter breakdown times in CO<sub>2</sub> compared to the other gases. Based solely on the classical streamer inception theory using Townsend coefficients, one would not expect CO<sub>2</sub> to possess the highest breakdown strength. Kumar *et al.* [39] showed that Meek's criterion fitted their breakdown data well for CO<sub>2</sub>, though their experimental arrangements incorporated considerably longer gaps, and with an arbitrarily chosen value of  $K = 13$ . The authors of [38] attributed the distinctly different field-time characteristic of their CO<sub>2</sub> dataset to statistical time, which was an aspect that was not controlled within their experimental arrangements. However, the largely unexplored domain of discharges within short sub-mm gaps motivates further study, as such, this work explores the possibility of other influencing factors over the discharge evolution that may be related to the observations in [38].

### 6.3.1 Computational Domain and Configuration

Aside from the two different working gases studied within the present simulations, two different 2D-axisymmetric electrode geometries were also included, shown in Figure 6.9. The first incorporated a needle-plane configuration, while the second mirrors the needle electrode to form a needle-needle configuration. All needles used within this set of simulations were approximated as hyperbolae of the form

$$\frac{(r - r_0)^2}{a^2} - \frac{(z - z_0)^2}{b^2} = 1 \quad (6.1)$$

with a radius of curvature of  $r_t = 80 \mu\text{m}$  (which was defined as the length of the *semi-latus rectum*,  $b^2/a$ ), as used in the experimental work of [38]. The gap distance considered was 250  $\mu\text{m}$ , which is of similar separation to those in [38] and among the smallest gaps used in [37]. The ramp voltage (5.48) was once again applied of both polarities, though with a new set of values of  $dU/dt$  corresponding to 10, 12.5, 16.67, 25, and 50 kV/ns informed by rising impulses typical to some pulsed power and plasma technologies [19]. Note that there was no requirement for the polarities to be changed for a second set of simulations in the needle-needle case due to the symmetry of the electrodes.

The choice of mathematical model was informed by the geometric characteristics of the utilised computational domain. Notably, the reader is reminded of the validity criteria presented as Figure 5.6 and Figure 5.7 of Chapter 5. Based solely on the former, where gap distance and pressure are the main determinators, the problem lies adequately within the *Fluid* simulation domain. This may be supported by a basic estimation of the electron free mean path in air

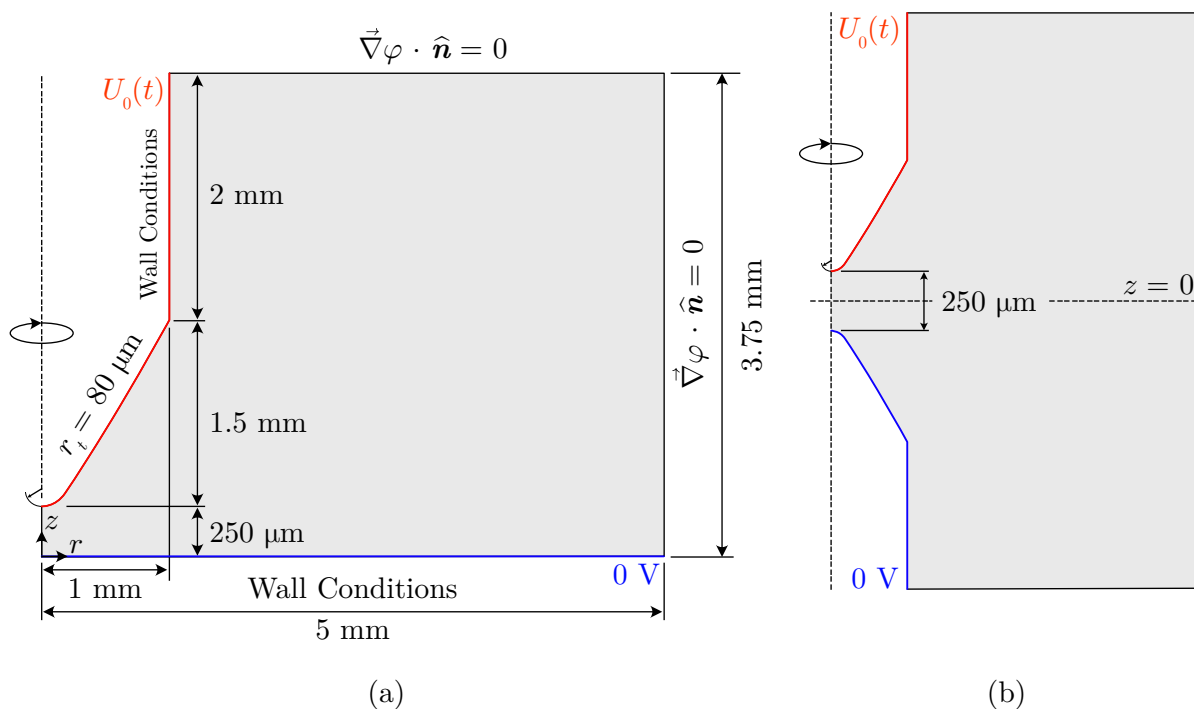


**Figure 6.9:** Cylindrically-symmetric domain used for the study of sub-mm ionisation waves in (a) needle-plane, (b) needle-needle electrode geometries, labelled with dimensions and boundary conditions. Image (a) adapted from [26] under CC BY 4.0.

and in  $\text{CO}_2$  according to [40] or in [41], which gives values on the order of  $10^{-7}$  m for electrons with energies of  $\lesssim 10$  eV. Compared to the electrode geometry with characteristic length of  $L \sim 10^{-4}$  m, the Knudsen number would also suggest that the fluid approach would be a suitable choice. Similarly, based on the analysis of Zhu *et al.* [42] as presented as Figure 5.10, the LMEA would be necessary for simulation accuracy using the conditions here, based on expected grid dimensions considering the already small gap distance.

More care has to be taken when applying the time-based criterion of Zhu *et al.* [42] shown in Figure 5.7. As will be seen within the results, the discharge timescales are on the order of picoseconds, which satisfies the criterion of (5.7), but places it close to the boundary between fluid and kinetic approaches since the discharge timescale is close to the electron energy relaxation time. That is, the simulation configuration here is on the edge of necessitating a kinetic description to be true to reality. There are reasons to believe, however, that the fluid model remains valid within this region which justifies its application. First of all, the criterion of Zhu *et al.* [42], as discussed in Section 5.2.2, was based on the assumption that the criterion is satisfied when  $10\nu_i < \nu$ , where  $\nu_i$  is the ionisation frequency and  $\nu$  is the inverse characteristic time. It is remarked that their

choice of the factor of 10 was arbitrary, and based on their original analysis, even a marginal relaxation of this factor would permit a far larger region of validity. From an experimental validation perspective, one may further compare the configuration here to that of Höft *et al.* [43], a study which featured in the counter-propagating streamer verification study of Chapter 5 - Section 5.8.4. The discharge simulated in [43] occurs over comparable (picosecond) timescales as those performed here, yet the authors found reasonable agreement between the characteristics of the simulated primary ionisation wavefront to that of ICCD images captured experimentally in the same configuration. The use of the fluid model, with the LMEA and enabled through StrAFE, was therefore considered valid for the discharges modelled herein. Incidentally, it is remarked that phenomena close to the fluid/kinetic validity boundary is poorly understood and forms part of the novelty of this work. This study thus also poses a significant opportunity for future modelling works to build upon the results presented in this section, possibly by using a kinetic approach.

Using the LMEA, the simulation incorporated simplified sets of reaction data for both air and CO<sub>2</sub>. The former utilised the same set of reactions as in Section 5.8.3 - Table 5.4, which once again included photoionisation based on the 3-term Helmholtz approximation using the parameters of Bourdon *et al.* [44] in Table 5.2. The latter was described using the simplified chemistry set adapted from Aerts, Somers, and Bogaerts [31] in their study of CO<sub>2</sub> splitting, incorporating tracked charged and neutral species including e<sup>-</sup>, CO, O, O<sub>2</sub>, O<sub>3</sub>, CO<sub>2</sub><sup>+</sup>, O<sub>2</sub><sup>-</sup>, and O<sup>-</sup>, partaking in 17 reactions tabulated in Table 6.1. In CO<sub>2</sub>, there remains some uncertainty regarding the role of photoionisation. Bagheri, Teunissen, and Ebert [47] suggested that photoionisation in CO<sub>2</sub> would be negligible based on their experimental measurements. They further argued that due to the short absorption lengths of photons in CO<sub>2</sub>, the photoelectron source may be limited in magnitude. More recently, however, simulation works including those by Li, Sun, and Teunissen [48] and Marskar [49] suggested otherwise; that photoionisation in CO<sub>2</sub>, although weak, may be sufficient to support the development of positive streamers under high-field conditions. It is remarked that the simulations presented here were conducted prior to the findings of [48] and [49], and photoionisation in CO<sub>2</sub> was therefore not included within the results shown here. Instead, as similarly assumed by Bagheri, Teunissen, and Ebert [47], an elevated level of background pre-ionisation with 10<sup>13</sup> m<sup>-3</sup> of CO<sub>2</sub><sup>+</sup> and e<sup>-</sup> (compared to 10<sup>9</sup> m<sup>-3</sup> of N<sub>2</sub><sup>+</sup> and e<sup>-</sup> used for air) was incorporated for CO<sub>2</sub> simulations. Based on the results of [47], streamers in CO<sub>2</sub> do not appear to exhibit great sensitivity to the level of background ionisation, though it may be important to branching behaviour. With the short sub-mm dimensions of the gap used here, it is unlikely that branching would be relevant. It was therefore concluded that using the

**Table 6.1:** Plasma chemical reactions used in simulations involving CO<sub>2</sub>. Notation  $f(\bar{\varepsilon})$  means that the reaction rate was an empirical function of the local electron energy. Chemical symbol M represents any neutral. Data from the BOLSIG+ solver [45] was computed using the Phelps' database [46].

R	Description	Reaction	Rate	Unit	Ref.
$R_1$	Impact Ionisation	$e^- + \text{CO}_2 \longrightarrow \text{CO}_2^+ + e^- + e^-$	BOLSIG+	m <sup>3</sup> /s	[45]
$R_2$	Dissociation	$e^- + \text{CO}_2 \longrightarrow \text{CO} + \text{O} + e^-$	$5 \times 10^{-17}$	m <sup>3</sup> /s	[31]
$R_3$	Attachment	$e^- + \text{CO}_2 \longrightarrow \text{CO} + \text{O}^-$	BOLSIG+	m <sup>3</sup> /s	[45]
$R_4$	Dissociation	$e^- + \text{O}_3 \longrightarrow \text{O} + \text{O}_2 + e^-$	$2 \times 10^{-15}$	m <sup>3</sup> /s	[31]
$R_5$	Dissociation	$e^- + \text{O}_2 \longrightarrow 2\text{O} + e^-$	$2 \times 10^{-15}$	m <sup>3</sup> /s	[31]
$R_6$	Dissociation	$e^- + \text{O}_2 \longrightarrow \text{O} + \text{O}^-$	$4 \times 10^{-17}$	m <sup>3</sup> /s	[31]
$R_7$	Attachment	$e^- + \text{O}_2 + \text{M} \longrightarrow \text{O}_2^- + \text{M}$	$3 \times 10^{-42}$	m <sup>6</sup> /s	[31]
$R_8$	Ion-Neutral Reaction	$\text{O}^- + \text{CO} \longrightarrow \text{CO}_2 + e^-$	$5.5 \times 10^{-16}$	m <sup>3</sup> /s	[31]
$R_9$	Ion-Neutral Reaction	$\text{O}^- + \text{O}_2 \longrightarrow \text{O}_3 + e^-$	$1 \times 10^{-18}$	m <sup>3</sup> /s	[31]
$R_{10}$	Ion-Neutral Reaction	$\text{O}^- + \text{O}_3 \longrightarrow 2\text{O}_2 + e^-$	$3 \times 10^{-16}$	m <sup>3</sup> /s	[31]
$R_{11}$	Electron-ion Recombination	$e^- + \text{CO}_2^+ \longrightarrow \text{CO} + \text{O}$	$6.5 \times 10^{-13}$	m <sup>3</sup> /s	[31]
$R_{12}$	Ion-Ion Recombination	$\text{O}_2^- + \text{CO}_2^+ \longrightarrow \text{CO} + \text{O}_2 + \text{O}$	$6 \times 10^{-13}$	m <sup>3</sup> /s	[31]
$R_{13}$	Neutral Reaction	$2\text{O} + \text{M} \longrightarrow \text{O}_2 + \text{M}$	$1.04 \times 10^{-45}$	m <sup>6</sup> /s	[31]
$R_{14}$	Neutral Reaction	$\text{O} + \text{O}_2 + \text{M} \longrightarrow \text{O}_3 + \text{M}$	$4.42 \times 10^{-46}$	m <sup>6</sup> /s	[31]
$R_{15}$	Neutral Reaction	$\text{O} + \text{O}_3 \longrightarrow 2\text{O}_2$	$7.56 \times 10^{-18}$	m <sup>3</sup> /s	[31]
$R_{16}$	Neutral Reaction	$\text{O} + \text{CO} + \text{M} \longrightarrow \text{CO}_2 + \text{M}$	$1.11 \times 10^{-47}$	m <sup>6</sup> /s	[31]
$R_{17}$	Neutral Reaction	$\text{O}_3 + \text{M} \longrightarrow \text{O}_2 + \text{O} + \text{M}$	$1.16 \times 10^{-32}$	m <sup>6</sup> /s	[31]

elevated pre-ionisation as an approximation for an additional (photo)electron source may not be unreasonable. In future, it would be of great interest to revisit the CO<sub>2</sub> simulations conducted here with a full characterisation of the photoionisation process and to perform comparative analysis.

Since the present work was focused on the type of working gas and on the effects of the waveform, no secondary emission nor photoemission at the electrodes were considered. Besides, secondary emission coefficients remain poorly characterised for many engineering materials, and further, cannot typically be controlled. Therefore, although a systematic study on the effects of secondary emission would undoubtedly be of great physical interest, it has been omitted here. It is also noted that the simulations here were terminated upon the contact of the primary ionisation front with the opposing electrode or cathode sheath, since the subsequent processes of cathode sheath collapse and those relating to the gas heating phase are not well known, nor can they be adequately captured using the present model. The resulting simulation results are presented in the sections that follow.

### 6.3.2 Ionisation Front Morphology, Inception, and Propagation

Results are firstly presented on the general morphological features of positive and negative ionisation fronts initiated from the electrode configurations studied here. Figure 6.10 shows the

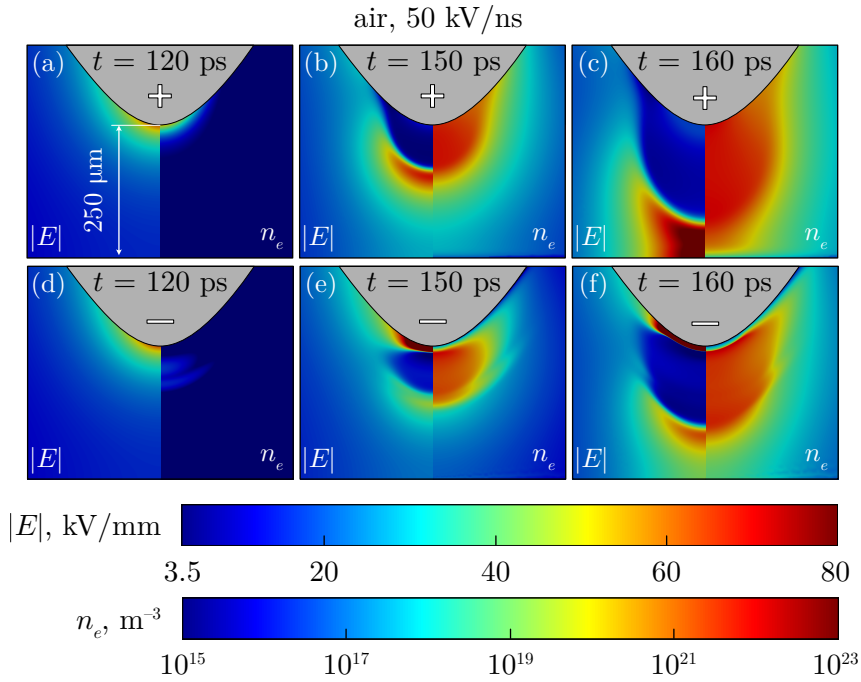


**Figure 6.10:** Time evolution of the ionisation front in an air-filled needle-plane gap. Panels are labelled with the moment in time the image was recorded, while the symbol printed on the needle electrode indicates the polarity of the applied voltage (top rows are positive, bottoms rows are negative). Showing  $dU/dt = 50$  kV/ns only. Image adapted from [26] under CC BY 4.0.

evolution of the electric field magnitude (left half of each panel) and the developed electron density (right half of each panel) at various times in air, magnified to the region containing the discharge near the needle tip for needle-plane electrodes. The case of  $dU/dt = 50$  kV/ns is shown only; all other (slower) rates of rise were morphologically identical, just shifted in time according to the additional time to rise. For a complete set of streak images for all other conditions, the reader is referred to the supplementary material of the publication [26]. The corresponding evolution of wavefronts in CO<sub>2</sub> are shown in Figure 6.11.

The significant overvolting of the electrode gap, from the application of the steep voltage ramp, led to the rapid onset of the primary streamer phase. For the studied range of  $dU/dt$ , the total time-of-flight was in the range of 30 ps to 60 ps which is in reasonable agreement with those obtained by Höft *et al.* [43] considering the smaller gap used here. The corresponding propagation velocities are discussed later in Section 6.3.3. Expectedly, positive wavefronts were initiated directly from the enhanced field near the needle tip, resulting from the needle-directed electron drift and induced impact ionisation near the high-field region. Accumulation of sufficient charge eventually distorts the local electric field at the needle tip, leading to the departure of the main

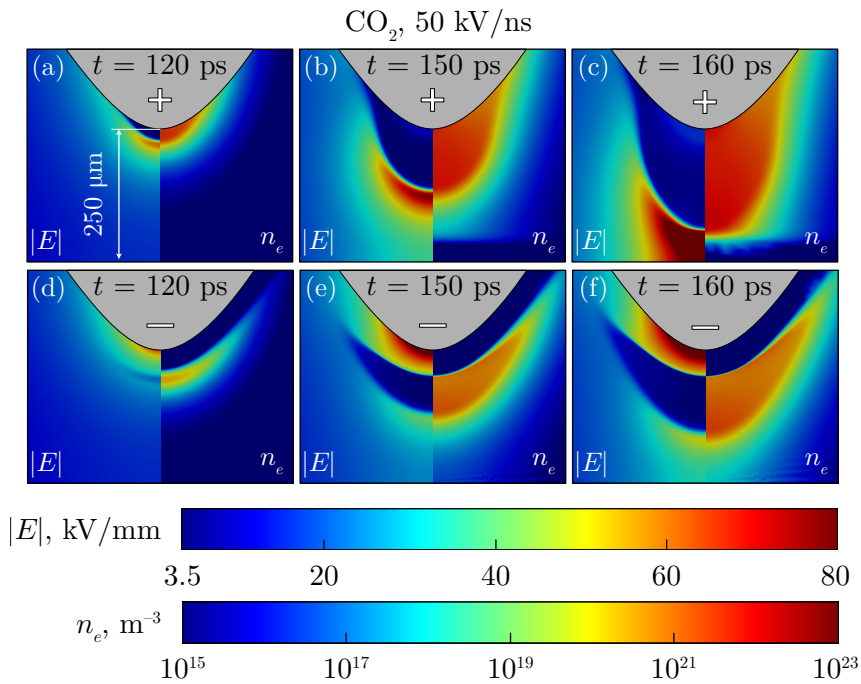


**Figure 6.11:** Time evolution of the ionisation front in a CO<sub>2</sub>-filled needle-plane gap. Panels are labelled with the moment in time the image was recorded, while the symbol printed on the needle electrode indicates the polarity of the applied voltage (top rows are positive, bottoms rows are negative). Showing  $dU/dt = 50 \text{ kV/ns}$  only. Image adapted from [26] under CC BY 4.0.

ionisation front, which then rapidly bridges the electrode gap. Note that direct contact of positive wavefronts with the cathode surface was not made, due to the formation of a cathode sheath with low electron density. Thus, positive wavefronts, upon close-approach, *spread out* along a region indicative of the boundary of the cathode sheath. For negative wavefronts, the cathode sheath formed over the needle electrode, disallowing the initiation of ionisation fronts directly from its surface. In these cases, the initial drift of electrons away from the needle tip caused an initial, and weakly ionising, wave of electrons to leave the needle tip before the formation of a main ionising front. This is particularly clear in Figure 6.10(d). These same electrons were those that drifted away from the needle and led to the eventual establishment of the cathode sheath. The subsequent initiation of the negative wavefront therefore occurred *ahead of the cathode sheath*, where the sheath itself acted as an extended cathode, before propagating and consuming the initial wave of electrons. In CO<sub>2</sub>, this effect was particularly evident due to the significantly thicker cathode sheath that developed (see Figure 6.11) compared to air. As the focus of this section is only on the broad morphology of the wavefronts, the proposed explanation for this difference, along with additional cathode sheath effects, are discussed separately—and in more

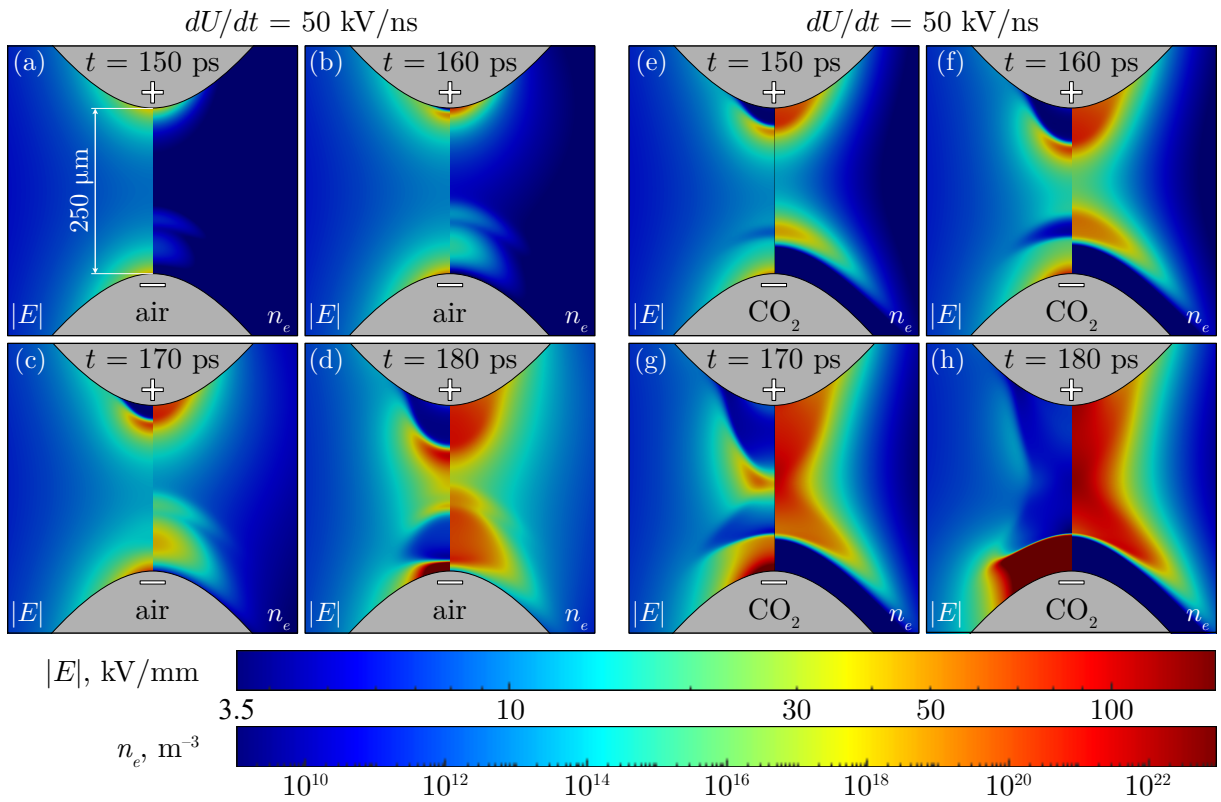


**Figure 6.12:** Time evolution of the ionisation front in (a)–(d) air-filled, (e)–(h) CO<sub>2</sub>-filled needle-needle gaps. Panels are labelled with the moment in time the image was recorded, distinction between anode and cathode is indicated by “+” and “-” symbols printed on the needle electrodes. Showing  $dU/dt = 50 \text{ kV/ns}$  only. Image adapted from [26] under CC BY 4.0.

detail—within Section 6.3.5.

The corresponding colour plots for the needle-needle case are included as Figure 6.12. The phenomenon of the initial electron wave is particularly clear within Figure 6.12(a) and 6.12(b) as seen propagating away from the cathode. In this symmetrical geometry, positive and negative wavefronts do not inception at the same time; negative wavefronts were delayed relative to the positive wavefronts due to the higher inception field associated with negative discharges, consistent with the conclusions of Höft *et al.* [43]. The subsequent counter-propagation of streamers after inception evolved like in [43], where the establishment of the plasma channel was ultimately resultant from the mid-gap merging of the positive and negative wavefronts.

Using the wavefront evolutions from the needle-plane case, let  $t_i$  be the time of wavefront inception. This was defined based on the moment that the wavefront velocity (point of maximum electric field at the head of the wavefront) first becomes non-zero, where it was found that  $t_i$  was

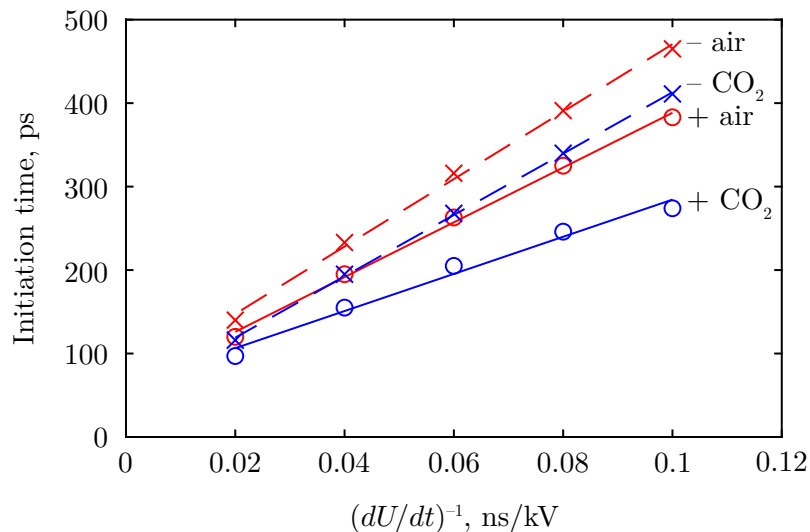


**Figure 6.13:** Plot of the observed linear scaling of streamer inception time with the  $(dU/dt)^{-1}$  in needle-plane gaps for all combinations of gas and polarity. Image adapted from [26] under CC BY 4.0.

inversely proportional to the rate of voltage rise,  $dU/dt$ , for the range of studied values, shown by the linear fittings of Figure 6.13. The reader is reminded that no charged seeds were used in the initiation of wavefronts here; the initial accumulation of charge around the needle tip was purely driven by the local field enhancement induced by the needle curvature. In this case, the initial stages may be considered similar to that of avalanche development as modelled in Chapter 4. In fact, it may be shown that the inverse proportion as observed from Figure 6.13 may be recovered from the improved avalanche-to-streamer model developed in Chapter 4—as follows. The reader is first reminded of the closed-form approximation of the time-to-breakdown (moment of avalanche-to-streamer transition) (4.35), which is reprinted here for convenience,

$$t_b = \frac{B_\alpha}{\mathcal{D}k_1\omega(\mathcal{D})}, \quad (6.2)$$

where  $\mathcal{D}$  is the rate-of-rise of the *electric field*,  $B_\alpha$  and  $k_1$  are constant for a given gas, and the function  $\omega(\mathcal{D})$  is related to the Lambert- $W$  product-log function following (4.36), though the exact analytical form is of less importance in the following analysis. Consider that (6.2) may be expressed as the proportionality

$$t_b \propto \frac{1}{\mathcal{D}\omega(\mathcal{D})} \quad (6.3)$$

since  $B_\alpha$  and  $k_1$  are constant for a given gas. The function  $\omega(\mathcal{D})$  is plotted over a representative

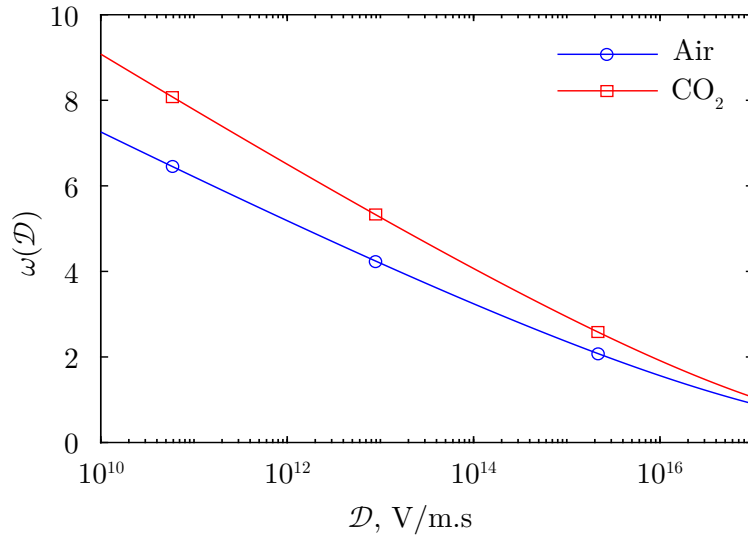


**Figure 6.14:** The function  $\omega(\mathcal{D})$  for air and CO<sub>2</sub> over several magnitudes of  $\mathcal{D}$ . The nearly linear character suggests  $\omega(\mathcal{D}) \propto \log(\mathcal{D}/c)$  is a good approximation. Image adapted with permission from [50], © IEEE 2024.

range of  $10^{10} \leq \mathcal{D} \leq 10^{17} \text{ V m}^{-1} \text{ s}^{-1}$  in Figure 6.14, where two features are of interest. Firstly, the almost linear relationship on the semi-log scale suggests that  $\omega(\mathcal{D})$  is well approximated, over several magnitudes of  $\mathcal{D}$ , by a relation of the form  $\omega(\mathcal{D}) \approx k \log(\mathcal{D}/c)$  where  $k$  is constant and  $c$  is independent of  $\mathcal{D}$  but has units  $\text{V m}^{-1} \text{ s}^{-1}$  to render the argument of the logarithm dimensionless. Considering this, the proportionality  $\omega(\mathcal{D}) \propto (\log \mathcal{D} - \log c)$  therefore applies. Secondly, comparing typical values of  $\omega(\mathcal{D})$  to the corresponding values of  $\mathcal{D}$  shows that the function is only weakly sensitive to changes in  $\mathcal{D}$ , which can be confirmed also by the derivative

$$\frac{\partial}{\partial \mathcal{D}} (\log \mathcal{D} - \log c) \propto \frac{1}{\mathcal{D}}. \quad (6.4)$$

For the ramp voltages simulated here, the values of  $\mathcal{D}$  lie in an estimated range of  $10^{16} \text{ V m}^{-1} \text{ s}^{-1}$  to  $10^{17} \text{ V m}^{-1} \text{ s}^{-1}$ , which in accordance to (6.4) would correspond to values of  $\omega(\mathcal{D})$  that are negligibly different. In fact, the consequence is that for any sufficiently small range of  $\mathcal{D}$ ,  $\omega(\mathcal{D})$  can be considered effectively constant. It follows that under these conditions, (6.3) reduces to the inverse proportionality

$$t_b \propto \frac{1}{\mathcal{D}}, \quad (6.5)$$

such that for any system where the electric field is generated in a static geometrical configuration\*—

\*Static geometries necessarily generate fields of the form  $E(\vec{r}, t) = \mathcal{G}(\vec{r})U(t)$ , where  $\mathcal{G}(\vec{r})$  is some geometry-only-dependent function, and  $U(t)$  is the time-only-dependent voltage. Thus,  $\partial_t E(t) = \mathcal{G}(\vec{r})\partial_t U(t)$  must hold.

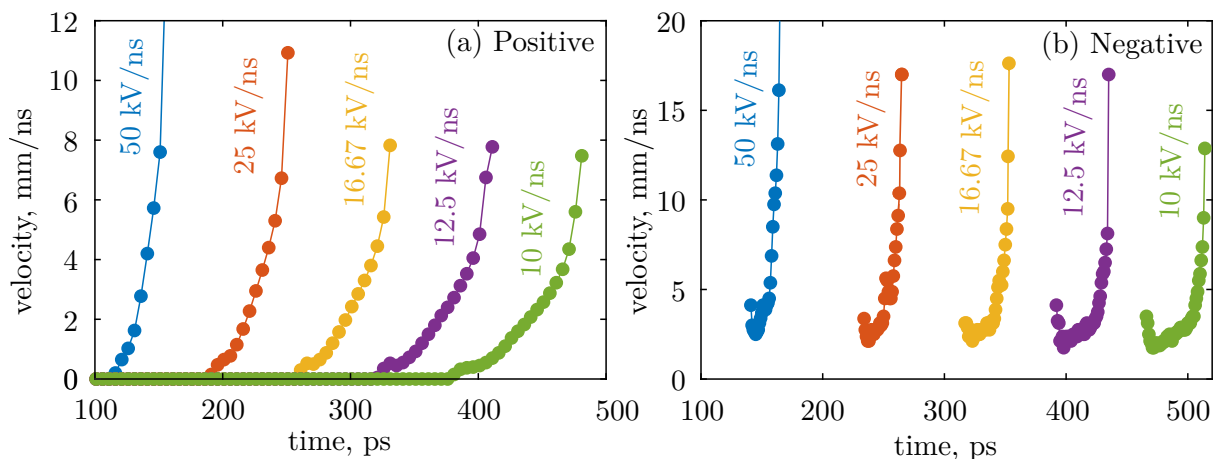


**Figure 6.15:** Instantaneous velocity over time of the (a) positive, (b) negative ionisation fronts in air-filled needle-plane gaps for the simulated rates of voltage rise. Negative fronts also have zero velocity before the first data-point, but markers have been removed for visibility. Image adapted from [26] under CC BY 4.0.

which is true in the vast majority of cases—the proportionality  $\mathcal{D} \propto dU/dt$  holds, and hence

$$t_b \propto \left( \frac{dU}{dt} \right)^{-1}, \quad (6.6)$$

in agreement with the simulated wavefront inception times shown in Figure 6.13.

### 6.3.3 Effects of $dU/dt$ on Velocity and Electric Field

Instantaneous propagation velocities for the developed ionisation waves were computed based on the  $z$ -position of the wavefront. For both polarities, this was defined as the point of maximum field strength ahead of the main wavefront, which are plotted for all the studied values of  $dU/dt$  in the needle-plane case in Figure 6.15(a) and 6.15(b). It is noted that due to the inception of negative wavefronts ahead of the cathode sheath, the location of the maximum electric field exhibits an abrupt jump from the needle surface to the location of the initiated wavefront. This manifested as the abrupt changes in velocity visible in Figure 6.15(b). This was not an issue for positive streamers, since they were initiated directly from the needle tip, resulting in no sudden transitions in the position of the maximum field.

Overall, the propagation velocities of all fronts grew rapidly after inception, owing to the high electric field magnitudes of between 60 kV/mm to 80 kV/mm driving the wavefront forward. Negative fronts appeared to experience significantly greater acceleration than their positive counterparts, and attained higher maximum velocities over the course of their propagation. This

appears to be related to the generally stronger inception field required for negative streamers. With slowing  $dU/dt$ , however, the effect on the maximum attained velocity for both polarities was inconclusive. During the propagation phase, lower values of  $dU/dt$  appeared to reduce the acceleration of wavefronts, indicated by the decreasing slope of velocity. A notable aspect for negative streamers is the initial reduction in the propagation velocity observed in Figure 6.15(b), which corresponds to the phase when the ionisation wave begins to initiate. During this phase, the plasma channel begins to develop ahead of the needle, but the front has yet to begin its propagation in a self-sustained manner driven by sufficiently intense ionisation at its head. Since the channel is also continuously expanding due to outward electronic diffusion (thus leading to a decrease in the wavefront field), these competing mechanisms contribute towards the initial decrease in propagation velocity, up until the point that ionisation becomes sufficiently intense to drive the wavefront forward. The simulated propagation velocities are in fair agreement with those measured and simulated in Höft *et al.* [43], and are further corroborated by those experimentally measured in Tardiveau *et al.* [51] also under voltages rising on the order of kV/ns.

Average velocities were further calculated from the simulated data, according to

$$v_{\text{avg}} = \frac{d}{t_c - t_i}, \quad (6.7)$$

where  $d$  is the distance covered by the wavefront (discounting the cathode sheath) over its propagation,  $t_c$  is the time of contact, and  $t_i$  is the time of inception as defined in Section 6.3.2. The time of contact,  $t_c$ , was taken to be the moment that the wavefront ceased to have a  $z$ -velocity upon close approach to the plane electrode. That is, at the point when the maximum electric field ceased its progression downward, but instead began to spread out along either the electrode itself (in the negative case), or across the cathode sheath (in the positive case). The streak image of Figure 6.16(a) provides several examples indicating the moments when these quantities were defined, while Figure 6.16(b) provides the computed average velocities plotted against  $dU/dt$  for each triplet of gas-polarity- $dU/dt$ .

Ionisation fronts initiated in air, on average, propagated faster than those in CO<sub>2</sub>, regardless of  $dU/dt$  or polarity. Comparing between air-initiated wavefronts alone, clear and consistent differences in the average velocities were found; negative fronts, on average, propagated faster than positive fronts under the same conditions. This was in contrast to CO<sub>2</sub>, which appeared to have no significant differences in average velocity between the two polarities. The reason appears related to the varying thickness of the cathode sheath developed exclusively in CO<sub>2</sub>, which was found to be greater for slower rising voltages and for negative-polarity discharges. For

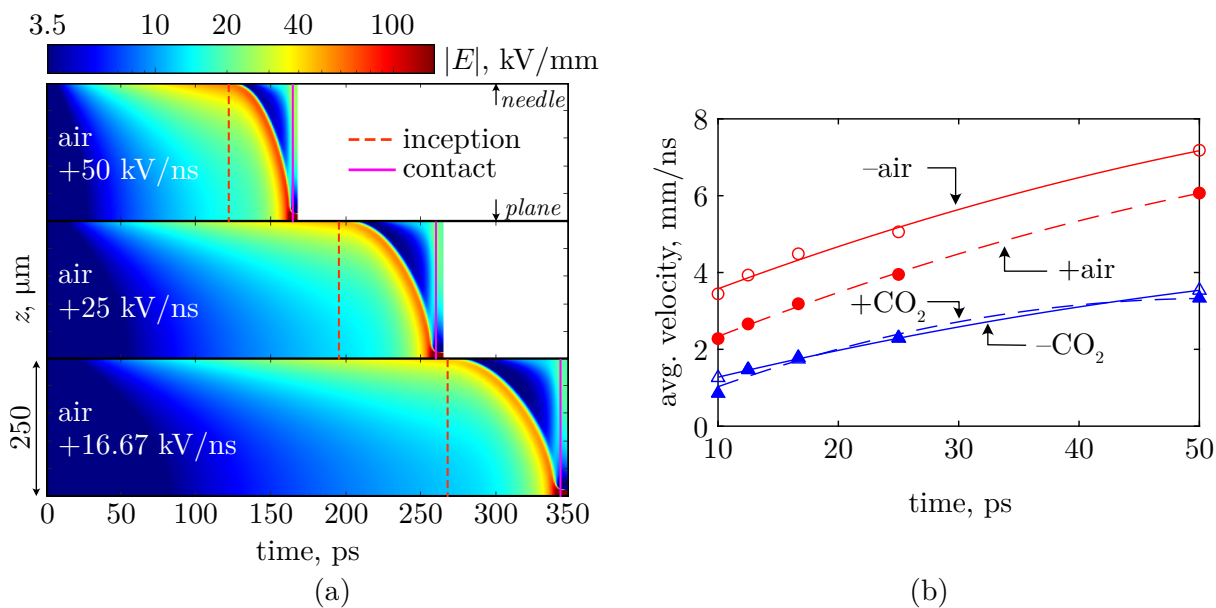


**Figure 6.16:** (a) Streak images of the electric field magnitude along the axis of symmetry for air-filled needle-plane gaps at  $dU/dt = 16.67, 25,$  and  $50 \text{ kV/ns}$ . Red dotted line indicated the time of inception, solid magenta lines indicate the time of contact. (b) Average propagation velocities for air and  $\text{CO}_2$  wavefronts in needle-plane gaps for both polarities. Markers are simulated data, lines are best-fit curves. Images adapted from [26] under CC BY 4.0.

the velocity calculation, despite the greater acceleration of negative  $\text{CO}_2$  wavefronts—leading to a shorter time-of-flight—the effective distance traversed by the front was reduced due to the sheath behaviour. The resulting calculation according to (6.7) was therefore rendered similar to the positive case. Since the cathode sheath thickness in air was found to be far less sensitive to polarity, and effectively experienced no variation with  $dU/dt$ , this appeared to explain the separation between average velocities seen for air that are absent in  $\text{CO}_2$ . The proposed mechanisms for the cathode sheath scaling are believed to result from aspects relating to the variation of electronic mobility, and to the existence of photoionisation. Their detailed discussion, however, warranted a dedicated section which is provided later as Section 6.3.5.

Moving to the analysis of wavefront electric field magnitudes, Figure 6.17 plots the maximum electric field strengths of the propagating wavefronts over time (along the axis of symmetry) and for each studied value of  $dU/dt$ . Upon voltage application, the electric field increases linearly for all cases, as expected from the linearly-rising voltage. The moment of inception becomes evident as the electric field becomes distorted, which occurs at a greater background field in air compared to  $\text{CO}_2$  regardless of polarity or  $dU/dt$ . Negative-polarity discharges also exhibited higher inception fields compared to their positive counterparts, for both air and  $\text{CO}_2$  regardless

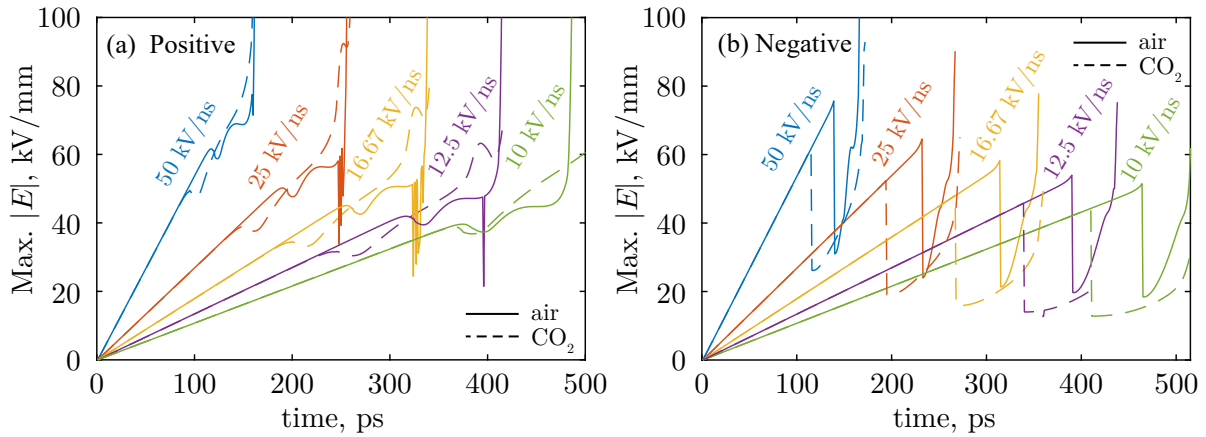


**Figure 6.17:** Maximum electric field over time for (a) positive, (b) negative energisation for ionisation waves simulated with  $dU/dt = 10, 12.5, 16.67, 25,$  and  $50$  kV/ns. Solid lines are for air, dashed lines are for CO<sub>2</sub>. Image adapted from [26] under CC BY 4.0.

of  $dU/dt$ . At the moment of inception (field distortion), positive wavefronts exhibited a marginal decrease in the electric field magnitude as the accumulation of critical space charge screened the electric field at the tip, before it was redistributed, forming the main ionisation front. A subsequent increase of the wavefront field was then found, corresponding to the propagation and traversal of the wavefront across the inter-electrode gap. Upon close-approach to the cathode sheath, the field experienced a second rapid increase as it became compressed within the sheath, such that most of the potential drop across the gap was across the sheath alone. Some numerical oscillations were also observed during this approach for positive fronts, likely due to the extreme field and charge density gradients that developed in the vicinity of the plane electrode. Despite this, the oscillations were minor and were adequately stabilised by StrAFE, such that the general tendencies of the field nearing this moment remained visible.

For negative wavefronts, the point of maximum electric field remained at the needle tip for the entire duration of the simulation, due to the formation of the cathode sheath over the electrode surface. Therefore, to track the wavefront propagation, the location of the tracked field was, upon inception, necessarily moved to be ahead of the cathode sheath. This explains the seemingly sudden drop of the electric field strength in Figure 6.17(b), which was due to the appearance of the wavefront ahead of the cathode sheath that has, initially, a lower field magnitude than that of the previously tracked field present at the needle tip. The electric field then behaved comparably to those of the positive wavefronts during the propagation phase, where the field exhibited an initial, slow, climb during traversal of the gap, before rapidly increasing upon close approach to the electrode.

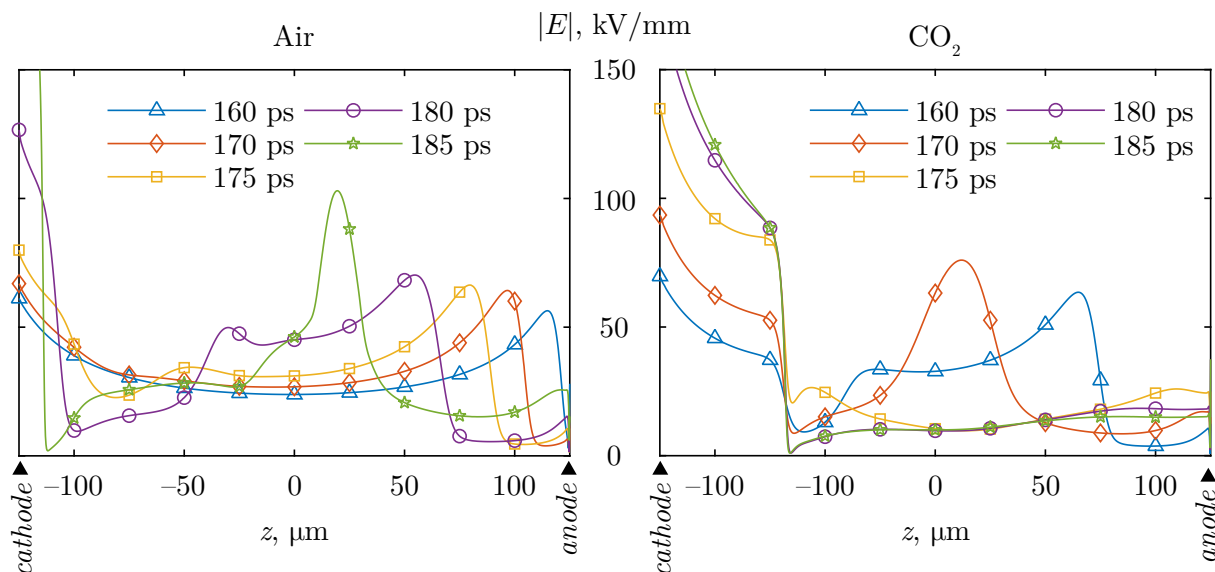


**Figure 6.18:** Electric field down the axis of symmetry for (a) air-filled, (b)  $\text{CO}_2$ -filled needle-needle gaps at various timesteps.  $dU/dt = 50 \text{ kV/ns}$  shown only. Image adapted from [26] under CC BY 4.0.

When simultaneous positive and negative streamers were initiated in the needle-needle case, the tendencies of the wavefront fields for the two streamers behaved identically to those described for the needle-plane case, but occurring separately at anode and cathode, respectively. Figure 6.18 further provides the plot of the electric field strength across the needle-needle plane gap at various timesteps for the case of  $dU/dt = 50 \text{ kV/ns}$ . In the same manner as in the verification study of Section 5.8.4, the initiation of the two wavefronts propagating towards each other enhances the electric field within the region between their heads, before it ultimately collapses upon the collision and combination of the wavefronts. The location of the wavefront merge was not centred within the gap, as was similarly observed in [43], due to the different inception times and propagation velocities of positive compared to negative wavefronts.

### 6.3.4 Developed Electron Density and Plasma Composition

The resulting electron density developed along the axis of symmetry (at the time of contact) is shown in Figure 6.19 for a selection of  $dU/dt$  values. In general, a positive, nonlinear, correlation between the electron density and  $dU/dt$  was found. This can be explained by the greater degree of overvoltage achieved with greater values of  $dU/dt$ , which acted not only to increase the inception field, but also contributed towards higher electric field strengths ahead of the wavefront. Higher field magnitudes naturally promote ionisation, increasing the overall density of generated

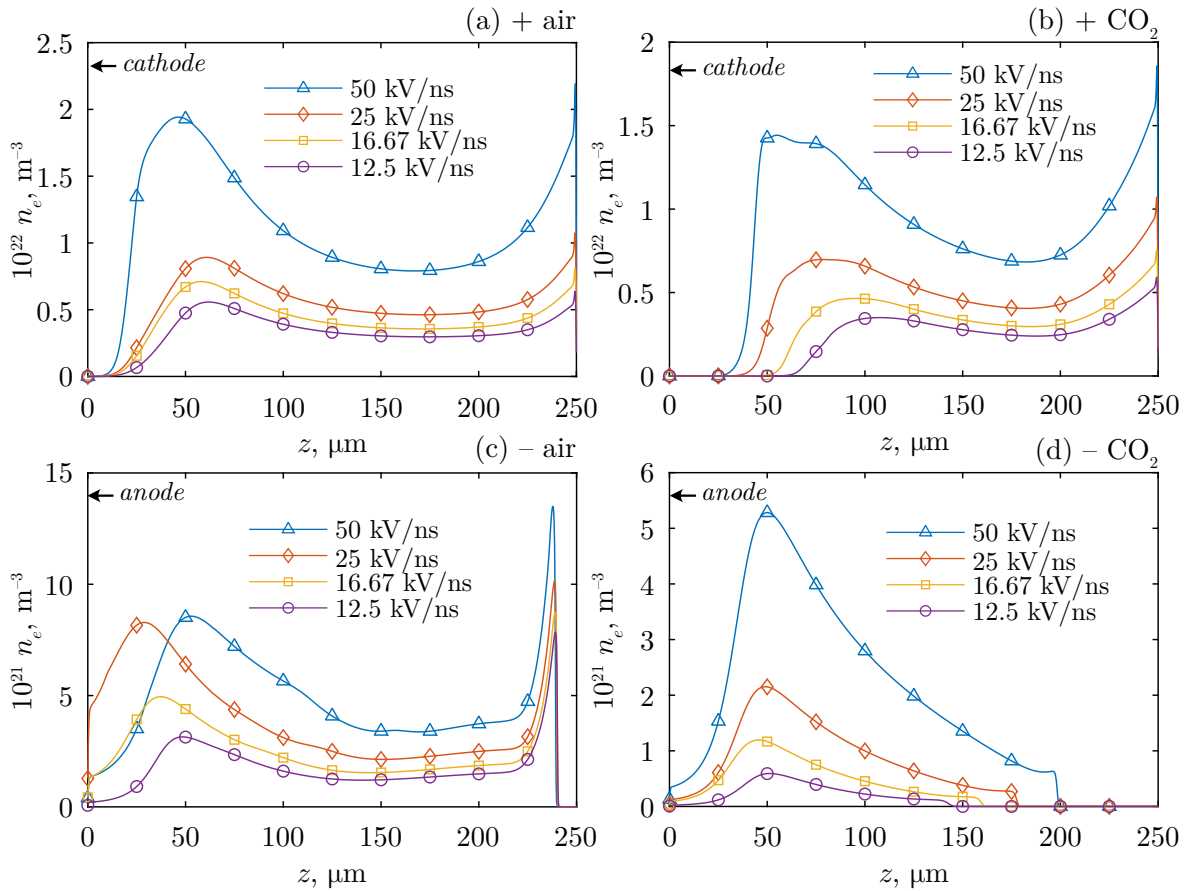


**Figure 6.19:** Electron density along the axis of symmetry at the time of contact for needle-plane gaps filled with air and CO<sub>2</sub>. Sub-figures are labelled with the gas type (“air” or “CO<sub>2</sub>”) and the polarity (“+” or “-”). Plotted for  $dU/dt = 12.5, 16.67, 25,$  and  $50$  kV/ns. Image adapted from [26] under CC BY 4.0.

electrons through impact ionisation. There may also be a type of cyclic and self-fulfilling behaviour here, wherein higher electric fields produce increased charge densities, which in turn cause an increase to the channel conductivity, further enhancing the field ahead of the streamer, which intensifies ionisation yet again. Comparing across polarities, positive discharges were found to generate greater electron densities compared to negative discharges, likely due to the differences in wavefront field magnitude. Despite possessing a higher inception field, negative fronts were able to propagate with a lower wavefront field magnitude compared to positive fronts, which was also seen in Figure 6.17. This has been previously linked to the more diffuse nature of negative discharges in the past [24], which generally lowers the electric field ahead of the wavefront. In consequence, the lower intensity of ionisation resulted in a plasma channel of lower density in the wake of negative wavefronts. Regardless of polarity, the overall plasma densities were also

found to be higher in air compared to CO<sub>2</sub>.

While the present work was not focused on the detailed analysis of specific plasma composition, for completeness, Figure 6.20 shows the proportion of all tracked species within the plasma chemistry model at the time of contact shown in Figure 6.19, for all simulated values of  $dU/dt$ . Alongside a generally higher overall plasma density, voltages rising with different  $dU/dt$  influenced the generation efficiency of certain species within a plasma discharge, see for example, the reducing proportion of O<sub>2</sub><sup>+</sup>N<sub>2</sub> with faster-rising voltages, or the differences in profile of CO and O produced within CO<sub>2</sub> discharges. These trends may be consequential to various chemical processing applications, for example, as described in [52].

### 6.3.5 Characteristics of the Cathode Sheath

Within Sections 6.3.2 and 6.3.3, the behaviour of the cathode sheath was alluded to; the full and detailed discussion of which is included within the present section. To more formally define the cathode sheath, it is formed due to the outward drift of electrons away from the negative electrode, thereby leaving a thin region of net positive charge. Characterised by a low electron density and a considerably high electric field magnitude, sheath regions may be formed over electrodes or solid dielectric surfaces [53]. The role of the cathode sheath in low-temperature electrode-bounded gas discharges is poorly understood, with studies generally focusing on discharge characteristics far from physical boundaries.

From the configuration studied here, it was found that the cathode sheath thickness varied with the rate of voltage rise,  $dU/dt$ , in CO<sub>2</sub> but not in air. While one can get an indication of the sheath thickness from Figure 6.19, Figure 6.21 directly plots the cathode sheath thickness as a function of  $dU/dt$  for all gas-polarity pairs in the needle-plane case. Sheaths formed in the needle-needle case were of similar dimension to those of negative needle-plane cases (since they equivalently saw the inception of a negative wavefront from a negatively-charged needle), the analysis here is therefore applicable also to the symmetrical case. Comparison between voltage polarities within the same working gas is first discussed.

In air, cathode sheaths formed over the plane electrode under positive voltages were thicker ( $\approx 40\ \mu\text{m}$ ) than those formed over the needle in the corresponding negative cases ( $\approx 25\ \mu\text{m}$ ). Since, under positive-polarity voltage, the wavefront must first initiate then propagate the full distance from needle to plane, it would be reasonable to conclude that electrons have longer to drift away from the cathode during positive needle energisation, depleting a larger region near

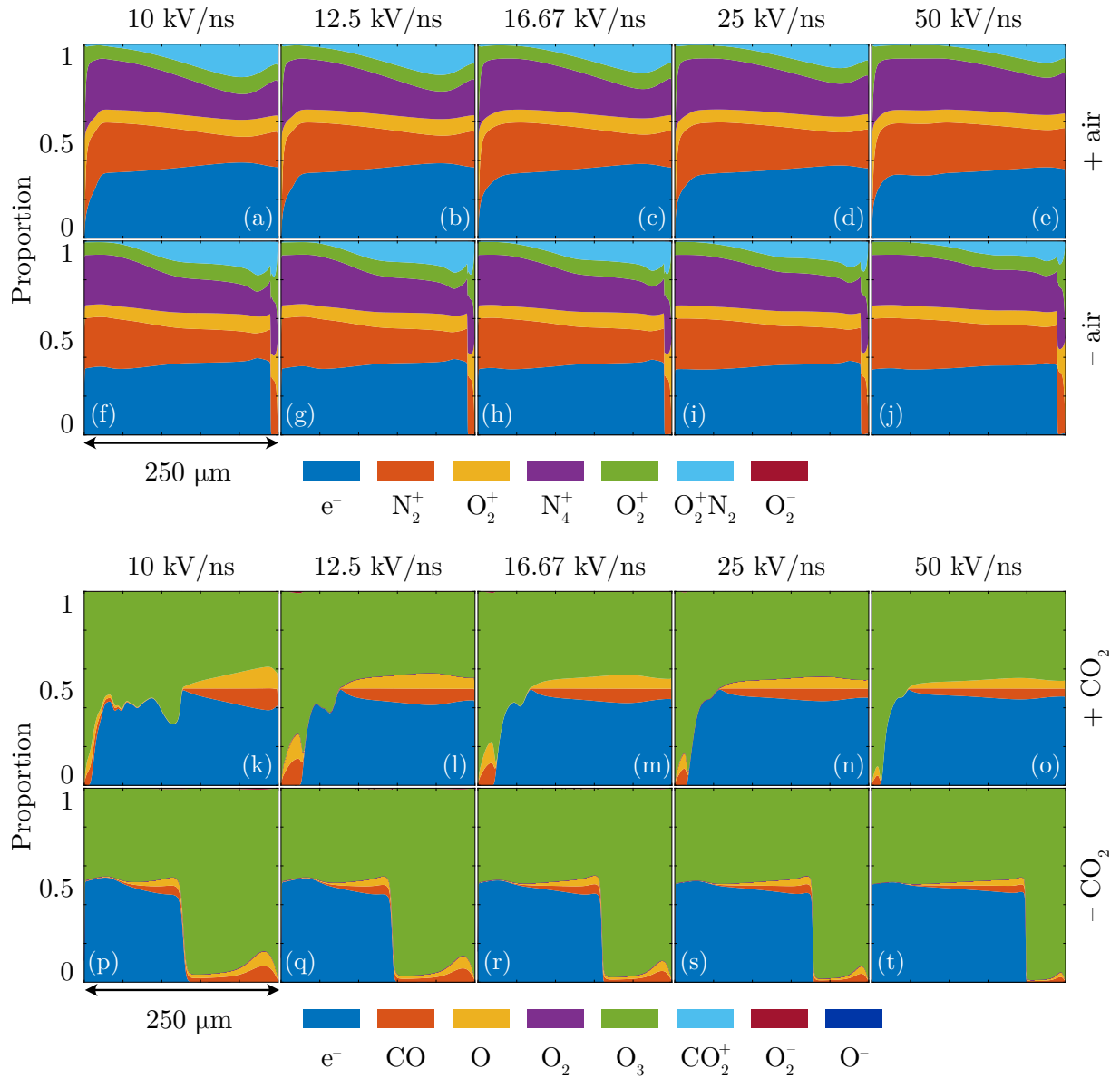


**Figure 6.20:** Plasma composition along the axis of symmetry for ionisation waves at the point of contact for (a)–(j) air-filled, (k)–(t) CO<sub>2</sub>-filled needle-plane gaps. Vertical axis is normalised by the total density of tracked species.

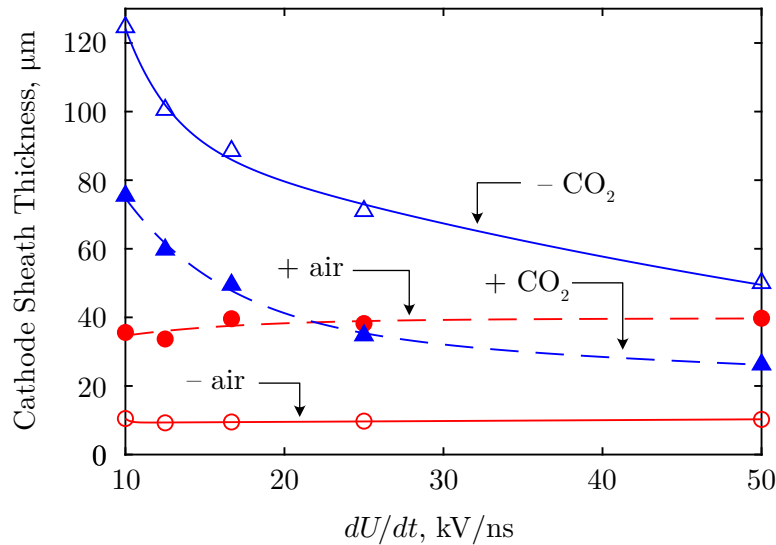


**Figure 6.21:** Cathode sheath thickness as a function of the voltage rate-of-rise, for wavefronts initiated in air- and  $\text{CO}_2$ -filled needle-plane gaps. Markers are simulated data, lines are best-fit curves. Image adapted from [26] under CC BY 4.0.

the plane. When under negative needle energisation, electrons may drift faster away from the needle due to enhanced drift velocity, however, the onset of ionisation coupled with the induced photoionisation in the near vicinity of the needle tip may lead to the injection of electrons into the developing sheath region, suppressing its growth.

This is in contrast to  $\text{CO}_2$ , for which negative needle energisation led to the formation of a far thicker sheath region than for positive cases, regardless of  $dU/dt$ . Two mechanisms are believed to govern this difference, beginning first with photoionisation. Since photoionisation was not included for  $\text{CO}_2$  (and in any case, the literature suggests that photoelectron production would be far weaker in  $\text{CO}_2$ ), the initiation of intensive ionisation processes cannot lead to the emission of ionising photons which may aid in the replenishment of the electron-depleted sheath region. See Figure 6.22(b) showing an example of the photoelectron source mid-way through a positive discharge in air. In particular, note the prediction of substantial photoelectron production in the region where the sheath would form, but is ultimately suppressed due to the replenishment of electrons that drift out of the region. Secondly, Figure 6.22(a) shows the electron mobility data used within the present simulations (as a function of electron energy, as per the use of the LMEA). Note the non-monotonic nature of the electron mobility relationship with energy in  $\text{CO}_2$ , particularly of the local maximum exhibited by the electron mobility at  $\approx 0.75$  eV. It follows

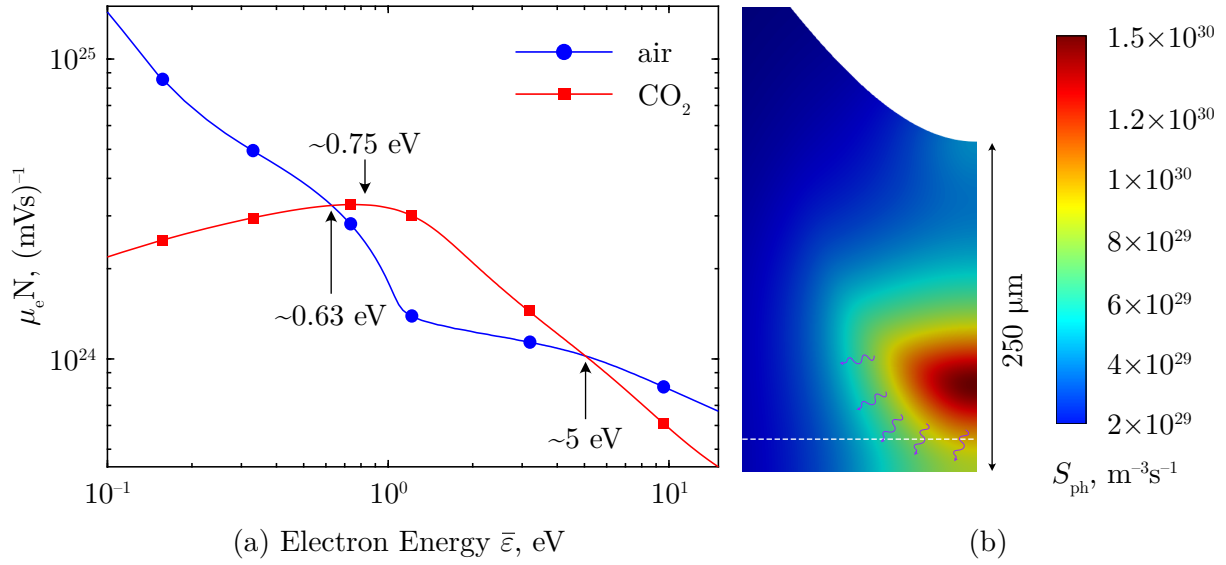


**Figure 6.22:** (a) Comparison between the electronic mobility scaled by the neutral gas density as a function of the electron energy for air and CO<sub>2</sub> (as computed via BOLSIG+ [45]). Note the critical region  $0.63 \leq \bar{\epsilon} \leq 5$  eV. (b) Example of the photoelectron source term ahead of the wavefront penetrating into the cathode sheath region, suppressing its growth. Image (a) adapted from [26] under CC BY 4.0.

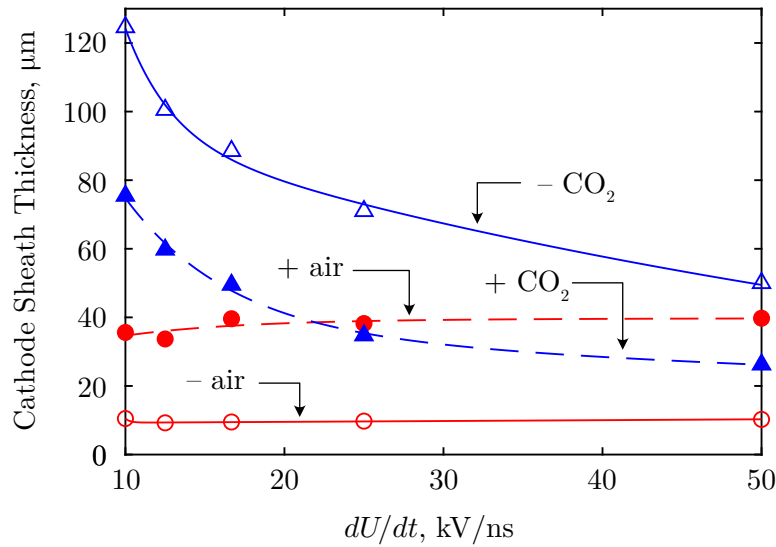
that for negative needle energisation, the enhanced field at the needle tip heats electrons rapidly into this region of enhanced mobility, allowing electrons to drift at an accelerated rate away from the needle tip. Without the aforementioned replenishment due to photoionisation, substantial sheaths are able to be developed across the needle. In the positive case, however, electrons do not drift as quickly away from the plane electrode, since there is an absence of significant field enhancement due to electrode curvature. Electrons near the plane therefore do not gain as much energy, drifting only slowly relative to those near the needle in the negative case, resulting in a thinner cathode sheath by the time the discharge traverses the gap.

Comparing across working gases, the clear difference in the sheath thickness as it varied with  $dU/dt$  shown in Figure 6.21 is addressed here. In air, the cathode sheath thickness for both discharge polarities remained identical over all simulated  $dU/dt$ . This contrasts the case of CO<sub>2</sub>, where the sheath thickness exhibited a significant increase at slower rates of voltage rise. To explain this phenomenon, the reader is once again referred to the electron mobility relation of Figure 6.22. Note particularly the region  $0.63 \lesssim \bar{\epsilon} \lesssim 5$  eV, where the electron mobility in CO<sub>2</sub> increases to a maximum and becomes significantly higher than that of air. The obtained simulation data indicates that this energy range may be entered by electrons while the electric

field remained below the critical field for both CO<sub>2</sub> and air, suggesting that for a period of time during the rising voltage slope, electrons in CO<sub>2</sub> drift at a greater velocity than in air at the same energy. With the linear time-increasing field used in this study, there must exist a duration when the local mean electron energy passes through this critical energy range. During this time, the maximisation of mobility in CO<sub>2</sub> allows the establishment of far larger region that is depleted of electrons due to the greater drift velocity compared to air. It follows, that for slower rising voltages, the time electrons spend within this energy range is prolonged, enhancing electron drift away from the cathode and resulting in the formation of a thicker sheath. Meanwhile, electrons in air, although also subject to drift in the field, do not drift as fast as those in CO<sub>2</sub>. Once ionisation activity initiates, photoionisation in air further suppresses the formation of a significant cathode sheath as discussed previously when comparing polarities. For both needle-plane and needle-needle simulations at the slowest rate-of-rise simulated here (10 kV/ns), the cathode sheath formed in CO<sub>2</sub> occupied almost half of the inter-electrode gap.

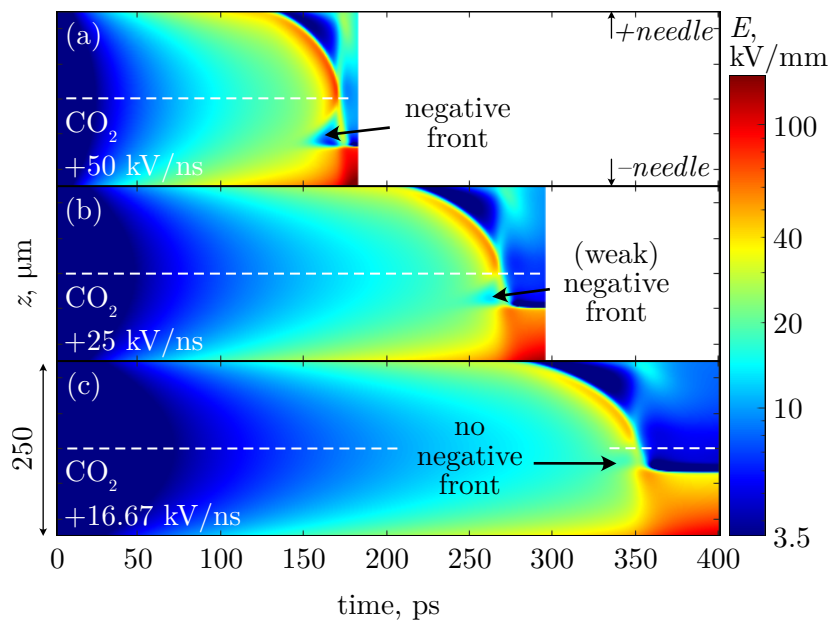
To complement and to test this explanation, further simulations in air with photoionisation disabled, and with background pre-ionisation levels increased to match that of the CO<sub>2</sub> simulations, were conducted. Based on the proposed mechanisms, it was hypothesised that in absence of photoionisation, the sheath distance in air would become larger, as there would be no photoelectron source that may suppress the sheath formation. The sheath distance should also be found to vary with  $dU/dt$ , since a longer period of time would be spent within the low-field region on slower-rising slopes, allowing more substantial electron drift, and with no replenishing electron source. The decreasing trend with higher values of  $dU/dt$  was expected to be similar to that of CO<sub>2</sub>, though the absence of the maximisation of electron mobility as found in CO<sub>2</sub> was theorised to give rise to a different tendency. The resulting cathode sheath thicknesses from this set of additional simulations are shown in Figure 6.23.

Figure 6.23 confirms that indeed, the process of photoionisation as modelled using the present techniques suppressed the formation of a thick cathode sheath in air. Confirming the hypothesis, air similarly exhibited scaling of the cathode sheath thickness when photoionisation was disabled, with a similar tendency to that of CO<sub>2</sub>. When comparing polarities, sheaths produced under negative energisation were generally thicker than those under positive energisation, in contrast to the results presented in Figure 6.21 with photoionisation enabled. This supports the proposition that sheaths produced under negative voltages were thinner *with* photoionisation due to the replenishment of electrons near the needle tip as the field became sufficiently enhanced. With photoionisation disabled, sheaths over the negatively-charged needle were found to be thicker,



**Figure 6.23:** Cathode sheath thickness as a function of the voltage rate-of-rise for wavefronts initiated in air- and CO<sub>2</sub>-filled needle-plane gaps. In this case, photoionisation in air was disabled and the background ionisation levels were increased to match that of CO<sub>2</sub>. Markers are simulated data, lines are best fit curves.

simply due to more significant outward electron drift—consistent with those simulated within CO<sub>2</sub>. Also notable from Figure 6.23 is the tendency for sheaths in air with no photoionisation to become similar in size regardless of polarity for higher values of  $dU/dt$ . This can be explained from the monotonically-decreasing mobility of air with electron energy, shown in Figure 6.22, where faster-rising voltages do not provide sufficient time within the low-energy range for the differences in electron drift distance to become significant between polarities prior to the inception of the main wavefront. On the other hand, the difference in sheath thickness between polarities in CO<sub>2</sub> was maintained due to the maximisation of electron mobility in the low- to mid-energy region. Incidentally, for  $dU/dt > 50$  kV/ns, it could be expected that the sheath thicknesses in CO<sub>2</sub> may also converge (as is implied by the tendencies of Figure 6.23), since the time spent within this critical energy range prior to the main wavefront initiation would become increasingly short. While photoionisation has been known for some time to be an important electron source for positive elementary streamers, it has been demonstrated here that photoionisation may also significantly influence the development of sub-mm discharges through different and previously-unknown mechanisms.



**Figure 6.24:** Streak images of the electric field magnitude along the axis of symmetry for a  $\text{CO}_2$ -filled needle-needle gap with  $dU/dt = 16.67, 25,$  and  $50 \text{ kV/ns}$ . Dashed white line shows the midpoint between the two needle electrodes. Negative wavefront did not form for  $dU/dt$  less than  $25 \text{ kV/ns}$ , as indicated. Image adapted from [26] under CC BY 4.0.

### 6.3.5.1 Cathode Sheath Suppression of Negative Wavefront Development

The cathode sheath scaling effects observed here may have consequences for the discharge evolution in short, sub-mm, or smaller gaps. One possibly important consequence is presented here, which was observed as part of the corresponding needle-needle simulations conducted during this work. Figure 6.24 shows streak images of the electric field magnitude for needle-needle discharges at various  $dU/dt$  in  $\text{CO}_2$ . As described in Section 6.3.2, simultaneous positive and negative wavefronts propagated towards each other and merged within the gap. This was true for all  $dU/dt$  values greater than  $25 \text{ kV/ns}$  in  $\text{CO}_2$ . Below this value, a negative wavefront did not develop due to the substantial size of the cathode sheath, which had occupied a significant proportion of the inter-electrode gap. Since negative wavefronts can only be initiated ahead of the cathode sheath, the reduction of available space due to the sizeable sheath region, occupying almost half the inter-electrode gap, suppressed the formation of a negative wavefront. The entire discharge evolution therefore resembled more of the inception of a solitary positive wavefront originating from the needle tip; which then collided and spread out over a now large cathode sheath region, acting like an extended virtual cathode.

The results on the cathode sheath scaling may help to explain some experimental observations. For example, the results of Liu *et al.* [38] reported higher breakdown strengths at shorter time-to-breakdown in CO<sub>2</sub> compared to air and N<sub>2</sub>, under the same nanosecond impulses within a 100 μm gap. As discussed at the beginning of this section, this is against conventional theories based solely on Townsend's ionisation parameters and associated critical field values. On the basis of the results here, it is theorised that in short sub-mm gaps, the enhanced mobility of electrons in CO<sub>2</sub> may lead to a significant reduction of the electron density during the rising edge of an impulse; prior to the onset of any substantial ionisation. This may possibly inhibit the formation of initial avalanches and ionisation fronts, delaying the breakdown process and leading to an observed increase in the breakdown strength. It is thought that in longer gaps these effects would be negligible, as the electron energy would have to remain within the critical range for a far longer duration to cause a meaningful reduction of the electron density ahead of any developing wavefronts. In other words, if there indeed exists an increased breakdown strength to CO<sub>2</sub> due to this phenomenon, it would only hold in the case when the developed electron-depleted sheath region is able to occupy a significant proportion of the inter-electrode gap. Of course, the simulations conducted here have omitted other potential electronic sources such as charge injection at the electrodes or secondary emission processes. It also forgoes the consideration of statistical processes before, and other processes beyond, the primary ionisation front. The comparison done here with practical breakdown data is therefore done with extreme caution; confirmation of these mechanisms would necessitate significant further experimental and theoretical modelling work.

## 6.4 Overstressed Surface Streamers Along a Sub-mm Dielectric Surface

Complementary to the simulations of Section 6.3, this section presents results arising from a similar and linked set of simulations to the sub-mm discharges analysed in Section 6.3. Note that the results presented here were partially adapted from the published work [54]. Briefer in nature, the simulations here incorporated a solid dielectric surface to the needle-plane domain of Figure 6.9. This set of simulations aimed to compare the case when discharges would be initiated directly at a solid-gas-electrode triple junction and develop directly as sub-mm surface ionisation waves. This configuration has particular relevance to technologies such as MEMS or other miniaturised electronic systems, where active electrode components may be embedded within (or attached atop) a substrate material and may be of close proximity, raising the probability of small-scale

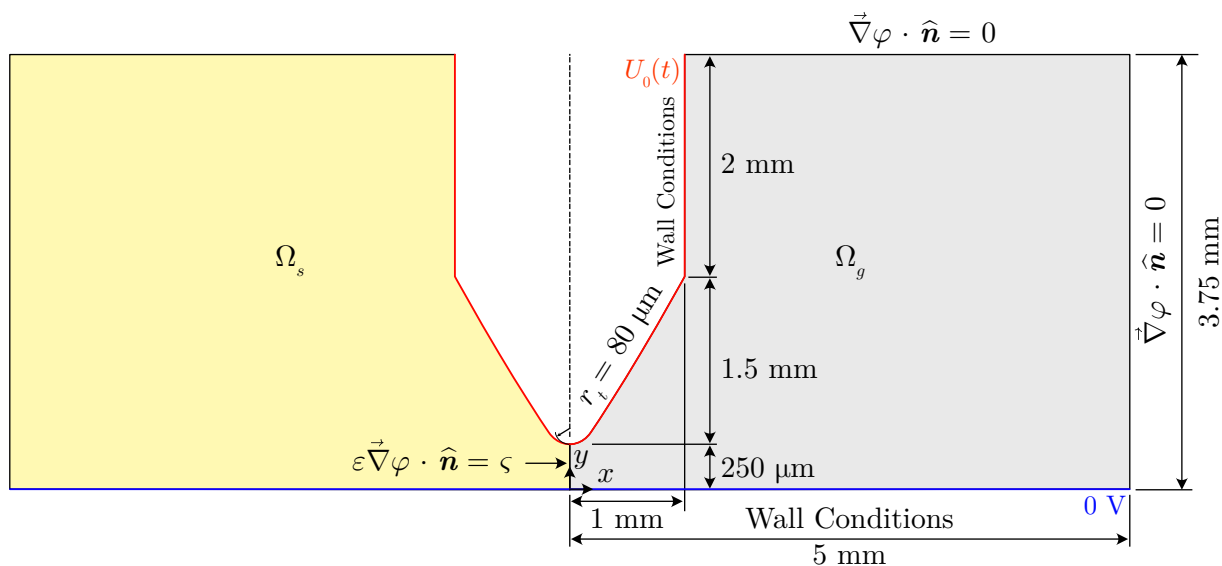


**Figure 6.25:** Plane-parallel domain used for the study of sub-mm surface ionisation waves. Image adapted with permission from [54], © IEEE 2023.

surface flashovers.

The revised domain used for the following simulations is shown as Figure 6.25. Note that due to the asymmetry of the revised domain, simulations were conducted in 2D-planar mode since cylindrical symmetry no longer holds. As such, the “needle” electrode is more akin to a razor blade, extending into and out of the page. This is very much an approximation to the cylindrically-symmetric case of Section 6.3, however, full 3D simulations would be necessary to accurately model an embedded needle electrode inside a surface. This possibility laid squarely outside the scope of this work and beyond the capabilities of the available computer hardware at the time of study.

The simulation parameters and settings were identical to those used in Section 6.3, including the plasma chemistry sets for both air and CO<sub>2</sub>. The solid surface relative permittivity was fixed at  $\epsilon_r = 2$  for all tests, and since the objective here was mainly to compare general wavefront morphologies and propagation characteristics, this value remained unchanged. Besides, the effect of various permittivity in similar configurations have already been established, for example, in the verification case study of Section 5.8.2 and references therein.

#### 6.4.1 Sub-mm Surface Discharge Morphology and Characteristics

Included as Figure 6.26 are colour plots showing the time-evolution of the electric field magnitude

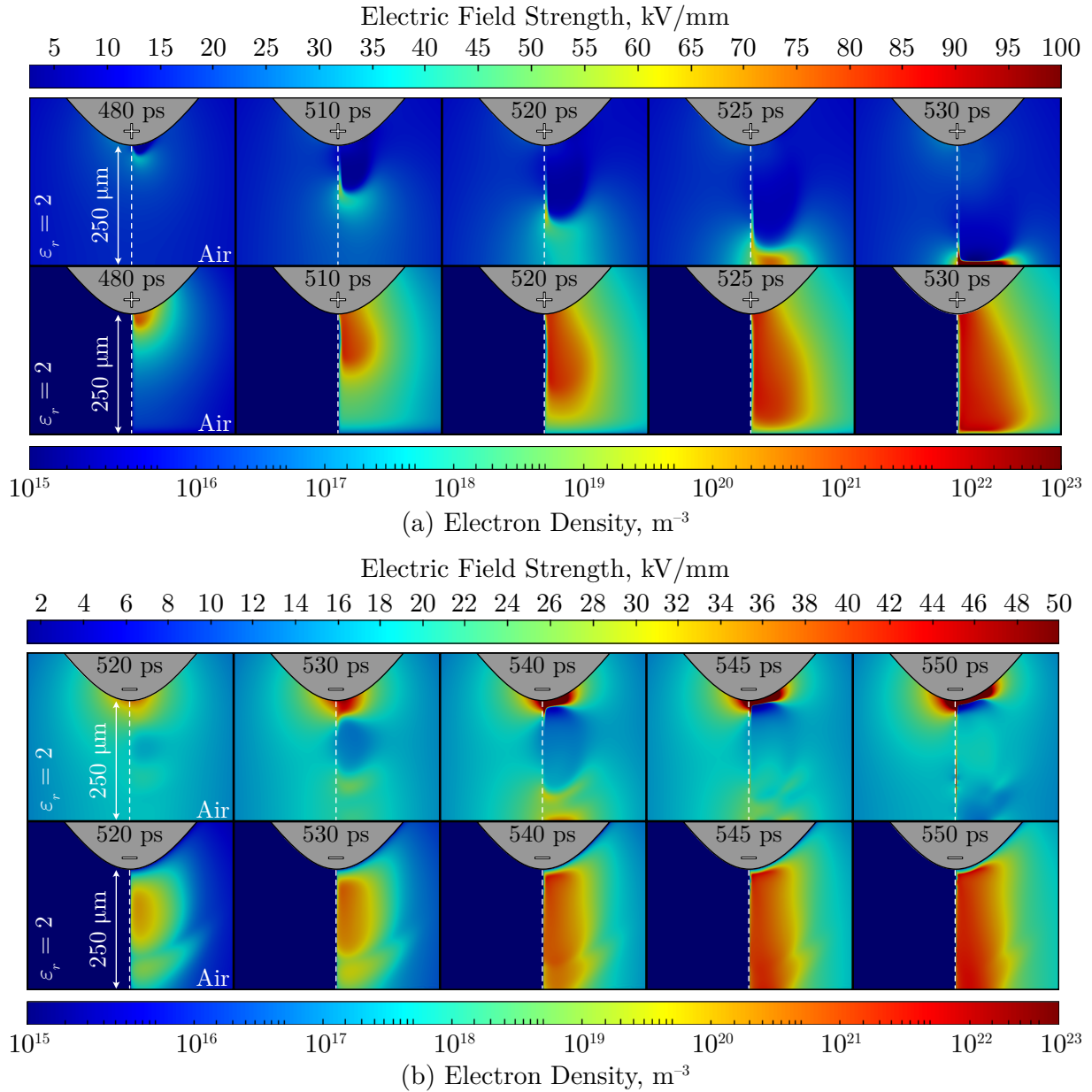


**Figure 6.26:** Spatio-temporal evolution of the electric field magnitude and electron density for sub-mm surface ionisation waves in air, for (a) positive, (b) negative ramp voltage energisation. Showing  $dU/dt = 10 \text{ kV/ns}$  only. Image adapted with permission from [54], © IEEE 2023.

and the electron density in air at various timesteps. Only the case of  $dU/dt = 10\text{ kV/ns}$  of both polarities are shown for brevity; discharges under faster-rising voltages were found to be morphologically identical, but scaled in time based on the rate at which the voltage increased.

With the inclusion of a dielectric surface, positive ionisation waves were developed at the solid-gas-anode triple junction. The embedded needle geometry ensured that discharges initiated directly as surface ionisation waves, in contrast to simulations such as the verification study of Section 5.8.2. For positive energisation, the initial development of space charge at the triple junction eventually led to the initiation of a surface ionisation wave, which then rapidly propagated across the surface and bridged the gap, in a similar manner to the simulations of Section 6.3. The difference here was that the point of maximum field remained above the solid surface, providing the means for intense collisional ionisation to drive the development of the surface discharge. Upon bridging the gap, positive surface discharges expand away from the surface and assume a cone-like shape, contrasting the general morphology of the negative surface discharges shown in Figure 6.26(b). Instead, due to the formation of the sheath across negatively-charged needles, the wavefront was able to make direct contact with the plane electrode when the gap was bridged, preventing the lateral spreading of the channel. The development of negative discharges also resembled less of a *propagation*, in the sense of moving from one electrode to the other. Due to the initial drift away from the needle electrode, the discharge appeared more akin to the appearance of an electron density almost mid-gap, which then grew in both directions towards both needle and plane. In air, the plasma channels developed under positively-charged needles therefore appeared more diffuse than their negative counterparts. This differed from the conventional knowledge of long filamentary streamer discharges away from boundaries, in which negative streamers tend to be more diffuse since electrons move away, rather than towards, streamer heads (see for example, those simulated in Section 6.2).

In  $\text{CO}_2$ , the corresponding colour plots are shown in Figure 6.27. The general morphology of  $\text{CO}_2$  surface discharges were found to be remarkably different from those in air. Most notably, the strong influence of the sizeable cathode sheath, as discussed in Section 6.3.5, greatly impacted the plasma channel development. Once again acting like an extended cathode, discharges could only form outside the sheath region where there existed sufficient electrons. For different values of  $dU/dt$ , the cathode sheath in  $\text{CO}_2$  scaled identically to the previous case with no dielectric surface, as shown in Figure 6.21.

Electron densities of  $\text{CO}_2$ , relative to air, remained the same as those found for the gas-only case, where the developed plasma densities were generally higher in air. Overall, however, the

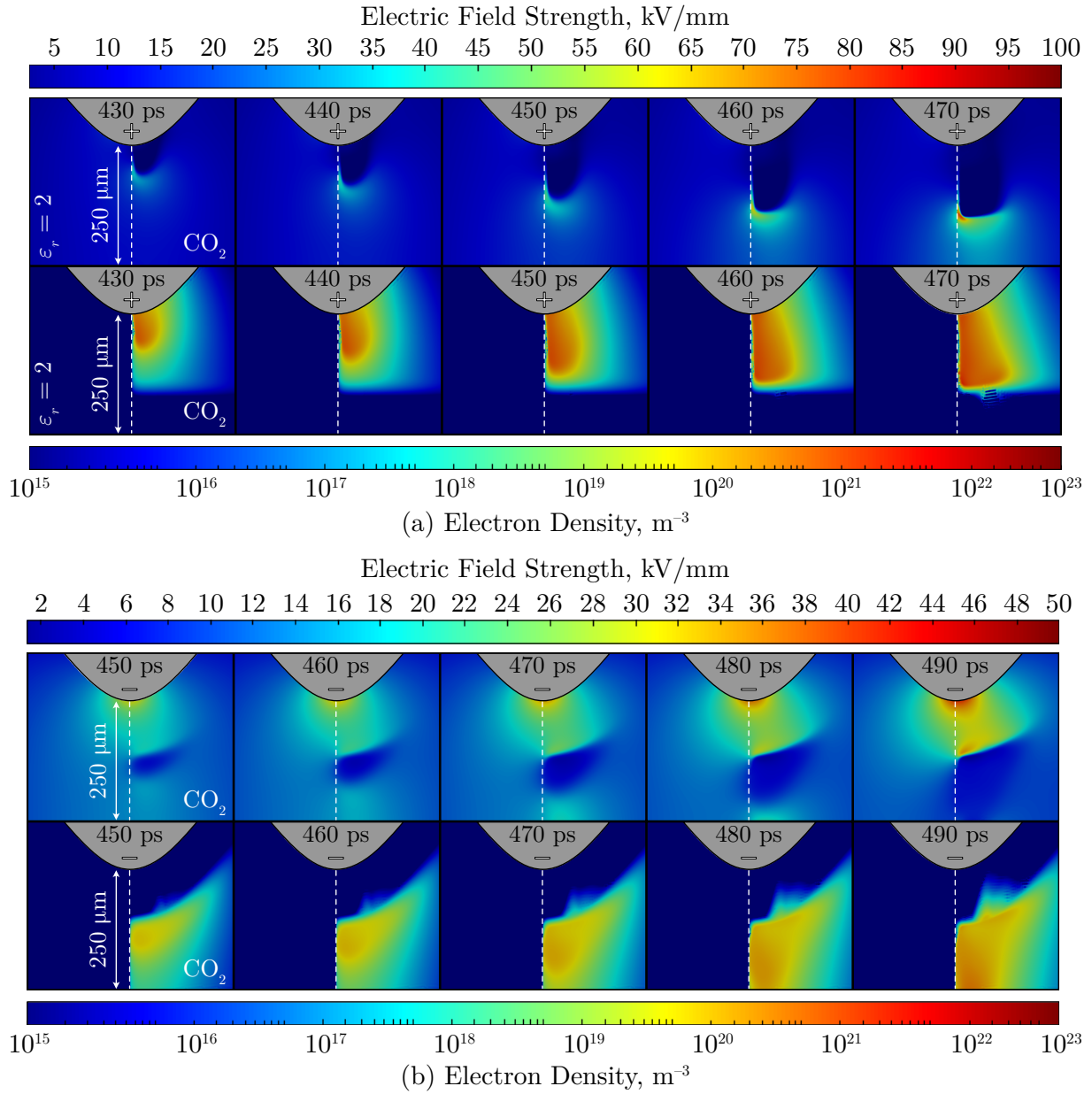


**Figure 6.27:** Spatio-temporal evolution of the electric field magnitude and electron density for sub-mm surface ionisation waves in  $\text{CO}_2$ , for (a) positive, (b) negative ramp voltage energisation. Showing  $dU/dt = 10 \text{ kV/ns}$  only.

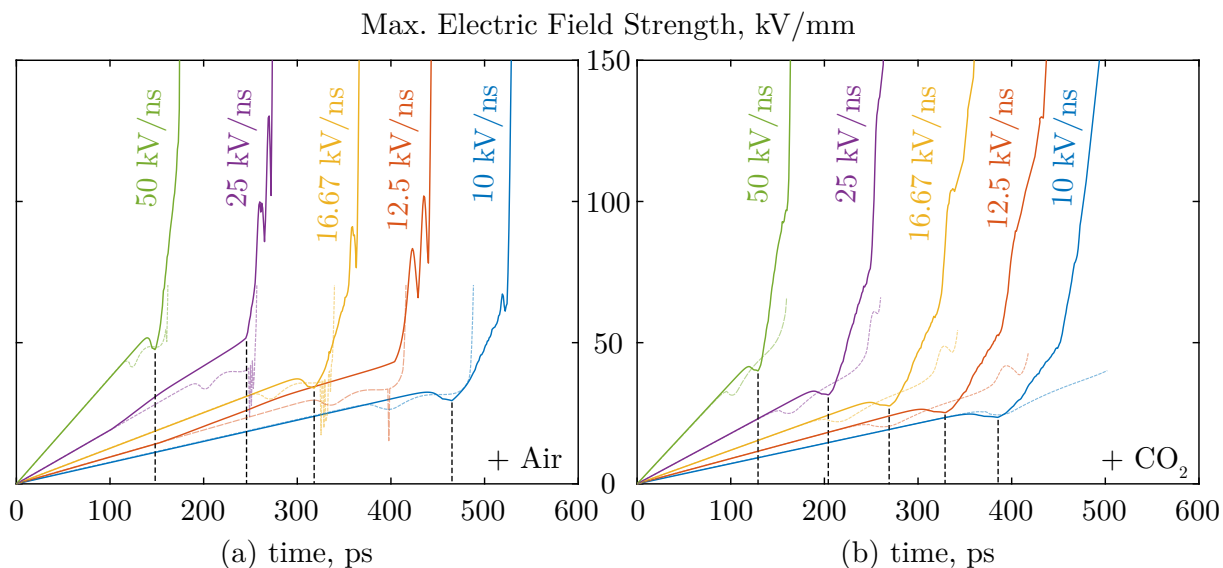


**Figure 6.28:** Maximum electric field over time for (a) air, (b)  $\text{CO}_2$  for surface ionisation waves simulated with  $dU/dt = 10, 12.5, 16.67, 25,$  and  $50 \text{ kV/ns}$ . Dotted transparent lines show field data from Figure 6.17 for the gas-only case, and normalised such that the initial rate of field rise is the same as the case with surface included. This was necessary due to the additional curvature of the axisymmetric domain which naturally imparts a greater overall field strength. Image (a) adapted with permission from [54], © IEEE 2023.

inclusion of the dielectric barrier increased the developed plasma density in every configuration compared to those in Section 6.3 simulated without a dielectric. This is consistent with the greater magnitudes of electric field as shown in Figures 6.26 and 6.27. The enhancement of the electric field strength over the needle-plane only case can be explained from two major effects: (i) the polarisation of the dielectric that redistributes and enhances the field at its surface, and (ii) the curvature of the streamer fronts that were significantly smaller due to the adherence of the wavefronts to the dielectric surface. The developed field near the dielectric surface was therefore far greater than those observed with no surface present, see for example, Figure 6.28 which plots the maximum electric field strength for all simulated positive discharges. Note that the maximum fields for negative discharges remained within the sheath region, and are therefore unrepresentative of the field at the wavefront and have not been shown. One may see from Figures 6.26 and 6.27, however, that typical negative wavefront maximum field values were factors of 2 to 3 times lower than those of the positive case. Since electrons were generally advected away from the surface for negative energisation, charge densities near the head of the growing wavefronts did not become as significant as the positive case, where electrons were accelerated into the wavefront. Coupled with the reduced distance available for development (due to the cathode sheath), negative wavefronts were far more diffuse in nature and did not produce plasma

channels with densities as high as the positive cases. The difference was also greater for  $\text{CO}_2$ , since there was no mechanism for photoionisation included, for the reasons discussed in Section 6.3.

It is remarked that for  $\text{CO}_2$  simulations, minor instabilities near the cathode sheath began to occur near the end of the simulation, mainly due to the steep density and field gradients at the sheath-plasma boundary. This resulted in the perceived collapse of the cathode sheath, where an upward wavefront would penetrate into the sheath and lead to the full bridging of the electrode gap. While sheath collapse must inevitably happen in practise, the present model is unlikely able to accurately simulate the dynamics of sheath collapse, nor be able to capture the fast gas heating processes that proceed from this point. The likelihood remains that the observed instabilities are purely numerical in nature, resulting from insufficient mesh density or mesh quality. Additional refinement may help to reduce these instabilities, however, may render the simulations prohibitively expensive. Considering that these instabilities only arose near the time when the simulations were terminated anyway, they were considered acceptable. From another perspective, these instabilities raise an important question regarding the nature of cathode sheath collapse: if minor numerical errors can lead to something similar to a sheath collapse, can unavoidable statistical instabilities and fluctuations near the sheath boundary contribute to a physical sheath collapse? Using a fully deterministic approach like the hydrodynamic model may not be able to provide an answer, but future studies involving the use of kinetic approaches would unquestionably be of great interest.

#### 6.4.2 Electric Field and Separation of Discharge Phases

This section focuses on the positive surface wavefront propagation, which, due to their direct inception from the needle tip, facilitated the tracking of the point of maximum electric field which corresponded to the head of the wavefront. Note that this was exclusive to positive energisation, as negative wavefronts developed in such a way that the position of the streamer head was initially ambiguous, and the sheath-confined maximum field magnitude provides little meaningful information relating to the wavefront position. It was found that based on the position of the maximum field, distinct phases of the positive wavefront development could be identified. Figure 6.29 shows the  $x$ - and  $y$ -position of the point of maximum field for the 10 kV/ns surface discharge in air. Five phases of the development and propagation of the discharge could be identified based on the signature of the field position; the characterising features of which were identified as listed below. See also the colour plots of Figure 6.30 which provides representative field plots

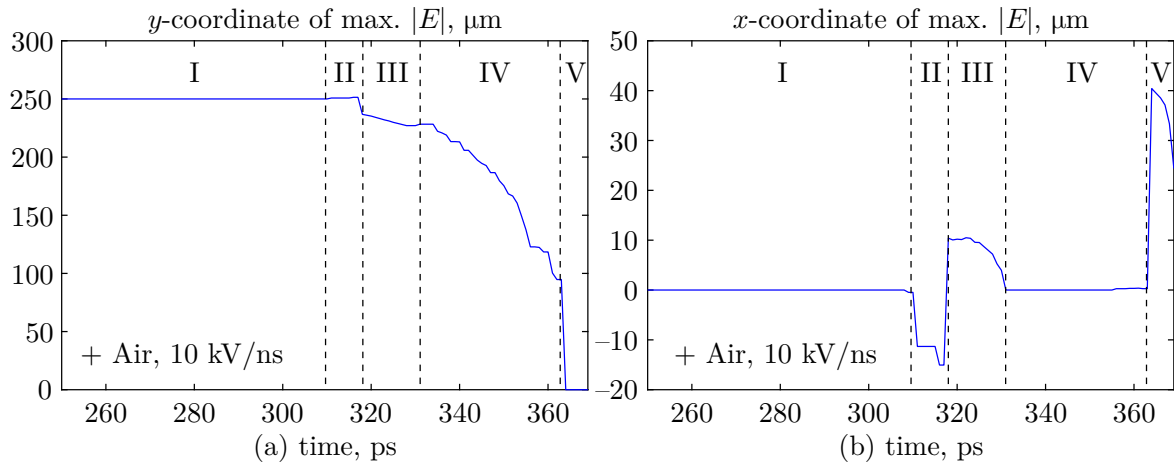


**Figure 6.29:** Example of the recorded  $x$ - and  $y$ -positions of the maximum electric field for surface ionisation waves initiated in air with  $dU/dt = 10 \text{ kV/ns}$ . Dashed lines indicate the identified phases of propagation given in the main text and labelled with Roman numerals.

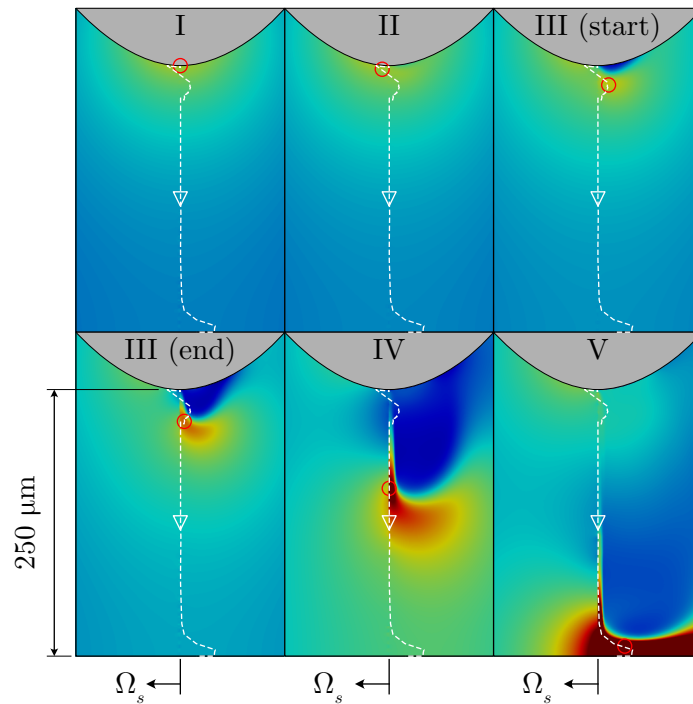


**Figure 6.30:** Spatio-temporal evolution of the electric field magnitude at selected times corresponding to the identified propagation phases. White dashed line delineates the path taken by the field maximum corresponding to Figure 6.29.

corresponding to each phase.

- I. *Pre-initiation Phase* — The maximum electric field maintains its position at the needle tip ( $x = 0 \mu\text{m}$ ,  $y = 250 \mu\text{m}$ ). Insufficient charge has accumulated to distort the field.
- II. *Inception Phase* — Accumulated charge at the needle tip screens the external field, the distortion momentarily causes the point of maximum field to *enter into the solid dielectric*, such that  $x$  becomes negative. The  $y$ -position also momentarily decreases as the field is redistributed from the needle tip to the head of the forming ionisation wavefront.
- III. *Surface Transition Phase* — The developing plasma channel causes the point of maximum field to transition from inside the solid to the head of the wavefront. The  $x$ -position therefore jumps from  $-x$  to  $+x$ , before decreasing close to  $x = 0^+$  which is located just above the solid surface. Meanwhile, the  $y$ -position initially decreases at this stage before experiencing a slight increase as the field moves into the dielectric sheath region upon its formation (which lies slightly behind the wavefront).
- IV. *Propagation Phase* — The enhanced field, now located inside the dielectric sheath, is sufficiently strong to drive the wavefront down the surface. The  $x$ -position maintains its location inside the sheath, while the  $y$ -position decreases as the wavefront travels towards the plane electrode.
- V. *Contact Phase* — The wavefront approaches the plane electrode, and begins to spread out along the cathode sheath. The  $x$ -position therefore increases as the main ionisation front now moves in the lateral  $x$ -direction into the dielectric sheath, while the  $y$ -position settles to a value related to the sheath thickness. In the case of air, this was located effectively at  $y = 0$ , since the cathode sheath was negligibly thin. For  $\text{CO}_2$ , the final  $y$ -position varies with  $dU/dt$  [see Figure 6.31(c)].

For positive discharges under each combination of working gas and  $dU/dt$ , the  $x$ - and  $y$ -positions of the maximum field are plotted in Figure 6.31, with the respective phases indicated according to the descriptions above. The rate of voltage rise,  $dU/dt$ , can be observed to influence every phase of the discharge development. Slower rates-of-rise led to the prolongation of all five phases, with a slower onset of ionisation and thus transition from I to II to III, a decrease in propagation velocity in phase IV, and further influenced the sheath thickness in phase V. Based on Figure 6.29(b) and (d), the extent to which the maximum field extends into the gas domain during phase III appears to exhibit a weak increase with decreasing  $dU/dt$ . However, due to the limited resolution of the measurement (solution data was only saved every 1 ps to reduce storage requirements), this would

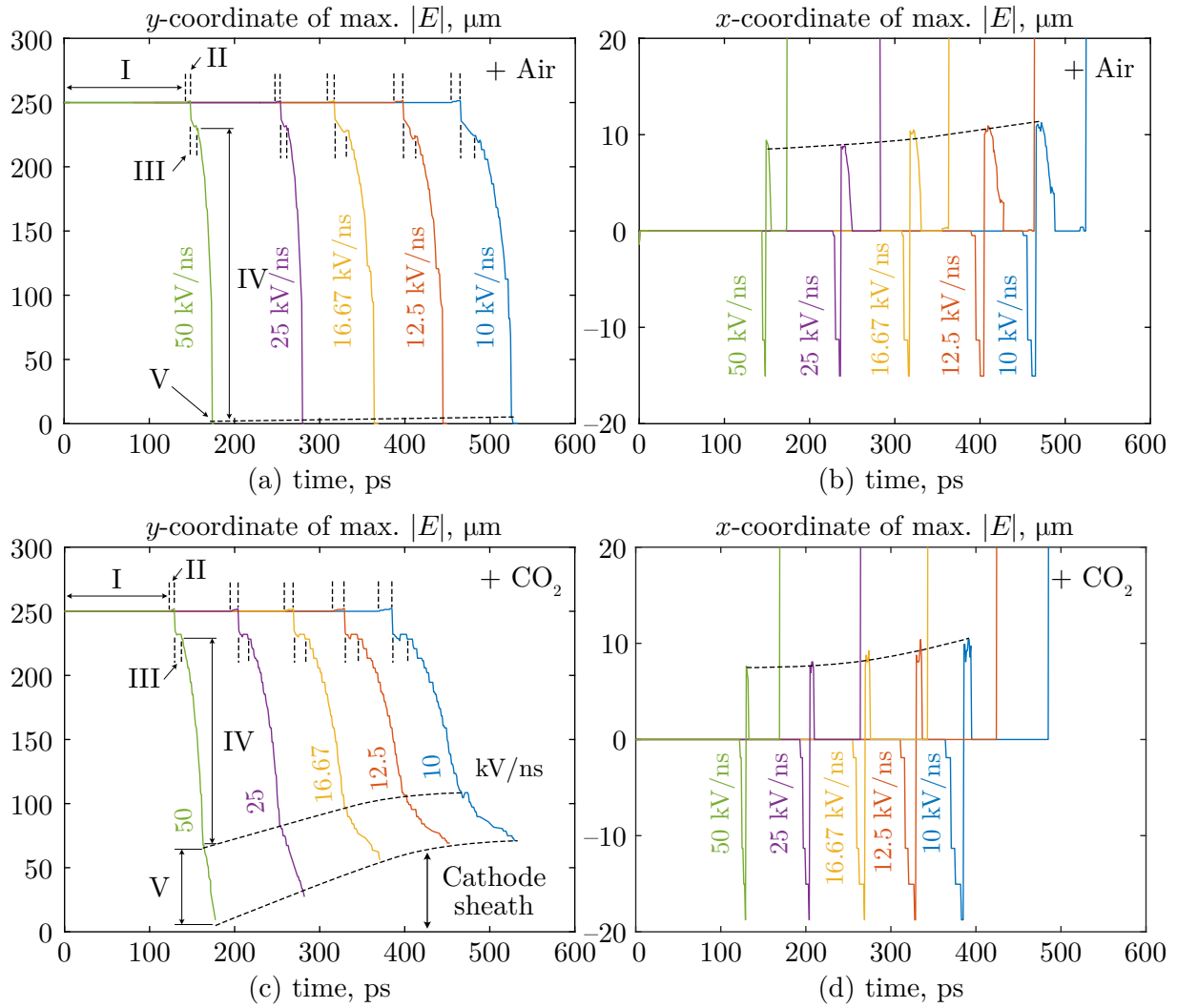


**Figure 6.31:** Recorded  $x$ - and  $y$ -positions of the point of maximum electric field for positive surface ionisation waves for  $dU/dt = 10, 12.5, 16.67, 25,$  and  $50$  kV/ns, for (a)–(b) air, (c)–(d) CO<sub>2</sub>. Labels included in plots (a) and (c) to indicate the identified propagation phases identified based on Figure 6.29.

benefit from further confirmation. Within the range of  $dU/dt$  simulated here, the difference also appears small and possibly inconsequential for the rest of the discharge development. Also notable is the the momentary increase of the electric field strength inside the solid dielectric during phase V, resulting from the compression of the field in the cathode sheath. Simulated field magnitudes were found to exceed 1 MV/cm, which enters into an order of magnitude where solid bulk breakdown becomes possible [55, 56]. However, considering the estimated picosecond timescales of the modelled ionisation events, this is equivalent to subjecting the solid dielectric to a rapid, almost instantaneous, HV impulse with picosecond rise-times. Since impulse breakdown strengths are typically higher for faster-rising voltages, it would not be unreasonable to assume that the solid breakdown strength could be far greater than the MV/cm order of magnitude found in [55, 56] for pulses of such duration.

The tendencies and identification of discharge propagation phases conducted here contributes towards a greater fundamental understanding of impulsive and overstressed surface ionisation waves. Moreover, the separation of the distinct phases of discharge may ultimately aid in the future development of diagnostics and instrumentation; those that aim to experimentally characterise fast ionisation phenomena along surfaces. The simulated discharge development and time-evolution may further provide important characterising information for low-temperature plasma applications incorporating surfaces [57].

### 6.4.3 Deposition of Surface Charge

Having included solid subdomains, StrAFE automatically considers the accumulation of surface charge due to inbound charge fluxes as per Section 5.4.5. Accordingly, the surface charge density was also included as output in the present set of simulations, allowing the visualisation of the estimated post-discharge charge density which was deposited onto the surface. It is first noted that for all positive discharges, irrespective of the working gas, the surface charge density was negligible. This was primarily due to the transport of electrons *away* from the dielectric surface during positive discharges, owing to the positively-charged wavefront head. This also explains the formation of the dielectric sheath for positive discharges only. Hence, electrons do not adhere onto the surface, and do not induce any significant surface charging over these timescales, as similarly observed in simulations from [53]. For negative discharges, however, electrons are accelerated from the plasma channel onto the surface, such that electrons generally bombard the dielectric surface, inducing a negative charge density. For all cases of negative discharge, Figure 6.32 plots the post-discharge surface charge densities, taken at the time of contact,  $t_c$ .

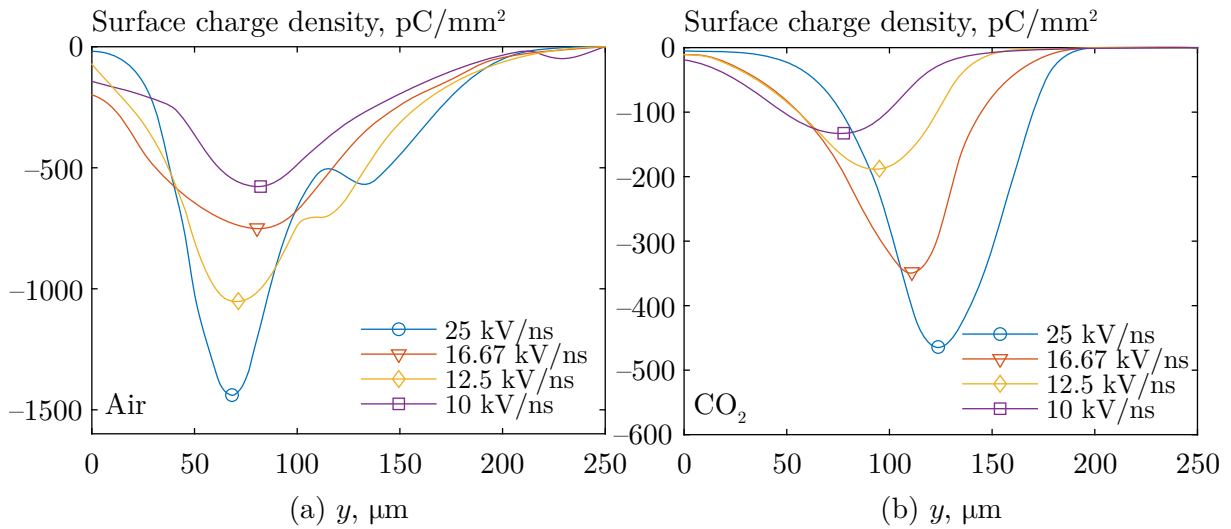


**Figure 6.32:** Deposited surface charge densities after passage of negative surface ionisation wavefronts in (a) air and (b)  $\text{CO}_2$  with  $dU/dt = 10, 12.5, 16.67,$  and  $25 \text{ kV/ns}$ , taken at the time of contact.

Since there were no included secondary emission processes, and heavy species were considered immobile over the simulation timescales, the sole mechanism for surface charging was electron bombardment originating from the discharge. The deposited surface charge density was found to be most significant near the head of the wavefront, where the most energetic electrons would be accelerated towards the surface. As the volumetric charge density increased over time, due to intensifying ionisation processes, so too did the deposited surface charge density. As a result, the maximum recorded surface charge density was always found at the end of the wavefront traversal, as shown in Figure 6.32. Faster-rising voltages were also found to increase the amount of deposited surface charge, resulting from the greater electron density produced due to the increased degree of overvoltage. The generally greater magnitude of the field may have also facilitated the acceleration of electrons towards the surface to a greater extent. Moreover, discharges in  $\text{CO}_2$  accumulated far less post-discharge surface charges in each case when compared to air, understood to be due to the lower charge densities that were developed in general. It should also be noted that the location of the maximum charge density shifts with  $dU/dt$  in  $\text{CO}_2$  (the shift in air is only due to the finite resolution of the saved timesteps, and the associated uncertainty in computing the time of contact from numerical data) because of the aforementioned scaling behaviour of the cathode sheath. The location where the wavefront initiates moves farther away from the needle with slower  $dU/dt$ , since the cathode sheath would begin to occupy much of the region immediately ahead of the needle in  $\text{CO}_2$ .

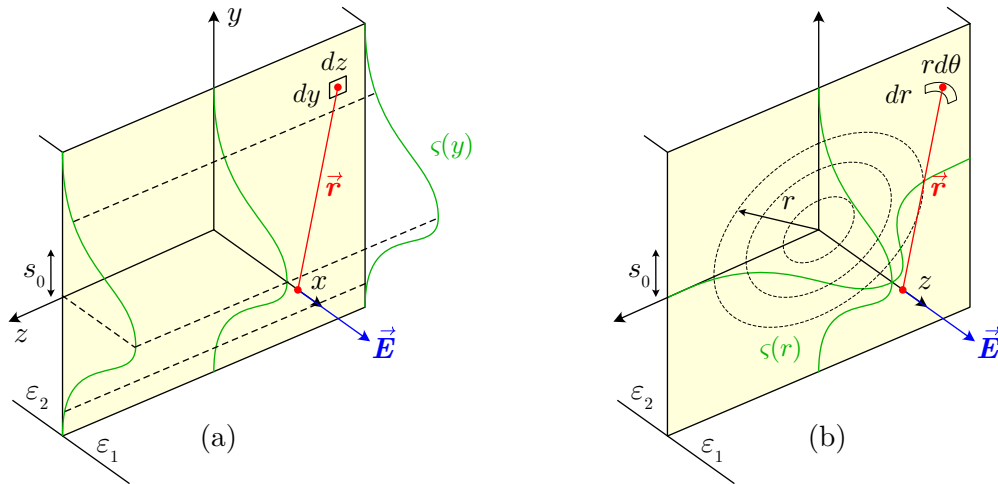


**Figure 6.33:** Diagrams depicting the calculation of the maximum surface charge induced electric field from a Gaussian-distributed surface charge density in (a) plane-parallel approximation with 1D charge density, (b) full 2D surface charge density.

Under the simulated conditions, the estimated magnitudes of surface charge density were found to be in reasonable agreement with those similarly deposited by surface streamers in [12]. In the following, it is further shown that such levels of surface charge are not negligible, and may be sufficient to substantially distort the local electric field. Consider that in the present 2D plane-parallel approximation, one may loosely approximate the accumulated charge density as a Gaussian-distributed surface charge of the form

$$\varsigma(y) = \varsigma_0 \exp\left(-\frac{(y - y_0)^2}{s_0^2}\right) \quad (6.8)$$

which prescribes a non-uniform charge density that decays along the  $y$ -direction, but does not vary in the  $z$ -direction which is of infinite length, i.e., as illustrated in Figure 6.33(a). An exact solution for the maximum electric field at the peak of the Gaussian density,  $y = y_0$ , at some distance  $x$  orthogonal to the surface can be sought by application of an integral over the real coordinate plane  $\mathbb{R}^2$ ,

$$\begin{aligned} \vec{E}_{\max}(x) &= \frac{x}{4\pi\epsilon_0\epsilon_r} \iint_{\mathbb{R}^2} \frac{\varsigma(y)}{|\vec{r}|^3} dz dy \cdot \hat{x} \\ &= \frac{x\varsigma_0}{4\pi\epsilon_0\epsilon_r} \int_{-\infty}^{+\infty} \exp\left(-\frac{y^2}{s_0^2}\right) \int_{-\infty}^{+\infty} \frac{dz}{(x^2 + y^2 + z^2)^{3/2}} dy \cdot \hat{x}, \end{aligned} \quad (6.9)$$

considering that the Gaussian is centred at the origin  $(z, y) = 0$ . The evaluation of (6.9) can be

found in Appendix A.13, yielding

$$\vec{\mathbf{E}}_{\max}(x) = \frac{\varsigma_0}{2\varepsilon_0\varepsilon_r} \frac{x}{|x|} \exp\left(\frac{x^2}{s_0^2}\right) \operatorname{erfc}\left(\left|\frac{x}{s_0}\right|\right) \cdot \hat{\mathbf{x}} \quad (6.10)$$

where  $\operatorname{erfc}(\cdot)$  is the complementary error function, and where the interface condition  $\varepsilon_1 \vec{\mathbf{E}}_1 \cdot \hat{\mathbf{n}} - \varepsilon_2 \vec{\mathbf{E}}_2 \cdot \hat{\mathbf{n}} = \varsigma$  can be shown to be satisfied at the surface, since

$$\begin{aligned} \lim_{x \rightarrow 0^+} \vec{\mathbf{E}}_1(x) \cdot \hat{\mathbf{n}} &= \frac{\varsigma_0}{2\varepsilon_0\varepsilon_1}, \\ \lim_{x \rightarrow 0^-} \vec{\mathbf{E}}_2(x) \cdot \hat{\mathbf{n}} &= -\frac{\varsigma_0}{2\varepsilon_0\varepsilon_2}, \end{aligned} \quad (6.11)$$

and therefore

$$\lim_{x \rightarrow 0} \left[ \varepsilon_0\varepsilon_1 \vec{\mathbf{E}}_1(x) \cdot \hat{\mathbf{n}} - \varepsilon_0\varepsilon_2 \vec{\mathbf{E}}_2(x) \cdot \hat{\mathbf{n}} \right] = \varsigma_0. \quad (6.12)$$

It is convenient to introduce the constant  $k$ , defined as the ratio  $k := |x/s_0|$  which provides a measure of the distance away from the surface as a  $k$  multiple of  $s_0$ . From (6.10), therefore, a critical peak level of surface charge,  $\varsigma_{\text{crit}}$ , which would induce an electric field of greater than a value  $|\vec{\mathbf{E}}_{\text{crit}}|$ , at a distance of  $ks_0$ , in this approximation may be given by

$$\varsigma_{\text{crit}} = \frac{2\varepsilon_0\varepsilon_r}{e^{k^2} \operatorname{erfc}(k)} |\vec{\mathbf{E}}_{\text{crit}}|. \quad (6.13)$$

The decay of the maximum field moving away from the surface in the positive  $x$ -direction is shown in Figure 6.34 as the blue line, where it may further be seen that directly at the surface, at the point of maximum charge density, the electric field converges to a value equal to that of an infinite charged plane with the uniform charge density  $\varsigma = \varsigma_0$ .

Hence, a peak level of surface charge necessary to enhance the electric field to an approximate critical field of  $|\vec{\mathbf{E}}_{\text{crit}}| = 3 \text{ kV/mm}$  in atmospheric air at a distance  $s_0$  away from the surface, would be approximately  $124 \text{ pC/mm}^2$ . It follows that the simulated charge distributions of Figure 6.32 induce fields that may be far above the ionisation threshold alone. Since the most significant charge deposition occurs during the passage of the primary ionisation front across the surface, the surface-charge induced field may not substantially affect the characteristics of the primary surface wavefront. However, the remaining charge deposited on the surface (which may have a long decay time, based on the conductivity of the solid material) may influence subsequent discharge behaviour in the same system, especially considering that the estimated charge densities were quite significant. In practise, the peak surface charge induced field would likely be overestimated

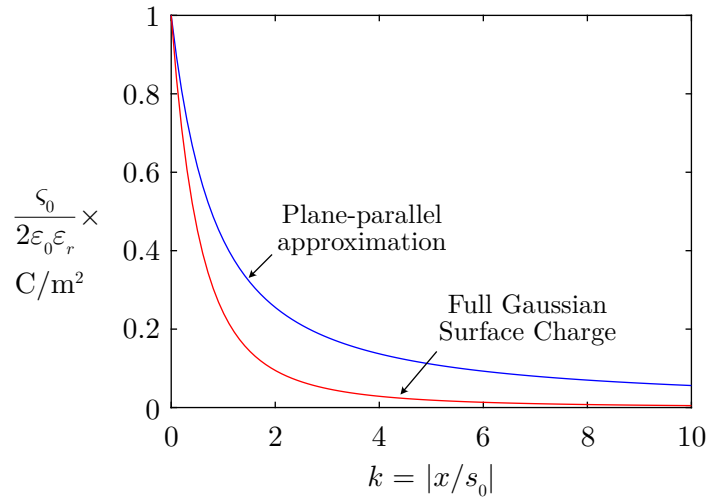


**Figure 6.34:** Variation of the electric field strength directly above Gaussian-distributed surface charge densities as a function of  $k = |x/s_0|$  for the plane-parallel approximation and full solution (where  $x \rightarrow z$  serves the same function). Note the convergence to  $\varsigma_0/2\varepsilon_0\varepsilon_r$  on the surface.

here, considering that decay of surface charge away from the surface would be greater with an additional dimension—see the following analysis. Consider the derivation of Appendix A.13, which repeats the integral of (6.9) but in the cylindrical coordinate space  $(r, \theta, z)$ , and computes the maximum electric field above a plane with a full 2D Gaussian surface charge centred at  $r = 0$  [see Figure 6.33(b)]. The peak field magnitude developed above the centre of the charge patch was found to be

$$\vec{E}_{\max}^{\text{full}}(z) = \frac{\varsigma_0}{2\varepsilon_0\varepsilon_r} \frac{z}{|z|} \left[ 1 - \left| \frac{z}{s_0} \right| \sqrt{\pi} \exp\left(-\frac{z^2}{s_0^2}\right) \operatorname{erfc}\left(\left| \frac{z}{s_0} \right|\right) \right] \cdot \hat{z} \quad (6.14)$$

which converges to the same limit on the surface ( $z = 0$ ), but decays in the  $z$ -direction faster than that of (6.10), as shown by the red line of Figure 6.34. The corresponding critical charge expression as an analogue to (6.13) becomes

$$\varsigma_{\text{crit}}^{\text{full}} = \frac{2\varepsilon_0\varepsilon_r}{1 - k\sqrt{\pi}e^{k^2} \operatorname{erfc}(k)} |\vec{E}_{\text{crit}}|, \quad (6.15)$$

which gives a higher threshold value of around 219 pC/mm<sup>2</sup> for a critical field of 3 kV/mm at the same distance,  $s_0$ , above the surface. It is remarked, however, that surface streamer heads in the full 3D case will likely possess higher electric fields due to increased curvature and enhancement at the wavefront [58]. In turn, this would increase the total charge deposited onto the surface due to the development of greater charge fluxes.

## 6.5 Influence of Non-uniform Surface Charge on Surface Streamer Development

The simulations conducted in Section 6.4 indicated that significant surface charge can be deposited by a surface discharge propagating across a solid interface (Figure 6.32). Coming away briefly from the focus on overstressed ionisation events, this section shifts the focus towards the interfacial aspect of this work. Presented in this section is an auxiliary set of simulations investigating the role of *non-uniform* surface charge, with a particular focus on subsequent surface streamer development under static voltages. Interest in surface charging phenomena has increased significantly, particularly for the development of HVDC transmission technologies and associated novel insulation accessories within the power industry. Whether accumulated by the prolonged presence of unipolar currents or resulting from previous partial (or complete) discharges like those in Figure 6.32, sufficient levels of surface charge are believed to affect the propagation of subsequent discharge events, as was discussed within the review of Chapter 2 - Section 2.4.1.

The effects of *non-uniform* surface charge on the propagation of surface streamers remain poorly understood. Yet, previous discharges clearly leave irregular and highly non-uniform distributions of surface charge on dielectric surfaces based on past literature [12,13,59] and the results of Section 6.4. Summarising the relevant simulation works reviewed in Section 2.4.1, Li *et al.* [12] simulated negative streamers initiated near a uniformly charged surface, concluding that same-polarity (*homocharge*) surface charge suppressed the development of streamers, while different-polarity (*heterocharge*) promoted and accelerated their development. This was similarly concluded in the experimental works [13] and [60]. Florkowski [61] simulated a short linear homocharge deposited on an inclined surface, showing what the author referred to as *airborne streamers*; discharges initiated from the surface charge spot, which briefly travelled through the gas, before re-attaching to the surface, in seemingly good agreement with the experimentally-imaged phenomena.

In general, however, the influence of non-uniform surface charge on surface streamer development has many unexplored facets. For one, neither of the charge distributions studied by Li *et al.* [12] or Florkowski [61] resemble the far more non-uniform distributions left by streamer discharges as simulated in Section 6.4 and similarly in [12,60]. Moreover, their simulations were conducted using the LFA which may limit their validity. Other factors such as the size, magnitude, distribution, field non-uniformity, and the location of the charge with respect to energising electrodes, remain unexplored. While the present study does not at all aim to explore all possible factors, in light

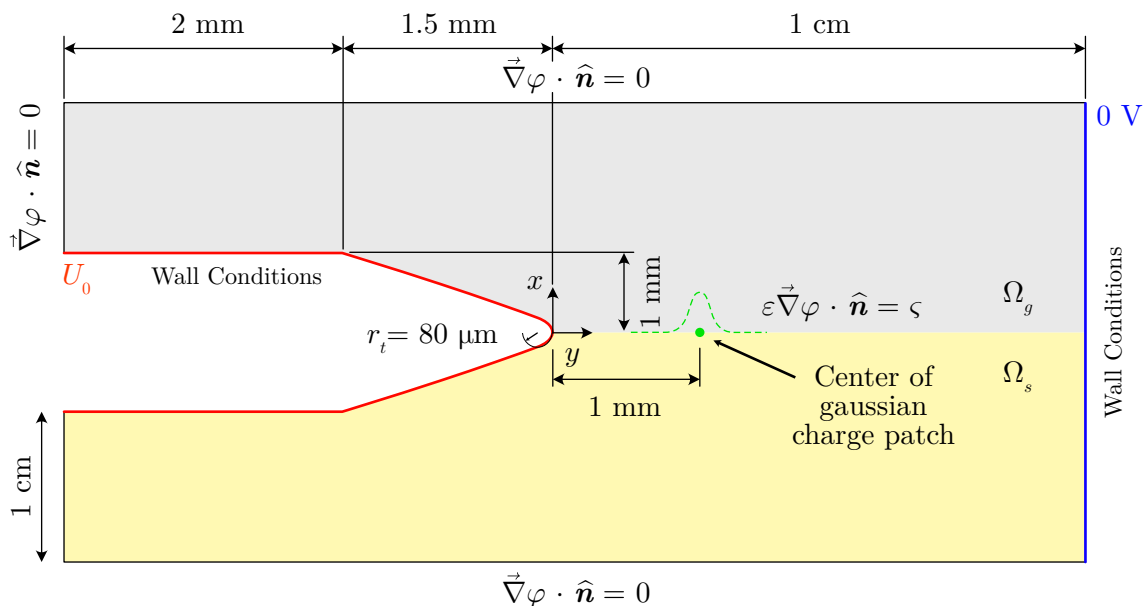


**Figure 6.35:** Plane-parallel domain used for the study of surface streamers interacting with non-uniform surface charge.

of the computed surface charge distributions of Figure 6.32, it seemed only appropriate to briefly address an undeniably important part of solid-gas interfacial phenomena, using an adapted version of the simulation configuration used in Section 6.4.

### 6.5.1 Computational Domain and Configuration

The same needle-plane electrode geometry of Section 6.4 was utilised with a number of changes shown in Figure 6.35. Namely, the gap distance was lengthened to a total inter-electrode gap of 1 cm; and at a distance 1 mm from the needle tip, a Gaussian-distributed charge patch in the form of (6.8) was placed as an initial condition. To isolate the influence of the charge patch, the previously time-dependent voltage applied to the needle electrode was instead replaced by a static voltage of  $U_0 = 20 \text{ kV}$ , and the relative permittivity of the dielectric remained fixed at  $\epsilon_r = 2$ . This study focused only on atmospheric air (using the plasma chemistry set of Table 5.4 and the LMEA) and exclusively on positive surface streamers for a number of reasons. Most importantly, the development of negative streamers from the needle electrode forms the cathode sheath region ahead of the electrode surface, as seen in Sections 6.3 and 6.4. Due to the need to resolve steep field gradients along a far longer gap (and for a correspondingly longer time), the total number of mesh elements required to successfully resolve the cathode sheath and streamer front, became prohibitively expensive on the available computer systems, even with the use of

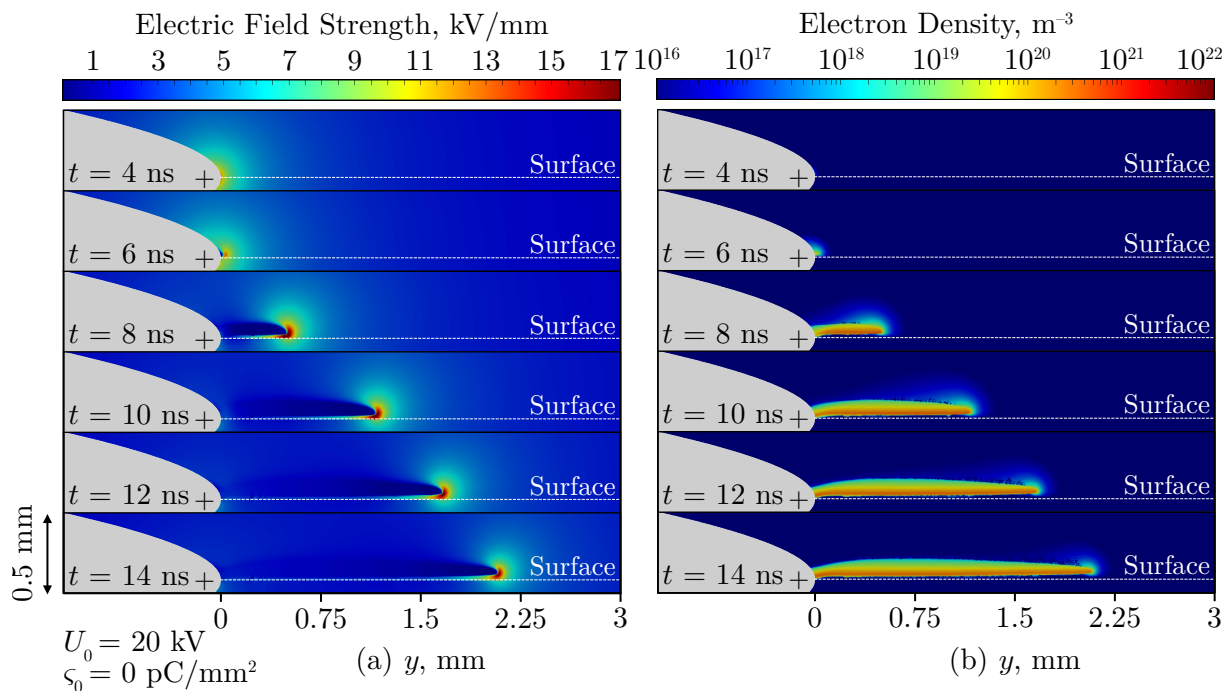


**Figure 6.36:** Spatio-temporal development of the (a) electric field magnitude and (b) electron density for a positive surface streamer, initiated with an initially uncharged surface from an embedded needle.

adaptive meshes. Computational load was less intensive for positive surface streamers due to the absence of the cathode sheath, and where the pre-refined mesh along the dielectric surface was alone sufficient to resolve the dielectric sheath.

### 6.5.2 Gaussian Distributed Homo- and Hetero-charge

A total of seven different simulations were conducted corresponding to peak charge densities of  $\varsigma_0 = \pm 400$ , 600, and 800 pC/mm<sup>2</sup>, with one additional case of no surface charge to act as a point of reference. The initial variance parameter of the charge patch was set to  $s_0 = 0.2$  mm, based on surface streamer charge accumulation simulated in [12]. Figure 6.36 first presents the reference case with no additional surface charge, showing the development of the electric field and electron density at various timesteps. Given the results from the previous sections of this chapter, the surface streamer develops across the dielectric surface in line with expectation. Streamer initiation was facilitated by the enhanced electric field at the solid-gas-electrode triple junction, causing the ionisation front to incept directly at the surface and subsequently propagate along the interface. Note the far lower field magnitude at the streamer head compared to Section 6.4, as these surface streamers were not developed under an overstressed discharge regime. The

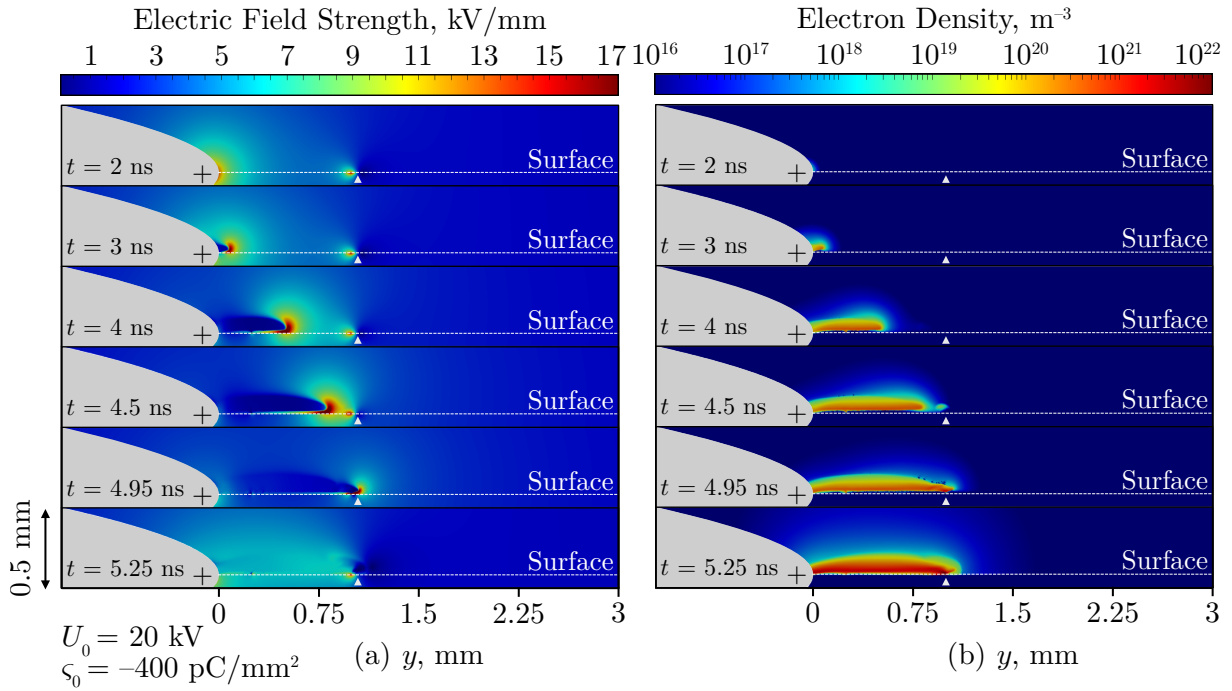


**Figure 6.37:** Spatio-temporal development of the (a) electric field magnitude and (b) electron density for a positive surface streamer, initiated with a peak Gaussian surface charge density of  $-400 \text{ pC/mm}^2$  at the shown location.

streamer velocity appeared to slow as it propagated into a region of decreasing background field, though it would be expected that, given sufficient time (note that the simulations were not run up to the point of electrode bridging), the streamer velocity would not decrease indefinitely, but rather successfully bridge the electrode gap, since the field across the length of the surface exceeded the typical value of the so-called streamer stability field of around  $4.5 \text{ kV/cm}$  [62]<sup>†</sup>.

### 6.5.2.1 Incomplete Streamer Discharges due to Non-uniform Heterocharge

The case that heterocharge distributions were introduced onto the surface is first discussed. Corresponding colour plots for the  $s_0 = -400$ ,  $-600$ , and  $-800 \text{ pC/mm}^2$  cases are presented in Figure 6.37 and 6.38, noting that the timesteps shown are different for each value of charge since the inception time and velocities were found to be influenced by the charge magnitude.

In comparison to the uncharged surface of Figure 6.36, the introduction of the charge patch distorted the net electric field around the charge location. As the charge density was of opposite

<sup>†</sup>It is remarked that this value is typically found for streamers propagating in gas only. It is currently unknown if the stability field value for surface streamers would be different.



polarity to the energising voltage, the electric field was enhanced in the region between the needle tip and the charge patch. In effect, the charge patch functioned as an elevated cathode, resulting in a shortening of the time for streamer inception with greater peak charge magnitude. While for the uncharged case almost 10 ns were necessary for the surface streamer to arrive at the location of where the charge patch was placed in the simulations including surface charge, all other cases with surface charge traversed the same distance in under half the time. A minor increase in the plasma density was also found, which aligns with expectation based on the greater field enhancement at the streamer head with greater surface charge. In the  $\varsigma_0 = -600 \text{ pC/mm}^2$  and  $-800 \text{ pC/mm}^2$  cases, the field induced by the charge patch itself was sufficiently strong to cause local and rapid ionisation. Beyond approximately 2 ns in Figure 6.38(b) and (d), a negative discharge can be observed to incept near the charge location, eventually merging with the positive streamer front originating from the needle. This is particularly clear at  $\varsigma_0 = -800 \text{ pC/mm}^2$ , where the magnitude of the surface charge induced field was significant, contributing strongly to the rapid development of the plasma channel during these initiating stages of the surface discharge. The observed behaviours are in general agreement with the conclusions of [7, 13, 63, 64] for heterocharge deposition.

Note that these simulations were terminated soon after the streamer reached the location of the charge patch. This was due to the observation that the rapid interaction between the streamer head and the charge patch appeared to result in the halting or interruption of the streamer channel. To explain this further, Figure 6.39 shows the evolution of the electric field near the time that the positive streamer reached the location of the surface charge distribution. Far from the charge patch, the positive surface streamer evolves as expected, fuelled primarily by electrons accelerated into the streamer channel from ahead of the ionising front (streamer head), corresponding to panel (I). Meanwhile, electrons near the charge patch are accelerated away due to the negative charge polarity; those which were originally located between the charge patch and the needle are soon also accelerated into the streamer head. Upon close approach of the streamer head to the charge patch, electrons are accelerated with increasing intensity due to the closing distance between the positively-charged streamer head and the negative charged patch (II).

As the streamer propagates over the centre location of the Gaussian (III), however, the simulation results indicated a significant increase in the electron density in the near vicinity of this surface location due to the inbound electrons. The subsequent increase in electron density appeared to induce a sufficiently intense field to reverse the direction of the net electric field at the streamer head (IV). The outward pointing field of the positively-charged layer, characteristic of the

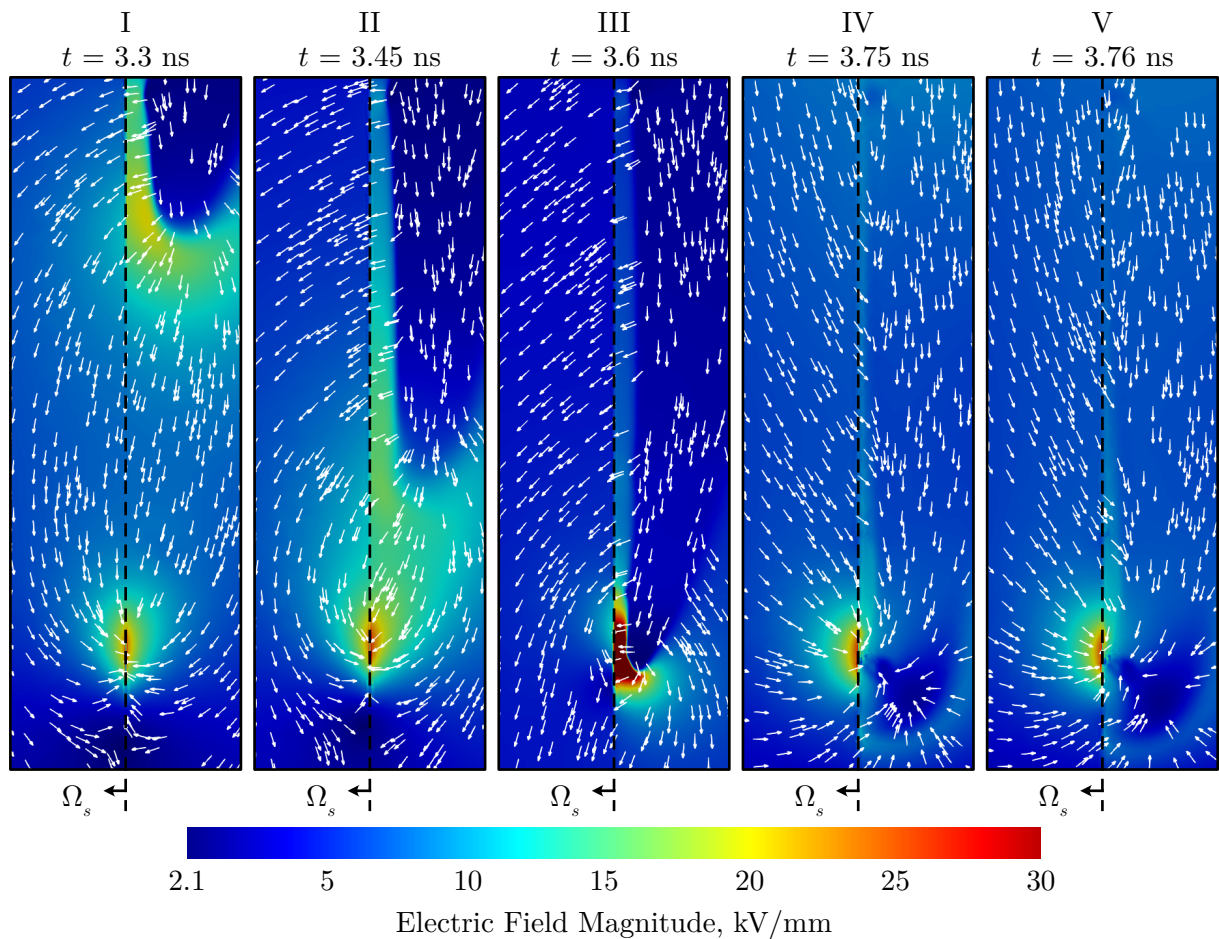


**Figure 6.39:** Magnified head of a positive surface streamer at various stages upon approaching the negatively charge patch. White arrows show the direction of the electric field. Black dashed line shows the location of the solid surface, where  $\Omega_s$  denotes the solid domain. Note the reversal of the electric field during stages IV and V, breaking up the coherent streamer structure and halting its propagation.

streamer head, was overcome by the intense negative field originating from the combined effects of the now significant electron density and negative surface charge. The streamer channel was then seen to collapse, as electrons around the charge patch location were subsequently accelerated *away* due to the inversion of the electric field direction—(IV) and (V). At this moment, the dielectric sheath local to the charge patch also collapses, which appeared to be a consequence of electrons being accelerated back towards the surface (V). The collapse of the coherent structure of the streamer channel led to the disruption and cessation of its propagation along the surface.

The observed halting of the surface streamer may manifest in practise as incomplete surface discharges, similar in nature to those simulated in [59]. Partial streamer discharges were largely

attributed to the loss of the stability field, stochastic fluctuations, or surface geometry acting as a form of inhibiting mechanism. However, the breakup of the streamer structure observed here caused by the interaction with the strong and non-uniform surface charge electric field, may contribute to the occurrence of incomplete streamer discharges. To the best of the authors knowledge, there exists no prior literature that conducted surface streamer simulations under similar combinations of field non-uniformity, dielectric surfaces, non-uniform charge distributions, and with the use of the LMEA. The simulated behaviours here appear consistent with the type of model used, however, would benefit significantly from future verification and validation. In particular, the use of kinetic models would be an important step towards ensuring that the observed behaviours are not solely an artefact of the hydrodynamic approach, or have resulted from computational deficiencies.

### 6.5.2.2 Counter-propagating Homocharge-initiated Surface Streamers

In the case where positive surface charge densities (of the same magnitudes as used previously) were deposited instead, the inception of the positive streamer was found to be significantly delayed. With  $\varsigma_0 = 400 \text{ pC/mm}^2$ , the streamer did not incept until around  $t = 15 \text{ ns}$  compared to  $t = 6 \text{ ns}$  in the charge-free case. The streamer morphology was otherwise identical to those shown in Figure 6.37, since the field up to the (now positive) charge location remained above the stability field. At  $\varsigma_0 = 600 \text{ pC/mm}^2$  and  $800 \text{ pC/mm}^2$ , however, the surface charge induced field was sufficiently strong for discharges to be developed at the charge spot location instead of the needle tip, since the field at the needle tip was now reduced from the counteracting surface charge field. Figure 6.40 shows the evolution of these rapid ionisation events for the  $\varsigma_0 = 600 \text{ pC/mm}^2$  charge density, which could not be simulated beyond the moment shown due to the significant field gradient formed within the abnormally thin dielectric sheath. The  $\varsigma_0 = 800 \text{ pC/mm}^2$  case was morphologically identical, but developed slightly earlier.

The developed ionisation waves originating from the positively-charged spots were of counter-propagating nature. Two ionisation fronts were found to propagate towards the needle and the plane simultaneously, similar to double-headed streamers as shown in Section 5.8.3. In [65], double-headed surface streamers were successfully simulated and experimentally imaged, the characteristics of their propagation similar to those known for streamers developed in gas alone. However, it should be noted that the discharges of Figure 6.39 possess a key difference: the two outbound surface streamers are *of the same polarity*. Due to the magnitude of surface charge present, the field strength in the vicinity of the charge location was stronger than at the needle

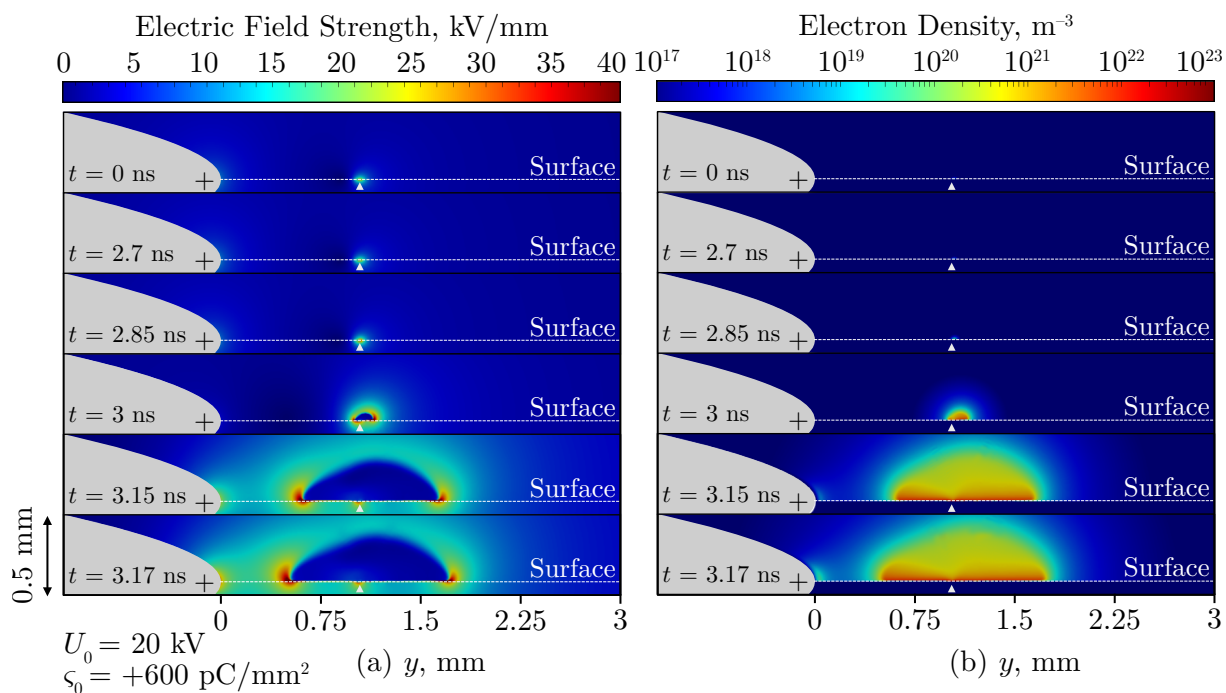


**Figure 6.40:** Spatio-temporal development of the (a) electric field magnitude and (b) electron density for a positive surface streamer, initiated with a peak Gaussian surface charge density of 600 pC/mm<sup>2</sup> at the shown location.

tip. Both the needle and the plane electrode therefore acted as cathodes to the charge patch “anode”, leading to the inception of two simultaneous *positive* streamers travelling in opposite directions, formed initially from the acceleration of electrons towards the charged patch. A cathode sheath can be seen beginning to form over the needle tip at  $t = 3.17$  ns in Figure 6.40, resulting from the reversal of the field and drift of electrons away from the needle, into the oncoming positive streamer channel instead.

The electric field driving both streamer heads forward were also found to be much stronger than those of needle-initiated positive streamers that were far from the negative charge patch, like those seen in the heterocharge case. However, comparing the field of needle-initiated positive streamers as they traverse over the charged patch (e.g., as shown in Figure 6.39), the magnitudes are comparable. It follows that the initially stronger field of the positive surface charge initiated streamers have likely resulted due to their direct inception from charges resting immediately on the surface. Both streamers also formed their respective dielectric sheaths which were found to be thinner than those formed between positive streamers originating from the needle. This substantially increased the computational requirements and ultimately resulted in numerical divergence due to an unphysical sheath collapse. With advancing computational power, it would

undoubtedly be of high interest to revisit such simulations in the future and to study the entire evolution in more depth.

The novel simulation results obtained here nonetheless reinforce the idea that significant accumulation of surface charge can drastically change discharge behaviours. While polarity effects are in agreement with well-known tendencies, the induced differences to positive streamer development near the charge patch were found to be characteristically different from cases of assumed uniform surface charge [12], and may help explain experimentally imaged discharge morphologies across solid-gas interfaces, e.g., in [66,67]. Overall, this work has contributed a stronger understanding of the potential impact of surface charges on the flashover behaviour of solid insulators. It is envisaged that, ultimately, this may help to inform the future design of high voltage solid insulation and charge tailoring techniques for power and pulsed power systems.

## 6.6 Chapter Conclusions, Contributions, and Outlook

Pre-breakdown phenomena in gas and solid-gas insulating systems remain poorly characterised, particularly within the domains of pulsed power engineering and in the overstressed breakdown regime. In the past, analysis of pre-breakdown phenomena under fast-rising overstressed conditions has largely been confined to experimental investigation. It was seen to be of significant benefit to utilise modern computational techniques to contribute towards a more fundamental understanding of low-temperature gas discharges under such conditions. Motivated by advances in computational power, and by the development of efficient multi-scale modelling techniques, this chapter has explored the development of non-thermal gas discharges in gas and across solid dielectric surfaces. Using the StrAFE framework developed in Chapter 5, fast ionisation wavefronts and filamentary streamer discharges, developed in several relevant system geometries, have been studied by means of computational simulation. Four sections comprise this chapter, each focused on the occurrence of low-temperature gas discharge phenomena associated either with development under overstressed conditions, or with their interaction with solid-gas interfaces. Novel results within each case study have contributed towards an increased understanding of gas pre-breakdown phenomena in non-standard system geometries, particularly those subjected to electrical stresses relevant to the development and optimisation of pulsed power and microscale electrical systems. The individual contributions of each section are described separately in the following.

### 6.6.1 Academic Significance and Contributions

As a first look into steamer discharges developed under fast-rising voltages, a first case study has studied the effect of the voltage rate-of-rise,  $dU/dt$ , on the propagation of positive streamers and the initiating behaviour of negative streamers in atmospheric air. Using the minimal hydrodynamic model, streamers initiated from a charged seed within a uniform electrode gap, subjected to ramp voltages rising with  $dU/dt$  between 2.5 kV/ns to 10 kV/ns, were simulated. Increased streamer propagation velocities of positive streamers were found with faster-rising voltages, attributed to the greater background field magnitude and associated increase to ionisation intensity at the streamer head. A corresponding increase to the developed electron densities inside the streamer channels at comparable propagation lengths has additionally been observed with faster-rising voltages. Streamer radius was also found to increase with  $dU/dt$  as a result of the larger ionising region developed at the streamer head. Comparing the velocity to squared-diameter ratio of overstressed positive streamers to the empirical relation suggested in [17], the relation  $v/d_{st}^2 \approx 1$  was found to be a better fit than the originally proposed  $v/d_{st}^2 \approx 0.5$  found for streamers under static voltages. For negative streamers initiated from a negative charge seed, the coupling between electron diffusion rate and the voltage rate-of-rise, as derived in Chapter 4, was found to hold. Under slower-rising voltages, sufficient time allowed the outward diffusion of the initial seed to reduce the curvature and electric field at the head of the streamer, delaying streamer onset. Together with the analytical results of Chapter 4, this further suggests that electron diffusion may continue to play a significant role under rising-voltage conditions depending on the rate-of-rise.

A second case study investigated fast ionisation wavefronts initiated in 250  $\mu\text{m}$  needle-plane and needle-needle gaps, under fast-rising ramp overvoltages in atmospheric air and  $\text{CO}_2$ , and using the extended hydrodynamic model with the inclusion of simplified plasma chemistry. It was found that ionisation fronts initiated in air developed stronger electric fields at their heads than in  $\text{CO}_2$  for negative voltages, but the opposite was found for positive voltages. Wavefronts developed in  $\text{CO}_2$  also appeared larger in radius, and incepted earlier, than those in air under the same conditions. The acceleration of ionising wavefronts was found to be affected by the voltage rate-of-rise, where slower rising voltages led to slower-accelerating wavefronts. Average propagation velocities increased with greater voltage rate-of-rise, though this was more significant in air than in  $\text{CO}_2$ . A nonlinear increase to the channel plasma density with increased rate-of-rise, which were, in general, higher for positive wavefronts than negative wavefronts in both gases, was found. The wavefront inception times were found to scale with the reciprocal of  $dU/dt$ , which

has been shown to be consistent with the predictions of the model presented in Chapter 4. In CO<sub>2</sub>, the cathode sheath thickness was found to increase with decreasing  $dU/dt$ , but little change was observed in air. This has been attributed to an enhancement of the electronic mobility in CO<sub>2</sub> within a specific range of electron energy during the rising slope, and due to the injection of electrons from the photoionisation process, which acted to replenish the depleted sheath region in air. This was confirmed with additional simulations without photoionisation enabled. It is believed that the relationship between rate-of-rise and the cathode sheath region may be consequential for the operation of systems utilising sub-mm electrode gaps. In a needle-needle simulation, the electron-depleted region occupied a significant portion of the inter-electrode gap and suppressed the formation of a negative wavefront. It is believed that the ratio between the sheath thickness and the total gap distance may be an important parameter in characterising this process, as is the voltage rate-of-rise.

Moving to the investigation of interfacial phenomena, a third set of simulations were conducted to study similarly short-gap needle-plane discharges, with the inclusion of a dielectric surface. Transient ionisation waves were therefore initiated from an embedded needle electrode at the solid-gas-electrode triple junction in a 2D approximation, again in air and CO<sub>2</sub>. These simulations exhibited similar tendencies to the gas-only gaps studied previously in terms of propagation characteristics with different rate-of-rise. Morphologically, however, the developed surface discharges were characteristically different from those initiated in gas only. Furthermore, plasma channel morphologies were found to differ significantly between discharge polarities, attributed to differences in electron transport in the near vicinity of the dielectric surface. Simulation results also indicated that, greater electron densities, relative to a gas-only gap, would be generated with the inclusion of a dielectric surface, due to the overall enhancement of the electric field at the solid surface that results from the polarisation of the dielectric. This is compounded by the adherence of the ionising wavefronts to the surface, such that the field strength at the wavefront head becomes notably stronger than in the gas-only case, acting to increase the ionisation intensity. Based on the position of the maximum electric field, the development of positive discharges could be separated into distinct phases corresponding to different features of its propagation. This included a momentary shift of the maximum electric field into the solid dielectric upon discharge inception.

Positive surface discharges were found to deposit negligible amounts of surface charge since electrons generally drifted away from the surface, and the generated heavy species were effectively immobile over the picosecond timescales involved. Over longer timescales with a sustained

surface-directed field component, heavy species would impinge on the surface and may begin to influence the surface charge distribution. Negative discharges, however, were found to deposit significant surface charge that increased in magnitude with propagation distance. The deposited charge was also found to be highly non-uniform across the surface, with a peak corresponding to the location of the propagating wavefront head. Fast-rising voltages also induced greater levels of surface charge, owing to the increased intensity of ionisation and charge bombardment of the surface. Analytical limits to the peak electric field generated by a Gaussian patch of surface charge were derived for 2D plane-parallel approximations and the full 3D case. From this, it could be concluded that the simulated discharges may have the potential to deposit sufficiently intense levels of surface charge; enough to have a substantial effect on subsequent discharges due to local field distortion. Obtained critical surface charge densities also suggested that surface charge alone may distort the field sufficiently to breach the ionisation threshold and initiate discharges directly from the solid surface.

In a fourth and final section, the idea of non-uniform surface charge and its effects on positive surface discharge behaviour was investigated. Also motivated by a distinct lack of understanding relating to the influence of non-uniform surface charge, which is far more likely to be found in practise, the embedded needle-plane geometry was extended to incorporate a gap distance of 1 cm. A Gaussian-distributed surface charge patch was introduced as an initial condition, and simulations of positive-needle energised discharges were conducted under a static 20 kV voltage under hetero- and homo- surface charge conditions of  $-400$ ,  $-600$ , and  $-800$  pC/mm<sup>2</sup> peak magnitude. Gaussian heterocharge was found to act as an extended cathode, promoting earlier streamer inception, and faster surface propagation, of positive streamers originating from the needle triple junction. This was found to agree with the literature. The extent of field enhancement in the region between the heterocharge patch and the needle increased with greater surface charge density, leading to a reduction of the streamer inception time, and time for the streamer to reach the charge patch location. At the highest levels of surface charge simulated, the possibility for a negative streamer to be formed from the charge patch was also found, which propagated briefly to meet the incoming positive streamer front, accelerating the channel connection process between the needle and the charge patch. Most importantly, for the heterocharge conditions simulated here, positive surface streamers were found to be interrupted upon reaching the surface charge location. Based on the electric field data, this was due to the rapid development of significant negative charge from the intense enhancement of the electric field as the positive streamer propagated over the charge patch. This localised negative charge density induced an opposing field with sufficient strength to locally invert the field direction, disrupt the

positive streamer charge sheath, and cease the propagation of the streamer. It is believed this may manifest in practise as incomplete surface streamer discharges, though significant future work would be necessary to confirm.

In the case of homocharge, these acted to reduce the electric field between the needle and the charge patch, suppressing streamer formation at the needle tip, and delaying the onset of surface discharge for lower surface charge densities. However, with sufficiently high surface charge, the simultaneous initiation and propagation of double-headed counter-propagating streamers, both of positive polarity, was observed. For this to occur, electric fields at the induced streamer heads must be greater than that of the field at the needle, such that the charge patch acts as an anode to both the needle and plane electrodes. The dielectric sheaths formed between these induced surface streamers were found to be thinner than streamers initiated from the needle electrode, posing a substantially greater computational challenge to resolve beyond the inception stage.

### 6.6.2 Industrial Relevance

The studies conducted within sub-mm electrode gaps are highly relevant to the development of miniaturised and compact electrical systems, whose reducing geometrical dimensions may place them within the realms of electrical discharge, despite low operating voltages. For example, modern semiconductor, power electronic, or micro-electromechanical systems [27, 68] are example applications beginning to face such issues. Electrical discharge phenomena within these systems may be detrimental to their operation or lead to outright system failure. The results attained in this work may provide critical design criteria in relation to clearance distances or insulating gas selection for microscale systems. Other beneficiaries include pulsed power equipment such as plasma-closing switches [28], which aim to induce controlled and precise electrical breakdown for high-speed switching of large electrical currents. Breakdown voltage under non-uniform electrode geometries, gas type, discharge byproducts, and pre-breakdown processes are critical for the reduction of switch jitter for many applications. The discharge characteristics including the cathode sheath behaviour and the scaling of inception time and sheath thickness with  $dU/dt$ , provides an important basis on which to develop the understanding of microscale discharge events. Moreover, CO<sub>2</sub> remains a potential candidate to be used within different gas mixtures in continued efforts to replace the potent greenhouse gas, SF<sub>6</sub>. As such, characterisation of CO<sub>2</sub> under overstressed pulse conditions, as conducted in this work, is of paramount importance.

Increasing the understanding of surface streamer phenomena, as studied in the latter two sections of this chapter, are of equal importance to industrial applications. The use of solid dielectric

material is unavoidable for high voltage power and pulsed power equipment, favoured for their unmatched dielectric strength and mechanical properties. The results presented here on the characteristics of primary surface discharges contributes towards a deeper understanding of solid-gas interfacial phenomena, particularly under non-uniform and fast-rising voltage stress, aiding in the development of future composite insulation systems for the enhancement of hold-off voltage, for example. Characterisation of surface streamer propagation phases, and understanding their relation to measurable quantities, may aid in the development of diagnostic equipment for discharge activity. This work has additionally presented novel results on the effects of non-uniform surface charge, with potential implications to charge tailoring methods [69, 70] and for deepening the fundamental understanding of charge deposition and interaction with surface streamer discharges. Advancing the understanding of plasma composition and surface interaction is also of particular importance to novel plasma applications, especially those involving chemical processing [31] or plasma-surface interactions, e.g., in surface treatment technologies using nanosecond pulsed discharges [57]. Here, results pertaining to the plasma density and how it may be influenced by factors such as  $dU/dt$  may be of significance.

### 6.6.3 Limitations and Future Outlook

Throughout the simulations presented in this chapter, particularly for the simulations involving sub-mm gaps, an effort was made to ensure that the configuration did not fall outside of model validity bounds. However, the reader is referred again to the beginning of Section 6.3, where the fuzzy boundary between kinetic and fluid approaches was discussed, in relation to the fast discharge timescales involved in this work. It is reiterated that the discharge conditions lie close to the expected boundary of validity, and ideally, the study would benefit from comparison to a kinetic approach to ensure the repeatability and validity of the conclusions. Limitations relating to these limits can also be considered to be part of the wider limitations to the hydrodynamic approach used in StrAFE. Incidentally, the reader should be reminded of those discussed within Chapter 5 - Section 5.9.3. Included within this category are the boundary conditions used for the Helmholtz sources, which have been shown to possibly influence the nature of the photoelectron source term. Zero-Neumann conditions for all three absorption lengths were assumed throughout the simulations of this chapter, which may have the tendency to overestimate the intensity of photoionisation near the boundary.

The majority of simulations presented here also involved solid boundaries, primarily in the form of electrodes and/or solid dielectric surfaces. It was previously mentioned that secondary

emission processes were not included due to poor characterisation of practical materials, and due to the focus of the work being largely placed on other other features such as the waveform, working gas, and surface charge. It cannot be ruled out that secondary emission processes (including from charge bombardment, photon bombardment (photoemission), or field emission) may have tangible effects on the discharge evolution near boundaries. This may be particularly relevant to behaviours affecting the cathode sheath, as discussed within Section 6.3.5, considering that electron emission from the cathode surface may contribute to the replenishment of the electron density in the depleted region. A more complete picture would also consider additional plasma-surface interactions, including the effects of surface chemistry, gas adsorption etc.; aspects that may further influence the surface discharge behaviour but remain poorly characterised.

For all simulations involving a dielectric surface, limitations on computational resources necessitated the use of the 2D plane-parallel approximation. This is of lesser issue for comparative studies as conducted here, however, it would be important to understand the differences should full 3D surface discharges be simulated (or indeed, where multiple streamers, possibly resulting from branching, may be important). The author remarks further on the limitations pertaining to the surface charge simulations of Section 6.5. The highly complex nature of this set of simulations proved computationally challenging and time-consuming, resulting in numerous unexplored aspects. Namely, this includes the expansion of the study to a wider range of surface charge densities and distributions. The results are unlikely representative of conditions outside of those simulated due to the narrow range that was investigated. Secondly, numerical divergence of simulations resulting from the collapse of the dielectric sheath (as in the case of the homocharge simulations) makes evident some additional limitations associated with the use of the continuous Galerkin (CG) method at interfaces, where the field may be discontinuous. Under these conditions, an abnormally (and potentially prohibitively) high mesh resolution is necessary due to the imposed continuity of CG elements at the surface. Resolving the simulation beyond the initial streamer inception is an important step towards characterising the full surface discharge evolution. Evidently, negative surface discharges and their interaction with surface charges also remain unexplored in this work.

In consideration of these limitations, and in relation to the contributions that this chapter has made towards fast, overstressed, ionisation events in gases and across surfaces, the present work has also identified numerous possibilities for further study:

- The empirical relation of streamer velocity to squared diameter,  $v/d_s^2 \approx c$ , where the value

of  $c$  appeared to depend on the rate-of-rise. What is the nature of the dependency, and can it be analytically approximated, or be understood from a fundamental perspective?

- Inclusion of secondary emission at solid boundaries. At what threshold would this have tangible effects on the cathode sheath, or on the discharge characteristics of surface streamers or streamers near electrodes?
- Can the effects discussed within this chapter be recreated using a kinetic scheme? In other words, does the extended hydrodynamic approach remain valid close to the analytical boundary? Are there significant non-local effects that have been neglected?
- Can the cathode-sheath scaling effects have tangible impacts on discharge evolution in very short gaps in practise? Can weak photoionisation in  $\text{CO}_2$  impact this process?
- The above point may be further explored with experimental study. An electrode gap pre-stressed with a voltage below the breakdown threshold would, in theory, reduce the electron density within the electrode gap as to delay the formation of discharges when subjected to a subsequent impulse.
- Can surface heterocharge (or any other distribution or polarity of charge, for that matter) truly lead to the disruption of surface streamers, despite potentially accelerating their initial development?
- Can surface charge be part of the explanation for different spark morphologies observed across solid-gas interface, for example, in [66, 67]?
- Extended modelling with the inclusion of plasma-surface interactions, e.g., chemical interactions, surface texture.
- Exploration of the effects of surface streamer propagation across multilayered graded materials, as explored in Chapter 3.
- While there is confidence that the simulations predicted behaviour consistent with the underlying methods implemented (and that the implemented physics is correct and representative), experimental validation of many of the observed phenomena remains of great importance.

## Chapter 6 References

- [1] S. Nijdam, J. Teunissen, and U. Ebert, “The physics of streamer discharge phenomena,” *Plasma Sources Sci. Technol.*, vol. 29, no. 10, p. 103001, 2020.
- [2] J. M. Meek, “A theory of spark discharge,” *Phys. Rev.*, vol. 57, pp. 722–728, 1940.
- [3] H. Raether, *Electron Avalanches and Breakdown in Gases*. Butterworths, London, 1964.
- [4] L. B. Loeb and J. M. Meek, “The Mechanism of Spark Discharge in Air at Atmospheric Pressure. I,” *J. Appl. Phys.*, vol. 11, no. 6, pp. 438–447, 1940.
- [5] L. B. Loeb and J. M. Meek, “The Mechanism of Spark Discharge in Air at Atmospheric Pressure. II,” *J. Appl. Phys.*, vol. 11, no. 7, pp. 459–474, 1940.
- [6] L. B. Loeb and J. M. Meek, *The Mechanism of the Electric Spark*. Stanford University Press, 1941.
- [7] X. Li, S. Dijcks, S. Nijdam, A. Sun, U. Ebert, and J. Teunissen, “Comparing simulations and experiments of positive streamers in air: steps toward model validation,” *Plasma Sources Sci. Technol.*, vol. 30, no. 9, p. 095002, 2021.
- [8] N. Y. Babaeva and G. V. Naidis, “Modeling of streamer dynamics in atmospheric-pressure air: Influence of rise time of applied voltage pulse on streamer parameters,” *IEEE Trans. Plasma Sci.*, vol. 44, no. 6, pp. 899–902, 2016.
- [9] N. Y. Babaeva and G. V. Naidis, “Simulation of subnanosecond streamers in atmospheric-pressure air: Effects of polarity of applied voltage pulse,” *Phys. Plasmas*, vol. 23, no. 8, p. 083527, 2016.
- [10] J. Jadidian, M. Zahn, N. Lavesson, O. Widlund, and K. Borg, “Effects of impulse voltage polarity, peak amplitude, and rise time on streamers initiated from a needle electrode in transformer oil,” *IEEE Trans. Plasma Sci.*, vol. 40, no. 3, pp. 909–918, 2012.
- [11] J. Jadidian, M. Zahn, N. Lavesson, O. Widlund, and K. Borg, “Effects of electrode size and solid barrier orientation on streamer discharge in transformer oil,” *J. Appl. Phys.*, vol. 115, no. 14, p. 143304, 2014.
- [12] X. Li, A. Sun, and J. Teunissen, “A computational study of negative surface discharges: Characteristics of surface streamers and surface charges,” *IEEE Trans. Dielectr. Electr. Insul.*, vol. 27, no. 4, pp. 1178–1186, 2020.
- [13] H. K. Meyer, F. Mauseth, R. Marskar, A. Pedersen, and A. Blaszczyk, “Streamer and surface charge dynamics in non-uniform air gaps with a dielectric barrier,” *IEEE Trans. Dielectr. Electr. Insul.*, vol. 26, no. 4, pp. 1163–1171, 2019.
- [14] H. K. H. Meyer, R. Marskar, H. Gjerdal, and F. Mauseth, “Streamer propagation along a profiled dielectric surface,” *Plasma Sources Sci. Technol.*, vol. 29, no. 11, p. 115015, 2020.
- [15] R. Marskar and H. K. H. Meyer, “A kinetic monte carlo study of positive streamer interaction with complex dielectric surfaces,” *Plasma Sources Sci. Technol.*, vol. 32, no. 8, p. 085010, 2023.
- [16] B. Bagheri, J. Teunissen, U. Ebert, M. M. Becker, S. Chen, O. Ducasse *et al.*, “Comparison of six simulation codes for positive streamers in air,” *Plasma Sources Sci. Technol.*, vol. 27, no. 9, p. 095002, 2018.

- [17] T. M. P. Briels, J. Kos, G. J. J. Winands, E. M. van Veldhuizen, and U. Ebert, “Positive and negative streamers in ambient air: measuring diameter, velocity and dissipated energy,” *J. Phys. D: Appl. Phys.*, vol. 41, no. 23, p. 234004, 2008.
- [18] T. Huiskamp, W. Sengers, F. J. C. M. Beckers, S. Nijdam, U. Ebert, E. J. M. van Heesch *et al.*, “Spatiotemporally resolved imaging of streamer discharges in air generated in a wire-cylinder reactor with (sub)nanosecond voltage pulses,” *Plasma Sources Sci. Technol.*, vol. 26, no. 7, p. 075009, 2017.
- [19] T. Huiskamp, “Nanosecond pulsed streamer discharges part I: Generation, source-plasma interaction and energy-efficiency optimization,” *Plasma Sources Sci. Technol.*, vol. 29, no. 2, p. 023002, 2020.
- [20] E. J. M. van Heesch, G. J. J. Winands, and A. J. M. Pemen, “Evaluation of pulsed streamer corona experiments to determine the  $o^*$  radical yield,” *J. Phys. D: Appl. Phys.*, vol. 41, no. 23, p. 234015, 2008.
- [21] K. Yoshinaga, S. Okada, D. Wang, T. Namihira, S. Katsuki, and H. Akiyama, “Effect of polarity and rise time of applies pulsed voltage on streamer discharge phenomena,” in *2nd Euro-Asian Pulsed Power Conference*, vol. 115, no. 6, 2008, pp. 1050–1052.
- [22] C. Li, U. Ebert, and W. Hundsdorfer, “3d hybrid computations for streamer discharges and production of runaway electrons,” *J. Phys. D: Appl. Phys.*, vol. 42, no. 20, p. 202003, 2009.
- [23] O. Chanrion and T. Neubert, “Production of runaway electrons by negative streamer discharges,” *J. Geophys. Res.: Space Phys.*, vol. 115, no. A6, 2010.
- [24] A. Luque, V. Ratushnaya, and U. Ebert, “Positive and negative streamers in ambient air: modelling evolution and velocities,” *J. Phys. D: Appl. Phys.*, vol. 41, no. 23, p. 234005, 2008.
- [25] S. Chen, L. C. J. Heijmans, R. Zeng, S. Nijdam, and U. Ebert, “Nanosecond repetitively pulsed discharges in N<sub>2</sub>-O<sub>2</sub> mixtures: inception cloud and streamer emergence,” *J. Phys. D: Appl. Phys.*, vol. 48, no. 17, p. 175201, 2015.
- [26] T. Wong, I. Timoshkin, S. MacGregor, M. Wilson, and M. Given, “A computational study on the effects of fast-rising voltage on ionization fronts initiated in sub-mm air and CO<sub>2</sub> gaps,” *Sci. Rep.*, vol. 14, p. 1185, 2024.
- [27] W. A. de Groot, J. R. Webster, D. Felhofer, and E. P. Gusev, “Review of device and reliability physics of dielectrics in electrostatically driven MEMS devices,” *IEEE Trans. Device Mat. Reliab.*, vol. 9, no. 2, pp. 190–202, 2009.
- [28] Y. Yao, I. V. Timoshkin, S. J. MacGregor, M. P. Wilson, M. J. Given, and T. Wang, “Breakdown characteristics of plasma closing switch filled with air, N<sub>2</sub>, CO<sub>2</sub>, and Ar/O<sub>2</sub>,” *IEEE Trans. Plasma Sci.*, vol. 46, no. 10, pp. 3574–3583, 2018.
- [29] A. C. Mermigkas, I. V. Timoshkin, S. J. MacGregor, M. J. Given, M. P. Wilson, and T. Wang, “Impulsive corona discharges for fine particles precipitation in a coaxial topology,” *IEEE Trans. Plasma Sci.*, vol. 42, no. 10, pp. 3089–3094, 2014.
- [30] N. Ibrahim, L. Vallet, F. M. Andre, L. Ariztia, M. Rivaletto, A. S. de Ferron *et al.*, “A subnanosecond pulsed electric field system for studying cells electroporation,” *IEEE Trans. Plasma Sci.*, vol. 48, no. 12, pp. 4242–4249, 2020.

- 
- [31] R. Aerts, W. Somers, and A. Bogaerts, “Carbon dioxide splitting in a dielectric barrier discharge plasma: A combined experimental and computational study,” *ChemSusChem*, vol. 8, no. 4, pp. 702–716, 2015.
- [32] H. E. Nechmi, A. Beroual, A. Girodet, and P. Vinson, “Fluoronitriles/CO<sub>2</sub> gas mixture as promising substitute to SF<sub>6</sub> for insulation in high voltage applications,” *IEEE Trans. Dielectr. Electr. Insul.*, vol. 23, no. 5, pp. 2587–2593, 2016.
- [33] S. Tian, X. Zhang, Y. Cressault, J. Hu, B. Wang, S. Xiao *et al.*, “Research status of replacement gases for SF<sub>6</sub> in power industry,” *AIP Adv.*, vol. 10, no. 5, p. 050702, 2020.
- [34] Z. Guo, S. Liu, Y. Pu, B. Zhang, X. Li, F. Tang *et al.*, “Study of the arc interruption performance of CO<sub>2</sub> gas in high-voltage circuit breaker,” *IEEE Trans. Plasma Sci.*, vol. 47, no. 5, pp. 2742–2751, 2019.
- [35] A. M. Loveless, G. Meng, Q. Ying, F. Wu, K. Wang, Y. Cheng *et al.*, “The transition to paschen’s law for microscale gas breakdown at subatmospheric pressure,” *Sci. Rep.*, vol. 9, no. 1, p. 5669, 2019.
- [36] M. G. Hogg, I. V. Timoshkin, S. J. MacGregor, M. P. Wilson, M. J. Given, and T. Wang, “Electrical breakdown of short non-uniform air gaps,” in *2013 19th IEEE Pulsed Power Conf. (PPC)*, 2013, pp. 1–4.
- [37] M. G. Hogg, I. V. Timoshkin, S. J. Mcgregor, M. P. Wilson, and M. J. Given, “Polarity effects on breakdown of short gaps in a point-plane topology in air,” *IEEE Trans. Dielectr. Electr. Insul.*, vol. 22, no. 4, pp. 1815–1822, 2015.
- [38] T. Liu, I. Timoshkin, M. P. Wilson, M. J. Given, and S. J. MacGregor, “The nanosecond impulsive breakdown characteristics of air, N<sub>2</sub> and CO<sub>2</sub> in a sub-mm gap,” *Plasma*, vol. 5, no. 1, pp. 12–29, 2022.
- [39] S. Kumar, T. Huiskamp, A. Pemen, M. Seeger, J. Pachin, and C. M. Franck, “Electrical breakdown study in CO<sub>2</sub> and CO<sub>2</sub>-O<sub>2</sub> mixtures in AC, DC and pulsed electric fields at 0.1–1 mpa pressure,” *IEEE Trans. Dielectr. Electr. Insul.*, vol. 28, no. 1, pp. 158–166, 2021.
- [40] S. C. Brown, *Basic Data of Plasma Physics: The Fundamental Data on Electrical Discharges in Gases*. American Institute of Physics, Melville, NY, 1994.
- [41] T. K. S. Wong and S. G. Ingram, “Observational of fowler-nordheim tunnelling at atmospheric pressure using Au/Ti lateral tunnel diodes,” *J. Phys. D: Appl. Phys.*, vol. 26, no. 6, p. 979, 1993.
- [42] Y. Zhu, X. Chen, Y. Wu, J. Hao, X. Ma, P. Lu *et al.*, “Simulation of ionization-wave discharges: a direct comparison between the fluid model and E-FISH measurements,” *Plasma Sources Sci. Technol.*, vol. 30, no. 7, p. 075025, 2021.
- [43] H. Höft, M. M. Becker, J. F. Kolb, and T. Huiskamp, “Double-propagation mode in short-gap spark discharges driven by HV pulses with sub-ns rise time,” *Plasma Sources Sci. Technol.*, vol. 29, no. 8, p. 085002, 2020.
- [44] A. Bourdon, V. P. Pasko, N. Y. Liu, S. Célestin, P. Ségur, and E. Marode, “Efficient models for photoionization produced by non-thermal gas discharges in air based on radiative transfer and the helmholtz equations,” *Plasma Sources Sci. Technol.*, vol. 16, no. 3, p. 656, 2007.

- [45] G. J. M. Hagelaar and L. C. Pitchford, "Solving the boltzmann equation to obtain electron transport coefficients and rate coefficients for fluid models," *Plasma Sources Sci. Technol.*, vol. 14, no. 4, p. 722, 2005.
- [46] Plasma Data Exchange Project: Lxcat. (2024) Phelps database. [Online]. Available: <http://lxcat.net/Phelps>
- [47] B. Bagheri, J. Teunissen, and U. Ebert, "Simulation of positive streamers in CO<sub>2</sub> and in air: the role of photoionization or other electron sources," *Plasma Sources Sci. Technol.*, vol. 29, no. 12, p. 125021, 2020.
- [48] X. Li, S. Dijcks, A. Sun, S. Nijdam, and J. Teunissen, "Investigation of positive streamers in CO<sub>2</sub>: experiments and 3d particle-in-cell simulations," arXiv, 2304.01531, 2024.
- [49] R. Marskar, "A 3d kinetic monte carlo study of streamer discharges in CO<sub>2</sub>," *Plasma Sources Sci. Technol.*, vol. 33, no. 2, p. 025023, 2024.
- [50] T. Wong, I. Timoshkin, S. MacGregor, M. Wilson, and M. Given, "An avalanche-to-streamer transition criterion for overstressed breakdown on a rising slope," *IEEE Transactions on Plasma Science*, vol. early access, pp. 1–13, 2024.
- [51] P. Tardiveau, L. Magne, E. Marode, K. Ouaras, P. Jeanney, and B. Bournonville, "Sub-nanosecond time resolved light emission study for diffuse discharges in air under steep high voltage pulses," *Plasma Sources Sci. Technol.*, vol. 25, no. 5, p. 054005, 2016.
- [52] D. Wang and T. Namihira, "Nanosecond pulsed streamer discharges: II. physics, discharge characterization and plasma processing," *Plasma Sources Sci. Technol.*, vol. 29, no. 2, p. 023001, 2020.
- [53] X. Li, A. Sun, G. Zhang, and J. Teunissen, "A computational study of positive streamers interacting with dielectrics," *Plasma Sources Sci. Technol.*, vol. 29, no. 6, p. 065004, 2020.
- [54] T. Wong, I. Timoshkin, S. MacGregor, M. Wilson, and M. Given, "Modelling of transient discharges along a sub-mm air-solid dielectric interface under fast-rising ramp voltages," in *2023 IEEE Pulsed Power Conf. (PPC)*, 2023, pp. 1–5.
- [55] L. Zhao, J. Su, X. Zhang, and Y. Pan, "Experimental investigation on the role of electrodes in solid dielectric breakdown under nanosecond pulses," *IEEE Trans. Dielectr. Electr. Insul.*, vol. 19, no. 4, pp. 1101–1107, 2012.
- [56] L. Zhao, G.-z. Liu, J.-c. Su, Y.-f. Pan, and X.-b. Zhang, "Investigation of thickness effect on electric breakdown strength of polymers under nanosecond pulses," *IEEE Trans. Plasma Sci.*, vol. 39, no. 7, pp. 1613–1618, 2011.
- [57] M. Bertin, E. M. Leitao, S. Bickerton, and C. J. R. Verbeek, "A review of polymer surface modification by cold plasmas toward bulk functionalization," *Plasma Process. Polym.*, vol. 21, no. 5, p. 2300208, 2024.
- [58] Z. Wang, A. Sun, and J. Teunissen, "A model comparison of 2d cartesian and 2d axisymmetric models for positive streamer discharges in air," arXiv, 2401.12353, 2024.

- 
- [59] J. Zhang, Y. Wang, D. Wang, and D. J. Economou, “Numerical simulation of streamer evolution in surface dielectric barrier discharge with electrode-array,” *J. Appl. Phys.*, vol. 128, no. 9, p. 093301, 2020.
- [60] S. Kumara, S. Alam, I. R. Hoque, Y. V. Serdyuk, and S. M. Gubanski, “DC flashover characteristics of a polymeric insulator in presence of surface charges,” *IEEE Trans. Dielectr. Electr. Insul.*, vol. 19, no. 3, pp. 1084–1090, 2012.
- [61] M. Florkowski, “Imaging and simulations of positive surface and airborne streamers adjacent to dielectric material,” *Measurement*, vol. 186, p. 110170, 2021.
- [62] H. Francisco, J. Teunissen, B. Bagheri, and U. Ebert, “Simulations of positive streamers in air in different electric fields: steady motion of solitary streamer heads and the stability field,” *Plasma Sources Sci. Technol.*, vol. 30, no. 11, p. 115007, 2021. [Online]. Available: <https://dx.doi.org/10.1088/1361-6595/ac2f76>
- [63] T. Shao, F. Kong, H. Lin, Y. Ma, Q. Xie, and C. Zhang, “Correlation between surface charge and DC surface flashover of plasma treated epoxy resin,” *IEEE Trans. Dielectr. Electr. Insul.*, vol. 25, no. 4, pp. 1267–1274, 2018.
- [64] M. Florkowski, D. Krześniak, M. Kuniewski, and P. Zydrón, “Surface discharge imaging in presence of deposited space charges in non-uniform DC electric field,” *High Volt.*, vol. 6, no. 4, pp. 576–589, 2021.
- [65] J. Jánský, D. Bessières, R. Brandenburg, J. Paillol, and T. Hoder, “Electric field development in positive and negative streamers on dielectric surface,” *Plasma Sources Sci. Technol.*, vol. 30, no. 10, p. 105008, 2021.
- [66] X. Meng, H. Mei, F. Yin, and L. Wang, “The development of the streamer discharge to flashover along the dielectric surfaces,” *IEEE Trans. Dielectr. Electr. Insul.*, vol. 30, no. 4, pp. 1733–1742, 2023.
- [67] Z. Wang, I. V. Timoshkin, M. P. Wilson, M. J. Given, T. Wang, and S. J. MacGregor, “Impulsive breakdown characteristics of solid–gas interfaces,” *IEEE Trans. Plasma Sci.*, vol. 49, no. 1, pp. 365–377, 2021.
- [68] Y.-L. Tsai, T.-C. Chang, Y.-C. Tsao, M.-C. Tai, H.-Y. Tu, Y.-T. Chien *et al.*, “Improving breakdown voltage in AlGaN/GaN metal-insulator-semiconductor HEMTs through electric-field dispersion layer material selection,” *IEEE Trans. Device Mat. Reliab.*, vol. 21, no. 3, pp. 320–323, 2021.
- [69] G. Teyssedre, D. Fabiani, Y. Cao, J. He, and C. Li, “Advances in interface charge tailoring techniques: fundamentals and applications,” in *Int. Conf. High Volt. Engr., Beijing, China, 2020*, pp. 1–5.
- [70] C. Li, J. Fu, Y. Zi, and Y. Cao, “Insulator surface charge behaviors: From hazards to functionality,” *IEEE Electr. Insul. Mag.*, vol. 38, no. 3, pp. 6–14, 2022.



# Impulsive Breakdown and Surface Roughness Characteristics of Solid-Solid Polymer Interfaces

---

IN practise, theoretical models like those developed in Chapters 3 to 6 are only able to represent the ideal case, disregarding the imperfect and often messy considerations of the physical world. In the first of two final technical chapters of this work, the results from two experimental studies focused on the impulsive breakdown of dielectric interfaces are presented. While the previous chapters have explored a variety of processes leading up to impulsive breakdown, these final chapters present experimental work aimed at the characterisation of the complete breakdown process across practical engineering surfaces. Where possible, the understanding gained from theoretical modelling has been compared to the observed experimental tendencies, or used to aid in the explanation of recorded behaviours. In addition to supplementing the present theoretical work, these chapters also contribute important experimental data on impulsive breakdown at practical interfaces, which often acts as crucial performance data that informs the design of high voltage (HV) pulsed power systems.

The present chapter investigates the overstressed impulsive breakdown of solid-solid interfaces,

---

This chapter was partially adapted, and may be quoted verbatim, from the following publication(s) with permission: T. Wong, I. Timoshkin, S. MacGregor, M. Wilson, and M. Given, “The Breakdown and Surface Characteristics of Polymer Interfaces Under HV Impulses,” *IEEE Trans. Dielectr. Electr. Insul.*, early access, doi: 10.1109/TDEI.2024.3407728, May 2024. © IEEE 2024.

formed between various polymers, under low (10's of kPa) mating pressure assembled in atmospheric pressure air. The studied materials included PVC (polyvinylchloride), Torlon (polyamide-imide), Delrin (polyoxymethylene), Perspex (polymethylmethacrylate), and Ultem (polyetherimide). Homogeneous interfaces (between the same material) were formed between these materials and subjected to two different HV impulsive waveforms with different rise characteristics. Prior to the presentation of experimental results, however, the theoretical basis for solid-solid breakdown is firstly introduced, alongside the proposal of a novel breakdown model for overstressed solid-solid breakdown based on surface roughness and tribological principles. Complementing this, the experimental characterisation of the pre-breakdown surface roughness profiles was also performed and included within the breakdown data analysis.

Under the investigated low mating pressure conditions (10's kPa), the data indicated that the effective breakdown strength across solid-solid interfaces may drop below that of an identical gap filled with air alone. A correlation between the estimated average aspect ratio of surface asperities at the interface and the interfacial breakdown strength was observed. Explanations have been proposed explaining both of these observations based on surface-asperity-driven field enhancement, leading to their departure from tendencies observed for interfaces formed under much higher mating pressure. Furthermore, the increased width of the post-breakdown affected region on the contacting surfaces was found to increase with slower-rising voltages. An explanation for this phenomenon is proposed based on space charge transport within interfacial voids prior to the moment of breakdown. In comparison to the developed theoretical breakdown model, results suggested that the rate-of-rise of the intra-void electric fields may be a dominant factor over surface texture in the determination of impulse-driven breakdown across solid-solid interfaces under the studied conditions.

### 7.1 Introduction and Motivation

As discussed within Chapter 2 - Section 7.3.2, pulsed power technology continues to experience rapid growth, and where safe and reliable operation is ultimately underpinned by electrical insulation. The analyses presented in the preceding chapters have provided theoretical insight into multiple pre-breakdown processes, based around effects relating to overvolted breakdown and dielectric interfaces. The development of practical systems, however, must also be supported by extensive empirical data as models are only representative up to certain limits. Empirical data also underpins the validation of theoretical models, which together, jointly support continued technological advancement. It was therefore only appropriate to complement the theoretical

analyses with systematic experimental studies of complete impulsive breakdown.

The reader is reminded of the review of Chapter 2 - Section 2.4.2; conducted on the state of the current understanding of solid-solid breakdown. Additional motivation to conduct impulse-driven solid-solid breakdown tests stemmed largely from the previously-discussed lack of exploration and characterisation outside of standard waveforms; those that have originated overwhelmingly from the power industry. That is, power-frequency AC, steady-state DC, or IEC lightning impulses as seen in studies such as [1–13]. Tests on non-standard materials are also far less prevalent and has resulted in a poor understanding of dielectric performance for materials outside of those typical for power applications. Those commonly studied, and can be considered reasonably well-characterised, include: XLPE, SiR, PP, and the rubbers EPR and EPDM. In many pulsed power applications, non-standard waveforms, atypical materials, and irregular geometries are commonplace, but the lack of available performance data hinders further advancement.

It follows that the materials used in the present experimental work were selected on the basis that they are commercially available, with characteristics that render them typical and/or ideal choices for various engineering applications. The chosen materials are provided in list form below, in which includes a mixture of standard engineering polymers and more specialised polymers that have seen successful application to several pulsed power applications, see for example, [14–16].

The materials studied were:

- **PVC** (polyvinylchloride).
- **Torlon** (polyamide-imide, aka. Duratron T4203).
- **Delrin** (polyoxymethylene).
- **Perspex** (polymethylmethacrylate, aka. Acrylic).
- **Ultem** (polyetherimide, aka. Duratron U1000).

The material parameters which are of relevance to the present work are tabulated in Table 7.1, which includes electrical and mechanical parameters which play a role in the later analyses presented in Section 7.2.

This chapter is organised as follows. Based on the theory of interfacial void-driven breakdown, the principles of rough surface contact theory, along with the approaches of Chapters 3 and 4, were first combined to form a breakdown model for solid-solid interfaces under impulsive energisation. This is introduced in Section 7.2 and its theoretical estimations are discussed. The description of the experimental methodology, including statistical treatment of breakdown

**Table 7.1:** Relevant properties for the materials investigated in this work. Materials were acquired in sheet form in commercially available thicknesses closest to 10 mm. Thicknesses shown here were subsequently measured using digital calipers. Elastic moduli were taken directly from the relevant specification sheets.

Material	Thickness $d_s$ , mm	Relative Permittivity, $\epsilon_r$	Elastic modulus, $Y$ , MPa
PVC	12.14	2.9	3400
Delrin	10.72	3.7	2800
Torlon	10.33	3.9	4200
Perspex	9.44	3.6	3200
Ultem	13.25	3.0	3500

data, is included within Section 7.3; Section 7.4 then presents the obtained results relating to breakdown field and time; discusses the observed effects on the post-breakdown material surfaces; before Section 7.5 compares between practise and theory. This chapter is concluded in Section 7.6 alongside a summary of the contributions, discussion of limitations, and identification of opportunities to extend this work in the future.

## 7.2 A Theoretical Model for the Impulsive Breakdown of Solid-Solid Interfaces

The analysis presented within this section follows from the reviewed breakdown mechanisms of Section 2.4.2. Summarising for convenience, the earlier works of [1–7, 17–20] led to the identification that surface condition, contact pressure, and material hardness were strong indicators of solid-solid interfacial breakdown strength, when subjected to a variety of standard AC and DC steady-state voltages. Interfacial breakdown strengths were found to be significantly inferior to that of bulk solids, particularly where there existed a strong field component parallel to the interfacial axis. Accumulated evidence strongly suggested that characteristics of an assembled solid-solid interface which would modify the shape, size, and distribution of the gas-filled void-like features formed between the interfaces, would lead also to a modification of the interfacial breakdown strength. Subsequent works conducted by Kantar *et al.* [8–13] combined tribological techniques with the principles of gas breakdown to test this idea with predictive success. It is now widely accepted that breakdown across solid-solid interfaces is primarily determined by initial discharges in the gas-filled interfacial voids, which are subsequently chained together to form a continuous conductive path across the interfacial contact. In other words, intra-void gas discharge precedes full interfacial breakdown, and largely determines the interfacial breakdown strength.

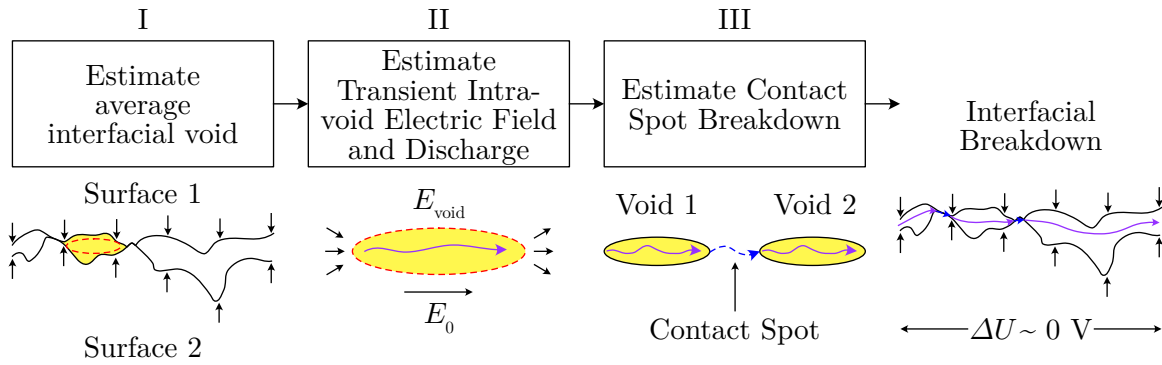


**Figure 7.1:** Diagram depicting the three main sub-models that form the developed solid-solid interfacial breakdown model based on the theory of interfacial gas-void driven breakdown.

Advances in the understanding of solid-solid interfaces came particularly with the contributions of Kantar *et al.* [8–13], who presented both deterministic [13] and statistical models [12] of the interfacial breakdown processes under power frequency AC energisation; reporting good correlations to experimentally measured data [12]. Using the models developed within Chapter 3 and Chapter 4, this section presents adaptations to the methods of Kantar *et al.* in pursuit of extending their modelling efforts to the domain of impulsive breakdown. As in [13], the complete interfacial breakdown model was considered to be comprised of three component sub-models as shown in Figure 7.1. Namely, based on the theory of interfacial void-driven discharge leading ultimately up to flashover across the contacting surfaces, the determination of the following factors were necessary:

- I. Using the known characteristics of the material combined with surface profilometry data of the surfaces in contact, an estimate of an average void shape\* and size that would be formed at the solid-solid interface.
- II. An estimation of the critical field at which this average interfacial void would discharge when subjected to an arbitrary impulse waveform.
- III. An estimation of the moment that tracking would occur across the *contact-spots* located between interfacial voids, in what is believed to immediately precede the chained connection of multiple voids, leading to complete interfacial breakdown.

The strategies dealing with each of the above points are detailed in the following subsections.

---

\*In practise, the exact nature of the interfacial voids that lead to interfacial breakdown will be system- and surface-dependent. It is assumed here that a void of average size is first to discharge, as similarly assumed in Kantar *et al.*, and which is assumed to be adequately representative of the general surface condition.

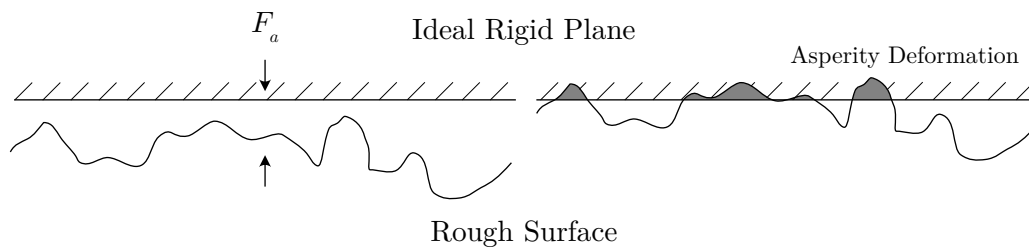


**Figure 7.2:** Graphical depiction of rough surface contact between a practical rough surface and an ideal, rigid, plane. Surface asperities are deformed based on the applied contact force.

### 7.2.1 Hertzian Contact and the Equivalent Surface Approximation

Sub-model I involves the estimation of a statistically average interfacial void based on the features of given practical interface. To do so, one must consider the roughness characteristics and mechanical parameters associated with both surfaces that form the interfacial contact. The study of mechanical contact and surface roughness lies within the broad field of *tribology*, from which several methods of analysis may be utilised. To begin, it must be assumed that surface profiles of reasonable accuracy are able to be obtained through the measurement of practical surfaces (see the later Section 7.3.2 for the method employed in the experimental procedure of this work). That is, a quantification of the surface heights along some evaluation length(s) relative to some ideally-flat reference plane must first be obtained. When two surfaces are placed in contact, asperities present on each surface may undergo deformation depending on the local contact pressure, see for example the diagram of Figure 7.2.

While direct simulation of asperity deformation can be achieved using various numerical techniques including mesh-based methods [21–23], or strategies which result in an energy optimisation formulation [13]; early approaches using statistical methods have also found success in describing the characteristics of rough surface contact, but which are generally simpler. Of particular importance to this work are the methods introduced by Robbe-Valloire [24] based on the contact theory of Greenwood and Williamson [25], which itself stems from the classical Hertzian theories of contact mechanics [26]. From Hertz [26], the contact of an elastic sphere with radius  $\beta$  with an elastic half-space, as depicted in Figure 7.3, which results in some deformation distance  $\delta$  and produces a circular contact area with radius  $r_c$ , such that

$$\pi r_c^2 = \sqrt{\beta \delta} \quad (7.1)$$

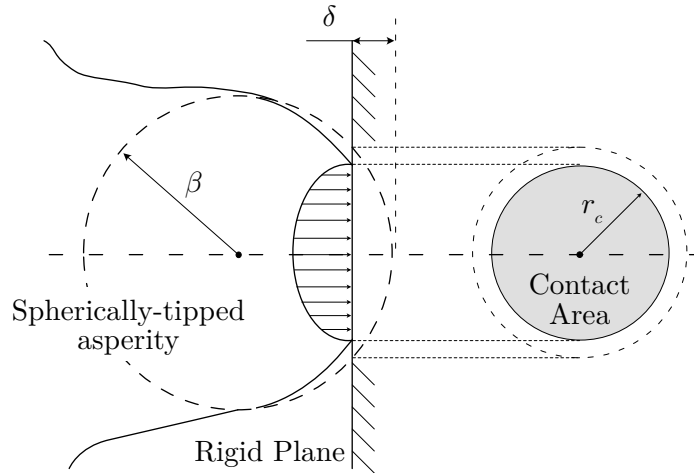


**Figure 7.3:** Diagram of the classical case of Hertzian contact assuming an elastic spherical surface asperity with tip radius  $\beta$  on an elastic half-space deforming by a distance  $\delta$  and associated circular contact area with radius  $r_c$ .

and where the applied load,  $F_a$ , may be described as a function of the deformation  $\delta$  by

$$F_a = \frac{4}{3} Y' \beta^{\frac{1}{2}} \delta^{\frac{3}{2}}, \quad (7.2)$$

where the composite elastic modulus,  $Y'$ , is given as a combination of the moduli and Poisson ratios of the two materials in contact, denoted  $Y_1$ ,  $Y_2$ , and  $\nu_1$ ,  $\nu_2$ , respectively, following

$$\frac{1}{Y'} = \frac{1 - \nu_1^2}{Y_1} + \frac{1 - \nu_2^2}{Y_2}. \quad (7.3)$$

The statistical analysis of Greenwood and Williamson [25] derives a number of relations on the limited case of elastic rough-surface contact with an ideally-flat plane. Based on some arbitrary probability distribution of asperity heights, estimations of the total real area of contact,  $A_r$ , and the total real load,  $F_r$ , at the interface were derived to be

$$A_r = \pi N \beta \int_d^\infty (z - d') \phi(z) dz, \quad (7.4)$$

$$F_r = \frac{4}{3} N Y' \beta^{\frac{1}{2}} \int_d^\infty (z - d')^{\frac{3}{2}} \phi(z) dz, \quad (7.5)$$

based on the Hertzian assumption of spherical asperity tips, where  $d'$  is the separation between the rigid plane and the reference plane of the rough surface. Here,  $N$  is the total number of asperities and  $\phi(z)$  is the probability distribution function of the asperity peak heights,  $z$ . In later work, Greenwood and Tripp [27] concluded that for two rough surfaces characterised by distributions

$\phi_1(z)$  and  $\phi_2(z)$ ; both which are normally distributed [ $\phi(z) := \mathcal{N}(\beta, \sigma)$ ]; their contact can be reduced to that of a single, equivalent, normal distribution,  $\mathcal{N}_{\text{eq}}(\beta^{[\text{eq}]}, \sigma^{[\text{eq}]})$ , in contact with an ideal plane such that  $\beta^{[\text{eq}]}$  and  $\sigma^{[\text{eq}]}$  are the mean peak radius and standard deviation of the *equivalent* surface<sup>†</sup>. Note that Greenwood and Williamson [25] remarked that experimental data suggested that normally-distributed peak heights were typical for most engineering surfaces. This was similarly confirmed through the analyses of O’Callaghan and Cameron [28] and Francis [29]. Appendix B.4 includes examples of height distributions measured for surfaces used in this work, which further corroborates these claims. Bhushan [30] conducted non-dimensional analysis using the Greenwood and Williamson [25] model assuming normally-distributed peak heights, from which was derived an approximation of the true contact area at the interface,

$$A_r^{\text{normal}} \approx \frac{3.2p_a A_a}{Y' \sqrt{\frac{\sigma^{[\text{eq}]}}{\beta^{[\text{eq}]}}}}, \quad (7.6)$$

where  $p_a$  and  $A_a$  are the apparent contact pressure and area, respectively (such that the apparent force applied to the contact is  $F_a = p_a A_a$ ). In the same analysis, Bhushan estimated the total number of expected contacts,  $N^{\text{normal}}$ , to be approximately

$$N^{\text{normal}} \approx 1.21\eta^{[\text{eq}]} A_a \left( \frac{p_a}{\eta^{[\text{eq}]} \sigma^{[\text{eq}]} \beta^{[\text{eq}]} Y' \sqrt{\frac{\sigma^{[\text{eq}]}}{\beta^{[\text{eq}]}}}} \right)^{0.88} \quad (7.7)$$

where  $\eta^{[\text{eq}]}$  is the density of surface asperities. It is further noted that the product  $\eta\sigma\beta$  had been previously discussed in the work of Archard [31], finding the phenomenological relation that  $\eta\sigma\beta \approx c$ , where  $c$  is a dimensionless constant that depends on the type of surface treatment. For most engineering surfaces, Archard suggested that  $c \approx 0.03$  to  $0.05$ .

To relate the above roughness characteristics to the dimensions of interfacial voids, Kantar *et al.* [12] assumed (based on 3D measurements of polymer profiles) that the most important void-like features formed at the solid contact were approximately elliptical in shape, with a minor to major axis ratio (which is denoted  $K$  here, as used in Chapter 3) of around 0.1 to  $0.125^{\ddagger}$  [12], see for example as depicted in Figure 7.4. Kantar *et al.* then assumed that the area of the

<sup>†</sup>The superscript and square brackets are used intentionally here to maintain consistency with the labelling scheme used later in Section 7.3.2 and should not be confused with exponentiation.

<sup>‡</sup>In Kantar *et al.* [12], the value of 8 to 9 is quoted for the major to minor axis ratio ( $1/K$ ) which has been converted here for consistency of notation.

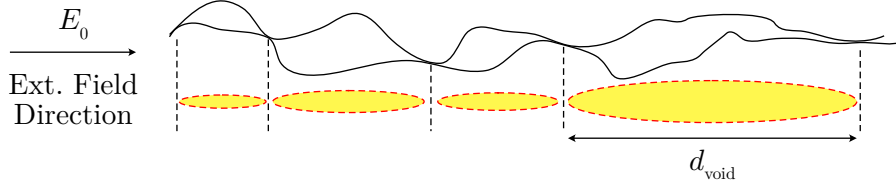


**Figure 7.4:** Graphical depiction of adjacent interfacial voids along an interfacial contact, alongside their approximation as high aspect ratio ellipsoids.

average void,  $\bar{A}_{\text{void}}$ , can be calculated based on Bhushan's estimated real contact area (7.6) and the total number of contact spots (7.7) with

$$\bar{A}_{\text{void}} = \frac{A_a - A_r}{N} \quad (7.8)$$

and further assumed, for simplicity, that the projected area is approximately square, such that the length of the average void would be

$$\bar{d}_{\text{void}} = \sqrt{\bar{A}_{\text{void}}} = \frac{\left( Y' \sqrt{\frac{\sigma^{[\text{eq}]}}{\beta^{[\text{eq}]}} - 3.2p_a} \right)^{0.5} (\beta^{[\text{eq}]})^{0.47} (\sigma^{[\text{eq}]})^{0.41}}{\sqrt{1.21Y'^{0.06} (\eta^{[\text{eq}]})^{0.06} p_a^{0.44}}}. \quad (7.9)$$

It is, however, unclear why the projected area was assumed to be square, which contrasts their previous approximation of interfacial voids as elliptical with reasonably high aspect ratio. By repeating the above analysis and alternatively projecting the area to that of an ellipse with area  $\bar{A}_{\text{void}}^{\text{ellip}} = \pi K \bar{r}_{\text{void}}^2$ , with  $\bar{r}_{\text{void}}$  being the semi-major axis length (aligned with the axis of the interface), the estimate of the void length according to (7.9) becomes

$$\bar{d}_{\text{void}}^{\text{ellip}} = 2\bar{r}_{\text{void}} = \frac{2}{\sqrt{\pi K}} \bar{d}_{\text{void}}, \quad (7.10)$$

which is (7.9) scaled by an additional factor of  $2/\sqrt{\pi K}$ . In the case where  $K = 0.1$ , the estimated void length is close to four times of that estimated using (7.9), while for voids approaching sphericity ( $K \approx 1$ ), the estimated length is just about 10% longer than (7.9). This exercise aims to show the sensitivity of this approach even to the assumed shape of this area, which can be significant. For consistency with the elliptical assumption, this work utilised the alternative definition of (7.10) for the cavity dimension estimation.

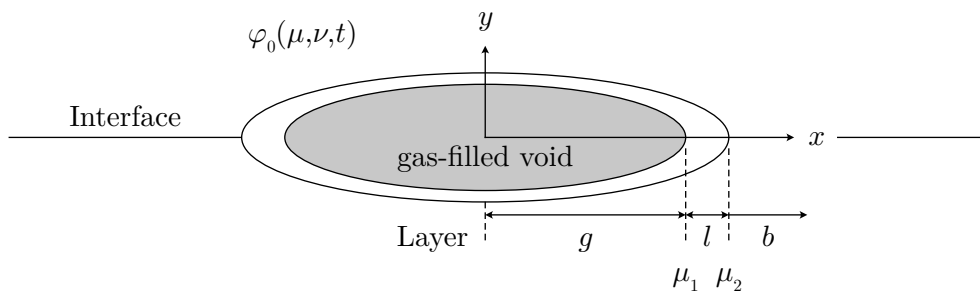


**Figure 7.5:** Diagram of a single, rotationally-symmetric, spheroidal inclusion with three layers as an approximation of various types of interfacial void modelled in this work.

### 7.2.2 Transient Electric Field and Breakdown of Interfacial Voids

Moving to sub-model II, the original model developed in Kantar *et al.* [12] applied Paschen's law to estimate the breakdown strength of the void based on the pressure-distance product,  $p\bar{d}_{\text{void}}$ , without the explicit modelling of the void geometry. Intra-void field enhancement in [12] was considered through the enhancement factors given in Crichton, Karlsson, and Pedersen [32]. This was a reasonable approach for the power frequency AC waveforms which formed the main focus of their work. However, as shown within Chapter 4, the classical approaches such as Paschen's law do not provide accurate estimations of breakdown strength in the (overstressed) impulsive regime. Moreover, no information can be extracted relating to the time-to-breakdown using models developed for static breakdown cases; the characterisation of which is often critical for pulsed power system design.

To address this, an explicit model for an isolated cavity, subject to an external impulsive electric field, was developed using the general solutions of Chapter 3. This allowed the full incorporation of time-dependency, the effects of void geometry, and the effects of dielectric relaxation. The approximation of an ellipsoidal void present at the interface can be represented using the spheroidal geometry introduced as part of the prolate-spheroidal set of solutions presented in Section 3.4.1, with its semi-major axis aligned parallel to the interface in a manner shown in Figure 7.5. Note that the limitations associated with azimuthal symmetry described in Section 3.4.1 remained, and the distinction between the term *spheroidal* compared to *ellipsoidal* is emphasised<sup>§</sup>. The opportunity for the theoretical model to generalise to the cases of dry-mate,

<sup>§</sup>The term *ellipsoid* refers to closed surfaces which may have all three principal axes of different length. *Spheroids* exclusively refer to closed surfaces where two out of three of the principal axes are equal in length, thus the cross-sectional slice through a plane formed by these two axes is always circular. For closed surfaces with all three principal axes of equal length, these are referred to as *spherical*.

wet-mate, and oil-mate interfaces was also taken. An inclusion incorporating three layers ( $n = 3$ ) was thus considered, corresponding to those labelled within Figure 7.5, as a simple representation of:

- *Layer b* — Represents the solid dielectric bulk of the materials forming the interface. Since only homogeneous interfaces were considered, this layer fills the entire region external to the void.
- *Layer l* — Represents an additional thin layer present on the internal wall of the void with thickness  $\Delta_l$ . This was included as a possible model for a damp or wet surface, e.g., due to the ingress of water, oil, or lubricant onto the assembled interface, whether by design or otherwise. It may also act as a model for a high degree of carbonisation on the void walls left over from previous (partial) discharge activity.
- *Layer g* — Represents the gas void formed between the cavities on the rough surfaces, with a relative permittivity of  $\varepsilon_g = 1$  and nominally assumed to be perfectly non-conductive under normal conditions.

It should be noted that, in practise, the bulk layer may not occupy the entire space between the void and the electrodes, which is the case in the later experimental work of Section 7.3 [see Figure 7.16(c)]. This is an approximation that the model must make, as the construction of an analytical boundary value problem that would be exactly representative of the practical geometry would be highly nontrivial. It may, however, be a reasonable assumption that the differences are not of significance for solid materials with relative permittivity  $\varepsilon_b \approx 2 - 3$ , as the effects of polarisation may not be substantial.

The external energising potential was assumed to be applied through a set of stationary electrodes on either side of the void, and thus assumed the form  $\varphi_0(\mu, \nu, t) = U_0(t)\mathcal{G}(\mu, \nu)$  where  $U_0(t)$  is the time-dependent applied voltage and  $\mathcal{G}(\mu, \nu)$  is some geometric function that must be cylindrically symmetric around the Cartesian  $x$  direction. In the experimental work presented within Section 7.3, the external field is developed between a sphere-plane electrode set. The derivation here therefore initially assumes an arbitrary  $\varphi_0$  to demonstrate how the method incorporates non-uniform external fields, before demonstrating the reduction of the model to the case of a uniform field which is subsequently shown to be a reasonable approximation for the configuration used in this work. This was justified through computation of intra-void field utilisation factors using the analytical solutions that follow. It remains, according to the strategy of Chapter 3 - Section 3.4.1, that the potential and electric fields need determined within each

of the above sub-regions. The full details of the derivation are enclosed in Appendix A.14 for brevity, with only the most important steps detailed in the following. Note that functional notation has once again been omitted for succinctness of expressions, except where it enhances understanding.

Considering the arbitrary external potential,  $\varphi_0$ , the Laplace equation (3.32) admits solutions inside the domains  $g$ ,  $l$ , and  $b$  following

$$\begin{aligned}\varphi_g &= \sum_{\ell=0}^{\infty} A_{\ell}^g P_{\ell}(\cosh \mu) P_{\ell}(\cos \nu), \\ \varphi_l &= \sum_{\ell=0}^{\infty} \left[ A_{\ell}^l P_{\ell}(\cosh \mu) + B_{\ell}^l Q_{\ell}(\cosh \mu) \right] P_{\ell}(\cos \nu), \\ \varphi_b &= \sum_{\ell=0}^{\infty} \left[ A_{\ell}^b(\mu) + B_{\ell}^b Q_{\ell}(\cosh \mu) \right] P_{\ell}(\cos \nu),\end{aligned}\tag{7.11}$$

where  $P_{\ell}$  and  $Q_{\ell}$  are the  $\ell$ -th degree Legendre functions of the first and second kinds, respectively, and the coefficients  $A_{\ell}^{g,l,b}$  and  $B_{\ell}^{l,b}$  are time-dependent; their solution characterising the developed layer potentials. The coefficient  $A_{\ell}^b(\mu)$  is dependent on  $\mu$  and arises from the Fourier-Legendre expansion of the external potential, alongside the application of the far-field condition (3.34) such that

$$\begin{aligned}A_{\ell}^b &= \frac{2\ell + 1}{2} \int_0^{\pi} \varphi_0 P_{\ell}(\cos \nu) \sin \nu \, d\nu \\ &= U_0(t) \frac{2\ell + 1}{2} \int_0^{\pi} \mathcal{G}(\mu, \nu) P_{\ell}(\cos \nu) \sin \nu \, d\nu,\end{aligned}\tag{7.12}$$

where  $U_0(t)$  can currently admit some arbitrary choice of time-dependent voltage. Since the interest was exclusively on impulsive waveforms, the double-exponential form according to (3.22) was once again used and is henceforth assumed, for which the reader is reminded takes the form

$$U_0(t) = A_0 U_0 \left( e^{-\hat{\alpha}t} - e^{-\hat{\beta}t} \right).\tag{7.13}$$

By comparison of Legendre coefficients from (7.11), the equivalent linear system of (3.6) may be recovered such that coefficients that satisfy

$$\begin{aligned}A_{\ell}^g &= A_{\ell}^l + B_{\ell}^l F_{\ell}^{\mu_1}, \\ A_{\ell}^l + B_{\ell}^l F_{\ell}^{\mu_2} &= \frac{A_{\ell}^b(\mu_2)}{P_{\ell}(\cosh \mu_2)} + B_{\ell}^b F_{\ell}^{\mu_2},\end{aligned}$$

$$\begin{aligned} \frac{(\sigma_g + \varepsilon_0 \varepsilon_g s)}{(\sigma_b + \varepsilon_0 \varepsilon_b s)} A_\ell^g &= A_\ell^l + B_\ell^l G_\ell^{\mu_1}, \\ \frac{(\sigma_l + \varepsilon_0 \varepsilon_l s)}{(\sigma_b + \varepsilon_0 \varepsilon_b s)} \left[ A_\ell^l + B_\ell^l G_\ell^{\mu_2} \right] &= \frac{\partial_\mu A_\ell^b(\mu_2)}{\partial_\mu P_\ell(\cosh \mu_2)} + B_\ell^b G_\ell^{\mu_2}, \end{aligned} \quad (7.14)$$

are the solutions to (7.11). Here, the Laplace transform has been applied,  $\partial_\mu$  is the spatial derivative along  $\mu$ , and the functions  $F_\ell$  and  $G_\ell$  are defined

$$F_\ell^\mu = F_\ell(\mu) = \frac{Q_\ell(\cosh \mu)}{P_\ell(\cosh \mu)}, \quad G_\ell^\mu = G_\ell(\mu) = \frac{\partial_\mu Q_\ell(\cosh \mu)}{\partial_\mu P_\ell(\cosh \mu)}, \quad (7.15)$$

which collapse to the definitions for the uniform field case of (3.41) and (3.43) when  $\ell = 1$  as assumed in Section 3.4.1. For the simple 3-layer system considered here, explicit solutions for each coefficient, following the derivation of Appendix A.14, can then be written

$$\begin{aligned} A_\ell^l &= A_0 U_0 \left[ G_\ell^{\mu_2} \frac{A_\ell^b(\mu_2)}{P_\ell(\cosh \mu_2)} - F_\ell^{\mu_2} \frac{\partial_\mu A_\ell^b(\mu_2)}{\partial_\mu P_\ell(\cosh \mu_2)} \right] \times \\ &\quad \frac{\sigma_b}{(\sigma_b G_\ell^{\mu_2} - \sigma_l F_\ell^{\mu_2}) \left( \tau_1 \tau_2 - \frac{F_\ell^{\mu_2}}{F_\ell^{\mu_1}} m_\ell \tau_3 \tau_4 \right)} \times \\ &\quad \left[ e^{-\frac{t}{\tau_5}} \left( \frac{\hat{\beta} - \hat{\alpha}}{\xi_1} \right) \left( 1 - \frac{\tau_b + \tau_1}{\tau_5} + \frac{\tau_b \tau_1}{\tau_5^2} \right) + e^{-\frac{t}{\tau_6}} \left( \frac{\hat{\beta} - \hat{\alpha}}{\xi_2} \right) \left( 1 - \frac{\tau_b + \tau_1}{\tau_6} + \frac{\tau_b \tau_1}{\tau_6^2} \right) \right. \\ &\quad \left. + \frac{e^{-\hat{\alpha}t}}{\xi_3} \left[ 1 - \hat{\alpha}(\tau_b + \tau_1) + \tau_b \tau_1 \hat{\alpha}^2 \right] - \frac{e^{-\hat{\beta}t}}{\xi_4} \left[ 1 - \hat{\beta}(\tau_b + \tau_1) + \tau_b \tau_1 \hat{\beta}^2 \right] \right], \end{aligned} \quad (7.16)$$

$$\begin{aligned} B_\ell^l &= A_0 U_0 \left[ G_\ell^{\mu_2} \frac{A_\ell^b(\mu_2)}{P_\ell(\cosh \mu_2)} - F_\ell^{\mu_2} \frac{\partial_\mu A_\ell^b(\mu_2)}{\partial_\mu P_\ell(\cosh \mu_2)} \right] \times \\ &\quad \frac{\sigma_b(\sigma_g - \sigma_l)}{(\sigma_b G_\ell^{\mu_2} - \sigma_l F_\ell^{\mu_2})(\sigma_l G_\ell^{\mu_2} - \sigma_g F_\ell^{\mu_2}) \left( \tau_1 \tau_2 - \frac{F_\ell^{\mu_2}}{F_\ell^{\mu_1}} m_\ell \tau_3 \tau_4 \right)} \times \\ &\quad \left[ e^{-\frac{t}{\tau_5}} \left( \frac{\hat{\beta} - \hat{\alpha}}{\xi_1} \right) \left( 1 - \frac{\tau_b + \tau_1}{\tau_5} + \frac{\tau_b \tau_1}{\tau_5^2} \right) + e^{-\frac{t}{\tau_6}} \left( \frac{\hat{\beta} - \hat{\alpha}}{\xi_2} \right) \left( 1 - \frac{\tau_b + \tau_1}{\tau_6} + \frac{\tau_b \tau_1}{\tau_6^2} \right) \right. \\ &\quad \left. + \frac{e^{-\hat{\alpha}t}}{\xi_3} \left[ 1 - \hat{\alpha}(\tau_b + \tau_1) + \tau_b \tau_1 \hat{\alpha}^2 \right] - \frac{e^{-\hat{\beta}t}}{\xi_4} \left[ 1 - \hat{\beta}(\tau_b + \tau_1) + \tau_b \tau_1 \hat{\beta}^2 \right] \right], \end{aligned} \quad (7.17)$$

with the final two coefficients determined due to (7.14) to be

$$A_\ell^g = A_\ell^l + B_\ell^l F_\ell^{\mu_1}, \quad (7.18)$$

$$B_\ell^b = \frac{A_\ell^l}{F_\ell^{\mu_2}} - \frac{A_\ell^b(\mu_2)}{F_\ell^{\mu_2} P_\ell(\cosh \mu_2)} + B_\ell^l, \quad (7.19)$$

and where the intrinsic time constants  $\tau_{b,l,g}$  are given by

$$\tau_{b,l,g} = \frac{\varepsilon_{b,l,g}}{\sigma_{b,l,g}} \varepsilon_0. \quad (7.20)$$

The time constants  $\tau_{1-4}$  have been introduced for brevity, relating to the interfacial charging times,  $\tau_{5,6}$ , corresponding to the two boundaries and given by

$$\begin{aligned} \tau_1 &= \frac{\varepsilon_l G_\ell^{\mu_1} - \varepsilon_g F_\ell^{\mu_1}}{\sigma_l G_\ell^{\mu_1} - \sigma_g F_\ell^{\mu_1}} \varepsilon_0, & \tau_2 &= \frac{\varepsilon_b G_\ell^{\mu_2} - \varepsilon_l F_\ell^{\mu_2}}{\sigma_b G_\ell^{\mu_2} - \sigma_l F_\ell^{\mu_2}} \varepsilon_0, \\ \tau_3 &= \frac{\varepsilon_g - \varepsilon_l}{\sigma_g - \sigma_l} \varepsilon_0, & \tau_4 &= \frac{\varepsilon_l - \varepsilon_b}{\sigma_l - \sigma_b} \varepsilon_0, \end{aligned} \quad (7.21)$$

such that  $\tau_{5,6}$  arise from the characteristic polynomial of order  $n - 1$  (in this case, equal to order 2) which was solved using the quadratic formula, yielding

$$\tau_{5,6} = \frac{2}{\gamma \mp \sqrt{\gamma^2 - 4\delta}} \quad (7.22)$$

where

$$\gamma = \frac{(\tau_1 + \tau_2) - \frac{F_\ell^{\mu_2}}{F_\ell^{\mu_1}} m_\ell (\tau_3 + \tau_4)}{\tau_1 \tau_2 - \frac{F_\ell^{\mu_2}}{F_\ell^{\mu_1}} m_\ell \tau_3 \tau_4}, \quad \delta = \frac{1 - \frac{F_\ell^{\mu_2}}{F_\ell^{\mu_1}} m_\ell}{\tau_1 \tau_2 - \frac{F_\ell^{\mu_2}}{F_\ell^{\mu_1}} m_\ell \tau_3 \tau_4}, \quad (7.23)$$

$$m_\ell = \frac{(\sigma_l - \sigma_b)(\sigma_g - \sigma_l)}{\left( \sigma_l \frac{G_\ell^{\mu_1}}{F_\ell^{\mu_1}} - \sigma_g \right) \left( \sigma_b - \sigma_l \frac{F_\ell^{\mu_2}}{G_\ell^{\mu_2}} \right)}, \quad (7.24)$$

and where the constants  $\xi_{1-4}$  have the definitions

$$\begin{aligned} \xi_1 &= \left( \frac{1}{\tau_6} - \frac{1}{\tau_5} \right) \left( \hat{\alpha} \hat{\beta} - \frac{\hat{\alpha} + \hat{\beta}}{\tau_5} + \frac{1}{\tau_5^2} \right), \\ \xi_2 &= \left( \frac{1}{\tau_5} - \frac{1}{\tau_6} \right) \left( \hat{\alpha} \hat{\beta} - \frac{\hat{\alpha} + \hat{\beta}}{\tau_6} + \frac{1}{\tau_6^2} \right), \\ \xi_3 &= \frac{1}{\tau_5 \tau_6} - \hat{\alpha} \left( \frac{1}{\tau_5} + \frac{1}{\tau_6} \right) + \hat{\alpha}^2, \\ \xi_4 &= \frac{1}{\tau_5 \tau_6} - \hat{\beta} \left( \frac{1}{\tau_5} + \frac{1}{\tau_6} \right) + \hat{\beta}^2. \end{aligned} \quad (7.25)$$

It follows from the set of potentials (7.11) that the electric fields are given by

$$\vec{E}_g = -\frac{1}{h} \left[ \sum_{\ell=0}^{\infty} A_{\ell}^g \frac{\partial P_{\ell}(\cosh \mu)}{\partial \mu} P_{\ell}(\cos \nu) \cdot \hat{\mu} + \sum_{\ell=0}^{\infty} A_{\ell}^g \frac{\partial P_{\ell}(\cos \nu)}{\partial \nu} P_{\ell}(\cosh \mu) \cdot \hat{\nu} \right], \quad (7.26)$$

$$\begin{aligned} \vec{E}_l = -\frac{1}{h} \left[ \sum_{\ell=0}^{\infty} \left( A_{\ell}^l \frac{\partial P_{\ell}(\cosh \mu)}{\partial \mu} + B_{\ell}^l \frac{\partial Q_{\ell}(\cosh \mu)}{\partial \mu} \right) P_{\ell}(\cos \nu) \cdot \hat{\mu} \right. \\ \left. + \sum_{\ell=0}^{\infty} \left[ A_{\ell}^l P_{\ell}(\cosh \mu) + B_{\ell}^l Q_{\ell}(\cosh \mu) \right] \frac{\partial P_{\ell}(\cosh \mu)}{\partial \nu} \cdot \hat{\nu} \right], \end{aligned} \quad (7.27)$$

$$\begin{aligned} \vec{E}_b = -\frac{1}{h} \left[ \sum_{\ell=0}^{\infty} \left( \frac{\partial A_{\ell}^b}{\partial \mu} + B_{\ell}^b \frac{\partial Q_{\ell}(\cosh \mu)}{\partial \mu} \right) P_{\ell}(\cos \nu) \cdot \hat{\mu} \right. \\ \left. + \sum_{\ell=0}^{\infty} \left[ A_{\ell}^b + B_{\ell}^b Q_{\ell}(\cosh \mu) \right] \frac{\partial P_{\ell}(\cos \nu)}{\partial \nu} \cdot \hat{\nu} \right], \end{aligned} \quad (7.28)$$

where  $h$  is the prolate-spheroidal scale factor,  $h = a_0 \sqrt{\cosh^2 \mu - \cos^2 \nu}$ .

### 7.2.3 On Intra-void Field Non-uniformity and the Uniform Approximation

The solutions developed in Section 7.2.2 have intentionally incorporated the arbitrary external potential  $\varphi_0$ . This was of particular importance to understand if there would be significant field non-uniformity within interfacial voids if the interface were to be subjected to a non-uniform field from, for example, sphere or needle electrodes. If the intra-void field exhibited strong non-uniformity, the suitability of applying the breakdown model of Chapter 4 would have been questionable. Since the main purpose for the present model was to provide theoretical support to the experimental work of Section 7.3 onwards, this brief section aims to show that for the electrode configuration used for practical tests, a negligible degree of intra-void field enhancement results from the non-uniformity of the external field. Hence, the assumption that the external field is uniform can be shown to be a suitable assumption, further allowing the infinite Fourier-Legendre series solutions to be collapsed to exact, and simpler, closed-form expressions.

Figure 7.6 shows two different non-uniform electrode topologies which were subject to analysis. The first are sphere-plane electrodes representing the topology used within the present experimental work, while the second set incorporates a needle-plane geometry with far greater tip curvature. While the latter electrode topology did not feature within the experimental work, it has been included for purposes of comparison. To analytically represent non-uniform electrode geometries, the Legendre expansion coefficients according to (7.12) must be obtained, requiring that the geometric function  $\mathcal{G}(\mu, \nu)$  be determined. The method to obtain this function is as

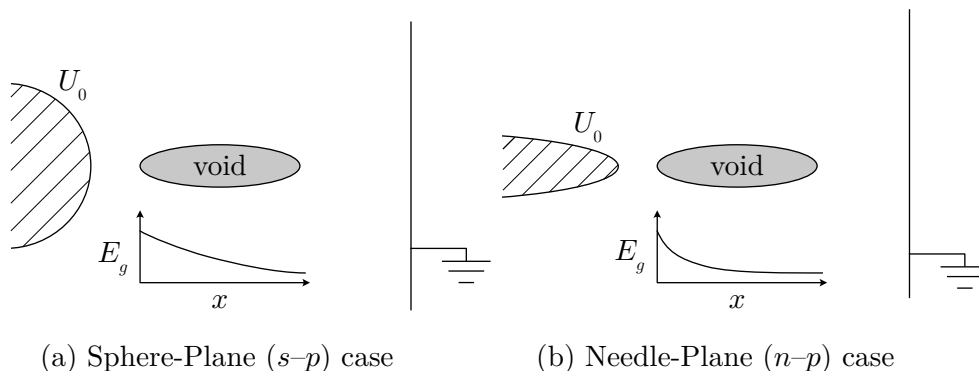


**Figure 7.6:** Graphical depiction of a spheroidal void in the proximity of a curved electrode in (a) a sphere-plane, (b) needle-plane configuration, indicating the nature of the field non-uniformity in the intra-void electric field.

follows:

1. Solve the Laplace equation on a separate (electrode) coordinate space  $\vec{q}$  that best represents the electrode geometry (i.e., where electrode surfaces can be well-represented by constant coordinate surfaces of  $q^j$ ), resulting in  $\varphi_0(\vec{q})$ .
2. Apply the coordinate transform  $(\vec{q} - \vec{q}') \rightarrow (\mu, \nu) : \varphi_0(\vec{q} - \vec{q}') \rightarrow \varphi_0(\mu, \nu)$  to be used as the external field within (7.12) on the void reference frame.  $\vec{q}'$  is an adjustable transform that controls the alignment of the electrode and void reference frames, for example, to change the position of the void in the inter-electrode gap.

For the case of the sphere-plane gap, the (axisymmetric) bi-spherical coordinate system  $\vec{q} = (\psi, \zeta)$  was used, while a secondary prolate-spheroidal system  $\vec{q} = (u, v)$  represented a hyperbolic needle-plane system using the coordinate  $v$ . Derivations for both systems can be found in Appendix A.15, from which the corresponding  $\mathcal{G}$  functions were found to be

$$\mathcal{G}^{s-p}(\psi, \zeta) = R(\psi, \zeta) \sum_{\ell=0}^{\infty} \frac{\sinh \left[ (\psi - \psi_2) \left( \ell + \frac{1}{2} \right) \right]}{\sinh \left[ (\psi_1 - \psi_2) \left( \ell + \frac{1}{2} \right) \right]} \frac{(2\ell + 1) P_{\ell}(\cos \zeta)}{2} \int_0^{\pi} \frac{P_{\ell}(\cos \zeta) \sin \zeta}{R(\psi, \zeta)} d\zeta \quad (7.29)$$

for sphere-plane systems (superscript  $s - p$ ), where  $R(\psi, \zeta) = \sqrt{\cosh \psi - \cos \zeta}$  and the potential  $U_0$  is applied to  $\psi_1$ , while the surface  $\psi_2$  is grounded. For a needle-plane ( $n - p$ ) system,

$$\mathcal{G}^{n-p}(v) = \frac{Q_0(\cos v) - Q_0(\cos v_2)}{Q_0(\cos v_1) - Q_0(\cos v_2)} \quad (7.30)$$

holds, where again  $U_0$  is applied to  $v_1$  and  $v_2$  is grounded. Note that in the ( $s - p$ ) case, the

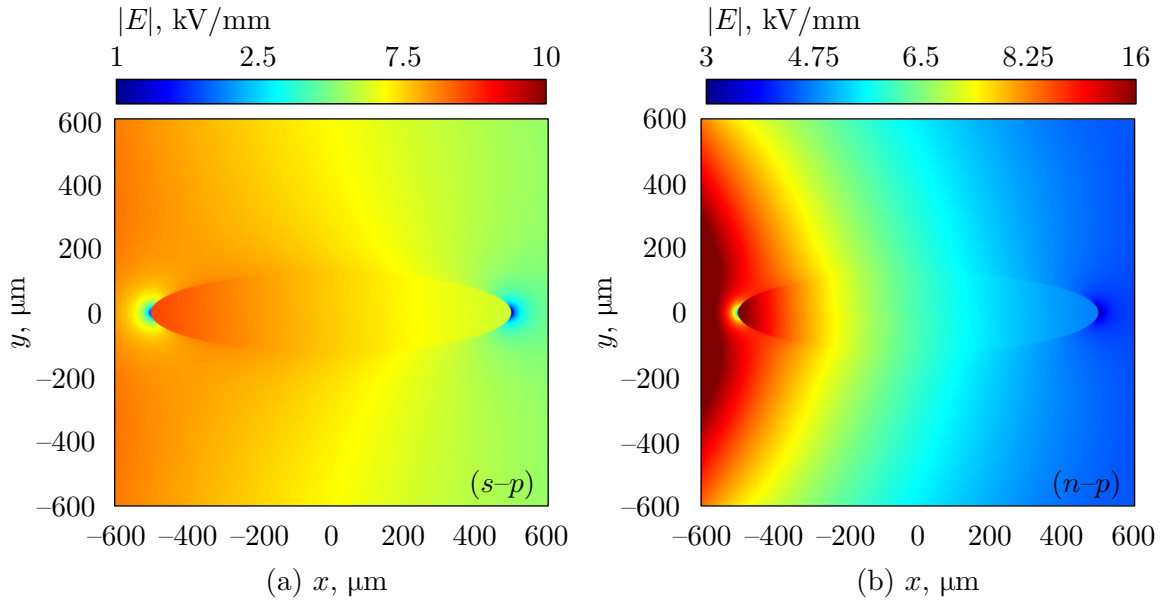


**Figure 7.7:** Examples of the electric field magnitudes for a spheroidal gas-filled void embedded within a solid bulk with  $\varepsilon_b = 2.5$  and  $\sigma_b = 10^{-12}$  S/m in (a) sphere-plane, (b) needle-plane electrode topologies using the Fourier-Legendre approach. Note the difference in the intra-void field non-uniformity.

Laplace equation is not fully separable, resulting in the series solution of (7.29). In both cases, Gauss-Legendre quadrature was used to evaluate the Legendre coefficients of (7.12). Figure 7.7 shows examples of the computed electric field distributions around micro-voids for the  $(s - p)$  and  $(n - p)$  cases with the indicated dimensions. In both cases, 10 terms of the Legendre series were used—a value determined by trial-and-error, observing that the solution exhibited negligible change with additional, higher-order, terms. Note that void and electrode dimensions were selected based on typical values measured during the experimental component of this work (Section 7.3 and onwards). Electrical parameters of the layers  $l$  and  $b$  were chosen to represent typical values for polymeric insulation like those of Table 7.1.

Qualitatively, the degree of non-uniformity inside the void may be significant only in the case of needle-plane electrodes and for larger voids close to the needle tip. For a more quantitative view, the *field utilisation factor*,  $\eta_E$ , was calculated according to

$$\eta_E = \frac{\text{mean } |\vec{E}_g|}{\text{max } |\vec{E}_g|} \quad (7.31)$$

as a measure of the degree of intra-void field non-uniformity, where  $\eta_E = 1$  corresponds to an entirely uniform field. For the  $(s - p)$  and  $(n - p)$  cases, Figure 7.8(a) and 7.8(b) plots the field

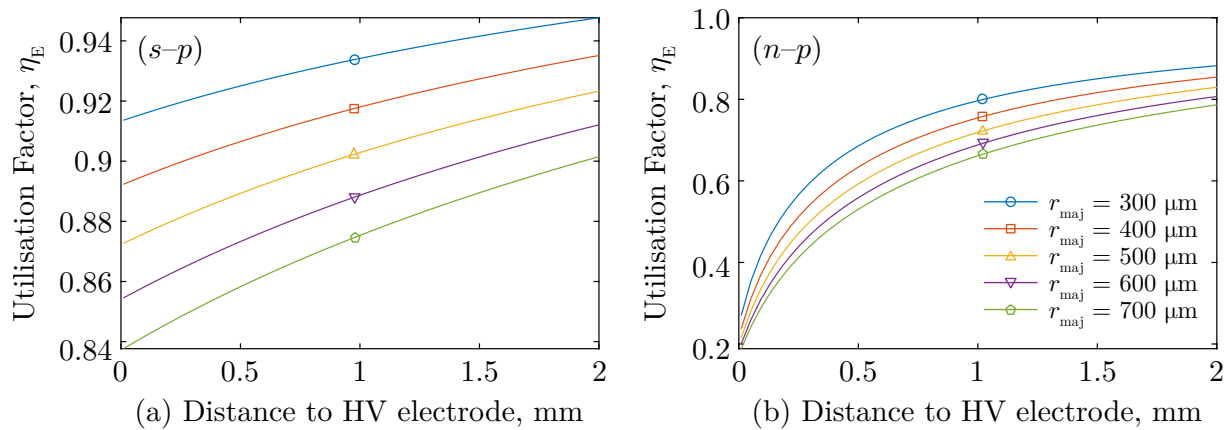


**Figure 7.8:** Intra-void field utilisation factor,  $\eta_E$ , as a function of the distance away from the curved electrode tip for (a) sphere-plane, (b) needle-plane electrodes, and with various representative void semi-major radii.

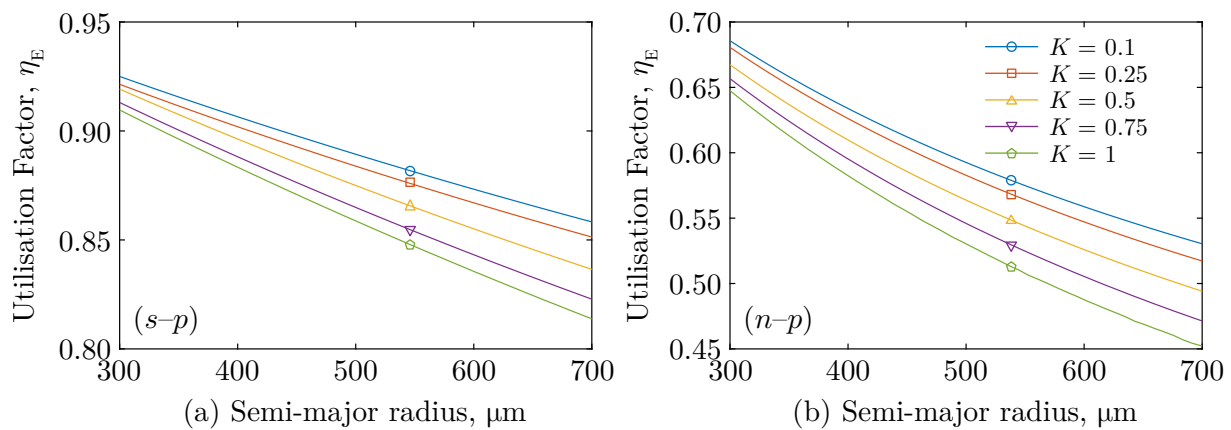


**Figure 7.9:** Intra-void field utilisation factor,  $\eta_E$ , as a function of void semi-major radius for (a) sphere-plane, (b) needle-plane electrodes, and across a range of axis ratio (eccentricity),  $K$ .

utilisation factor as a function of the proximity of the void to the sphere or needle electrode (assuming  $K = 0.1$  as per [12]), respectively. Figure 7.9(a) and 7.9(b) also plots the factor as a function of the void size at a fixed distance of 500  $\mu\text{m}$  away from the curved electrode and for a range of values of  $K$ . In general, the intra-void field exhibits greater uniformity when located farther away from the curved electrode, where the  $(s - p)$  case was, overall, more uniform than that of the  $(n - p)$  case. This aligned with expectations, considering that the uniformity of the external field also increases away from the curved electrode—the location with the most divergent field would be located at the point of maximum electrode curvature. Fields with a greater degree of non-uniformity were found to develop within larger voids of the same eccentricity, an effect which was stronger the closer the void was to the curved electrode. The axis ratio,  $K$ , of the

void only had a weak effect on the intra-void field utilisation factor compared to the far more dominant factors of the void proximity and size. Based upon the magnitudes of field utilisation factor, the  $(n - p)$  case exhibited a significant degree of field non-uniformity and would be poorly represented by an equivalent system energised using a uniform external field. The  $(s - p)$  case, which has been modelled to represent the practical geometry of the experimental work (from Section 7.3 onward), however, exhibited only weak field non-uniformity due to the relatively small void size compared to the size of the spherical electrode. The approximation of the  $(s - p)$  configuration with that of plane-parallel electrodes was therefore deemed reasonable to apply and adequately representative.

Returning therefore to the analytical solutions of Section 7.2.2, if the external potential,  $\varphi_0$ , assumed the form

$$\varphi_0 = -a_0 \frac{U_0(t)}{d} \cosh \mu \cos \nu, \quad (7.32)$$

then it would represent the  $+x$ -directed uniform field,  $E_0(t)$ , of magnitude  $U_0(t)/d$ , where  $d$  is the electrode separation. It follows that the Legendre expansion requires only the zero- and first-degree ( $\ell = 0, 1$ ) terms in (7.12) since

$$\begin{aligned} A_0^b &= U_0(t) \frac{1}{2} \int_0^\pi -\frac{a_0}{d} \cosh \mu \cos \nu \cdot P_0(\cos \nu) \sin \nu \, d\nu \\ &= U_0(t) \frac{1}{2} \int_0^\pi -\frac{a_0}{d} \cosh \mu \cos \nu \sin \nu \, d\nu \\ &= 0, \end{aligned} \quad (7.33)$$

$$\begin{aligned} A_1^b &= U_0(t) \frac{3}{2} \int_0^\pi -\frac{a_0}{d} \cosh \mu \cos \nu \cdot P_1(\cos \nu) \sin \nu \, d\nu \\ &= U_0(t) \frac{3}{2} \int_0^\pi -\frac{a_0}{d} \cosh \mu \cos^2 \nu \sin \nu \, d\nu \\ &= -a_0 \frac{U_0(t)}{d} \cosh \mu, \end{aligned} \quad (7.34)$$

where the geometric component of the external potential is evidently  $\mathcal{G}(\mu, \nu) = -(a_0/d) \cosh \mu \cos \nu$  in this case. Thus, the two-term expansion exactly represents the external field with finite terms. The field coefficients therefore follow (7.16) to (7.25) with  $\ell = 0, 1$ ; with the potential and field expressions simplifying precisely to the uniform case presented in Chapter 3 - Section 3.4.1.1 for  $i = 1, 2$ , and 3. The opportunity is taken here to

further remark on the significance of the factor

$$\mathcal{F}_\ell = \frac{G_\ell^{\mu_2} \frac{A_\ell^b(\mu_2)}{P_\ell(\cosh \mu_2)} - F_\ell^{\mu_2} \frac{\partial_\mu A_\ell^b(\mu_2)}{\partial_\mu P_\ell(\cosh \mu_2)}}{(\sigma_b G_\ell^{\mu_2} - \sigma_l F_\ell^{\mu_2})} \quad (7.35)$$

as featured in the coefficients for the arbitrary field case of (7.16) and (7.17), which has been labelled  $\mathcal{F}_\ell$  for convenience. Evaluating (7.35) for the first-degree term  $\ell = 1$  (since this is the only non-zero term of the two-term expansion in the case of the uniform external field, as  $\mathcal{F}_0 = 0$ ) yields

$$\mathcal{F}_1 = \frac{G_1^{\mu_2} - F_1^{\mu_2}}{\sigma_b G_1^{\mu_2} - \sigma_l F_1^{\mu_2}}, \quad (7.36)$$

which by further considering the limits

$$\begin{aligned} \lim_{\sigma_b \gg \sigma_l} \mathcal{F}_1 &= \frac{1}{\sigma_b} \left( 1 - \frac{F_1^{\mu_2}}{G_1^{\mu_2}} \right) \propto 1 - \frac{F_1^{\mu_2}}{G_1^{\mu_2}}, \\ \lim_{\sigma_l \gg \sigma_b} \mathcal{F}_1 &= \frac{1}{\sigma_l} \left( 1 - \frac{G_1^{\mu_2}}{F_1^{\mu_2}} \right) \propto 1 - \frac{G_1^{\mu_2}}{F_1^{\mu_2}}, \end{aligned} \quad (7.37)$$

shows that the field enhancement factors derived in Chapter 3 - Section 3.4.2 are recovered for a 2-layer inclusion<sup>¶</sup>. The implication here is that  $\mathcal{F}_\ell$  is an analog of the field enhancement factor relative to a uniform field, but which considers two separate sources of field non-uniformity: (i) due to the non-uniformity of some arbitrary external field, and (ii) due to the electrical characteristics and geometry of the inclusion. The generality of this result allows the application of (7.35) to arbitrary fields (with the limitation of cylindrical symmetry as imposed during derivation), enabling field enhancement factors around voids or particles to be estimated under certain non-uniform external fields, see for example in the related work [33]. Additional field enhancement plots may further be found in Appendix C.5 for a selection of non-uniform external fields.

To summarise the analysis up to this point, the transient electric field developed within a void at a solid-solid interface was ultimately estimated using

$$\vec{E}_g(\mu, \nu, t) = -\frac{A_1^g(t)}{h} (\sinh \mu \cos \nu \cdot \hat{\mu} - \cosh \mu \sin \nu \cdot \hat{\nu}) \quad (7.38)$$

<sup>¶</sup>Although the system here has 3 layers, the limiting behaviour is identical since the two layers being considered ( $l$  and  $b$ ), are directly adjacent. For example, the limit  $\sigma_l \gg \sigma_b$  is unaffected by the value of  $\sigma_g$ , since the high conductivity of layer  $l$  would nullify the field in the innermost layer  $g$  regardless.

such that the intra-void field magnitude is uniform, given by

$$|\vec{\mathbf{E}}_g| = \sqrt{[\vec{\mathbf{E}}_g \cdot \hat{\boldsymbol{\mu}}]^2 + [\vec{\mathbf{E}}_g \cdot \hat{\boldsymbol{\nu}}]^2} = \frac{A_1^g(t)}{a_0} \quad (7.39)$$

which was derived under the assumption of a double-exponential energising voltage. In the sequence of events leading up to interfacial breakdown, the uniform field given by (7.39) was then used as input to the improved avalanche-to-streamer model of Chapter 4 to estimate the moment of void discharge. The type of gas trapped within the interfacial void was therefore incorporated by the use of electron swarm parameters, defined in the same format as was used in Chapter 4.

Upon void discharge, the intra-void conductivity was assumed to rise significantly due to the production of free charges from ionisation, to the point that the condition  $\sigma_g \gg \sigma_b$  becomes satisfied. The maximum field developed in the bulk at the void extremities along the semi-major axis ( $\nu = 0$ ,  $\mu = \mu_2$ , the location of the contact spots between adjacent voids) may then be estimated from

$$\max |\vec{\mathbf{E}}_b| = |\vec{\mathbf{E}}_b(\mu = \mu_2, \nu = 0)| = \left| -\frac{1}{h} \left[ \partial_\mu A_1^b(\mu_2) + B_1^b \partial_\mu Q_1(\cosh \mu_2) \right] \right|. \quad (7.40)$$

The moment of void discharge was assumed to rapidly screen the intra-void field [34], fast enough that the void conductivity,  $\sigma_g$ , could be assumed to exhibit a step change at the void discharge moment,  $t_v$ , like

$$\sigma_g(t) = \sigma_{\max} H(t - t_v), \quad (7.41)$$

where  $H(t)$  is the Heaviside step function, and  $\sigma_{\max}$  is the conductivity of the discharged void; chosen to be large enough that  $\sigma_g \gg \sigma_b$ . Based on the discharge shielding times estimated in [35], the sudden void discharge was assumed to be followed immediately by the collapse of the intra-void field which is well approximated by

$$\vec{\mathbf{E}}_g^{\text{break}}(t) = \vec{\mathbf{E}}_g(\sigma_g = 0, t) + \left[ \vec{\mathbf{E}}_g(\sigma_g = \sigma_{\max}, t) - \vec{\mathbf{E}}_g(\sigma_g = 0, t) \right] H(t - t_v) \quad (7.42)$$

and the where the corresponding bulk field is also well represented by the step change

$$\vec{\mathbf{E}}_b^{\text{break}}(t) = \vec{\mathbf{E}}_b(\sigma_g = 0, t) + \left[ \vec{\mathbf{E}}_b(\sigma_g = \sigma_{\max}, t) - \vec{\mathbf{E}}_b(\sigma_g = 0, t) \right] H(t - t_v). \quad (7.43)$$

Equation (7.42) and (7.43) essentially represent an instantaneous transition from the transient field evolution in the case that  $\sigma_g = 0$  to that of  $\sigma_g = \sigma_{\max}$  at the moment  $t_v$  (see Appendix B.5). This description is advantageous in the sense that it not only incorporates dry-mate interfaces

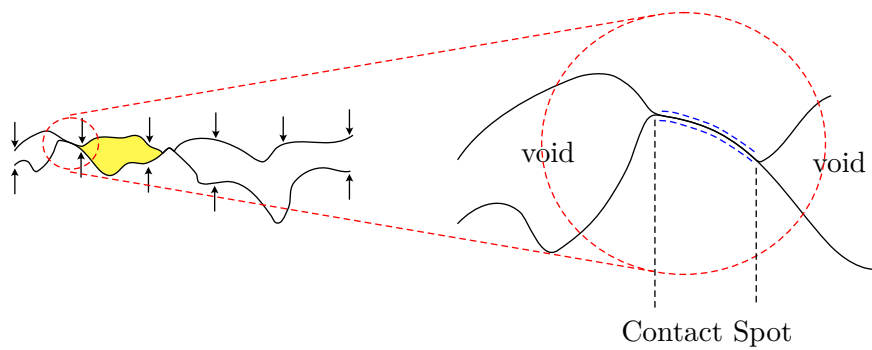


**Figure 7.10:** Graphical depiction of the interfacial contact spots, regions of contacting bulk material (dashed blue line) in between interfacial voids along the rough surface contact.

(with gas-filled voids), but can also be applied to cases where void discharge may not occur first (e.g., within water-filled voids), but rather initiate due to the already-enhanced field at the interfacial contact spots. In the latter case,  $t_v \rightarrow \infty$  and thus  $H(t - t_v) = 0 \forall t$ , however, the expression (7.43) remains valid and simply describes the time-evolution of the electric field at the contact spots assuming water-filled voids, which beyond a threshold strength (discussed in Section 7.2.4) may induce direct breakdown across the contacting regions between the voids. Characteristics of, and predictions relating to, wet-mate (oil or water) interfaces are presented in Section 7.2.5 as part of a wider discussion of theoretical estimations.

#### 7.2.4 Breakdown of Contact Spots

Returning to the model outline as detailed at the beginning of Section 7.2, the occurrence of void discharge was assumed to be followed by processes pertaining to breakdown across the *contact spots* (sub-model III), which ultimately facilitates the connection of adjacent discharged voids, creating a breakdown path. The term *contact spot* was used in the literature to refer to regions along the interface which were fully in contact, as depicted in Figure 7.10. In the works of Kantar *et al.*, no specific means to estimate what was referred to as the *tracking strength* was attempted, a term given to the dielectric strength of the contact spots. Instead, Fothergill's filamentary electromechanical breakdown model [36], which was developed for bulk solids, was used as an order-of-magnitude indication of the contact spot dielectric strength within their analyses. Fothergill [36] estimates the electromechanical breakdown strength as

$$E_b \approx \left[ \frac{16GY'}{(\varepsilon_0\varepsilon_r)^2r'} \right]^{1/4}, \quad (7.44)$$

where  $G$  is the toughness of the solid, and  $r'$  is the radius of the head of the growing filamentary breakdown channel. Note that the composite modulus  $Y'$  has been used here for the assembled interface according to (7.3).

In general, it is difficult to estimate the failure mode and characteristics of these contacting regions for several reasons. Primarily, regardless of the contact pressure, the two sides of the solid dielectrics at the contact spots are not completely fused together, such that their treatment as simply a bulk solid material is unlikely to be representative. Fothergill's [36] analysis was based upon an energy balance criterion—that for the propagation of a micro-filament through the solid material would require the sum of the *surface energy* and *plastic deformation energy* to be exceeded. The former refers to the energy necessary to create a new surface in a solid material based on classical fracture mechanics [26], while the latter describes the energy required for the material to locally, and permanently, deform. It is argued here that Fothergill's approach would not be appropriate here, since no new surfaces would be formed from the breakdown across a contact spot, which by definition, is a feature formed from two already separate surfaces. One may remove the surface energy term when repeating Fothergill's analysis (see Appendix A.16), which would yield an alternative estimation of

$$E_b \approx \sqrt{\frac{\sqrt{8}Y'}{\varepsilon_0\varepsilon_r}} \quad (7.45)$$

if only plastic deformation is assumed necessary and the surface energy need not be overcome. Figure 7.11 compares (7.44) to (7.45) over a range of effective modulus,  $Y'$ , where the grey region of Figure 7.11 identifies the range of elastic moduli relevant to the materials used in this work (from Table 7.1). It is shown that the revised version of Fothergill's approximation decreases the estimated tracking strength substantially for softer, more elastic, materials. However, it becomes similar within the range of interest demarcated by the grey region, corresponding to the range of  $Y'$  for the materials used in this work. It is argued that this may be more representative of tracking failure across contact spots, especially when the interfacial mating pressure is not particularly high. However, whether the revised model is representative of breakdown across contact spots remains questionable. The estimated breakdown strength increases indefinitely with  $Y'$ , and further, does not incorporate the effects of mating pressure; a parameter which almost certainly plays a role. In general, it remains challenging to derive good approximations to the contact spot breakdown strength due to the irregularity of practical rough surface morphologies. These features may induce a great degree of local field enhancement at the interface that is challenging to estimate. There also exist the problem of proximity effects of two (or more) voids

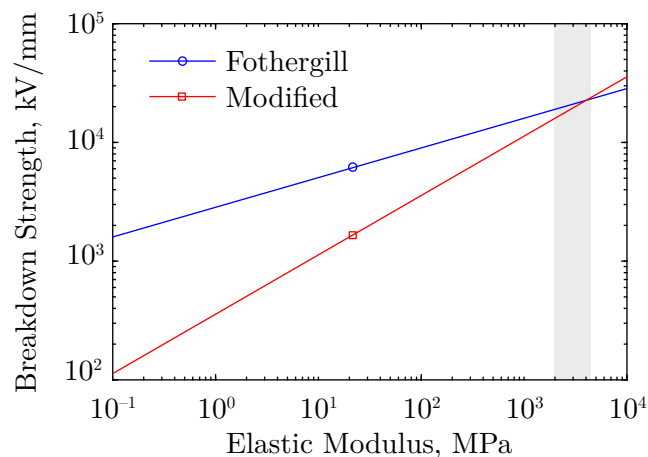


**Figure 7.11:** Comparison of the estimated breakdown strength as a function of elastic modulus based on Fothergill’s filamentary electromechanical breakdown model (7.44) [36] to the revised Fothergill model (7.45) removing the surface energy term. The former assumed a toughness of  $G = 15 \text{ kJ/m}^2$  and  $r' = 10 \text{ }\mu\text{m}$  based on manufacturer quoted values and estimations from the experimental results of Section 7.3. Grey box shows the region of elastic modulus relevant to the materials used in this work.

that may be separated by a distance far smaller than their respective dimensions. In this case, the field enhancement between multiple discharged and conducting voids would reach far beyond those that can be estimated for a single void, see Appendix B.6.

Additionally, the analyses of Majumdar and Bhushan [37] reveals that rough surface contact exhibits fractal-like properties and can be characterised using the tools and methods of fractal mathematics. Correspondingly, one may consider that upon the magnification of an interfacial contact spot, one would find smaller and smaller sets of void-like features exhibiting scale-independent, fractal-like geometry. Quantification of discharge behaviour across such features is therefore highly nontrivial, and to the best of the author’s knowledge, no such method currently exists that would allow these features to be accurately modelled. Despite this, and in the absence of more sophisticated models, Fothergill’s original model (7.44) and the revised model (7.45) provides an *order of magnitude* estimate that remains useful as a reference. However, the time between void discharge and full interfacial breakdown was assumed to be negligible, such that the occurrence of void breakdown was taken to correspond to interfacial breakdown, as was similarly assumed in [12].

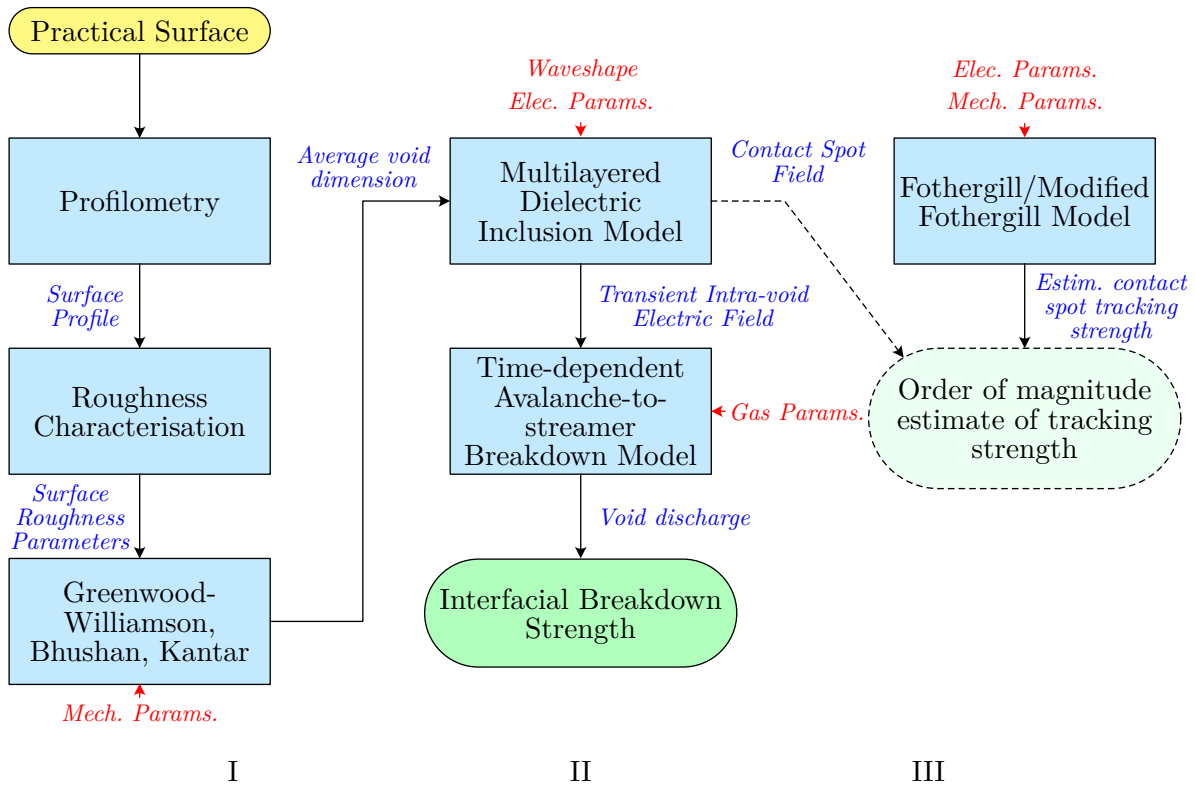


**Figure 7.12:** Expanded flowchart representing the modelling process of the developed solid-solid interfacial breakdown model. Blue text shows the outputs of each process that feeds into the proceeding step. Red text shows the locations where external system parameters are introduced. Note that the contact spot model was not directly integrated as part of the main model, as discussed in the main text.

### 7.2.5 Model Predictions and Estimations

To summarise, the various sub-models represented previously in the high-level flow diagram of Figure 7.1 is repeated with specific details relating to input data and model type in Figure 7.12. To consolidate, the method requires five main sets of data as input parameters relating to the various mechanisms present in the system, described below.

- *Surface Roughness Parameters:* Determined from the measurement of surface roughness profiles of practical sample surfaces. Namely, the equivalent surface parameters  $\sigma^{[eq]}$ ,  $\beta^{[eq]}$ , and  $\eta^{[eq]}$  allow an average interfacial void dimension to be estimated. The method employed in this work is described in Section 7.3.2.
- *Material Mechanical Properties:* The elastic moduli,  $Y_1$  and  $Y_2$ , are necessary to compute the effective modulus  $Y'$  and also in the estimation of void size; as are the apparent contact pressure  $p_a$  which may be found from the contact force  $F_a$  and apparent contact area  $A_a$

determined from measurement.

- *Material Electrical Properties:* The relative permittivity,  $\varepsilon_{g,l,b}$ , and electrical conductivity,  $\sigma_{g,l,b}$ , of the three layers included within the model determines the transient field response of the void. Most importantly, these parameters partially influence the development of the field in the void,  $\vec{E}_g(t)$ , and the field in bulk (contact spots),  $\vec{E}_b(t)$ .
- *Waveshape Parameters:* The assumption that the energising voltage was of double exponential form necessitates the inclusion of the waveshaping parameters  $A_0$ ,  $\hat{\alpha}$ , and  $\hat{\beta}$  which determine the rise and fall characteristics of the applied field. Necessarily, the peak voltage  $U_0$  and the inter-electrode distance  $d$  must also be defined. Alternatively, a field of peak strength,  $E_0$ , may also be used.
- *Gas Transport Parameters:* The use of the time-dependent avalanche model of Chapter 4 requires initial conditions relating to the electron distribution:  $n_0(t_0)$ ,  $\sigma_0$ , and the electron transport parameters for the gas that is assumed to occupy the inside of the voids—electron mobility,  $\mu_e$ ; diffusion coefficient,  $D_e$ ; and the net ionisation coefficient,  $\bar{\alpha}$ . Naturally, the thermodynamic conditions of the gas: pressure,  $P$ , and temperature,  $T$ , are also necessary to determine the neutral density. In practise, these parameters depend entirely on the type of gas environment in which the solid-solid interface was assembled.

The model outputs consist of the estimated formative time-to-breakdown of the interface,  $t_b$ , and the corresponding breakdown field magnitude,  $E_b$  (and voltage,  $V_b$ , if some electrode separation  $d$  was assumed). Note that the parameters characterising the interior of the void (and the void wall) may also be set to represent some medium other than gas. For example, water or various dielectric liquids may be present at the interface under wet-mate conditions, or if a form of oil lubricant was used during the joining process. Each of these cases are briefly explored in the following subsections. Unless otherwise stated, the default parameters used to generate the results shown in Sections 7.2.5.1 to 7.2.5.3 are tabulated in Table 7.2. These parameters were selected based on typical values for the polymers used in this work, drawn from the material properties of Table 7.1 and the surface roughness data later presented in 7.4.5. Wave-shaping parameters were chosen to represent a standard IEC-60060 lightning impulse [38] for demonstration, and air at STP conditions was assumed for all cases that incorporated a gas-filled void. For each case, the main quantity of interest was the maximum values of  $|\vec{E}_g|$  and  $|\vec{E}_b|$ , and their evolution over the course of the impulse.

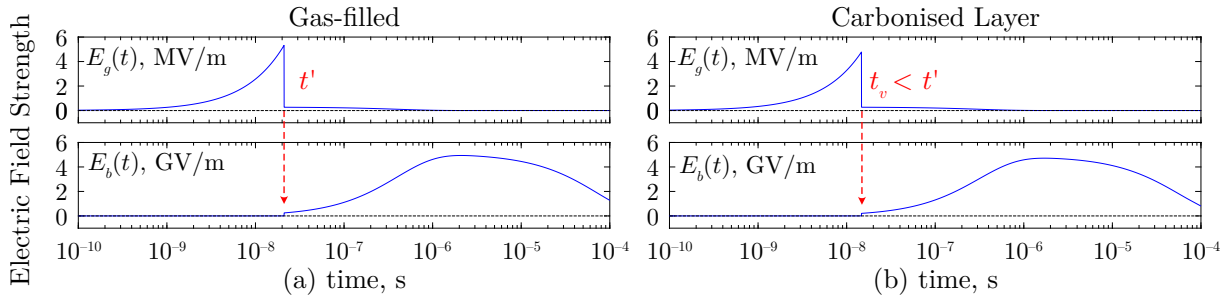


**Figure 7.13:** Example time-course of the maximum electric field magnitudes in the interfacial void and at the contact spot for a dry-mate interface where (a) the void is gas-filled, (b) the void has a carbonised layer but is otherwise gas-filled.

### 7.2.5.1 Dry-mate/Carbonised Interface

Under configurations where an interface is assembled in a dry environment, two cases are of relevance and are demonstrated here. The first is the standard case that two fresh and dry samples are placed into contact. Thus, the additional layer included on the void inner wall was assumed to be part of the bulk with identical properties. To aid comparison, the breakdown time estimated for the standard dry-mate and gas-filled case is assigned the symbol  $t'$ , allowing subsequent cases to be expressed relative to this value.

Figure 7.13(a) shows the transient field responses  $|\vec{E}_g|$  and  $|\vec{E}_b(\mu = \mu_2, \nu = 0)|$  over time (where for brevity, the symbols have been simplified to  $E_g(t)$  and  $E_b(t)$ , respectively) according to (7.42) and (7.43). The moment of void discharge is indicated by the collapse of the electric field inside the void, leading to field enhancement in the bulk. Note that the estimated field magnitudes at the contact spots are within the GV/m range, even with the present simplification of an ideal spheroidal void that incorporates no additional surface irregularities. Considering that two additional sources of field enhancement are likely present at practical interfaces: (i) due to

**Table 7.2:** Default parameters used for the examples of Section 7.2.5. Unless otherwise stated, these parameters were used. Parameters were based on practical system parameters and measurements conducted within Section 7.3.

Parameter	Value	Parameter	Value
$U_0$	100 kV	$\varepsilon_g$	1
$A_0$	1.037	$\varepsilon_l$	2.5
$\hat{\alpha}$	$1.47 \times 10^4 \text{ s}^{-1}$	$\varepsilon_b$	2.5
$\hat{\beta}$	$2.47 \times 10^6 \text{ s}^{-1}$	$\sigma_g$	0 S/m
$d$	10 mm	$\sigma_l$	$10^{-12} \text{ S/m}$
$\bar{d}_{\text{void}}$	1.5 mm	$\sigma_b$	$10^{-12} \text{ S/m}$
$K$	0.1	$\Delta_l$	1 $\mu\text{m}$

adjacent voids being in close proximity, and (ii) due to far more irregular and likely higher aspect ratio geometry present at multiple scales along the contact, an additional factor of enhancement of  $10^1$  to  $10^2$  may not be entirely unreasonable. The field at the contact spot may therefore rapidly enter into the region where breakdown becomes possible after void discharge based on the values of Figure 7.11 from Fothergill's theory. It is remarked again that additional modelling to incorporate either of these sources of enhancement would be highly nontrivial, but methods to do so would be of interest for future work. The reader may additionally refer to Appendix B.6 for some numerical results on estimating approximate enhancement factors between two voids, the magnitudes of which support the idea that the contact spot field may be enhanced to such an extent that allows contact spot tracking to rapidly proceed from void discharge.

In a related case, the additional layer (with subscript  $l$ ) was assigned the parameters  $(\varepsilon_l, \sigma_l) = (2.3, 10^{-5} \text{ S/m})$  to represent the existence of a thin layer of carbonised material possibly resulting from multiple previous (partial) discharges across the interface [39] in an otherwise gas-filled void. Figure 7.13(b) encloses the corresponding results, showing the field evolving in a similar manner to the standard gas-filled case, with the key difference that the estimated moment of void discharge occurred sooner,  $t_v < t'$ , than in Figure 7.13(a). The presence of a moderately conductive layer acted to enhance the field inside the void, leading to stronger ionisation that ultimately shortened the time for void discharge to occur. For fast-rising impulses, small differences in the time-to-breakdown may correspond to substantial changes to the corresponding breakdown field strength. It should be noted, however, that the effect of the intermediate layer on the intra-void field as predicted by this model depends on the specific layer properties. For example, were the layer to assume values representing a substantially more conductive medium, void discharge is prevented completely as the layer acts to screen the intra-void field in Faraday cage-like behaviour. Further reading on the sensitivity of the fields to the various layer parameters can be found in Appendix B.7. In practise, carbonised trails would also link between voids along previous breakdown paths, likely leading to further a reduction of the overall breakdown strength. This is a limitation of the single-void model used here, as interactions between neighbouring voids are not considered.

### 7.2.5.2 Full/Partial Wet-mate Interface

Ingress of water onto interfacial contacts may be likely for some applications, whether through direct introduction during assembly, or by reasons relating to the operating conditions, e.g., submerged operation, condensation, or environmental humidity. Two cases were considered here,

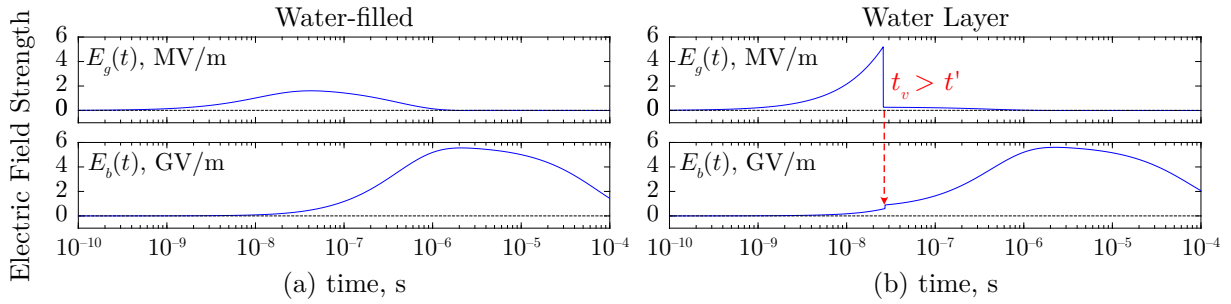


**Figure 7.14:** Example time-course of the maximum electric field magnitudes in the interfacial void and at the contact spot for a wet-mate interface where (a) the void is water-filled, (b) the void has a wetted layer but is otherwise gas-filled.

representing water present at the interfacial contact of different levels of severity. The first assumed that all gas that would be trapped within the interfacial voids are instead filled with water, such that  $(\varepsilon_g, \sigma_g = 80, 3.0 \text{ S/m})$ , where the conductivity value has been chosen to represent seawater [40]. Figure 7.14(a) shows the far diminished strength of the intra-void field owing to the increased void conductivity. As a result, the field at the contact spots exhibits no step change due to sudden void discharge, but begins in an already-enhanced state. The breakdown of the interface would therefore follow soon after the failure of the contact spots as the bulk field rises, chaining the water-filled cavities together along the interface. Due to the redistributed field, this may occur far sooner than the gas-filled case, which is believed to explain the lower breakdown strength of wet-mate interfaces seen in, for example, [41, 42] and references therein.

In the complementary case, parameter values of  $(\varepsilon_l, \sigma_l = 80, 0.15 \text{ S/m})$  were assumed for the void inner wall only, representing a thin layer of water representative of less significant water ingress or of damp surfaces prior to interface assembly. With the higher permittivity and more significant electrical conductivity of the layer, Figure 7.14(b) suggests a delay in the time to void discharge compared to the dry-mate case, resulting from a reduced intra-void electric field. Unlike the gas-filled case, however, the bulk field prior to  $t_v$  is not negligible but is enhanced in the same way as the water-filled case of Figure 7.14(a). With sufficiently strong field enhancement, the contact spot strength may be exceeded before the intra-void field reaches its discharge threshold. In practise, this is made more likely due to the the many adjacent voids (in some distribution of completely water-filled, gas-filled, and with wetted layers) of different scales along the interface. Thus, as it is generally understood, penetration of any type of fluid of moderate conductivity or higher onto the interface should be avoided.

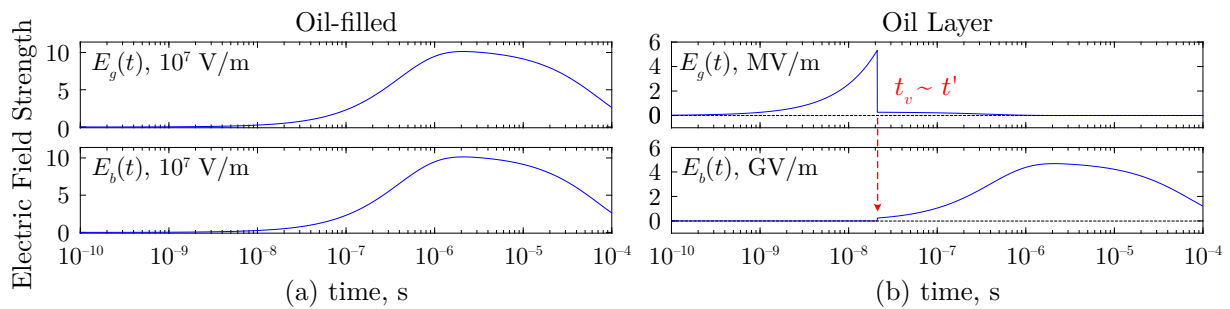


**Figure 7.15:** Example time-course of the maximum electric field magnitudes in the interfacial void and at the contact spot for an oil-mate interface where (a) the void is oil-filled, (b) the void has a wetted oil layer but is otherwise gas-filled.

### 7.2.5.3 Full/Partial Oil-mate Interface

The scenario that some form of dielectric fluid or oil exists at the interface was additionally considered. Such cases may arise, for example, if some form of lubricant or grease were to be used during interfacial mating. Once again, separate cases where the interfacial voids were assumed saturated with fluid, or had only a thin surface layer over the void walls, were considered with the parameters  $(\epsilon_{g,l}, \sigma_{g,l}) = (2.3, 10^{-12} \text{ S/m})$  for typical dielectric fluids [43, 44]. In this case, Figure 7.15(a) shows that for a completely oil-filled void, the close match between the void parameters and the bulk results in negligible field enhancement. Moreover, the field within the entire gap becomes essentially uniform with a magnitude equal to the external field. Different types of insulating fluid will result in differences to the degree of non-uniformity and field enhancement, but generally, if the parameters of the void are only marginally different from that of the bulk, the external field does not become distorted in the vicinity of the void. Incidentally, this provides a reasonable explanation for experimental observations that oil-mate interfaces generally possess greater dielectric strength than their dry-mate and wet-mate counterparts [41].

Figure 7.15(b) provides the corresponding field evolutions for the case where only a thin layer of oil was considered, in an otherwise gas-filled void. The field responses in this case are identical to those of the dry-mate case alone (Figure 7.13), since the oil layer of similar properties to the bulk act only to extend the bulk by a distance equal to the thickness of the oil layer. The field responses are effectively identical to those of a slightly smaller void under dry-mate conditions, and are otherwise unremarkable. These results do suggest, however, that in practise, the use of dielectric fluids for solid-solid interfacial mating should be recommended where possible and should adhere to two best-practises for highest dielectric performance:

- The electrical parameters of the fluid used should match, as closely as possible, the solid

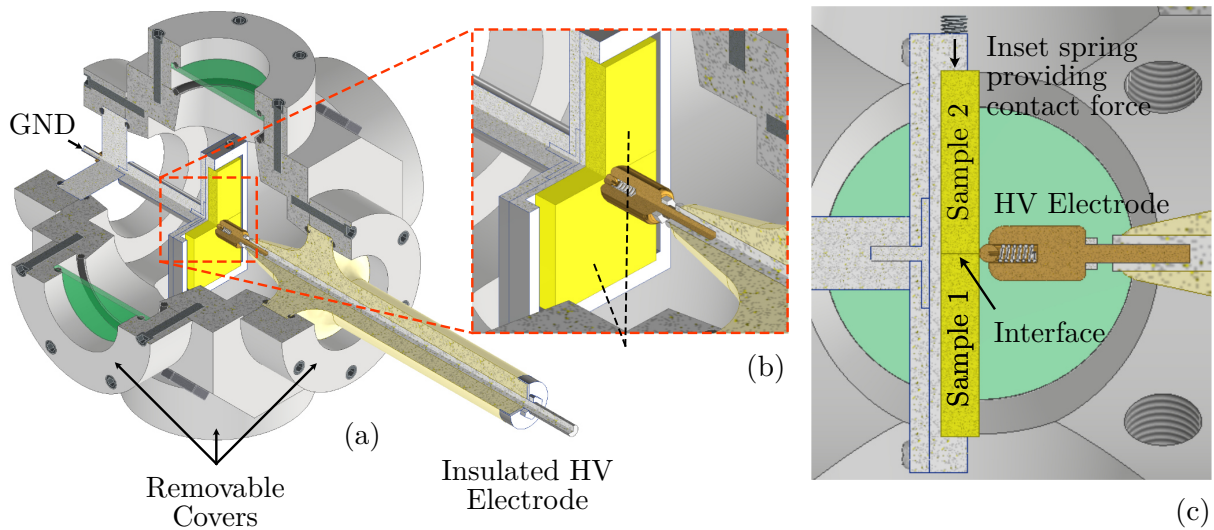


**Figure 7.16:** (a) 3/4 cutaway view of a 3D model of the utilised test chamber for solid-solid interface breakdown tests, (b) magnified image showing the location of the solid samples forming the solid interface and the spring-loaded HV electrode, (c) sectional view through the centre of the solid sample holder, indicated are the locations of the inset springs providing the sample holding force. Image adapted with permission from [45], © IEEE 2024.

bulk dielectrics being connected.

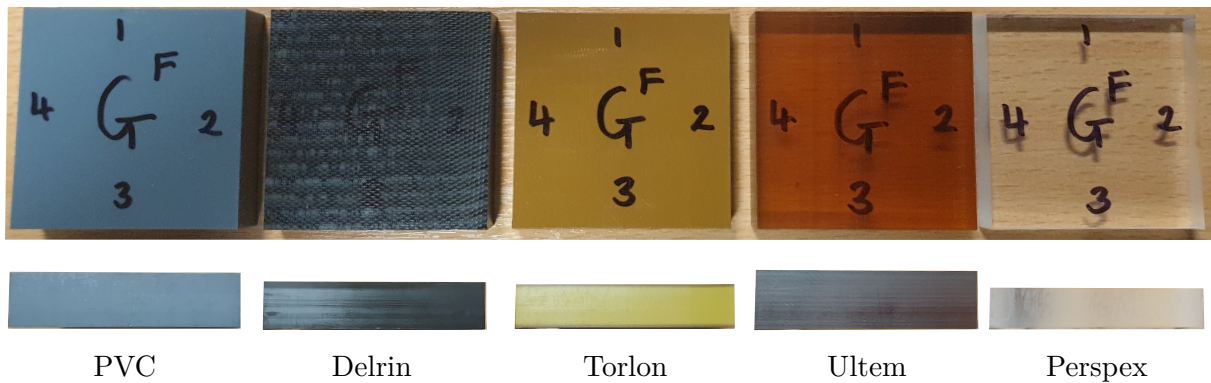
- The conditions of the fluid application should, as far as possible, ensure that the mating surfaces are sufficiently saturated, such that all potential gas-filled interfacial voids should be replaced with completely fluid-filled voids upon mating.

## 7.3 Experimental Methodology

Theoretical model at hand, the remainder of this chapter turns the focus towards the experimental characterisation of impulsive solid-solid interfacial breakdown. The present section provides an overview of the experimental methodology, which includes details pertaining to surface roughness characterisation, experimental design, and arrangements relating to the conduction of breakdown experiments.

### 7.3.1 Test Chamber and Circuit

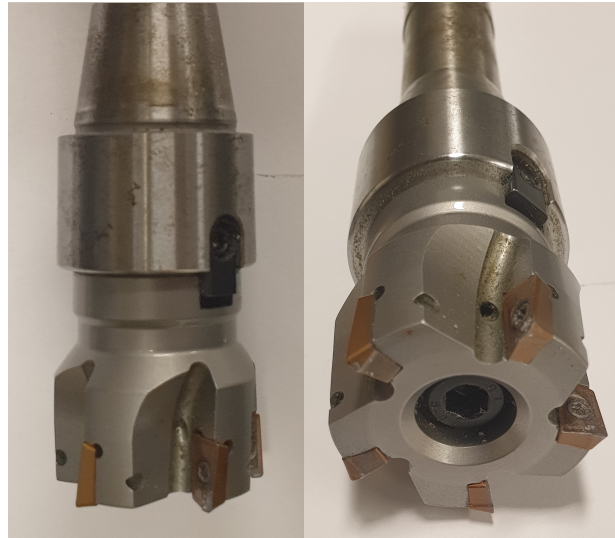
Breakdown tests were conducted on the assembled interfaces using the test chamber shown in Figure 7.16. The sealed main chamber housed a custom-designed sample holder that accommodated two 50 by 50 mm square samples cut from large sheets (Figure 7.17), where the relevant surfaces to be placed in contact were treated using a shoulder mill [46], pictured in



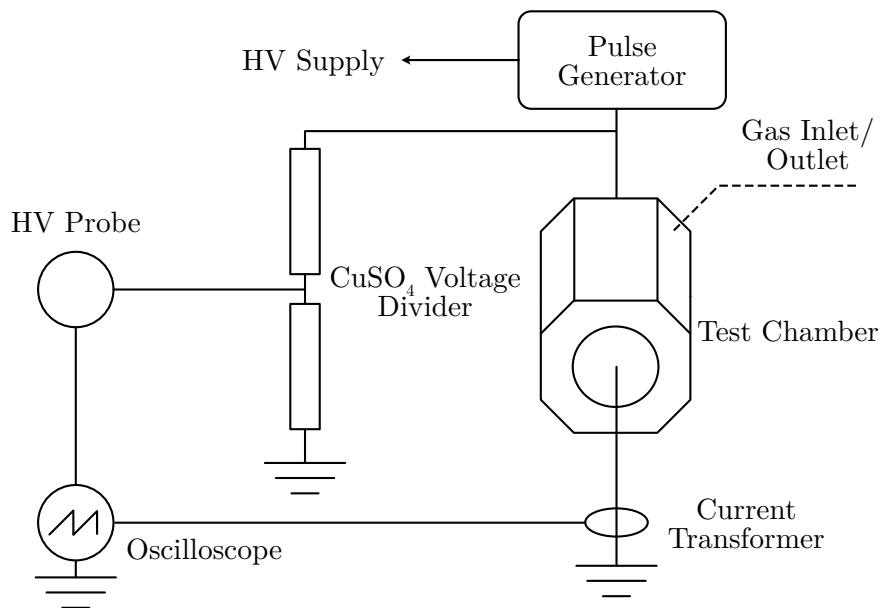
**Figure 7.17:** Photographs of the five types of material samples used within this experimental work, labelled with the material name. Markings on the samples also shows the method used for sample and data management. Interfaces were identified by means of their material, a letter identifier, and a numerical value for the face number. These were used internally only, and have been omitted for simplicity in the presentation of the results.

Figure 7.18. Each pair of samples were held in contact by two spring-loaded ball bearings fitted inside the top edge of the holder. The apparent contact pressure at the interface was therefore kept consistent via the downforce exerted by the deformation of the springs, estimated in the range of 10's of kPa based on the measured spring constant and deformation distance. The assembled sample holder was secured inside the sealed chamber, where an adjustable brass ball-bearing electrode of radius 3.5 mm was positioned in light contact with the interface formed between the solid samples. The base of the sample holder therefore also acted as the ground (plane) electrode. While the chamber can be pressurised with different gases, the present work focused only on breakdown in laboratory air at atmospheric pressure.

The test chamber was connected in accordance with the circuit diagram shown in Figure 7.19. Two variations of the circuit were used, corresponding to the two different rates of voltage rise,  $dU/dt$ , which were investigated in this work. The first incorporated a custom-built stacked Blumlein pulse forming line following the topology shown in [47], charged to 30 kV using a Glassman HV power supply through a  $1\text{ M}\Omega$  charging resistor, and with a nominal multiplication factor of 4. The generator was triggered using a self-breaking spark-gap, and was used in combination with a copper sulphate ( $\text{CuSO}_4$ ) divider (1:8) and a Northstar PVM-5 HV probe (1:1000, 80 MHz nominal bandwidth) for voltage monitoring. The second circuit substituted the Blumlein generator for a Samtech TG-01 trigger generator capable of generating impulses with a peak voltage of 35 kV. For this configuration, only the PVM-5 probe was used since the peak voltage was sufficiently low to not necessitate the divider. The Blumlein generator provided impulses of  $\approx 50\text{ ns}$  rise-time corresponding to approximately  $2400\text{ kV}/\mu\text{s}$ , while the



**Figure 7.18:** Photographs of the shoulder mill from [46] used to cut and treat each of the mating surfaces.



**Figure 7.19:** Circuit diagram of the experimental test circuit for solid-solid interface breakdown tests. The pulse generator was either a custom-built stacked Blumlein [47] triggered using a self-breaking spark-gap, or a Samtech TG-01 trigger generator. In the latter case, the  $\text{CuSO}_4$  voltage divider was not necessary due to the lower peak voltage. Image adapted with permission from [45], © IEEE 2024.

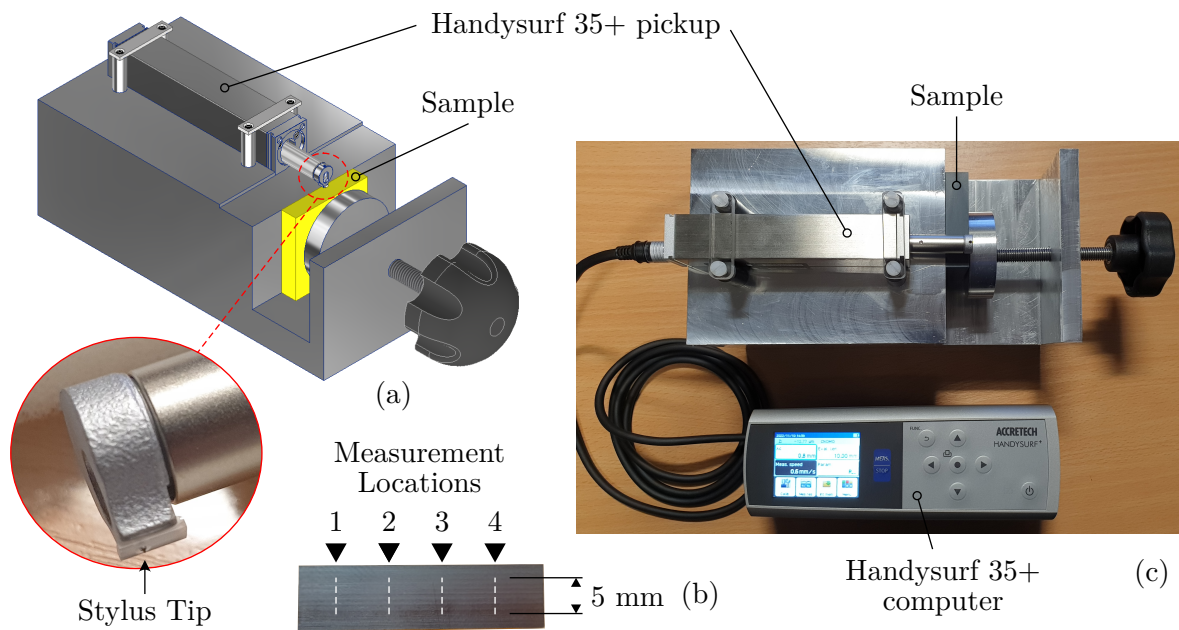


**Figure 7.20:** (a) 3D CAD model of the Handysurf 35+ manual profilometer [48] and measurement system, including a solid sample shown in yellow and magnified photograph of the diamond measurement tip, (b) Diagram showing the four measurement locations used for roughness measurements, and (c) photograph of the full roughness measurement system, including the included computer for data export and processing.

Samtech TG-01 produced impulses of  $\approx 100 \mu\text{s}$  resulting in a value of  $dU/dt$  of  $\approx 0.35 \text{ kV}/\mu\text{s}$ . For both circuits, current waveforms were recorded using a Pearson model 6600 current transformer ( $0.1 \text{ V/A}$ , useful rise-time  $5 \text{ ns}$ ), which were simultaneously captured alongside voltage waveforms on a Tektronix TDS3045C digital oscilloscope ( $500 \text{ MHz}$  bandwidth,  $5 \text{ GS/s}$ ).

### 7.3.2 Surface Roughness Characterisation using Motifs

As has been discussed in Chapter 2 and again in Section 7.1, the roughness characteristics of the surfaces in contact can impact the interfacial breakdown strength, due to their role in determining the nature of interfacial voids. Prior to breakdown experiments (which are destructive by nature), all surfaces used in this work were subjected to surface characterisation.

To do so, surface profiles at four evenly-spaced intervals across each material sample were taken using the Accretech “Handysurf 35+” profilometer [48] across evaluation lengths of  $5 \text{ mm}$ , details of which are shown in Figure 7.20. The instrument features a diamond-tipped mechanical stylus of  $2 \mu\text{m}$  tip radius, and although the profilometry method is mechanical in nature, the downward stylus force of only  $0.75 \text{ mN}$  (estimated pressure of  $\approx 60 \text{ MPa}$ , far lower than the ball indentation

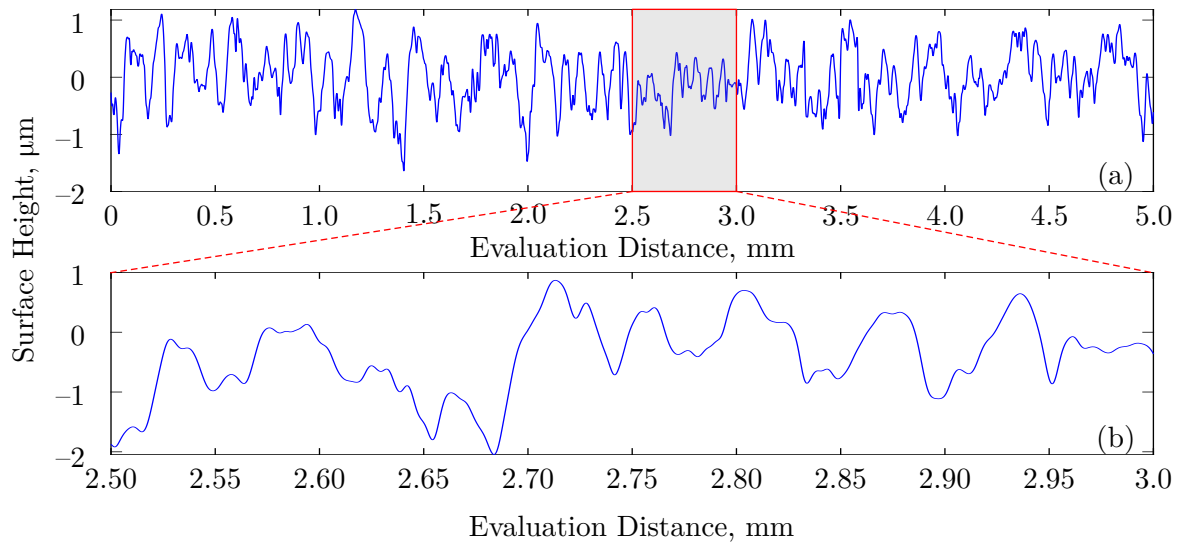


**Figure 7.21:** Example of a measured primary height profile using the Handysurf 35+ across an evaluation length of 5 mm alongside a magnified segment to show detail. This example profile was taken from a PVC sample.

hardness of all materials involved) was sufficiently small to not inscribe any of the surfaces, and therefore would not affect the breakdown results. An example of a typical surface height profile measured across one surface is shown in Figure 7.21. Broadly, two sets of information were required from the raw surface profile data (also referred to as the *primary profile* which is used interchangeably here): (i) appropriate and representative measure(s) of the surface condition of a given surface, and (ii) the surface parameters characterising the interface as the contact between an equivalent surface and an ideal rigid plane [49]. The method of *motif profiles* as described in the ISO-12085 standard [50] was used for this purpose, an outline of which is provided in the following.

Using the example primary profile of Figure 7.21 as reference, a single *motif* represents a single *feature* of the primary profile, where the entire profile can be decomposed into a chain of motifs, shown in Figure 7.22(a) and (b). Corresponding to the labels of Figure 7.22, the parameters defining the  $i$ -th motif along the profile are as follows [50]:

- $H_i$  : Height between the leftmost motif peak and the deepest motif valley.
- $H_{i+1}$  : Height between the rightmost motif peak and the deepest motif valley.
- $T_i$  : The *motif depth*,  $T_i = \min(H_i, H_{i+1})$ .
- $R_i, W_i$  : Mean height,  $R_i = (H_i + H_{i+1})/2$ , of the motif peaks.
- $AR_i, AW_i$  : Horizontal distance between the left and right peaks of the motif.

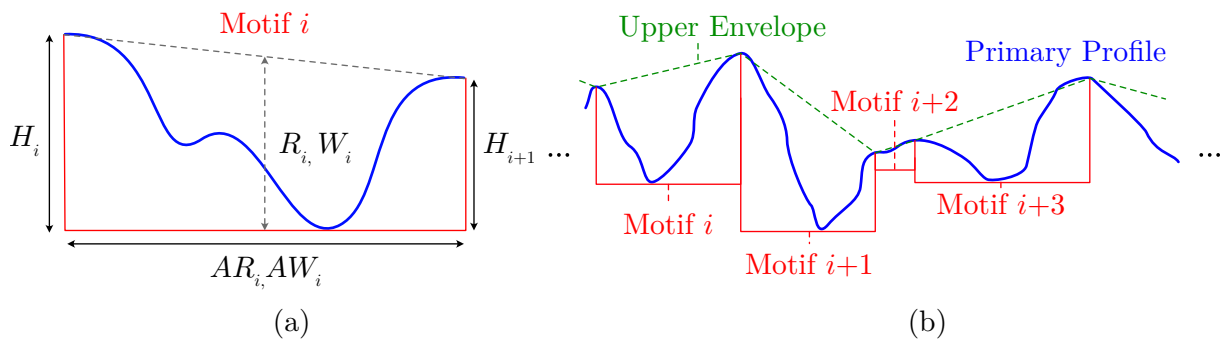


**Figure 7.22:** Diagram of an example (a) single motif characterising a single surface feature, labelled with relevant parameters listed in the main text, (b) motif profile composed of a chain of single motifs that can be extracted from the primary profile, and the upper envelope based on the connection of the motif profile. Imaged adapted with permission from [45], © IEEE 2024.

Conceptually, the chain of motifs along the primary profile are collectively named the *roughness motif profile*, representing the short wavelength variations of the surface. The *upper envelope* [Figure 7.22(b)] is an additional profile formed by connecting the peaks of all *roughness motifs*. By repeating the motif decomposition of the upper envelope, the *waviness motif profile* can be extracted, providing a quantitative measure of the longer wavelength, larger undulations, of the rough surface profile. The decomposition algorithm is hereby summarised for completeness.

The process to obtain the roughness and waviness motif profiles differ only by a single step, therefore, it will be described for the former only, with the necessary changes for the waviness computation appended at the end of the description. As outlined by the ISO-12085 [50] standard, the motif algorithm involves an iterative process over *segments* of the primary profile. A *segment* is defined as a portion of the primary profile that may contain one or more *motifs*, as illustrated in Figure 7.22(b). To divide the primary profile into a set of initial segments, a *limit value* of  $A = 0.5$  mm is first defined according to the standard, then the algorithm is as follows:

1. Divide the total length of the primary profile into sections of  $A/2$ , which provides  $n$  consecutive *segments*, ignoring any non-integer excess.
2. Compute the total  $y$ -bound,  $HR_j$ , of each segment with index  $j$ , based on the maximum and minimum heights of the segment.
3. Peaks and valleys of each segment must be determined based on the peak prominence value,  $H_{\min}$ , defined as 5% of the average value of  $HR_j$ , such that

$$H_{\min} = \frac{0.05}{n} \sum_{j=1}^n HR_j. \quad (7.46)$$

4. The profile between consecutive peaks which were identified in the previous step are considered temporary motifs. The initial segments formed from step 1 are then re-defined based on the motif heights contained within the segments  $j$  based on the next step.
5. Iterating over each motif regardless of the segment in which it is contained, a new segment is formed if the leftmost peak of a motif has no other peak higher than it within a distance  $A$  of the selected peak. This is repeated for each motif until all motifs are part of a segment.

The next stage is to combine the motifs within each segment. Iterating over each segment, the following conditions must be met for two motif candidates inside one segment to be combined into a single motif:

1. When considering two adjacent motifs as a single motif, their shared peak must be lower than or equal to either the leftmost or rightmost peaks, i.e.,  $(H_{i+1} \leq H_i) \vee (H_{i+1} \leq H_{i+2})$ .
2. When considering two adjacent motifs as a single motif, the motif depth of the *combined* motif,  $T_c = \min(H_i, H_{i+2})$ , must be greater than or equal to the motif depths,  $T_i$ , of *both* individual motifs treated separately, i.e.,  $(T_c \geq T_i) \wedge (T_c \geq T_{i+1})$ .
3. When considering two adjacent motifs as a single motif, the motif depths of the individual motifs treated separately,  $T_i$ , must be lower than or equal to a value of  $0.6T_c$ , i.e.,  $(T_i \leq 0.6T_c) \vee (T_{i+1} \leq 0.6T_c)$ .

The above criteria is applied over each segment and repeated, until no additional connections can be made within each segment. Once complete, *all* motifs within the evaluation range must be connected. To do so, a fourth condition is required to be met for two adjacent motifs to be combined:

4. When considering two adjacent motifs as a single motif, the combined motif width should be shorter than or equal to the limit value  $A$ , i.e.,  $(AR_i + AR_{i+1}) \leq A$ .

All four conditions are repeatedly checked on each pair of motifs along the evaluation length until no additional motifs can be combined. One final corrective step must then be applied to ensure that no individual peak or valley, which are unusually high (or low), disproportionately affects the final computed motif profile. Visiting each motif once again:

1. Determine the *standard height*,

$$h_s = \mu_T + 1.65\sigma_T, \quad (7.47)$$

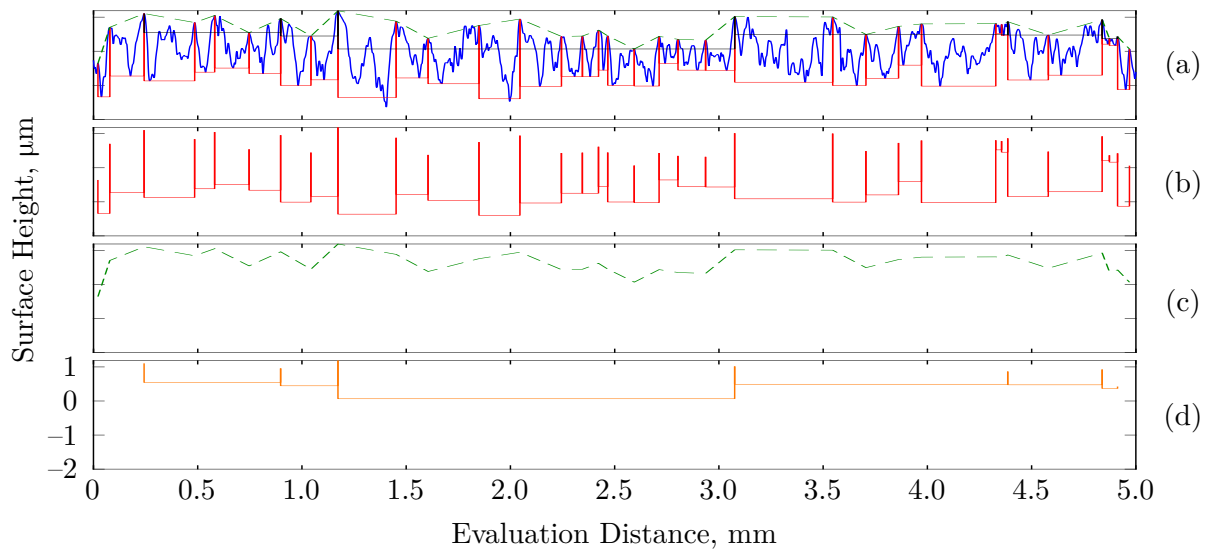


**Figure 7.23:** Example of the decomposed primary profile of Figure 7.21 using the motif method. (a) Combined plot of primary profile, roughness motif, upper envelope, and waviness motif, (b) extracted roughness motif profile, (c) extracted upper envelope, (d) extracted waviness motif profile.

where  $\mu_T$  and  $\sigma_T$  are the mean and standard deviation of all motif depths along the profile.

2. For each motif, if either  $H_i$  or  $H_{i+1}$  is greater than  $h_s$ , the corresponding peak or valley enclosed within this motif should be lowered so that its height equals  $h_s$  relative to its adjacent peaks and valleys.

Once the correction process is complete, the remaining motif profile is the final *roughness motif* of the primary surface profile, comprised of a string of motifs along the evaluation length as shown in Figure 7.23. To determine the *waviness motif*, the entire algorithm is repeated using the *upper envelope* in place of the primary profile and using a limit value of  $B = 2.5$  mm instead of  $A$ . An example of an extracted waviness motif has been included within Figure 7.23. Consider now two rough surfaces in contact, both with roughness and waviness motif profiles obtained using the above algorithm. A number of *motif parameters* can be calculated based on the characteristics of the motif profiles. Let the superscript  $[s]$ <sup>||</sup> denote the index for either the first surface ( $[s] = 1$ ) or second surface ( $[s] = 2$ ), then:

- $R^{[s]}$  — Average roughness motif heights across all  $R_i^{[s]}$ .
- $W^{[s]}$  — Average waviness motif height across all  $W_i^{[s]}$ .

<sup>||</sup>Where the superscript position and square brackets have been used here to differentiate between the parameters associated with individual motifs, not to be confused with exponentiation.

- $AR^{[s]}$  — Average roughness motif width across all  $AR_i^{[s]}$ .
- $AW^{[s]}$  — Average waviness motif width across all  $AW_i^{[s]}$ .
- $SR^{[s]}$  — RMS of roughness motif heights across all  $R_i^{[s]}$ .
- $SW^{[s]}$  — RMS of waviness motif heights across all  $W_i^{[s]}$ .
- $SAR^{[s]}$  — RMS of roughness motif widths across all  $AR_i^{[s]}$ .
- $SAW^{[s]}$  — RMS of roughness motif widths across all  $AW_i^{[s]}$ .

The parameters for the equivalent surface are then given by [49]

$$\begin{aligned}
R^{[eq]} &= R^{[1]} + R^{[2]}, & W^{[eq]} &= W^{[1]} + W^{[2]}, \\
AR^{[eq]} &= \frac{1}{2} (AR^{[1]} + AR^{[2]}), & AW^{[eq]} &= \frac{1}{2} (AW^{[1]} + AW^{[2]}), \\
SR^{[eq]} &= \sqrt{SR^{[1]2} + SR^{[2]2}}, & SW^{[eq]} &= \sqrt{SW^{[1]2} + SW^{[2]2}}, \\
SAR^{[eq]} &= \sqrt{SAR^{[1]2} + SAR^{[2]2}}, & SAW^{[eq]} &= \sqrt{SAW^{[1]2} + SAW^{[2]2}},
\end{aligned} \tag{7.48}$$

where [eq] represents the equivalent surface. According then to [49] following the methods of [24], the equivalent surface properties  $\eta$ ,  $\sigma$ , and  $\beta$  required as input for the breakdown model of Section 7.2 can be estimated as

$$\begin{aligned}
\eta^{[eq]} &= \frac{1.2}{AR^{[eq]}}, \\
\sigma^{[eq]} &= 0.35 \sqrt{W^{[eq]2} + SW^{[eq]2}}, \\
\beta^{[eq]} &= \frac{AR^{[eq]2} + SAR^{[eq]2}}{16R^{[eq]}},
\end{aligned} \tag{7.49}$$

where the reader is reminded that  $\eta$ ,  $\sigma$ , and  $\beta$  are the surface asperity density, standard deviation of asperity heights, and mean asperity radius, respectively. One additional measure of general surface morphology is introduced here, the *mean asperity aspect ratio* [45] defined by

$$a^{[eq]} = \frac{R^{[eq]}}{\beta^{[eq]}}, \tag{7.50}$$

which is the ratio of the mean motif height to the mean asperity radius, hereby used as an indication of the aspect ratio of the equivalent surface asperity. This dimensionless ratio can be used as measure of the *sharpness* of the asperity, as it provides an indication of the width of an asperity tip compared to its height, as illustrated in Figure 7.24. The reader is reminded of the surface height distributions included as Appendix B.4 that support the use of the equivalent

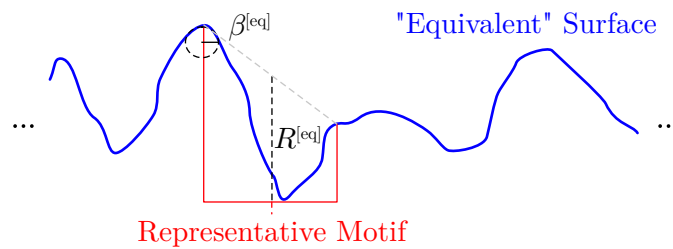


**Figure 7.24:** Diagram showing the features used to characterise the asperity aspect ratio.

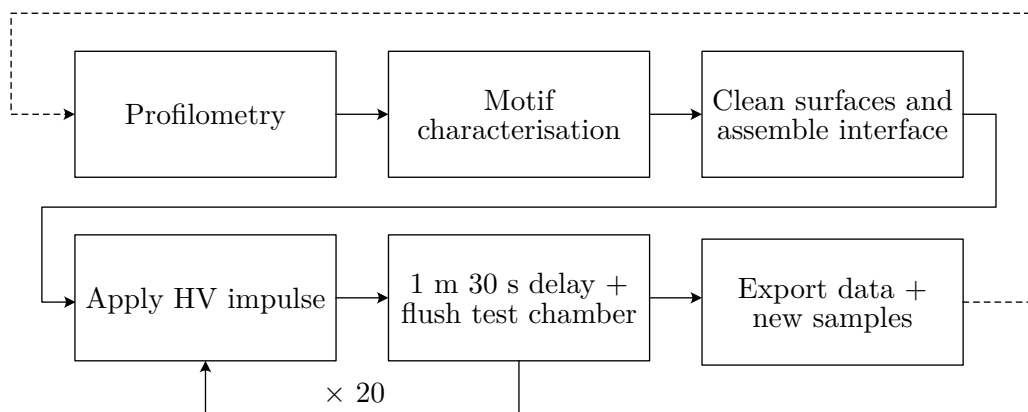


**Figure 7.25:** Flowchart of the experimental procedure followed for the impulse breakdown tests of solid-solid interfaces.

surface method. The parameters described by equations (7.48) to (7.50) are those most important in characterising the equivalent surface roughness of the interface, and are referred to within the analysis and discussion of Section 7.4, and within Chapter 8.

### 7.3.3 Experimental Procedure

Figure 7.25 provides an outline of the experimental procedure. Sample preparation involved first taking surface roughness measurements of the sample surfaces, following Section 7.3.2. Each surface was then cleaned using a 70% ethanol-water solution and with low-lint paper, with care taken to remove any residue or other foreign material that may become caught between the surface when contact is made. The holder with dried and assembled samples was then secured, with the HV electrode positioned such that it would be in light contact with the samples, before the chamber was sealed.

Each interface (formed between one pair of samples) was subjected to 20 HV shots, with a 1 min

30 s delay between each shot to ensure that any residual charges could fully dissipate. This was confirmed using a Trek 346 electrostatic voltmeter during initial tests, which saw the surface potential drop to negligible levels rapidly after interfacial discharge. During this time, the test chamber was also flushed and replaced with fresh air. As the stored energy for either of the pulse generation systems used in this work was quite low, 20 shots could be applied to one interface without significant surface damage. The reader is referred to the supplementary material of the publication [45], which show breakdown voltages plotted against the shot number, confirming that these experimental arrangements avoided the skewing of results with repeated shots.

For each polarity, a total of 40 shots were applied to two different interfaces. This was done to ensure that the breakdown characteristics would largely be the same for an interface of the same material. However, it is emphasised that the first 20 shots on the first interface may not be directly comparable to the second 20 shots on the second interface, since their surface roughness characteristics would not be identical. Thus, the distinction between the first 20 and second 20 shots for each material-polarity pair is maintained within the results of Section 7.4.

#### 7.3.4 Breakdown Data Processing and Statistical Treatment

Using the instrumentation described in Section 7.3.1, breakdown voltage waveforms were recorded for each shot. Examples of typical raw oscillograms attained from the 2400 kV/ $\mu$ s and 0.35 kV/ $\mu$ s cases are shown in Figure 7.26(a) and 7.26(b), respectively. To extract the value of breakdown voltage from each waveform, raw oscillograms (i.e., those shown in Figure 7.26) were filtered using a simple moving-average to reject noise and oscillations around the peak. A filter window length of 10 was used in all cases, corresponding to low-pass cut-off frequencies of approximately 200 MHz and 2 MHz for the 2400 kV/ $\mu$ s and 0.35 kV/ $\mu$ s waveforms, respectively. The peak position of filtered waveforms then becomes unambiguous and was taken to be the breakdown voltage. The corresponding time between the beginning of the voltage rise (first zero-crossing of the waveform) and the peak voltage was recorded as the time-to-breakdown. It is remarked that this process is effectively an algorithmic and fully reproducible method of implementing *visual averaging* as often done for breakdown waveforms. Note that the output of the algorithm for every waveform was also subjected to manual inspection to ensure that the correct points were identified.

Each set of 20 breakdown voltage and time-to-breakdown datapoints per dataset were fit to two-parameter Weibull distributions (where it is assumed that the formative time is effectively zero in comparison to the statistical time lag; itself assumed to be given by the Weibull scale parameter in the following), informed by both Kolmogorov-Smirnov and Lilliefors goodness-of-fit

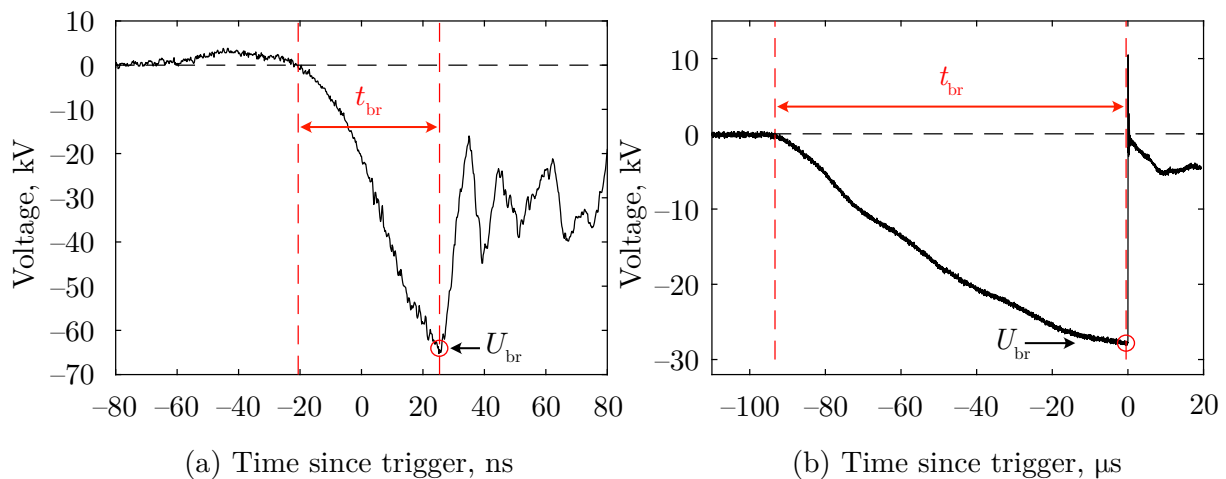


**Figure 7.26:** Oscillograms of typical voltages obtained during breakdown for (a) 50 ns rise-time stacked Blumlein, (b) 100  $\mu$ s rise-time Samtech TG-01 trigger generator. Red circles indicate the identified breakdown voltages, red dashed lines show the identified time-to-breakdown. Both examples shown here are from interfaces formed from Torlon, but were largely similar for all other materials. Image adapted with permission from [45], © IEEE 2024.

tests at 95% confidence. The probability distribution (PDF) was therefore of the form

$$f(p; \alpha, \beta) = \frac{\beta}{\alpha} \left(\frac{p}{\alpha}\right)^{\beta-1} \exp\left[-\left(\frac{p}{\alpha}\right)^\beta\right], \quad (7.51)$$

where  $p$  represents either voltage or time,  $\alpha$  is the scale parameter, and  $\beta$  is the dimensionless shape parameter. The fitting was conducted using the maximum likelihood estimation (MLE) method, which seeks the maximisation of the log-likelihood function  $L$ :

$$\mathbb{L} = \prod_{i=1}^n f_i(p_i, \bar{\theta}), \quad \frac{d \log \mathbb{L}}{d \bar{\theta}} = 0, \quad (7.52)$$

where  $\bar{\theta}$  are the optimal parameters  $\bar{\alpha}$  and  $\bar{\beta}$  that maximise the likelihood function with the number of observations  $n$ , thereby describing the best-fitting distribution and enabling the Confidence Intervals (CIs) to be computed. Within the present context,  $\bar{\alpha}$  is equal to the voltage or time at which 63.2% of samples had failed, which is taken to be the characteristic breakdown voltage or time of the interface ( $\bar{\alpha} = V_b$  or  $\bar{\alpha} = t_b$ , depending on the dataset). It is remarked that a comparison was made between the MLE method and the commonly employed least-squares (LSQ) linear fitting and median ranks approximation, finding that MLE was generally superior at outlier reject for the data handled in this work. For data with no significant outliers, the LSQ and MLE methods provided essentially identical fittings. The reader is referred to Appendix B.8

for example Weibull plots and for a comparison between LSQ and MLE fittings.

To compensate for the varying thicknesses of the different materials (see Table 7.1), a nominal breakdown field value,  $E_{br}$ , was calculated from each obtained breakdown voltage following  $E_{br} = V_{63.2}/d_s$ , where  $d_s$  is the sample thickness and equal to the minimum inter-electrode gap distance. This value is used as a means of comparison between different materials in Section 7.4 as a representative value of the interfacial breakdown strength.

## 7.4 Impulsive Breakdown Results and Discussion

This section moves to discuss the obtained breakdown strength and time-to-breakdown measurements, split into a number of subsections separately discussing the effects of material,  $dU/dt$ , and voltage polarity. Note that a complete set of the raw data, including captured waveforms and roughness data, is available and can be found deposited at the repository [51]. Computed Weibull parameters for all datasets have additionally been included as Appendix B.9.

### 7.4.1 Impulse Breakdown Strength and Material Choice

Figure 7.27 shows  $E_{br}$  and  $t_{63.2}$  with 95% CIs for the 2400 kV/ $\mu$ s and 0.35 kV/ $\mu$ s cases, and for all material-polarity pairs. Dashed and dash-dot lines further show  $E_{br}$  in absence of any solid interface at 10 mm separation for negative and positive polarities, respectively. Note that in the specific electrode configuration used here, the 2400 kV/ $\mu$ s case saw almost identical negative and positive breakdown voltages in the no-solid case. This suggests that the gap distance (10 mm) used for the no-solid tests in the 2400 kV/ $\mu$ s case is close to the *critical gap distance*,  $d_{crit}$ , of this electrode topology, where the breakdown strengths become the same regardless of polarity as described in Hogg *et al.* [52]. The authors of [52], and references therein, indicated that this phenomenon may be attributed to the development and transport of space charge in non-uniform fields. This explanation is supported by the observed differences in breakdown time between positive and negative impulses shown in Figure 7.27(a) and 7.27(c), despite near-identical breakdown voltages. Development of sufficient space charge may affect the overall  $dU/dt$  of the voltage across the gap when nearing the moment of breakdown, leading to a difference in the time-to-breakdown despite the breakdown occurring at the same voltage magnitude. It should be noted that additional no-solid breakdown tests were conducted using a range of gap distances (around 10 mm, since materials were not of equal thickness), and little variation in the normalised breakdown field was found. The relative positions of  $E_{br}$  between the no-solid case

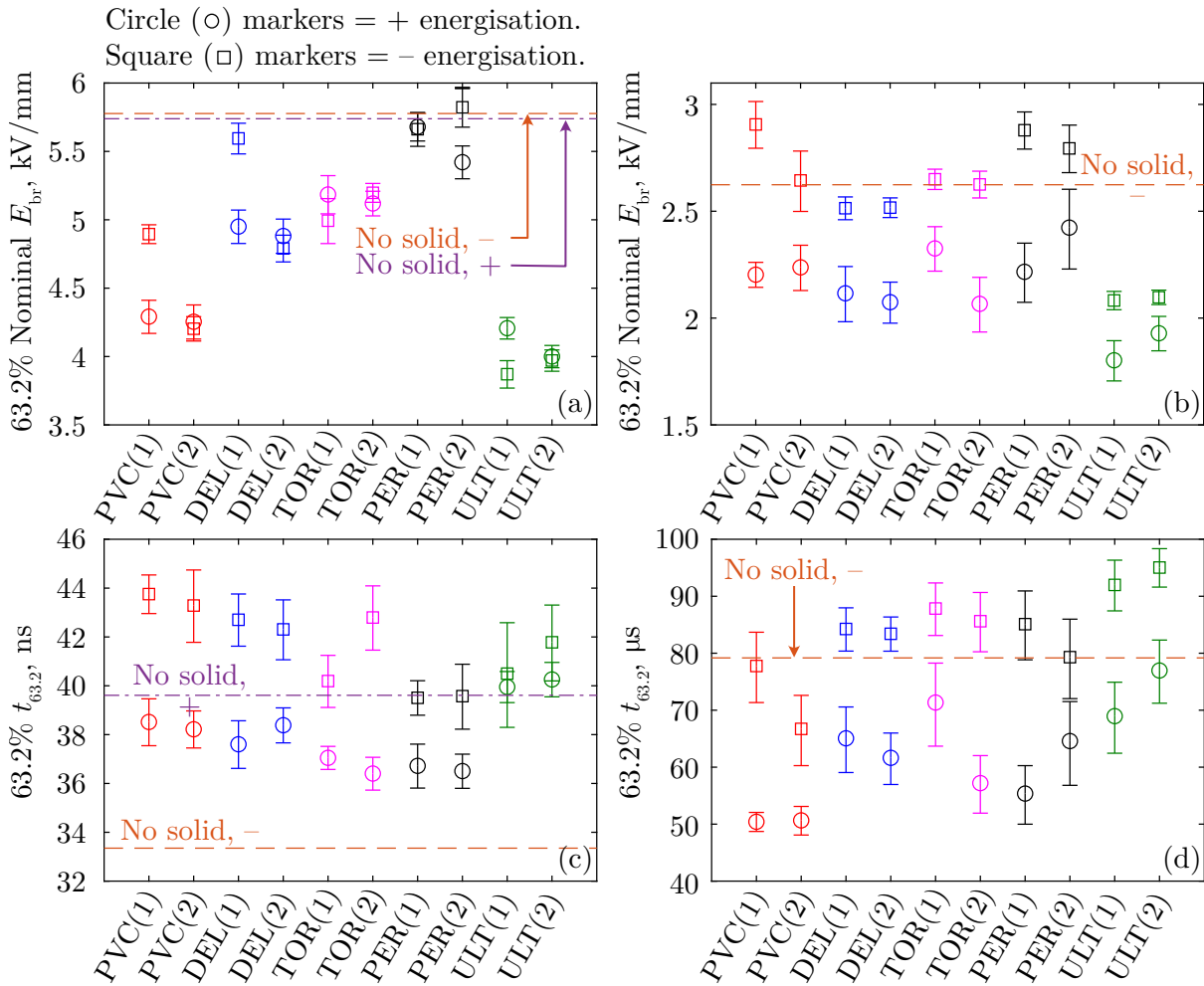


**Figure 7.27:** Nominal breakdown fields,  $E_{br}$ , for all materials and both polarities in the (a) 2400 kV/ $\mu$ s case, (b) 0.35 kV/ $\mu$ s case. Time to breakdown,  $t_{63.2}$ , for all materials and both polarities in the (c) 2400 kV/ $\mu$ s case, (d) 0.35 kV/ $\mu$ s case. Orange and purple dash-dot lines indicate the corresponding  $E_{br}$  and  $t_{63.2}$  values in the case of an air gap with no solid included. These are absent for positive polarity in sub-figures (b) and (d) since breakdown did not occur. Error bars show the 95% confidence intervals. Image adapted with permission from [45], © IEEE 2024.

and breakdown including an interface of Figure 7.27 would therefore remain the same.

Believed to be resulting from the same phenomenon, positive breakdown could not be attained in the no-solid case for 0.35 kV/ $\mu$ s impulses, but negative breakdown occurred consistently; indicating that in this case, 10 mm may in fact be smaller than  $d_{\text{crit}}$  as defined in [52]. This suggests that  $d_{\text{crit}}$  may also be dependent on  $dU/dt$ . It should further be noted that upon the introduction of a solid interface, the 0.35 kV/ $\mu$ s case sees negative breakdown be consistently higher than positive breakdown [Figure 7.27(b)], but the 2400 kV/ $\mu$ s case remains inconclusive [Figure 7.27(a)]. This further suggests that the existence of the solid interface may also affect the critical distance, but investigation of this phenomenon is left as a subject for future work.

Based on Figures 7.27(a) and 7.27(b), it was observed that the impulsive breakdown strengths of the solid interfaces were not only vastly inferior to that of bulk solids (typically in the range of MV/cm, e.g., see [53, 54]), but in the majority of cases, reduced the system breakdown strength to significantly below that of just air alone. In [8], authors have suggested that the tracking resistance of the interfacial contact spots may be important in determining the overall breakdown strength of a solid interface. This was under the consideration that the interfacial voids which partially discharge must subsequently be chained together via breakdown of the contact spots, leading to full interfacial breakdown as was discussed within Section 7.2.4. In this work, the low interfacial mating pressure ( $\approx 10$ 's kPa) is believed to have the equivalent effect of significantly reducing the contact-spot tracking strength. In this way, it is theorised that under these conditions, the interfacial contact spots do very little to obstruct the evolution of breakdown across the length of the interface. Initial discharges which form within the interfacial voids (due to the enhancement of the electric field inside them) can readily chain together, such that the breakdown strength of the interfacial voids alone essentially determine the breakdown strength of the whole interface. Now considering that the electric field is enhanced due to dielectric polarisation inside the voids (and therefore for the same voltage stress, the field will be higher at the solid interface than in the no-solid case), it explains the observed reduction of the interfacial breakdown strength below that of just air under the same electrode and voltage conditions. This may be a critical design issue for insulating systems which incorporate solid dielectric interfaces, showing that a loss of interfacial pressure may result in the reduction of the system breakdown strength to below that of solely gas insulation.

When comparing across materials, one should do so with caution as the surface roughness conditions (even between the same materials) will not be identical. However, the breakdown results of Figure 7.27 are reasonably consistent for interfaces of the same material, suggesting

that the surface morphologies were also of fair consistency between samples. Since the resulting surface condition after cutting is also a characteristic of the material itself, it would therefore not be unreasonable to draw some form of comparison. Considering the 95% CIs (and across breakdown results of the same polarity), PVC, Delrin, and Torlon interfaces appeared to have similar breakdown strengths and times-to-breakdown in the 0.35 kV/ $\mu$ s case. For the 2400 kV/ $\mu$ s case, Delrin and Torlon interfaces remained similar, with PVC falling below by approximately 1 kV/mm in nominal breakdown field for three out of four tests. Perspex interfaces could be considered the highest performing of the materials tested, with a generally higher nominal breakdown strength. Most notably, however, is that Ultem interfaces were significantly weaker than those formed by all other materials. A difference of  $\approx 2$  kV/mm compared to Perspex interfaces was observed in the 2400 kV/ $\mu$ s case, and  $\approx 1$  kV/mm in the case of 0.35 kV/ $\mu$ s impulses. Inspection of the raw values of  $V_{63.2}$  rather than nominal fields indicated that Ultem interfaces possessed similar breakdown voltages to all other materials, despite being almost 4 mm thicker when compared to the thinnest materials (Torlon and Perspex).

For the 2400 kV/ $\mu$ s case, the emergence of this ranking is believed to be the difference in sample thickness. A direct correlation between the sample thicknesses of Table 7.1 and  $E_{br}$  can be seen, where a thicker sample resulted in a lower value for  $E_{br}$ , despite being normalised by the gap distance. It is believed that the most important factor here is the *rate of change of field*,  $dE/dt$ , rather than the applied  $dU/dt$ . The developed field for thinner samples at a certain fixed value of  $dU/dt$  will rise with a greater value of  $dE/dt$ , which likely results in a higher  $E_{br}$  based on the typical behaviour of gas breakdown in the present overstressed impulsive regime. The reader is reminded of the conclusions of Chapter 4 relating to the effects of  $dE/dt$  (or denoted  $\mathcal{D}$  as used in Chapter 4) on overstressed breakdown in gas. Considering that the interfacial breakdown is determined by intra-cavity gas discharge, the results would suggest that the increased  $E_{br}$  of thinner interfaces due to the effects of greater  $dE/dt$  is dominant over any corresponding reduction of  $E_{br}$  resulting from decreased  $d_s$ . This observation, however, is not entirely clear for the 0.35 kV/ $\mu$ s case, suggesting that the above is only a partial explanation, or that the aforementioned behaviour is dominant only for the faster-rising regime. In both cases, Ultem was also observed to possess a far lower  $E_{br}$  compared to the other materials, even when accounting for the greater thickness. It is believed that the surface roughness characteristics of Ultem may provide a secondary process which explains this observation, and is discussed further in Section 7.4.5.

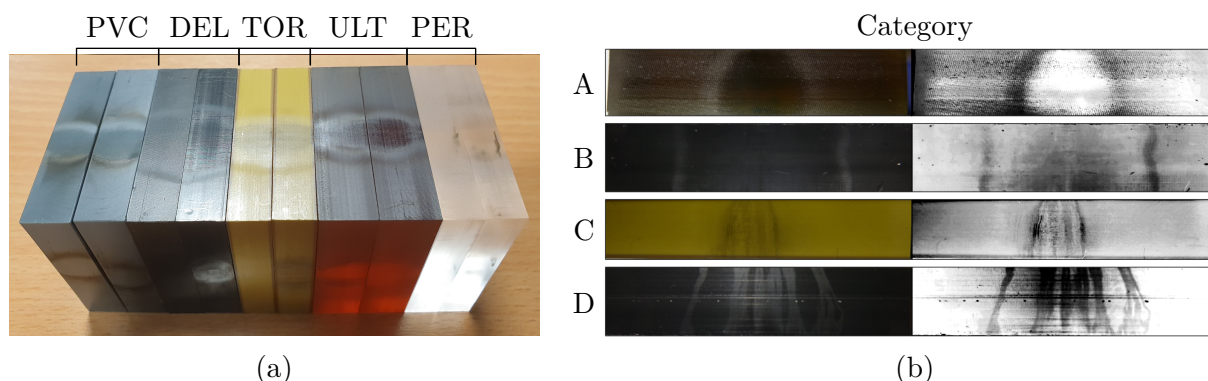


**Figure 7.28:** Photographs of (a) each type of solid-solid interface after 20 breakdown shots, (b) the four identified categories of post-breakdown traces left after 20 shots. Descriptions are given in the main text. Left images show photographs, right images are contrast and brightness adjusted greyscale versions for clarity. Materials shown from top to bottom: Ultem, Delrin, Torlon, Delrin. Image (b) adapted with permission from [45], © IEEE 2024.

#### 7.4.2 Post-breakdown Surface Analysis

As previously mentioned, the low energy output of both generators used in this work ensured that no significant surface damage was induced by repeated breakdown (in terms of burning or drastic modification of the surface texture). However, the discharge plasma channels left visible marks across the interface which show the discharge path(s) taken over the 20 breakdown shots. Only PVC and Torlon exhibited (light) carbonisation, and only for positive 2400 kV/ $\mu$ s impulses. Figure 7.28 shows several examples of the surfaces photographed after testing. Considering all experiments that were conducted, four separate and distinct cases could be identified based on the shape, number, and size of the visible traces on the post-breakdown surfaces; descriptions of which are listed below (following the labels of Figure 7.28):

- A) Central plasma channel with a small region of lateral expansion. Indicates that the discharge paths were focused down the line of maximum (Laplacian) field for all 20 shots applied to the interface.
- B) One single, central, plasma channel; but the expansion region was significant wider (two to three times the width) than those in (A).
- C) Multiple plasma channels originate from the spherical HV electrode that branch across the interface following the Laplacian field lines. Indicates that repeated discharges did not necessarily follow the same path.
- D) Multiple plasma channels bridge the gap as in (C), however, some channels originate not from the spherical HV electrode, but from the electrode edges (see Figure 7.29). This

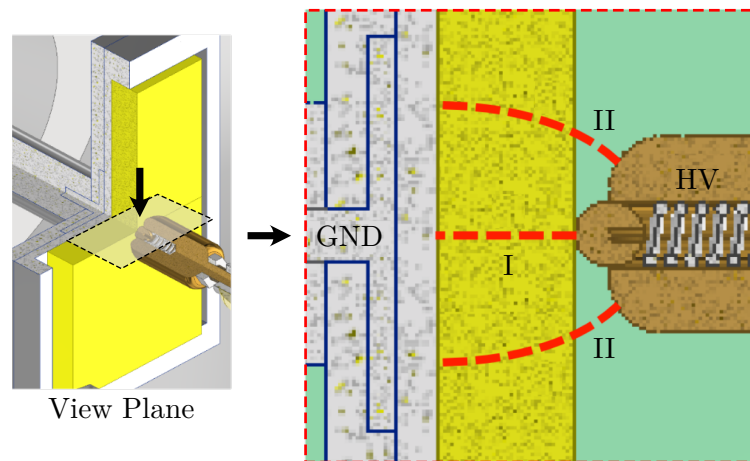


**Figure 7.29:** Magnified image of the contact between the HV electrode and the interface. Breakdown path labelled I corresponds to categories A and B, while paths labelled II delineates the longer path taken (through the gas first) as in category D. Image adapted with permission from [45], © IEEE 2024.

indicates that some shots took a far longer discharge path (through the air first) to bridge the interface that did not necessarily align with the critical path based on the Laplacian field.

The analyses and discussion of the following Sections 7.4.3 and 7.4.4 make reference to the post-breakdown trace definitions above and the breakdown results of Figure 7.27.

### 7.4.3 Effects of Voltage Polarity

For the  $0.35 \text{ kV}/\mu\text{s}$  case [Figure 7.27(b)], the negative nominal breakdown fields were consistently higher than that of positive polarity for all materials. This appears consistent with the theory of gas-void discharge driven interfacial breakdown, though clearly indicates that the critical distance (as discussed in Section 7.4.1) must now be different, considering that this contrasts the results in just air. Higher negative-polarity breakdown voltages compared to positive-polarity for the same voltage magnitude is a well-known phenomenon in electronegative gases, generally attributed to negative space-charge effects and higher inception voltages for negative streamers [52], but as discussed in Section 7.4.1, applies only if the configuration is far from the critical gap distance. Comparing negative breakdown to positive breakdown for the  $2400 \text{ kV}/\mu\text{s}$  case [Figure 7.27(a)], this tendency was not observed, and the results were mixed. No notable correlations were observed between the polarity and the discharge path category for either value of  $dU/dt$ .

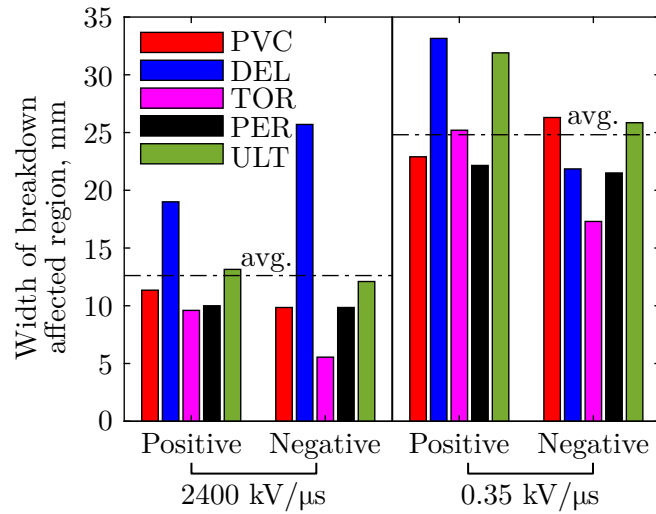


**Figure 7.30:** The maximum width of the region affected by breakdown on the sample surfaces after 20 shots over all cases. Values shown are the averaged widths of the first and second interfaces per material-polarity pair (20 shots each). Image adapted with permission from [45], © IEEE 2024.

#### 7.4.4 Effects of $dU/dt$

As is evident from Figure 7.27(a) and 7.27(b), increased breakdown voltages were recorded for the faster-rising impulse, behaviour of which is consistent with the impulsive breakdown of gases alone. The same was found for all materials irrespective of polarity, attributed to the magnitude of  $dU/dt$  affecting the amount to which the voltage may additionally increase after the initiation of breakdown, prior to voltage collapse (i.e., the overvoltage, see again the analysis of rates from Chapter 4).

The two different values of  $dU/dt$  used in this work also had significant effects on the paths taken by the discharges, indicated by inspection of the post-breakdown surfaces. All breakdown events induced using the 2400 kV/ $\mu$ s impulse had discharge paths that fell only into category A or B, and those that belonged to category B were exclusively Delrin interfaces. For the discharge paths of 0.35 kV/ $\mu$ s breakdown, these fell exclusively into category C or D, where category C was dominated mainly by Torlon and Perspex interfaces, and D was found for the majority of PVC and Delrin interfaces. The maximum widths of the surface region affected by the breakdown (after all 20 shots) were also measured for each interface, and the average of the two values obtained was calculated for each triplet of  $dU/dt$ , polarity, and material. The resulting data is shown in Figure 7.30.

It is believed that this preference between A/B and C/D is caused by space charge effects: for lower  $dU/dt$ , the slower-rising voltages result in a net charge density near the HV electrode-dielectric-gas triple junction, including inside interfacial voids in its vicinity. The mechanism for this is believed to be electron transport on the rising slope prior to the onset of significant ionisation, similar to the cathode sheath formation simulated in Chapter 6. The net charge accumulated within this region is believed to change the preferential path of breakdown due to the local distortion of the Laplacian electric field. The field at the curved edges of the enclosure which holds the sphere electrode may therefore become enhanced and act as an initial site for avalanches to form, propagating briefly through the gas before reaching the surface (corresponding to paths labelled II in Figure 7.29). The degree to which the field can be distorted before discharge inception may be far lower for high  $dU/dt$ , and the electric field may therefore not stray far from the Laplacian field up to the time of breakdown. This may explain why multiple discharge channels were seen exclusively for the 0.35 kV/ $\mu$ s case, and equally explain the occurrence of case D, where the discharge paths were initiated from the edge of the electrode rather than from the HV tip—also only observed for 0.35 kV/ $\mu$ s impulses. In consequence, the average width of the affected region over all shots for the 0.35 kV/ $\mu$ s case was found to be approximately two times wider than that of the 2400 kV/ $\mu$ s case, as indicated in Figure 7.30—a factor that would be even greater were Delrin to be excluded in the averaging of the 2400 kV/ $\mu$ s data, since it was a clear outlier in this case with the majority of Delrin traces falling into category B rather than A. Delrin, under 2400 kV/ $\mu$ s impulses, formed far wider regions around the central breakdown channel than all other materials. The present data suggests that this is a material-specific property, but further study which potentially explores specific plasma-surface interaction would have to be undertaken to confirm this, which is outside the scope of the present work.

#### 7.4.5 Relationship with Surface Roughness Characteristics

Of the equivalent surface parameters computed following Section 7.3.2, those relevant in capturing the overall morphology of the interfaces include  $R^{[eq]}$ ,  $W^{[eq]}$  and  $AR^{[eq]}$ ,  $AW^{[eq]}$  [12], since the first two provides an indication of the degree of protrusion of surface asperities from the surface median, while the latter two gives an indication of the larger undulations of the surface profile, both of which are related to the size of the void-like gaps formed at the interface which may facilitate the discharge process. As it would be excessive to provide individual measured values for the numerous tested surfaces, Table 7.3 provides averages of these parameters for each material, computed from the average across all samples of the same material, as representative values of the roughness conditions found on the samples used in this work. Based on Figure 7.31,

**Table 7.3:** Representative averages of equivalent surface motif parameters for the materials used in this work. All units are  $\mu\text{m}$ .

Material	$R^{[\text{eq}]}$	$W^{[\text{eq}]}$	$AR^{[\text{eq}]}$	$AW^{[\text{eq}]}$
PVC	6.556	3.881	163.2	960.4
Delrin	2.264	3.472	110.3	879.6
Torlon	5.342	5.131	158.5	1036.5
Perspex	2.823	3.689	122.4	973.4
Ultem	5.026	4.492	128.1	848.5

which plots the nominal breakdown field against the computed values of  $R^{[\text{eq}]}$ ,  $W^{[\text{eq}]}$ ,  $AR^{[\text{eq}]}$ , and  $AW^{[\text{eq}]}$ ; representing the two-surface contact, no clear correlations were found directly between any of the motif parameters and the nominal field. This contrasts the conclusions of past work, e.g., [9]. However, this is primarily believed to be the result of the low contact pressure used in this work. The contact pressure exerted by the holder is much lower compared to other studies (in the range of kPa rather than MPa). Each interface was held together only through a parallel spring arrangement which could easily be overcome by pushing against the samples by hand. In accordance with current theories, low mating pressure tends to increase the size of the interfacial voids, decreases the effective contact area, and reduces the contact spot tracking resistance, hence decreasing the breakdown strength [9].

Under these conditions, however, it is believed that a different characteristic of the rough surfaces may be more impactful in determining the interfacial breakdown strength. Figure 7.32 plots the nominal breakdown strength for all material-polarity pairs against the mean asperity aspect ratio,  $a^{[\text{eq}]}$ , as defined in (7.50). A negative Pearson's correlation coefficient was found for both 2400 kV/ $\mu\text{s}$  and 0.35 kV/ $\mu\text{s}$  cases. Since a higher value of  $a^{[\text{eq}]}$  corresponds to smaller and sharper asperity peaks, it is believed that the higher aspect ratio of these surface features increases the degree of local field enhancement at the interface. Coupled with the low contact pressure and consequent low tracking resistance, it may possibly play a significant role in interfacial breakdown under the conditions studied here. This is in contrast to studies conducted under high mating pressure, wherein many more of these high aspect ratio asperities may be deformed and themselves become the interfacial contact spots. This would act to increase both the total number of contact spots—due to the deformation of more surface asperities—and also to increase the tracking resistance of existing contact spots due to higher local pressure, leading to an overall increase to the interfacial breakdown strength.

The significantly lower breakdown strength of Ultem interfaces is believed to be partially explained

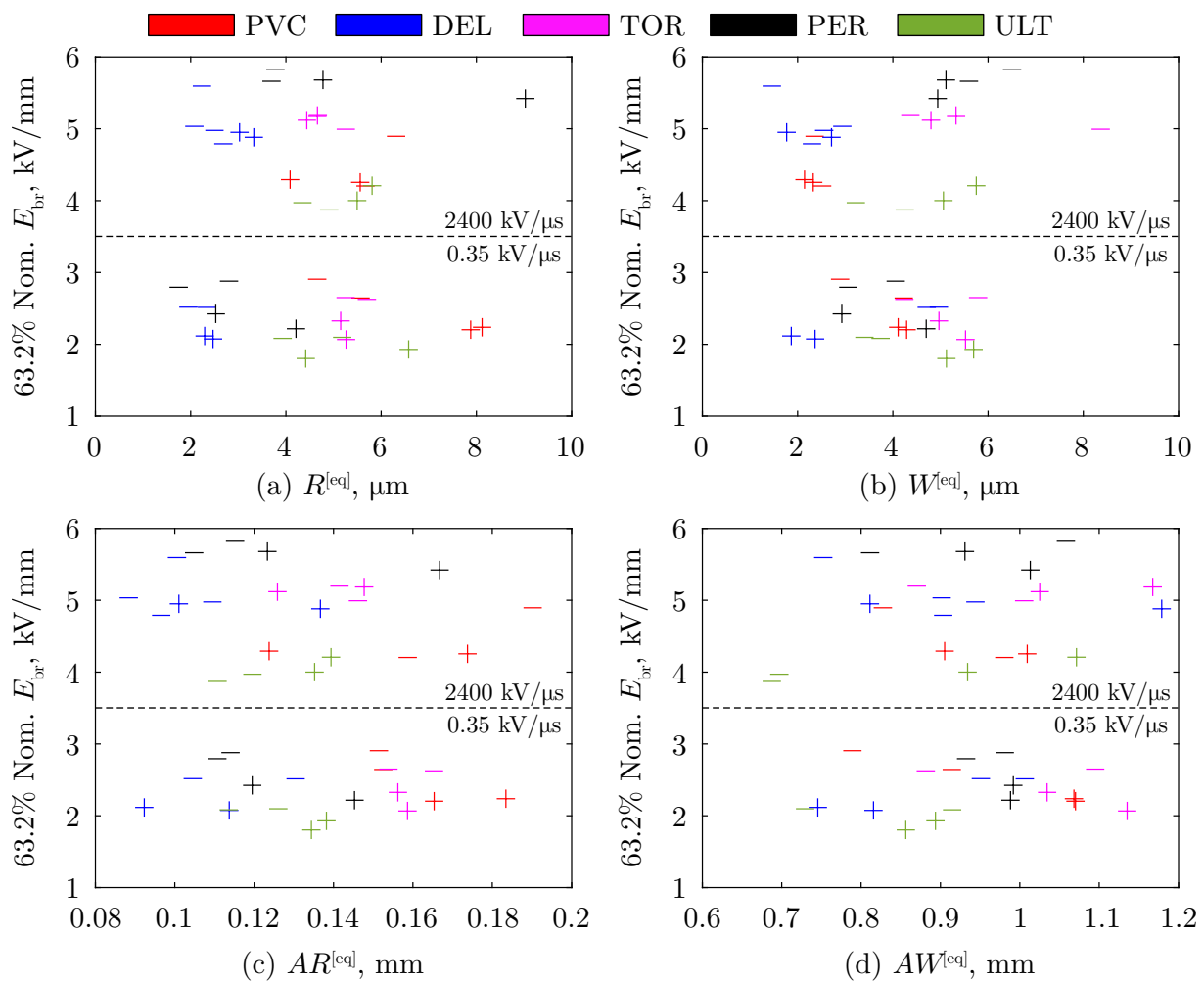


**Figure 7.31:**  $E_{br}$  plotted against (a)  $R^{[eq]}$ , (b)  $W^{[eq]}$ , (c)  $AR^{[eq]}$ , (d)  $AW^{[eq]}$  for all tested interfaces. Marker symbol indicated the polarity (either “+” or “-”).

by the asperity aspect ratio, which in general was higher for Ultem than the other materials (Figure 7.27). This was further evidenced by the visual inspection of the Ultem surfaces, which show faint diagonal serrations left behind by the cutting tool (e.g., Figure 7.28, case A; visible also in the additional photographs that have been included as Appendix C.6) used to treat the dielectric samples—contrasting that of all the other materials where these serrations were not as evident. Considering that all materials were cut using the same tool and procedure, this suggests that there exists some mechanical property of Ultem that determines the surface condition when subjected to machining action, and as a consequence, tended to leave sharper features on Ultem surfaces. One possibility is the material brittleness: materials which are more brittle would be far more likely to exhibit local brittle fracture during machining from the impact of the cutting tool.

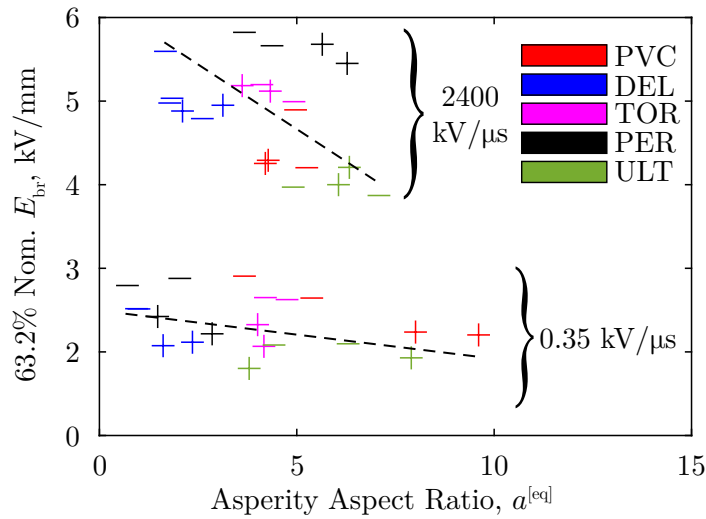


**Figure 7.32:**  $E_{br}$  plotted against the estimated equivalent asperity aspect ratio,  $a^{[eq]}$ , for all tested interfaces. Marker symbol indicates polarity (either “+” or “-”). Dashed black lines indicate the tendency for surfaces with higher aspect ratio asperities to result in lower breakdown strength. Image adapted with permission from [45], © IEEE 2024.

Brittleness is typically inferred from the stress-strain curve of a material, the measurement of which was not performed in the present work. However, the brittleness of a material is known to be related to its impact strength, often measured using the Charpy impact test (ISO-179 [55]) and reported in specification sheets. The impact strength is typically provided as a single numerical value with units  $\text{kJ/m}^2$ , a measure of energy absorption during fracture. Lower impact strength generally suggests that the material is brittle rather than ductile. For the materials involved here, PVC, Delrin, Torlon, and Perspex have reported Charpy impact strengths between  $10 \text{ kJ/m}^2$  and  $14 \text{ kJ/m}^2$ ; while for Ultem, it is significantly lower at just  $3.5 \text{ kJ/m}^2$ . This would support the hypothesis that Ultem may be more brittle than the other materials, leading to sharper surface asperities after machining due to local brittle fracture, resulting in the observed lowering of the interfacial breakdown strength. It is, however, clear from Figure 7.32 that the asperity aspect ratio is unlikely to be the only determinant of solid interfacial breakdown, but appears to offer at least a partial explanation of the observed tendencies.

## 7.5 Comparison with Modelling Results

This section returns to the solid-solid interfacial breakdown model presented in Section 7.2 and compares the modelled results to the experimentally-determined results of Figure 7.27.

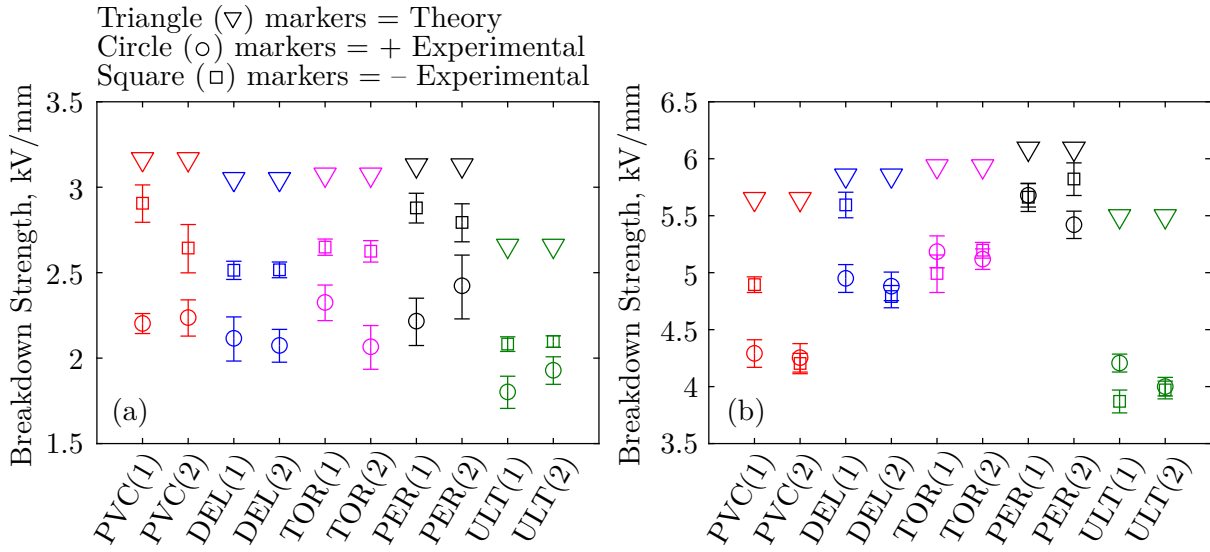


**Figure 7.33:** Comparison of the predicted interfacial breakdown strength using the solid-solid breakdown model to the experimentally measured values for the (a) 0.35 kV/ $\mu$ s case, (b) 2400 kV/ $\mu$ s case. Note that the model does not incorporate the effects of polarity, hence only one set of markers are shown per plot.

### 7.5.1 Comparison of Theoretical and Practical Interfacial Breakdown Strengths

As no measures were taken to reduce the statistical time-lag during experimental tests (e.g., UV irradiation or radioactive sources), the modelled times-to-breakdown from the developed deterministic model were not directly comparable. Instead, the comparison is focused on the estimated and measured values of 63.2% nominal breakdown field. For modelling purposes, the practical waveforms were represented using the double-exponential form as described in Section 7.2; waveshaping parameters of which are tabulated in Table 7.4. Figure 7.33 compares the theoretical values and experimental results reprinted from Figure 7.27 complete with the original 95% CIs. Note that because the model does not include polarity effects, only one point per interface is shown.

**Table 7.4:** Waveshaping parameters calculated to represent the practical impulses used the experimental solid-solid interfacial breakdown tests. These were computed following the strategy described in Appendix B.1.

Waveform	$A_0$	$\hat{\alpha}, s^{-1}$	$\hat{\beta}, s^{-1}$
Blumlein	1.2245	2466518.908	53831008.51
Samtech TG-01	1.3372	1537.9494	20830.8352

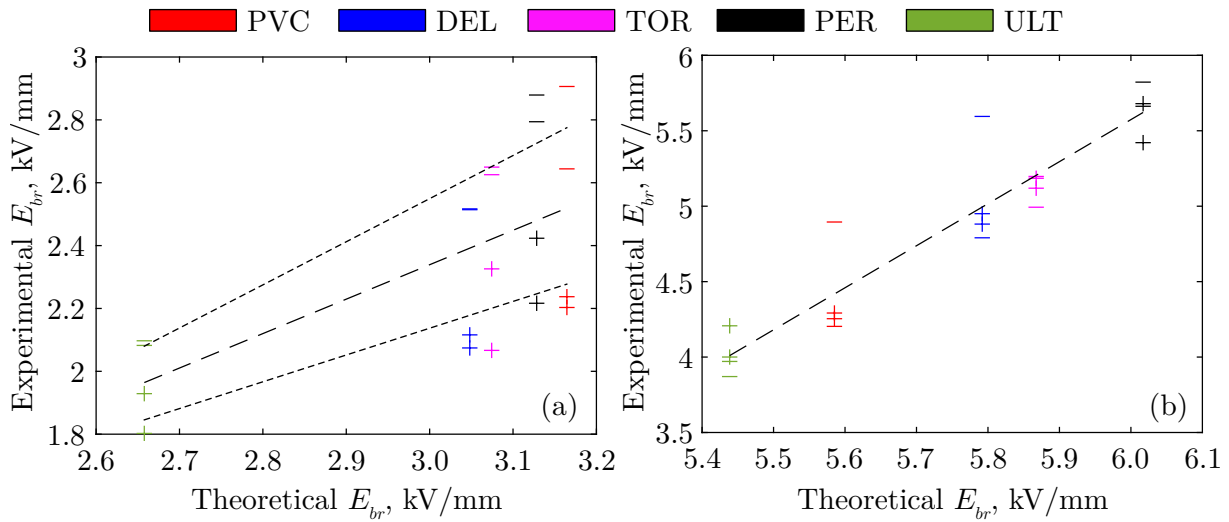


**Figure 7.34:** Plots of the measured nominal breakdown field strengths against the theoretically-estimated values (using the solid-solid breakdown model) for the (a)  $0.35 \text{ kV}/\mu\text{s}$  case, (b)  $2400 \text{ kV}/\mu\text{s}$  case. Due to the greater difference between polarities for the  $0.35 \text{ kV}/\mu\text{s}$  case, additional per-polarity linear fits have been provided for visual guidance.

It is firstly noted that between two interfaces of the same material, the predicted breakdown strength is essentially identical (the differences are negligible and imperceptible on the scale of the diagram). This therefore suggests that the differences in estimated void dimension between two interfaces of the same material were negligible, further supporting the consistency of the surface conditions between the first 20 and second 20 shots. In other words, any differences that were present did not lead to sufficiently significant changes to the predicted breakdown strength.

Overall, the model generally overestimates the breakdown strength for all cases. However, considering that the model has a number of parameters (e.g., initial electron density and spread) that come with significant uncertainty, alongside a number of applied approximations (e.g., constant diffusion), the predicted values were remarkably close to the measured experimental values. More important are the modelled tendencies. For both cases of  $dU/dt$ , the relative relationships between the estimated breakdown strengths of the different materials are identical to those observed experimentally. This is made more evident in Figure 7.34, where both the modelled and measured breakdown strengths have been plotted against each other. The experimentally-obtained breakdown strengths were found to be positively correlated to the theoretical estimations, and furthermore, the model appeared to correctly predict the lower breakdown strength of Ultem interfaces. A stronger correlation was found between the model and the  $2400 \text{ kV}/\mu\text{s}$  data over all tests regardless of polarity. This is due to the greater difference in measured breakdown strengths between polarities in the  $0.35 \text{ kV}/\mu\text{s}$  data. Taken separately,

however, the strong positive correlation once again emerges as shown in Figure 7.34(a).

The predictions for Ultem interfaces were yet again of particular interest. Despite correctly predicting an overall lower breakdown strength for Ultem interfaces, the experimental data indicates that, relative to the other materials, Ultem interfaces exhibited breakdown strengths that were lower by an additional factor than estimated by the model. This discrepancy supports the idea that additional factors lead to the further reduction of breakdown strength for Ultem interfaces, which was proposed to be sharp asperity features as explained in Section 7.4.5. This explanation may be reasonable since the modelling approach does not directly consider surface asperities and only models a representative void formed between asperities. Intra-void field enhancement is due purely to polarisation and surface charge accumulation, neglecting any additional enhancement due to sharp asperity features or irregular geometry. This would explain the further underestimation of the breakdown strength when sharper surface features are present, as in the case of Ultem.

It may be said that the model captures the effects of the impulsive waveform well, and the method of estimating interfacial breakdown based on intra-void discharge proves to be reasonably effective. However, it has also been shown that external factors like abnormally sharp surface features may further influence the evolution of interfacial breakdown, and is a clear limitation of the simple interfacial void approximation.

## 7.6 Chapter Conclusions, Contributions, and Outlook

This chapter has presented an experimental study on the impulsive breakdown characteristics of homogeneous solid-solid dielectric interfaces formed between five polymers: PVC, Delrin, Torlon, Ultem, and Perspex. Motivated by the lack of empirical design data for impulse-driven interfacial breakdown and particularly the gap in knowledge relating to breakdown across loosely-fit interfaces, this work focused on the effects of voltage rate-of-rise and surface roughness on their overstressed breakdown characteristics. Complementing the experimental work, a semi-deterministic model, which extends previous work on combining high voltage engineering techniques with the principles of tribology, was developed and presented. This made use of the novel methods developed in Chapters 3 and 4 to produce an integrated predictive model for impulsive solid-solid interfacial flashover based on the theory of void-driven breakdown.

Impulse-driven breakdown tests using a sphere-plane electrode configuration were conducted in laboratory air under atmospheric pressure using two different pulse generators. Results were

obtained under two different  $dU/dt$  values of approximately 2400 kV/ $\mu$ s and 0.35 kV/ $\mu$ s and in the overstressed breakdown regime. Analyses on the breakdown strength and time-to-breakdown were performed using Weibull statistics, complemented with surface characterisation data obtained from the measurement of the pre-breakdown surface profiles using a mechanical profilometer. Inspection and categorisation of the nature of post-breakdown surface traces was also conducted. This work has contributed towards the understanding of mechanisms responsible for solid-solid interfacial breakdown under impulse action, by extending characterisation work to non-standard impulse waveforms and atypical materials used in pulsed power system design. Detailed surface characterisation data has furthered the understanding of the effects of surface texture on the performance of solid-solid interfaces found within high voltage insulating systems.

### 7.6.1 Academic Significance and Contributions

A number of novel results have arisen from the work presented within this chapter, which have contributed towards a deeper understanding of impulse-driven breakdown processes across solid-solid interfaces. Overall, solid interfaces at low mating pressure (10's kPa) acted to reduce the impulsive breakdown strength of the system to lower than that of air alone in almost all cases. This is believed to be a result of intra-void field enhancement at the interface, combined with a significant reduction of the tracking resistance due to low contact force. Under these conditions, equivalent roughness and waviness parameters arising from the motif characterisation method ( $R^{[eq]}$ ,  $W^{[eq]}$ ,  $AR^{[eq]}$ ,  $AW^{[eq]}$ ) appeared to have no correlation with the interfacial breakdown strength alone, contrasting studies performed under MPa pressures. However, a negative correlation between the estimated equivalent asperity ratio,  $a^{[eq]}$ , and the breakdown strength was found over all tests. It has been posited that at low contact pressure, the nature of the asperities' radii have a stronger effect in determining interfacial breakdown, since the surfaces are not compressed with sufficient force to cause significant deformation of surface asperities to form strong contact spots. As a result, the field enhancement at the interface is determined by the size and radius of asperities—the higher the asperity aspect ratio, the greater the degree of local field enhancement, and the lower the interfacial breakdown strength.

This theory is in part supported by the much-reduced interfacial breakdown strength observed for Ultem interfaces. The asperity aspect ratios of Ultem interfaces were among the highest of all tested interfaces, suggesting the existence of sharper and higher aspect ratio asperities at the contact. The reason is believed to be linked to the brittleness of Ultem compared to other materials, which has been inferred from its Charpy impact strength that is 3–4 times lower

than other materials used in this work. Local brittle fracture during machining is thought to explain the sharper surface features. Observed discrepancies between the theoretical void-driven breakdown model and experimental data for Ultem provides further support. The predicted breakdown strengths of Ultem interfaces, relative to other materials, were correctly estimated to be lower, largely believed to be due to its additional thickness and corresponding modification of the intra-void  $dE/dt$ . However, the experimental results exhibited an abnormal reduction that was greater than predicted by the model when compared to the differences found for other materials. It is believed that the underestimation from the model arises, at least partially, due to the neglect of these high aspect ratio features found experimentally. It was thus concluded that the applicability of the void-driven discharge model for solid-solid interfaces may be limited when additional factors may influence the breakdown evolution, despite the reasonable predictions found for some of the other materials and as reported in previous literature.

Inspection of post-breakdown traces left by the plasma breakdown channels indicated that under 2400 kV/ $\mu$ s impulses, a single, central, breakdown channel was far more likely to result after repeated breakdown events. In contrast, under 0.35 kV/ $\mu$ s impulses, multiple different (longer) discharge paths were taken, some of which originated from the edges of the electrode rather than down the centre (i.e., critical path considering only the Laplacian field). It is believed that the additional time available on the rising edge of 0.35 kV/ $\mu$ s impulses allowed sufficient space charge transport prior to breakdown that redistributes the field, explaining the redirection of the breakdown path as the electric field becomes distorted from its Laplacian state near the HV tip. As a result, the mean width of the breakdown-affected region for 0.35 kV/ $\mu$ s impulses were on average about twice as wide as those in the 2400 kV/ $\mu$ s case.

### 7.6.2 Industrial Relevance

First and foremost, the breakdown data generated and analysed as part of this work contributes additional empirical design data that is critical to the development of pulsed power systems incorporating interfaces. This work provides an additional set of performance data for PVC, Delrin, Torlon, Ultem, and Perspex, under a non-standard configuration and poorly characterised breakdown regime.

The obtained results and conclusions are also of consequence to insulation design and coordination for high voltage and pulsed power systems. This work further emphasises the necessity to maintain mating pressure where solid interfaces cannot be avoided, as its reduction may lead to the weakening of the effective dielectric strength below that of only gas insulation, risking

catastrophic failure. They further indicate that under conditions like those studied in this work, the roughness and waviness parameters alone may play less of a role in the determination of interfacial breakdown strength, since discharges can readily form and propagate with little to impede them. The analyses conducted here also suggest (depending on how materials are cut or treated) the possibility that material brittleness plays a role in determining the aspect ratio of surface asperities, which under low mating pressures, appears important for interfacial breakdown. Given that in many applications, no specific treatment will be used to attain specific surface roughness conditions prior to mating, this work may provide additional information for appropriate material selection for the design of HV pulsed power insulating systems.

The observed differences in the post-breakdown channels widths may be of critical importance for compact pulsed power system design, as the effective width of the discharge region has been shown to be dependent on the pulse rise-time and on the interface material. There is the additional suggestion that this may be a material-dependent property, with the possible implication that certain materials are superior in suppressing the channel expansion at the interface during breakdown. This may further impact the development of plasma surface treatment systems and inform future understanding of plasma-surface interaction.

### 7.6.3 Limitations and Future Outlook

While the present work makes progress towards the wider characterisation of impulse solid-solid interfacial breakdown, the study is inevitably limited by various factors. A number of these are described in the following.

In relation to experimental procedure, particularly to the mating force provided by the inset springs of the interface holder, an accurate measurement of the contact force was not performed for each interface tested. The approximate range of  $\approx 10$ 's kPa given within this work was calculated based on an estimation of the spring constant and approximate deformation distance when the samples were inserted. In general, this value likely varies for different interfaces due to the dimensional tolerances of the cut samples. An improved configuration would ensure that an accurate measurement of the contact pressure could be achieved and recorded for each test. Along similar lines, the differing sample thicknesses used in this work were intentionally maintained based on what was commercially available, and considering materials such as Torlon which had an additional outer layer, using these materials “as received” was deemed most representative of practical conditions. However, better consistency in the experimental method could be gained if samples were machined to the same size and thickness to a defined precision, and would remove

the need for the obtained voltages to be normalised by thickness when compared.

For surface characterisation, it was assumed that four separate measurements across each surface would provide representative averages for the roughness parameters. The consistency in the measurements appear to support that the general morphology at each site were mostly similar for each material, however, higher fidelity (e.g., optical 2D measurements across the entire surface) measurements would be desirable to better characterise surface features, with the potential to allow the influence of cavity and asperity distributions to be investigated. It is also well known that the results of surface roughness measurements is sensitive to the resolution of the instrument and to the processing method [56], such that the profilometry data obtained within this work may vary if an instrument other than the Handysurf 35+ were to be used. This is, however, a widespread challenge relating to tribology and the fractal-like nature of rough surfaces which, in general, is difficult to completely avoid. For the present comparative study, however, all roughness measurements were obtained using the same instrument and processed using the same algorithm, ensuring comparability.

On statistical treatment of breakdown data, voltage and time data were fit to 2-parameter Weibull distributions informed by Kolgomorov-Smirnov and Lilliefors goodness-of-fit tests as explained in Section 7.3.4. While other distributions may be equally valid (and may also pass goodness-of-fit tests), the 2-parameter Weibull distribution was selected also for its prevalence as a well-accepted method for handling breakdown statistics. It is reiterated that in using the 2-parameter Weibull distribution for breakdown time data, the formative time has been assumed to be negligible compared to the statistical time.

The limitations surrounding the interfacial breakdown model had previously been alluded to. The results have indicated that modelling the interfacial breakdown processes as purely gas-void driven only accounts partially for the underlying breakdown mechanisms. For low mating pressures or surfaces with sharper surface features, the dominant mechanism may be local field enhancement along asperity tips, which cannot be accounted for using the this class of void-based model.

Given the above, the following list outlines a number of aspects that would benefit from further study that have been identified from this investigation; suggesting also future possibilities that may address remaining knowledge gaps relating to impulse-driven solid-solid breakdown:

- On the critical distance parameter: does  $dU/dt$  affect the critical distance, as suggested from the present results?

- Does the critical distance parameter even exist when a solid-solid interface is introduced? What about for bulk solids?
- Why does Delrin develop an abnormally wide post-breakdown region under the 2400 kV/ $\mu$ s case, behaviour which differs from all other materials?
- More conclusive confirmation of the effects of material brittleness, perhaps from more detailed analysis of the freshly-cut surface morphologies and the use of stress-strain curves.
- Characteristics of impulsive breakdown under high contact pressures ( $\sim$ MPa), and on whether a similar increase to the breakdown strength will be observed, as was found for past steady-state experiments.
- Expansion of this study to include different materials, different values of  $dU/dt$ , or other electrode geometries.
- Expansion of this study to include wet-mate and oil-mate interfaces, for which the theoretical model has predictions for but without validation.
- Further exploration of rough surface characteristics of the interface, particularly of the distribution and general morphological characteristics of interfacial voids and asperities.
- On further modelling: How can the proposed mechanism of local field enhancement at interfacial asperities be incorporated into physical models to account for configurations where it may be dominant?
- On further modelling: Can streamer re-ignition between interfacial voids be a significant process governing the discharge evolution?

## Chapter 7 References

- [1] D. Fournier and L. Lamarre, “Effect of pressure and length on interfacial breakdown between two dielectric surfaces,” in *Conf. Rec. 1992 IEEE Int. Symp. Electr. Insul.*, 1992, pp. 270–272.
- [2] D. Fournier, C. Dang, and L. Paquin, “Interfacial breakdown in cable joints,” in *Proc. IEEE Int. Symp. Electr. Insul.*, 1994, pp. 450–452.
- [3] D. Fournier, “Effect of the surface roughness on interfacial breakdown between two dielectric surfaces,” in *Conf. Rec. 1996 IEEE Int. Symp. Electr. Insul.*, vol. 2, 1996, pp. 699–702 vol.2.
- [4] C. Dang and D. Fournier, “A study of the interfacial breakdown in cable joints,” in *Proc. IEEE Conf. Electr. Insul. and Dielectr. Phenom. - (CEIDP’94)*, 1994, pp. 518–523.
- [5] C. Dang and D. Fournier, “Dielectric performance of interfaces in premolded cable joints,” *IEEE Trans. Power Deliv.*, vol. 12, no. 1, pp. 29–32, 1997.
- [6] T. Takahashi, T. Okamoto, Y. Ohki, and K. Shibata, “Breakdown strength at the interface between epoxy resin and silicone rubber—a basic study for the development of all solid insulation,” *IEEE Trans. Dielectr. Electr. Insul.*, vol. 12, no. 4, pp. 719–724, 2005.
- [7] D. Kunze, B. Parmigiana, R. Schroth, and E. Gockenbach, “Macroscopic internal interfaces in high voltage cable accessories,” *Int. Council Large Electr. Syst.*, 2000.
- [8] E. Kantar, D. Panagiotopoulos, and E. Ildstad, “Factors influencing the tangential AC breakdown strength of solid-solid interfaces,” *IEEE Trans. Dielectr. Electr. Insul.*, vol. 23, no. 3, pp. 1778–1788, 2016.
- [9] E. Kantar, F. Mauseth, E. Ildstad, and S. Hvidsten, “Longitudinal AC breakdown voltage of XLPE-XLPE interfaces considering surface roughness and pressure,” *IEEE Trans. Dielectr. Electr. Insul.*, vol. 24, no. 5, pp. 3047–3054, 2017.
- [10] E. Kantar, E. Ildstad, and S. Hvidsten, “Effect of material elasticity on the longitudinal AC breakdown strength of solid-solid interfaces,” *IEEE Trans. Dielectr. Electr. Insul.*, vol. 26, no. 2, pp. 655–663, 2019.
- [11] E. Kantar, E. Ildstad, and S. Hvidsten, “Effect of elastic modulus on the tangential AC breakdown strength of polymer interfaces,” *IEEE Trans. Dielectr. Electr. Insul.*, vol. 26, no. 1, pp. 211–219, 2019.
- [12] E. Kantar, S. Hvidsten, F. Mauseth, and E. Ildstad, “A stochastic model for contact surfaces at polymer interfaces subjected to an electrical field,” *Tribol. Int.*, vol. 127, pp. 361–371, 2018.
- [13] E. Kantar and S. Hvidsten, “A deterministic breakdown model for dielectric interfaces subjected to tangential electric field,” *J. Phys. D: Appl. Phys.*, vol. 54, no. 29, p. 295503, 2021.
- [14] J. Lehr, M. Abdalla, J. Burger, J. Elizondo, J. Fockler, F. Gruner *et al.*, “Design and development of a 1 MV, compact, self break switch for high repetition rate operation,” in *Digest of Technical Papers. 12th IEEE International Pulsed Power Conference. (Cat. No.99CH36358)*, vol. 2, 1999, pp. 1199–1202 vol.2.

- 
- [15] “K-modules: Modules designer for high energy x-ray of electron beam generating devices,” Los Alamos National Laboratory, Technology Snapshot, 2022. [Online]. Available: <https://www.lanl.gov/projects/feynman-center/technology-techsnapshots.php?id=61d66103f1b9050a1aab8ee9>
- [16] R. Timmermans, H. Mastwijk, L. Berendsen, A. Nederhoff, A. Matsers, M. Van Boekel *et al.*, “Moderate intensity pulsed electric fields (PEF) as alternative mild preservation technology for fruit juice,” *Int. J. Food Microbiol.*, vol. 298, pp. 63–73, 2019.
- [17] K. Shibata, Y. Ohki, T. Takahashi, and T. Okamoto, “Breakdown strength at the interface between epoxy resin and silicone rubber,” in *2003 Ann. Rep. Conf. Electr. Insul. Dielectr. Phenom.*, 2003, pp. 289–292.
- [18] B. Du and L. Gu, “Effects of interfacial pressure on tracking failure between XLPE and silicon rubber,” *IEEE Trans. Dielectr. Electr. Insul.*, vol. 17, no. 6, pp. 1922–1930, 2010.
- [19] S. M. Hasheminezhad, E. Ildstad, and A. Nysveen, “Breakdown strength of solid | solid interface,” in *2010 10th IEEE Int. Conf. Solid Dielectr.*, 2010, pp. 1–4.
- [20] M. Hasheminezhad and E. Ildstad, “Application of contact analysis on evaluation of breakdown strength and PD inception field strength of solid-solid interfaces,” *IEEE Trans. Dielectr. Electr. Insul.*, vol. 19, no. 1, pp. 1–7, 2012.
- [21] R. Sayles and T. Thomas, “Computer simulation of the contact of rough surfaces,” *Wear*, vol. 49, no. 2, pp. 273–296, 1978.
- [22] R. I. Taylor, “Rough surface contact modelling—a review,” *Lubricants*, vol. 10, no. 5, 2022.
- [23] B. Bhushan, “Contact mechanics of rough surfaces in tribology: multiple asperity contact,” *Tribol. Lett.*, vol. 4, pp. 01–35, 1998.
- [24] F. Robbe-Valloire, B. Paffoni, and R. Proghi, “Load transmission by elastic, elasto-plastic or fully plastic deformation of rough interface asperities,” *Mech. Mater.*, vol. 33, no. 11, pp. 617–633, 2001.
- [25] J. A. Greenwood, J. B. P. Williamson, and F. P. Bowden, “Contact of nominally flat surfaces,” *Proc. Royal Soc. London. A. Math. Phys. Sci.*, vol. 295, no. 1442, pp. 300–319, 1966.
- [26] H. Hertz, “Ueber die berührung fester elastischer körper.” *Journal für die reine und angewandte Mathematik*, no. 92, pp. 156–171, 1882.
- [27] J. A. Greenwood and J. H. Tripp, “The contact of two nominally flat rough surfaces,” *Proc. Inst. Mech. Engr.*, vol. 185, no. 1, pp. 625–633, 1970.
- [28] “Static contact under load between nominally flat surfaces in which deformation is purely elastic,” *Wear*, vol. 36, no. 1, pp. 79–97, 1976.
- [29] “Application of spherical indentation mechanics to reversible and irreversible contact between rough surfaces,” *Wear*, vol. 45, no. 2, pp. 221–269, 1977.
- [30] B. Bhushan, “Analysis of the real area of contact between a polymeric magnetic medium and a rigid surface,” *J. Tribol.*, vol. 106, no. 1, pp. 26–34, 1984.
- [31] J. Archard, “Surface topography and tribology,” *Tribology*, vol. 7, no. 5, pp. 213–220, 1974.
- [32] G. Crichton, P. Karlsson, and A. Pedersen, “Partial discharges in ellipsoidal and spheroidal voids,” *IEEE Trans. Electr. Insul.*, vol. 24, no. 2, pp. 335–342, 1989.

- [33] T. Wong, I. Timoshkin, S. MacGregor, M. Wilson, and M. Given, “Electrostatic modelling of gas-filled voids and conductive particles in highly non-uniform electric fields,” in *23rd Int. Symp. High Volt. Engr.* Institution of Engineering and Technology, 2023, pp. 1022–1028.
- [34] D. Levko, R. R. Arslanbekov, and V. I. Kolobov, “Modified paschen curves for pulsed breakdown,” *Phys. Plasmas*, vol. 26, no. 6, p. 064502, 2019.
- [35] D. S. Nikandrov, L. D. Tsendin, V. I. Kolobov, and R. R. Arslanbekov, “Theory of pulsed breakdown of dense gases and optimization of the voltage waveform,” *IEEE Trans. Plasma Sci.*, vol. 36, no. 1, pp. 131–139, 2008.
- [36] J. Fothergill, “Filamentary electromechanical breakdown,” *IEEE Trans. Electr. Insul.*, vol. 26, no. 6, pp. 1124–1129, 1991.
- [37] A. Majumdar and B. Bhushan, “Role of fractal geometry in roughness characterization and contact mechanics of surfaces,” *J. Tribol.*, vol. 112, no. 2, pp. 205–216, 1990.
- [38] “High-voltage test techniques - part 1: General definitions and test requirements,” International Electrotechnical Commission (IEC), Geneva, CH, International Standard, 2010.
- [39] E. Kantar, “Longitudinal AC electrical breakdown strength of polymer interfaces,” Theses, Department of Electric Power Engineering, University of Science and Technology, Trondheim, Norway, 2019.
- [40] Z. Zheng, Y. Fu, K. Liu, R. Xiao, X. Wang, and H. Shi, “Three-stage vertical distribution of seawater conductivity,” *Sci. Rep.*, vol. 8, 2018.
- [41] E. Kantar, “Dielectric strength of polymeric solid–solid interfaces under dry-mate and wet-mate conditions,” *Energies*, vol. 14, no. 23, 2021.
- [42] S. M. Hasheminezhad, “Breakdown strength of solid | solid interfaces,” in *2011 IEEE Trondheim PowerTech*, 2011, pp. 1–7.
- [43] T. Judendorfer, A. Pirker, and M. Muhr, “Conductivity measurements of electrical insulating oils,” in *2011 IEEE Int. Conf. Dielectr. Liq.*, 2011, pp. 1–4.
- [44] I. V. Timoshkin, M. J. Given, M. P. Wilson, and S. J. MacGregor, “Review of dielectric behaviour of insulating liquids,” in *44th Int Univer. Power Engr. Conf. (UPEC)*, 2009, pp. 1–4.
- [45] T. Wong, I. Timoshkin, S. MacGregor, M. Wilson, and M. Given, “The breakdown and surface characteristics of polymer interfaces under HV impulses,” *IEEE Trans. Dielectr. Electr. Insul.*, pp. 1–1, 2024.
- [46] *Square shoulder mills brochure: EMP02-040-A16-AP11-05C*, ZCC Cutting Tools Europe GmbH. [Online]. Available: <https://www.zcct-europe.com>
- [47] I. C. Somerville, S. J. MacGregor, and O. Farish, “An efficient stacked-blumlein HV pulse generator,” *Meas. Sci. Technol.*, vol. 1, no. 9, p. 865, 1990.
- [48] *HANDYSURF+*, Accretech Europe. [Online]. Available: <https://www.accretech.eu/en/surface-measuring-systems/roughness-measuring-systems/handysurf-354045/>
- [49] S. Belghith, S. Mezlini, H. BelhadjSalah, and J.-L. Ligier, “Modeling of contact between rough surfaces using homogenisation technique,” *Comptes Rendus Mécanique*, vol. 338, no. 1, pp. 48–61, 2010.

- 
- [50] “Geometrical product specifications (GPS) - surface texture: Profile method - motif parameters,” International Organization for Standardization (ISO), Geneva, CH, International Standard, 1996.
- [51] T. Wong, I. Timoshkin, and S. MacGregor, “Data for: “the breakdown and surface characteristics of polymer interfaces under hv impulses”,” doi: 10.15129/eed7c188-4c26-430e-986c-5e3785c46f9f, 2024.
- [52] M. G. Hogg, I. V. Timoshkin, S. J. Mcgregor, M. P. Wilson, and M. J. Given, “Polarity effects on breakdown of short gaps in a point-plane topology in air,” *IEEE Trans. Dielectr. Electr. Insul.*, vol. 22, no. 4, pp. 1815–1822, 2015.
- [53] L. Zhao, J. Su, X. Zhang, and Y. Pan, “Experimental investigation on the role of electrodes in solid dielectric breakdown under nanosecond pulses,” *IEEE Trans. Dielectr. Electr. Insul.*, vol. 19, no. 4, pp. 1101–1107, 2012.
- [54] L. Zhao, G.-z. Liu, J.-c. Su, Y.-f. Pan, and X.-b. Zhang, “Investigation of thickness effect on electric breakdown strength of polymers under nanosecond pulses,” *IEEE Trans. Plasma Sci.*, vol. 39, no. 7, pp. 1613–1618, 2011.
- [55] “Plastics - determination of charpy impact properties - part 1: Noninstrumented impact test,” International Organization for Standardization (ISO), Geneva, CH, International Standard, 2023.
- [56] A. Sanner, W. G. Nöhring, L. A. Thimons, T. D. Jacobs, and L. Pastewka, “Scale-dependent roughness parameters for topography analysis,” *Appl. Surf. Sci. Adv.*, vol. 7, p. 100190, 2022.



## Effects of Surface Condition on the Impulsive Flashover of Polymer-Gas Interfaces

---

SUPPLEMENTING the work on solid-solid interfacial breakdown of Chapter 7, this chapter presents a second study of impulse-driven breakdown, focused instead on the flashover characteristics of solid-gas interfaces. Following a similar experimental methodology as used in Chapter 7, a new test configuration has been developed to investigate impulsive flashover characteristics across the same set of polymeric materials: PVC, Delrin, Torlon, Ultem, and Perspex. Two different impulsive waveforms were again generated using the same stacked Blumlein and trigger generator from Chapter 7, though with minor adjustments to the values of  $dU/dt$ , appropriate for the new test configuration. Surface roughness characterisation was once again employed, where the purpose of the experimental work was to investigate the differences in the impulsive flashover behaviour between “*as received*” and “*machined*” surfaces.

Results arising from this study has indicated that the machining action used to treat the polymers had significantly increased the roughness and waviness motif heights of all polymers, but had a weaker effect on the motif widths; supported by significance tests. Results from impulsive flashover tests showed strong polarity effects, believed to be due primarily to the use of asymmetric electrodes, but also from differences induced by different values of  $dU/dt$ . A theory

---

This chapter was partially adapted, and may be quoted verbatim, from the following publication(s) with permission: T. Wong, I. Timoshkin, S. MacGregor, M. Wilson, and M. Given, “Characteristics of Impulse-driven Surface Flashover across Polymers with Different Surface Conditions,” in preparation, Aug. 2024.

based on the corresponding asymmetry in streamer propagation has been proposed to explain these results. Tendencies have additionally been observed that imply an increase in surface flashover strength with greater short-wavelength surface height variations, while long-wavelength variations appeared, comparatively, of lesser importance.

## 8.1 Introduction and Motivation

Better characterisation of impulse-driven surface flashover behaviour is equally as important to pulsed power system design as the solid-solid interfaces explored within Chapter 7. The reader is first reminded of the review of Chapter 2 - Section 2.4.1, many issues of which relate to the motivation behind this study of solid-gas breakdown. To reiterate, the prevalence of gas-insulated apparatus in both HV power and pulsed power systems cannot be understated. The issue of surface flashover across unavoidable mechanical supports has long been known; made more pressing with increases in operational field stresses and miniaturisation. Over time, and particularly within the power industry, various techniques have been explored in efforts to increase the breakdown strength across solid-gas interfaces and to enhance their hold-off capabilities. Incidentally, the method of non-uniform field grading and control is one such advancement that was previously explored in Chapter 3; to which the reader may refer. Other examples include geometrical modification of insulator topologies [1] or surface grading [2]. Several works have considered the possibility of surface texture modification as a means to increase breakdown voltage by increasing the effective discharge path length [3–5]. In addition, issues relating to poor characterisation under non-standard waveshapes and atypical geometries—as has been the running theme throughout this work—apply similarly to solid-gas surface flashover. Some recent works have progressed this understanding, for example, in [3,4,6–8], but more must be done to develop robust design rules and recommendations relevant to practical system design.

On that account, this chapter is organised as follows. Section 8.2 describes the experimental configuration and outlines the modifications from that of Chapter 7 that were made to accommodate the new test geometry which involved cylindrical material samples. Details are provided on the new scheme developed for surface roughness characterisation, including the adaptation of the surface measurement rig for the new geometry, and the revised test procedures. Before the presentation of breakdown results, Section 8.3 discusses aspects relating to the two types of surface condition tested in this work, including a quantification of the measured differences between “as received” and “machined” surfaces. Impulse surface flashover tests reporting on the breakdown voltage and times are presented in Section 8.4.1; observations of

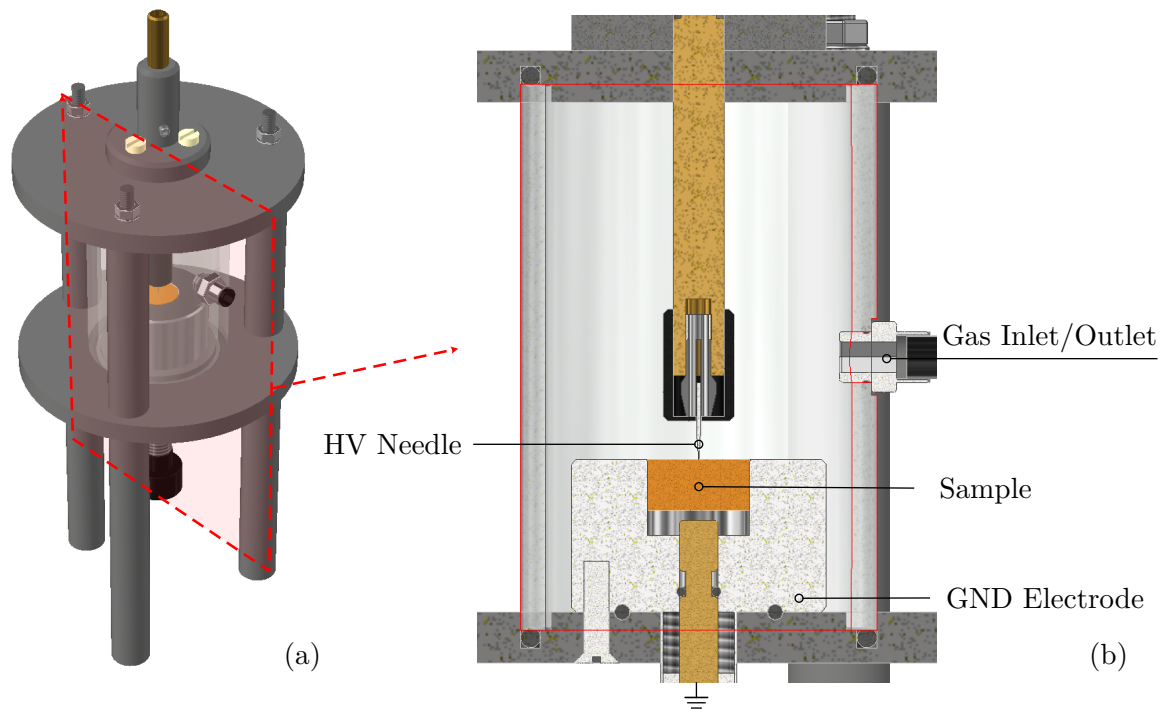


**Figure 8.1:** 3D CAD model of the test cell used for impulsive solid-gas flashover tests. (a) Perspective view of the full test cell, (b) sectional view cut through the centre plane, showing the ground electrode acting also as the holder for solid cylindrical samples, energised through a HV needle electrode held at the sample surface.

which are supported by additional modelling work. Observed correlations between the flashover behaviour and surface characteristics are then discussed in Section 8.4.2, before the chapter is concluded in Section 8.5 with the contributions, limitations, and outlook, in the usual manner.

## 8.2 Experimental Methodology

While the arrangements and methods used in this work largely mirror those of the solid-solid case of Section 7.3, there were a few key differences described in the section that follows.

### 8.2.1 Solid-Gas Test Cell and Circuit

Figure 8.1 shows a 3D model of the test cell used for surface flashover tests, including a sectional view detailing the nature of the electrode setup. Material samples (see Figure 8.2) were cut to be cylindrical in shape with a diameter of 20 mm and were inset into the ground electrode, such that the surface under test would sit flush with its top surface. The ground connection was designed to allow the height adjustment of a rod that kept the sample from sinking into



**Figure 8.2:** Photograph of the cylindrical solid samples cut from the same materials as used in Chapter 7. Inset image shows a magnified image of Torlon samples with the original surface finish and the exposed inner material once the machined.

the bore. Since the samples were cut from the same sheets as in Chapter 7 - Section 7.3, their thicknesses were different, following those of Table 7.1. By allowing sample height adjustment, the problem of different sample thicknesses was resolved, as the rod could simply be adjusted to ensure that any sample was flush with the surface regardless of its height. A small piece of fabric was additionally placed between the rod and the bottom surface of the sample, preventing the rod from damaging the surface when samples were adjusted or removed.

Breakdown was induced across the sample surfaces by application of HV impulses to the needle electrode of approximately  $80\ \mu\text{m}$  tip radius, held directly above the centre of the sample. Effort was made to ensure that the needle tip would be as centred as possible, to reduce the chance of preferential breakdown paths due to one side of the needle being closer to the ground electrode edge. The resulting triple junction formed between the needle, dielectric, and air ensured that discharges would initiate from the needle tip and propagate across the sample with greatest probability. Surface flashover was visually verified for every shot before data was recorded. “Soft tone” gramophone needles were used as the HV electrode, where five needles closest to the target  $80\ \mu\text{m}$  tip radius were selected from a pack, done via the inspection of each needle under a microscope and a measurement of the tip radius. The final five needles had a mean tip radius of  $80.38 \pm 5.59\ \mu\text{m}$ , and which were replaced after every 16 tests that were completed ( $16 \times 20$  shots per interface = 320 shots per needle). To ensure that needle degradation was acceptable over hundreds of repeated shots, a dummy sample was subjected to  $> 600$  shots with a single test needle and was subsequently re-inspected for tip deformation or damage. Due to the low

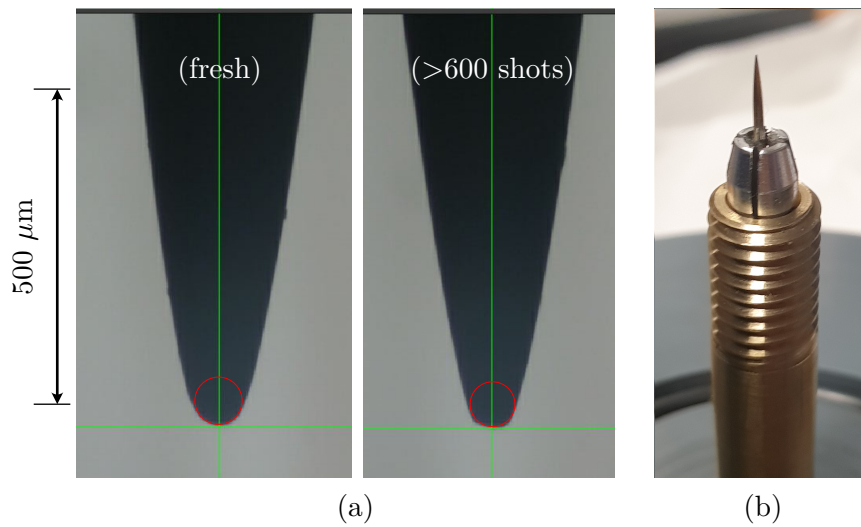


**Figure 8.3:** (a) Microscope images of magnified gramophone needles used as the HV electrode, comparing between a fresh needle and the same needle after over 600 HV shots with no degradation, (b) Photograph of the needle held within the brass HV connection, with the securing PVC cover removed.

pulse energy, the needle geometry was found to be unchanged with no visible damage, providing confidence in the consistency of each test. Figure 8.3 compares two microscope images of this test needle, before and after degradation testing.

The test circuit remained largely identical to that of Chapter 7 with the same two generators (stacked Blumlein and Samtech TG-01) used, see Figure 8.4. The TG-01 waveform remained identical to before, rising to around 35 kV over approximately 100 μs of both polarities. The charging voltage for the Blumlein, however, was reduced to 15 kV (compared to 30 kV used in Chapter 7) with the spark-gap distance correspondingly reduced. The reason for this change was related to the observation that the original value of  $dU/dt$  could not consistently break the gap under the new test configuration. The reduced charging voltage therefore also reduced the  $dU/dt$ , allowing repeated breakdown to occur. An additional 675 pF capacitor bank was also connected in parallel with the test cell, in earlier attempts to slow the voltage rise further. However, while breakdown on the rising slope was readily attained using the TG-01, this was not the case for the Blumlein, despite the adjusted waveshape. Even in air alone, consistent breakdown could only be achieved for both polarities when the inter-electrode gap was reduced down to several millimetres. Thus, breakdown voltages could not be obtained for the fast-rising case using the Blumlein. Using the breakdown current waveforms, however, an alternative method was implemented to allow the extraction of the time-to-breakdown. Details are provided later within Section 8.4.1.

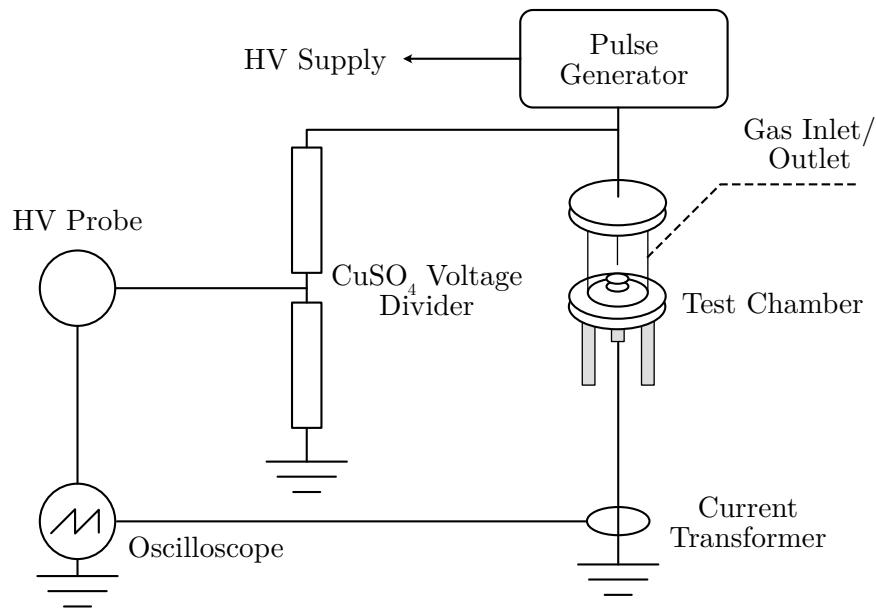


**Figure 8.4:** Circuit diagram of the experimental test circuit for solid-gas interfacial flashover tests. The pulse generator was either a custom-built stacked Blumlein [9] triggered using a self-breaking spark-gap, or a Samtech TG-01 trigger generator. In the latter case, the CuSO<sub>4</sub> voltage divider was not necessary due to the lower peak voltage.

Diagnostics for the Blumlein tests remained the same as Chapter 7 (Northstar PVM-5, CuSO<sub>4</sub> divider), while TG-01 voltage monitoring was provided through a Tektronix P6015A high voltage probe. Current monitoring was only introduced after completion of the TG-01 tests, using a Pearson 6585 current transformer for all Blumlein tests. All waveforms were once again captured on a Tektronix TDS3054C digital oscilloscope.

### 8.2.2 Sample Preparation and Roughness Characterisation

As mentioned, one of the main objectives of this study was to investigate the effects of the surface condition on the impulse-driven flashover behaviour. Since the cylindrical samples were cut from “as received” flat sheets, both of the flat cross-sectional surfaces of the samples inherited the “as received” surface condition of the original sheet. To produce the “machined” condition, one out of each pair of flat surfaces per cylindrical sample was treated by removing a thin layer of material using the same shoulder mill shown in Chapter 7 (Figure 7.18) [10]. To summarise, each cylindrical sample therefore had two surfaces, each with different conditions:

1. “As received” surface. Aside from light cleaning using a 70% ethanol-water mixture prior to testing, no treatment was applied. Used regardless of condition *as received* from the

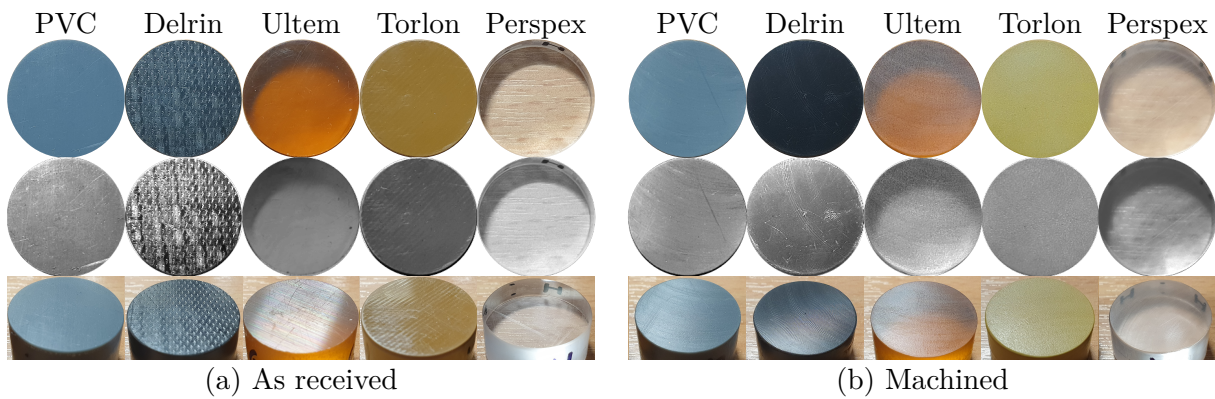


**Figure 8.5:** Photographs and contrast/brightness adjusted photographs of representative sample surfaces used in this work for (a) “as received” surfaces from the supplier/manufacturer, (b) machined surfaces with a thin layer removed. Note that Perspex has high optical clarity, preventing the surface texture to be easily captured on camera. The wood grain visible in the photograph is that of the table underneath.

supplier/manufacturer.

2. “Machined” surface. Due to the action of the tool, any pre-existing scratches or marks that were present on the original surface would therefore be removed, replaced by faint machining marks.

Figure 8.5 encloses photographs showing representative samples of both surface conditions and for each type of material.

Visually, the “as received” surfaces of PVC and Perspex appeared most similar, with a mostly smooth appearance and very minor, randomly-oriented, scratches. Ultem and Torlon also appeared similar, but with clear uni-directional parallel lines across their entire surfaces, in contrast to PVC and Perspex. The “as received” surfaces of Delrin were unlike any other material, as the entire surface was covered with small indentations. These indentations are uniformly spaced, and evidently, intentionally placed. However, their size, shape, and density varied across different samples of Delrin. Some samples had indentations that appeared closer to a diamond shape, while others were more circular in nature, and varied in both depth and in size. The exact source of these surface features remains unclear, but undoubtedly results from some process during manufacture.

The “machined” surfaces appeared visually similar across all materials, with faint machining marks that appear curved due to the rotary nature of the tool used. It is important to note that the Torlon samples used here were comprised of three layers, the thinner dark-brown top

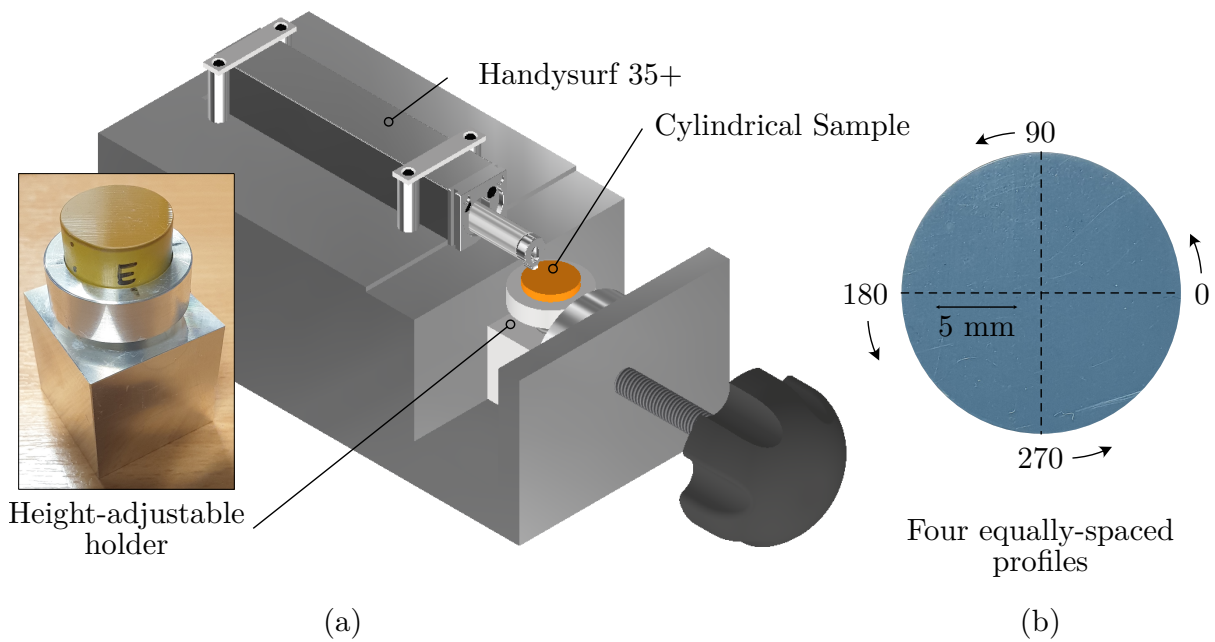


**Figure 8.6:** Revised 3D CAD model of the Handysurf 35+ profilometry system, (a) showing the custom-made holder to accommodate for the measurement cylindrical samples, (b) diagram showing the four new measurement locations considering the cylindrical geometry.

and bottom layers result from curing processes during production [11]. The machining process strips away one of the outer layers and exposes the inner material as shown in Figure 8.5. The opportunity was therefore taken to evaluate whether the exposure of the inner layer of Torlon would make any tangible difference to its surface flashover properties. A number of additional photographs of the pre-breakdown surfaces are available in Appendix C.7.

### 8.2.3 Experimental Procedure

The number of shots per surface was kept consistent with the solid-solid tests of Chapter 7, again subjecting each surface to 20 shots, for two independent surfaces of the same material and condition, to ensure consistency. It is again emphasised that the first 20 and second 20 shots cannot be combined into a single dataset, since the surface characteristics may be different. Surface roughness profiles were measured prior to breakdown using the Handysurf 35+ introduced in Section 7.3.2. Figure 8.6 shows an additional holder designed to secure the cylindrical samples during surface profilometry, which for this study were taken across four 5 mm evaluation lengths along the radius of each surface at 90 degree angular intervals. Roughness and waviness parameters, like in Section 7.3.2, were computed using the motif method and averaged across the four measurement locations.

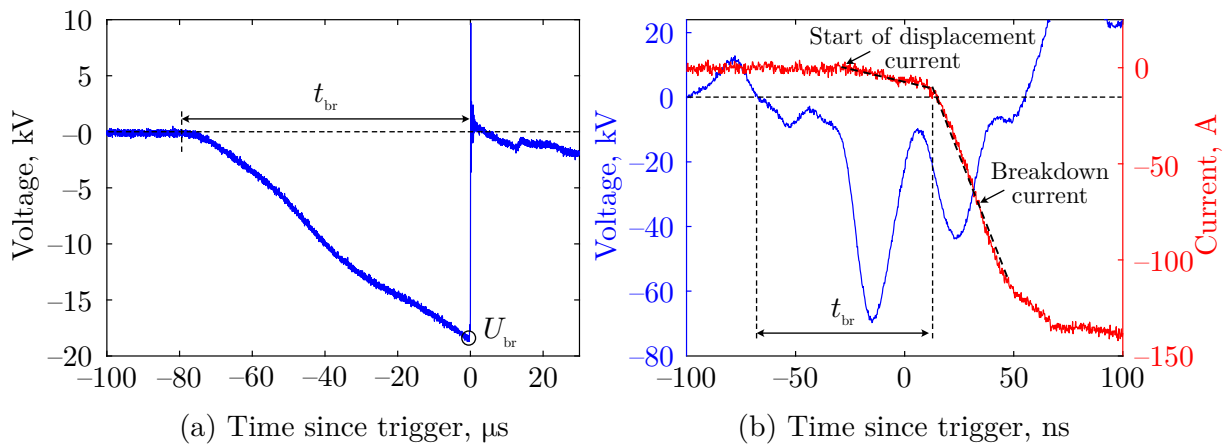


**Figure 8.7:** Typical breakdown oscillograms for (a) Samtech TG-01 and (b) Blumlein tests. Current waveforms were only recorded for Blumlein tests. Labels of figure (b) show the separation between that is believed to be the start of the displacement current and the main superimposed breakdown current. Breakdown voltage,  $U_{br}$ , and time-to-breakdown,  $t_{br}$  were determined based on the indicated points.

As was done in Chapter 7, each sample was cleaned using a 70% ethanol-water solution and low-lint paper before it was inserted into the test cell, height adjusted, and needle electrode lowered to rest on the sample surface. As before, the test cell was sealed and flushed with fresh laboratory air after each shot, which were similarly separated by 1 min 30 s in time as informed by the tests described in Section 7.3.3. Following Section 8.2.1, the needle was replaced after every 320 shots (16 surfaces).

#### 8.2.4 Data Processing and Statistics

For tests conducted using the TG-01, breakdown voltages and times-to-breakdown were obtained using the same method as for the solid-solid interface tests, see Section 7.3.4. Summarising for convenience, raw voltage waveforms were passed through a moving average (low-pass) filter to reject noise, before taking (i) the unambiguous filtered peak as the breakdown voltage, and (ii) the duration between the zero-crossing nearest the voltage rise to the moment of the voltage peak as the time-to-breakdown, see Figure 8.7(a).

For Blumlein tests, the mentioned inability to trigger breakdown on the rising slope resulted in only times-to-breakdown being successfully recorded. These were inferred using the voltage and current waveforms together, by defining the time-to-breakdown as the time between the nearest zero-crossing of the voltage rise, to the first *significant* rise in current. Emphasis is placed on *significant* rise in current that was indicative of the breakdown current. This is made clear

due to the existence of an initial, slower, rise in current that accompanied the steepest rise in voltage for all captured waveforms; believed to be the capacitive displacement current, see Figure 8.7(b). However, the displacement current did not appear to reduce near the peak of the voltage waveform according to  $I_D = C \cdot dU/dt$ . Instead, it is believed that in the present configuration, the displacement current was superimposed with the main breakdown current, where the initial slow rise in current was followed by a sudden change in gradient as the main breakdown current became significant. The system capacitance was also estimated from electrostatic simulations (see model presented later in Section 8.4) to be approximately 3 pF, which gives an estimated magnitude of displacement current in the range of 10 A to 20 A based on the approximate  $dU/dt$  of the applied voltage, in agreement with typical magnitudes recorded for the initial rise in current. The change in gradient between the displacement current and main breakdown current was therefore taken as an indicator of the moment of breakdown. This was identified using the MATLAB `findchangepts` function, based on sudden changes to the gradient, to ensure repeatability. Once again, algorithmically determined points were also subject to manual inspection to ensure correct identification.

Results arising from roughness characterisation and flashover results are presented in the following sections. A complete set of the raw data, including captured waveforms and roughness data, has been made available at the repository [12]. The reader is once again reminded that the computed Weibull parameters for all datasets has additionally been included as Appendix B.9.

### 8.3 Roughness and Waviness of “As received” and “Machined” Surfaces

Since there were two distinct surface conditions tested in this study, it is instructive to first draw an initial comparison of the obtained roughness characteristics as a separate matter to surface flashover. The parameters which characterised each sample surface were the same as those described in Section 7.3.2, though it is remarked that the *equivalent* surface parameter theory does not apply here, as there were no interfaces between solids that were formed. The parameters  $R$ ,  $W$ ,  $AR$ ,  $AW$  therefore directly describe the short- and long-wavelength characteristics of individual sample surfaces. A total of 80 surfaces (5 materials  $\times$  2 surface conditions  $\times$  2 polarities  $\times$  2 values of  $dU/dt$   $\times$  2 samples per surface condition) were characterised using the motif algorithm of Section 7.3.2 and averaged across the four measurement locations per sample. In the following, the calculated surface parameters and their distributions are compared between “as received” and “machined” surfaces. For all samples, Figure 8.8 plots the computed motif

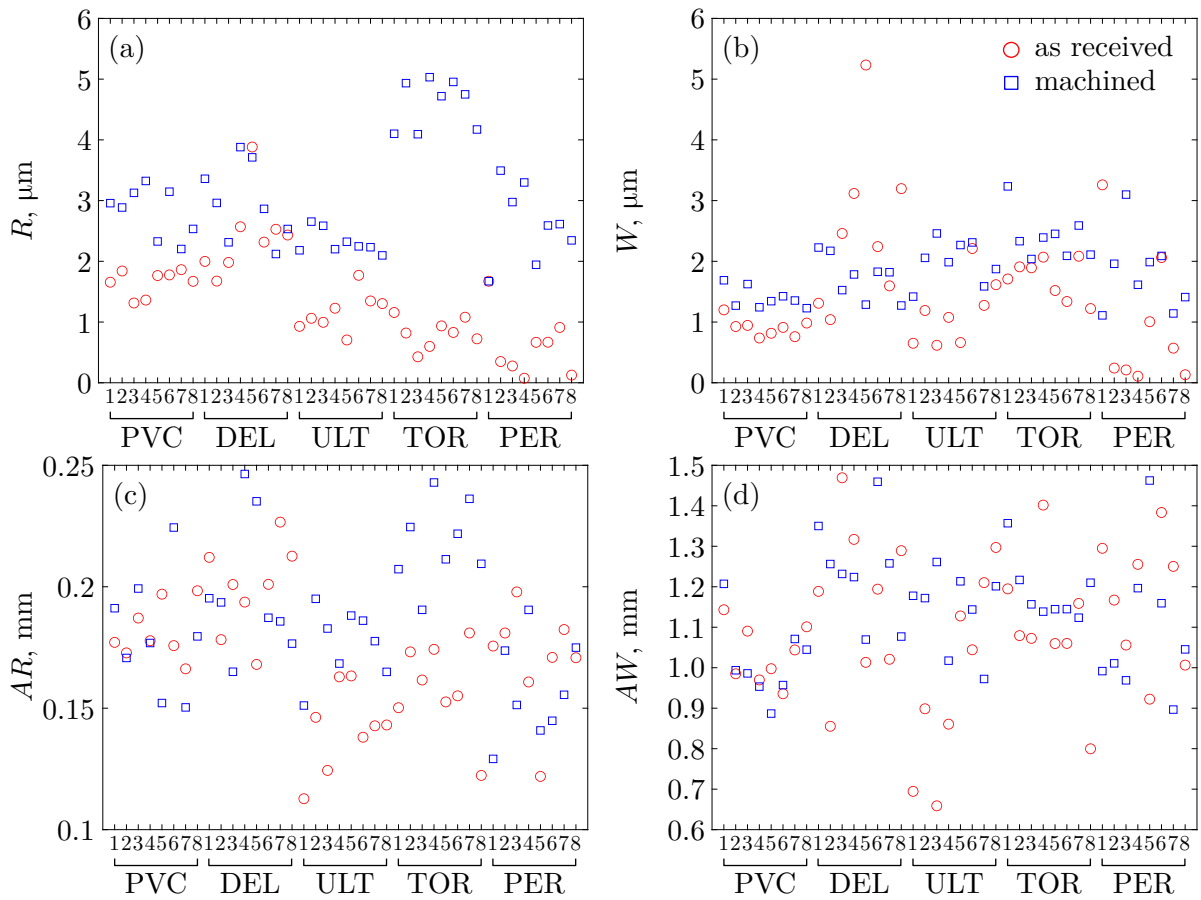


**Figure 8.8:** Plots of the motif parameters (a)  $R$ , (b)  $W$ , (c)  $AR$ , and (d)  $AW$  averaged over all four measurement locations for all samples used in this study. Marker shape and colour differentiates between “as received” and “machined” surface conditions.

parameters  $R$ ,  $W$ ,  $AR$ , and  $AW$ , differentiating between the two surface conditions.

A clear increase in the roughness motif height,  $R$ , was observed, in qualitative agreement with their visual appearance as shown in Figure 8.5. The action of machining tended to introduce deeper grooves onto the material surfaces which were visible to the naked eye. These were visibly deeper and had greater spatial uniformity when compared to the randomly oriented markings found on “as received” surfaces. The waviness motif height,  $W$ , also appeared to exhibit a small but consistent increase as a result of machining. Based on Figures 8.8(c) and 8.8(d), the motif widths  $AR$  and  $AW$  appear largely unaffected, suggesting that the machining method used had little effect on the longer-wavelength undulations of the surface profile. It is noted that Torlon appears in Figure 8.8 to exhibit a significant increase in  $R$  after machining, which results from the removal of the top, fully-cured, layer, which was visibly (and measurably) smoother than the

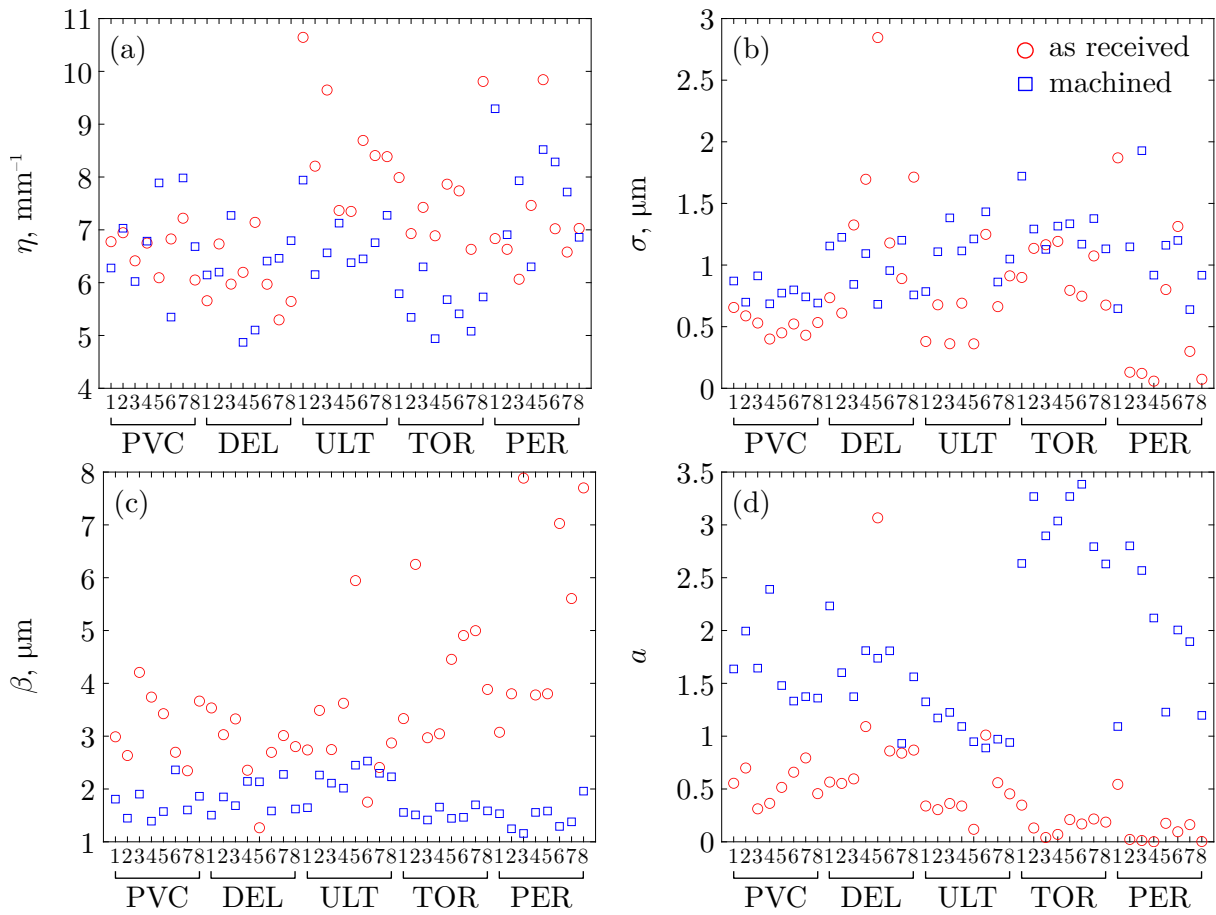


**Figure 8.9:** Plots of the compound roughness parameters (a)  $\eta$ , (b)  $\sigma$ , (c)  $\beta$ , and (d)  $a$  averaged over all four measurement locations for all samples used in this study. Marker shape and colour differentiates between “as received” and “machined” surface conditions.

exposed material underneath. The compound roughness parameters  $\eta$ ,  $\sigma$ ,  $\beta$ , and  $a$ , for which the reader is reminded represent the asperity density, standard deviation of asperity heights, asperity tip radius, and asperity aspect ratio, respectively, are similarly plotted in Figure 8.9. General tendencies for  $\eta$  suggests a small decrease in asperity density after machining, though this is inconclusive from the plot alone. Similarly, there is a general tendency for  $\sigma$  to increase with machining, but the distributions do not appear, at least qualitatively, very distinct. A clear decrease in asperity radius was observed based on Figure 8.9(c), which imply sharper surface features introduced through machining. This is supported by the clear increase in the asperity aspect ratio, which is made more distinct due to the increase in asperity height seen in Figure 8.8(a). In almost all cases, the “as received” surfaces had  $a \leq 1$ , implying asperities wider than they are tall, in contrast to “machined” surfaces which almost exclusively have  $a \geq 1$ , suggestive of thinner and taller surface protrusions.

**Table 8.1:** Results from 2-parameter Kolmogorov-Smirnov hypothesis tests on the empirical distributions of “as received” and “machined” surfaces at 95% significance. As such,  $p < 0.05$  was considered statistically significant.

Parameters	Probably Distinct (95% Confidence)	$p$ -value
$R$	Y	$5.017 \times 10^{-13}$
$W$	Y	$1.330 \times 10^{-4}$
$AR$	Y	0.0431
$AW$	N	0.5313
$\eta$	Y	0.0431
$\sigma$	Y	$3.565 \times 10^{-4}$
$\beta$	Y	$1.339 \times 10^{-14}$
$a$	Y	$2.888 \times 10^{-16}$

In Figure 8.10, histograms of the computed surface data are plotted to facilitate comparison of “as received” and “machined” distributions. By comparing across all materials, any change in the distribution represents, in general, the effects of machining action on the gross surface morphology. Each pair of distributions were subjected to 2-parameter Kolmogorov-Smirnov tests, which tests the null hypothesis that the two sets of data are likely to belong to the same distribution. Tests at 95% confidence were conducted, with the results and significance ( $p_s$ ) values shown in Table 8.1, where  $p_s < 0.05$  was considered statistically significant.

For the roughness heights  $R$ , Figure 8.10 indicates a clear shift in distribution after machining with an overall increase in the  $R$  value. This shift is supported by the hypothesis test, indicating that the two datasets are likely drawn from distinct distributions with high statistical likelihood. The visual shift in the  $W$  distribution was similarly reflected within the hypothesis test, where Figure 8.8 also shows that the variance of the waviness motif heights decreased, suggesting that machining tended to introduce long wavelength undulations that were higher and of more consistent size. Visually, distributions of  $AR$  and  $AW$  appear similar and unchanged. Hypothesis tests suggest that only  $AW$  was less likely affected, and that the distributions of  $AR$  are distinct; though the significance values for these tests indicate the uncertainty in these results. All four compound roughness parameters  $\eta$ ,  $\sigma$ ,  $\beta$  and  $a$  passed the hypothesis test at 95% confidence, however, far greater statistical significance (lower  $p_s$  value) was found for  $\beta$  and  $a$ . Thus, with reasonable confidence, one may conclude that changes induced by the present machining method to the short-wavelength surface features were more significant than changes to the long-wavelength profile variations. Similarly, the motif profile heights were modified to a greater extent than the profile widths.

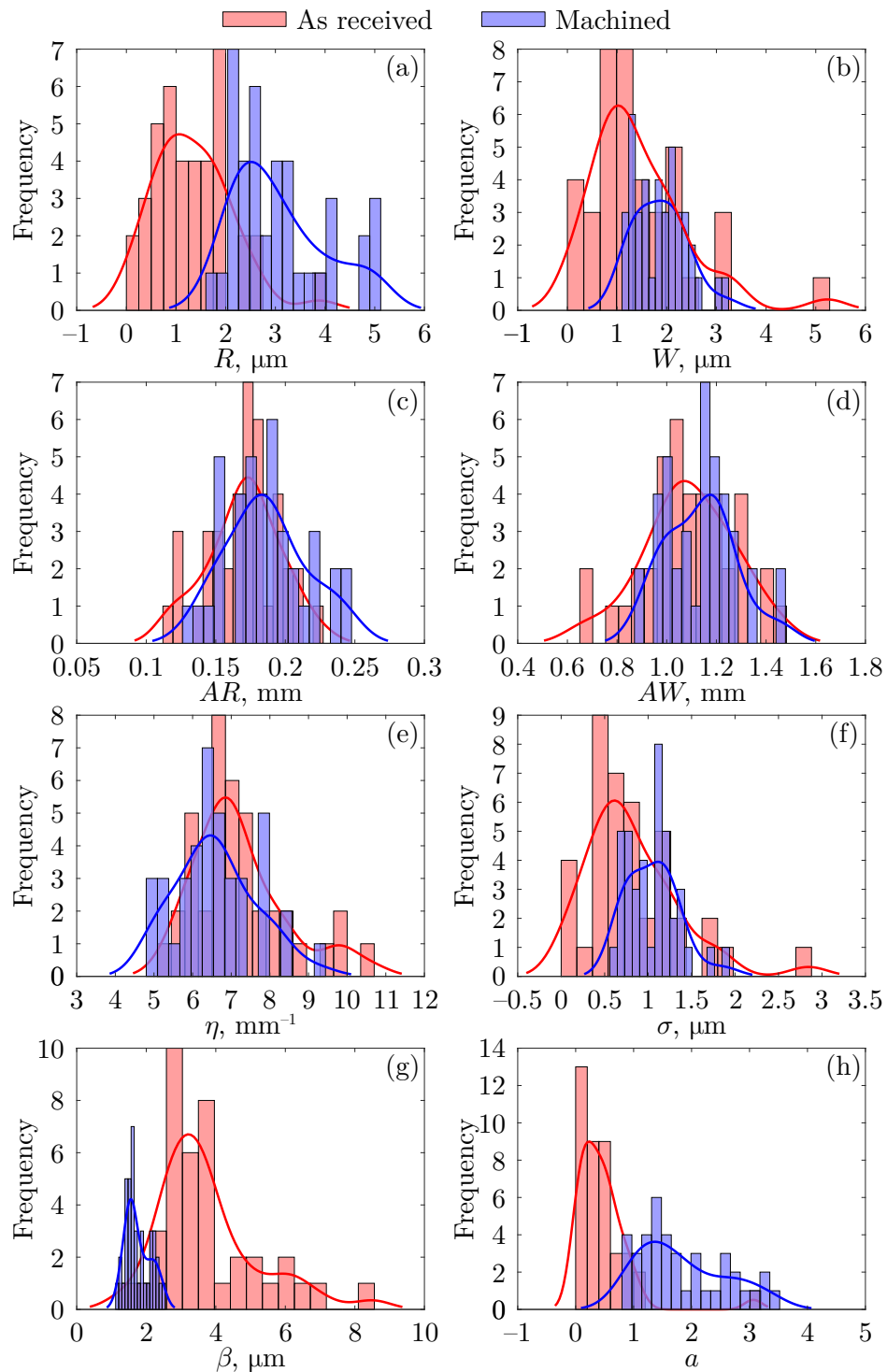


**Figure 8.10:** Histograms of the averaged motif parameters (a)  $R$ , (b)  $W$ , (c)  $AR$ , (d)  $AW$ , and compound roughness parameters, (e)  $\eta$ , (f)  $\sigma$ , (g)  $\beta$ , and (h)  $a$  for all samples (regardless of material) split into “as received” and “machined” surfaces. Solid lines are kernel density estimates (KDE) fitted to the empirical distributions, for visual guidance.

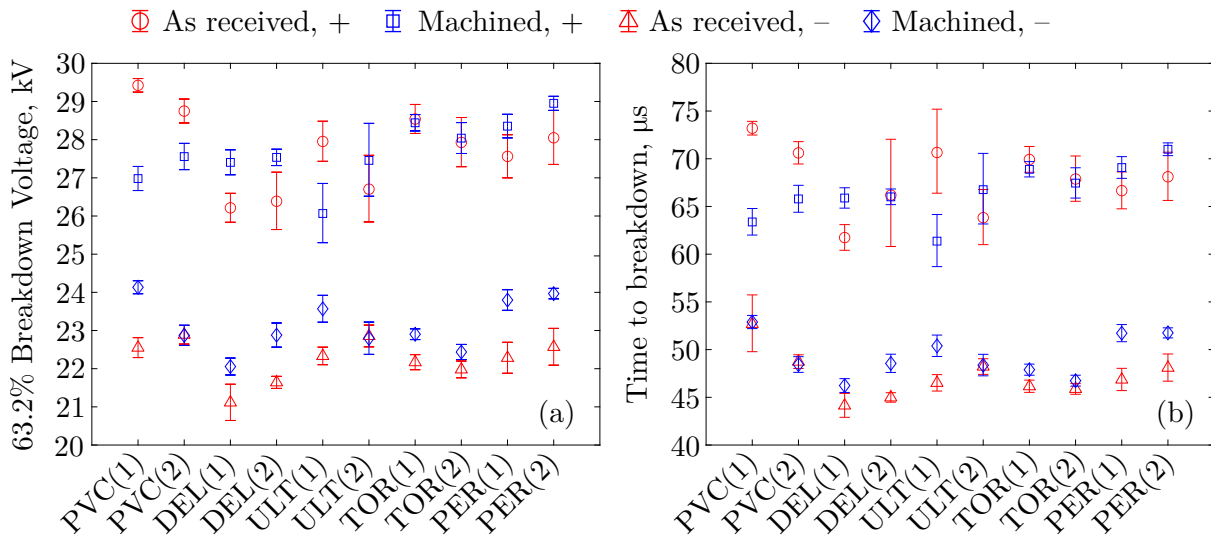


**Figure 8.11:** 63.2% (a) breakdown voltage and (b) time-to-breakdown for surface flashover events using the TG-01 for both surface conditions. Error bars show the 95% confidence intervals.

## 8.4 Surface Flashover Results

This section concerns itself with the presentation and interpretation of the impulsive surface flashover results. These are broadly split into three subsections: Section 8.4.1 includes discussion of the statistically-processed breakdown voltages and times, which are supported by additional modelling work. Section 8.4.2 then details the tendencies observed between the flashover characteristics and the measured surface roughness parameters.

### 8.4.1 Comparison of Breakdown Voltages and Times

Breakdown voltages and times-to-breakdown for tests conducted using the TG-01 generator are first presented as Figure 8.11. It is clear, from Figure 8.11(a), that under this configuration, negative-polarity breakdown voltages were several kV lower than positive breakdown voltages for all tests. Given that asymmetric electrodes were employed in this study, it is unsurprising to find clear polarity effects. In this case, the difference can be explained using streamer theory and by considering that the utilised electrode geometry incorporates two triple junctions. The first is located at the tip of the needle electrode where it sits in contact with the sample; and the second, where the dielectric sample meets the inner edge of the ground electrode. Figure 8.12 shows the simulated electric field distribution in the test cell, numerically computed using QuickField Professional [13] at a peak voltage of 30 kV. Labelled on the figure is also a contour along the breakdown path. The field strength along this contour is plotted in Figure 8.13, showing that the

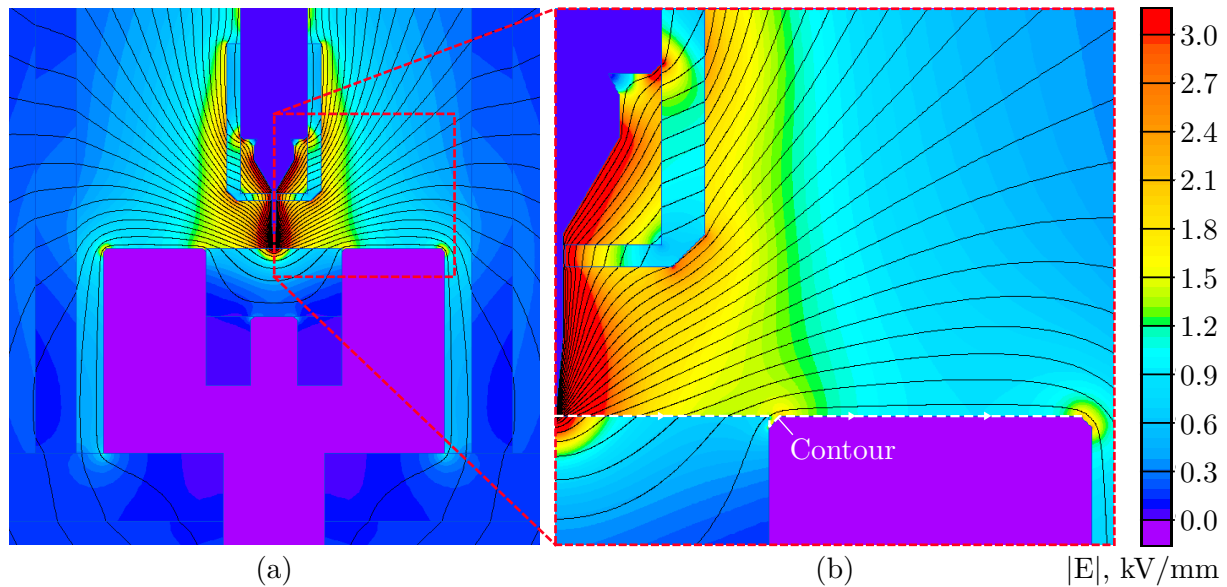


**Figure 8.12:** (a) QuickField [13] simulated electric field distribution inside the test cell at a peak applied voltage of 30 kV, (b) magnified image showing the two triple junctions and a measurement contour for the plot of Figure 8.13.

electric field at both junctions can exceed the critical field of air when the voltage pulse reaches its maximum. Positive and negative streamers therefore have the potential to initiate from both points during the pre-breakdown phase and propagate towards each other, in much the same manner as those simulated in Chapter 5 - Section 5.8.4.

However, the asymmetry and vastly different geometries of the electrodes imparts a far stronger field at the needle triple junction compared to the ground triple junction. As is well-established in the literature (e.g., [14] and references therein) and in the simulation work of Chapter 6, positive streamers tend to initiate at lower field magnitudes, but negative streamers typically exhibit greater acceleration and attain higher propagation velocities than their positive counterparts once incepted. It follows that under positive impulse action, a positive streamer may incept far earlier at the needle and begin to propagate along the surface, while the negative streamer remains within its initiating phase near the ground electrode triple junction. To bridge the electrode gap, the positive streamer must therefore traverse a greater proportion of the inter-electrode gap before combining with the negative streamer. Based on the results of Chapter 4, the lower  $dU/dt$  of the TG-01 impulses may additionally suppress the formation of a negative streamer altogether, due to the action of outward diffusion during the rising slope. In this case, the positive streamer

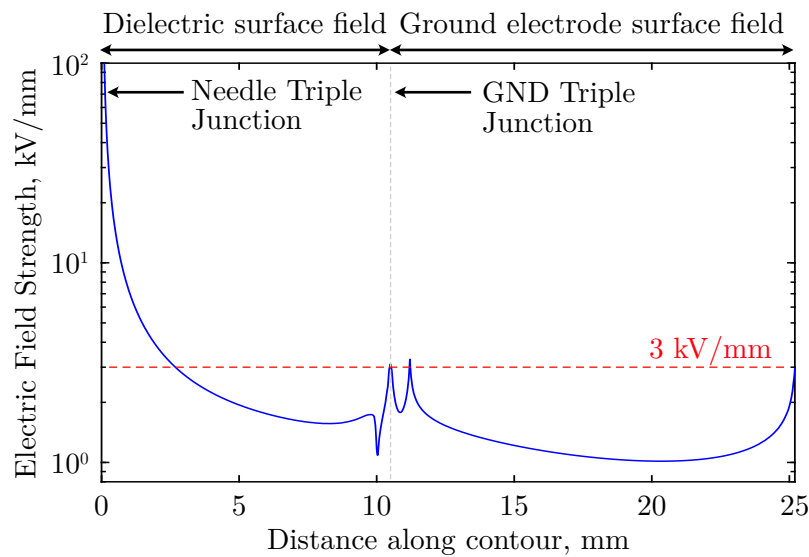


**Figure 8.13:** Simulated electric field magnitude across the dielectric surface and ground electrode corresponding to the contour of Figure 8.12. Red dashed line shows 3 kV/mm as an approximate reference value for the static breakdown voltage of atmospheric air.

would be required to traverse the entire 1 cm gap distance before the conductive plasma channel becomes established.

In contrast, under negative-polarity impulses, negative streamers are believed to reach the propagation phase at almost the same time (or earlier) as a positive streamer initiated from the ground triple junction. The greater electric field strength at the needle compensates for the typical initiation delay observed for negative streamers. As such, a pair of positive and negative streamers may simultaneously develop across the surface, each traversing some proportion of the inter-electrode gap distance, leading to a shorter breakdown time and lower breakdown voltage. As an aspect for future work, the use of the StrAFE framework presented in Chapter 5 could be used to test this idea further by simulating surface streamers in a computational domain representative of the experimental conditions.

For the faster-rising impulses of the Blumlein, Figure 8.14 shows the extracted times-to-breakdown. Positive-polarity tests tended to break earlier and closer to the voltage peak, while negative impulses consistently broke only on the falling edge. This explains the significant time difference between positive and negative times-to-breakdown in Figure 8.14(a) and 8.14(b). This difference suggests that the negative impulse breakdown voltage would be higher than the positive, if both were to be achieved on the rising slope, which contrasts the case of the TG-01. However, this may also be a result of breakdown on the falling edge and be related to a minimum field

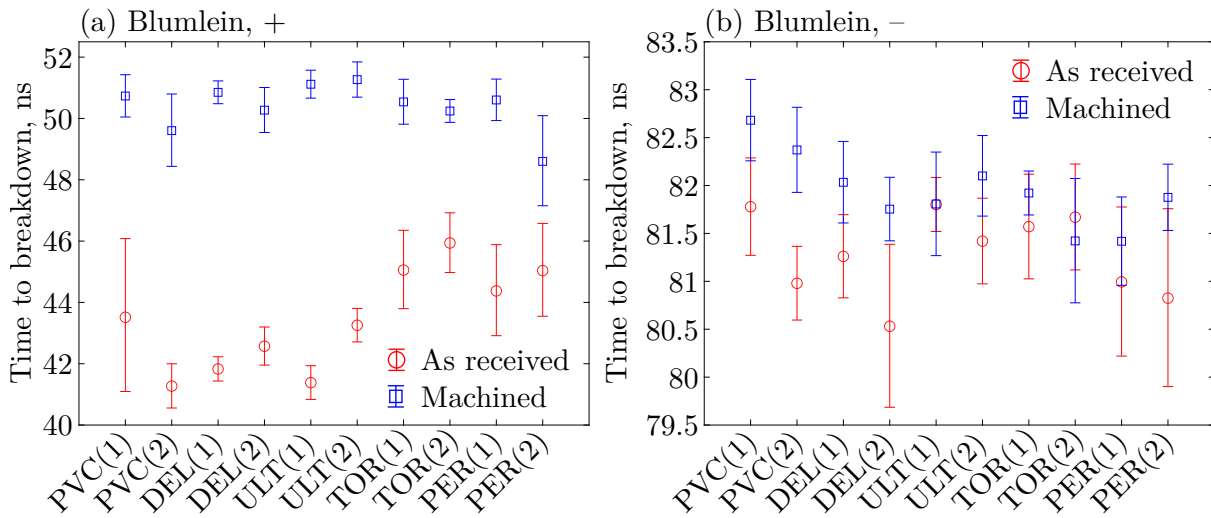


**Figure 8.14:** 63.2% time-to-breakdown for (a) positive, (b) negative surface flashover events using the Blumlein for both surface conditions. Error bars show the 95% confidence intervals.

required to sustain streamer propagation. Due to the more diffuse nature of negative streamers, a higher electric field strength is typically necessary to both initiate and sustain negative streamer propagation. As the voltage begins to decrease from the peak, it may be the case that the decrease in the field acts to slow the development of negative streamers to greater effect than on positive streamers; the latter of which have more compact wavefronts and can generally be sustained at lower field magnitudes. This may explain the delay of negative polarity breakdown as a result of breakdown occurring on the falling edge.

Notable tendencies can additionally be observed when comparing between “as received” and “machined” surfaces. For the TG-01 tests, “as received” surfaces tended to exhibit flashover at a generally lower voltage than “machined” surfaces, but exclusively for negative impulses. For positive-polarity tests, no such distinction was found. It is possible that the more diffuse nature of negative streamer fronts are more prone to be interrupted by changes in surface morphology, and may be more difficult to reignite once interrupted compared to their positive counterparts. However, this does not align with the tendencies observed for the Blumlein tests, suggesting other mechanisms at play that should be explored in further detail in subsequent investigations. In the case of Blumlein tests, this tendency emerges in the time-to-breakdown data for both polarities, the “as received” surfaces typically experienced flashover earlier than “machined” surfaces, with positive Blumlein impulses breaking earlier, on average, by around 9 ns compared to a difference of 1 ns to 3 ns for the negative case. The differences in surface roughness conditions are believed to be responsible for the tendencies of TG-01 negative, and Blumlein results of both polarities;

as explained in the following.

In consideration of the profilometry results of Section 8.3, it is believed that the increase in surface roughness ( $R$  and  $W$ ) may act to impede surface discharges by increasing the discharge path length. Pre-breakdown streamers tend to adhere to surfaces, as shown in [15, 16] and demonstrated in Chapter 5 - Section 5.8.2. Thus, any additional amount of surface corrugation or irregularity tends to increase the total length a streamer must travel to bridge the electrode gap, believed to prolong the time-to-breakdown [3, 4, 6].

Additional arguments may be further based on the series of combined works conducted by Meyer *et al.* [2, 3, 7, 8] and Marskar [6], who investigated streamer propagation along profiled surfaces of various geometry (as was included in the review of Chapter 2 - Section 2.4.1). The corrugated surfaces of various profiles used in [6, 7] had surface features which were far more uniform and of a significantly larger characteristic scale (minimum 500  $\mu\text{m}$  between corrugations) than typical surface asperities found on the present samples. However, reported effects of the impeding and suppression of surface streamers is believed to be highly relevant to this work. The authors of [6] concluded that smaller spacing between profile features reduced the streamer propagation distance over the same time, which aligned with the increased breakdown strengths observed experimentally in [3] and observed in the tests conducted here. Simulations in [6] indicated that the main driving mechanisms could be attributed to the increase in discharge path length and the inability for streamer re-ignition and subsequent re-connection between adjacent surface features. Their theory is largely consistent with the majority of the results found here, considering that a rough surface is morphologically similar to a corrugated surface, with the difference that the distribution of features are non-uniform, and surface features are instead on the scale of several micrometres. However, their work did not consider the effects of impulse rate-of-rise and cannot explain several discrepancies in the present data. Namely, why positive flashover across the PVC(1), PVC(2) and ULT(1) surfaces for the TG-01 tests (Figure 8.11) were found to stray from this behaviour, with “as received” surfaces outperforming those that were machined. These may be statistical anomalies, or suggests behaviour specific to longer-rising positive impulses. It would nonetheless be of great interest to expand the range of surface roughness conditions under test to supplement the present results.

#### 8.4.2 Effect of Surface Characteristics

To better understand the effects of individual surface characteristics on the measured flashover voltages and times, this section combines the breakdown data of Section 8.4.1 and the surface

data of Section 8.3 in a discussion of their correlations and of their implications. The method used here was as follows. For each data set, the extracted 63.2% breakdown voltage and breakdown times were correlated against the set of motif parameters,  $R$ ,  $W$ ,  $AR$ ,  $AW$ , and the set of compound roughness parameters  $\eta$ ,  $\sigma$ ,  $\beta$ , and  $a$ . Visual, qualitative, correlation was evaluated by inspection of the plotted data (which are provided here), supported by calculated values of Spearman’s correlation coefficient,  $\rho_c$ , given by

$$\rho_c = \frac{\text{cov}[\mathcal{R}(x), \mathcal{R}(y)]}{\bar{\sigma}_{\mathcal{R}(x)}\bar{\sigma}_{\mathcal{R}(y)}}, \quad (8.1)$$

where  $\text{cov}(\cdot, \cdot)$  is the covariance between its arguments, the function  $\mathcal{R}(\cdot)$  represents the *rank* of the variable within the data vector, and  $\bar{\sigma}_{\mathcal{R}(\cdot)}$  is the standard deviation of the extracted variable ranks. Spearman’s coefficient can be considered a measure of whether variables  $x$  and  $y$  are correlated by a monotonic function which is not necessarily linear (unlike Pearson’s correlation coefficient, which measures linear correlation only). Data points within each plot has been labelled with shortened labels to indicate the material type: V = PVC, D = Delrin, U = Ultem, T = Torlon, and P = Perspex; and a subscript indicating whether it was the first 20 or second 20 shots of the pair of samples used per experimental condition. The surface condition and polarity have additionally been indicated based on the colour and marker shape. Visual correlations are first discussed for all results before the correlation coefficients are compared.

Results from the TG-01 tests are first presented. Figure 8.15 plots the breakdown voltage against the motif parameters  $R$ ,  $W$ ,  $AR$ ,  $AW$ , for all tested surfaces. Note that since the negative and positive breakdown voltages were close in value, they have been plotted on the same plot, such that there appears a divide between the top group and bottom group of data delineated by a grey line. These were treated separately when calculating the correlation coefficient.

As a first observation, many material pairs (subscript 1 and 2 of the same letter identifier) were found to be in close proximity of each other. This implies that samples of the same material had similar “as received” surface conditions, reacted similarly to the machining action, and behaved electrically similar. A clear separation between “as received” surfaces and “machined” surfaces is evident for the roughness parameters  $R$  and  $W$ , which reflects the trends discussed within Section 8.3. The observed tendency for negative breakdown voltages to be higher with “machined” surfaces is reflected in the slight upward tendency observed in the bottom group of Figure 8.15(a) for  $R$ , and to a lesser degree Figure 8.15(d) for  $W$ . No such relationship is evident for  $AR$  or  $AW$ , suggesting that the motif *heights* represented by the parameters  $R$  and  $W$  are

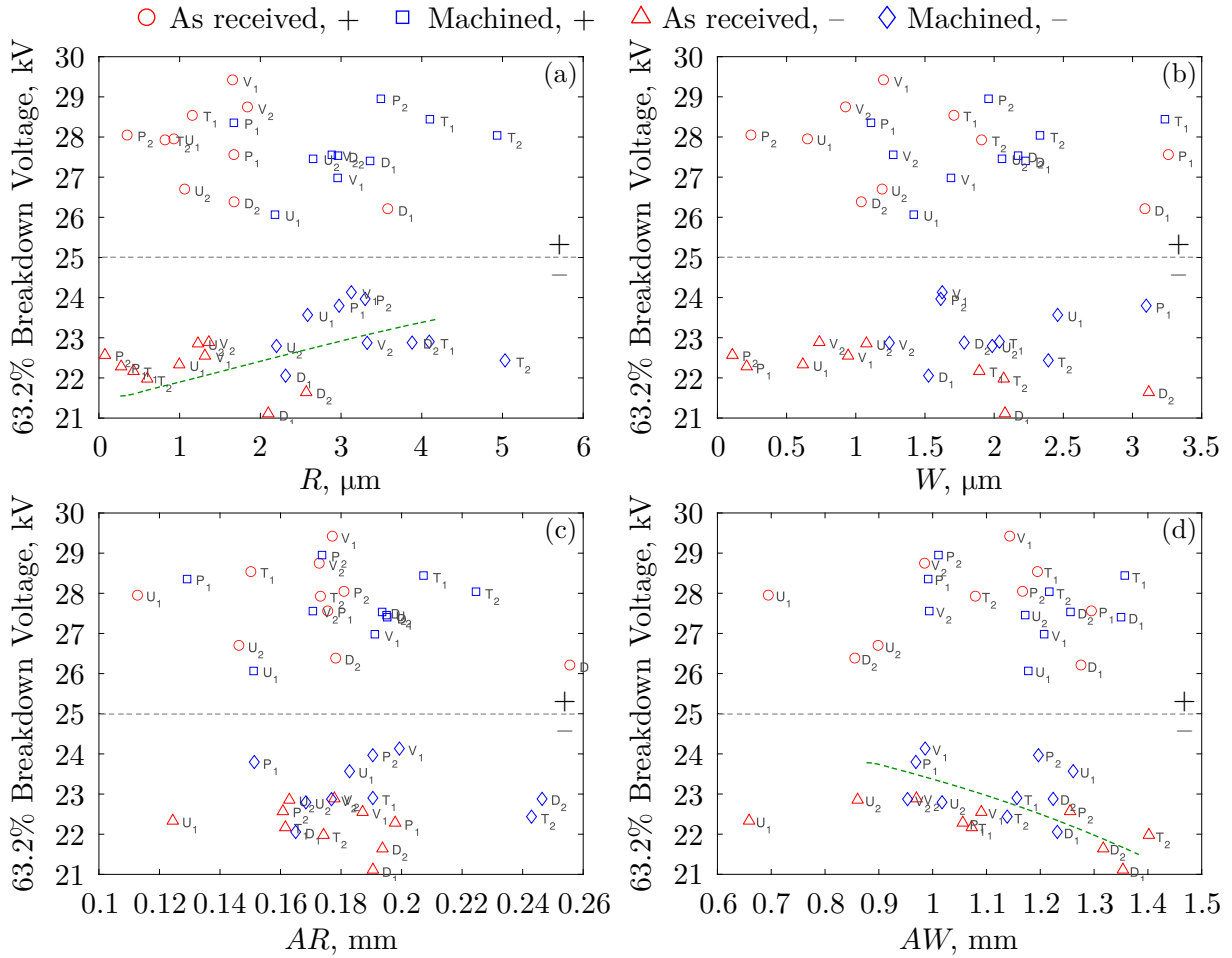


**Figure 8.15:** Plots of 63.2% breakdown voltages recorded for all TG-01 surface flashover events against the motif parameters (a)  $R$ , (b)  $W$  (c)  $AR$ , and (d)  $AW$ . Dashed green lines are for visual guidance only, indicating the observed tendencies discussed in the main text and corresponding to those deemed of interest in Table 8.2.

stronger determinators of surface flashover voltage.

Figure 8.16 plots the breakdown voltages against the compound surface parameters  $\eta$ ,  $\sigma$ ,  $\beta$ , and  $a$ . Overall, no clear correlations were found for the asperity density,  $\eta$ , or the asperity height deviation,  $\sigma$ . However, correlations appear present for the mean asperity radii,  $\beta$ , and the mean asperity aspect ratio,  $a$ . This once again suggests that the degree of *protrusion* away from the surface median is of greater importance to surface flashover behaviour than larger surface undulations. This seems reasonable from the perspective of the streamer inhibition, since higher asperities (and sharper, higher aspect ratio asperities) on a similar dimensional scale to typical features of streamers (e.g., charge sheaths and streamer head radii) present quite significant

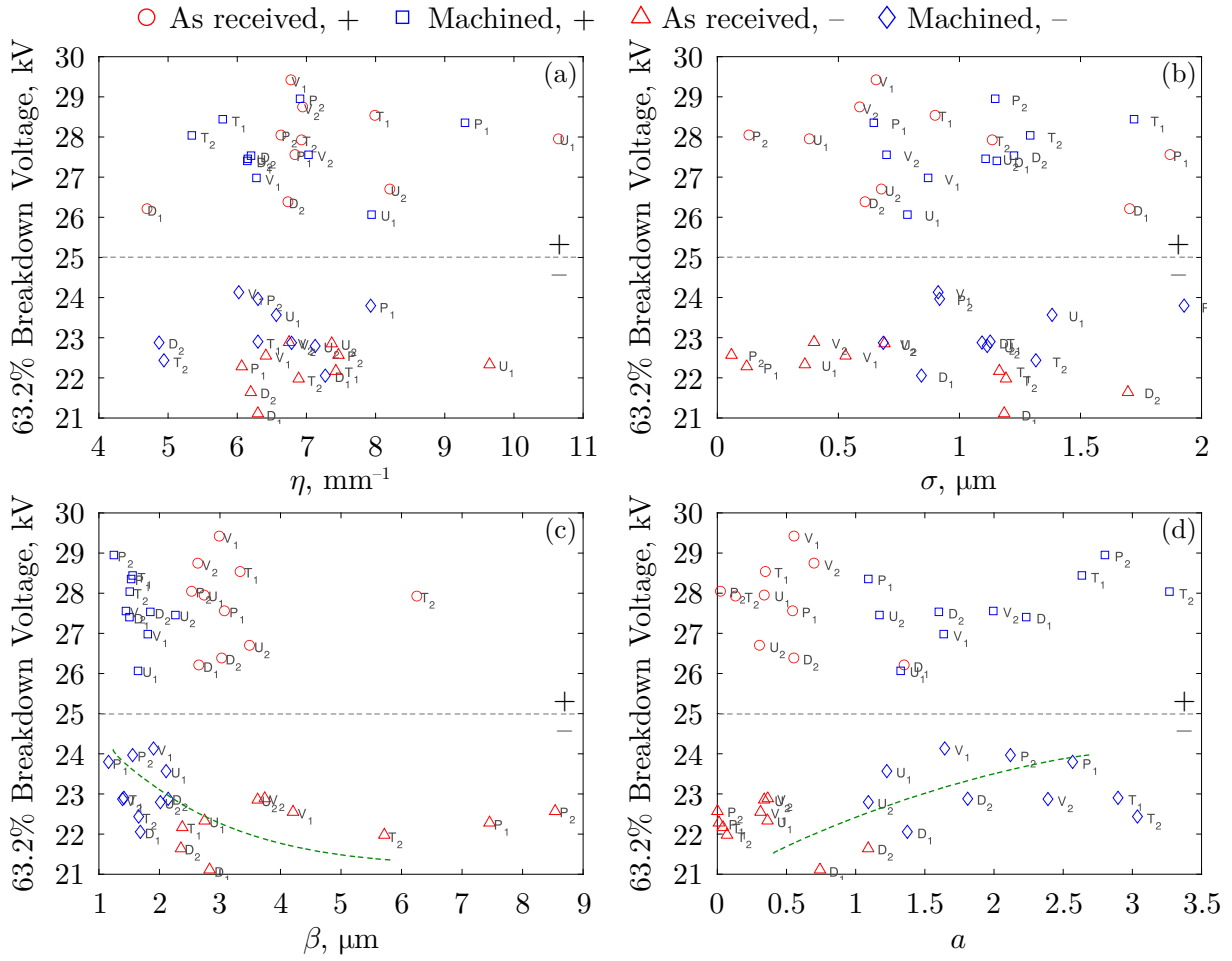


**Figure 8.16:** Plots of 63.2% breakdown voltages recorded for all TG-01 surface flashover events against the compound roughness parameters (a)  $\eta$ , (b)  $\sigma$  (c)  $\beta$ , and (d)  $a$ . Dashed green lines are for visual guidance only, indicating the observed tendencies discussed in the main text and corresponding to those deemed of interest in Table 8.2.

obstacles for surface streamer propagation. However, larger changes to the surface morphology across distances far larger than streamer characteristic scales, may ultimately provide little contribution to an increase of the effective path length, limiting their effectiveness to suppress streamer development. It is also important to note that Ultem was not found to have significantly sharper surface features after machining, in contrast to the solid-solid study of Chapter 7, and neither did it exhibit an abnormally different flashover strength in either set of tests. This is believed to be, at least in part, due to differences in the method used to treat the surfaces in Chapter 7 compared to the present chapter. While the same shoulder mill of Figure 7.18 was used to remove the thin surface layers, the process is thought to be substantially more gentle than that used to treat the square sample edges in Chapter 7. It is believed that this reduced

**Table 8.2:** Matrix of calculated Spearman’s correlation coefficients and significance for all surface flashover datasets against the motif parameters  $R$ ,  $W$ ,  $AR$ ,  $AW$ , and the compound roughness parameters,  $\eta$ ,  $\sigma$ ,  $\beta$ ,  $a$ . Those highlighted blue and in italics represent the most significant across all correlations, satisfying  $|\rho_c| \gtrsim 0.3$  and  $p_s \lesssim 0.25$ .

TG-01 +	$R$	$W$	$AR$	$AW$	$\eta$	$\sigma$	$\beta$	$a$
$\rho_c$	-0.149	-0.135	-0.183	-0.123	0.183	-0.132	-0.038	-0.021
$p_s$	0.530	0.568	0.437	0.603	0.437	0.577	0.876	0.932
Blumlein +	$R$	$W$	$AR$	$AW$	$\eta$	$\sigma$	$\beta$	$a$
$\rho_c$	<i>0.293</i>	0.227	0.185	<i>0.299</i>	-0.185	0.156	-0.205	<i>0.262</i>
$p_s$	<i>0.209</i>	0.334	0.433	<i>0.199</i>	0.433	0.509	0.385	<i>0.264</i>
TG-01 -	$R$	$W$	$AR$	$AW$	$\eta$	$\sigma$	$\beta$	$a$
$\rho_c$	<i>0.504</i>	-0.038	0.071	<i>-0.392</i>	-0.071	-0.039	<i>-0.501</i>	<i>0.510</i>
$p_s$	<i>0.025</i>	0.876	0.767	<i>0.088</i>	0.767	0.871	<i>0.022</i>	<i>0.023</i>
Blumlein -	$R$	$W$	$AR$	$AW$	$\eta$	$\sigma$	$\beta$	$a$
$\rho_c$	<i>0.268</i>	0.212	-0.238	-0.057	0.238	0.253	<i>-0.561</i>	<i>0.501</i>
$p_s$	<i>0.253</i>	0.368	0.312	0.811	0.312	0.281	<i>0.011</i>	<i>0.026</i>

the occurrence of local fracture and resulted in less extreme surface asperities, diminishing the overall impact that brittleness may have in generating sharper asperity peaks. This is supported by comparing the range of asperity aspect ratios measured for all square samples in Figure 7.32 of Chapter 7 to the cylindrical samples of Figure 8.16, which were found to be lower in general.

Since the TG-01 tests exhibited breakdown exclusively on the rising edge, there was a direct correlation between breakdown voltage and time (i.e., longer time-to-breakdown means higher breakdown voltage). As such, there is no need to plot the breakdown time against roughness characteristics as the observed trends are identical to those of Figure 8.15 and 8.16. On the other hand, for the results obtained using the Blumlein, Figure 8.17 and 8.18 plot the obtained times-to-breakdown against the motif and compound roughness parameters, respectively. One finds that the general tendencies as discussed for the TG-01 results apply equally to the breakdown times measured using the faster-rising Blumlein generator.

As a more quantitative means to measure these correlations, the Spearman’s correlation coefficient was calculated for each dataset according to (8.1). Table 8.2 presents the calculated coefficients for all cases and across all motif and roughness parameters. For the TG-01 tests, this involves the correlation between roughness parameters and the breakdown voltage; substituted for breakdown time in the case of the Blumlein tests. The reader is reminded that the range of  $\rho_c$  is  $[-1, +1]$ , where a value close to  $-1$  indicates a strong monotonically decreasing correlation, while a value close to  $+1$  suggests a strong monotonically increasing correlation. Corresponding significance

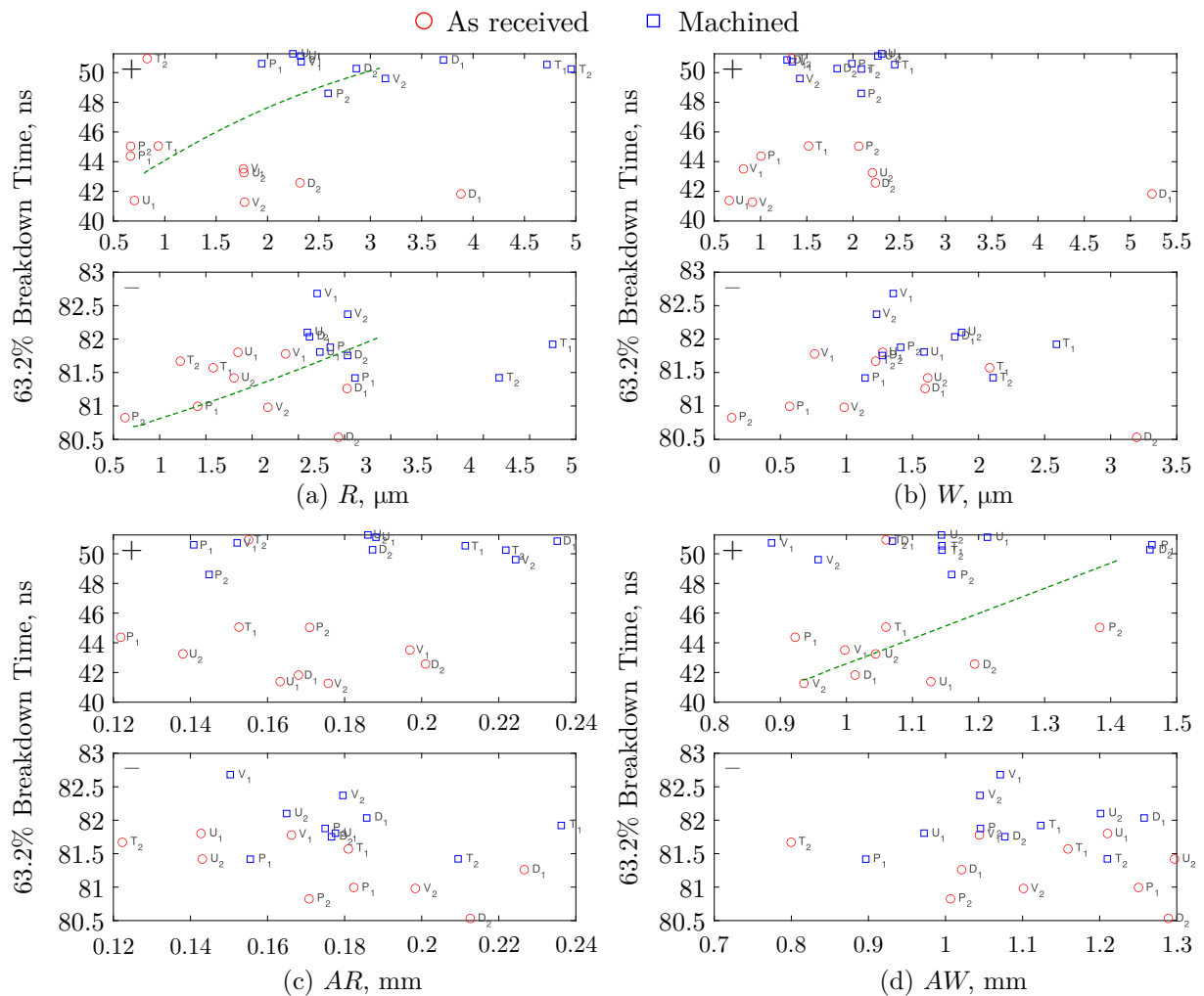


**Figure 8.17:** Plots of 63.2% times to breakdown recorded for all Blumlein surface flashover events against the motif parameters (a)  $R$ , (b)  $W$  (c)  $AR$ , and (d)  $AW$ . Dashed green lines are for visual guidance only, indicating the observed tendencies discussed in the main text and corresponding to those deemed of interest in Table 8.2.

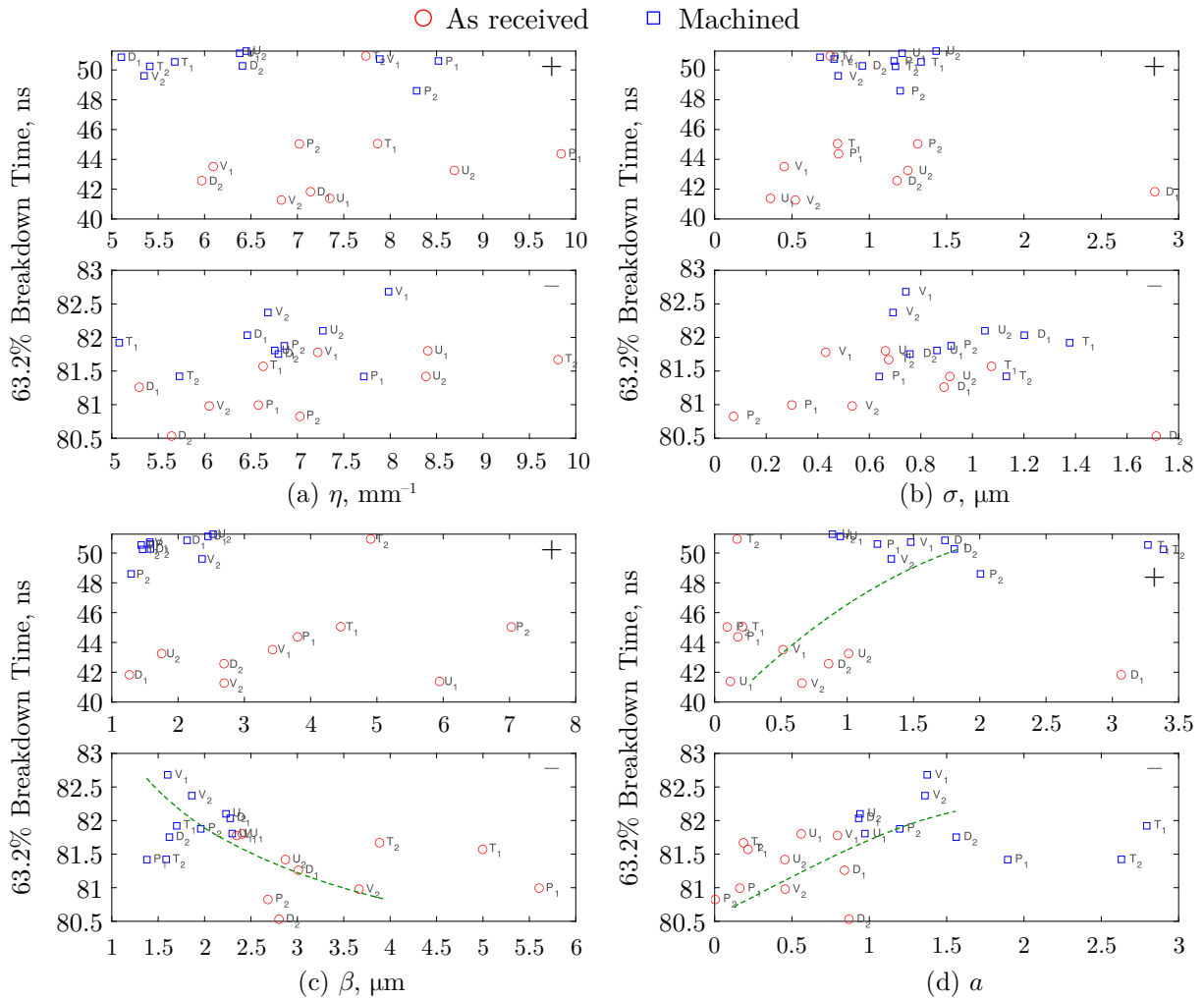


**Figure 8.18:** Plots of 63.2% times to breakdown recorded for all Blumlein surface flashover events against the compound surface parameters (a)  $\eta$ , (b)  $\sigma$  (c)  $\beta$ , and (d)  $a$ . Dashed green lines are for visual guidance only, indicating the observed tendencies discussed in the main text and corresponding to those deemed of interest in Table 8.2.

values have also been indicated for each correlation coefficient, as a measure of the confidence that the calculated correlation is indeed different from zero.

It is remarked that at a sample size of 20 points per set, this is generally lower or near to the minimal recommended sample size for effective correlation analysis to be conducted. As such, to attain statistical significance at high confidence was unlikely. This analysis is nonetheless presented here, as the correlation coefficients with greatest significance were found to largely agree with the qualitative tendencies. Based on the range of values obtained for  $\rho_c$  and  $p_s$ , all datasets resulting in values of  $|\rho_c| \gtrsim 0.3$  and with a significance of  $p \lesssim 0.25$  (75% confidence) were considered moderately correlated with sufficient confidence to warrant discussion. The values that satisfied this criteria are coloured blue within Table 8.2. It can be seen that the parameters that appear most impactful (with with greatest confidence that a correlation does exist) to the surface flashover behaviour are, broadly, the roughness motif heights,  $R$ ; the asperity radii,  $\beta$ ; and the asperity aspect ratio,  $a$ . In fact, statistical significance at >95% confidence was found for  $\beta$  and  $a$  parameters for all negative flashover tests, providing reasonable grounds to suggest that there are moderate ( $|\rho_c| \approx 0.5$ ) correlations between these features to the breakdown voltage and time. This was, however, less clear for all positive tests regardless of  $dU/dt$ , which may suggest that these sharper surface features have a greater inhibition effect for the more diffuse, negative-polarity, streamers. Two other highlighted values were for the waviness motif width,  $AW$ . However, the nature of these correlations are of opposite sign between the positive Blumlein dataset and the TG-01 negative dataset—which seemingly suggests an increase to the flashover voltage (time) for the former case but decrease for the latter. Considering also the low confidence of the other two correlation coefficients concerning the  $AW$  parameter, these two statistics are perhaps best interpreted with some caution. Additionally, despite the statistically significant change in distribution of the  $W$  parameter after machining, there is little suggestion that this correlated to a change in the flashover voltage or time. The correlation coefficients were found to be generally higher for Blumlein tests, but the significance values lend little confidence to this observation. Since  $W$  measures the height of the *waviness* motif, it supports the idea that the long-wavelength features are of lesser impact. For the TG-01 positive dataset, none of the calculated correlation coefficients satisfied the above criteria, which is likely due to the (possibly anomalous) PVC(1), PVC(2) and ULT(1) results as briefly discussed in Section 8.4.1. Overall, however, the loose correlations calculated here are in agreement with the qualitative analysis and are generally supportive of the proposed mechanisms.

## 8.5 Chapter Conclusions, Contributions, and Outlook

In accompaniment to Chapter 7, this chapter has presented the results gathered from surface flashover experiments under HV impulse action in atmospheric air. Motivated by the increasing interest in surface texture modification to achieve higher flashover voltage, the present work focused on the comparison between fresh, “as received”, surfaces and treated, “machined”, surfaces that were of different surface conditions.

Minor modifications to the experimental arrangements of Chapter 7 were made to accommodate for a new test cell configuration and sample geometry. Cylindrical samples of the polymers (PVC, Delrin, Torlon, Ultem, and Perspex) were fabricated, leaving one side untreated and “as received”, while a thin layer was removed from the opposite face to produce two unique surface conditions. Surface profilometry and characterisation using the motif method of Section 7.3.2 indicated substantial changes to the surface texture and roughness parameters on all materials after the machining. Once again, impulses of different  $dU/dt$  and of both polarities were tested, with the breakdown voltage and time-to-breakdown data treated using Weibull statistics. Field modelling was further conducted to explain the observed breakdown tendencies and polarity effects. Correlations were found between the surface conditions and the measured impulsive flashover voltages and times, largely in agreement with other results found in the literature. Most importantly, the comprehensive surface characterisation data obtained within this work contributed towards a greater understanding of the driving mechanisms behind surface-texture-enhanced flashover strength.

### 8.5.1 Academic Significance and Contributions

A main contribution of this work is the application of surface profilometry to gain a deeper quantitative understanding of the effects of surface condition on impulse-driven flashover strength. This work also contributed towards a greater understanding of flashover behaviours across important polymeric materials used in pulsed power system design and under non-standard impulsive waveforms.

For the materials used here, surface profilometry and motif characterisation showed a statistically significant increase to the heights of short- and long-wavelength surface features after machining action. The long-wavelength undulations were affected to a lesser extent, and lesser change was also found for motif profile widths. The changes to surface parameters were supported using 2-parameter hypothesis tests to 95% confidence on the pre- and post- machining parameter

distributions. As such, the machining method used in this work can be considered to have increased the surface asperity heights and asperity radii of the “as received” material samples, producing surfaces with generally greater overall *roughness* but with lesser changes to *waviness*.

Results of impulsive breakdown tests did not indicate substantial differences in flashover strength between materials, though it is noted that breakdown on the rising slope was achieved using the Samtech TG-01 generator but not with the stacked Blumlein pulse forming line, where the latter breakdown strengths were instead inferred from measurements of the time-to-breakdown based on breakdown current waveforms. In addition, there did not appear to be substantial differences in flashover behaviour between different  $dU/dt$  aside from an expected increase to the overall breakdown strength, characteristic of overstressed pulsed breakdown as discussed in Chapter 4. Clear polarity effects were found, attributed to the asymmetry of the electrode configuration which induced higher flashover voltages for positive-polarity impulses compared to negative cases for almost all tests, regardless of  $dU/dt$  or surface condition. This was supported by a numerical simulation of the electric field distribution, which allowed an explanation of these effects to be based on typical characteristics of pre-breakdown streamer development. Breakdown results further suggested that “machined” surfaces generally experienced flashover at higher voltages than “as received” surfaces, an aspect investigated further in a correlation analysis between the flashover data and the measured profilometry data. Using Spearman’s correlation as a measure of possible monotonic relationships, results suggested that short-wavelength surface features have stronger influence on the surface flashover voltage than long-wavelength variations. Rougher surfaces therefore increase the surface flashover voltage, in agreement with the theory of increased path length and suppression of surface streamer development. Wavier surfaces alone are believed to have far lesser effect, since the effective path length is not substantially increased. Based upon the novel results obtained here, however, it has been proposed that surface features with length scales on a similar order of magnitude to typical features of surface streamers (e.g, streamer charge sheaths or head radii) may be most effective in inhibiting streamer development and propagation along rough surfaces. Greater surface asperity heights also appear to be a contributing factor to surface streamer inhibition, though this seems to apply more to the closely-spaced features of the roughness profile than to the sparser height features of the long-wavelength waviness profile. This ultimately leads to the enhancement of the surface flashover strength.

### 8.5.2 Industrial Relevance

The conclusions of the present investigation may be of consequence to the future coordination and optimisation of high voltage and pulsed power insulating systems. In particular, solid dielectric spacers used in various gas-insulated equipment and apparatuses. Various methods, including surface texture modification, have gained significant research attention to evaluate their effectiveness to enhance surface flashover strength.

The conclusions from this study relating to the effects of roughness and waviness may provide critical design knowledge for surface-modified solid insulators. For instance, the results may aid in the development of specific surface profiles to be applied to solid dielectric spacers in terms of the shape, size, and distribution of surface features for greatest effect. Moreover, for the five materials used in this work (PVC, Delrin, Torlon, Ultem, and Perspex), the set of obtained impulsive breakdown data suggested little difference between the material flashover strengths in the present configuration, but emphasised the importance of surface condition. This may aid in the selection of appropriate materials for the development of pulsed power systems employing similar geometries and waveforms as used in this work. In any case, this study has contributed an additional set of performance data for the impulse-driven surface flashover behaviour and surface roughness characteristics of several polymeric materials important to pulsed power systems development.

### 8.5.3 Limitations and Future Outlook

Limitations associated with this experimental study shares several aspects to those of Chapter 7 - Section 7.6, particularly with respect to the method of surface characterisation and statistical treatment of data. The reader is thus referred to Section 7.6 for details.

Specific limitations uniquely identified for this work firstly includes the described inability for breakdown on the rising edge to be induced for both cases of  $dU/dt$ . While this did not limit comparisons between polarity and between surface types, an ideal case would see the direct comparison of the same quantities, i.e., breakdown voltage. It would be highly beneficial in future work to consider configurations and waveforms that would allow such consistency to be achieved.

Other limitations include issues relating to the test cell. When changing samples, the entire top half of the test cell (which housed the needle electrode) required removal before a new sample could be inserted; then the removed cover replaced. Although effort was made to ensure that the needle was re-centred, it was not rigorously measured, nor in general can it be perfectly centred.

Samples were judged to have no preferential breakdown pathway after the completion of 20 shots based on the visual inspection of the angular distribution of the post-breakdown traces. Data was accepted if these were judged adequately spaced and suggested no one path was repeatedly traversed (thus, the needle was not significantly closer to one side). However, formal analysis of these distributions was not conducted. Whether this would be necessary, or at all useful, is unclear, since other factors such as spatially non-uniform surface roughness across the surface may additionally affect the distribution of paths, even in an ideal case where the needle could be perfectly centred. While there is no evidence to suggest that this may have skewed the obtained results, an improvement could potentially be made by using a test cell that does not require removal of the needle nor ground electrode during the sample change procedure. In this case, the electrodes would be maintained at precisely the same location for each sample under test.

Further to this is the correlation analysis conducted for the breakdown voltage and time-to-breakdown data against the motif and surface parameters. The limited number of samples used in this work exists on the lower bound of a typically accepted number of samples required for meaningful correlation analysis. Substantially more data would have been beneficial for this analysis, and may give significantly greater confidence in the observed tendencies. It is remarked that despite this, the parameters which were identified from the loosening of correlation and significance thresholds aligned well with qualitative analysis and expectation. Additional data possibly gathered from future work, however, would undoubtedly be valuable to the extension of this analysis and to the confirmation of the suspected tendencies.

There of course exists significant scope for future study, owing to the many facets of impulsive surface flashover that remain poorly understood. Some particular aspects identified from the present work include:

- Systematic discharge modelling studies, over complex surfaces designed to emulate practical rough surfaces, would be highly beneficial to further understand the effects of surface condition on surface streamer development. At the time of writing, this remains squarely within the domain of high-performance computing and is not yet easily conducted.
- Given past and present results on the posited influence of surface texture on streamer inhibition across interfaces, what are the optimal profiles that should be used over solid spacers to enhance flashover strength? This should relate to spacing, distribution, and shape.
- How does the distribution of surface asperities affect the discharge development? For

example, would there be benefits to be gained by grading the surface roughness along the discharge direction, such as increasing the roughness over the propagation distance?

- If the size and nature of surface asperities influence the streamer inhibition effectiveness, as is believed based on the results of the present work and past works, where are the limits? For example, consider an initially *wavy* surface with long-wavelength undulations far longer than any characteristic streamer scale. As the feature wavelength decreases, at what point do the features of the waviness profile become sufficiently short to be classified as roughness? Decreasing further, what effects do features with wavelength significantly shorter than that of streamer characteristic lengths have on the discharge evolution, if any?
- In relation to the above point, a limit must exist as wavelength decreases, as the surface becomes fractal-like in nature with a theoretically infinite path length (which cannot lead to an infinite breakdown voltage). Can mathematical analysis of this limiting theoretical case lead to important realisations that inform engineering design, see for instance, the progress seen in [17].
- Expansion of this study to include different materials, other values of  $dU/dt$ , and additional electrode geometries.
- Expansion of this study to compare the effects of different types of industrial surface treatment, to understand the changes they may have on the surface condition depending on the tool or method used, and corresponding effects (if any) on the surface flashover voltage.

## Chapter 8 References

- [1] H. Li, N. Zebouchi, M. Haddad, A. Reid, and E. Ekkel, “Development of future compact and eco-friendly HVDC gas insulated systems,” *Energies*, vol. 15, no. 22, 2022.
- [2] B. X. Du, H. C. Liang, and J. Li, “Surface coating affecting charge distribution and flashover voltage of cone-type insulator under DC stress,” *IEEE Trans. Dielectr. Electr. Insul.*, vol. 26, no. 3, pp. 706–713, 2019.
- [3] H. K. Meyer, R. Marskar, H. G. Osberg, and F. Mauseth, “Surface flashover over a microprofiled cylinder in air,” *IEEE Trans. Dielectr. Electr. Insul.*, vol. 30, no. 6, pp. 2862–2869, 2023.
- [4] R. W. Macpherson, M. P. Wilson, I. V. Timoshkin, M. J. Given, and S. J. MacGregor, “Flashover of smooth and knurled dielectric surfaces in dry air,” *IEEE Trans. Dielectr. Electr. Insul.*, vol. 31, no. 1, pp. 204–211, 2024.
- [5] J. O. Rossi, M. Ueda, A. R. Silva, and L. P. S. Neto, “Improvement on UHMWPE and PMMA surface flashover under atmospheric pressure using piii processing,” *IEEE Trans. Plasma Sci.*, vol. 48, no. 10, pp. 3386–3391, 2020.
- [6] R. Marskar and H. K. H. Meyer, “A kinetic monte carlo study of positive streamer interaction with complex dielectric surfaces,” *Plasma Sources Sci. Technol.*, vol. 32, no. 8, p. 085010, 2023.
- [7] H. K. H. Meyer, R. Marskar, and F. Mauseth, “Evolution of positive streamers in air over non-planar dielectrics: experiments and simulations,” *Plasma Sources Sci. Technol.*, vol. 31, no. 11, 2022.
- [8] H. K. H. Meyer, R. Marskar, H. Gjerdal, and F. Mauseth, “Streamer propagation along a profiled dielectric surface,” *Plasma Sources Sci. Technol.*, vol. 29, no. 11, p. 115015, 2020.
- [9] I. C. Somerville, S. J. MacGregor, and O. Farish, “An efficient stacked-blumlein HV pulse generator,” *Meas. Sci. Technol.*, vol. 1, no. 9, p. 865, 1990.
- [10] *Square shoulder mills brochure: EMP02-040-A16-AP11-05C*, ZCC Cutting Tools Europe GmbH. [Online]. Available: <https://www.zccct-europe.com>
- [11] Drake Plastics Ltd. Co. (2019) Post curing torlon wear parts reduces wear. [Online]. Available: <https://drakeplastics.com/2019/03/25/>
- [12] T. Wong, I. Timoshkin, and S. MacGregor, “Data for: “characteristics of impulse-driven surface flashover across polymers with different surface conditions”,” doi: 10.15129/c1523bc8-647d-4752-b18f-973a82c108c4, 2024.
- [13] Tera Analysis. Quickfield professional v. 6.4. [Online]. Available: <https://quickfield.com>
- [14] S. Nijdam, J. Teunissen, and U. Ebert, “The physics of streamer discharge phenomena,” *Plasma Sources Sci. Technol.*, vol. 29, no. 10, p. 103001, 2020.
- [15] X. Li, A. Sun, G. Zhang, and J. Teunissen, “A computational study of positive streamers interacting with dielectrics,” *Plasma Sources Sci. Technol.*, vol. 29, no. 6, p. 065004, 2020.
- [16] A. Dubinova, “Modeling of streamer discharges near dielectrics,” Ph.D. dissertation, Applied Physics and Science Education, Technische Universiteit Eindhoven, 2016, proefschrift.
- [17] A. Majumdar and B. Bhushan, “Role of Fractal Geometry in Roughness Characterization and Contact Mechanics of Surfaces,” *J. Tribol.*, vol. 112, no. 2, pp. 205–216, 1990.

## Concluding Remarks, Contributions, and Perspectives

---

MOTIVATED by the rapid expansion of pulsed power engineering, this work recognised the existence of significant gaps in understanding related to dielectric phenomena under impulse waveforms, and relating to electrical breakdown phenomena under fast-rising overstressed conditions. Issues of which, if left unaddressed, greatly hinders the further development and advancement of pulsed power technology. The present work has made progress in addressing key issues pertaining to gas discharge phenomena within pulsed power systems, advancing the theoretical and practical understanding that underpins the realisation and development of next-generation pulsed power systems. In conclusion, the overall contributions of this work are summarised in the following. The reader is referred back to the individual chapter conclusions for full and specific details.

Starting from the application of an impulse to an arbitrary system, this work has made novel analytical progress in methods to estimate the time-dependent field distributions developed in multilayer, poorly-conducting, composite materials. For the first time, theoretical results relating to the calculation of  $n$ -layer interfacial relaxation times were attained and have been generalised to a number of geometrical configurations. The successful application of these models to multilayered field graders under impulsive energisation shows the importance of considering the dielectric relaxation time, and of its coupling to the applied impulse rise and fall characteristics. These are of practical significance relating to the estimation of insulator performance for pulsed

power systems, where the methods developed here are envisaged to provide convenient methods for the coordination and optimisation of composite insulation.

A second set of brand-new analytical results have arisen from the theoretical analysis of electron avalanche development under a fast-rising and linearly-increasing electric field. In a number of successive approximations, an analytical model, semi-empirical expression, and closed-form equations have been developed that provide an alternative to the Meek-Raether criterion for overstressed impulsive breakdown. The novel model not only progresses the theoretical explanation of increasing breakdown voltage with faster rate-of-rise, but is further demonstrated to be capable of predicting the upward shift to Paschen's curve; be able to recreate the field-time scaling characteristic of pulsed breakdown, with good agreement with experimental data; and to correctly describe the scaling of streamer inception time with  $dU/dt$  when compared to simulated data. The role that electron diffusion may play in impulse-driven breakdown was further elucidated through mathematical arguments, indicating that it may not always be negligible. The approximations developed in this work have provided expressions able to be directly evaluated for reasonable estimations of gas breakdown strength under overstressed conditions, based only on empirical fits of gas transport parameters and the rate-of-field-rise. They are therefore synonymous with classical breakdown criteria, extended for the first time to the domain of overstressed breakdown and improving upon fully phenomenological expressions that have been prevalent within pulsed power engineering.

A novel framework for simulating low-temperature gas discharge phenomena, based on an open-source package, has been developed and is documented in this work. In the form of a Python library, StrAFE (**Streamers on Adaptive Finite Elements**) is a fully-featured, simple-to-use, and scalable software package designed to computationally simulate gas discharge phenomena using the finite element method. Comparison of simulation outputs from StrAFE to known problems from literature indicated that StrAFE is comparable to state-of-the-art custom codes and commercially-available software, in terms of capabilities and accuracy. StrAFE therefore has great potential to be used in future work, offering a highly capable platform in which gas discharge phenomena can be explored in greater depth. Moreover, its physics-agnostic nature facilitates future modification with relative ease, bringing with it the possibility to explore gas discharge and plasma phenomena coupled to other physics, in simulations of considerable complexity.

Subsequent simulation studies were conducted using StrAFE on overstressed ionisation wavefronts and streamer discharges. A new velocity-to-diameter scaling relationship for overstressed streamer discharges in air has been found, where streamers generally propagated faster of similar diameter,

---

different to a well-known empirical expression previously found for streamers initiated in static fields. Comparison of simulated ionisation waves, initiated under sub-millimetre needle-plane and needle-needle gaps, has contributed additional understanding of cathode sheath scaling behaviour in CO<sub>2</sub> with different rates of voltage rise. This work has further provided important technical insights into computational aspects relating to the representation of photoionisation. Surface streamers have additionally been studied within short and long electrode gaps, contributing towards understanding of surface charge dynamics and on the effects of non-uniform deposited charge on subsequent surface streamer propagation. This includes both the expedition and suppression of subsequent streamers based on polarity, and the possibility for accumulated surface charge to contribute partially to incomplete surface streamers. The simulated characteristics and tendencies of these ionisation events, especially under varying voltage rate-of-rise, are of particular significance to novel technologies that aim to harness the properties of low-temperature plasmas. They further contribute to a deeper fundamental understanding of primary ionisation phenomena as a preceding mechanism to complete electrical breakdown in gas-insulated systems.

In experimental work, a systematic experimental study of the impulse-driven breakdown characteristics across solid-solid interfaces and solid-gas interfaces formed from PVC, Delrin, Ultem, Torlon, and Perspex, under impulses rising at different rates, has been conducted. Included within this study was the application of surface profilometry techniques which characterised the pre-breakdown surface roughness of solid surfaces, aiding in the understanding of its effects. Solid-solid interfaces, assembled under low mating pressure, were found to largely exhibit breakdown strengths lower than gas alone due to interfacial field enhancement. Novel effects relating to the aspect-ratio of surface asperities have been found to possibly reduce the solid-solid interfacial breakdown strength under low mating pressure, and explanations justifying its difference to the case of high mating pressure have been proposed. While material permittivity and conductivity appeared largely unimportant to the breakdown strength, a dependence of the widths of breakdown traces with rate of voltage rise was found, with some indication that it may additionally be material-dependent. The theory of gas-void driven breakdown across solid-solid surfaces appeared to largely hold, where a novel theoretical model was found to provide reasonable estimations of the interfacial breakdown strength. The solid-solid study has highlighted the importance of different material's mechanical response to cutting and machining, which in general, do not affect materials in the same way. For the majority of applications where effort is not generally made to attain specific surface conditions, merely the way in which the cutting tool modifies the surface texture (particularly for brittle materials) may leave unfavourable surface conditions that promote interfacial discharge. Within

solid-gas experiments, the impulsive flashover characteristics between “as-received” surfaces and treated, “machined”, surfaces were compared. The use of surface roughness data reinforced past studies that reported on enhanced flashover strengths with increased surface roughness. By separation of surface profiles using the motif characterisation method, this work found that short-wavelength surface features appear more effective in impeding surface streamers than long-wavelength surface undulations. Importantly, this work contributes towards the optimisation of specific surface profiles to achieve the greatest streamer suppression effect, based on the knowledge that certain sizes of roughness features may have greater impact. Ultimately, this moves towards the development of optimal profiles for surface flashover suppression or prevention.

There is, undoubtedly, significant progress still to be made as pulsed power technology looks to the future. Within the technical conclusions contained within each of the Chapters 3–8, aspects deemed of greatest importance for future investigation were outlined extensively, and the reader is encouraged to revisit these sections for details. Summarising over the entirety of this work, however, areas deemed of exceptional importance to future pulsed power research and development activities—those that have been identified from the present work—include:

- Experimental validation of the multilayered models of Chapter 3. This would incidentally require the development of novel diagnostics capable of directly measuring or inferring the electric field strengths within composite layers. Success, alongside the advancement of manufacturing techniques for multilayer laminates, would be significant progress towards novel high-performance insulation solutions.
- Extension of the type of analysis conducted in Chapter 4 on electron avalanches to consider electric fields with a high degree of non-uniformity. Given that non-uniform fields are far more prevalent in practise, understanding avalanche dynamics (and transition) within these geometries is of considerable importance.
- Development of novel and efficient algorithms to speed up full 3D simulations of gas discharge phenomena. Some progress has been made towards this as discussed within Chapter 5, however, it remains generally challenging with current algorithms and accessible computing power (outside of supercomputing facilities).
- Complete description of the streamer-to-leader transition from a physical perspective, which may possibly be implemented into numerical solver routines and advance the understanding of the breakdown phase beyond those of primary wavefronts like in Chapter 6. This currently forms a significant unknown within pulsed power, and more generally, in the

---

fields of high voltage engineering and gas discharge physics. Successful characterisation of this process would be a noteworthy leap forward.

- Significantly expanded studies in terms of materials, impulse waveshapes, mating pressures, etc., on the impulsive flashover studies of Chapter 7 and 8. Lack of performance data is a significant bottleneck to the design of practical systems, critical also for model validation purposes to compare against new theoretical approaches that may be developed.
- Move towards understanding optimal surface modifications that may maximise voltage hold-off capabilities across solid-gas interfaces. This seems a promising direction based on the numerous studies which have reported similar effects. If specific types of surface features are found to lead to significant increases in flashover strength, this would be a simple and cost-effective method that may address significant issues relating to solid-gas interfaces.

Overall, this work has contributed towards a greater understanding of composite dielectric phenomena, charge transport, and (pre-)breakdown events under fast-rising impulse action. The findings of this work have made progress towards the optimisation of mixed-phase and composite materials for HV pulsed applications, the behaviours of low-temperature pulsed gas discharges, and towards the development of novel surface-modified insulating materials for next-generation pulsed power equipment. The utilisation of a diverse set of methodologies encompassing analytical, computational, and experimental work has laid a foundation on which future research can be built.

---

## Appendix

---

### A Mathematical Derivations

#### A.1 Electrode-bounded Multilayered Composite - General Result

Starting from (3.9), it is evident from the second equation that

$$\alpha_k^i(s) = \lambda_i \alpha_k^{i+1}(s), \quad (\text{A.1})$$

since the equality must hold if, for each term  $k$ , (A.1) is satisfied. This first order recurrence allows any coefficient  $\alpha_k^i$  to be written in terms of the first,  $\alpha_k^1$ ,

$$\alpha_k^i(s) = \frac{\alpha_k^1(s)}{\prod_{j<i} \lambda_j} = \frac{\sigma_1 + \varepsilon_0 \varepsilon_1 s}{\sigma_i + \varepsilon_0 \varepsilon_i s} \alpha_k^1(s). \quad (\text{A.2})$$

Next, the first equation of (3.9) may be rearranged such that

$$\begin{aligned} \beta^i &= \beta^{i+1} + \sum_k \alpha_k^{i+1}(s) f_k(q_i^j) - \alpha_k^i(s) f_k(q_i^j) \\ &= \beta^{i+1} + \sum_k f_k(q_i^j) \left[ \alpha_k^{i+1}(s) - \alpha_k^i(s) \right] \end{aligned} \quad (\text{A.3})$$

which, from the recurrence relation in  $\beta^i$  allows  $\beta^n$  to be introduced such that

$$\begin{aligned} \beta^1 - \beta^n &= \sum_{\ell=1}^n \sum_k f_k(q_\ell^j) \left[ \alpha_k^{\ell+1}(s) - \alpha_k^\ell(s) \right] \\ &= \sum_{\ell=1}^n \sum_k \alpha_k^\ell(s) \left[ f_k(q_\ell^j) - f_k(q_{\ell+1}^j) \right], \end{aligned} \quad (\text{A.4})$$

where one may reintroduce (A.2) twice to give

$$\beta^1 - \beta^n = \sum_{\ell=1}^n \sum_k \alpha_k^1(s) \frac{\sigma_1 + \varepsilon_0 \varepsilon_1 s}{\sigma_\ell + \varepsilon_0 \varepsilon_\ell s} \left[ f_k(q_\ell^j) - f_k(q_{\ell+1}^j) \right]$$

$$\begin{aligned}
&= \sum_{\ell=1}^n \sum_k \alpha_k^i(s) \frac{\sigma_i + \varepsilon_0 \varepsilon_i s}{\sigma_\ell + \varepsilon_0 \varepsilon_\ell s} \frac{\sigma_1 + \varepsilon_0 \varepsilon_1 s}{\sigma_\ell + \varepsilon_0 \varepsilon_\ell s} [f_k(q_\ell^j) - f_k(q_{\ell+1}^j)] \\
&= \sum_{\ell=1}^n \sum_k \alpha_k^i(s) \frac{\sigma_i + \varepsilon_0 \varepsilon_i s}{\sigma_\ell + \varepsilon_0 \varepsilon_\ell s} [f_k(q_\ell^j) - f_k(q_{\ell+1}^j)], \tag{A.5}
\end{aligned}$$

as given in the main text.

## A.2 One-dimensional Multilayered Stack—Time Domain Solution

From the one-dimensional general solution (3.21) and the double exponential form (3.22), the coefficient  $A_i(s)$  becomes

$$A_i(s) = \frac{A_0 U_0}{c_0} (\hat{\beta} - \hat{\alpha}) \left[ \frac{1}{(s + \hat{\alpha})(s + \hat{\alpha}) \prod_{\ell=1}^{n-1} \left(s + \frac{1}{\tau_\ell}\right)} \right]. \tag{A.6}$$

One may thus expand (A.6) in partial fractions of the form

$$\begin{aligned}
\frac{1}{(s + \hat{\alpha})(s + \hat{\alpha}) \prod_{\ell=1}^{n-1} \left(s + \frac{1}{\tau_\ell}\right)} &= \frac{A}{(s + \hat{\alpha})} + \frac{B}{(s + \hat{\beta})} + \sum_{\ell=1}^{n-1} \frac{K_\ell}{\left(s + \frac{1}{\tau_\ell}\right)} \\
\Rightarrow 1 &= A(s + \hat{\beta}) \prod_{\ell=1}^{n-1} \left(s + \frac{1}{\tau_\ell}\right) + B(s + \hat{\alpha}) \prod_{\ell=1}^{n-1} \left(s + \frac{1}{\tau_\ell}\right) + \prod_{m=1}^{n-1} \left(s + \frac{1}{\tau_m}\right) \cdot \sum_{\ell=1}^{n-1} \frac{K_\ell}{\left(s + \frac{1}{\tau_\ell}\right)}, \tag{A.7}
\end{aligned}$$

from which one deduces if  $s = -\hat{\beta}$ ,  $s = -\hat{\alpha}$  or  $s = -1/\tau_\ell$ :

$$\begin{aligned}
1 &= B(\hat{\alpha} - \hat{\beta}) \prod_{\ell=1}^{n-1} \left(\frac{1}{\tau_\ell} - \hat{\beta}\right) \rightarrow B = \frac{1}{(\hat{\alpha} - \hat{\beta}) \prod_{\ell=1}^{n-1} \left(\frac{1}{\tau_\ell} - \hat{\beta}\right)} \\
1 &= A(\hat{\beta} - \hat{\alpha}) \prod_{\ell=1}^{n-1} \left(\frac{1}{\tau_\ell} - \hat{\beta}\right) \rightarrow A = \frac{1}{(\hat{\beta} - \hat{\alpha}) \prod_{\ell=1}^{n-1} \left(\frac{1}{\tau_\ell} - \hat{\beta}\right)} \\
1 &= \left(\hat{\beta} - \frac{1}{\tau_\ell}\right) \left(\hat{\alpha} - \frac{1}{\tau_\ell}\right) K_\ell \prod_{m=1, m \neq \ell}^{n-1} \left(\frac{1}{\tau_m} - \frac{1}{\tau_\ell}\right) \\
\rightarrow K_\ell &= \frac{1}{\left(\hat{\beta} - \frac{1}{\tau_\ell}\right) \left(\hat{\alpha} - \frac{1}{\tau_\ell}\right) \prod_{m=1, m \neq \ell}^{n-1} \left(\frac{1}{\tau_m} - \frac{1}{\tau_\ell}\right)}, \tag{A.8}
\end{aligned}$$

hence the time-domain solution after application of the inverse Laplace transform to (A.6):

$$E_i(t) = \mathcal{L}^{-1} \{A_i(s)\} = \frac{A_0 U_0 (\hat{\beta} - \hat{\alpha})}{c_0} \left[ A e^{-\hat{\alpha}t} - B e^{-\hat{\beta}t} + \sum_{\ell=1}^{n-1} K_\ell e^{-\frac{t}{\tau_\ell}} \right], \quad (\text{A.9})$$

where the factor  $(\hat{\beta} - \hat{\alpha})$  may cancel with those contained in coefficients  $A$  and  $B$  if distributed through the exponential terms. The notational differences from the present derivation compared to [31] (Chapter 3) is due to the inclusion or exclusion of the layer-dependent term within the characteristic polynomial. In other words, the leading coefficient  $a_0$  from [31] (Chapter 3) is independent of  $i$ , while the coefficient  $c_0$  in the present formulation is dependent on  $i$ . These are related through

$$c_0 = \frac{a_0}{(\hat{\beta} - \hat{\alpha}) \prod_{k=1, k \neq i}^n \sigma_k (1 + \tau_k s)}, \quad (\text{A.10})$$

where  $k$  runs over all  $n$  layers where  $\tau_k$  are the intrinsic time constants  $\tau_k = \varepsilon_0 \varepsilon_k / \sigma_k$ . This explains the additional terms introduced through the  $P$ ,  $Q$  and  $R$  of (3.24), which arise when the partial fraction expansion is performed using the  $a_0$  formulation, since the additional terms in the denominator of (A.10) appear within the expansion. The formulation published in [31] (Chapter 3) is used within the main text for consistency despite the slightly simpler formulation attained from the general solution. Regardless, it is important to note that these two expressions are identical.

### A.3 Laplace Equation in Prolate-Spheroidal Coordinates

Starting from the Laplace equation (3.32) in  $(\mu, \nu)$  coordinates, one may use the substitution  $\sigma = \cosh \mu$ ,  $\tau = \cos \nu$  to transform (3.32) into

$$\vec{\nabla} \varphi = \frac{1}{a_0^2 (\sigma^2 - \tau^2)} \left\{ \frac{\partial}{\partial \sigma} \left[ (\sigma^2 - 1) \frac{\partial \varphi}{\partial \sigma} \right] + \frac{\partial}{\partial \tau} \left[ (1 - \tau^2) \frac{\partial \varphi}{\partial \tau} \right] \right\}. \quad (\text{A.11})$$

Assuming separability, the ansatz  $\varphi = \Sigma(\sigma)T(\tau)$  separates the equation like

$$\begin{aligned} T(\tau) \frac{\partial}{\partial \sigma} \left( (\sigma^2 - 1) \frac{\partial \Sigma(\sigma)}{\partial \sigma} \right) + \Sigma(\sigma) \frac{\partial}{\partial \tau} \left( (1 - \tau^2) \frac{\partial T(\tau)}{\partial \tau} \right) &= 0 \\ \Rightarrow \frac{1}{\Sigma(\sigma)} \left( 2\sigma \frac{d\Sigma(\sigma)}{d\sigma} + (\sigma^2 - 1) \frac{d^2 \Sigma(\sigma)}{d\sigma^2} \right) + \frac{1}{T(\tau)} \left( -2\tau \frac{dT(\tau)}{d\tau} + (1 - \tau^2) \frac{d^2 T(\tau)}{d\tau^2} \right) &= 0, \end{aligned} \quad (\text{A.12})$$

thus giving two separated differential equations of the Legendre type

$$\begin{aligned} (1 - \sigma^2) \frac{d^2 \Sigma(\sigma)}{d\sigma^2} - 2\sigma \frac{d\Sigma(\sigma)}{d\sigma} + k\Sigma(\sigma) &= 0, \\ (1 - \tau^2) \frac{d^2 T(\tau)}{d\tau^2} - 2\tau \frac{dT(\tau)}{d\tau} + kT(\tau) &= 0, \end{aligned} \quad (\text{A.13})$$

where customarily one sets  $k = \ell(\ell + 1)$ ,  $\ell \in \mathbb{Z}$ ; solutions of which are Legendre's functions

$$\begin{aligned} \Sigma(\sigma) &= AP_\ell(\sigma) + BQ_\ell(\sigma), \\ T(\tau) &= CP_\ell(\tau) + DQ_\ell(\tau), \end{aligned} \quad (\text{A.14})$$

thus giving the full general solution due to linearity,

$$\varphi = \sum_{\ell=0}^{\infty} [A_\ell P_\ell(\cos \nu) + B_\ell Q_\ell(\cos \nu)] [C_\ell P_\ell(\cosh \mu) + D_\ell Q_\ell(\cosh \mu)], \quad (\text{A.15})$$

where the original definitions  $\sigma = \cosh \mu$ ,  $\tau = \cos \nu$  have been restored, as given in the main text.

#### A.4 Legendre Expansion Coefficients

For a function  $f$  expanded in Legendre polynomials,

$$f = \sum_{n=0}^{\infty} a_n P_n(x), \quad (\text{A.16})$$

one may exploit the orthogonality of Legendre polynomials with respect to the inner product, i.e.,

$$\int_{-1}^1 P_n(x) P_m(x) dx = \delta_{nm} = \begin{cases} 0 & n \neq m \\ \frac{2}{2n+1} & n = m \end{cases} \quad (\text{A.17})$$

where  $\delta_{mn}$  is the Kronecker delta function. In this work, the substitution  $x = \cos \nu$  is used, giving corresponding form with a change of variable

$$\int_0^\pi P_n(\cos \nu) P_m(\cos \nu) \sin \nu d\nu = \delta_{nm} = \begin{cases} 0 & n \neq m \\ \frac{2}{2n+1} & n = m \end{cases}. \quad (\text{A.18})$$

It follows that from (A.16), one may multiply both sides by  $P_\ell(\cos \nu)$  and integrate such that

$$f = \sum_{n=0}^{\infty} a_n P_n(\cos \nu) \quad (\text{A.19})$$

$$\begin{aligned}
&\Rightarrow \int_0^\pi f \cdot P_m(\cos \nu) \sin \nu \, d\nu = \int_0^\pi \sum_{n=0}^{\infty} a_n P_n(\cos \nu) P_m(\cos \nu) \sin \nu \, d\nu \\
&\Rightarrow \int_0^\pi f \cdot P_m(\cos \nu) \sin \nu \, d\nu = \sum_{n=0}^{\infty} a_n \frac{2}{2m+1} \delta_{nm} \\
&\therefore a_m = \frac{2m+1}{2} \int_0^\pi f \cdot P_m(\cos \nu) \sin \nu \, d\nu
\end{aligned} \tag{A.20}$$

as given in the main text.

## A.5 Multilayer Prolate-Spheroidal Solution

From the two-term Fourier-Legendre solution in the prolate-spheroidal system, one has

$$\varphi_i = A_i \cosh \mu \cos \nu + B_i \cos \nu \left( 1 - \cosh \mu \ln \sqrt{\frac{\cosh \mu + 1}{\cosh \mu - 1}} \right) \tag{A.21}$$

as a general solution, which has been simplified to

$$\varphi_i = [A_i + B_i F_i] \cosh \mu \cos \nu \tag{A.22}$$

by factoring out the trigonometric terms and introducing the definition of  $F_i$  as in (3.41). It follows that in the notation of the general solution (3.5),  $\Phi^1 := [A_i + B_i F_i] \cosh \mu$  and from (3.9) one finds

$$\begin{aligned}
&[A_i + B_i F_i] \cosh \mu = [A_{i+1} + B_{i+1} F_i] \cosh \mu \\
&\left[ A_i \sinh \mu + B_i \frac{\partial}{\partial \mu} (F_i \cosh \mu) \right] = \lambda_i \left[ A_{i+1} \sinh \mu + B_{i+1} \frac{\partial}{\partial \mu} (F_i \cosh \mu) \right],
\end{aligned} \tag{A.23}$$

where the definition for  $G_i$  can be substituted to yield

$$\begin{aligned}
A_i + B_i F_i &= A_{i+1} + B_{i+1} F_i \\
A_i + B_i G_i &= \lambda_i (A_{i+1} + B_{i+1} G_i).
\end{aligned} \tag{A.24}$$



and where  $\bar{d}_1 = d_1/b_1$ ; though it is evident that  $\bar{d}_i$  for  $i = 1, 2, \dots, N - 2$  will all be zero. From the algorithm, solutions  $x_i$  are found according to

$$x_i = \bar{d}_i - \bar{c}_i x_{i+1}, \quad x_N = \bar{d}_N, \quad (\text{A.30})$$

which, from the definitions of  $\bar{c}$  and  $\bar{d}$  above, may be used to calculate the first coefficient  $x_1$  as a product over  $N - 2$   $-\bar{c}_i$  coefficients, since most of  $\bar{d}_i = 0$  with the exception of  $\bar{d}_{N-1}$  and  $\bar{d}_N$  which are factored out of the product like

$$x_1 = (\bar{d}_{N-1} - \bar{c}_{N-1}\bar{d}_N) \prod_{m=1}^{N-2} -\bar{c}_m = (\bar{d}_{N-1} - \bar{c}_{N-1}\bar{d}_N) \prod_{m=1}^{N-2} \frac{c_m}{b_m - a_m \bar{c}_{m-1}} \quad (\text{A.31})$$

from the system matrix, coefficients  $c_m$  may be substituted based on the knowledge that

$$c_m = \begin{cases} \lambda_m(F_m - G_m), & \text{for } m \text{ odd} \\ G_m \lambda_m - F_m, & \text{for } m \text{ even} \\ 0 & \text{for } m = N - 1, N \end{cases} \quad (\text{A.32})$$

yields

$$\begin{aligned} x_1 &= (\bar{d}_{N-1} - \bar{c}_{N-1}\bar{d}_N) \underbrace{\prod_{m=1}^{N-2} \frac{c_m}{b_m - a_m \bar{c}_{m-1}}}_{=} \\ &= \prod_{m=1}^{N-2} \frac{1}{b_m - a_m \bar{c}_{m-1}} \cdot \prod_{m=1}^{N-2} c_m \\ &= \prod_{m=1}^{N-2} \frac{1}{b_m - a_m \bar{c}_{m-1}} \cdot \prod_{m=1}^{n-2} \lambda_m(F_m - G_m) \cdot \prod_{m=1}^{n-2} G_m \lambda_m - F_m. \end{aligned} \quad (\text{A.33})$$

From the matrix,  $\bar{c}_{N-1} = 0$ , while  $\bar{d}_{N-1}$  can be simplified to

$$\bar{d}_{N-1} = \frac{d_{N-1} - a_{N-1} \cancel{d_{N-2}}^0}{b_{N-1} - a_{N-1} \bar{c}_{N-2}} = \frac{a_0 E_0 [\lambda_{N-1}(F_{N-1} - G_{N-1})]}{b_{N-1} - a_{N-1} \bar{c}_{N-1}}. \quad (\text{A.34})$$

The factor  $(\bar{d}_{N-1} - \bar{c}_{N-1}\bar{d}_N)$  can therefore be absorbed into the first and second  $\Pi$  operators, yielding

$$x_1 = a_0 E_0 \prod_{m=1}^{N-1} \frac{1}{b_m - a_m \bar{c}_{m-1}} \cdot \prod_{m=1}^{n-1} \lambda_m(F_m - G_m) \cdot \prod_{m=1}^{n-2} G_m \lambda_m - F_m$$

$$\begin{aligned}
&= -a_0 E_0 \prod_{m=1}^{n-1} \lambda_m (F_m - G_m) \cdot \left[ \prod_{m=1}^{2n-3} (a_m \bar{c}_{m-1} - b_m) \cdot \prod_{m=1}^{n-2} \frac{1}{G_m \lambda_m - F_m} \right]^{-1} \\
&= -\frac{a_0 E_0}{P_n} \prod_{m=1}^{n-1} \lambda_m (F_m - G_m), \tag{A.35}
\end{aligned}$$

where the substitution  $N = 2(n - 1)$  has been made and a factor of  $-1$  has been taken out. Also to match the form given in the main text, the reciprocal power  $-1$  has been introduced. The double product contained within the the square brackets is therefore the full form of the characteristic polynomial. From this, one attains the results of the main text,

$$\begin{aligned}
P_1 &= \prod_{m=1}^{2(1)-3} (a_m \bar{c}_{m-1} - b_m) \cdot \prod_{m=1}^{1-2} \frac{1}{G_m \lambda_m - F_m} = (1) \cdot (1) = 1 \\
P_2 &= \prod_{m=1}^1 (a_m \bar{c}_{m-1} - b_m) \cdot \prod_{m=1}^0 = (a_1 \bar{c}_{m-1} - b_1) = -(G_1 \lambda_1 - F_1) = F_1 - G_1 \lambda_1 \\
P_3 &= \prod_{m=1}^3 (a_m \bar{c}_{m-1} - b_m) \cdot \prod_{m=1}^1 \frac{1}{G_m \lambda_m - F_m} = \frac{(a_1 \bar{c}_0 - b_1)(a_2 \bar{c}_1 - b_2)(a_3 \bar{c}_2 - b_3)}{G_1 \lambda_1 - F_1} \\
&= (F_2 - G_2 \lambda_2)(F_1 - G_1 \lambda_1) - F_2 G_2 (\lambda_2 - 1)(\lambda_1 - 1) \\
&\vdots \\
P_n &= \dots \text{etc.} \tag{A.36}
\end{aligned}$$

## A.6 Fickian Diffusion of Gaussian Density using Green's Function

For brevity, the derivation here is done for a constant diffusion coefficient,  $D$ . The time-dependent case is straightforward to obtain by the substitutions provided at the end of the following. Fick's second law was solved using the corresponding 3-dimensional Green's function,

$$u(\vec{x}, t) = \frac{1}{(4\pi Dt)^{3/2}} \int_{\mathbb{R}^3} g(\vec{y}) \cdot \exp \left[ -\frac{(\vec{x} - \vec{y})^2}{4Dt} \right] d^3 \vec{y}, \tag{A.37}$$

where  $g(\vec{y})$  is the initial condition

$$g(\vec{x}) = g_0(t_0) \exp \left( -\frac{\vec{x}^2}{2s_0^2} \right) \tag{A.38}$$

re-labelled from Chapter 4. It follows that

$$\begin{aligned} u(\vec{x}, t) &= \frac{1}{(4\pi Dt)^{3/2}} \int_{\mathbb{R}^3} g_0(t_0) \exp\left(-\frac{\vec{y}^2}{2s_0}\right) \exp\left[-\frac{(\vec{x} - \vec{y})^2}{4Dt}\right] d^3\vec{y} \\ &= \frac{g_0(t_0)}{(4\pi Dt)^{3/2}} \int_{\mathbb{R}^3} \exp\left\{-\left[\frac{\vec{y}^2}{2s_0^2} + \frac{(\vec{x} - \vec{y})^2}{4Dt}\right]\right\} d^3\vec{y}, \end{aligned} \quad (\text{A.39})$$

where the integrand may be simplified as

$$\begin{aligned} &\rightarrow \underbrace{\exp\left(-\frac{\vec{x}^2}{(2s_0^2 + 4Dt)}\right)}_{\vec{y}\text{-independent}} \exp\left[-\left(\frac{(2s_0^2) \vec{x}^2}{4Dt(2s_0^2 + 4Dt)} + \vec{y}^2 \frac{(2s_0^2 + 4Dt)}{2s_0^2(4Dt)}\right) - \frac{2\vec{x} \cdot \vec{y}}{4Dt}\right] \\ &= \exp\left(-\frac{\vec{x}^2}{(2s_0^2 + 4Dt)}\right) \exp\left[-\frac{(2s_0^2 + 4Dt)}{2s_0^2(4Dt)} \left(\vec{y} - \frac{2s_0^2}{(2s_0^2 + 4Dt)}\vec{x}\right)^2\right]. \end{aligned} \quad (\text{A.40})$$

Let

$$\vec{z} = \sqrt{\frac{2s_0^2 + 4Dt}{2s_0^2(4Dt)}} \left(\vec{y} - \frac{2s_0^2}{2s_0^2 + 4Dt}\vec{x}\right), \quad (\text{A.41})$$

then one may make the change of integration limits

$$d^3\vec{z} = \left[\frac{2s_0^2(4Dt)}{2s_0^2 + 4Dt}\right]^{3/2} d^3\vec{y}. \quad (\text{A.42})$$

Thus,

$$\begin{aligned} u(\vec{x}, t) &= \frac{g_0(t_0)}{(4\pi Dt)^{3/2}} \exp\left(-\frac{\vec{x}^2}{(2s_0^2 + 4Dt)}\right) \int_{\mathbb{R}^3} \exp(-\vec{z}^2) \left[\frac{2s_0^2(4Dt)}{2s_0^2 + 4Dt}\right]^{3/2} d^3\vec{z} \\ &= \frac{g_0(t_0)}{(4\pi Dt)^{3/2}} \exp\left(-\frac{\vec{x}^2}{(2s_0^2 + 4Dt)}\right) \left[\frac{2s_0^2(4Dt)}{2s_0^2 + 4Dt}\right]^{3/2} \underbrace{\int_{\mathbb{R}^3} \exp(-\vec{z}^2) d^3\vec{z}}_{=\pi^{3/2}}, \end{aligned} \quad (\text{A.43})$$

and finally,

$$\begin{aligned} u(\vec{x}, t) &= \frac{g_0(t_0)}{(4\pi Dt)^{3/2}} \exp\left(-\frac{\vec{x}^2}{2s_0^2 + 4Dt}\right) \left[\frac{2s_0^2(4Dt)}{2s_0^2 + 4Dt}\right] \pi^{3/2} \\ &= g_0(t_0) \frac{\pi^{3/2}}{(4\pi Dt)^{3/2}} \frac{[2s_0^2(4Dt)]^{3/2}}{(2s_0^2 + 4Dt)^{3/2}} \exp\left(-\frac{\vec{x}^2}{2s_0^2 + 4Dt}\right) \end{aligned}$$

$$= g_0(t_0) \frac{[2\pi s_0^2 (4Dt)]^{3/2}}{[2s_0^2\pi(4Dt) + \pi(4Dt)^2]^{3/2}} \exp\left(-\frac{\vec{x}^2}{2s_0^2 + 4Dt}\right), \quad (\text{A.44})$$

yielding the result of the main text, where  $u(\vec{x}, t) \rightarrow n_e(\vec{r}, t)$  and  $g_0(t_0) \rightarrow n_0(t_0)$ , one has

$$n_e(\vec{r}, t) = n_0(t_0) \frac{(2\pi s_0^2)^{3/2}}{(2\pi s_0^2 + 4\pi Dt)^{3/2}} \exp\left(-\frac{\vec{x}^2}{2s_0^2 + 4Dt}\right). \quad (\text{A.45})$$

Note that  $n_0(t_0)$  here is the initial condition of the peak electron density, which itself is then assumed to evolve in time,  $n_0(t)$ . For field-dependent (thus time-dependent) diffusion, the substitution

$$Dt \rightarrow \int_{t_0}^t D(t') dt' \quad (\text{A.46})$$

only need made.

### A.7 Initial Conditions for Gaussian Electron Transport

Integration over  $\mathbb{R}^3$  using spherical coordinates:

$$\begin{aligned} N_e &= \int_{\mathbf{S}} n_e(r, t_0) d^3\mathbf{S} \\ &= \int_0^{2\pi} \int_0^\pi \int_0^\infty n_0(t_0) \exp\left(-\frac{r^2}{2s_0^2}\right) r^2 \sin\theta dr d\theta d\phi \\ &= 4\pi n_0(t_0) \int_0^\infty r^2 \exp\left(-\frac{r^2}{2s_0^2}\right) dr \\ &= (2\pi s_0^2)^{3/2} n_0(t_0). \end{aligned} \quad (\text{A.47})$$

### A.8 Analytical Solution for Gaussian Under Ramp Field

From the general form of the electron source equation,

$$\frac{\partial n_0(t)}{\partial t} = \bar{\alpha}(t) |\vec{v}_d(t)| n_0(t), \quad (\text{A.48})$$

one substitutes the empirical fitting functions, and the ramp field  $E(t) = \mathcal{D}t$ ,

$$\begin{aligned} \bar{\alpha}(t) &\approx A_\alpha \exp\left[-\frac{B_\alpha}{E(t)}\right] - C_\alpha, \\ \mu_e(t) &\approx A_\mu E(t)^{-B_\mu}, \end{aligned} \quad (\text{A.49})$$

such that

$$\begin{aligned}
 \frac{\partial n_0(t)}{\partial t} &= \left\{ A_\alpha \exp \left[ -\frac{B_\alpha}{E(t)} \right] - C_\alpha \right\} \cdot \left[ A_\mu E(t)^{-B_\mu} E(t) \right] n_0(t) \\
 &= \left\{ A_\alpha A_\mu E(t)^{-B_\mu} E(t) \exp \left[ -\frac{B_\alpha}{E(t)} \right] - C_\alpha A_\mu E(t)^{-B_\mu} E(t) \right\} n_0(t) \\
 &= \left[ A_\alpha A_\mu (\mathcal{D}t)^{-B_\mu} \mathcal{D}t \exp \left( -\frac{B_\alpha}{\mathcal{D}t} \right) - C_\alpha A_\mu (\mathcal{D}t)^{-B_\mu} \mathcal{D}t \right] n_0(t) \\
 &= \left[ A_\alpha A_\mu \mathcal{D}^{1-B_\mu} t^{1-B_\mu} \exp \left( -\frac{B_\alpha}{\mathcal{D}t} \right) - C_\alpha A_\mu \mathcal{D}^{1-B_\mu} t^{1-B_\mu} \right] n_0(t). \tag{A.50}
 \end{aligned}$$

Then introducing the constants  $k_{1-4}$  as in (4.16), one arrives at

$$\frac{\partial n_0(t)}{\partial t} = t^{k_1-1} \left[ k_2 \exp - \left( \frac{k_3}{t} \right) - k_4 \right] n_0(t) \tag{A.51}$$

which remains in the form of a first-order relaxation equation, with the solution

$$\begin{aligned}
 n_0(t) &= n_0(t_0) \exp \left\{ \int_t^t t'^{k_1-1} \left[ k_2 \exp \left( -\frac{k_3}{t'} \right) - k_4 \right] dt' \right\} \\
 &= n_0(t_0) \exp \left\{ \underbrace{\int_0^t k_2 t'^{k_1-1} \exp \left( -\frac{k_3}{t'} \right) dt'}_I - \int_0^t k_4 t'^{k_1-1} dt' \right\}. \tag{A.52}
 \end{aligned}$$

The indicated integral can be transformed into the form of the upper incomplete gamma function according to the definition (4.18) by the substitution  $\bar{\tau} = k_3/t'$  as follows:

$$\begin{aligned}
 I &= \int_0^t k_2 t'^{k_1-1} \exp \left( -\frac{k_3}{t'} \right) dt' \\
 &= \int_\infty^{k_3/t} \left( \frac{k_3}{\bar{\tau}} \right)^{k_1-1} \exp(-\bar{\tau}) \cdot \left( -\frac{t^2}{k_3} \right) d\bar{\tau} \\
 &= k_2 k_3^{k_1-2} \int_{k_3/t}^\infty \frac{k_3^2}{\bar{\tau}^2} \cdot \frac{1}{\bar{\tau}^{k_1-1}} \exp(-\bar{\tau}) d\bar{\tau} \\
 &= k_2 k_3^{k_1} \int_{k_3/t}^\infty \bar{\tau}^{-k_1-1} \exp(-\bar{\tau}) d\bar{\tau} \\
 &= k_2 k_3^{k_1} \Gamma \left( -k_1, \frac{k_3}{t} \right), \tag{A.53}
 \end{aligned}$$

where it is noted that the upper and lower integration limits could be interchanged due to absorption of the negative sign from  $(-t^2/k_3)$ . Recombining with the trivial second integral, one

arrives at the solution

$$n_0(t) = n_0(t_0) \exp \left[ k_2 k_3^{k_1} \Gamma \left( -k_1, \frac{k_3}{t} \right) - \frac{k_4}{k_1} t^{k_1} \right] \quad (\text{A.54})$$

as printed in the main text.

### A.9 Closed form approximation for Overstressed Breakdown

From (4.34), one may expand using the definition of  $\mathcal{I}(t)$  to yield

$$\begin{aligned} {}_t \frac{\partial \mathcal{I}(t)}{\partial t} &= \frac{f}{g} \\ {}_t \frac{\partial}{\partial t} \left\{ \frac{\gamma_1}{\mathcal{D}} \Gamma \left( -k_1, \frac{B_\alpha}{\mathcal{D}t} \right) \right\} &= \frac{f}{g} \\ \frac{\gamma_1}{\mathcal{D}} \left( \frac{B_\alpha}{\mathcal{D}t} \right)^{-k_1} \exp \left( -\frac{B_\alpha}{\mathcal{D}t} \right) &= \frac{f}{g} \\ t \exp \left( -\frac{B_\alpha}{k_1 \mathcal{D}} t^{-1} \right) &= \frac{B_\alpha}{\mathcal{D}} \left( \frac{f \mathcal{D}}{g \gamma_1} \right)^{1/k_1}. \end{aligned} \quad (\text{A.55})$$

The substitution

$$u = -\frac{B_\alpha}{k_1 \mathcal{D}} t^{-1} \quad (\text{A.56})$$

can be used to reduce the equation to the form

$$\begin{aligned} -\frac{B_\alpha}{u k_1 \mathcal{D}} \exp(u) &= \frac{B_\alpha}{\mathcal{D}} \left( \frac{f \mathcal{D}}{g \gamma_1} \right)^{1/k_1} \\ u^{-1} \exp(u) &= -k_1 \left( \frac{f \mathcal{D}}{g \gamma_1} \right)^{1/k_1}, \end{aligned} \quad (\text{A.57})$$

and with a final substitution  $-u = z$ , one has

$$z \exp(z) = \frac{1}{k_1} \left( \frac{g \gamma_1}{f \mathcal{D}} \right)^{1/k_1}, \quad (\text{A.58})$$

which follows the definition of the Lambert- $W$  (product-log) function, which is the solution  $W(x) \exp[W(x)] = x$ , thus, re-substituting all dummy variables:

$$z = W \left[ \frac{1}{k_1} \left( \frac{g \gamma_1}{f \mathcal{D}} \right)^{1/k_1} \right] \Rightarrow u = -W \left[ \frac{1}{k_1} \left( \frac{g \gamma_1}{f \mathcal{D}} \right)^{1/k_1} \right]$$

$$\Rightarrow t = \frac{B_\alpha}{k_1 \mathcal{D} W \left[ \underbrace{\frac{1}{k_1} \left( \frac{g\gamma_1}{f\mathcal{D}} \right)^{1/k_1}}_{\omega(\mathcal{D})} \right]}$$

$$\therefore t_b = \frac{B_\alpha}{k_1 \mathcal{D} \omega(\mathcal{D})}, \quad (\text{A.59})$$

as given in the main text.

### A.10 Pulsed Paschen Proportionality

Consider that  $B_\alpha \propto N \propto p$ ,  $A_\alpha \propto N \propto p$ , and  $A_\mu \propto 1/N^{1-B_\mu}$ . Consider also that  $\mathcal{D} \propto 1/d$ . Thus, the ratio

$$\frac{\gamma_1}{\mathcal{D}} \propto p^a d \quad (\text{A.60})$$

holds. It follows that the argument to the Lambert- $W$  function has the proportion

$$\frac{1}{k_1} \left( \frac{g\gamma_1}{f\mathcal{D}} \right)^{1/k_1} \propto (p^a d)^b, \quad (\text{A.61})$$

where the approximate symbol is due to the uncertainty in the dependencies of  $g$ . Then,

$$V_b = \frac{B_\alpha d}{k_1 \omega(\mathcal{D})}$$

$$V_b \propto \frac{pd}{\ln [k(p^a d)^b] - \ln [\ln k(p^a d)^b]}, \quad (\text{A.62})$$

as featured in the main text.

### A.11 New Field-Time Scaling Characteristic

Since

$$t_b = \frac{B_\alpha}{\mathcal{D} k_1 \omega(\mathcal{D})}, \quad E_b = \frac{B_\alpha}{k_1 \omega(\mathcal{D})}, \quad (\text{A.63})$$

then

$$N t_b \times \frac{E_b}{N} = \frac{B_\alpha^2}{k_1^2 \mathcal{D} \omega^2(\mathcal{D})}$$

$$\therefore N t_b = \frac{B_\alpha^2}{k_1^2 \mathcal{D} \omega^2(\mathcal{D})} \cdot \frac{1}{E_b/N}, \quad (\text{A.64})$$

as required.

### A.12 Weak Formulation of ADR-Poisson Equations

Process: Multiply by test function  $v$  then integrate over domain  $\Omega$ , reduce all second-order derivatives to first order. Specific indices for  $v_1, v_2, \dots, v_i$  are omitted here for brevity. Two important vector calculus identities required for the following:

$$\vec{\nabla} \cdot (\phi \vec{\nabla} u) = \phi \vec{\nabla}^2 u + \vec{\nabla} \phi \cdot \vec{\nabla} u, \quad (\text{A.65})$$

$$\int_{\Omega} \phi \vec{\nabla}^2 u \, d\Omega = \int_{\partial\Omega} \phi (\vec{\nabla} u \cdot \hat{\mathbf{n}}) \, dS - \int_{\Omega} \vec{\nabla} u \cdot \vec{\nabla} \phi \, d\Omega. \quad (\text{A.66})$$

Starting from the Poisson Equation,

$$-\vec{\nabla} \cdot (\varepsilon \vec{\nabla} u) = \rho. \quad (\text{A.67})$$

Multiply both sides by test function  $v$  and integrate over  $\Omega$ ,

$$\int_{\Omega} -v \vec{\nabla} \cdot (\varepsilon \vec{\nabla} u) \, d\Omega = \int_{\Omega} \rho v \, d\Omega, \quad (\text{A.68})$$

then using (A.65) split the  $\vec{\nabla} \cdot (\varepsilon \vec{\nabla} u)$  term into

$$\begin{aligned} \int_{\Omega} -v(\varepsilon \vec{\nabla}^2 u + \vec{\nabla} \varepsilon \cdot \vec{\nabla} u) \, d\Omega &= \int_{\Omega} \rho v \, d\Omega \\ - \left[ \int_{\Omega} v \varepsilon \vec{\nabla}^2 u \, d\Omega + \int_{\Omega} v \vec{\nabla} \varepsilon \cdot \vec{\nabla} u \, d\Omega \right] &= \int_{\Omega} \rho v \, d\Omega. \end{aligned} \quad (\text{A.69})$$

Then, from (A.66), split the first integral term into

$$\begin{aligned} - \left[ \int_{\partial\Omega} v \varepsilon \vec{\nabla} (u \cdot \hat{\mathbf{n}}) \, dS - \int_{\Omega} \vec{\nabla} u \cdot \vec{\nabla} (v \varepsilon) \, d\Omega + \int_{\Omega} v \vec{\nabla} \varepsilon \cdot \vec{\nabla} u \, d\Omega \right] &= \int_{\Omega} \rho v \, d\Omega \\ \int_{\Omega} v \vec{\nabla} \varepsilon \cdot \vec{\nabla} u \, d\Omega + \int_{\Omega} \rho v \, d\Omega - \int_{\Omega} \vec{\nabla} u \cdot \vec{\nabla} (v \varepsilon) \, d\Omega + \int_{\partial\Omega} v \varepsilon \vec{\nabla} (u \cdot \hat{\mathbf{n}}) \, dS &= 0. \end{aligned} \quad (\text{A.70})$$

Since the  $(\cdot)$  operator is commutative in real vector space:  $\vec{\nabla} u \cdot \vec{\nabla} (v \varepsilon) = \vec{\nabla} (v \varepsilon) \cdot \vec{\nabla} u$ ,

$$\int_{\Omega} v \vec{\nabla} \varepsilon \cdot \vec{\nabla} u \, d\Omega + \int_{\Omega} \rho v \, d\Omega - \int_{\Omega} \vec{\nabla} (v \varepsilon) \cdot \vec{\nabla} u \, d\Omega + \int_{\partial\Omega} v \varepsilon \vec{\nabla} (u \cdot \hat{\mathbf{n}}) \, dS = 0, \quad (\text{A.71})$$

where the charge density  $\rho$  is also written in terms of a summation over all charged species in the main text.

The strong form of the Advection-Diffusion-Reaction equation is stated as

$$\frac{\partial n}{\partial t} - \vec{\nabla} \cdot [\text{sgn}(q)n\mu\vec{\nabla}\varphi + D\vec{\nabla}n] = S, \quad (\text{A.72})$$

where the advective and diffusive parts are dealt with separately here. For the advective component,

$$-\vec{\nabla} \cdot [\text{sgn}(q_i)n\mu\vec{\nabla}\varphi] \Rightarrow -\text{sgn}(q_i) \int_{\Omega} v\vec{\nabla} \cdot (n\mu\vec{\nabla}\varphi) d\Omega. \quad (\text{A.73})$$

Using (A.65) one expands:

$$= -\text{sgn}(q_i) \int_{\Omega} v [n\mu\vec{\nabla}^2\varphi + \vec{\nabla}(n\mu) \cdot \vec{\nabla}\varphi] d\Omega \quad (\text{A.74})$$

$$= -\text{sgn}(q_i) \left[ \int_{\Omega} vn\mu\vec{\nabla}^2\varphi d\Omega + \int_{\Omega} v\vec{\nabla}(n\mu) \cdot \vec{\nabla}\varphi d\Omega \right]. \quad (\text{A.75})$$

Using identity (A.66) expand the Laplacian:

$$= -\text{sgn}(q_i) \left[ \int_{\partial\Omega} vn\mu(\vec{\nabla}\varphi \cdot \hat{\mathbf{n}}) dS - \int_{\Omega} \vec{\nabla}\varphi \cdot \vec{\nabla}(vn\mu) d\Omega + \int_{\Omega} v\vec{\nabla}(n\mu) \cdot \vec{\nabla}\varphi d\Omega \right]. \quad (\text{A.76})$$

The diffusive term follows

$$-\vec{\nabla} \cdot [D\vec{\nabla}n] \Rightarrow - \int_{\Omega} v\vec{\nabla} \cdot (D\vec{\nabla}n) d\Omega. \quad (\text{A.77})$$

Using identity (A.65) again:

$$\Rightarrow - \int_{\Omega} v (D\vec{\nabla}^2n + \vec{\nabla}D \cdot \vec{\nabla}n) d\Omega \quad (\text{A.78})$$

$$\Rightarrow - \int_{\Omega} vD\vec{\nabla}^2n d\Omega - \int_{\Omega} v\vec{\nabla}D \cdot \vec{\nabla}n d\Omega, \quad (\text{A.79})$$

then applying identity (A.66);

$$- \int_{\partial\Omega} vD(\vec{\nabla}n \cdot \hat{\mathbf{n}}) dS + \int_{\Omega} \vec{\nabla}n \cdot \vec{\nabla}(vD) d\Omega - \int_{\Omega} v\vec{\nabla}D \cdot \vec{\nabla}n d\Omega. \quad (\text{A.80})$$

The trivial time derivative and source terms simply becomes

$$\int_{\Omega} \frac{\partial n}{\partial t} v d\Omega, \quad \int_{\Omega} Sv d\Omega, \quad (\text{A.81})$$

respectively. Collating all parts together, one arrives at the full weak formulation

$$\begin{aligned}
& \int_{\Omega} \frac{\partial n}{\partial t} v \, d\Omega - \operatorname{sgn}(q) \left[ \int_{\partial\Omega} vn\mu(\vec{\nabla}\varphi \cdot \hat{\mathbf{n}}) \, dS - \int_{\Omega} \vec{\nabla}\varphi \cdot \vec{\nabla}(vn\mu) \, d\Omega \right. \\
& \quad \left. + \int_{\Omega} v\vec{\nabla}(n\mu) \cdot \vec{\nabla}\varphi \, d\Omega \right] - \int_{\partial\Omega} vD(\vec{\nabla}n \cdot \hat{\mathbf{n}}) \, dS \\
& \quad + \int_{\Omega} \vec{\nabla}n \cdot \vec{\nabla}(vD) \, d\Omega - \int_{\Omega} v\vec{\nabla}D \cdot \vec{\nabla}n - \int_{\Omega} S_i v \, d\Omega = 0. \tag{A.82}
\end{aligned}$$

Further note that the boundary integral terms (second and fifth integrals from the left) form

$$-\operatorname{sgn}(q) \int_{\partial\Omega} vn\mu(\vec{\nabla}\varphi \cdot \hat{\mathbf{n}}) \, dS - \int_{\partial\Omega} vD(\vec{\nabla}n \cdot \hat{\mathbf{n}}) \, dS, \tag{A.83}$$

which is equivalent to

$$\int_{\partial\Omega} -\operatorname{sgn}(q)vn\mu(\vec{\nabla}\varphi \cdot \hat{\mathbf{n}}) - vD(\vec{\nabla}n \cdot \hat{\mathbf{n}}) \, dS \tag{A.84}$$

$$\Rightarrow \int_{\partial\Omega} v \left[ -\operatorname{sgn}(q)n\mu(\nabla\varphi \cdot \hat{\mathbf{n}}) - D(\vec{\nabla}n \cdot \hat{\mathbf{n}}) \right] \, dS \tag{A.85}$$

$$\Rightarrow \int_{\partial\Omega} v(\vec{\Gamma} \cdot \hat{\mathbf{n}}) \, dS, \tag{A.86}$$

giving the term for normal boundary flux as appears in the main text. The Helmholtz equation for photoionisation terms follow similarly. From the strong form

$$\begin{aligned}
& \vec{\nabla}^2 S_{\text{ph},j} - (\lambda_j p_{\text{O}_2})^2 S_{\text{ph},j} = -A_j p_{\text{O}_2}^2 I(\vec{\mathbf{r}}) \\
\Rightarrow & \int_{\Omega} v \vec{\nabla}^2 S_{\text{ph},j} \, d\Omega - \int_{\Omega} v (\lambda_j p_{\text{O}_2})^2 S_{\text{ph},j} \, d\Omega = - \int_{\Omega} v A_j p_{\text{O}_2}^2 I(\vec{\mathbf{r}}) \, d\Omega, \tag{A.87}
\end{aligned}$$

application of (A.66) immediately yields the result

$$\begin{aligned}
& \int_{\Omega} \vec{\nabla}v \cdot \vec{\nabla}S_{\text{ph},j} \, d\Omega + \int_{\Omega} v (p_{\text{O}_2} \lambda_j)^2 S_{\text{ph},j} \, d\Omega \\
& \quad - \int_{\Omega} v \left( A_j p_{\text{O}_2}^2 \frac{p_q}{p + p_q} \xi \frac{\nu_u}{\nu_i} \right) S_{\text{ion}} \, d\Omega - \int_{\partial\Omega} v (\vec{\nabla}S_{\text{ph},j} \cdot \hat{\mathbf{n}}) \, dS = 0, \tag{A.88}
\end{aligned}$$

where  $I(\vec{\mathbf{r}})$  has been expanded to its full form, and  $S_{\text{ph},j}$  is used instead of  $u_i$  in the main text.

### A.13 Surface Charge Integrals

For the planar case (extending infinitely into- and out- of the plane), one has from the main text (6.9)

$$\begin{aligned}
 \vec{E}_{\max}(x) &= \frac{x}{4\pi\epsilon_0\epsilon_r} \iint_{\mathbb{R}^2} \frac{\varsigma(y)}{|\vec{r}|^3} dz dy \cdot \hat{\mathbf{x}} \\
 &= \varsigma_0 \frac{x}{4\pi\epsilon_0\epsilon_r} \int_{-\infty}^{+\infty} \exp\left(-\frac{y^2}{s_0^2}\right) \int_{-\infty}^{+\infty} \frac{dz}{(x^2 + y^2 + z^2)^{3/2}} dy \cdot \hat{\mathbf{x}} \\
 &= \varsigma_0 \frac{x}{4\pi\epsilon_0\epsilon_r} \int_{-\infty}^{+\infty} \exp\left(-\frac{y^2}{s_0^2}\right) \underbrace{\left[ \frac{z}{(x^2 + y^2) \sqrt{x^2 + y^2 + z^2}} \right]_{-\infty}^{+\infty}}_{=2/(x^2+y^2)} dy \cdot \hat{\mathbf{x}} \\
 &= \varsigma_0 \frac{2x}{\pi\epsilon_0\epsilon_r} \int_{-\infty}^{+\infty} \frac{1}{x^2 + y^2} \exp\left(-\frac{y^2}{s_0^2}\right) dy \cdot \hat{\mathbf{x}} \\
 &= \varsigma_0 \frac{x}{2\pi\epsilon_0\epsilon_r} \cdot \frac{\pi}{|x|} \exp\left(\frac{x^2}{s_0^2}\right) \operatorname{erfc}\left(\left|\frac{x}{s_0}\right|\right) \cdot \hat{\mathbf{x}} \\
 &\therefore \frac{\varsigma_0}{2\epsilon_0\epsilon_r} \frac{x}{|x|} \exp\left(\frac{x^2}{s_0^2}\right) \operatorname{erfc}\left(\left|\frac{x}{s_0}\right|\right) \cdot \hat{\mathbf{x}}, \tag{A.89}
 \end{aligned}$$

as in the main text. For the cylindrically-symmetric version, one has

$$\begin{aligned}
 \vec{E}_{\max}^{\text{full}}(z) &= \frac{z}{4\pi\epsilon_0\epsilon_r} \iint_{\mathbb{R}^2} \frac{\varsigma(r)}{|\vec{r}|^3} r dr d\theta \cdot \hat{\mathbf{z}} \\
 &= \varsigma_0 \frac{z}{4\pi\epsilon_0\epsilon_r} \int_0^{2\pi} \int_0^{\infty} \frac{r dr}{(r^2 + z^2)^{3/2}} \exp\left(-\frac{r^2}{s_0^2}\right) d\theta \cdot \hat{\mathbf{z}} \\
 &= \varsigma_0 \frac{2\pi z}{4\pi\epsilon_0\epsilon_r} \left\{ \frac{\exp\left(-\frac{r^2}{s_0^2}\right)}{\sqrt{r^2 + z^2}} \left[ \exp\left(\frac{r^2 + z^2}{s_0^2}\right) \sqrt{\frac{r^2 + z^2}{s_0^2}} \Gamma\left(\frac{1}{2}, \frac{r^2 + z^2}{s_0^2}\right) - 1 \right] \right\}_0^{\infty} \cdot \hat{\mathbf{z}} \\
 &= \frac{\varsigma_0 z}{2\epsilon_0\epsilon_r} \left[ \frac{1}{|z|} - \frac{\sqrt{\pi} \exp\left(\frac{z^2}{s_0^2}\right) \operatorname{erfc}\left|\frac{z}{s_0}\right|}{|s_0|} \right] \cdot \hat{\mathbf{z}} \\
 &\therefore \frac{\varsigma_0}{2\epsilon_0\epsilon_r} \frac{z}{|z|} \left[ 1 - \left|\frac{z}{s_0}\right| \sqrt{\pi} \exp\left(\frac{z^2}{s_0^2}\right) \operatorname{erfc}\left(\left|\frac{z}{s_0}\right|\right) \right] \cdot \hat{\mathbf{z}}, \tag{A.90}
 \end{aligned}$$

as given in the main text.

### A.14 Three Layer Spheroidal Void in an Arbitrary Field

From the general solution (3.33) which was also derived in Appendix A.3, application of the far-field conditions of Chapter 3 - Section 3.2.2 provides the Fourier-Legendre series solutions for the potential in layers  $g$ ,  $b$ , and  $l$ ,

$$\begin{aligned}\varphi_g &= \sum_{\ell=0}^{\infty} A_{\ell}^g P_{\ell}(\cosh \mu) P_{\ell}(\cos \nu), \\ \varphi_l &= \sum_{\ell=0}^{\infty} \left[ A_{\ell}^l P_{\ell}(\cosh \mu) + B_{\ell}^l Q_{\ell}(\cosh \mu) \right] P_{\ell}(\cos \nu), \\ \varphi_b &= \sum_{\ell=0}^{\infty} \left[ A_{\ell}^b(\mu) + B_{\ell}^b Q_{\ell}(\cosh \mu) \right] P_{\ell}(\cos \nu).\end{aligned}\tag{A.91}$$

The continuity conditions require:

$$\begin{aligned}\sum_{\ell=0}^{\infty} A_{\ell}^g P_{\ell}(\cosh \mu_1) &= \sum_{\ell=0}^{\infty} \left[ A_{\ell}^l P_{\ell}(\cosh \mu_1) + B_{\ell}^l Q_{\ell}(\cosh \mu_1) \right], \\ \sum_{\ell=0}^{\infty} \left[ A_{\ell}^l P_{\ell}(\cosh \mu_2) + B_{\ell}^l Q_{\ell}(\cosh \mu_2) \right] &= \sum_{\ell=0}^{\infty} \left[ A_{\ell}^b(\mu_2) + B_{\ell}^b Q_{\ell}(\cosh \mu_2) \right], \\ \sum_{\ell=0}^{\infty} A_{\ell}^g \frac{\partial P_{\ell}(\cosh \mu_1)}{\partial \mu} &= \sum_{\ell=0}^{\infty} \left( A_{\ell}^l \frac{\partial P_{\ell}(\cosh \mu_1)}{\partial \mu} + B_{\ell}^l \frac{\partial Q_{\ell}(\cosh \mu_1)}{\partial \mu} \right), \\ \sum_{\ell=0}^{\infty} \left( A_{\ell}^l \frac{\partial P_{\ell}(\cosh \mu_2)}{\partial \mu} + B_{\ell}^l \frac{\partial Q_{\ell}(\cosh \mu_2)}{\partial \mu} \right) &= \sum_{\ell=0}^{\infty} \left( \frac{\partial A_{\ell}^b(\mu_2)}{\partial \mu} + B_{\ell}^b \frac{\partial Q_{\ell}(\cosh \mu_2)}{\partial \mu} \right),\end{aligned}\tag{A.92}$$

where  $P_{\ell}(\cos \nu)$  terms have been cancelled out on the basis that equality can only be satisfied if each  $\ell$ -th Legendre term have equal coefficients. Thus, the  $\ell$ -th coefficient must also satisfy

$$A_{\ell}^g = A_{\ell}^l + B_{\ell}^l F_{\ell}^{\mu_1},\tag{A.93}$$

$$A_{\ell}^l + B_{\ell}^l F_{\ell}^{\mu_2} = \frac{A_{\ell}^b(\mu_2)}{P_{\ell}(\cosh \mu_2)} + B_{\ell}^b F_{\ell}^{\mu_2},\tag{A.94}$$

$$\frac{(\sigma_g + \varepsilon_0 \varepsilon_g s)}{(\sigma_b + \varepsilon_0 \varepsilon_b s)} A_{\ell}^g = A_{\ell}^l + B_{\ell}^l G_{\ell}^{\mu_1},\tag{A.95}$$

$$\frac{(\sigma_l + \varepsilon_0 \varepsilon_l s)}{(\sigma_b + \varepsilon_0 \varepsilon_b s)} \left[ A_{\ell}^l + B_{\ell}^l G_{\ell}^{\mu_2} \right] = \frac{\partial_{\mu} A_{\ell}^b(\mu_2)}{\partial_{\mu} P_{\ell}(\cosh \mu_2)} + B_{\ell}^b G_{\ell}^{\mu_2},\tag{A.96}$$

where the functions  $F_{\ell}$  and  $G_{\ell}$  have been introduced as defined in (7.15). What remains is an algebraic exercise of epic proportions to solve for coefficients  $A_{\ell}^g$ ,  $A_{\ell}^l$ ,  $B_{\ell}^l$ , and  $B_{\ell}^b$ . The major steps are outlined here, but the full manipulation is left as an exercise for the reader. Rearranging

(A.95), one finds

$$B_\ell^l = A_\ell^l \left[ \frac{(\sigma_g + \varepsilon_0 \varepsilon_g s) - (\sigma_l + \varepsilon_0 \varepsilon_l)}{G_\ell^{\mu_1} (\sigma_l + \varepsilon_0 \varepsilon_l) - F_\ell^{\mu_1} (\sigma_g + \varepsilon_0 \varepsilon_g s)} \right]. \quad (\text{A.97})$$

Combining (A.94) and (A.96),

$$\begin{aligned} A_\ell^l \left[ \frac{(\sigma_l + \varepsilon_0 \varepsilon_l s)}{(\sigma_b + \varepsilon_0 \varepsilon_b s)} - \frac{G_\ell^{\mu_2}}{F_\ell^{\mu_1}} \right] + B_\ell^l \left[ G_\ell^{\mu_2} \frac{(\sigma_l + \varepsilon_0 \varepsilon_l s)}{(\sigma_b + \varepsilon_0 \varepsilon_b s)} - G_\ell^{\mu_2} \right] \\ = \frac{dA_\ell^b(\mu_2)}{\partial P_\ell(\cosh \mu_2)} - \frac{G_\ell^{\mu_2}}{F_\ell^{\mu_2}} \frac{A_\ell^b(\mu_2)}{P_\ell(\cosh \mu_2)} \end{aligned} \quad (\text{A.98})$$

and substituting (A.97) and rearranging, the solution for  $A_\ell^l$  is achieved,

$$\begin{aligned} A_\ell^l = \left[ G_\ell^{\mu_2} \frac{A_\ell^b(\mu_2)}{P_\ell(\cosh \mu_2)} - F_\ell^{\mu_2} \frac{dA_\ell^b(\mu_2)}{dP_\ell(\cosh \mu_2)} \right] \times \left[ \frac{\sigma_b}{(\sigma_b G_\ell^{\mu_2} - \sigma_l F_\ell^{\mu_2})} \right] \\ \times \frac{(1 + \tau_b s)(1 + \tau_1 s)}{(1 + \tau_1 s)(1 + \tau_2 s) - F_\ell^{\mu_2} G_\ell^{\mu_2} \frac{(\sigma_g - \sigma_l)(\sigma_l - \sigma_b)}{(\sigma_l G_\ell^{\mu_1} - \sigma_g F_\ell^{\mu_1})(\sigma_b G_\ell^{\mu_2} - \sigma_l F_\ell^{\mu_2})} (1 + \tau_3 s)(1 + \tau_4 s)}, \end{aligned} \quad (\text{A.99})$$

where the reason for why the substitution of the many constants defined in (7.25) was necessary should now be evident. The denominator of (A.99) is the characteristic polynomial defined within Chapter 3.3; the factorisation of which is trivially done with the quadratic formula. Hence, the  $s$ -domain solution is recovered as

$$\begin{aligned} A_\ell^l = A_0 U_0 \left[ G_\ell^{\mu_2} \frac{A_\ell^b(\mu_2)}{P_\ell(\cosh \mu_2)} - F_\ell^{\mu_2} \frac{\partial_\mu A_\ell^b(\mu_2)}{\partial_\mu P_\ell(\cosh \mu_2)} \right] \times \\ \frac{\sigma_b}{(\sigma_b G_\ell^{\mu_2} - \sigma_l F_\ell^{\mu_2}) \left( \tau_1 \tau_2 - \frac{F_\ell^{\mu_2}}{F_\ell^{\mu_1}} m_\ell \tau_3 \tau_4 \right)} \left[ \frac{(1 + \tau_b s)(1 + \tau_1 s)}{\left( s + \frac{1}{\tau_5} \right) \left( s + \frac{1}{\tau_6} \right)} \right], \end{aligned} \quad (\text{A.100})$$

from which the time-domain solution as presented in the main text is obtained from the inverse Laplace transform of (A.100), aided by a partial fraction expansion in the same method following Appendix A.2. All other coefficients are found by re-substitution of  $A_\ell^l$  into the set of equations (7.14).

### A.15 Nonuniform External Field Derivations

For the representation of a sphere-plane system, the rotationally-symmetric bi-spherical coordinate system was used where the Laplace equation is

$$\nabla^2 \varphi(\psi, \zeta) = \frac{(\cosh \psi - \cos \zeta)^3}{a_0^2 \sin \zeta} \left[ \frac{\partial}{\partial \zeta} \left( \frac{\sin \zeta}{\cosh \psi - \cos \zeta} \frac{\partial \varphi}{\partial \zeta} \right) + \sin \zeta \frac{\partial}{\partial \psi} \left( \frac{1}{\cosh \psi - \cos \zeta} \frac{\partial \varphi}{\partial \psi} \right) \right], \quad (\text{A.101})$$

which is  $R$ -separable using the ansatz

$$\begin{aligned} \varphi(\psi, \zeta) &= R(\psi, \zeta) E(\psi) Z(\zeta), \\ R(\psi, \zeta) &= \sqrt{\cosh \psi - \cos \zeta}, \end{aligned} \quad (\text{A.102})$$

which separates the equation such that

$$\begin{aligned} -\frac{\sin^2 \zeta}{4} + \cos \zeta \sin \zeta \frac{1}{Z(\zeta)} \frac{dZ(\zeta)}{d\zeta} + \sin^2 \zeta \frac{1}{Z(\zeta)} \frac{d^2 Z(\zeta)}{d\zeta^2} + \sin^2 \zeta \frac{1}{E(\psi)} \frac{d^2 E(\psi)}{d\psi^2} &= 0 \\ \Rightarrow \frac{\cot \zeta}{Z(\zeta)} \frac{dZ(\zeta)}{d\zeta} + \frac{1}{Z(\zeta)} \frac{d^2 Z(\zeta)}{d\zeta^2} - \frac{1}{4} + \frac{1}{E(\psi)} \frac{d^2 E(\psi)}{d\psi^2} &= 0, \end{aligned} \quad (\text{A.103})$$

and the equations

$$\begin{aligned} E(\psi) &= A e^{-\psi(\ell+\frac{1}{2})} + B e^{\psi(\ell+\frac{1}{2})}, \\ Z(\zeta) &= C P_\ell(\cos \zeta) + D Q_\ell(\cos \zeta), \end{aligned} \quad (\text{A.104})$$

yield a general solution of the form

$$\varphi = R(\psi, \zeta) \sum_{\ell=0}^{\infty} \left[ A_\ell e^{-\psi(\ell+\frac{1}{2})} + B_\ell e^{\psi(\ell+\frac{1}{2})} \right] \left[ C_\ell P_\ell(\cos \zeta) + D_\ell Q_\ell(\cos \zeta) \right], \quad (\text{A.105})$$

where  $Q_\ell(\cos \zeta)$  is necessarily zero to satisfy the non-singular condition for the potential. The Dirichlet conditions  $\varphi(\psi_1, \zeta) = U_0$  and  $\varphi(\psi_2, \zeta) = 0$  must be prescribed, yielding the particular solution in the main text. In this work, the surface  $\psi_2 \gg \psi_1$  to approximate a plane.

A similar strategy was used for needle-plane, where the Laplace equation was solved again in prolate-spheroidal coordinates, but using the surfaces of constant  $\nu$ . Following from the general solution shown in Appendix A.3,  $Q_\ell(\cosh \mu)$  violates the non-singular condition, thus  $D_\ell$  must

be zero. With a constant potential  $U_0$  on some  $\nu$ , an expansion of order  $\ell = 0$  suffices and hence  $P_\ell(\cos \nu)$  and  $P_\ell(\cosh \mu)$  collapse to unity. What remains is of the form

$$\varphi = A + BQ_\ell(\cosh \mu), \quad (\text{A.106})$$

where upon application of appropriate conditions  $\varphi(\nu_1) = U_0$  and  $\varphi(\nu_2) = 0$  yields the simple solution in the main text for needle-planes. Once again, the coordinate  $\nu_2$  is set to represent an infinitely-stretched hyperbola approximating a flat plane.

### A.16 Fothergill's Model without Surface Energy

From Fothergill, one has

$$E^4 \frac{\varepsilon_0^2 \varepsilon_r^2 \pi r^2}{8Y} \delta l > \cancel{2G\pi r \delta l} + Y\pi r^2 \delta l, \quad (\text{A.107})$$

where the scored-out term is the surface energy term which is ignored here. It follows then

$$\begin{aligned} E_b^4 \frac{\varepsilon_0^2 \varepsilon_r^2 \pi r^2}{8Y} \delta l &= Y\pi r^2 \delta l \\ E_b^4 &= \frac{8Y^2}{(\varepsilon_0 \varepsilon_r)^2} \\ E_b &= \left[ \frac{8Y^2}{(\varepsilon_0 \varepsilon_r)^2} \right]^{1/4} \\ \therefore E_b &= \sqrt{\frac{\sqrt{8Y}}{\varepsilon_0 \varepsilon_r}} \end{aligned} \quad (\text{A.108})$$

as shown in the main text.

## B Additional and Supporting Material

### B.1 Swarm-like Monte-Carlo Optimisation for Waveshaping

Three parameters are necessary to define a double-exponential waveform as in (3.22):  $A_0$ ,  $\hat{\alpha}$  and  $\hat{\beta}$ , which must be sought for a desired rise-time,  $t_r$ , time-to-half,  $t_h$ , and peak voltage,  $U_0$ . A multivariate optimisation technique based on particle-swarm optimisation was used to compute parameters for all waveforms used within this work. Consider the optimal parameters describing the desired waveshape to be  $A'_0$ ,  $\hat{\alpha}'$ , and  $\hat{\beta}'$ , which minimises some measure of absolute error  $E(A'_0, \hat{\alpha}', \hat{\beta}') \approx 0$ .

The algorithm begins by constructing a search space  $\mathcal{S} = [\vec{x}_{\min}, \vec{x}_{\max}]$  that is large compared to the range of the parameters, where  $\vec{x} = [A_0, \hat{\alpha}, \hat{\beta}]$ .  $N$  uniformly spaced points are randomly spawned within  $\mathcal{S}$  and their errors,  $E$ , computed. The point which produces minimum error is recorded, and the search space is reduced according to

$$\mathcal{S}_{k+1} = f(T) \cdot \mathcal{S}_k, \quad (\text{A.109})$$

where  $f(T) \leq 1$  is dependent on the specified tolerance and the number of points which produced an error within said tolerance, and  $\mathcal{S}_{k+1}$  is constructed to be centred at the previous particle of lowest  $E$ . This ensures the successive reduction of the parameter search space, such that when  $N$  particles are spawned within the restricted search space near the previous most-optimal value, the probability of landing on a more-optimal point is greater, from which the algorithm repeats until a point with acceptable error is found. The error metric used in this work was simply

$$E(A_0, \hat{\alpha}, \hat{\beta}) = \left| \frac{t_f - t_f^d}{t_f^d} \right| + \left| \frac{t_h - t_h^d}{t_h^d} \right| + \left| \frac{U_0 - U_0^d}{U_0^d} \right|, \quad (\text{A.110})$$

where the parameters labelled  $d$  are the desired parameters.  $E < 0.01$  was deemed acceptable, corresponding to no greater than 1% error for any one of the computed parameters. This is a variation of the traditional particle swarm algorithm, where the difference is Monte-Carlo like sampling is employed instead of moving the particles towards the direction most likely to produce an optimal solution.

## B.2 Comparison of Field Enhancement Expressions for Spheroid

Crichton, Karlsson, and Pedersen ([55] of Chapter 3) give the enhancement factor as

$$K = \frac{2\nu^3}{(1 - \nu^2) \left( \ln \frac{1+\nu}{1-\nu} - 2\nu \right)}, \quad (\text{A.111})$$

where  $\nu$  is the eccentricity. Similarly, Lekner ([62] of Chapter 3) gives the expression

$$\frac{E_{\max}}{E_0} = \frac{e^3/(1 - e^2)}{\frac{1}{2} \ln \frac{1+e}{1-e} - e}, \quad (\text{A.112})$$

where  $e$  is the eccentricity as defined in this work; this expression is evidently the same as Crichton *et al.* by dividing by 2. Lekner further provides an asymptotic approximation of

$$\frac{E_{\max}}{E_0} = \frac{(1/K)^2}{\ln \left( \frac{2}{K} \right) - 1} + \mathcal{O}(1). \quad (\text{A.113})$$

Figure A.1 compares these three expressions to equation (3.54) of Chapter 3.

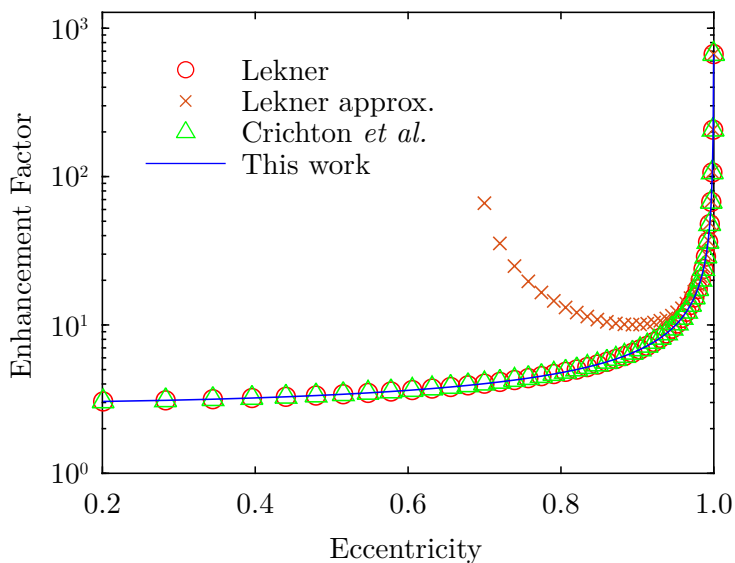


**Figure A.1:** Comparison of the field enhancement factor on the surface of a conducting spheroidal void to expressions in literature.

### B.3 All Discharge Simulation Settings and Stats

Table A.1 encloses all settings associated with simulations presented within this work.

**Table A.1:** All miscellaneous discharge simulation settings for computational studies.

Simulation Parameter	Comparison Study Section 5.8.1	Surface Attachment Study Section 5.8.2	Double-headed Study Section 5.8.3	Counterprop. Study Section 5.8.4
Timestep	dynamic	1 ps	1 ps	0.01 ps
Min timestep	1 ps	n/a	n/a	n/a
Max timestep	5 ps	n/a	n/a	n/a
Time adaptation $k$	3	1 ns	n/a	n/a
AMR	✓	✓	✓	✓
Min mesh size	2.2 $\mu\text{m}$	2 $\mu\text{m}$	2 $\mu\text{m}$	0.1 $\mu\text{m}$
Mesh adaptation $k$	30	30	30	30
Refinement functions	$E/E_{\text{max}}, \rho, n_e/n_0$	$E/E_{\text{max}}, \rho, n_e/n_0$	$E/E_{\text{max}}, \rho, n_e/n_0$	$E/E_{\text{max}}, \rho, n_e$
Refinement tolerances*	[1.2, 1.5, $\infty, \infty, \infty$ ] [15, 17, 19, 20, 20] [0.4, 0.7, 0.8, 0.9, $\infty$ ]	[1.2, 1.5, $\infty, \infty, \infty$ ] [15, 17, 19, 20, 20] [0.4, 0.7, 0.8, 0.9, $\infty$ ]	[ $\infty, \infty, 0.5, 0.6, 0.7$ ] [15, 17, 19, 20, 20] [0.4, 0.7, $\infty, \infty, \infty$ ]	[0.4, 0.5, $\infty, \infty$ ] [18, 29, 20, 21] [ $10^{18}, \infty, \infty, \infty$ ]
Refinement levels	[1,1,1,2,1]	[1,1,1,2,1]	[1,1,1,2,1]	[1,1,1,1]
Refinement radii, mm	0.2	0.2	0.2	[0.5, 0.6, 0.7, 0.8]
$n$ processes	16	16	18	18
Approx. runtime/sim <sup>†</sup>	3 h to 4 h	$\approx 70$ h	$\approx 80$ h	$\approx 5$ h
Max. mesh elements	$\approx 7.8 \times 10^5$	$\approx 1.8 \times 10^6$	$\approx 2.1 \times 10^6$	$\approx 5.7 \times 10^5$
CPU Speed	3.4–4.9 GHz	3.4–4.9 GHz	3.0–4.6 GHz	3.0–4.6 GHz
Equipped Memory	64 GB	64 GB	64 GB	64 GB

Simulation Parameter	Streamer First-look Study Section 6.2	Sub-mm Air/CO <sub>2</sub> Study Section 6.3	Sub-mm-dielectric Study Section 6.4	Surface Charge Study Section 6.5
Timestep	dynamic	0.01 ps	0.01 ps	0.075 ps
Min timestep	1 ps	n/a	n/a	n/a
Max timestep	5 ps	n/a	n/a	n/a
Time adaptation $k$	3	1 ns	n/a	n/a
AMR	✓	✓	✓	✓
Min mesh size	2.2 $\mu\text{m}$	0.1 $\mu\text{m}$	0.1 $\mu\text{m}$	0.75 $\mu\text{m}$
Mesh adaptation $k$	30	30	30	30
Refinement functions	$E/E_{\text{max}}, \rho, n_e/n_0$	$E/E_{\text{max}}, \rho, n_e$	$E/E_{\text{max}}, \rho, n_e$	$E/E_{\text{max}}, \rho$
Refinement tolerances*	[1.2, 1.5, $\infty, \infty, \infty$ ] [15, 17, 19, 20, 20] [0.4, 0.7, 0.8, 0.9, $\infty$ ]	[1.2, 1.5, $\infty, \infty, \infty$ ] [15, 17, 19, 20, 20] [0.4, 0.7, 0.8, 0.9, $\infty$ ]	[0.4, 0.5, $\infty, \infty$ ] [18, 19, 20, 21] [ $10^{18}, 10^{19}, \infty, \infty$ ]	[0.4, 0.5, $\infty, \infty$ ] [18, 19, 20, 21]
Refinement levels	[1,1,1,2,1]	[1,1,1,2,1]	[1,1,1,1]	[1,1,1,1]
Refinement radii, mm	0.2	[0.05,0.05,0.05,0.02]	[0.02,0.02,0.02,0.01]	0.04
$n$ processes	18	16	18	16
Approx. runtime/sim <sup>†</sup>	3 h to 8 h	2 h to 3 h	2 h to 3 h	60 h to 70 h
Max. mesh elements	$10^6$ to $3.4 \times 10^6$	$\approx 7 \times 10^5$	$\approx 8 \times 10^5$	$\approx 1 \times 10^6$
CPU Speed	3.0–4.6 GHz	3.4–4.9 GHz	3.0–4.6 GHz	3.4–4.9 GHz
Equipped Memory	64 GB	64 GB	64 GB	64 GB

\*Charge density expressed in  $\log_{10}(\rho/q_e)$ . <sup>†</sup>Runtimes were not specifically recorded for most cases. Given values are (very) rough estimations.

## B.4 Surface Height Distributions for Solid Materials

Figure A.2 shows representative histograms of the measured surface height distributions for material surfaces used in the solid-solid interface study of Chapter 7. The surface heights were found to be normally-distributed supported by normality tests, such that the equivalent surface method could be considered valid. These would also be representative of the machined cylindrical surfaces of Chapter 8, however, is of less importance as there is no necessity for those surfaces to be normally-distributed since the equivalent surface algorithm is not used.

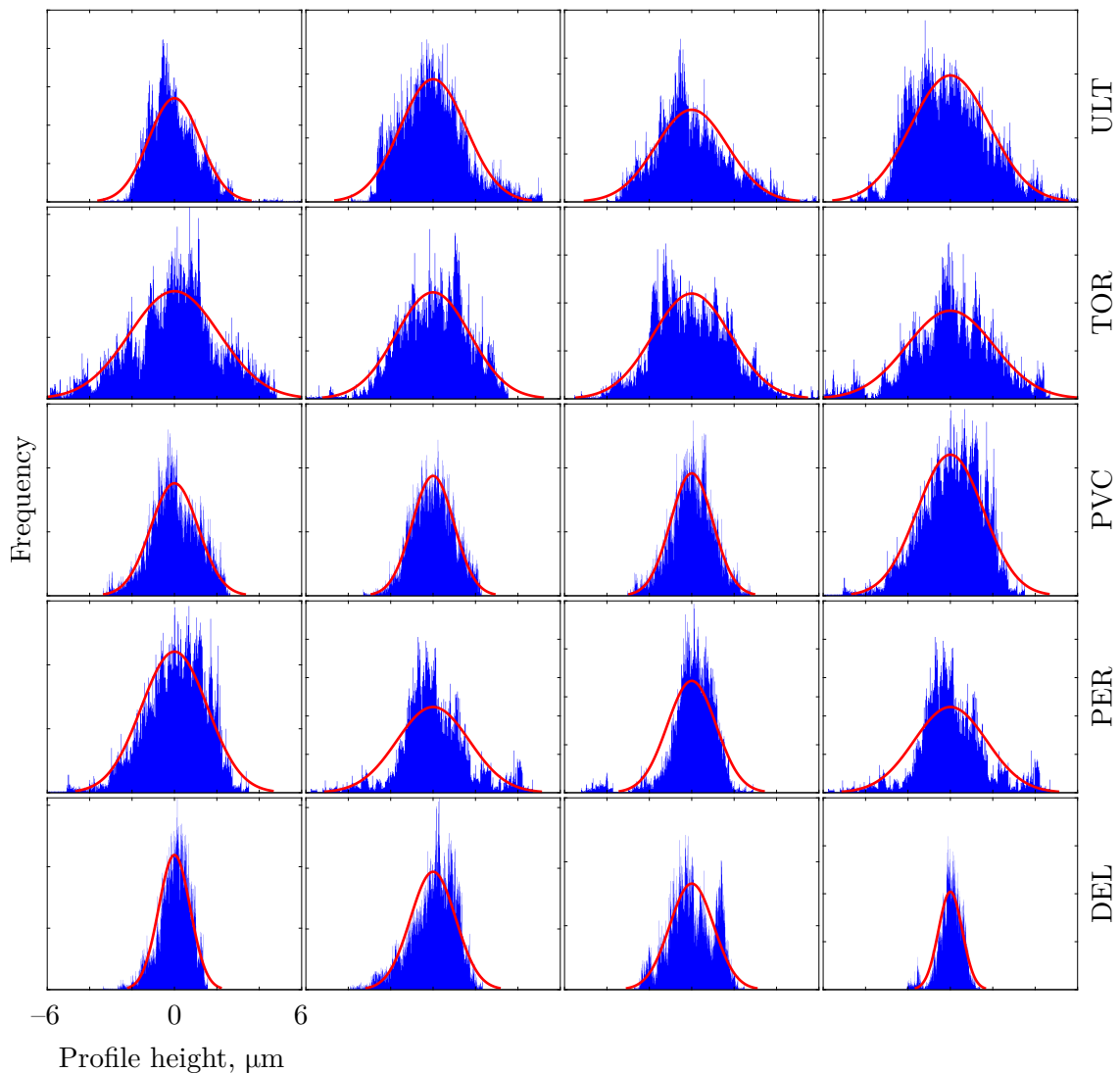


**Figure A.2:** Representative surface height distributions for the machined surfaces used in the solid-solid interface study of Chapter 7. Each row corresponds to the same material.

### B.5 Intra-void Field Shielding Model

Figure A.3 shows the results of the numerically-computed void and bulk electric fields using MATLAB Simulink, allowing a fully time-dependent void conductivity to be incorporated. Note that the bulk field transitions from the  $\sigma_g = 0$  case to the  $\sigma_g = \sigma_{\max}$  case when the conductivity rises (which was assumed to be a simple ramp in this case—the roughly 100 ns rise time here was chosen to be far longer than the estimated shielding times from reference [35] of Chapter 7 for demonstration. Thus, assuming an instantaneous rise near this time (shown by the orange dashed line) approximates the pre- and post-breakdown fields reasonably well.

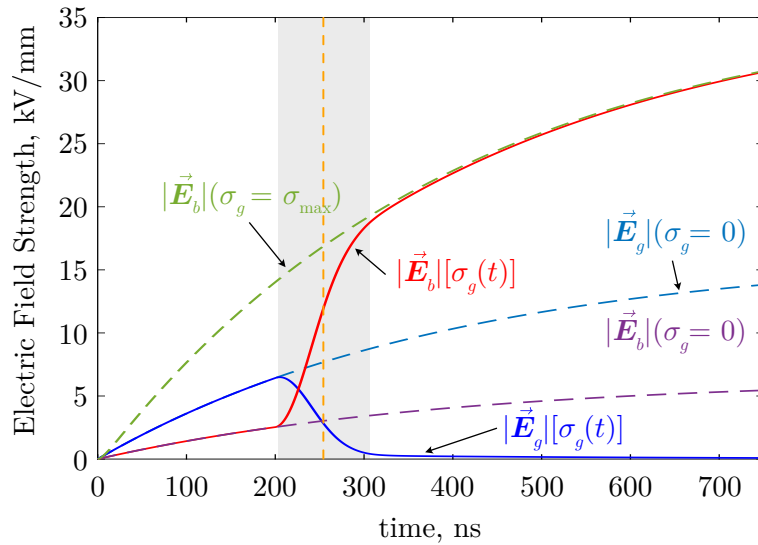


**Figure A.3:** Demonstration of void-shielding at moment of discharge, showing the (solid lines) maximum bulk and void fields during discharge, and the corresponding (dashed lines) pre-discharge  $\sigma_g = 0$  and post-discharge  $\sigma_g = \sigma_{\max}$  fields.

## B.6 Enhancement Between Two Voids

Figure A.4 shows the numerically-computed field enhancement factor between two conductive spheroidal voids, as a function of the ratio between the void separation and the semi-major axis,  $s/r_m$ , and the void axis ratio (eccentricity),  $K$ . Note that in the  $s/r_m \gg 1$  case, this converges to the expected value of  $f_\infty$  for the enhancement on the surface of a single void, as the voids become sufficiently far away from each other as to not have any influence. The convergence to  $f = 3$  in the large-separation and spherical limit is shown, as expected. When brought into close proximity, however, note the substantially higher degree of field enhancement that may be induced at the contact spot. This may become sufficient to cause breakdown even at the high breakdown strengths predicted using Fothergill's model.

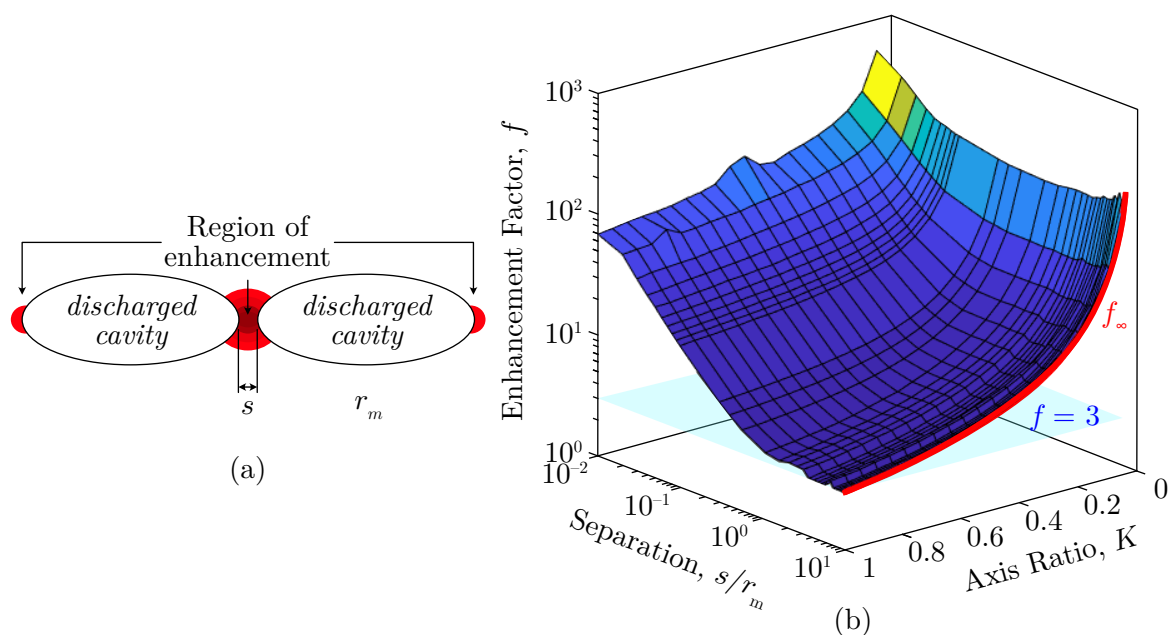


**Figure A.4:** (a) Diagram depicting the numerical simulation setup, of enhancement between two discharged voids, (b) computed enhancement curve as a function of  $s/r_m$  and  $K$ . Red line indicates  $f_\infty$  in the large-separation limit, blue surface indicates the surface  $f = 3$ .

### B.7 Sensitivity of Interfacial Void Model to Electrical Parameters

Figures A.5 and A.6 shows the results of a systematic study on the three-layer void model, showing the variation of the peak electric field strength recorded within the void and in the bulk when either the bulk or intermediate layer permittivity/conductivity is varied. The default parameters used here (when not parametrically-swept) were  $\sigma_g, \sigma_l, \sigma_b = 0, 10^{-9},$  and  $10^{-12}$  S/m and  $\varepsilon_g, \varepsilon_l, \varepsilon_b = 1, 4.5,$  and  $3.2,$  and under  $1.2/50 \mu\text{s}$  double exponential impulse with peak field magnitude of  $25 \text{ kV/mm}.$  Spheroidal ( $K = 0.25$ ) and spherical cases are shown, at angles of  $\nu = 0$  and  $\nu = \pi/2,$  since the position of the field maximum may shift by  $\pi/2$  radians depending on the layer parameters. The intermediate layer thickness was set to  $0.5 \mu\text{m}.$

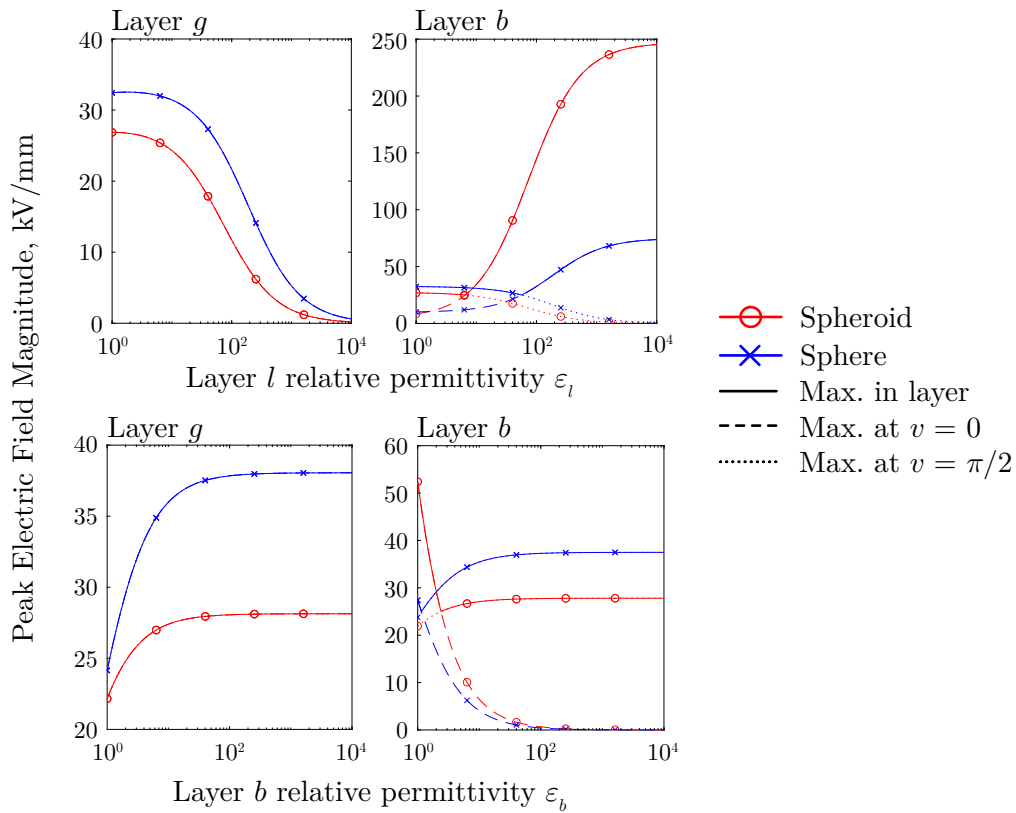


**Figure A.5:** Peak void and bulk electric field magnitudes for spheroidal and spherical voids when varying the layer or bulk relative permittivity values. Dashed lines show the maximum field at  $\nu = 0$ , dotted lines show the maximum field at  $\nu = \pi/2$ . Solid lines shows the net maximum, defined as the maximum between those at  $\nu = 0$  and  $\nu = \pi/2$ .

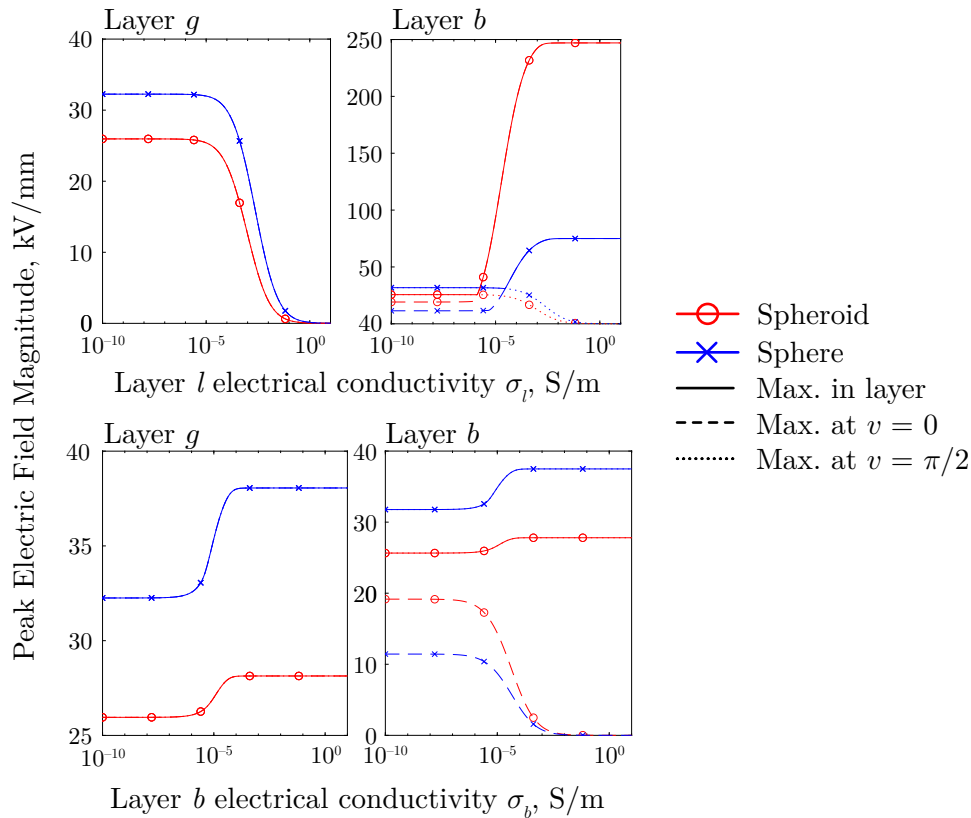


**Figure A.6:** Peak void and bulk electric field magnitudes for spheroidal and spherical voids when varying the layer or bulk electrical conductivity values. Dashed lines show the maximum field at  $\nu = 0$ , dotted lines show the maximum field at  $\nu = \pi/2$ . Solid lines shows the net maximum, defined as the maximum between those at  $\nu = 0$  and  $\nu = \pi/2$ .

## B.8 LSQ Compared to MLE Weibull Fitting

Figure A.7 compares two Weibull plots generated from two different solid-solid interfacial breakdown tests. Both LSQ with median ranks and MLE fittings were used to fit 2 parameter Weibull distributions, with the fitted parameters indicated on the plots. Note the sensitivity of the LSQ method from in Figure A.7(a) from a single outlier, which comparatively has little effect on the MLE fitting. Despite this, the fitted  $\alpha$  values remain similar, but LSQ provides a far greater shape parameter  $\beta$  due to the wider confidence bounds that resulted from outlying data. Figure A.7(b) aims to show that when the data is well-behaved with no extreme values, LSQ and MLE perform almost identically in terms of both parameter estimation and confidence bounds. However, MLE was preferred throughout for its robustness when faced with outliers.

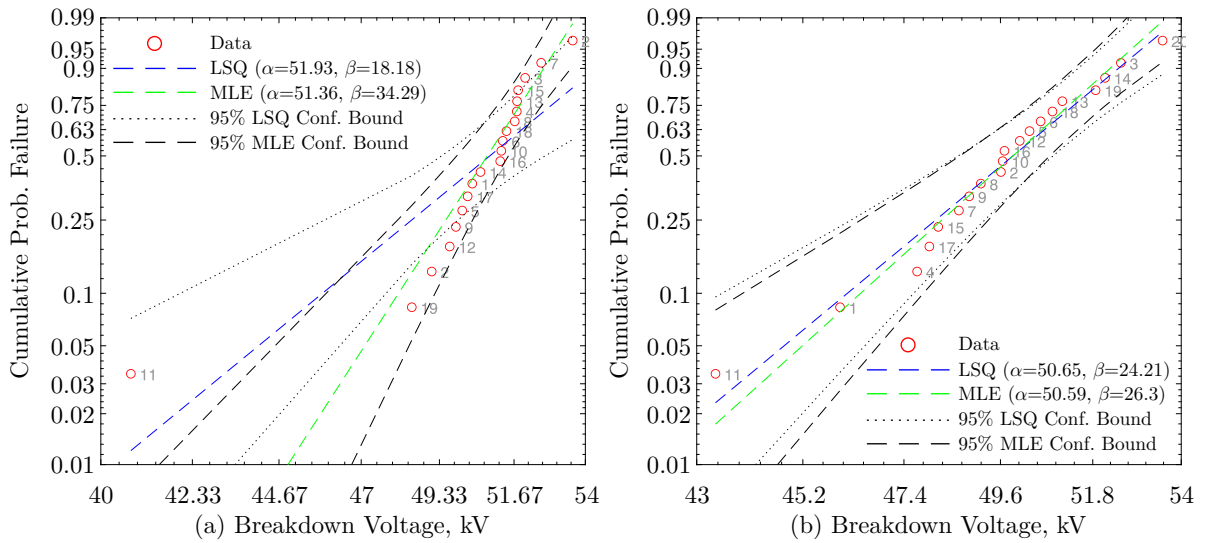


**Figure A.7:** Comparison of LSQ and MLE fittings for Weibull distributions. (a) In the presence of outliers in the dataset, (b) near-identical results from LSQ and MLE when data exhibits no clear outliers, which was true in the vast majority of cases.

## B.9 All MLE-fitted Weibull Parameters for Experimental Work

Table A.2 shows the MLE-computed two-parameter Weibull parameters for all solid-solid interface tests of Chapter 7. Table A.3 and A.4 provides the same set of parameters for all solid-gas flashover tests of Chapter 8, for “as received” and “machined” surface conditions, respectively.

**Table A.2:** MLE-fitted Weibull parameters: solid-solid experiments.

	Interface 1		Interface 2		Interface 1		Interface 2		
	$V_{63.2}$ , kV	$\bar{\beta}_V$	$V_{63.2}$ , kV	$\bar{\beta}_V$	$t_{63.2}$ , $\mu\text{s}$	$\bar{\beta}_t$	$t_{63.2}$ , $\mu\text{s}$	$\bar{\beta}_t$	
Samtech TG-01	+PVC	19.56	17.47	19.87	9.85	50.42	14.01	50.66	9.40
	+DEL	22.68	7.62	22.24	10.08	65.07	5.26	61.64	6.37
	+TOR	24.03	10.37	21.35	7.53	71.35	4.57	57.20	5.29
	+PER	20.92	7.48	22.88	6.00	55.37	5.04	64.58	4.08
	+ULT	23.88	8.92	25.56	11.06	68.96	5.17	76.97	6.43
	-PVC	25.81	12.30	23.48	8.67	77.76	5.86	66.72	5.04
	-DEL	26.95	21.75	26.98	25.36	84.26	10.28	83.41	12.91
	-TOR	27.37	25.76	27.12	19.33	87.84	8.85	85.62	7.65
	-PER	27.18	15.29	26.38	11.66	85.10	6.54	79.31	5.31
	-ULT	27.59	22.17	27.79	28.76	91.99	9.49	95.04	13.01

	Interface 1		Interface 2		Interface 1		Interface 2		
	$V_{63.2}$ , kV	$\bar{\beta}_V$	$V_{63.2}$ , kV	$\bar{\beta}_V$	$t_{63.2}$ , ns	$\bar{\beta}_t$	$t_{63.2}$ , ns	$\bar{\beta}_t$	
Blumlein	+PVC	52.10	16.34	51.65	15.88	44.50	3.62	38.96	6.70
	+DEL	53.07	18.63	52.33	18.06	36.89	9.18	40.89	4.02
	+TOR	53.56	17.21	52.88	26.30	36.72	10.31	38.74	5.36
	+PER	53.62	25.43	51.18	20.98	40.85	5.06	45.17	4.21
	+ULT	55.75	24.76	53.00	22.73	42.58	4.78	44.41	4.56
	-PVC	59.43	32.97	51.03	21.69	44.43	27.19	46.17	7.87
	-DEL	59.98	22.97	51.36	22.72	43.52	16.72	43.66	12.61
	-TOR	51.58	13.95	53.69	34.29	40.93	15.91	43.50	15.78
	-PER	53.45	21.09	54.96	18.71	40.61	26.00	40.26	15.52
	-ULT	51.29	17.93	52.62	23.74	41.40	8.24	42.68	10.86

**Table A.3:** MLE-fitted Weibull parameters: solid-gas experiments—“as received”.

	Interface 1		Interface 2		Interface 1		Interface 2		
	$V_{63.2}$ , kV	$\bar{\beta}_V$	$V_{63.2}$ , kV	$\bar{\beta}_V$	$t_{63.2}$ , $\mu$ s	$\bar{\beta}_t$	$t_{63.2}$ , $\mu$ s	$\bar{\beta}_t$	
Samtech TG-01	+PVC	29.42	76.89	28.75	42.41	73.20	47.48	70.61	27.88
	+DEL	26.21	31.03	26.39	16.03	61.74	20.72	66.19	5.48
	+TOR	28.54	33.65	27.93	19.55	69.92	23.17	67.88	12.92
	+PER	27.56	22.69	28.05	18.13	66.66	15.89	68.11	12.31
	+ULT	27.95	24.45	26.70	14.20	70.66	7.49	63.82	10.25
	-PVC	22.55	40.00	22.89	43.66	52.67	8.29	48.74	31.71
	-DEL	21.11	20.19	21.64	63.38	44.14	16.14	44.99	41.93
	-TOR	22.17	52.22	21.98	46.51	46.16	33.40	45.88	37.86
	-PER	22.28	25.02	22.57	21.53	46.86	18.45	48.10	15.56
	-ULT	22.33	45.21	22.86	37.30	46.51	25.22	48.22	27.36
	Interface 1		Interface 2		Interface 1		Interface 2		
	$V_{63.2}$ , kV	$\bar{\beta}_V$	$V_{63.2}$ , kV	$\bar{\beta}_V$	$t_{63.2}$ , ns	$\bar{\beta}_t$	$t_{63.2}$ , ns	$\bar{\beta}_t$	
Blumlein	+PVC	–	–	–	–	43.52	8.16	41.27	26.35
	+DEL	–	–	–	–	41.83	49.14	42.57	31.99
	+TOR	–	–	–	–	45.06	16.41	50.94	23.86
	+PER	–	–	–	–	44.37	13.92	45.04	13.85
	+ULT	–	–	–	–	41.38	34.84	43.25	36.91

Blumlein	-PVC	-	-	-	-	81.78	72.22	80.98	97.03
	-DEL	-	-	-	-	81.26	87.29	80.53	43.71
	-TOR	-	-	-	-	81.57	67.57	81.67	67.92
	-PER	-	-	-	-	80.99	47.97	80.82	40.03
	-ULT	-	-	-	-	81.80	133.85	81.42	83.36

**Table A.4:** MLE-fitted Weibull parameters: solid-gas experiments—“machined”.

	Interface 1		Interface 2		Interface 1		Interface 2		
	$V_{63.2}$ , kV	$\bar{\beta}_V$	$V_{63.2}$ , kV	$\bar{\beta}_V$	$t_{63.2}$ , $\mu$ s	$\bar{\beta}_t$	$t_{63.2}$ , $\mu$ s	$\bar{\beta}_t$	
Samtech TG-01	+PVC	26.98	39.36	27.56	36.95	63.38	21.02	65.79	21.46
	+DEL	27.40	37.83	27.54	59.29	65.88	27.76	66.01	37.23
	+TOR	28.44	61.19	28.04	32.01	68.89	39.52	67.45	19.57
	+PER	28.35	41.11	28.95	72.19	69.08	27.20	70.99	48.93
	+ULT	26.07	15.61	27.46	13.08	61.37	10.45	66.76	8.26
	-PVC	24.13	65.43	22.87	40.07	52.89	35.47	48.43	27.33
	-DEL	22.06	46.19	22.88	33.75	46.23	29.68	48.55	23.66
	-TOR	22.90	75.10	22.44	52.61	47.89	38.09	46.74	38.01
	-PER	23.80	40.80	23.97	78.11	51.72	26.63	51.75	44.53
	-ULT	23.57	31.10	22.79	25.18	50.39	20.85	48.37	20.04
	Interface 1		Interface 2		Interface 1		Interface 2		
	$V_{63.2}$ , kV	$\bar{\beta}_V$	$V_{63.2}$ , kV	$\bar{\beta}_V$	$t_{63.2}$ , ns	$\bar{\beta}_t$	$t_{63.2}$ , ns	$\bar{\beta}_t$	
Blumlein	+PVC	-	-	-	-	50.73	33.32	49.60	19.32
	+DEL	-	-	-	-	50.85	61.92	50.27	31.11
	+TOR	-	-	-	-	50.54	30.99	50.24	60.40
	+PER	-	-	-	-	50.60	33.96	48.60	15.30
	+ULT	-	-	-	-	51.12	50.76	51.27	40.17
	-PVC	-	-	-	-	82.68	88.24	82.37	84.23
	-DEL	-	-	-	-	82.03	88.14	81.75	113.04
	-TOR	-	-	-	-	81.92	164.39	81.42	56.86
	-PER	-	-	-	-	81.42	80.02	81.88	109.65
	-ULT	-	-	-	-	81.81	69.11	82.10	89.01

## C Miscellaneous Points of General Interest

### C.1 1D Multilayered Dielectric in the Continuous Limit

First consider the Laplace equation with a spatially-nonuniform permittivity,

$$\vec{\nabla} \cdot [\varepsilon(\vec{r}) \vec{\nabla} \varphi] = 0. \quad (\text{A.114})$$

In the one dimensional case, this simplifies to

$$\begin{aligned} \frac{d}{dx} \left[ \varepsilon(x) \frac{d}{dx} \varphi(x) \right] &= 0 \\ \varepsilon(x) \frac{d^2 \varphi(x)}{dx^2} + \varepsilon'(x) \frac{d\varphi(x)}{dx} &= 0 \\ \frac{d^2 \varphi(x)}{dx^2} + \frac{\varepsilon'(x)}{\varepsilon(x)} \frac{d\varphi(x)}{dx} &= 0, \end{aligned} \quad (\text{A.115})$$

which can be shown to admit the general solution

$$\begin{aligned} \varphi(x) &= \int C_1 \exp \left[ \int \frac{\varepsilon'(x)}{\varepsilon(x)} dx \right] dx + C_2 \\ &= \int \frac{C_1}{\varepsilon(x)} dx + C_2. \end{aligned} \quad (\text{A.116})$$

Applying simple conditions like in the case of Section 3.3.1, where  $\varphi(x=0) = U_0$  and  $\varphi(x=d) = 0$ , one finds  $C_1$  and  $C_2$ ,

$$\varphi(x) = U_0 - \frac{U_0}{\int_0^d \frac{1}{\varepsilon(x')} dx'} \int_0^x \frac{1}{\varepsilon(x'')} dx''. \quad (\text{A.117})$$

The corresponding electric field,  $E(x)$  may thus be recovered,

$$\begin{aligned} E(x) &= -\frac{d\varphi(x)}{dx} = \frac{U_0}{\int_0^d \frac{1}{\varepsilon(x')} dx'} \cdot \frac{1}{\varepsilon(x)} \\ &= \frac{U_0}{\varepsilon(x) \int_0^d \frac{1}{\varepsilon(x')} dx'}. \end{aligned} \quad (\text{A.118})$$

Now consider the multilayered approach of Section 3.3.1, the one-dimensional solution provided as (3.21), repeated here with  $z \rightarrow x$  and applying  $E_i(s) = -A_i(s)$ ,

$$E_i(s) = \frac{U_0(s)}{\sum_{\ell=1}^n \frac{\sigma_\ell + \varepsilon_0 \varepsilon_\ell s}{\sigma_\ell + \varepsilon_0 \varepsilon_\ell s} (x_{\ell+1} - x_\ell)}. \quad (\text{A.119})$$

In the non-conductive limit, one has

$$E_i(s) = \frac{U_0(s)}{\sum_{\ell=1}^n \frac{\varepsilon_i}{\varepsilon_\ell} (x_{\ell+1} - x_\ell)}, \quad (\text{A.120})$$

where  $x_{\ell+1} - x_\ell = \Delta x$  is the layer thickness. If  $\Delta x$  is allowed to tend to zero (in the sense of a Riemann sum) and  $n \rightarrow \infty$ , one recovers the integral

$$E(x) = \lim_{\Delta x \rightarrow 0} \frac{U_0}{\sum_{\ell=1}^{\infty} \frac{\varepsilon_i}{\varepsilon_\ell} \Delta x} = \frac{U_0}{\int_0^d \frac{\varepsilon(x)}{\varepsilon(x')} dx'} = \frac{U_0}{\varepsilon(x) \int_0^d \frac{1}{\varepsilon(x')} dx'}, \quad (\text{A.121})$$

where  $\varepsilon_i$  has been replaced with  $\varepsilon(x)$ , since, by definition  $\varepsilon_i$  was the permittivity of the layer  $i$  which is now infinitesimally small at location  $x$ . Note that this is *exactly* the solution found from directly solving the Laplace equation with a nonuniform coefficient. This implies that the general solutions derived within Chapter 3 may be applicable to continuous nonuniform materials in geometries of considerable complexity. Whether this continues to hold with non-zero conductivity would also be important to determine, as it may suggest that, in the limit, the computed surface charge distributions may reconstruct certain continuous space charge distributions for continuous materials.

## C.2 Examples of Adaptive Meshes for StrAFE Simulations

Figure A.8 shows several examples of dynamic meshes generated during StrAFE runtime for several simulations shown within this work.

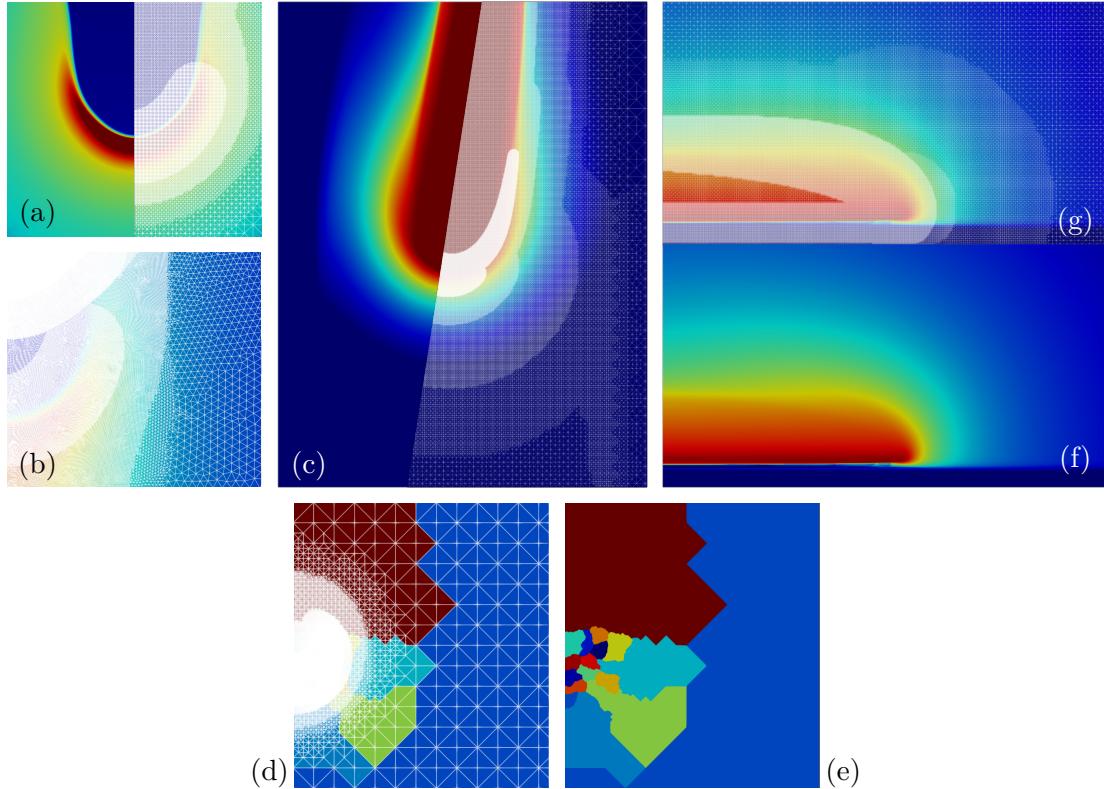


**Figure A.8:** Examples of dynamic meshes generated in StrAFE during (a) the comparison simulation of Section 5.8.1, (b) the sub-mm needle-plane gap study of Section 6.3, (c) the surface streamer study (before attachment) of Section 5.8.2, (d) same simulations as (a) but showing the parallel and load-balanced mesh partitions, as in (e) without the mesh, (g) and (f) from the surface streamer study of Section 5.8.2 post-attachment.

### C.3 Parallel Scaling Test for StrAFE

Figure A.9 shows a basic parallel scaling test, up to 16 processes, for StrAFE. This refers only to physical processors; enabling logical processors did not appear to provide any additional speedup.

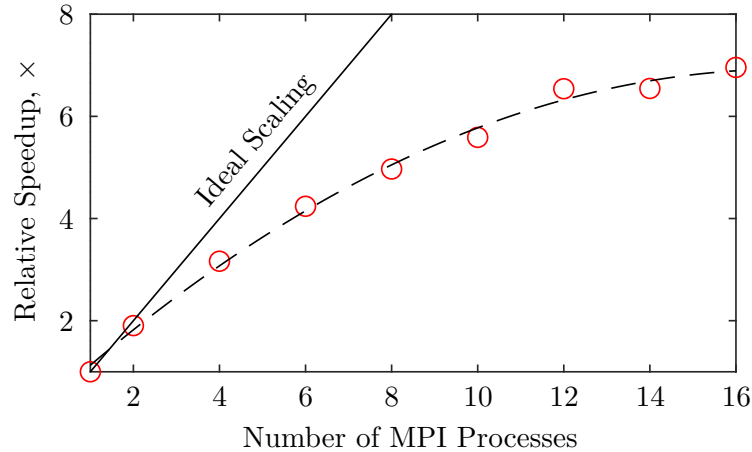


**Figure A.9:** Results from basic parallel scaling test of StrAFE up to 16 MPI processes. Image adapted from [60] of Chapter 5 under CC BY 4.0.

### C.4 Examples Plasma Chemistry File Format

Figure A.10 shows an example of .txt file chemistry input processable by StrAFE for configuring plasma simulations.

```

TRACKED SPECIES: e,N2+,O2+,N4+,O4+,O2+N2,O2-
CHARGE NUMBER: 1,1,1,1,1,1
MASS: 9.10938356e-31,4.65e-26,2.66e-26,9.3e-26,5.32e-26,7.31e-26,2.66e-26
MOBILITY: 80_20_air_300k/electron_mobility.txt,0,0,0,0,0,0
DIFFUSION: 80_20_air_300k/electron_diffusion.txt,0,0,0,0,0,0
NEUTRALS: M,N2,O2
PROPORTION: 1,0,0.8,0.2
DEPENDENT_PLASMA_PARAMETER: E
-- REACTIONS
INDEX  DESCRIPTION REACTANTS  TARGET  RATE TYPE  RATE  LOSS_TYPE  ENERGY_LOSS_COEFF
1      Ionisation  e,N2      N2+,e,e  Tabulated  80_20_air_300k/N2_15.6eV_Ionisation.txt  Tabulated  80_20_air_300k/N2_InelasticEnergyLoss.txt
2      Ionisation  e,N2      N2+,e,e  Tabulated  80_20_air_300k/N2_18.8eV_Ionisation.txt  Constant   0
3      Ionisation  e,O2      O2+,e,e  Tabulated  80_20_air_300k/O2_12.06eV_Ionisation.txt  Tabulated  80_20_air_300k/O2_InelasticEnergyLoss.txt
4      Rapid O2+ Production  N2+,N2,M  N4+,M    Constant  5e-41      Constant   0
5      Rapid O2+ Production  N4+,O2    O2+,N2,N2  Constant  2.5e-16    Constant   0
6      Rapid O2+ Production  N2+,O2    O2+,N2     Constant  6e-17      Constant   0
7      O2+ to O4+ Conversion  O2+,N2,N2  O2+,N2,N2  Constant  9e-43      Constant   0
8      O2+ to O4+ Conversion  O2+N2,N2  O2+,N2,N2  Constant  4.3e-16    Constant   0
9      O2+ to O4+ Conversion  O2+N2,O2  O4+,N2     Constant  1e-15      Constant   0
10     O2+ to O4+ Conversion  O2+,O2,M  O4+,M     Constant  2.4e-42    Constant   0
11     Electron-ion Recombination  e,O4+    O2,O2     Tabulated  80_20_air_300k/e_O4+_recombination.txt  Constant   0
12     Electron-ion Recombination  e,O2+    O2         Tabulated  80_20_air_300k/e_O2+_recombination.txt  Constant   0
13     Attachment  e,O2,O2  O2-,O2    Tabulated  80_20_air_300k/air_attachment.txt  Constant   0
14     Ion-ion Recombination  O2-,O4+  O2,O2,O2  Constant  1e-13      Constant   0
15     Ion-ion Recombination  O2-,O4+,M  O2,O2,O2,M  Constant  2e-37      Constant   0
16     Ion-ion Recombination  O2-,O2+,M  O2,O2,M    Constant  2e-37      Constant   0
END

```

**Figure A.10:** Example plasma chemistry input file for oxygen-nitrogen mixtures readable by StrAFE to automatically configure complex plasma simulations.

### C.5 Additional Nonuniform Field Enhancement Plots

Figure A.11 shows several additional examples of non-uniform field distributions around dielectric inclusions calculated using the models developed in this work.

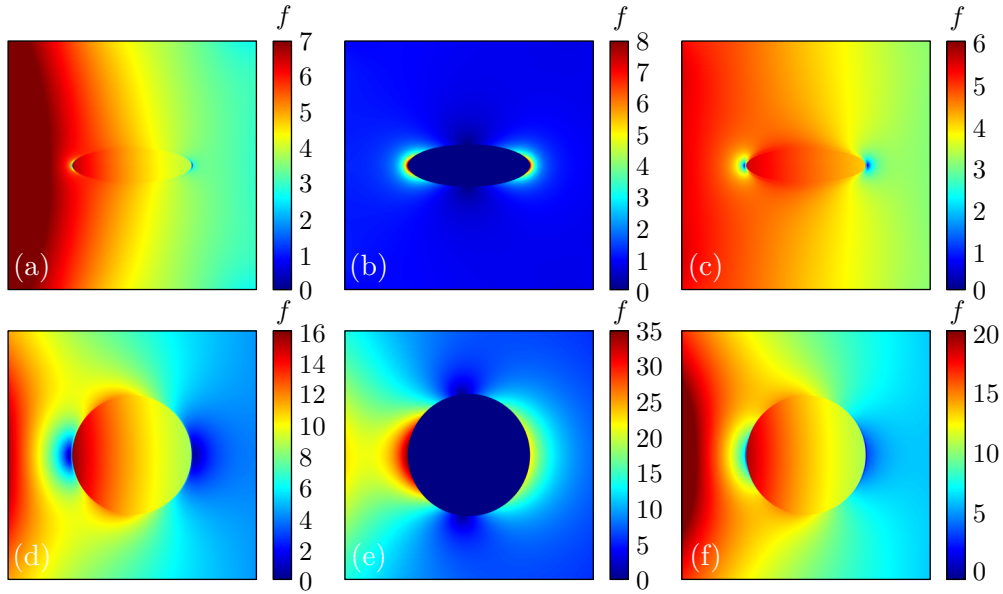


**Figure A.11:** Additional field enhancement plots around dielectric inclusions under nonuniform external electric fields, calculated using the model of Chapter 7 based on Chapter 3. Images (a)-(c) are for spheroidal inclusions under needle-needle electrodes, (d)-(f) are spherical inclusions under needle-plane electrodes. From left to right: gas void in dielectric; conductive particle in gas; gas void in conductive bulk.

### C.6 Additional Photographs from Solid-Solid Breakdown Tests

Figure A.12 provides several additional post-breakdown photographs of each material type in the solid-solid interfacial breakdown study.

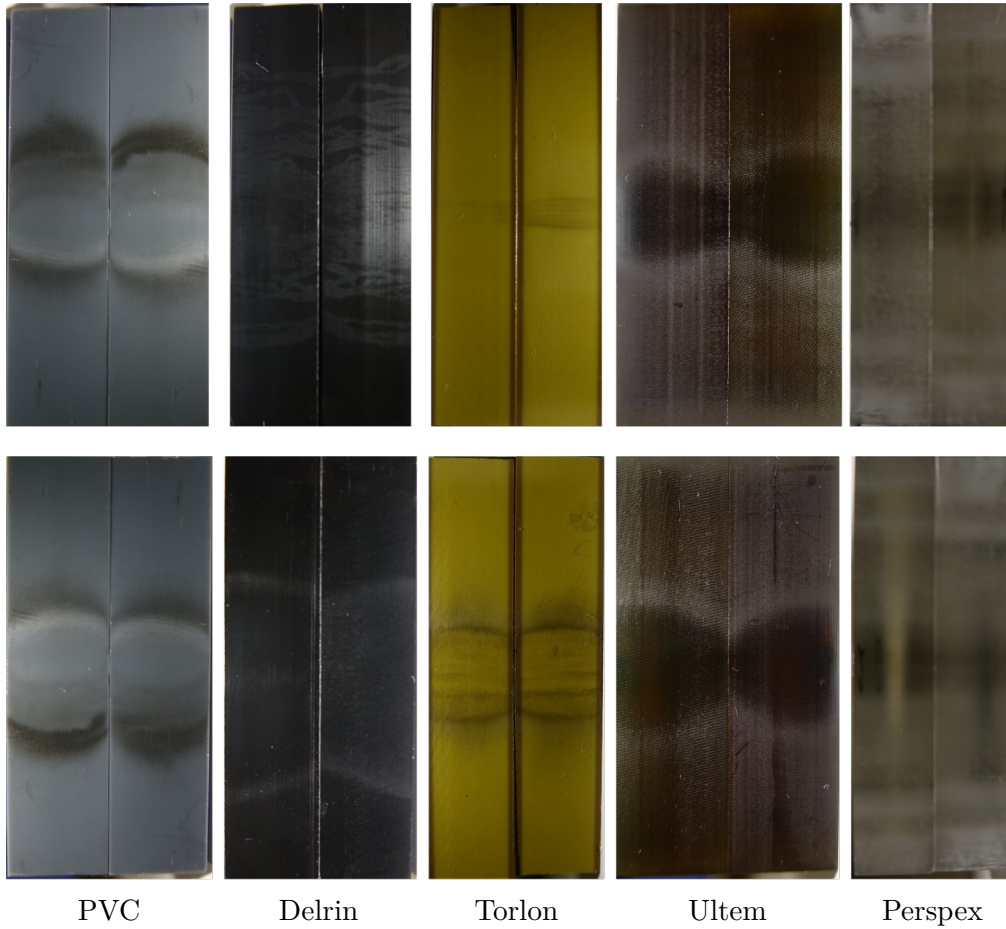


**Figure A.12:** Additional post-breakdown photographs of solid-solid interfaces.

### C.7 Additional Photographs of Solid-Gas Flashover Samples

Figure A.13 provides several additional post-breakdown photographs of each material type in the solid-solid interfacial breakdown study.

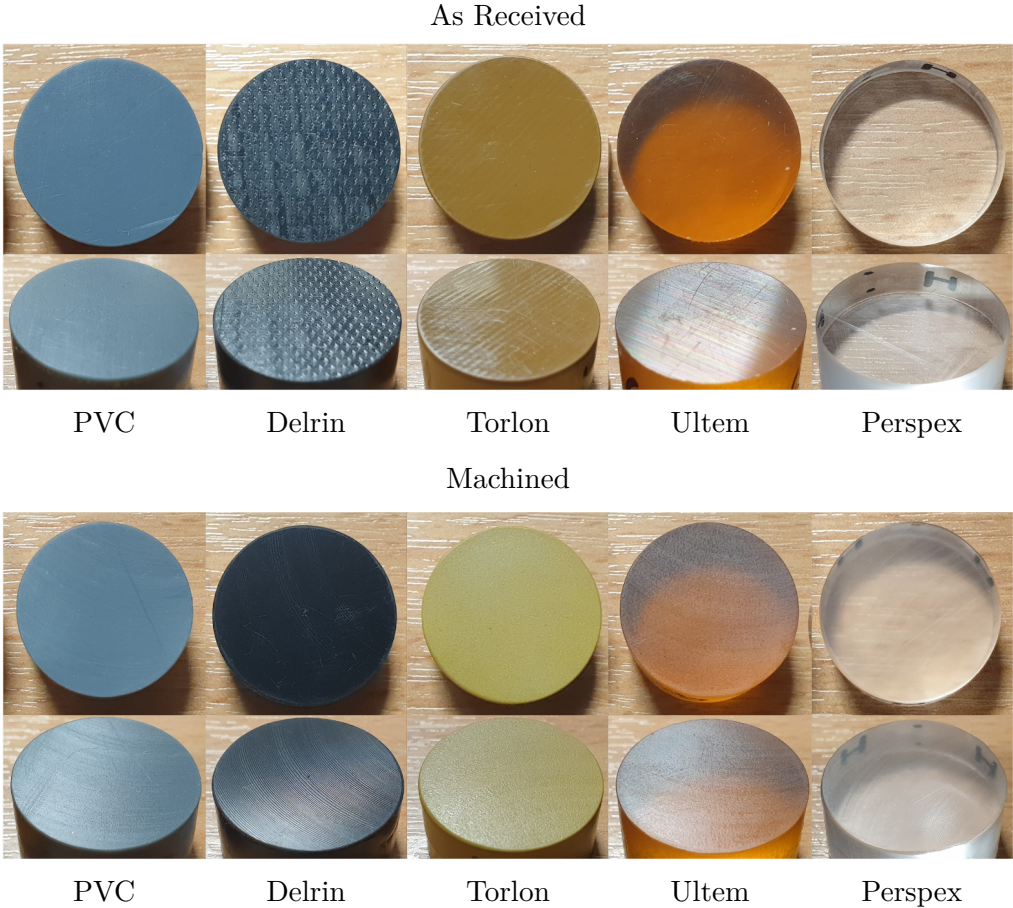


**Figure A.13:** Additional pre-breakdown photographs of cylindrical solid-gas sample surfaces.

